THE OCEANIC PARTICLE FLUX AND ITS CYCLING WITHIN THE DEEP WATER COLUMN

EDITED BY: Maureen H. Conte, Rut Pedrosa Pàmies, Makio Honda and Gerhard Josef Herndl

PUBLISHED IN: Frontiers in Earth Science

frontiers Research Topics

frontiers

ISSN 1664-8714
ISBN 978-2-83250-299-0
DOI 10.3389/978-2-83250-299-0

About Frontiers

Frontiers is more than just an open-access publisher of scholarly articles: it is a pioneering approach to the world of academia, radically improving the way scholarly research is managed. The grand vision of Frontiers is a world where all people have an equal opportunity to seek, share and generate knowledge. Frontiers provides immediate and permanent online open access to all its publications, but this alone is not enough to realize our grand goals.

Frontiers Journal Series

The Frontiers Journal Series is a multi-tier and interdisciplinary set of open-access, online journals, promising a paradigm shift from the current review, selection and dissemination processes in academic publishing. All Frontiers journals are driven by researchers for researchers; therefore, they constitute a service to the scholarly community. At the same time, the Frontiers Journal Series operates on a revolutionary invention, the tiered publishing system, initially addressing specific communities of scholars, and gradually climbing up to broader public understanding, thus serving the interests of the lay society, too.

Dedication to Quality

Each Frontiers article is a landmark of the highest quality, thanks to genuinely collaborative interactions between authors and review editors, who include some of the world's best academicians. Research must be certified by peers before entering a stream of knowledge that may eventually reach the public - and shape society; therefore, Frontiers only applies the most rigorous and unbiased reviews.
Frontiers revolutionizes research publishing by freely delivering the most outstanding research, evaluated with no bias from both the academic and social point of view. By applying the most advanced information technologies, Frontiers is catapulting scholarly publishing into a new generation.

What are Frontiers Research Topics?

Frontiers Research Topics are very popular trademarks of the Frontiers Journals Series: they are collections of at least ten articles, all centered on a particular subject. With their unique mix of varied contributions from Original Research to Review Articles, Frontiers Research Topics unify the most influential researchers, the latest key findings and historical advances in a hot research area! Find out more on how to host your own Frontiers Research Topic or contribute to one as an author by contacting the Frontiers Editorial Office: frontiersin.org/about/contact

THE OCEANIC PARTICLE FLUX AND ITS CYCLING WITHIN THE DEEP WATER COLUMN

Topic Editors:
Maureen H. Conte, Bermuda Institute of Ocean Sciences, Bermuda
Rut Pedrosa Pàmies, Marine Biological Laboratory (MBL), United States
Makio Honda, Japan Agency for Marine-Earth Science and Technology (JAMSTEC), Japan
Gerhard Josef Herndl, University of Vienna, Austria

Citation: Conte, M. H., Pàmies, R. P., Honda, M., Herndl, G. J., eds. (2022). The Oceanic Particle Flux and its Cycling Within the Deep Water Column. Lausanne: Frontiers Media SA. doi: 10.3389/978-2-83250-299-0

Table of Contents

frontiers | Frontiers in Earth Science

TYPE Editorial
PUBLISHED 09 September 2022
DOI 10.3389/feart.2022.1020065

OPEN ACCESS

EDITED AND REVIEWED BY
Timothy Ian Eglinton,
ETH Zürich, Switzerland

*CORRESPONDENCE
Maureen H Conte,
mconte@mbl.edu

SPECIALTY SECTION
This article was submitted to Biogeoscience, a section of the journal Frontiers in Earth Science

RECEIVED 15 August 2022
ACCEPTED 25 August 2022
PUBLISHED 09 September 2022

CITATION
Conte MH, Pedrosa Pàmies R, Honda M and Herndl GJ (2022), Editorial: The oceanic particle flux and its cycling within the deep water column. *Front. Earth Sci.* 10:1020065. doi: 10.3389/feart.2022.1020065

Editorial: The oceanic particle flux and its cycling within the deep water column

Maureen H Conte[1,2]*, Rut Pedrosa Pàmies[2], Makio Honda[3] and Gerhard J. Herndl[4]

[1]Bermuda Institute of Ocean Sciences, Saint Georges, Bermuda, [2]Ecosystems Center, Marine Biological Laboratory, Woods Hole, MA, United States, [3]Japan Agency for Marine-Earth Science and Technology (JAMSTEC), Yokosuka, Japan, [4]Department of Functional and Evolutionary Ecology, University of Vienna, Vienna, Austria

KEYWORDS

particle flux, deep ocean, marine particles, ocean biogeochemistry, carbon cycling, marine chemistry

Editorial on the Research Topic
The oceanic particle flux and its cycling within the deep water column

The oceanic particle flux transfers energy and material from the surface through the water column to the seafloor. (See review by Conte (2019) and references therein). The particle flux fuels life below the sunlit photic zone, exerts a major control on the global cycling of carbon and particle-associated elements, and also plays a major role in long-term carbon sequestration. In this Research Topic we present a collection of articles that provide a broad overview of current research on the interlinked processes controlling the magnitude and composition of the oceanic particle flux, and its cycling and depth attenuation within the deep water column.

Several articles focus on physical processes that influence seasonal and nonseasonal variability in particle flux generation in surface waters and particle export flux to depth. Shih et al. and Tan et al. examine how atmospheric and mesoscale eddy forcing influence euphotic zone nutrient supply, primary production and, in turn, particulate organic carbon (POC) export flux in the northern South China Sea (SCS). Tan et al. show that during the northeast monsoon, a deep mixed-layer depth and surface cooling, together with cyclonic eddy forcing, promote a strong winter flux peak. Conversely, an anticyclonic eddy in spring suppressed nutrient upwelling and primary production, decreasing summer fluxes. In autumn, aerosol optical depth in the SCS increases due to higher dust transport, suggesting that mineral ballasting of sinking particles varies seasonally. Shih et al. find that nutrient upwelling within cold eddies in the SCS fuels growth of large centric diatoms and dinoflagellates, increasing POC export. Conversely, downwelling within warm eddies intensifies stratification and reduces the nutrient supply, favoring small phytoplankton species and reducing POC export. Zúñiga et al. combine sediment trap observations in the Southern Ocean with a data-assimilative model to investigate how physical forcing of diatom ecology drives silicon vs. carbon sequestration efficiencies and

nutrient stoichiometry in the flux. They report on an anomalous sea-ice episode that induced (*via* re-stratification due to sea-ice melt) a massive, rapidly sinking bloom of *Corethron pennatum*, which greatly increased the biogenic silica to organic carbon export ratio.

Lopez et al. compare the seasonality of the POC export flux with deep water total organic carbon (TOC) concentrations in the northeast Pacific Ocean, a highly productive region of extreme seasonality. They find that deep (>1,000 m depth) TOC concentrations correlate with the POC export flux, and that this export also contributes to the dissolved organic carbon pool. Similar rates of TOC net accumulation and removal within deep waters indicates efficient remineralization of the seasonally exported carbon.

The study of Pedrosa-Pàmies et al. in the eastern Mediterranean Sea underscores the importance of atmospheric forcing in deep ocean carbon sequestration. Using lipid biomarkers to partition marine, terrestrial and anthropogenic particle flux sources, they show that extreme weather and dust deposition events trigger significant episodic flux pulses to the deep Mediterranean Sea.

Honda and Weber and Bianchi focus on carbon transfer efficiency through the water column. Honda compares POC fluxes at subarctic-eutrophic and subtropical-oligotrophic sites in the western Pacific. Although primary production and mesopelagic fluxes were similar at both sites, the deep (5,000 m) POC flux was 2–3 times higher at the subarctic-eutrophic site despite its much larger zooplankton carbon demand. Honda suggests that carbon transfer efficiencies may be higher in subarctic regions due to greater mineral ballasting and armoring of opal-rich particles and lower remineralization rates within subarctic mesopelagic waters due to colder water temperatures and lower dissolved oxygen concentrations.

Weber and Bianchi also report the influence of dissolved oxygen concentration on carbon transfer efficiency. They find that oxygen minimum zones (OMZs) of the Eastern Tropical Pacific and Arabian Sea have much lower mesopelagic carbon flux attenuation than surrounding waters and sequester carbon twice as efficiently. They suggest three mechanisms are responsible: decreased remineralization at the transition from aerobic to anaerobic respiration, exclusion of zooplankton-mediated particle disaggregation, and reduced diffusive supply of oxidants (oxygen and nitrate). Because each mechanism uniquely alters particle size distributions, particle optical profiling could help distinguish between them.

Chaikalis et al. combine particle optical profiling with traditional biochemical measurements to better elucidate particle cycling processes. They find that particle optical and biogenic properties in the Mediterranean Sea covary among water masses and that both are lower in the eastern than in the western Mediterranean Sea, consistent with stable isotopic evidence for different particle pools in the two sub-basins. POC concentration was positively correlated with beam attenuation and negatively correlated with particle median diameter, indicating that particles are primarily biogenic and small particles are especially POC-rich. Particle aggregation in deep waters was indicated by low particle size distribution slopes and increasing particle mean diameter with depth.

Thomson et al. focus on particle remineralization within the water column, specifically the extracellular phosphatases (phosphomonoesterase, MEA and phosphodiesterase, DEA) that hydrolyze and release phosphorus from particles. They find that in subantarctic waters DEA and MEA are equally important in organic phosphorus hydrolysis, both in surface waters and at mesopelagic depths. Variations in the MEA:DEA ratio suggest variability in availability and/or utilization of P-monoester and P-diester pools. The observed negative correlation of the MEA:DEA ratio to phosphate and the positive correlation to the inorganic N:P ratio, suggesting that the relative importance of DEA vs. MEA is linked to inorganic phosphorus availability and N:P stoichiometry.

Two articles evidence the importance of lateral advection on deep particle fluxes in regions having high spatial gradients. Aristegui et al. studied epipelagic and mesopelagic microbial respiration along two zonal transects extending from the northwest African coastal upwelling to open ocean waters. Except at the coastal upwelling site, mesopelagic respiration exceeded satellite-derived net primary production (NPP), with the imbalance increasing offshore. They show that in offshore waters mesopelagic respiration is supported by lateral advection of suspended POC from coastal upwelling areas, either *via* deep circulation and/or mesoscale eddy transport. Kim et al. find that ~40% of the deep mass flux in the central basin of the East Sea/Japan Sea is resuspended lithogenic material. Radiocarbon data and excess Mn concentration show that the lithogenic flux at 500 m depth has a shallower source region than that at 2,000 m depth. Mesoscale eddies are suggested to transport material from the Korea Strait and/or western basin shelf and upper slope to the site.

Yamaoka et al. present a particle flux study at an oligotrophic site in the subtropical northwest Pacific. Very low vertical flux attenuation suggests that remineralization mainly occurs near the sediment interface in this region. Fluxes reflect lithogenic inputs, carbonate production, biogenic carbon incorporation and scavenging, with >85% of Mn, Co, Ni, Cu, Zn, Cd, and Pb fluxes attributable to scavenging. They speculate that blooms fueled by nitrogen fixation or typhoon activity induce late summer fluxes.

Xu et al. use ultrahigh resolution mass spectrometry to unravel the particle chemistry relevant to Fe scavenging. Their study shows that particles play an important role in controlling the distribution and flux of Fe and particle-reactive radionuclides having similar chemistry (e.g., thorium). They find that potential iron-carrying moieties comprise ~14% of identifiable molecules in particles and appear to be incorporated via ion complexation, hydrophobic interaction, and/or interlayered "occlusion." Molecular features and depth compositional changes suggest that surface photochemical reactions produce precursors that

are subsequently modified during particle cycling. A notable finding is the presence of hydroxamate-like moieties in particles, the key functionality of strong iron-binding in dissolved ligands.

Martinez-Ruiz et al. present a study of authigenic barite distributions in the Pacific, Atlantic and Indian Oceans. They find that barite is mainly associated with organic aggregates and extracellular polymeric substances and is universally most abundant at mesopelagic depths of intense organic matter remineralization, regardless of barite saturation state. Their study provides strong evidence that microbially mediated organo-accumulation of barium in decaying particles leads to saturated microenvironments and nucleation sites promoting barite precipitation, and supports experimental studies that show barium binds to phosphate groups on cell surfaces and within the extracellular polymeric substances of microbial biofilms.

Two final articles synthesize multidecadal particle flux time series in contrasting oceanographic regions. These studies demonstrate the immense value of long time-series to elucidate the overarching role of climate drivers on the oceanic particle flux. Wynn-Edwards et al. present a 20-years particle flux record at the subantarctic Australian Southern Ocean Time Series site (SOTS, 47°S, 142°E, 4,600 m water depth). They show that the subantarctic Southern Ocean is a significant carbon sink despite its high-nutrient, low chlorophyll characteristics. The carbonate counter-pump is estimated to reduce carbon sequestration by ~8%. Fluxes, dominated by carbonate (>60%), opal (~10%) and organic matter, vary seasonally with an early spring peak (October/November) and a smaller late summer peak (January/February). However, the annually-averaged flux is relatively constant year to year and shows no temporal trend. Flux variability exceeds variability in satellite-estimated net primary production (NPP), providing additional evidence that processes independent of NPP significantly modulate surface flux export and vertical transport efficiencies. The SOTS time-series provides an important baseline in a region predicted to experience large future climate perturbations.

Fischer et al. present an 18-years particle flux record at the oligotrophic ESTOC site (29°N, 15.5°W, ~3,600 m water depth) in the eastern subtropical Atlantic, and compare fluxes at ESTOC with those at a mesotrophic site further south. At ESTOC, fluxes at 1,000 m depth record oligotrophic conditions of overlying waters whereas deep (3,000 m) fluxes also record advective influences of the coastal Cape Ghir filament. At ESTOC, increases in spring biogenic flux and particle compositional changes correlate with North Atlantic Oscillation variability. Fluxes further south show no North Atlantic Oscillation correlation, indicating that coastal upwelling systems along the African margin respond differently to basin-scale climate forcing depending on location.

Author contributions

Topic coeditor MC was the lead author of this editorial. Topic coeditors RP, MH and GH reviewed and contributed to the editorial content.

Conflict of interest

The authors declare that the research was conducted in the absence of any commercial or financial relationships that could be construed as a potential conflict of interest.

Publisher's note

Reference

Conte, M. H. (2019). "Oceanic particle flux," in *Encyclopedia of ocean sciences*. Editors J. Kirk Cochran, J. Henry Bokuniewicz, and L. Yager Patricia. 3rd Ed. (Oxford: Elsevier), 4, 192–200. doi:10.1016/b978-0-12-409548-9.11481-2

frontiers in Earth Science

ORIGINAL RESEARCH
published: 27 March 2020
doi: 10.3389/feart.2020.00080

High Temporal Variability of Total Organic Carbon in the Deep Northeastern Pacific

Chelsi N. Lopez[1], Marie Robert[2], Moira Galbraith[2], Sarah K. Bercovici[3,4,5], Monica V. Orellana[3,4] and Dennis A. Hansell[1]*

[1] Department of Ocean Sciences, Rosenstiel School of Marine and Atmospheric Sciences, University of Miami, Miami, FL, United States, [2] Department of Fisheries and Oceans, Institute of Ocean Sciences, Sidney, BC, Canada, [3] Applied Physics Laboratory, University of Washington, Seattle, WA, United States, [4] Institute for Systems Biology, Seattle, WA, United States, [5] Institute for Chemistry and Biology of the Marine Environment, Carl von Ossietzky University of Oldenburg, Oldenburg, Germany

The interseasonal and interannual variability of total organic carbon (TOC) was assessed in the deep northeastern Pacific Ocean, an area characterized by high primary production and organic matter export. Samples were collected from throughout the deeper water column (>250 m) seasonally in 2017 and 2018 along the Line P transect, as well as one distribution of dissolved organic carbon (DOC) in spring 2018. High heterogeneity was observed in TOC concentrations at depths greater than 1,000 m, both within seasons (concentration differences of ∼2–6 μmol kg^{-1}) and across seasons (∼2–12 μmol kg^{-1}), coinciding with changes in fluorescence in the overlying waters. Such observations suggest that biogenic particles sinking from the upper ocean are seasonally delivering observable TOC to depth. The presence of these particles also appeared to contribute to the DOC pool, as suggested by differences in the TOC and DOC distributions in spring 2018. Seasonal TOC net accumulation and removal rates differed between the years: 0.5 and 2.1 μmol kg^{-1} day^{-1} (accumulation) and 0.6 and 2.1 μmol kg^{-1} day^{-1} (removal) for 2017 and 2018, respectively. The rate estimates indicated that introduction of organic carbon to the bathypelagic occurred at approximately the same rate as removal post-bloom, demonstrating the efficient removal of seasonally produced organic carbon. High abundances of gelatinous zooplankton in spring 2018, supported by higher abundances of phytoplankton, enhanced the export of organic carbon to the bathypelagic zone during the seasonal bloom, resulting in localized TOC concentrations up to 148 μmol kg^{-1} in the bathypelagic. These results indicate high variability in bathypelagic TOC concentrations at high latitude, unlike oligotrophic systems.

Keywords: total organic carbon, dissolved organic carbon, North Pacific, export, Ocean Station Papa, carbon seasonality, deep carbon dynamics, marine biogeochemistry

OPEN ACCESS

Edited by:
Rut Pedrosa Pàmies, Marine Biological Laboratory (MBL), United States

Reviewed by:
Antoni Calafat, University of Barcelona, Spain
Felipe Sales de Freitas, University of Bristol, United Kingdom

****Correspondence:***
Chelsi N. Lopez
chelsi.lopez@rsmas.miami.edu

Specialty section:
This article was submitted to Biogeoscience, a section of the journal Frontiers in Earth Science

Received: *11 November 2019*
Accepted: *09 March 2020*
Published: *27 March 2020*

Citation:
Lopez CN, Robert M, Galbraith M, Bercovici SK, Orellana MV and Hansell DA (2020) High Temporal Variability of Total Organic Carbon in the Deep Northeastern Pacific. Front. Earth Sci. 8:80. doi: 10.3389/feart.2020.00080

INTRODUCTION

Marine organic matter, a product of ocean primary production, plays a vital role in the sequestration and export of carbon. It is produced in the euphotic layer via primary production by autotrophic organisms with most of it respired near-contemporaneously (Ducklow et al., 2001). However, a fraction of organic material is exported below the euphotic

zone and remineralized by heterotrophic organisms back to inorganic forms (i.e., the biological pump). Other residue of the biological pump is sedimented onto the seafloor, or potentially added to the refractory dissolved organic carbon (DOC) pool (Druffel et al., 1992; Ducklow et al., 2001; Jiao et al., 2010). Each of these processes sequesters carbon in the deep ocean, aiding in oceanic uptake of atmospheric carbon dioxide. In today's changing climate, consideration and understanding of such processes is increasingly important.

Since the longest-running time-series programs with measurements of total organic carbon (TOC) and DOC are located in oligotrophic regions (Hansell and Carlson, 2001), there is a gap in knowledge on the temporal variability of these parameters in waters underlying productive areas, such as the North Pacific. To remedy this, we analyzed TOC distributions in this region on a seasonal time scale. Located within a productive area, Ocean Station Papa (OSP) is a well-studied site (50.0°N and 145.0°W) in the northeastern Pacific that began as an ocean weather station in 1949, operated by the United States Weather Bureau (Tabata et al., 1986; Freeland, 2007). Located ∼1,200 km off the coast of British Columbia, OSP is on the southern edge of the subpolar gyre and within an area with weak currents (Pelland et al., 2016). The monitoring program for OSP underwent many changes over the years (Freeland, 2007), in particular the addition of several regularly occupied hydrographic sampling stations between OSP and the coast, now referred to as "Line P," that are currently monitored by the Canadian Department of Fisheries and Oceans (DFO) tri-annually. More recently, this area has been the site for many Argo float and Seaglider deployments, as well as a NOAA-monitored mooring, providing robust data that indicate constantly changing hydrological and biologic conditions (Pelland et al., 2016; Bif and Hansell, 2019). These processes near OSP are now being considered further by the NASA-supported EXPORTS research program (Siegel et al., 2016). Our analysis includes the first organic carbon measurements collected as a time-series along Line P, providing contextual information about seasonal and local organic carbon dynamics. Analyses such as this are vital for furthering our understanding of the ocean's ability to sequester carbon at depth.

Most particulate biogenic matter produced in the upper ocean does not reach great depths (Gardner, 2015), however, periodic fluxes of up to 43% of exported organic material have been observed at depths down to 3,400 m in the northeastern Pacific within only a few days of leaving the euphotic zone (Smith et al., 2018). Past measurements of sinking particles in sediment traps have indicated higher productivity at OSP versus stations further south, as average annual POC fluxes from traps at 1,000 m ranged from 138 to 246 mmol m^{-2} yr^{-1} (Honjo et al., 2008). At 31.7°N, 124.6°W, located within an oligotrophic zone in the North Pacific, POC flux was estimated to be 82 mmol m^{-2} yr^{-1}, much lower than fluxes at OSP. Climatologies of sediment flux at OSP have shown sporadic and seasonally dependent carbon export events, measured by deep-moored sediment traps (Wong et al., 1999; Timothy et al., 2013). In addition to sediment trap data, zooplankton collections and carbon export estimates indicate that a rapid sinking rate (up to 800 m per day) can transport high levels of organic material to the bathypelagic quickly (Robison et al., 2005), a factor that is overlooked in single-season hydrographic observing programs.

Seasonal trends in the bathypelagic may be more prominent than we currently understand based on observations in oligotrophic systems alone, given the differences in particle export. The data presented in this analysis provides insight on the seasonal dynamics and physical processes by which carbon reaches the deeper water column with sinking particles, some of which leaves a signal as DOC. Comparing TOC distributions at depth to upper layer parameters, such as fluorescence, nutrients, and zooplankton abundance provides an advantage in understanding the impact of vertical input of organic carbon via sinking particles, as well as understanding the variability of local organic carbon on a seasonal time-scale.

MATERIALS AND METHODS

Samples were collected along the Line P transect (**Figure 1**), occupied tri-annually by the Canadian Department of Fisheries and Oceans (DFO). The cruises departed from Sidney, British Columbia and continued out to Ocean Station Papa (P26/OSP: 50.0°N, 145.0°W), during winter (February), spring (June), and summer (August/September) of 2017 and 2018. Fluorescence data collected continuously during downcasts were provided by DFO while TOC and DOC were measured at the University of Miami. The fluorescence data are reported in mg m^{-3}, though according to DFO data reports the values of fluorescence do not always compare well with bottle chlorophyll data. Distributions of chlorophyll are qualitatively comparable to fluorescence values so we use the latter as a reasonable indicator of chlorophyll distributions. Data employed here are available at https://www.waterproperties.ca/linep/cruises.php. Most stations were occupied during daylight hours.

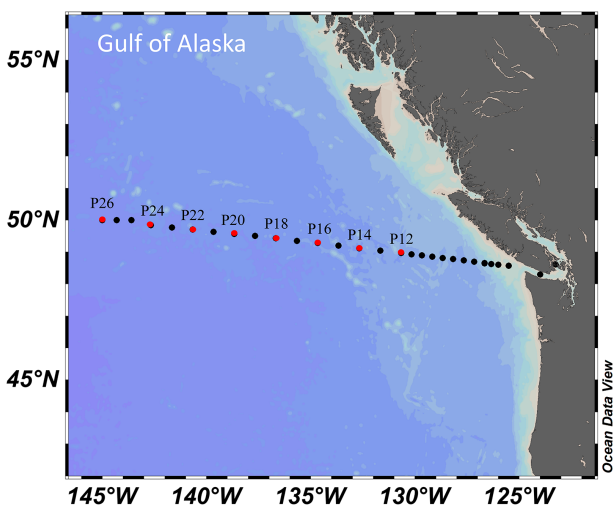

FIGURE 1 | Locations of Line P stations; those considered in this analysis are highlighted in red. This figure was created using Ocean Data View (Schlitzer, 2019).

The section of Line P of interest in this analysis is that of the open ocean. Line P stations considered were P12 to P26 (**Figure 1**). Salinity at the surface was used to indicate coastal impacts versus open ocean conditions, with oceanic stations holding salinities of ∼32.5 while the coastal stations were seasonally lower. Of the stations evaluated here, Station P12 is located closest to the coast, giving it the most potential for exposure to those influences. However, as the station is ∼100 km west of low salinity surface waters, it is evaluated here as an open ocean station.

Samples for TOC analysis were collected as whole-water directly from the Niskin bottles aboard the ship, placed into 40 mL pre-combusted vials and fixed with 100 μL of 4N HCl. Given our focus on the export of organic matter to the deeper water column, we report TOC concentrations only at depths >250 m. This analysis is restricted to stations away from the continental shelf (i.e., westward of Line P Station 11) to minimize variability due to coastal influences (e.g., fluvial inputs, filaments, shelf resuspension, etc.). Samples collected as DOC were filtered in-line from the Niskin bottles using a pre-combusted GF/F filter (0.7 μm nominal pore size) and then treated similarly to TOC. All samples were analyzed with Shimadzu TOC-L systems as previously described (Dickson et al., 2007). Reference materials from the Hansell Certified Reference Material (CRM) program (Hansell, 2005) were utilized to ensure accuracy. The uncertainty of TOC and DOC measurements is ±1.5 μmol L^{-1}. Concentrations were converted to μmol kg^{-1} by dividing by potential density, σ_θ.

Seasonal TOC profiles were modeled using the piece-wise linear least-squares statistical analysis tool in Ocean Data View (Schlitzer, 2019), with a 30-gridpoint output. Data employed were from stations P12 to P26 (**Figure 1**). TOC concentrations at depths ≥250 m did not exceed 80 μmol kg^{-1} for all stations and seasons analyzed, except for three data with very high concentrations observed during spring 2018, which were omitted in the model. The difference in TOC and DOC for these omitted stations/depths exceeded 1 standard deviation from the mean.

The calculations for TOC accumulation and removal rate estimates are shown in Equations 1 and 2, respectively.

$$\frac{TOC_{spring\ average} - TOC_{winter\ average}}{Days\ between\ cruises} = Accumulation\ rate \quad (1)$$

$$\frac{TOC_{summer\ average} - TOC_{spring\ average}}{Days\ between\ cruises} = Removal\ rate \quad (2)$$

These are net rates as they do not include variations in concentrations that may have occurred over time frequencies shorter than our occupations.

Zooplankton samples were collected using vertical hauls with 0.56 m diameter bongo nets, fitted with 0.236 mm black mesh. Samples were collected from 250 m to the surface. The bongo net consists of two black cylindrical–conical nets mounted on a central towing frame and weight. Each net has a 0.25 m^2 mouth area, a filtering area/mouth area ratio of 11.5, and 0.23 mm aperture black mesh. Volume filtered is measured by a TSK flowmeter mounted in the mouth of one net. Due to time constraints, bongo tows were collected both day and night. However, for many of the taxa considered, diel migration was either weak or was confined to movement within the upper 200 m.

The catch from one net of the bongo pair was preserved immediately in 10% formalin, and returned to shore for analysis. Quantitative subsamples were counted to species level and life stage. Subsample size varies with taxa to give approximately uniform expected abundance estimation error (about 20%) for all of the dominant groups. Flowmeter, net diameter, and tow depth were used to convert abundance per sample to abundance per cubed meter.

Zooplankton were also collected using a Multi Plankton Sampler (MPS) from Hydro-Bios (0.25 m^2 mouth area) at several stations along the line, towed 2,500 m to the surface with a speed of ∼1 m s^{-1}. The MPS was equipped with five white nets (250 μm mesh size) that can be opened and closed on command from the ship via conducting cable attachment. The volume of water filtered by the net was measured with Hydro-Bios flowmeters fitted in the mouth of each net. All MPS tows were done during daytime hours to take advantage of any layering of taxa at depth. The only data reported in this analysis from an MPS net, as opposed to a bongo net, was Station P26 in 2018.

RESULTS

We report TOC concentrations in the bathypelagic water column, with focus here on depths from 1,000 m to the seafloor, along with fluorescence within the euphotic zone providing a qualitative measure of chlorophyll (**Figures 2**, **3**). DOC concentrations from spring 2018 are also reported.

Distributions in 2017

Relative to spring and summer, winter concentrations of both fluorescence and TOC were most consistent along Line P, with upper ocean fluorescence (**Figure 2A**) ranging from 0.5 to 1 mg m^{-3} in the upper 100 m. TOC concentrations were ∼40 μmol kg^{-1} at >1,000 m, with several localized areas of elevated TOC (∼42 μmol kg^{-1}; **Figure 2B**). By spring, the deep chlorophyll maximum (DCM) developed with fluorescence concentrations up to 1.5 mg m^{-3}, mainly near 50 m (**Figure 2C**). Heterogeneity in the TOC distribution was prominent (**Figure 2D**), with a minimum of 38 μmol kg^{-1} (P20, 3,000 m) and a maximum of 46 μmol kg^{-1} (P12, 3,000 m). Observed in the deep bathypelagic at stations such as P24, P20, and P12, summertime TOC concentrations were elevated by ∼2–6 μmol kg^{-1} relative to neighboring concentrations (**Figure 2F**). Concentrations at P16 were particularly low throughout the water column, reaching a minimum of 37 μmol kg^{-1}. Fluorescence decreased to 1–1.5 mg m^{-3}, except near P26 where a localized maximum of 4 mg m^{-3} was observed toward the surface (**Figure 2E**).

Distributions in 2018

The lowest wintertime concentrations of fluorescence were again 0.5–1 mg m^{-3} (**Figure 3A**), except near P22, where

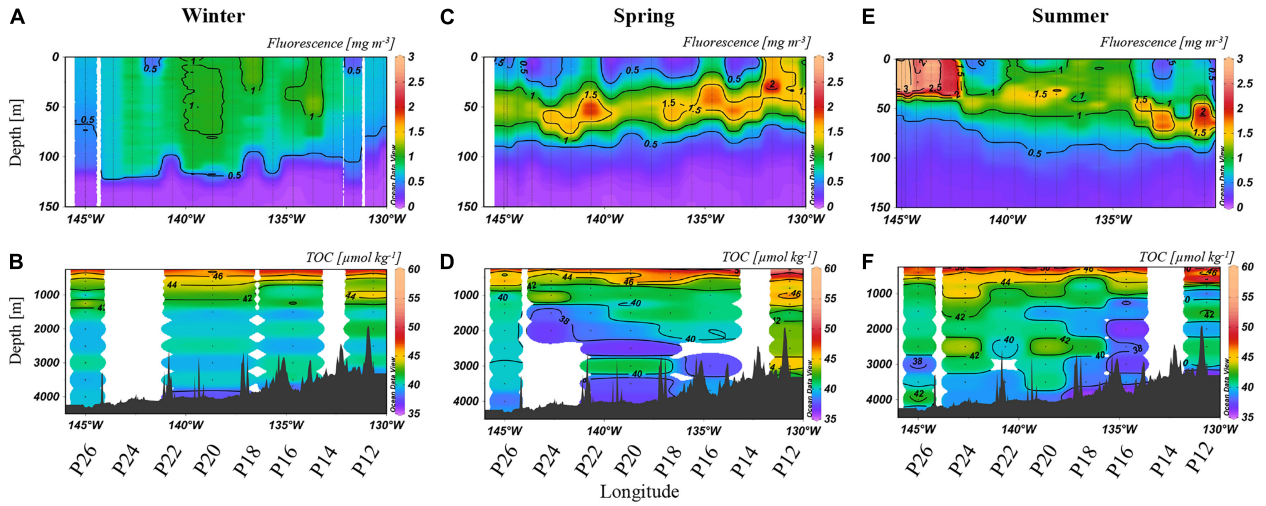

FIGURE 2 | Fluorescence to 150 m **(A,C,E)** [mg m^{-3}] and TOC [µmol kg^{-1}] at depths >250 m **(B,D,F)** from 2017. The color scales are non-linear to better visualize small changes in concentrations in the deeper water column. Note that fluorescence was measured at all stations while TOC was determined at selected stations, as labeled below the *x*-axis.

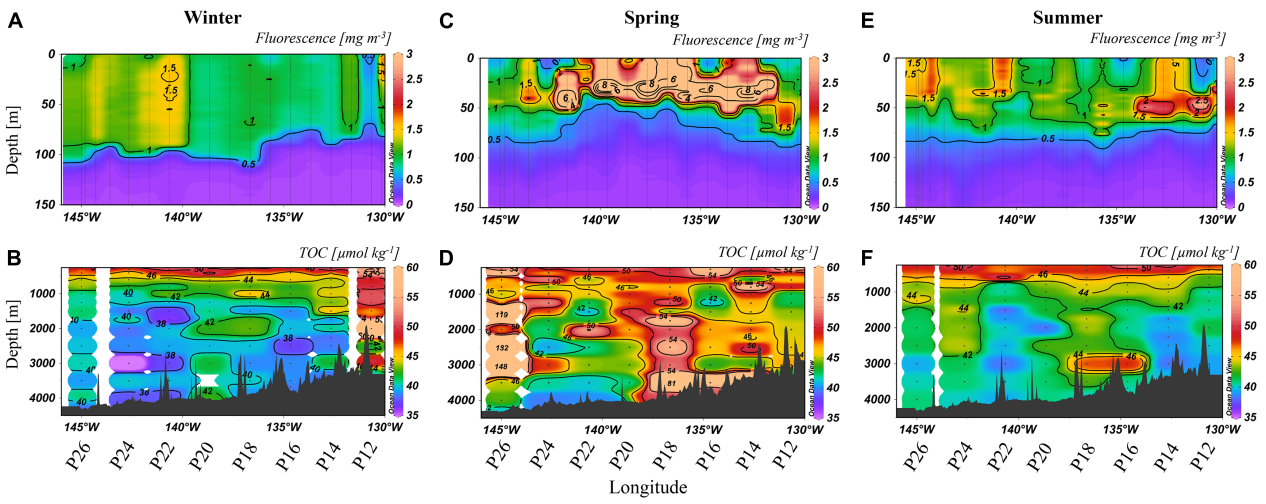

FIGURE 3 | Fluorescence to 150 m **(A,C,E)** [mg m^{-3}] and TOC [µmol kg^{-1}] at depths >250 m **(B,D,F)** from 2018. The color scales are non-linear, with some values off scale (>60 µmol kg^{-1} for TOC, >3 mg m^{-3} for fluorescence). Note that fluorescence was measured at all stations while TOC was determined at selections stations, as labeled below the *x*-axis.

the maximum concentration (~1.5 mg m^{-3}) was observed. The TOC distribution was heterogenous laterally and vertically (**Figure 3B**), with concentrations ranging from 35 to 44 µmol kg^{-1}, except for P12 where there were high concentrations down the water column, up to 74 µmol kg^{-1} (2,000 m). High variability in TOC concentrations was observed throughout the transect in spring (**Figure 3D**), with the highest concentrations at P26 (up to 146 µmol kg^{-1}) and P18 (up to 81 µmol kg^{-1}). Fluorescence concentrations were also enhanced (**Figure 3C**), ranging from 2 to 8 mg m^{-3} in the upper 50 m, except at P26 where concentrations were ~1 mg m^{-3}. TOC concentrations in summer (**Figure 3F**) in the bathypelagic ranged from 39 to 49 µmol kg^{-1}, with the highest concentrations observed at P16 to P20 and P24. Fluorescence returned to lower concentrations of 0.5–1 mg m^{-3} (**Figure 3E**) except at localized areas such as P12 and P14 (2 mg m^{-3}).

Distributions of DOC in Spring 2018

Dissolved organic carbon concentrations were highly variable along Line P, ranging from 37 to 60 µmol kg^{-1} at depths >1,000 m (**Figure 4**). Deep waters at stations P20 and P22 held relatively low values (<40 µmol kg^{-1}), concentrations consistent with prior reports for the northern North Pacific (Hansell and Carlson, 1998; Hansell et al., 2009). Isolated stations and depths along the transect held elevated DOC concentrations, demonstrating high heterogeneity. Maximum concentrations in

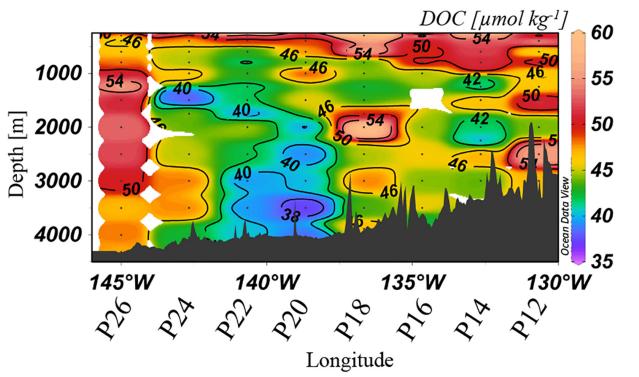

FIGURE 4 | Dissolved organic carbon [μmol kg^{-1}] distribution at >250 m in spring 2018 along Line P. The color scales are non-linear.

the bathypelagic were observed at Station P26, where DOC reached up to 50–55 μmol kg^{-1}, as well as at P18, which reached 58 μmol kg^{-1}.

DISCUSSION

To understand the trends observed in organic carbon and their contributing mechanisms, we discuss the data in terms of both interseasonal and interannual variability for 2017 and 2018, considering a multitude of parameters and rates that incorporate TOC, DOC, euphotic zone fluorescence and satellite-derived surface chlorophyll.

Trends in TOC and Fluorescence

Seasonality in 2017

Between winter and spring (**Figures 2A,C**), fluorescence increased (from 0.5 mg m^{-3} in winter to up to 2 mg m^{-3} in spring) across the transect, with a particular enhancement in the deep chlorophyll maximum (DCM; near 50 m). Organic matter export was evidenced by TOC enrichment and variability in the deep water column (**Figure 2B**). In spring, extensive enrichment of TOC, up to 46 μmol kg^{-1}, was observed at P12 (**Figure 2D**), values higher than in winter (**Figure 2B**). Elevated TOC at depth in spring coincided with an increase in fluorescence, suggesting that production in the euphotic zone was contributing to vertical export. Relative to winter values, minima in deep TOC were observed in spring as well, possibly due to further TOC removal between winter and spring by heterotrophic respiration or by horizontal displacement with low TOC waters. TOC was transported deep into the water column, as concentrations observed in the mesopelagic (up to 46 μmol kg^{-1}) reached depths of 2,000 m at several stations (P16, P18, and P20). Enhanced TOC concentrations were also apparent down to 3,000 m at some stations, indicating deep export of organic carbon via vertically sinking particles in connection with higher abundances of phytoplankton, as indicated by high fluorescence. In summer, isolated enrichments of TOC became even more noticeable (**Figure 2F**). These seasonal enrichments of TOC concentrations are consistent with increased fluorescence in the euphotic zone (**Figure 2E**), which again suggested that blooms of phytoplankton were producing organic carbon capable of reaching the bathypelagic ocean, supporting the long-term sequestration of carbon.

Seasonality in 2018

Winter 2018 (**Figure 3B**) had higher heterogeneity in TOC along Line P. Again, fluorescence averaged around 0.5–1 mg m^{-3}, though slightly higher concentrations (∼1.5 mg m^{-3}) were apparent further to the west in 2018, coinciding with heterogeneity in bathypelagic TOC in that area. The differences in wintertime TOC distributions between 2017 and 2018 suggested a more productive year in 2018. During winter, Station P12 had the highest deep TOC concentrations, averaging ∼50 μmol kg^{-1} (**Figure 3B**). These high TOC concentrations at P12 were not accompanied by elevated fluorescence in the euphotic zone at that station (**Figures 3C,D**), perhaps indicating a role for lateral input, such as terrestrial input from the margin. However, local surface conditions, such as fluorescence, do not have to align vertically with the associated exported organic carbon at depth given the great spatial separation possible between the site of particle export and its eventual location in the deep ocean (Siegel et al., 2008). Particularly elevated TOC concentrations at P12 were observed in spring 2017 as well, though less prominent (**Figures 2B,D**). We included this station for analysis because it was in deep water (>3,000 m; **Figure 1**), however, it is adjacent to, and possibly impacted by, adjacent shelf waters, as high coastal fluorescence was observed in spring 2017 (∼11 mg m^{-3}) and winter 2018 (∼5 mg m^{-3}). It was also nearest the area where the southward flow of the bifurcation of the North Pacific Current (NPC) originates which may have contributed to high TOC levels, as the remainder of the Line P stations analyzed are closer to the northward flow of the NPC (Pelland et al., 2016).

Exceptionally high fluorescence occurred in spring 2018, reaching levels above 8 mg m^{-3} (**Figure 3C**). This enhancement was evidence of a strong seasonal phytoplankton bloom, which appeared to export high levels of organic carbon to depth (**Figure 3D**). Chlorophyll-a concentrations obtained from satellite data (Hu et al., 2012) for spring 2018 were higher than 2017 on average as well (**Figure 5**). In 2017, chlorophyll concentrations on the western side of the transect were ∼0.15 mg m^{-3}, and 0.3 mg m^{-3} at the eastern stations. In contrast, concentrations in 2018 ranged from 0.3 to 0.6 mg m^{-3}, supporting our observations of higher fluorescence in 2018 and ultimately higher abundance phytoplankton. TOC levels at P26 were exceptionally high during this season, reaching 148 μmol kg^{-1}, though it did not correspond with enhanced fluorescence at that station. However, this station had a unique feature, as it contained high numbers of heterotrophic salps (discussed further in section "Contribution of Gelatinous Zooplankton to Organic Carbon Export"), which have been correlated with lower levels of phytoplankton due to consumption (Li et al., 2016), consistent with this observation. Elevated TOC values in this season were observed in the deep water column, even down to 3,500 m, suggesting the production and downward propagation of fast-sinking particulate matter. Past studies in the northeastern Pacific

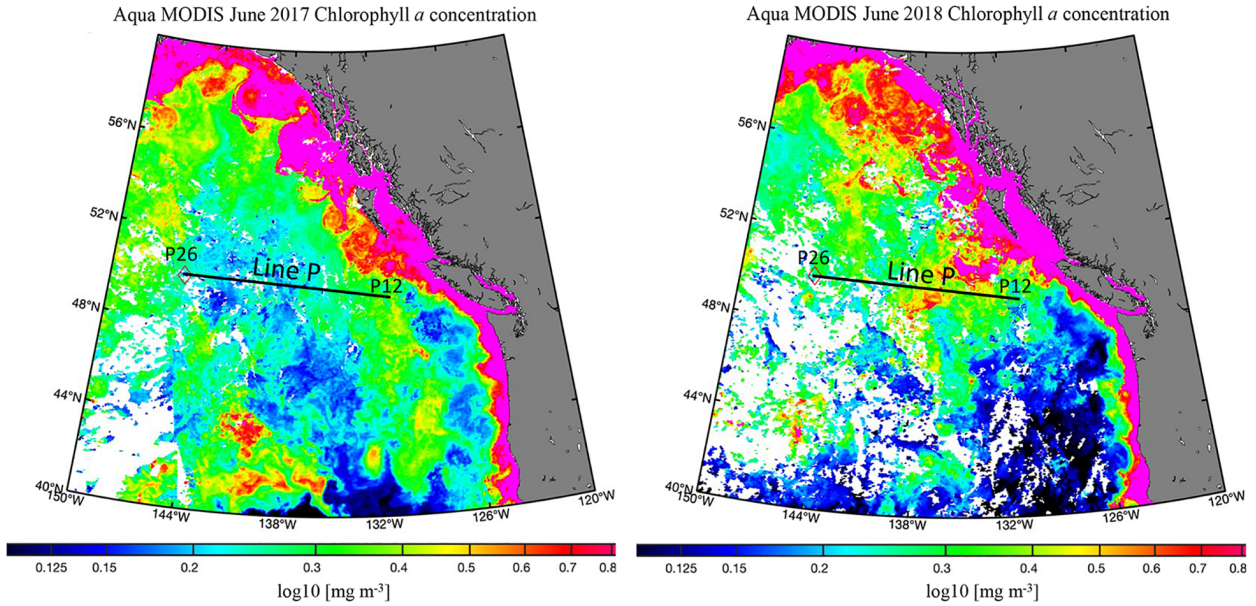

FIGURE 5 | Satellite chlorophyll distributions [mg m^{-3}] for June 2017 and 2018. The analyzed portion of Line P is represented by a black line. Aqua MODIS data from https://oceancolor.gsfc.nasa.gov/l3/ (Hu et al., 2012). Map made with M_Map (https://www.eoas.ubc.ca/~rich/map.html).

have identified a correlation of upper water column processes, such as chlorophyll and net primary production, to export flux in the deep bathypelagic (50 m from seafloor) as well as seafloor deposits (Smith et al., 2008), suggesting that carbon export in this area is a largely vertical process. Fluorescence was highest in the spring season for both 2017 and 2018 (**Figures 2C**, **3C**), spanning nearly the entire transect in both years, while elevated fluorescence was more variable across the transect in other seasons. These results indicate that spring was the most productive season in this region, and more productive than 2017.

By summer 2018, much of the TOC enhancement from springtime had dissipated (**Figure 3F**), potentially through heterotrophic remineralization, sedimentation to the sea floor, or lateral export away from the study site. Evidence of enhanced fluorescence still existed, though lower in intensity (**Figure 3E**). Higher TOC concentrations were observed intermittently at P16, P18, and P24, near where the highest TOC concentrations from spring were present. There was a trend in fluorescence in summer of both 2017 and 2018, as both years exhibited the maximum concentrations near stations P12 and P24/26, suggesting an interannual trend. In parallel with fluorescence, TOC was heterogeneous throughout the water column, particularly at P16 and P24.

Modeled Comparison of TOC Between Years

To better characterize variability between years, vertical profiles of TOC were modeled using a piece-wise linear least squares statistical analysis (Schlitzer, 2019). Vertical profiles of modeled TOC concentrations (**Figure 6**) provide insight on trends in the variability of TOC with depth; the differences between years and seasons became more visually apparent.

In both winters (**Figure 6A**), TOC profiles were comparable and variability in TOC with depth was mostly synchronous. For example, concentrations were somewhat lower at specific depths such as ∼1,700, 3,250, and 3,750 m in both years. TOC concentrations remained close in concentration at all depths, never exceeding a difference of 1.5 μmol kg^{-1} between years, a value approximating the uncertainty of the measurement. In contrast, there was high variability between 2017 and 2018 during the spring season (**Figure 6B**). Differences in TOC concentrations at similar depth ranged from 1.8 to 11.5 μmol kg^{-1}, with an average offset of ∼5 μmol kg^{-1} down the profiles. As was also apparent from the observed TOC distributions (**Figures 2D**, **3D**), higher concentrations in 2018 were estimated by the model. The sporadic changes in concentration with depth were similar for both years in the deeper bathypelagic, such as the decrease in TOC concentrations from roughly 2,750–3,000 m and the subsequent increase to 3,250 m. In summer, differences in concentration narrowed between the years, not exceeding 2 μmol kg^{-1}, except below ∼2,300 m where differences in concentration reached up to 6 μmol kg^{-1} (**Figure 6C**). These depths were located where the highest variability was also observed in spring, which likely contributed to variability in summer due to residual organic carbon. The TOC introduced in spring of both years returned to lower concentrations (∼36–42 μmol kg^{-1}) in the bathypelagic by summer, similar to winter observations. The disappearance of TOC between these seasons was evidence of organic carbon removal from the deeper water column, driven by heterotrophic respiration, lateral transport, or sedimentation of particles onto the seafloor, all of which sequester carbon produced in the upper water column into the bathypelagic ocean. The

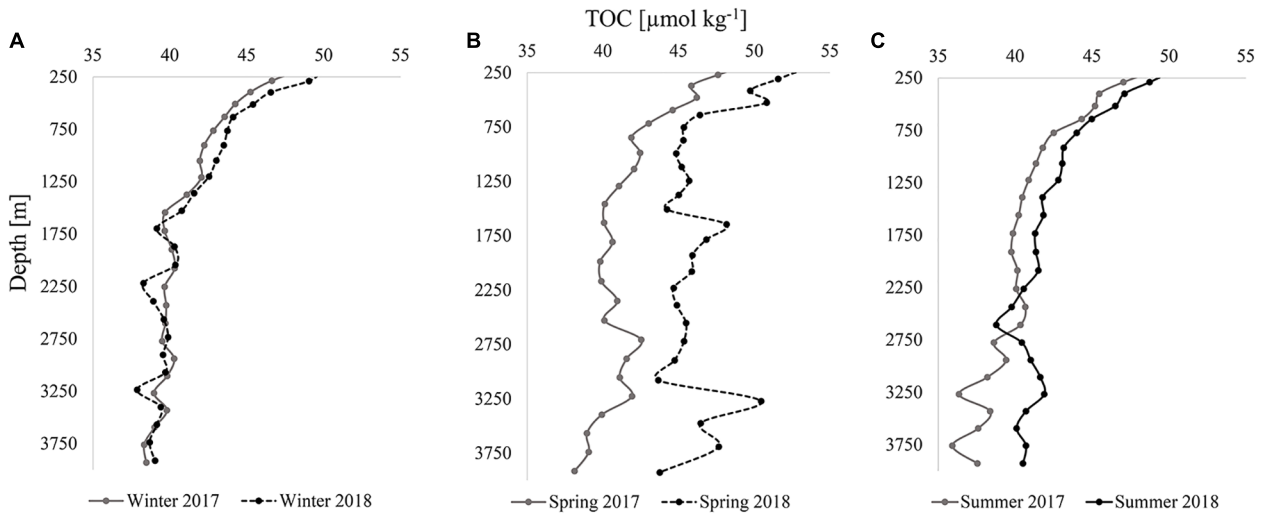

FIGURE 6 | Internannual comparisons (2017 and 2018) of modeled TOC [µmol kg^{-1}] vertical profiles for all stations in the analysis in winter **(A)**, spring **(B)**, and summer **(C)**.

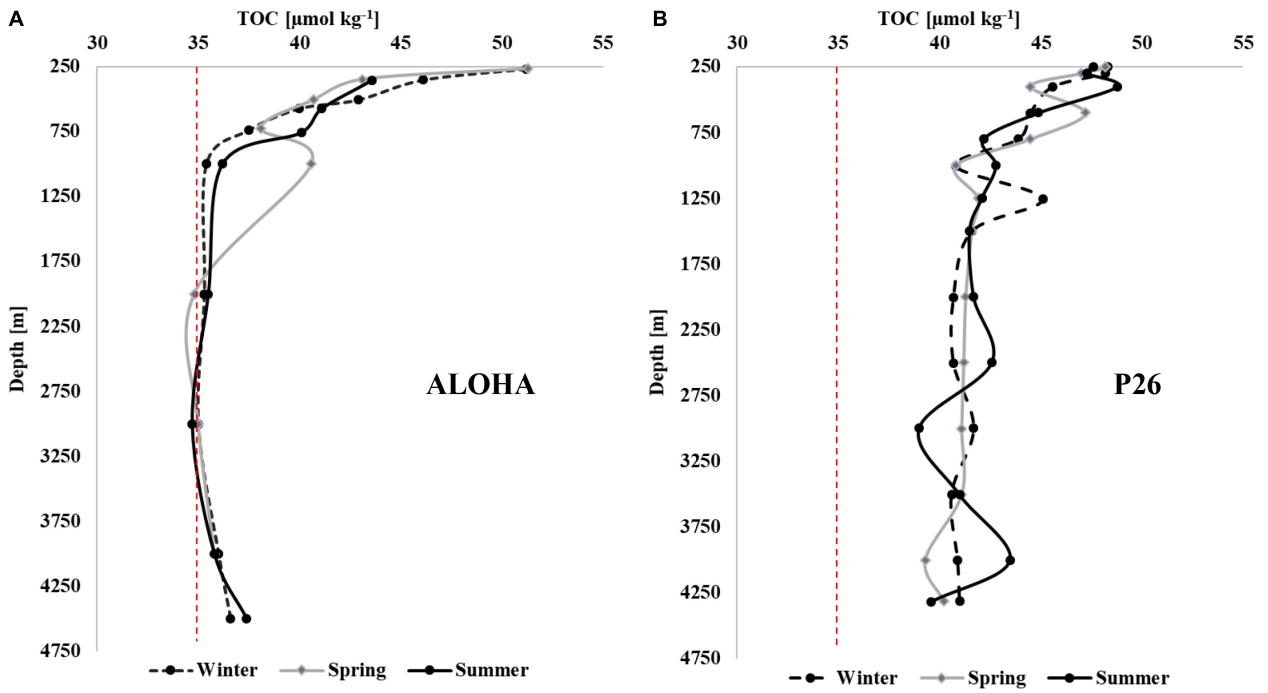

FIGURE 7 | Seasonal TOC [µmol kg^{-1}] profiles (winter, spring, and summer) at Station ALOHA **(A)** and at Station P26 along Line P **(B)** in 2017. The red dashed line at 35 µmol kg^{-1} provides a visual reference point emphasizing the differences in concentrations between subtropical and subpolar systems. HOT data are accessible at http://hahana.soest.hawaii.edu/hot/hot-dogs/bextraction.html. Concentrations at Station ALOHA are referred to here as TOC, rather than DOC as listed at the HOT data archive, since the samples were collected and analyzed as whole-water.

pattern in TOC between seasons for both years demonstrated an interannual trend.

The seasonality and variability in TOC concentrations at depth at P26 in 2017 (**Figure 7B**) was more prominent than changes in deep water at oligotrophic Station ALOHA of the Hawaii Ocean Time-series (HOT), located in the subtropical North Pacific (**Figure 7A**). Though deep TOC at Station ALOHA showed a single elevated value at ∼1,000 m in spring, seasonality in concentrations was largely not evident. In contrast, concentrations along Line P deviated considerably between seasons at all depths below 250 m (**Figure 2**). Such observations indicate that the deep water column of the northeastern Pacific

was more impacted by seasonal variability in carbon export in comparison to less productive oceanic areas such as the subtropical Pacific. The concentrations at Line P were also considerably higher at depth, ranging from 40 to 49 μmol kg^{-1}, while concentrations at HOTS were $\sim$35 μmol kg^{-1} in the deep water column with very low variability.

Contribution of Gelatinous Zooplankton to Organic Carbon Export

Sampling for abundances of zooplankton was completed at offshore stations P12, P16, P20, and P26 for three size classes of larvaceans, doliolids, and salps. The counts provided in **Table 1** are those that showed large increases from 2017 to 2018 (i.e., count increased by >1 individuals m^{-3}). The complete data are provided in **Supplementary Material**.

The presence of salps, larvaceans, and doliolids were correlated with high levels of TOC in the deep layers. The abundance of larvaceans during winter of 2018 was slightly higher than the low/non-observable counts during winter 2017, perhaps accounting for the minor increase in heterogeneity of TOC at depth observed in 2018 in this season. In contrast, abundances in spring were considerably higher in 2018 compared to 2017. Larvaceans were substantially more numerous at P16 and P20, where counts reached up to 187 individuals m^{-3} (P16, 2018), while very low numbers were observed in 2017. Doliolids were more abundant at these stations as well as at P12, also reaching a maximum at P16 ($\sim$95 individuals m^{-3}), providing potential for higher amounts of carbon to be exported to depth, which we observed in the TOC distribution (**Figure 3D**). Notably high abundances of large salps (>10 mm, some reaching $\sim$10 cm) were observed at P26, both from the bongo nets and visually apparent at the surface. High abundances of these gelatinous zooplankton were associated with high levels of organic carbon, higher than any other season, throughout the water column in spring 2018. Enrichment of TOC was likely due to sinking houses, fecal pellets, and carcasses of these organisms. As previously mentioned in Section "Seasonality in 2018," exceptionally high TOC concentrations were observed at P26 (i.e., 148 μmol kg^{-1} at 3,000 m, 131 μmol kg^{-1} at 2,500 m) that did not correlate with high surface fluorescence. However, this was the only station with large salps capable of quickly transporting carbon to the bathypelagic, perhaps scavenging much of the plant biomass in the process, which resulted in low fluorescence ($\sim$1 mg m^{-3} compared to 8 mg m^{-3} at other stations during this season). Salps were not observed in winter or summer of both years and we did not observe TOC concentrations as high as those in spring 2018 anywhere else in the distributions, a sign that salps were a major contributor to vertical carbon export within their bloom area and contributors to bathypelagic carbon.

TABLE 1 | Counts of larvaceans, doliolids, and salps (individuals m^{-3}) in the upper 250 m that showed important increase between 2017 and 2018.

	Station	Type	2017	2018
Winter	P12	Larvaceans	0.20	2.42
	P16	Larvaceans	NP	1.45
	P26	Larvaceans	0.42	3.10
Spring	P12	Doliolids	0.18	41.84
	P16	Larvaceans	0.05	187.17
	P16	Doliolids	0.21	95.11
	P20	Larvaceans	1.33	13.16
	P20	Doliolids	0.61	5.48
	P26	Salps	NP	6.08
Summer	P12	Larvaceans	6.37	0.91
	P12	Doliolids	36.37	NP
	P16	Larvaceans	1.69	6.42
	P16	Doliolids	16.75	39.82
	P20	Larvaceans	0.45	22.36
	P20	Doliolids	0.55	118.11

The data here contain combined abundances of all class sizes; more detailed information is available in ***Supplementary Material****. Samples that did not contain the specified organisms are labeled as "not present" (NP).*

In summer 2017, abundances of larvaceans and doliolids at P12 were higher than counts from 2018, though there was no substantial difference in TOC concentrations between years at this station. However, particularly high TOC concentrations (up to 71 μmol kg^{-1}, 2,000 m) were observed at P12 in the subsequent season (winter 2018), possibly due to the presence and resultant export of organic matter by these organisms from the previous season, which would suggest slower sinking rates of organic matter. Larvaceans were higher in abundance during 2018 at P16 and particularly at P20, however, where numbers reached 112 individuals m^{-3}. High TOC concentrations ($\sim$44–47 μmol kg^{-1}) were observed in these areas, likely correlated to the presence of these individuals during spring, but concentrations were considerably less prominent. No salps were observed in summer 2018, indicating that the large salp bloom had dissipated, likely allowing the phytoplankton community to recover, as indicated by elevated fluorescence levels (up to 4 mg m^{-3}).

A phenomenon noted within this area in the past (Li et al., 2016), the presence of larvaceans, doliolids, and salps, was observed, particularly during spring 2018. These organisms are gelatinous zooplankton that feed by siphoning water, typically secreting DOC and contributing to the detrital TOC pool through sinking carcasses and reworking of particulate material (Hamner and Robison, 1991). High phytoplankton abundances provide ample food for these heterotrophic organisms. Additionally, higher quantities of them can indicate strong autotrophic bloom conditions (Heron, 1972). Export flux estimates for each type of organism are typically $\sim$20 mg C m^{-2} d^{-1} (Wiebe et al., 1979; Matsueda et al., 1986; Robison et al., 2005; Takahashi et al., 2015; Stone and Steinburg, 2016), highlighting the magnitude of their potential contribution to the deep carbon pool. However, the flux is highly dependent on factors such as species, location, year, and bloom intensity. They range widely in size, as salps can reach up to 10 cm in length, and their colony chains can be as long as a few meters (Bone, 1998; Wrobel and Mills, 1998), making them capable of producing large, dense fecal pellets. Larvaceans can contribute to the sinking particulate pool through rapid disposal of their mucopolysaccharide-comprised houses, while salps and doliolids are efficient at digesting and packaging dense fecal pellets that can propagate down the water

column quickly. Sinking rates have been estimated from 450 to 1,210 m day^{-1} for these groups (Bruland and Silver, 1981; Silver et al., 2003; Robison et al., 2005), accounting for rapid vertical export of organic carbon to the bathypelagic. Given the fragility of gelatinous larvacean houses, past studies have indicated that they do not survive collection in sediment traps, leading to a potential underestimate of true carbon flux (Robison et al., 2005). Conservative estimates of the contribution to POC flux by larvacean houses was 7.6 g C m^{-2} yr^{-1} in Monterey Bay along the central California coast, where estimates for total export by sediment traps in that area were 14.4–24.0 g C m^{-2} yr^{-1}, highlighting the potential magnitude of POC supply missing in flux estimates (Silver et al., 2003; Robison et al., 2005). The estimate was considered conservative, as the authors stated that sampling was biased toward unfragmented and smaller sinkers. High abundances of these organisms have been observed in various regions, such as the Southern Ocean and the tropical North Pacific, and have been increasing in recent years (Atkinson et al., 2004; Hereu et al., 2010). Their increase in abundance is likely due to their ability to tolerate warmer waters (Atkinson et al., 2004), and in a warming ocean, may be increasingly important to the flux of carbon to depth within various regions of the ocean. From the data in this analysis, the contribution of gelatinous zooplankton to organic carbon export to the deep ocean when high in abundance appears to be quite important.

Sinking Particles Delivering DOC to Depth

Samples for both TOC and DOC were collected and analyzed during spring 2018, when we observed the extensive seasonal bloom of phytoplankton. Comparing the distributions of TOC and DOC provided insight on the impact of particulate carbon on the DOC pool within the bathypelagic ocean. Collection for both parameters was completed only during spring 2018 due to time and funding constraints.

Concentrations of TOC in spring 2018 (**Figure 3D**) were highly anomalous compared to both 2017 observations (lower TOC concentrations) and those previously observed in less productive areas of the North Pacific such as 30°N (Swift et al., 2014), where concentrations are both lower (∼36–38 μmol kg^{-1}) and more homogeneous. Elevated DOC was apparent at similar depths and stations (**Figure 4**) as in the distribution of TOC. For example, at Station P26 at 3,000 m, TOC was 148 μmol kg^{-1} and DOC was 50 μmol kg^{-1}, both of which were considerably higher than concentrations observed in wintertime (TOC values of ∼40 μmol kg^{-1}). These observations were evidence of the presence of sinking particulate matter, originally produced by the large phytoplankton bloom, which delivered DOC to depth either through biological modification or physical disaggregation of the particles. As discussed in Section "Contribution of Gelatinous Zooplankton to Organic Carbon Export," high abundances of salps were measured at P26, where we observed the most elevated TOC and DOC concentrations. It appeared that the export of particulate carbon into the bathypelagic originating from salps was particularly susceptible to contributions of organic matter to the bathypelagic. The differences between TOC and DOC were often considerable, beyond the measurement uncertainty of ±1.5 μmol kg^{-1}, indicating particulate matter enrichment at these locations. However, our methods do not provide an accurate measure of particulate organic matter (POC), as that measurement requires filtration of large volumes of water; the difference between TOC and DOC here must be considered as a qualitative representation of particulates in the water column. High levels of fluorescence (∼8 mg m^{-3}) also supported the occurrence of a particularly strong bloom during this year (2018), with the capacity to supply the deeper water column with organic matter. This observation provides evidence for sinking particulate matter to contribute to the bulk DOC pool on a short time scale.

Annual Net TOC Accumulation and Removal Rates

If TOC added to the deeper water column during the spring bloom was removed by heterotrophic respiration, there would be a commensurate decrease in oxygen concentration between spring and summer. However, oxygen in the bathypelagic along Line P increased during both summers (based upon CTD sensor data), likely due to renewal by transport of high oxygen water. This phenomenon overshadowed any observable change in oxygen that was due to biological activity, so we cannot discern whether TOC was remineralized in the water column, transported laterally, or sedimented onto the seafloor, thus leaving the removal mechanism, or combination of mechanisms, uncertain.

Despite this limitation, we can discern the efficiency of these mechanisms, whatever they may be, to accumulate and subsequently remove seasonal TOC to the bathypelagic. In 2017, TOC accumulated from winter to spring at a rate of ∼0.5 μmol kg^{-1} day^{-1}, and was removed at the nearly the same rate (∼0.6 μmol kg^{-1} day^{-1}) from spring to summer (**Figure 8**). The accumulation and removal rates during 2018 were also approximately the same: ∼2.1 μmol kg^{-1} day^{-1}. The rate estimates indicated that most, if not all, of the TOC introduced in

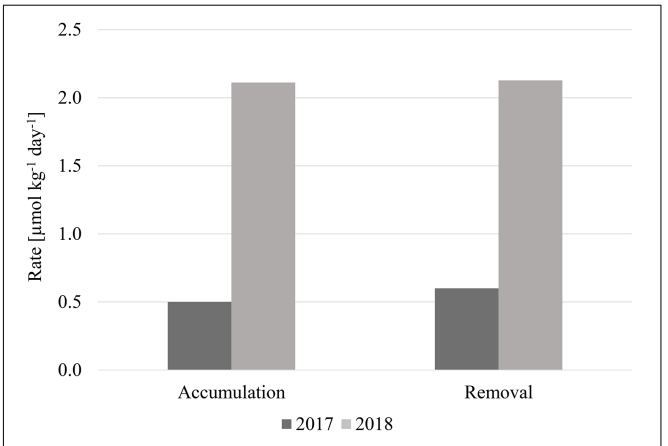

FIGURE 8 | Rates of net seasonal TOC accumulation and removal [μmol kg^{-1} day^{-1}] for 2017 and 2018.

spring is subsequently removed from the water column by summer since the accumulation and removal rates were the roughly same for each respective year. However, the rates for 2018 were four times higher than 2017, supporting the conclusion that a stronger spring phytoplankton bloom occurred during that year. This bloom introduced more organic carbon into the deeper water column, however, it was still efficiently removed by summer despite higher concentrations, demonstrating the proficiency of organic carbon removal within this area.

CONCLUSION

Distributions of TOC in the bathypelagic water column from 2017 and 2018 in the northeastern Pacific indicated high seasonal and spatial heterogeneity, as well as higher and more variable concentrations than those observed in the oligotrophic North Pacific (**Figure 7A**). A correlation between increased concentrations and heterogeneity of both TOC and fluorescence concentrations indicated that organic carbon produced in the upper ocean was vertically exported into the deep ocean. Fueled by a particularly strong phytoplankton bloom in spring 2018 (supported by fluorescence and satellite chlorophyll data), high abundances of gelatinous zooplankton aided in export of quickly sinking particulate matter, which also added DOC to the water column, evidenced by differences in TOC and DOC distributions during this season. Net TOC accumulation and removal rates indicated a fast, efficient removal of recently produced organic carbon, despite higher rates observed in 2018 (0.6 μmol kg^{-1} day^{-1} in 2017, 2.1 μmol kg^{-1} day^{-1} in 2018).

These seasonal observations in organic carbon dynamics shed light on the ability for the northeastern Pacific to produce and export TOC to the bathypelagic water column, as we observed that organic carbon concentrations can change vastly on a relatively short time scale; therefore, we cannot rely solely on single-season distributions to adequately characterize eutrophic ocean systems. Measurements of TOC and DOC at bathypelagic depths across the global ocean typically find low concentrations (38–42 μmol kg^{-1}; Hansell et al., 2009), but these observations often come from few single-season cruises dominated by oligotrophic and typically summer conditions, where the production and export of organic matter is less prominent. Given the observations in this analysis, the addition of both particulate and DOC into their respective bulk pools in the deep ocean may be larger than we are currently accounting for, or that it is more dynamic than we assume. Another critical factor to consider is the influence a warming climate has on production of organic matter, as we have a minimal understanding of its impact on TOC distributions and export, particularly in productive areas where the effect may be greater than within oligotrophic regions (Honjo et al., 2008). The high abundance of gelatinous zooplankton appeared to export high levels of organic matter to the deep ocean on a short timescale, and as these organisms outcompete others in warmer temperatures, they may play a significant role in the sequestration of marine organic matter in the future ocean (Atkinson et al., 2004). Technological advances in our analytical instruments have also improved our ability to discern smaller differences in TOC and DOC concentrations, allowing us to understand oceanic organic carbon variability better. Given such advancements and our constrained knowledge of both seasonality and the impact of climate change, we must be careful not to let limited observations of the ocean in past efforts bias our understanding of current ocean carbon dynamics, as this analysis indicates that productive areas can be quite variable.

DATA AVAILABILITY STATEMENT

The datasets analyzed for this study can be found in the Line P repository (https://www.waterproperties.ca/linep/) or by request to the author.

AUTHOR CONTRIBUTIONS

CL, DH, and MV conceived the idea and designed the project. MR, MG, CL, and SB collected data aboard cruises. CL completed the data analysis and wrote the manuscript. All authors aided in editing.

FUNDING

This work was supported by National Science Foundation Grant OCE 1634250 to DH and OCE 1634009 to MO, as well as NASA Grant 80NSSC18K0437 supporting CL and DH.

ACKNOWLEDGMENTS

We thank the Canadian Department of Fisheries and Oceans for sample collection and providing metadata and zooplankton counts, the crew and science party aboard the CCGS Tully and Laurier, and to Lillian Custals and Abigale Tinari for TOC/DOC analyses. Figures for satellite chlorophyll data were generated by Andrew Margolin.

SUPPLEMENTARY MATERIAL

The Supplementary Material for this article can be found online at: https://www.frontiersin.org/articles/10.3389/feart.2020.00080/full#supplementary-material

REFERENCES

Atkinson, A., Siegel, V., Pakhomov, E., and Rothery, P. (2004). Long-term decline in krill stock and increase in salps within the Southern Ocean. *Nature* 432, 100–103. doi: 10.1038/nature02996

Bif, M. B., and Hansell, D. A. (2019). Seasonality of dissolved organic carbon in the Northeast Pacific Ocean. *Glob. Biogeochem. Cycles* 33, 526–539. doi: 10.1029/2018GB006152

Bone, Q. (ed.) (1998). *The Biology of Pelagic Tunicates*. New York, NY: Oxford University Press, 1–24.

Bruland, K. W., and Silver, M. W. (1981). Sinking rates of fecal pellets from gelatinous zooplankton (Salps, Pteropods, Doliolids). *Mar. Biol.* 63, 295–300. doi: 10.1007/BF00395999

Dickson, A. G., Sabine, C. L., and Christian, J. R. (eds) (2007). Guide to best practices for ocean CO_2 measurements. *PICES Special Publ.* 3, 191.

Druffel, E. R. M., Williams, P. M., Bauer, J. E., and Ertel, J. R. (1992). Cycling of dissolved and particulate organic matter in the open ocean. *J. Geophys. Res.* 97, 15639–15659. doi: 10.1029/92JC01511

Ducklow, H. W., Steinburg, D. K., and Buessler, K. O. (2001). Upper ocean carbon export and the biological pump. *Oceanography* 14, 50–58. doi: 10.5670/oceanog.2001.06

Freeland, H. (2007). A short history of Ocean station Papa and Line P. *Prog. Oceanogr.* 75, 120–125. doi: 10.1016/j.pocean.2007.08.005

Gardner, W. D. (2015). The flux of particles to the deep sea: methods, measurement, and mechanisms. *Oceanography* 10, 116–121. doi: 10.5670/oceanog.1997.03

Hamner, W. M., and Robison, B. H. (1991). In situ observations of giant appendicularians in Monterey Bay. *Deep Sea Res.* 39, 1299–1313. doi: 10.1016/0198-0149(92)90070-A

Hansell, D., and Carlson, C. (1998). Deep-ocean gradients in the concentration of dissolved organic carbon. *Nature* 395, 263–266. doi: 10.1038/26200

Hansell, D. A. (2005). Organic carbon reference material program. *EOS* 86, 318. doi: 10.1029/2005EO350003

Hansell, D. A., and Carlson, C. A. (2001). Biogeochemistry of total organic carbon and nitrogen in the Sargasso Sea: control by convective overturn. *Deep Sea Res. Part II Top. Stud. Oceanogr.* 48, 1649–1667. doi: 10.1016/s0967-0645(00)00153-3

Hansell, D. A., Carlson, C. A., Repeta, D. J., and Schlitzer, R. (2009). Dissolved organic matter in the ocean: a controversy stimulates new insights. *Oceanography* 22, 52–61.

Hereu, C. M., Lavaniegos, B. E., and Goericke, R. (2010). Grazing impact of salp (Tunicata, Thaliacea) assemblages in the eastern tropical North Pacific. *J. Plankton Res.* 32, 785–804. doi: 10.1093/plankt/fbq005

Heron, A. C. (1972). Population ecology of a colonizing species—pelagic tunicate *Thalia democratica*. *Oecologia* 10, 269–293. doi: 10.1007/BF00345733

Honjo, S., Manganini, S. J., Krishfield, R. A., and Francois, R. (2008). Particulate organic carbon fluxes to the ocean interior and factors controlling the biological pump: a synthesis of global sediment trap programs since 1983. *Prog. Oceanogr.* 76, 217–285. doi: 10.1016/j.pocean.2007.11.003

Hu, C., Lee, Z., and Franz, B. A. (2012). Chlorophyll-a algorithms for oligotrophic oceans: a novel approach based on three-band reflectance difference. *J. Geophys. Res.* 117:C01011. doi: 10.1029/2011JC007395

Jiao, N., Herndl, G. J., Hansell, D. A., Benner, R., Kattner, G., Wilhelm, S. W., et al. (2010). Microbial production of recalcitrant dissolved organic matter: long-term carbon storage in the global ocean. *Nat. Rev. Microbiol.* 8, 593–599. doi: 10.1038/nrmicro2386

Li, K., Doubleday, A. J., Galbraith, M. D., and Hopcroft, R. R. (2016). High abundance of salps in the coastal Gulf of Alaska during 2011: a first record of bloom occurrence for the northern Gulf. *Deep Sea Res. Part II* 132, 136–145. doi: 10.1016/j.dsr2.2016.04.009

Matsueda, H., Handa, N., Inoue, I., and Takano, H. (1986). Ecological significance of salp fecal pellets collected by sediment traps in the eastern North Pacific. *Mar. Biol.* 91, 421–431. doi: 10.1007/bf00428636

Pelland, N. A., Eriksen, C. C., and Cronin, M. F. (2016). Seaglider surveys at Ocean Station Papa: circulation and water mass properties in a meander of the North Pacific Current. *J. Geophys. Res. Oceans* 121, 6816–6846. doi: 10.1002/2016JC011920

Robison, B. H., Reisenbichler, K. R., and Sherlock, R. E. (2005). Giant Larvacean Houses: rapid carbon transport to the deep sea floor. *Science* 308, 1609–1611. doi: 10.1126/science.1109104

Schlitzer, R. (2019). *Ocean Data View*. Available online at: https://odv.awi.de (accessed January 30, 2020).

Siegel, D. A., Fields, E., and Buesseler, K. O. (2008). A bottom-up view of the biological pump: modeling source funnels above ocean sediment traps. *Deep Sea Res. Part I Oceanogr. Res. Pap.* 55, 108–127. doi: 10.1016/j.dsr.2007.10.006

Siegel, D. A., Buesseler, K. O., Behrenfeld, M. J., Benitez-Nelson, C. R., Boss, E., Brzezinski, M. A., et al. (2016). Prediction of the export and fate of global ocean net primary production: the EXPORTS science plan. *Front. Mar. Sci.* 3:22. doi: 10.3389/fmars.2016.00022

Silver, M. W., Coale, S. L., Pilskaln, C. H., and Steinburg, D. R. (2003). Giant aggregates: importance as microbial centers and agents of material flux in the mesopelagic zone. *Limnol. Oceanogr.* 44, 498–507. doi: 10.4319/lo.1998.43.3.0498

Smith, K. L. Jr., Ruhl, H. A., Huffard, C. L., Messié, M., and Kahru, M. (2018). Episodic organic carbon fluxes from surface ocean to abyssal depths during long-term monitoring in NE Pacific. *PNAS* 48, 12235–12240. doi: 10.1073/pnas.1814559115

Smith, K. L. Jr., Ruhl, H. A., Kaufmann, R. S., and Kahru, M. (2008). Tracing abyssal food supply back to upper-ocean processes over a 17-year time series in the northeast Pacific. *Limnol. Oceanogr.* 53, 2655–2667. doi: 10.4319/lo.2008.53.6.2655

Stone, J. P., and Steinburg, D. K. (2016). Salp contributions to vertical carbon flux in the Sargasso Sea. *Deep Sea Res. Part 1 Oceanogr. Res. Pap.* 113, 90–100. doi: 10.1016/j.dsr.2016.04.007

Swift, J., Mecking, S., Feely, R., Dickson, A., Carlson, C., Jenkins, W., et al. (2014). *Carbon Dioxide, Hydrographic, and Chemical Data Obtained During the R/V Melville Cruise in the Pacific Ocean on GO-SHIP Repeat Hydrography Sections P02_2013 (21 March – 1 June, 2013)*. Oak Ridge, Tenn: Carbon Dioxide Information Analysis Center, Oak Ridge National Laboratory, US Department of Energy, doi: 10.3334/CDIAC/OTG.GOSHIP_P02_318M20130321

Tabata, S., Thomas, B., and Ramsden, D. (1986). Annual and interannual variability of steric sea level along Line P in the Northeast Pacific Ocean. *J. Phys. Oceanogr.* 16, 1378–1398. doi: 10.1175/1520-04851986016<1378:AAIVOS<2.0.CO;2

Takahashi, K., Ichikawa, T., Fukugama, C., Yamane, M., Kakehi, S., Okazaki, Y., et al. (2015). In situ observations of a doliolid bloom in a warm water filament using a video plankton recorder: bloom development, fate, and effect on biogeochemical cycles and planktonic food webs. *Limnol. Oceanogr.* 60, 1763–1780. doi: 10.1002/lno.10133

Timothy, D. A., Wong, C. S., Barwell-Clarke, J. E., Page, J. S., White, L. A., and Macdonald, R. W. (2013). Climatology of sediment flux and composition in the subarctic Northeast Pacific Ocean with biogeochemical implications. *Prog. Oceanogr.* 116, 95–129. doi: 10.1016/j.pocean.2013.06.017

Wiebe, P. H., Madin, L. P., Haury, L. R., Harbison, G. R., and Philbin, L. M. (1979). Diel vertical migration by *Salpa aspersa* and its potential for large-scale particulate organic matter transport to the deep sea. *Mar. Biol.* 53, 249–255. doi: 10.1007/BF00952433

Wong, C. S., Whitney, F. A., Crawford, D. W., Iseki, K., Matear, R. J., Johnson, W. K., et al. (1999). Seasonal and interannual variability in particle fluxes of carbon, nitrogen and silicon from time series of sediment traps at Ocean Station P, 1982–1993: relationship to changes in subarctic primary productivity. *Deep Sea Res. Part II Top. Stud. Oceanogr.* 46, 2735–2760. doi: 10.1016/S0967-0645(99)00082-X

Wrobel, D., and Mills, C. (1998). *Pacific Coast Pelagic Invertebrates: A guide to the Common Gelatinous Animals*. Monterey, CA: Sea Challengers.

Conflict of Interest: The authors declare that the research was conducted in the absence of any commercial or financial relationships that could be construed as a potential conflict of interest.

frontiers in Earth Science

ORIGINAL RESEARCH
published: 21 April 2020
doi: 10.3389/feart.2020.00074

Deep Ocean Particle Flux in the Northern South China Sea: Variability on Intra-Seasonal to Seasonal Timescales

Shiru Tan[1,2], Jingjing Zhang[2,3], Hongliang Li[2], Lin Sun[2], Zezhou Wu[2], Martin G. Wiesner[2], Hao Zheng[1] and Jianfang Chen[2,4]**

[1] Ocean College, Zhejiang University, Zhoushan, China, [2] Key Laboratory of Marine Ecosystem Dynamics, Second Institute of Oceanography, Ministry of Natural Resources, Hangzhou, China, [3] Southern Marine Science and Engineering Guangdong Laboratory (Zhuhai), Zhuhai, China, [4] State Key Laboratory of Satellite Ocean Environment Dynamics, Second Institute of Oceanography, Ministry of Natural Resources, Hangzhou, China

OPEN ACCESS

Edited by:
Maureen H. Conte,
Bermuda Institute of Ocean Sciences, Bermuda

Reviewed by:
Kazuhiko Matsumoto,
Japan Agency for Marine-Earth Science and Technology (JAMSTEC), Japan
Ronny Lauerwald,
Université libre de Bruxelles, Belgium

***Correspondence:**
Hongliang Li
lihongliang@sio.org.cn
Jianfang Chen
jfchen@sio.org.cn

Specialty section:
This article was submitted to Biogeoscience, a section of the journal Frontiers in Earth Science

Received: 05 October 2019
Accepted: 28 February 2020
Published: 21 April 2020

Citation:
Tan S, Zhang J, Li H, Sun L, Wu Z, Wiesner MG, Zheng H and Chen J (2020) Deep Ocean Particle Flux in the Northern South China Sea: Variability on Intra-Seasonal to Seasonal Timescales. Front. Earth Sci. 8:74. doi: 10.3389/feart.2020.00074

Based on a time-series sediment trap observation at a depth of 1,003-m in the northern South China Sea from 2014 to 2015, we used sinking particle flux combined with remote sensing-derived environmental data to infer the mechanisms of the biological carbon pump. Total particle flux, particulate organic carbon, $CaCO_3$, and lithogenic (inorganic) fluxes peaked in winter and autumn but showed minima in summer, ranging from 59.7 to 413.2 mg m^{-2} d^{-1}, 2.1 to 18.2 mg m^{-2} d^{-1}, 32.9 to 197.9 mg m^{-2} d^{-1}, and 12.0 to 73.6 mg m^{-2} d^{-1}, respectively. Similarly, opal flux varied from 6.9 to 109.6 mg m^{-2} d^{-1}, with a prominent peak in winter and minimum in summer. However, a secondary maximum of opal in autumn was barely noticeable compared with other components. A deeper mixed-layer depth related to the northeast monsoon and surface cooling, overlapping with the effect of cyclonic eddies, is responsible for strong winter fluxes. When an anticyclonic eddy suppresses the subsurface nutrient supply, primary production and subsequent export flux in summer were reduced substantially. With respect to maximum lithogenic and $CaCO_3$ fluxes in autumn, a large aerosol optical depth suggests scavenging and mineral ballast effects as potential causes. This study highlights the importance of intra-seasonal physical processes (e.g., mesoscale eddies and aerosol deposition) to the deep particle flux in the South China Sea, as well as monsoonal transition.

Keywords: particle flux, biological pump, monsoon, mesoscale eddy, South China Sea

INTRODUCTION

The overuse of fossil fuels by human activities and the destruction of the natural environment such as deforestation has increased the atmospheric concentration of CO_2 from 280 ppm before the Industrial Revolution, to around 406 ppm today[1]. This has led to global warming and a rise in sea level. Among the most important factors driving global atmospheric concentration of CO_2 and climate change during the glacial-interglacial period were biogeochemical processes in the ocean

[1]https://scripps.ucsd.edu/programs/keelingcurve/

(Broecker, 1982; Sigman and Boyle, 2000). The key to the removal of atmospheric CO_2 is the marine "biological pump" in which oceanic photosynthetic organisms take up inorganic matter as inorganic carbon and inorganic nutrients to synthesize particulate organic matter and export it to the deep sea (Volk and Hoffert, 1985).

Most of the settling particulate organic carbon (POC) in the deep ocean is composed of fine organic residues, including phytoplankton debris and zooplankton fecal pellets. In general, the export of organic matter from surface water is mainly controlled by net primary productivity (NPP) in the euphotic layer (Eppley and Peterson, 1979), particle sinking, and degradation rates (Francois et al., 2002). First, the NPP level is subjected to physical processes of different spatial and temporal scales that regulate the supply of nutrients to the overlying water, affecting the type and flux of subsequent carbon export (Nair et al., 1989; Archer and Maier-Reimer, 1994; Honjo et al., 1999). Next, biogenic (calcium carbonate, $CaCO_3$ and biogenic silica, opal) and lithogenic (aluminosilicates for example) minerals in the ocean have an impact on the formation, sedimentation, and preservation of POC (Armstrong et al., 2002; Francois et al., 2002; Klaas and Archer, 2002; Passow et al., 2006). When a mineral aggregated with POC, it had a "ballasting effect" on the particle. On one hand, it can increase the density of the settling particles, thereby accelerating the sinking rate. In addition, the mineral can provide physical protection and reduce the microbial degradation of organic matter (Lee et al., 2009). On a global scale, this effect is most relevant to the flux of biogenic minerals, especially $CaCO_3$ (Klaas and Archer, 2002; Barker et al., 2003), but in the marginal seas strongly affected by trade winds, monsoons and large rivers, like the Atlantic coastal regions, POC export is remarkably influenced by the ballast effect of lithogenic material from atmospheric deposition (Fischer and Karaka, 2009; Salter et al., 2010).

Located between the western Pacific warm pool and Qinghai–Tibet Plateau, the South China Sea (SCS) has an area of $\sim 3.5 \times 106$ km^2 and maximum water depth of ~5,500 m. The sea receives intense solar radiation and there is high sea surface temperature (SST) year-round, resulting in a strong vertical stratification of the water. The SCS is a typical surface oligotrophic area with surface nitrate, phosphate and silicate concentration below 1, 0.1, and 5 μmol/L, respectively (Wong et al., 2002) and of weak productivity (Liu et al., 2002; Wong et al., 2007). Because of distinct land–sea thermal differences, the East Asian monsoon prevails over the SCS. Under the persistent influence of monsoonal winds, a large-scale cyclonic circulation gyre develops across the entire SCS during the winter (northeast) monsoon and an anticyclonic circulation gyre covering the southern half of the sea during the summer (southwest) monsoon (Shaw and Chao, 1994; Xue et al., 2004). Meanwhile, there is upwelling along the Sunda Shelf and off Luzon Island of the Philippines during winter and off the southeastern coasts of the Indochinese Peninsula during the summer monsoon (Liu et al., 2002; Xie et al., 2003). At present, the long-term record of total particulate flux (TPF), POC, $CaCO_3$, and opal fluxes based on sediment traps in the northern SCS shows a distinct winter maximum pattern (Wiesner et al., 1996; Wong et al., 2007). The pronounced winter peak might be induced by the combined interaction of surface cooling and wind-induced mixing, which pumps eutrophic subsurface water to the euphotic layer and promotes primary production (Tseng et al., 2005). Findings from sediment trap samples in the SCS area have shown a strong winter signal in amino acid fluxes (Lahajnar et al., 2007), $\delta^{18}O$ of planktonic foraminifera (Lin et al., 2004, 2011), mean $\delta^{15}N$ values at various depths (Kao et al., 2012), nitrogen flux (Gaye et al., 2009), downward fluxes of coccoliths (Ran et al., 2015), and ^{210}Pb flux which correlates with particulate fluxes positively (Chung et al., 2004). Besides the winter peak, the central SCS has a secondary maximum of downward carbon fluxes during the summer monsoon (Lahajnar et al., 2007). Notwithstanding a lack of consensus, the summer secondary maximum may be driven by the horizontal advection of nutrients and biogenic particles from the summer jet off Vietnam to the central basin (Chen and Wang, 2015).

Moreover, the monsoon transports numerous airborne particles from the Asian mainland (Duce and Tindale, 1991). Studies have revealed that atmospheric dust from the eastern Asian continent can be carried distances in excess of 1,000 km (Wang et al., 2011). Dust input not only acts as mineral ballast material but also transfers macronutrients and bio-available iron to oligotrophic surface water (Wong et al., 2007; Zhang et al., 2018), which can stimulate the growth of phytoplankton in the upper layer. Owing to the uncertainty of dust loading time and scarcity of *in situ* investigations, the relationship between atmospheric input in the SCS and carbon export in the deep sea is not sufficiently explicit and has received inadequate attention. Furthermore, a high frequency of mesoscale eddies affects the biogeochemistry of the SCS (Xiu et al., 2010). Cyclonic eddies can replenish nutrients by central upwelling and trigger phytoplankton blooms, whereas anticyclonic eddies may suppress phytoplankton growth (Ning et al., 2004). The episodic strong sinking flux during the inter-monsoon period and deviation of inter-annual variations of long-term data both suggest that POC export in the SCS is not only dominated by monsoon transience but also governed by intra-annual physical processes such as aerosol deposition, mesoscale eddies, tropical cyclones, and short-term internal waves. The relationship between physical forcing and the biological pump for seasonal scale in this unique marginal sea is worth further exploration.

We aroused questions for the seasonal scales like: is monsoon transition being the most contributive and significant factor to the northern SCS all year around? Are these intra-annual physical processes overlapped with monsoon or functioned separately? Will marginal sea respond to some result of anthropogenic activity like dust deposition just in time? Through 1-year *in situ* investigation data from sediment traps, our study focuses on seasonal variations of settling particulate flux in the mesopelagic SCS. Factors affecting temporal variations of carbon export are analyzed, which aids understanding of the biological pump in response to intra-annual physical processes and the rapid change of global climate.

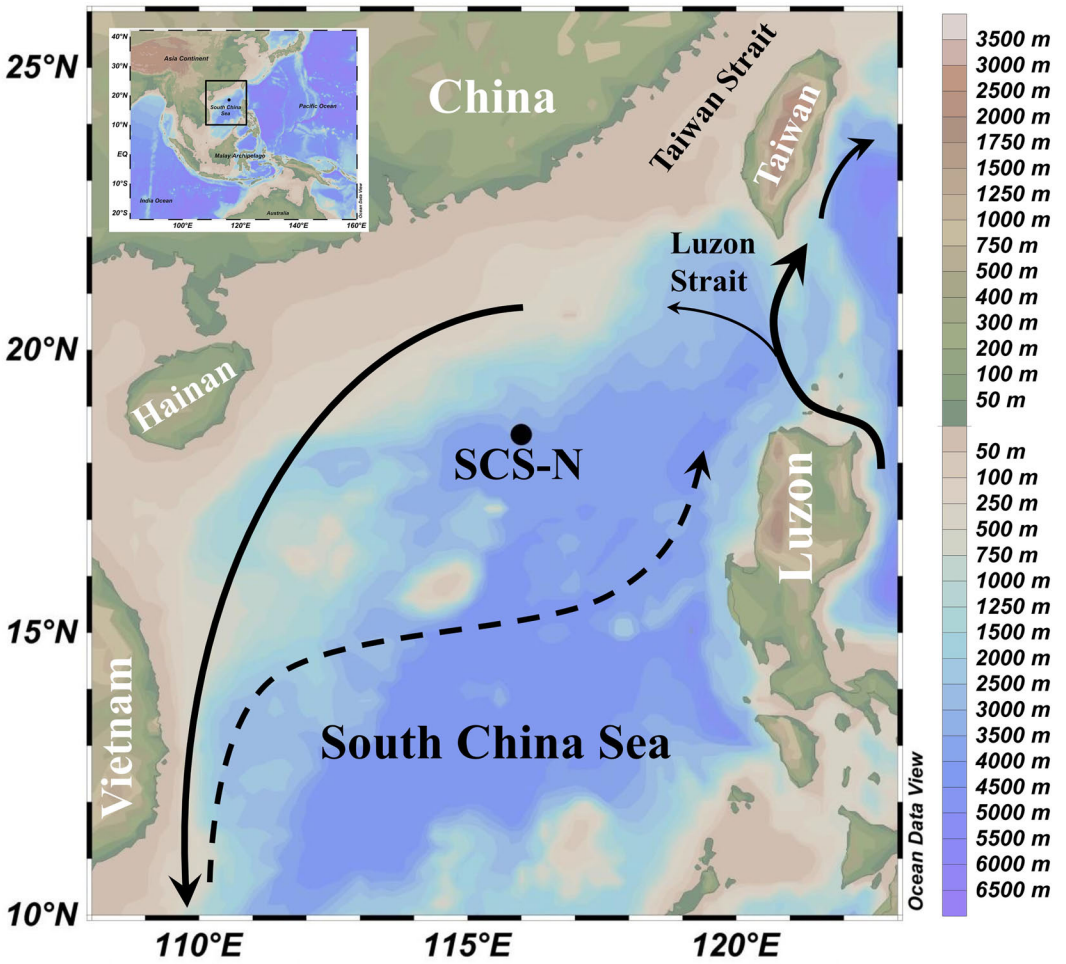

FIGURE 1 | Location of SCS-N sediment trap mooring station in northern SCS (116.0°E, 18.5°N). Solid line with arrow indicates basin-wide winter cyclonic gyre in northern SCS and Kuroshio with its intrusions around Luzon Strait. Dashed line represents eastward jet off the coast of Vietnam in summer. Overview map at upper left shows location of SCS, and black box represents the study area.

MATERIALS AND METHODS

Sample Collection

Our data were obtained from a Mark VI (McLane, United States) time-series sediment trap deployed in the northern SCS (116.0°E, 18.5°N) at depth 1,003 m, from May 01, 2014 to April 06, 2015 (**Figure 1**). The collection area and sampling interval of the sediment trap were 0.5 m^2 and 17 days, respectively. According to the sample collection and processing procedure described by Wiesner et al. (1996) and Li et al. (2017), 250-ml polyethylene sampling bottles were filled with trap-depth filtered seawater, with analytical grade NaCl (35 g l^{-1}) and $HgCl_2$ (3.3 g l^{-1}) added prior to deployment. This was aimed at minimizing diffusive processes and hindering microbial degradation in the trapped material. After recovery, wet samples were sifted through a 1-mm mesh nylon sieve to eliminate zooplankton that accidently entered the bottle. The <1 mm fractions were subsequently split into four equivalent aliquots by a high-precision rotary splitter (McLane WSD-10) and filtered by pre-weighed polycarbonate filters (0.45-μm pore size). These filtered samples were dried at 45°C for 72 h, and the dry weights were used for measuring total particle flux.

Elemental Analysis

The elemental analytical procedures were implemented by Wiesner et al. (1996); Lahajnar et al. (2007), and Li et al. (2017). Particulate total carbon (TC) and particulate nitrogen (PN) were measured by a Carlo Erba Science 1500 CNS Analyzer, whose running standard deviations were <0.15% for carbon and <0.005% for nitrogen. POC samples were treated by 1 M HCL and centrifuged six times to ensure that all carbonate carbon was removed. $CaCO_3$ fluxes were taken to be change in TC and POC.

Biogenic silica analysis followed the modified methods described by Mortlock and Froelich (1989) and Wiesner et al. (1996). Briefly, the dry samples were first treated with 1 M HCl and H_2O_2 (10%) to remove carbonate together with organic matter. Then, Na_2CO_3 solution (7%) was used to leach samples in a water bath at 85°C for 5 h. The dissolved silicate concentration

in the supernatant was analyzed by spectrophotometer using the silicomolybdenum blue method. The water content of biogenic opal was assumed to be 10% (Mortlock and Froelich, 1989), so biogenic silica was calculated from the Si concentration by multiplying by 2.4 (water-bound coefficient). The fluxes of lithogenic matter were obtained by subtracting other component fluxes (carbonate, organic matter, and biogenic opal) from the total sample fluxes.

Remote-Sensing and Modeling Data

In order to infer the mechanisms of seasonal variation for the biological carbon pump, remote sensing-derived environmental data were attained from satellite and model analyses. Wind speed (WS) data with spatial resolution 1/4° × 1/4° were obtained from the National Oceanic Data Center of the National Oceanic and Atmospheric Administration (NOAA[2]) for May 2014 to April 2015. The presented WS data were computed from the daily dataset. SST was calculated from a daily value of 0.25° × 0.25° resolution from Advanced Very High Resolution Radiometer (AVHRR) from NOAA. Net heat flux (NHF) data with spatial resolution 1.0° × 1.0° for the same period were taken from the NCEP/NCAR Reanalysis of Surface Flux Dataset provided by the NOAA Earth System Research Laboratory. Daily average surface chlorophyll-a (Chl-a) concentrations were provided by the NASA Ocean Biogeochemical Model with 0.67° × 1.25° horizontal resolution. Mixed-layer depth (MLD) and NPP of the euphotic layer were calculated from the Hybrid Coordinate Oceanic Circulation Model on the Ocean Productivity website[3], with 1/4° × 1/4° resolution. Aerosol optical thickness (AOT) was downloaded from the National Aeronautics and Space Administration[4] with 4-km horizontal resolution. Sea surface height anomaly (SSHA) data of 1/4° × 1/4° resolution were from the Archiving, Validation, and Interpretation of Satellite Data in Oceanography (AVISO[5]). Precipitation was derived from the Aerial Imagery for Roof Segmentation dataset of the Asia-Pacific Data Research Center[6], with 1.0° × 1.0° horizontal resolution.

RESULTS

Particle Fluxes

Time-series sediment trap data are shown in **Figure 2**. TPF at 1,003-m depth in the northern SCS ranged from 59.7 to 413.2 mg m^{-2} d^{-1} (**Figure 2A**), with a prominent peak during December 2014–January 2015 and a secondary maximum (196.0 mg m^{-2} d^{-1}) during October–November 2014. Bulk fluxes during spring and summer were <100 mg m^{-2} d^{-1} except in May (120.4 mg m^{-2} d^{-1}), and the minimum (59.7 mg m^{-2} d^{-1}) was recorded in July. TPF were mainly composed of carbonate (40–58%), and lithogenic matter also comprised a large proportion (14–40%) (**Figure 3A**). An exception was February 2015, which had a large proportion of biogenic opal (32%), greater than that of lithogenic matter (20%, **Figure 3A**).

Similar to total particulate fluxes, POC, $CaCO_3$, and lithogenic fluxes peaked in winter and autumn, but had small values in summer, with respective ranges 2.1–18.2, 32.9–197.9, and 12.0–73.6 mg m^{-2} d^{-1} (**Figures 2B,C,E**, respectively). The seasonal distributions of POC and $CaCO_3$ fluxes were nearly identical, with both maximizing in January 2015 and a small peak in October (91.5 mg m^{-2} d^{-1} for $CaCO_3$ fluxes and 9.1 mg m^{-2} d^{-1} for POC) compared to the winter maximum. The only difference was a pronounced minimum of POC fluxes in July, whereas $CaCO_3$ fluxes remained nearly constant with small values over the entire summer. Slightly different from POC and $CaCO_3$ fluxes, two peaks of lithogenic matter fluxes in winter and autumn were essentially equal, and the maximum was in autumn (73.0 mg m^{-2} d^{-1} in winter and 73.6 mg m^{-2} d^{-1} in autumn). Overall small values of lithogenic material in summer fluctuated noticeably. Similarly, biogenic opal fluxes (**Figure 2D**) varied from 6.9 to 109.6 mg m^{-2} d^{-1}, with a prominent peak in winter and minimum in summer. However, the secondary maximum of opal in autumn was barely noticeable compared to other components. Mole ratio of opal/$CaCO_3$ in sinking particulate fluxes is shown in **Figure 3B** with minimum in November, 2014 and maximum in February, 2015.

Particulate nitrogen fluxes from 28 January through 13 February maximized at 2.6 mg m^{-2} d^{-1}, and the daily mean from 8 December to 2 March was 1.8 mg m^{-2} d^{-1} (**Figure 2F**). A secondary peak in autumn was also notable, with a range of 1.1–1.4 mg m^{-2} d^{-1} and greatest minimum (0.5 mg m^{-2} d^{-1}) were found during summer (July).

Environmental Parameters

Figure 4 shows seasonal variations of environmental data, including SST, WS, NHF, MLD, NPP, Chl-a concentration, SSHA, AOT, and precipitation. There were distinct winter maxima of WS, MLD, NPP, and Chl-a, with ranges of 2.9–14.3 m s^{-1}, 12.6–53.3 m, 235.9–744.0 mg C m^{-2} d^{-1}, and 0.02–0.25 mg m^{-3}, respectively. SST showed the minimum in winter and ranges from 21.8 to 29.9°C. NHF and SSHA exhibited analogous cosine patterns. SSHAs were positive from July through November 2014, with a positive maximum in August and negative at other times, with the negative maximum in January (**Figure 4G**). NHF data were negative from October 2014 through January 2015, with fluctuating positive values in summer (**Figure 4C**). The distribution of AOT (**Figure 4H**) was bimodal in autumn (0.18) and winter (0.16), which nearly matched that of lithogenic matter (**Figure 2E**). Spring had the greatest precipitation (as shown in **Figure 4I**) compared to other seasons and maximum precipitation (89.0 kg m^{-2}) occurred in June.

When the data were analyzed in detail, three periods (1–18 October, 8–24 December, and 28 January to 13 February) were remarkable. First, WS from 1–18 October increased 59% relative to prior levels and NHF changed from negative to positive, both reaching their maximum (absolute) values at the period of 8th to 24th December. The temporal variation of MLD followed those of WS and NHF, with a notable increase of 48% in October and a maximized value

[2]http://www.ncdc.noaa.gov/

[3]http://orca.science.oregonstate.edu

[4]https://oceancolor.gsfc.nasa.gov

[5]https://www.aviso.altimetry.fr

[6]http://apdrc.soest.hawaii.edu

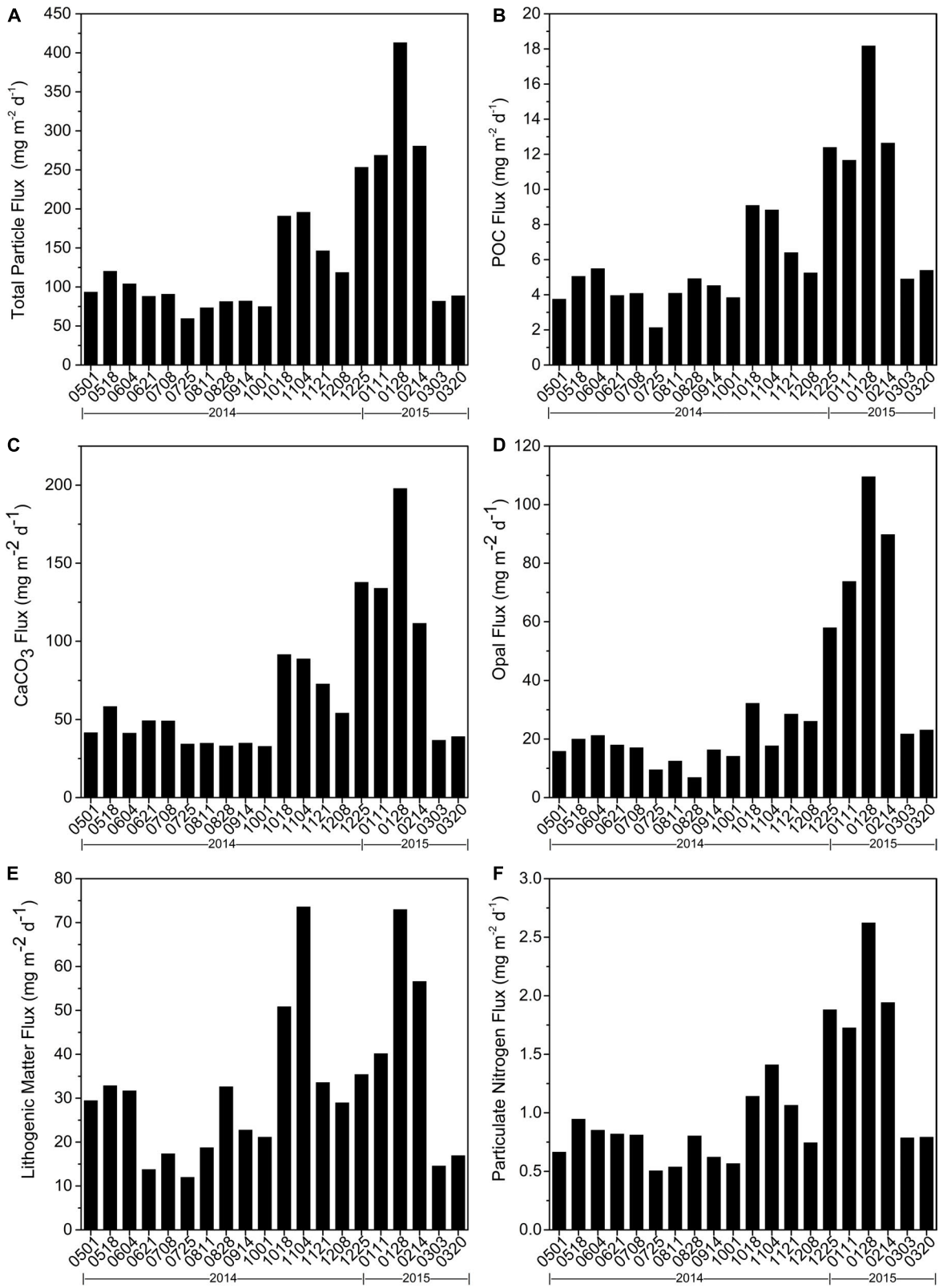

FIGURE 2 | Time Time series of particle fluxes derived from sediment trap at SCS-N station from May 01, 2014 to April 06, 2015. **(A)** total particle flux, **(B)** POC flux, **(C)** $CaCO_3$ flux, **(D)** opal flux, **(E)** lithogenic matter flux, and **(F)** particulate nitrogen flux. Date labels on x axis are marked as mmdd for first date of each sampling period (for this and subsequent similar figures).

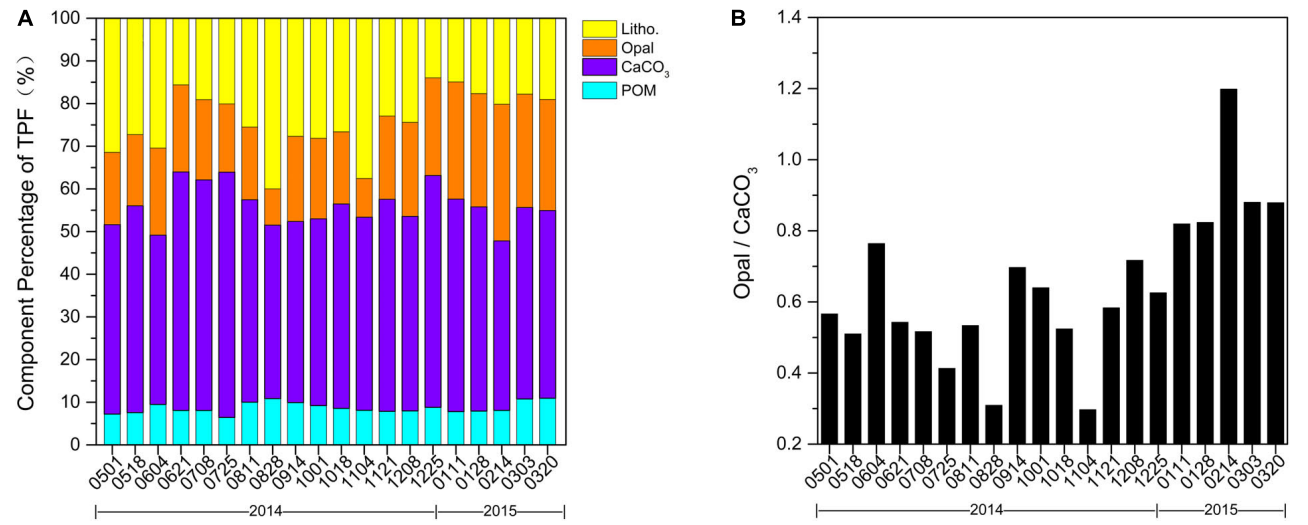

FIGURE 3 | (A) Component percentage of total particle fluxes (TPF) and **(B)** mole ratio of opal/$CaCO_3$ in sinking particulate fluxes at station SCS-N, May 01, 2014 to April 06, 2015. POM symbolizes particulate organic matter.

(53.3 m) from 8–24 December. But MLD was constantly deeper than 50 m in the following 30 days. SST showed obvious winter minimum while NPP and Chl-a concentration had simple winter peaks with maxima from 28 January to 13 February. The largest negative values of SSHA were also during that period.

DISCUSSION

The vast majority of long-term records of mesopelagic and abyssal fluxes based on sediment traps in the northern SCS have depicted a distinct winter maximum pattern and revealed the great influence of the East Asian Monsoon. However, there are a few physical processes that have a potentially strong impact on carbon export at intra-seasonal to seasonal timescales, and the specific influences of these processes have not been clearly revealed. Therefore, we focused on a 1-year observation of settling particulate fluxes and factors adjusting their temporal variations.

We observed maximum fluxes in winter, a secondary peak in autumn, and an abnormal decline in summer. For example, POC fluxes in winter and autumn were 12.0 and 7.0 mg m^{-2} d^{-1}, respectively, 1.6 and 1.2 times greater than the fluxes in 2011-2012. Summer POC flux was only 4.0 mg m^{-2} d^{-1} in contrast to the 5.1 mg m^{-2} d^{-1} in 2011, and was comparable to the flux in the year of El Niño during which the nutrient supply was limited to the photic zone (**Tables 1**, **2**).

The obvious seasonal variations raised several questions, as follows. Are the extremely high export fluxes in winter driven by monsoon-induced water mixing and, if so, is this the only control? Why is there a secondary peak during the inter-monsoon period (October to November) and which process plays the major role? What is the forcing mechanism behind the abnormal small values of POC and $CaCO_3$ fluxes on summer monsoon days?

Controls on Peak Flux in Winter

Vertical Mixing

Our trap data and environmental parameters both displayed obvious winter characteristics (**Figures 2**, **4**). The winter monsoon period represented only 25% of the year but accounted for nearly half of the annual measured fluxes: 46% for TPF, 44% for POC flux, 46% for $CaCO_3$ flux, 57% for opal flux, and 36% for lithogenic matter flux (**Table 1**). TPF, POC, $CaCO_3$, and opal fluxes greatly increased beginning in December by more than 110%, and all components peaked during January 28, to February 13, 2015.

There were also conspicuous increases in environmental data, including WS, MLD, NPP, and surface chlorophyll concentrations. In order to determine the relationship between physical forcing and biogenic activities, we did a Pearson relationship analysis of the data (**Table 3**). First, the MLD maxima correlated closely with WS (positively) and SST (negatively):

$$\mathrm{MLD} = 62.224 + 2.911\mathrm{WS} - 2.041\mathrm{SST},$$
$$(R^2 = 0.874, p < 0.001, N = 20) \quad (1)$$

The multi-linear regression (1) confirmed that the deepening of the mixed layer in the SCS was driven by the combined interaction of convective overturn by surface cooling and wind-induced mixing (Tseng et al., 2005, 2009). The partial correlation coefficients for WS and SST as independent variables to MLD was 0.851 and −0.714 (both $P < 0.01$, **Supplementary Table S3**), indicating the dependent influence of these two on the MLD (the analysis process was presented in **Supplementary Material**).

During the northeast monsoon when the surface water cooled down and the strongest winds occurred over the Strait of Luzon, curving across the SCS basin, the MLD was deepest and broached

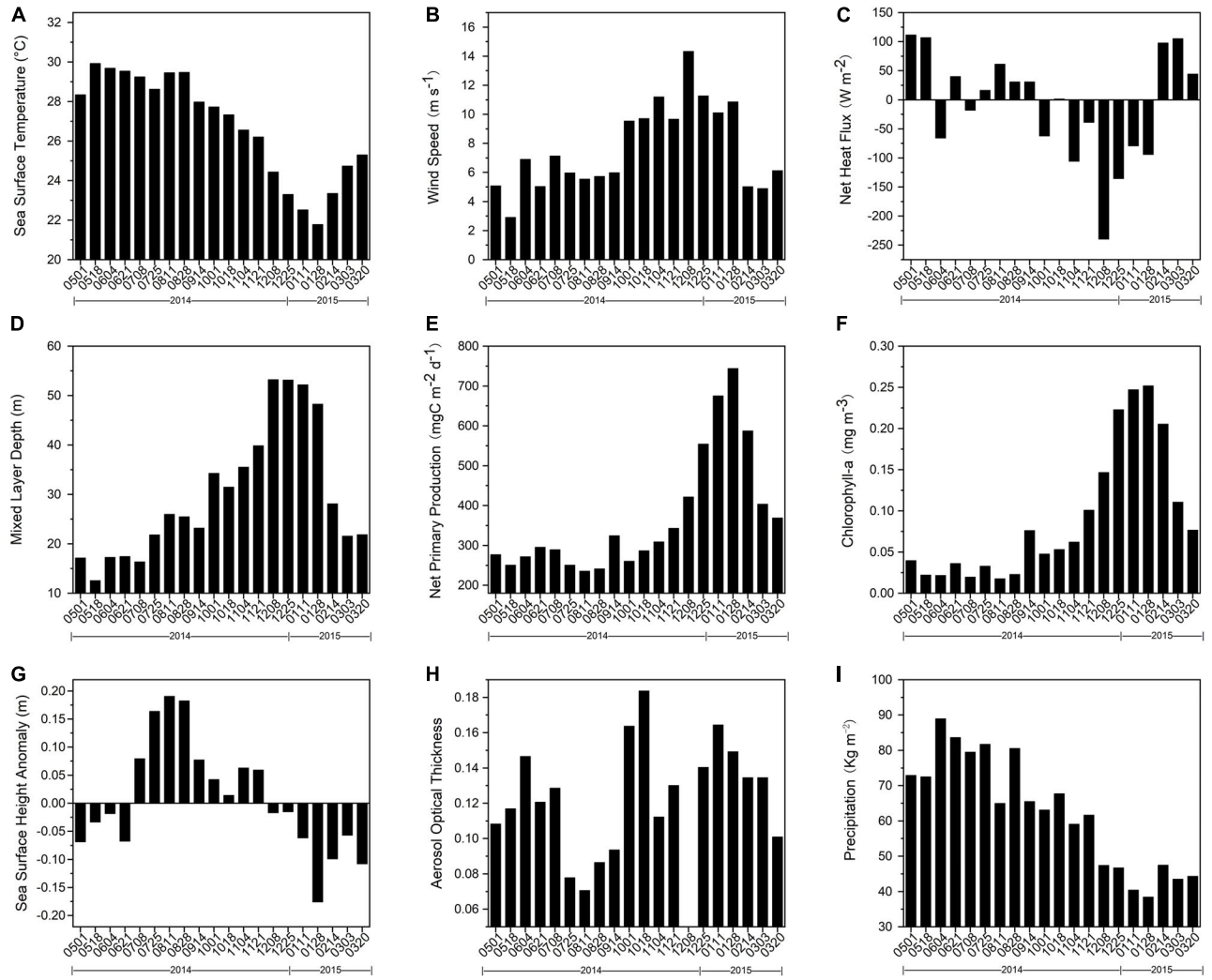

FIGURE 4 | Temporal variations of environmental parameters measured around SCS-N station from May 01, 2014 to April 06, 2015. **(A)** sea surface temperature, **(B)** wind speed, **(C)** net heat flux, **(D)** mixed-layer depth, **(E)** net primary productivity, **(F)** total surface chlorophyll-a concentration (Chlorophyll-a), **(G)** sea surface height anomaly, **(H)** aerosol optical thickness, and **(I)** precipitation.

TABLE 1 | Characteristics of seasonal variations of total particles, POC, $CaCO_3$, opal, lithogenic matter and particulate nitrogen fluxes observed at SCS-N station during May 2014 to March 2015.

			Average daily flux (mg m^{-2} d^{-1}) for each period and percentage of year-round flux (%)			
	1 year total flux (mg m^{-2})	Average daily flux (mg m^{-2} d^{-1})	Baseline condition (non-event period)	Summer 08 July–30 September	Autumn 01 October–7 December	Winter 08 December –01 March
Total particulate matter	49459.4	145.5	96.2 (20%)	77.6 (13%)	152.5 (21%)	267.0 (46%)
POC	2323.4	6.8	4.8 (21%)	4.0 (14%)	7.0 (21%)	12.0 (44%)
$CaCO_3$	23370.0	68.7	44.4 (19%)	37.3 (14%)	71.5 (21%)	127.1 (46%)
Opal	10750.5	31.6	20.0 (19%)	12.5 (10%)	23.2 (15%)	71.5 (56%)
Lithogenic matter	11156.7	32.8	23.2 (21%)	20.7 (16%)	44.8 (27%)	46.8 (36%)
Particulate nitrogen	361.3	1.1	0.8 (23%)	0.7 (15%)	1.0 (20%)	1.8 (42%)

Average daily flux was calculated as average of each sapling period. Proportions of each season of 1-year total flux were calculated by multiplying each average daily flux by its sampling days and dividing by corresponding total flux. Baseline condition was defined as non-event period, which included May 01 to July 07, 2014 and March 02 to April 06, 2015.

TABLE 2 | Comparison of Total particulate fluxes (TPF), POC fluxes and biogenic matter (Bio., sum of organic matter, $CaCO_3$ and opal fluxes) fluxes calculated for different season in 2014–2015, 2009–2010, 2011–2012 (data from Ran et al., 2015; Priyadarshani et al., 2019).

		Summer			Autumn			Winter		
		2009–2010	2011–2012	2014–2015	2009–2010	2011–2012	2014–2015	2009–2010	2011–2012	2014–2015
Duration		**27 June–30 August**	**20 May–08September**	**08 July–30 September**	**15 September–17 November**	**09 September–11 November**	**01 October–07 December.**	**18 November–06 February**	**12 November–15 February**	**08 December–01 March**
TPF	Maximum (mg m^{-2} d^{-1})	97.2	135.2	91.0	202.3	161.6	196.0	294.7	297.4	413.2
	Minimum (mg m^{-2} d^{-1})	45.4	46.6	59.7	56.9	30.9	75.1	56.9	109.9	118.7
	Total amount in the period (mg m^{-2})	6230.7	9331.1	6597.2	7001.3	7698.6	1034.7	17758.3	18463.7	22698.5
	Daily average (mg m^{-2} d^{-1})	77.9	83.3	77.6	109.4	120.3	152.2	185.0	192.3	267.0
	Period total flux/1 year total flux (%)	14.3	21.7	13.3	16.1	17.9	20.9	40.9	42.9	45.9
POC flux	Maximum (mg m^{-2} d^{-1})	4.7	8.3	4.9	9.6	8.8	9.1	12.5	11.6	18.2
	Minimum (mg m^{-2} d^{-1})	2.9	2.8	2.1	2.5	1.4	3.8	2.5	3.8	5.3
	Total amount in the period (mg m^{-2})	322.0	572.8	336.1	311.4	366.2	479.2	698.7	705.1	1022.3
	Daily average (mg m^{-2} d^{-1})	4.0	5.1	4.0	4.9	5.7	7.1	7.3	7.3	12.0
	Period total flux/1 year total flux (%)	17.7	29.3	14.5	17.1	18.7	20.6	38.5	36.1	44.0
Bio. flux	Maximum (mg m^{-2} d^{-1})	84.3	91.9	73.6	139.6	112.1	140.2	240.2	195.7	340.2
	Minimum (mg m^{-2} d^{-1})	38.9	33.0	47.7	44.9	25.9	54.0	42.2	82.3	87.9
	Total amount in the period (mg m^{-2})	5056.3	6970.9	4837.3	5309.8	5114.2	7300.3	13081.8	14101.8	18717.2
	Daily average (mg m^{-2} d^{-1})	63.2	62.2	56.9	83.0	79.9	107.4	136.3	146.9	220.2
	Period total flux/1 year total flux (%)	16.0	22.2	12.6	16.8	16.3	19.1	41.5	45.0	48.9

Total amount was calculated as the sum of each period and daily average fluxes were calculated as average of each sapling period.

TABLE 3 | Pearson correlation coefficient (*R*) between daily total particle flux (TPF), particulate organic carbon (POC), $CaCO_3$ fluxes, opal fluxes, lithogenic matter fluxes (Litho. Mat.), surface chlorophyll-a concentration (Chl-a), mixed layer depth (MLD), net primary production (NPP), sea surface temperature (SST), wind speed (WS) and net heat flux (NHF) at SCS-N site.

	TPF	POC	$CaCO_3$	Opal	Litho. Mat.	Chl-a	MLD	NPP	SST	WS	NHF
TPF	1	0.99**	0.99**	0.94**	0.82**	0.84**	0.64**	0.88**	−0.77**	0.46*	−0.34
POC		1	0.97**	0.94**	0.81**	0.84**	0.65**	0.88**	−0.79**	0.45*	−0.34
$CaCO_3$			1	0.92**	0.76**	0.84**	0.68**	0.87**	−0.76**	0.50*	−0.39
Opal				1	0.64**	0.90**	0.58**	0.94**	−0.82**	0.32	−0.23
Litho. Mat.					1	0.50*	0.46*	0.52*	−-0.49*	0.44	−0.31
Chl-a						1	0.78**	0.98**	−0.95**	0.50*	−0.41
MLD							1	0.69**	−0.77**	0.88**	−0.79**
NPP								1	−0.92**	0.42	−0.34
SST									1	−0.55*	0.41
WS										1	−0.94**
NHF											1

*The annotation ** designates significant correlation at 0.01 level ($p < 0.01$), and * shows significant correlation at 0.05 level ($p < 0.05$).*

the nutricline, which was recorded at 60 m year-round at the nearby SEATS station (115.5°E, 18.3°N, 0.5° south of station SCS-N) (Wong et al., 2007). Thus, the strengthened vertical mixing overturned subsurface nutrients into the overlying oligotrophic water and stimulated phytoplankton growth as indicated by maximized Chl-a during December 2014 to January 2015. The correlation between NPP and MLD ($r = 0.688$, $p < 0.01$) effectively confirmed the above process. The increase in surface productivity hence generated more numerous downward particles than in any other period.

Our data concurred with discoveries of previous studies in this area. An intensified upward nutrient supply in winter was certified by the increase of $\delta^{15}N$ in suspended particulate matter (Kao et al., 2012) and minimum $\delta^{13}C$ values with relatively large $\delta^{18}O$ values of planktonic foraminifera (Lin et al., 2004, 2011). Primary production rates in winter were estimated at 545.2 ± 408.2 mg C m^{-2} d^{-1} (Ning et al., 2004), in contrast with the 465.8 mg C m^{-2} d^{-1} annual average at the SEATS station (Ning et al., 2004). About 12% of the primary production (38.4–68.5 mg C m^{-2} d^{-1}) is said to be exported (Liu et al., 2002), and POC fluxes from the euphotic zone were reported at a large value of 44.4 mg m^{-2} d^{-1} in January (Cai et al., 2015). Deep ocean fluxes were recorded at station SCS-N by Lahajnar et al. (2007) during 1987–1988, and by Ran et al. (2015) during 2009–2010. Both showed peak POC fluxes from November through January (4.9 mg m^{-2} d^{-1} in 1987 and 12.5 mg m^{-2} d^{-1}in 2009), in accord with our data for 2014–2015.

However, total particulate fluxes in winter 2014–2015 were much higher in maximum, average daily values and total winter fluxes amount than in 2009–2010 and 2011–2012, as presented by Ran et al. (2015) and Priyadarshani et al. (2019), respectively. The comparison was listed in **Table 2**. The maximum amount of particulate fluxes in winter was 413.2 mg m^{-2} d^{-1} with a daily average of 267.0 mg m^{-2} d^{-1} while the maximum values in 2009 and 2011 were 294.7 and 297.4 with a daily average of 185.0 and 192.3 mg m^{-2} d^{-1}, respectively. The winter period daily flux in POC and opal in 2014 were 1.7- and 1.5-fold to those in 2009 (7.3 mg m^{-2} d^{-1} for POC and 48.2 mg m^{-2} d^{-1} for opal fluxes, respectively) (Priyadarshani et al., 2019). Despite the fact that the winter period in 2014 (85 days) was shorter than in 2009 and 2011 (96 days), POC flux in winter 2014 accounted for 44% of annual total POC flux and was larger than those in 2009 and 2011 (38 and 36%, respectively). In contrast to the strengthened sediment fluxes, the environmental parameters showed little differences. The average annual wind speed was comparable (7.1 m s^{-1} for 2009–2010 and 7.6 m s^{-1} for 2014–2015), indicating little difference in monsoon strength. MLD were around 50 m for both 2009–2010 and 2014–2015. The MLD was even deeper in the winter of 2011–2012 (>70 m) (Priyadarshani et al., 2019). Thus, the question arose as to why the fluxes in 2014 were so much higher than other years under similar monsoon conditions.

Additionally, there were slight mismatches in the timing of MLD, Chl-a, and downward fluxes, whereas there were good time relations in previous years (Ran et al., 2015; Li et al., 2017; Priyadarshani et al., 2019). No distinct time lag (longer than 1 month) here may be owing to a characteristic of marginal sea where huge terrestrial materials in the particles are large enough to accelerate the settling velocity (Goutx et al., 2007). The time mismatches in our study were too obvious to be ignored. First, the maximum surface Chl-a concentration occurred between 28 January and 13 February, about 34 days after the MLD maximum in December. In both 2009–2010 and 2011–2012, surface Chl-a concentration changed almost immediately when MLD changed during winter time (Priyadarshani et al., 2019). Second, bulk fluxes were collected in mid-to-late February, showing POC fluxes at 12.6 mg m^{-2} d^{-1} (**Figure 2B**) with a MLD just greater than 20 m (**Figure 4D**). In the meantime opal flux was the second highest of the year (**Figure 2D**), and Chl-a concentration was 0.21 mg m^{-3} (**Figure 4F**), 133% greater than average of 0.09 mg m^{-3}. Logically, nutrients cannot be effectively transported by a shoaled MLD, so productivity and export should have been cut off. If the high fluxes collected over the 1,000 depth are caused by the delayed settlement progress in the previous winter bloom, then the high chlorophyll value in the surface layer is contradictory. All these unusual phenomena leave the possibility of another positive mechanism

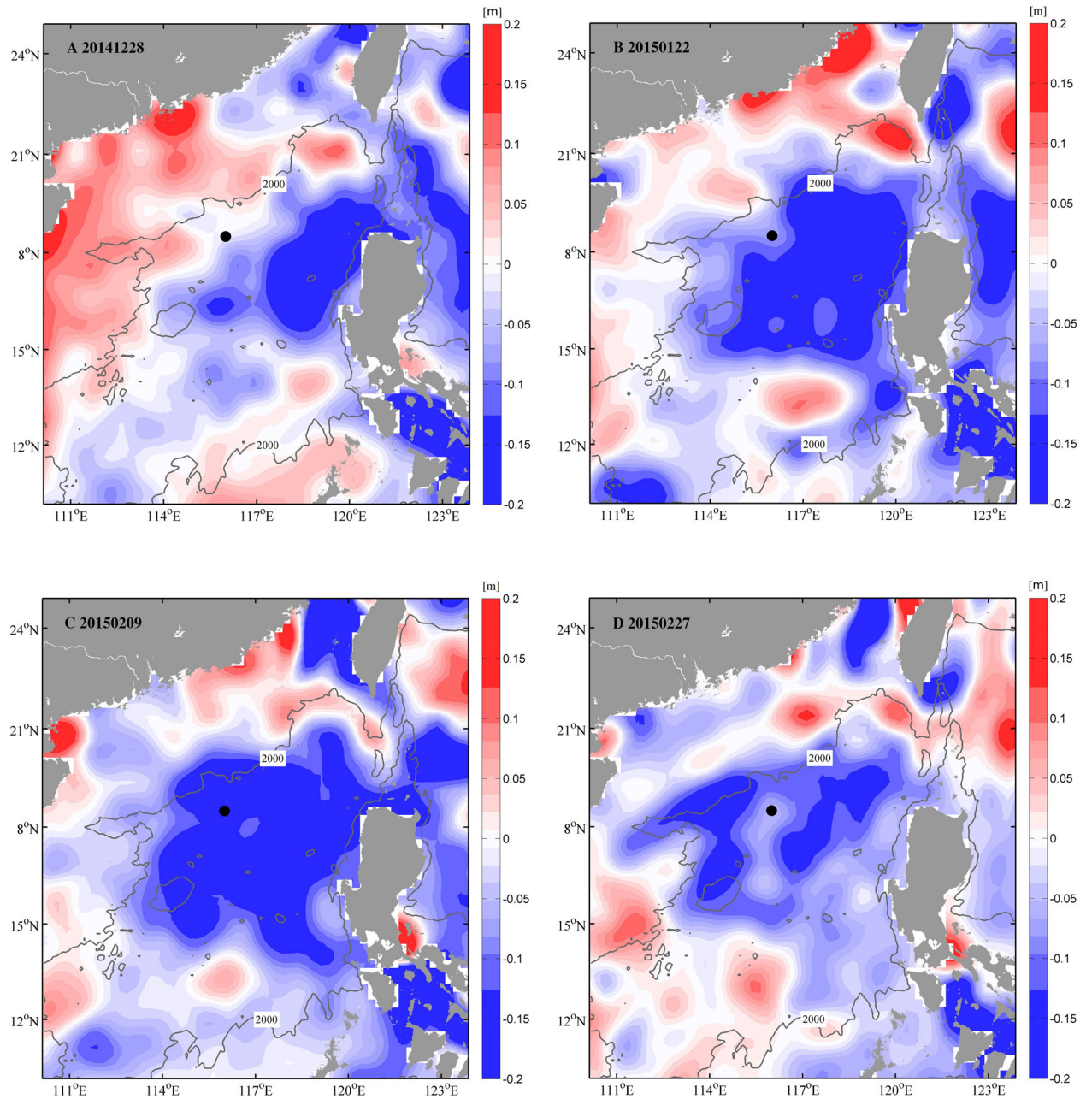

FIGURE 5 | Satellite images of daily sea surface height anomaly (SSHA, m) in northern SCS from AVISO product on **(A)** December 28, 2014, **(B)** January 22, 2015, **(C)** February 09, 2015, and **(D)** February 27, 2015, exhibiting cyclonic eddy activity during winter period of 2014–2015 in study area. Dots on map represent 1/4° × 1/4° grid around station SCS-N and gray line with label 2,000 indicates water isobaths of 2,000 m.

for downward particles superimposed on the primary role of the northeast monsoon.

Cyclonic Eddy

What factors could have contributed to a higher flux than the previous year and the mismatch in timing of the MLD, Chl-a, and downward fluxes.

Mesoscale cyclonic eddies, which can transport nutrients to the surface layer by upwelling within the eddy center (McGillicuddy et al., 1998), seemed to be possible. Indeed, a strong cyclonic eddy appeared to have occurred during the period in the northern SCS, according to subtractive SSHA (**Figure 4G**). Using a manual method of eddy tracking, a relatively large mesoscale eddy (radius = 48–174 km) formed northwest of Luzon Island during mid-December 2014 (**Figure 5A**). This eddy matured about 20 days later and began to split into small eddies during early-to-mid January. During this period the eddy moved westward, but our station was out of its

control. It wasn't until 22 January that the eddy exerted an influence on our station (**Figure 5B**), as shown by a sharp decrease (by 16%) in daily SSHA at SCS-N. One of the small cyclonic eddies that split from the northwest part of the large eddy developed very near our sampling station, beginning 26 January. The central part of the small eddy reached SCS-N in early February during its mature stage (**Figure 5C**). The station SSHA was <-0.18 m beginning 2 February and the minimum SSHA (-0.20 m) appeared between 7 and 9 February (**Figure 6**). This cold-core eddy continued to influence our station through 27 February (**Figures 5D**, **6**). The close match between the kinetic energy of this small eddy and the negative SSHA of our sampling station is a strong indication of cyclonic effects (**Figure 6**).

Cyclonic eddies could remarkably increase surface biomass (Chen et al., 2007; Xiu and Chai, 2011; Wang et al., 2016; Honda et al., 2018). Positive Chl-a anomalies from 1998 to 2011 were associated with cyclonic eddies in the SCS (He et al., 2016). There is phytoplankton enhancement of 10.5% in total Chl-a biomass in water column at the surface layer within the eddy center of SSHA $<$ 0.20 m (Wang et al., 2016). Elevation in productivity caused by cyclonic eddies in spring could even catch up with the maximum level in winter in SCS (Chen et al., 2007).

In our sampling winter period, from the end of January through mid-February, the SCS-N station was affected by a combination of cyclonic eddies and northeast monsoons. Under the resultant strong vertical mixing, the accelerated upward nutrient transport caused by eddy pumping allowed for deeper nutrient replenishment in the mixed layer (He et al., 2016). This replenishment of nutrient conspicuously increased productivity within the euphotic layer and contributed to a higher level in fluxes compared with previous years. Then, from mid-to-late February when the MLD seemed to be shoaled, our station was directly under the eddy center upwelling area. It was found that the water column-integrated biomass of diatoms was 21.3-fold greater at the center of a cyclonic eddy relative to its outside (Wang et al., 2016). The direct nutrient input by upwelling stimulated the growth of phytoplankton in the upper layer as observed in the high concentration of surface chlorophyll, leading to the strong fluxes seen during the sampling period from 14 February through 1 March. The upwelling effect of the cold water may also make the potential temperature line move upward, thus the MLD resulting from potential temperature seems to be shoaled. Further, one biological signal of the cold-core eddy is that it functioned preferentially as a selective silica pump (Thunell et al., 2007), although calcareous plankton may also benefit. Li et al. (2017) revealed that the cyclonic eddy in the SCS could contribute to 44–59% of opal and 17–54% of POC fluxes. The daily average opal fluxes in winter in our sampling time was 71.5 mg m^{-2} d^{-1} with a percentage of period to the annual amount as 56% in contrast to the number of 48.2 mg m^{-2} d^{-1} (43%) in 2009–2010 and 49.2 mg m^{-2} (44%) in 2011–2012 (Priyadarshani et al., 2019). The period daily average flux of $CaCO_3$ also increased to 127.1 mg m^{-2} d^{-1} in contrast to 74.9 mg m^{-2} d^{-1} (2009-2010) and 84.4 mg m^{-2} d^{-1} (2011-2012), while the percentage of period to the annual amount in $CaCO_3$ showed little difference (41-48%).

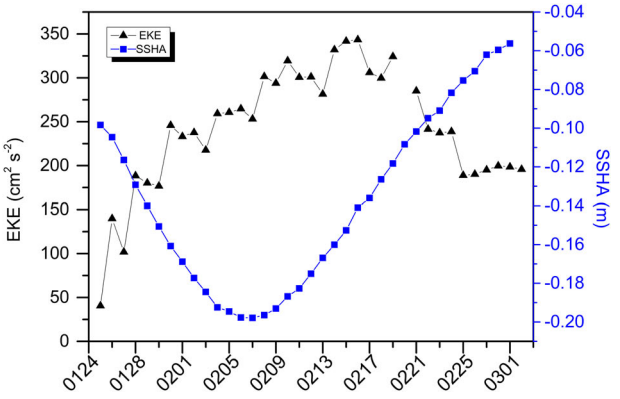

FIGURE 6 | Variations of eddy kinetic energy (EKE) at center of relatively small mesoscale cyclonic eddy (split from the original large one) near station SCS-N, using manual tracking method and daily sea surface height anomaly (SSHA) of 1/4° × 1/4° grid area around sampling station from January 25, to March 02, 2015.

The mole rate of opal/$CaCO_3$ was over 0.8 since January and the maximum of 1.3 appeared in mid-to-late February (**Figure 3B**). The maximized biological signal of cyclonic eddies in mid-to-late February was due to the direct influence of eddy upwelling and the weakened monsoon wind. Thus, this mechanism allowed a clear interpretation of secondary maximum opal flux (89.8 mg m^{-2} d^{-1}) and the maximum mole rate of opal/$CaCO_3$ (**Figure 3B**) during mid-to-late February, when the MLD was shallower than 20 m.

Compared with previous years, stronger signal in SSHA was recorded in our sampling year (2014–2015). SSHA data in 2009 and 2011 were >-0.10 m during the winter monsoon period (Ran et al., 2015; Priyadarshani et al., 2019). The larger fluxes in the winter of 2014-2015 compared to previous years were well interpreted by the extra replenishment of nutrients upwelled by cyclonic eddy.

Apart from cold-core eddy, atmospheric aerosol deposition may be another candidate, because strong flux of lithogenic matter and increased aerosol thickness were observed in winter (**Figures 2E**, **4H**). However, little precipitation in the study period impeded atmospheric aerosol reaching the ocean surface (**Figure 4I**). Wet deposition was reported to be the main route for atmospheric deposition in the area (Jung et al., 2011). So, the atmospheric aerosol deposition wasn't the answer to our findings in winter.

A third possibility lies in lateral transportation from the river and the Luzon Strait. First, our study site is distant from any river influence (Wong et al., 2007). In addition, water in the Luzon Strait comes from the West Pacific and has more oligotrophic characteristics than the SCS. An export of 1×10^{11} mol $year^{-1}$ of phosphate and 1.4×10^{12} mol $year^{-1}$ of nitrate is estimated from the SCS to the western Philippine Sea at intermediate depths between 350 and 1,350 m (Chen et al., 2001). Low nutrients cannot support the bloom of diatom and transport as large a flux of opal. However, the ratio of opal/$CaCO_3$ (**Figure 3B**) in our recorded fluxes peaked in February 2015, which showed a

TABLE 4 | Biogenic matter fluxes in sinking particles (calculated as sum of organic matter, $CaCO_3$, and opal fluxes) and particle composition of particulate nitrogen (PN) in biogenic matter fluxes during different seasons of 2014–2015.

Parameter	1-year means	Baseline condition (non-event period)	Summer 08 July–30 September	Autumn 01 October–07 December	Winter 08 December–01 March
Biogenic matter fluxes (mg m^{-2} d^{-1})	112.7	73.0	56.9	107.4	220.2
PN (% of biogenic matter)	1.03	1.11	1.17	0.99	0.81

large amount of diatom growth. Therefore these particles weren't attributed to lateral transportation from the Luzon Strait.

In summary, the winter peak flux in our data was the result of vertical mixing from convective overturn and monsoon, overlapped with a mesoscale cyclonic eddy. Vertical mixing by the winter monsoon played the critical role, while the cold-core eddy also had positive effects. It was precisely because of the coincidence of these factors that winter fluxes during 2014–2015 were much stronger than in previous years. Unfortunately, the contributions of those factors remain uncertain and more research, including *in situ* observation, is necessary for more detailed exploration.

Autumn Secondary Maximum Fluxes Owing to Aerosol Deposition

TPF, $CaCO_3$ flux, and POC flux showed pronounced secondary maxima during the autumn inter-monsoon. Daily average fluxes were 152.2, 71.5, and 7.0 mg m^{-2} d^{-1} for TPF, $CaCO_3$, and POC fluxes, surpassing values in non-event periods (including May 01–July, 07, 2014 and March 02–April, 06, 2015) by 58, 61, and 48%, respectively (**Table 1**). The lithogenic flux was even maximized in November (73.6 mg m^{-2} d^{-1}). This is a very interesting phenomenon, different from other observations of small values in autumn. Lahajnar et al. (2007) and Ran et al. (2015) indicated TPF and POC autumn fluxes of less than 100 and 4 mg m^{-2} d^{-1}, respectively. At this time, the mixed layer was mostly shallower than 40 m, despite a slight deepening compared to summer, but this was much shallower than the top of the nutricline depth (50–70 m) measured at the SEATS station (Wong et al., 2007). It was impossible to support upper production through reverse mixing of subsurface nutrients, and the tiny fluctuation in sea level further excluded the influence of mesoscale eddies.

The main sources of lithogenic matter are river input, atmospheric deposition, and sediment re-suspension. First, our study site is distant from any river influence (Wong et al., 2007). The most influential river emptying into the northern part of the SCS was Pearl River, with flow rates of 316 km^3 $year^{-1}$ reaching the SCS at 22°N (Wong et al., 2007). The lesser rivers that flow into the SCS in the Hainan and Taiwan islands were the Wanquan river and the Choshui river with an annual flow of 5.8 and 5.2 km^3 $year^{-1}$ (Liang and Ye, 2015), and the Cagayan Rio River which empties into the SCS from Luzon Island. The distance between the estuary of Pearl River, Cagayan Rio River, Wanquan River, Choshui River, and our site were 515.3, 478.4, 590.8, and 738.8 km, respectively. The basin-wide circulation gyres effectively isolate the interior of the SCS proper from the influence of the land-runoff (Wong et al., 2007). Moreover, although most lithogenic matter in the northern SCS might result from modern transport and the resuspension of sediments by the Kuroshio intrusion along the Taiwan Strait (Liu et al., 2014), there was little seasonal variability (especially during the autumn peak) in the upper layer. Therefore, atmospheric deposition was the most likely source of the sharp increase (2.4-fold) in autumn lithogenic matter. The pattern of lithogenic flux was in phase with aerosol optical thickness (**Figure 4H**), in which large amounts of airborne particles were observed during autumn. These atmospheric aerosol particles could effectively deposit to the ocean surface via relatively frequent precipitation (59.1–67.7 kg m^{-2}) as shown in **Figure 4I**.

Our data are consistent with Lin et al. (2007), who showed a powerful influence of atmospheric deposition in the study area, relating it to a northern source of eastern China fossil fuel together with Asia Desert Dust. Large-scale combustion of biomass usually takes place in October, and fossil fuel aerosol contains large amounts of nitrogen which acts as a direct source of nutrient input (Zhang et al., 2018). Additionally, micronutrients like iron in desert dust that are deposited on the ocean surface in the form of bioavailable Fe(II) can trigger upper-ocean nitrogen fixation (Chavagnac et al., 2007). This fixation can convert di-nitrogen to fixed nitrogen in the presence of iron and lead in order to increase phytoplankton biomass. Strong nitrogen fixation in the SCS that can support 3–13% of net primary production was revealed by Wong et al. (2002) at the SEATS station, and the availability of iron during seasons of strong aerosol deposition could substantially enhance nitrogen fixation (Wong et al., 2007). The increased percentage of PN in biogenic matter during autumn (0.99%, **Table 4**) was 22.2% greater than average in the winter high-flux period (0.81%), which might indicate strengthened primary production caused by nitrogen fixation. From a microcosm incubation experiment with aerosol event scales on deck, Guo et al. (2012) observed positive responses in biomass in the SCS and a shift in dominant phytoplankton assemblages from picoplankton to microphytoplankton (Guo et al., 2012). According to model data in the SCS, enhancement of Chl-a during a dust event and dust deposition could contribute ∼20% of annual biological new production (Kim et al., 2014). A strong association between Chl-a and AOT variability in non-winter months at the SEATS station was presented by Lin et al. (2009), implying an important role for aerosol input in the northern SCS. The absence of large values of surface Chl-a concentration in our remote-sensing data may be attributed to a limitation of satellite observation, meaning the subsurface water bloom cannot be detected. The subsurface chlorophyll maximum was distinct in the nearby SEATS station

(Gong et al., 2014) and different physical processes may enhance the phenomenon in the SCS (Chen et al., 2006; Lu et al., 2010).

Additionally, same as biogenic minerals, lithogenic minerals in surface water could have a ballasting effect in the form of increasing the sedimentation rate of particulate matter and protecting organic matter from decomposition in marginal seas (Fischer and Karaka, 2009). The composition percentage of total particle fluxes in **Figure 3A** effectively confirms this. Although $CaCO_3$ was the most abundant component of particles during most of the year, the proportion of lithogenic matter increased from 27 to 38% in autumn. This increase was because of the effect of substantial atmospheric loading on the stimulation of primary production and further aggregated with organisms settling into the deep sea. Our data corresponded to the findings of Lee et al. (2009) for the Mediterranean Sea, which revealed that dust greatly increased downward export flux by particle aggregation. In the low-nutrient low-chlorophyll area where there is a definite fertilization effect by dust, >50% of the increase in particulate organic matter was related to the aggregation process (Bressac et al., 2013).

The autumn secondary peak occurred for every flux except that of opal, and there was a minimum of opal/$CaCO_3$ in early November. There are two potential reasons for this. The first is that airborne aerosol might be more likely to promote the growth of calcareous organisms than siliceous plankton. This was supported by the fact that the daily average $CaCO_3$ flux in autumn was 1.6-fold to the baseline value (**Table 1**, baseline condition was defined as non-event period, which included May 01 to July 07, 2014 and March 02 to April 06, 2015). The second reason is related to the various ballasting effects from different types of minerals (Salter et al., 2010). Carbonate was important in increasing particle density and thus accelerated the sinking of particles while most of the aggregate formed by opal was re-mineralized before reaching the bottom (Francois et al., 2002). Hence, opal does not increase organic matter flux as effectively as carbonate.

Our study highlights the vital function of aerosol deposition for carbon export in the form of nutrient replenishment, improvement of nitrogen fixation, and strengthening of the ballasting effect via extra lithogenic mineral supply in the marginal sea. Limited by sparse *in situ* data from a time-series observation of vertical particle flux below the euphotic layer, investigation of the mineral ballast effect and atmospheric particle deposition is still in its infancy, so further research is recommended.

Small Values in Summer Induced by Anticyclonic Eddy

During the summer monsoon (June–September), total particle, POC, and lithogenic matter fluxes showed clear minima of 59.7, 2.1, and 12.0 mg m^{-2} d^{-1} in July, and a minimal opal flux of 6.9 mg m^{-2} d^{-1} in August. The average summer daily TPF was 77.6 mg m^{-2} d^{-1}, in contrast with the annual daily average of 145.5 mg m^{-2} d^{-1}. Furthermore, the daily average biological flux in summer was 56.9 mg m^{-2} d^{-1}, contributing only 13% to the annual figure, while in the previous years the value was 63.2 and 62.2 mg m^{-2} d^{-1} with an annual percentage of 16 and 23% for 2009 and 2011 (Priyadarshani et al., 2019), respectively.

Very few factors substantially suppressed carbon export, except for the mesoscale anticyclonic eddy (Lasternas et al., 2012). Our SSHA data (**Figure 4G**) exceeded 0.07 m at the beginning of July, directly suggesting the influence of the anticyclonic eddy (Roemmich and Gilson, 2001; Huang et al., 2010). As shown in **Figure 7**, the sampling station was affected by a mesoscale warm-core eddy moving from south to northwest, beginning July 14. The station was at the eddy center from August 9, with a maximum sea level anomaly of 0.19 m. This eddy lasted 1 month and began to dissipate in September. The characteristics of central downwelling (Samuelsen et al., 2012) within the anticyclonic eddy weakened the upward nutrient transportation, thus led to the small values of fluxes in summer.

Based on the Bermuda Atlantic Time-series Study of the Sargasso Sea, Sweeney et al. (2003) clearly showed that the 1994 spring bloom was suppressed by the passage of anticyclonic eddies with SSHA around 0.20 m. In the Norwegian Sea, warm-core eddies could delay the phytoplankton bloom by about 2 weeks (Hansen et al., 2010). Lasternas et al. (2012) not only observed a considerable enhancement of dissolved organic carbon (DOC) concentration in the anticyclonic eddy center, but also diatom cell mortality rates of 60%. They proposed that the high mortality and cell lysis rates mainly resulted in the DOC increase, thereby reducing carbon export. This is consistent with Moutin and Prieur (2012) and Bressac et al. (2013) for the Mediterranean, emphasizing weak primary production and carbon export but large values of DOC concentration in anticyclonic eddies. Although the anticyclonic eddy was revealed to have a positive biological effect within the subtropical gyre (Dufois et al., 2016), the negative relative difference Rd (%) in Dufois's research of the northern SCS indicated the counteraction of the anticyclonic eddy. The SCS is a typical surface oligotrophic and low-productivity area in which productivity is mainly fueled by various physical processes providing nutrients to the upper layer. The characteristic downward flow in an anticyclonic eddy center substantially inhibits the growth of phytoplankton (Xiu and Chai, 2011; Guo et al., 2015). The model data of Ning et al. (2004) indicate that a warm-core eddy can reduce phytoplankton growth by 31%.

Unlike anticyclonic eddies, other processes like typhoon, monsoon, and dust deposition can only supply nutrients to the surface other than restrain. Furthermore, there were no major differences in environmental data of WS and NHF compared with the 2009–2010 data of Ran et al. (2015), apart from conspicuously large values of SSHA. This reflected the only influence of warm-core eddy.

There is a secondary peak of carbon output during the summer monsoon in some long-term records from the SCS (Chung et al., 2004; Li et al., 2017), in contrast with our study. However, these records are from the central basin area where the southwestern monsoon has a strong impact. Our study site was in the northern SCS, outside the summer circulation area (Shaw and Chao, 1994), and there was little impact from upwelling (Liu et al., 2002; Ning et al., 2004). Moreover, there were no apparent summer features in studies of the nearby SEATS station

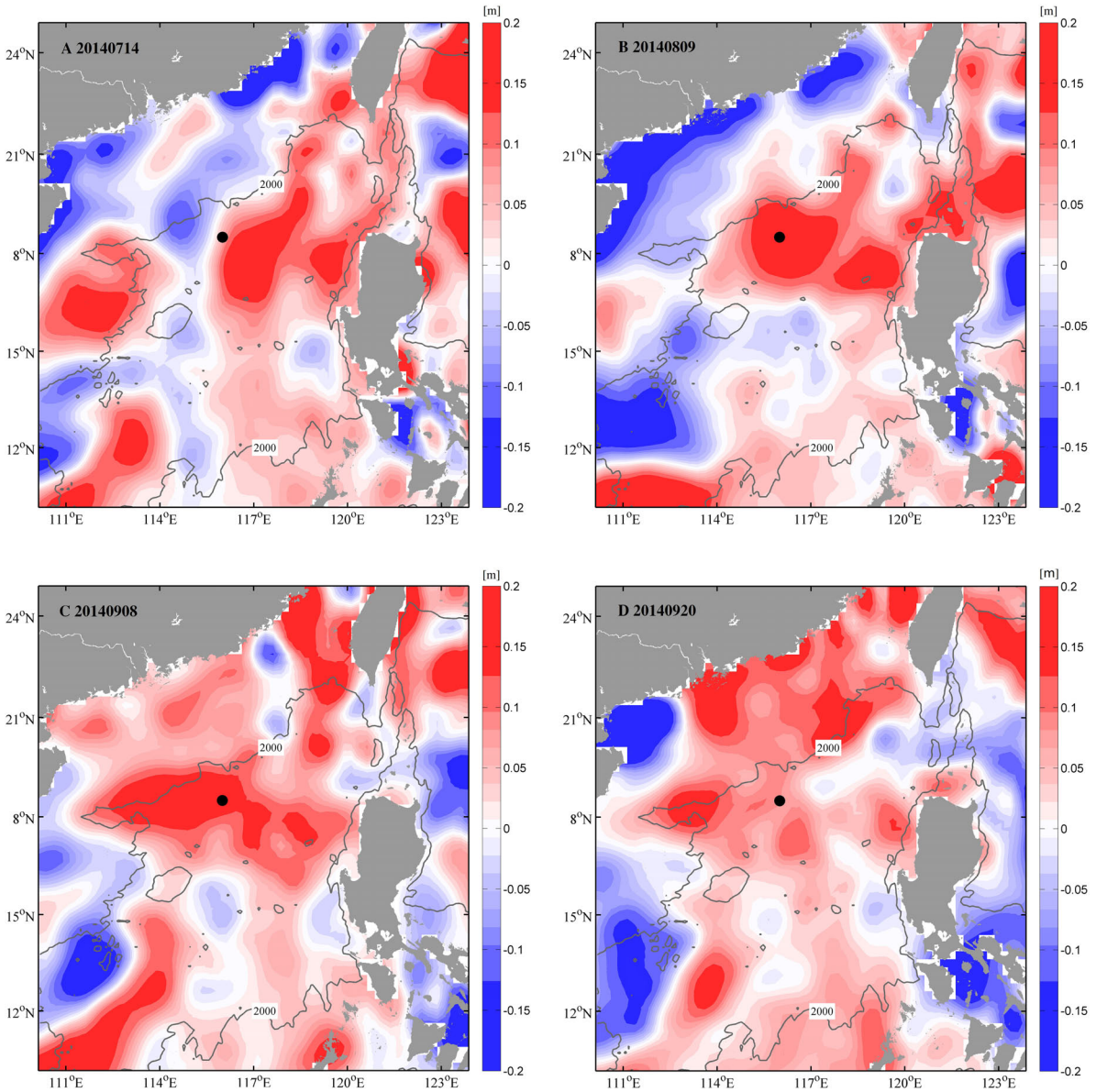

FIGURE 7 | Satellite images of daily sea surface height anomaly (SSHA, m) in northern SCS from AVISO product on **(A)** July 14, 2014, **(B)** August 09, 2014, **(C)** September 08, 2014, and **(D)** September 20, 2014, exhibiting anticyclonic eddy activity during summer period of 2014 in study area. Black dots on map represented 1/4° × 1/4° area around station SCS-N. Gray line with label 2,000 indicates water isobaths of 2,000 m.

(Tseng et al., 2005; Wong et al., 2007). The small summer export value in the present study is likely attributable to the influence of the mesoscale anticyclonic eddy.

CONCLUSION

Total particle flux, particulate organic carbon, $CaCO_3$ and lithogenic fluxes peaked in winter and autumn, but exhibited minima in summer. Opal flux was similar to those fluxes, with a prominent maximum in winter and a minimum in summer, whereas a secondary maximum of opal in autumn was barely noticeable compared with other components. A deeper mixed layer was related to the northeast monsoon and surface cooling, overlapped with the cyclonic eddy effect, which may be responsible for the strong winter fluxes. However, an anticyclonic eddy would suppress the subsurface nutrient supply, primary production, and subsequent export flux in summer. With respect to the autumn flux peaks of lithogenic and $CaCO_3$, the scavenging of atmospheric particles and mineral ballast effect are potential causes. Our study highlights that in addition to monsoonal transition, intra-seasonal physical processes (e.g., mesoscale eddies and aerosol deposition) are important to deep particle fluxes in the SCS.

DATA AVAILABILITY STATEMENT

The raw data supporting the conclusions of this article will be made available by the authors, without undue reservation, to any qualified researcher.

AUTHOR CONTRIBUTIONS

ST analyzed the data and led the writing of the manuscript under the instruction of JC and HL. JZ and LS accomplished the laboratory work with the cooperation of MW. ZW provided some environmental parameter data and contributed to track eddies by manual methods. MW and HZ made modifications for the manuscript.

FUNDING

This study was carried out in the financial support of the State Key R&D Project of China (2016YFA0601101), the National Natural Science Foundation of China (41906045 and 91528304), the Special Fund for Basic Scientific Research of the Second Institute of Oceanography, Ministry of Natural Resources (JT1501 and JG1514), and the Project of State Key Laboratory of Satellite Ocean Environment Dynamics, Second Institute of Oceanography, MNR (SOEDZZ1901), and the National Program on Global Change and Air-Sea Interaction (GASI-03-01-06-02).

ACKNOWLEDGMENTS

We are grateful to Institute of Geology, University of Hamburg for helpful instructions and laboratory cooperation in elemental analysis and the crews of R/V Tianying for their assistance during the mooring deployment. We appreciate the National Oceanic and Atmospheric Administration for providing SST, WS, and NHF data; Ocean Productivity for providing MLD and NPP data (http://orca.science.oregonstate.edu); National Aeronautics and Space Administration for providing AOT data; Asia-Pacific Data Research Center for providing precipitation water data (http://apdrc.soest.hawaii.edu); and Reiner Schlitzer with his group for sharing the Ocean Data View graphics program (odv.awi.de). We would like to thank LetPub (www.letpub.com) for providing linguistic assistance during the preparation of this manuscript.

SUPPLEMENTARY MATERIAL

The Supplementary Material for this article can be found online at: https://www.frontiersin.org/articles/10.3389/feart.2020.00074/full#supplementary-material

REFERENCES

Archer, D., and Maier-Reimer, E. (1994). Effect of deep-sea sedimentary calcite preservation on atmospheric CO2 concentration. *Nature* 367, 260–263. doi: 10.1038/367260a0

Armstrong, R. A., Lee, C., Hedges, J. I., Honjo, S., and Wakeham, S. G. (2002). A new, mechanistic model for organic carbon fluxes in the ocean based on the quantitative association of particulate organic matter with ballast minerals. *Deep Sea Res.* 49, 219–236. doi: 10.1016/s0967-0645(01)00101-1

Barker, S., Higgins, J. A., and Elderfield, H. (2003). The future of the carbon cycle: review, calcification response, ballast and feedback on atmospheric CO2. *Philos. T. R. Soc. A: Math. Phys. Eng. Sci.* 361, 1977–1998. doi: 10.1098/rsta.2003.1238

Bressac, M., Guieu, C., Doxaran, D., Bourrin, F., Desboeufs, K., Leblond, N., et al. (2013). Quantification of the lithogenic carbon pump following a dust deposition event. *Biogeosci. Discuss.* 10, 13639–13677. doi: 10.5194/bgd-10-13639-2013

Broecker, W. S. (1982). Ocean chemistry during glacial time. *Geochim. Cosmochim. Acta* 46, 1689–1705. doi: 10.1016/0016-7037(82)90110-7

Cai, P., Zhao, D., Wang, L., Huang, B., and Dai, M. (2015). Role of particle stock and phytoplankton community structure in regulation particulate organic matter export in a large marginal sea. *J. Geophys. Res. Oceans* 120, 2063–2095. doi: 10.1002/2014JC010432

Chavagnac, V., Waniek, J. J., Atkin, D., Milton, J. A., Leipe, T., Green, D. R. H., et al. (2007). Anti-Atlas Moroccan Chain as the source of lithogenic-derived micronutrient fluxes to the deep Northeast Atlantic Ocean. *Geophys. Res. Lett.* 34:L21604. doi: 10.1029/2007GL030985

Chen, C., and Wang, G. (2015). Interannual variability of the eastward current in the western South China Sea associated with the summer Asian monsoon. *J. Geophys. Res. Oceans* 119, 5745–5754. doi: 10.1002/2014JC010309

Chen, C. C., Shiah, F. K., Chung, S. W., and Liu, K. K. (2006). Winter phytoplankton blooms in the shallow mixed layer of the South China Sea enhanced by upwelling. *J. Mar. Syst.* 59, 97–110. doi: 10.1016/j.jmarsys.2005.09.002

Chen, C. T. A., Wang, S. L., Wang, B. J., and Pai, S. C. (2001). Nutrient budgets for the South China Sea basin. *Mar. Chem.* 75, 281–300. doi: 10.1016/s0304-4203(01)00041-x

Chen, Y. L. L., Chen, H. Y., Lin, I. I., Lee, M. A., and Chang, J. (2007). Effects of cold eddy on phytoplankton production and assemblages in Luzon strait bordering the South China Sea. *J. Oceanogr.* 63, 671–683. doi: 10.1007/s10872-007-0059-9

Chung, Y., Chang, H. C., and Hung, G. W. (2004). Particulate flux and 210Pb determined on the sediment trap and core samples from the northern South China Sea. *Cont. Shelf Res.* 24, 673–691. doi: 10.1016/j.csr.2004.01.003

Duce, R. A., and Tindale, N. W. (1991). Atmospheric transport of iron and its deposition in the ocean. *Limnol. Oceanogr.* 36, 1715–1726. doi: 10.4319/lo.1991.36.8.1715

Dufois, F., Hardman-Mountford, N. J., Greenwood, J., Richardson, A. J., Feng, M., and Matear, R. J. (2016). Anticyclonic eddies are more productive than cyclonic eddies in subtropical gyres because of winter mixing. *Sci. Adv.* 2:e1600282. doi: 10.1126/sciadv.1600282

Eppley, R. W., and Peterson, B. J. (1979). Particulate organic matter flux and planktonic new production in the deep ocean. *Nature* 282, 677–680. doi: 10.1038/282677a0

Fischer, G., and Karaka, G. (2009). Sinking rates and ballast composition of particles in the Atlantic Ocean: implications for the organic carbon fluxes to the deep ocean. *Biogeosciences* 6, 159–160. doi: 10.5194/bg-6-85-2009

Francois, R., Honjo, S., Krishfield, R., and Manganini, S. (2002). Factors controlling the flux of organic carbon to the bathypelagic zone of the ocean. *Glob. Biogeochem. Cycle* 16, 34–31. doi: 10.1029/2001GB001722

Gaye, B., Wiesner, M. G., and Lahajnar, N. (2009). Nitrogen sources in the South China Sea, as discerned from stable nitrogen isotopic ratios in rivers, sinking particles, and sediments. *Mar. Chem.* 114, 72–85. doi: 10.1016/j.marchem.2009.04.003

Gong, X., Shi, J., and Gao, H. (2014). Modeling seasonal variations of subsurface chlorophyll maximum in South China Sea. *J. Ocean Univ. China* 13, 561–571. doi: 10.1007/s11802-014-2060-4

Goutx, M., Wakeham, S. G., Lee, C., Duflos, M., and Guigue, C. (2007). Composition and degradation of marine particles with different settling

velocities in the northwestern Mediterranean Sea. *Limnol. Oceanogr.* 52, 1645–1664. doi: 10.4319/lo.2007.52.4.1645

Guo, C., Yu, J., Ho, T. Y., Wang, L., and Song, S. (2012). Dynamics of phytoplankton community structure in the South China Sea in response to the East Asian aerosol input. *Biogeosciences* 9, 1519–1536. doi: 10.5194/bg-9-1519-2012

Guo, M., Chai, F., Xiu, P., Li, S., and Rao, S. (2015). Impacts of mesoscale eddies in the South China Sea on biogeochemical cycles. *Ocean Dynam.* 65, 1335–1352. doi: 10.1007/s10236-015-0867-1

Hansen, C., Kvaleberg, E., and Samuelsen, A. (2010). Anticyclonic eddies in the Norwegian Sea: their generation, evolution and impact on primary production. *Deep Sea Res. Oceanogr. Res. Pap.* 57, 1079–1091. doi: 10.1016/j.dsr.2010.05.013

He, Q., Zhan, H., Cai, S., and Li, Z. (2016). Eddy effects on surface chlorophyll in the northern South China Sea: mechanism investigation and temporal variability analysis. *Deep Sea Res.* 112, 25–36. doi: 10.1016/j.dsr.2016.03.004

Honda, M. C., Sasai, Y., Siswanto, E., Kuwano-Yoshida, A., Aiki, H., and Cronin, M. F. (2018). Impact of cyclonic eddies and typhoons on biogeochemistry in the oligotrophic ocean based on biogeochemical/physical/meteorological time-series at station KEO. *Prog. Earth Planet. Sc.* 542. doi: 10.1186/s40645-018-0196-3

Honjo, S., Dymond, J., Prell, W., and Ittekkot, V. (1999). Monsoon-controlled export fluxes to the interior of the Arabian Sea. *Deep Sea Res.* 46, 1858–1902. doi: 10.1016/S0967-0645(99)00047-8

Huang, B., Hua, J., Xu, H., Cao, Z., and Wang, D. (2010). Phytoplankton community at warm eddies in the northern South China Sea in winter 2003/2004. *Deep Sea Res.* 57, 1792–1798. doi: 10.1016/j.dsr2.2010.04.005

Jung, J., Furutani, H., and Uematsu, M. (2011). Atmospheric inorganic nitrogen in marine aerosol and precipitation and its deposition to the North and South Pacific Oceans. *J. Atmos. Chem.* 68, 157–181. doi: 10.1007/s10874-012-9218-5

Kao, S. J., Yang, J. Y. T., Liu, K. K., Dai, M. H., Chou, W. C., Lin, H. L., et al. (2012). Isotope constraints on particulate nitrogen source and dynamics in the upper water column of the oligotrophic South China Sea. *Glob. Biogeochem. Cycle* 26:GB2033. doi: 10.1029/2011GB004091

Kim, T. W., Lee, K., Duce, R., and Liss, P. (2014). Impact of atmospheric nitrogen deposition on phytoplankton productivity in the South China Sea. *Geophys. Res. Lett.* 41, 3156–3162. doi: 10.1002/2014GL059665

Klaas, C., and Archer, D. E. (2002). Association of sinking organic matter with various types of mineral ballast in the deep sea: implications for the rain ratio. *Glob. Biogeochem. Cycle* 16:63. doi: 10.1029/2001GB001765

Lahajnar, N., Wiesner, M. G., and Gaye, B. (2007). Fluxes of amino acids and hexosamines to the deep South China Sea. *Deep Sea Res.* 54, 2120–2144. doi: 10.1016/j.dsr.2007.08.009

Lasternas, S., Piedeleu, M., Sangrà, P., Duarte, C. M., and Agustí, S. (2012). Carbon fluxes forced by anticyclonic mesoscale eddies generated by islands at the subtropical NE Atlantic Ocean. *Biogeosci. Discuss.* 9, 10241–10283. doi: 10.5194/bgd-9-10241-2012

Lee, C., Peterson, M. L., Wakeham, S. G., Armstrong, R. A., and Cochran, K. (2009). Particulate organic matter and ballast fluxes measured using time-series and settling velocity sediment traps in the northwestern Mediterranean Sea. *Deep Sea Res.* 56, 1420–1436. doi: 10.1016/j.dsr2.2008.11.029

Li, H., Wiesner, M. G., Chen, J., Zheng, L., Zhang, J., and Ran, L. (2017). Long-term variation of mesopelagic biogenic flux in the central South China Sea: impact of monsoonal seasonality and mesoscale eddy. *Deep Sea Res.* 126, 62–72. doi: 10.1016/j.dsr.2017.05.012

Liang, B., and Ye, C. Q. (2015). The Variation and Influencing Factors of Discharge into the Sea from Wanquan River in Tropical Island, China. *Rural Water Hydrop.* 1:15.

Lin, H. L., Sheu, D. D., Yang, Y., Chou, W. C., and Hung, G. W. (2011). Stable isotopes in modern planktonic foraminifera: sediment trap and plankton tow results from the South China Sea. *Mar. Micropaleontol.* 79, 15–23. doi: 10.1016/j.marmicro.2010.12.002

Lin, H. L., Wang, W. C., and Hung, G. W. (2004). Seasonal variation of planktonic foraminiferal isotopic composition from sediment traps in the South China Sea. *Mar. Micropaleontol.* 53, 447–460. doi: 10.1016/j.marmicro.2004.08.004

Lin, I. I., Chen, J. P., Wong, G. T. F., Huang, C. W., and Lien, C. C. (2007). Aerosol input to the South China Sea: results from the MODerate resolution imaging spectro-radiometer, the quick scatterometer, and the measurements of pollution in the troposphere sensor. *Deep Sea Res.* 54, 1589–1601. doi: 10.1016/j.dsr2.2007.05.013

Lin, I. I., Wong, G. T. F., Lien, C. C., Chien, C. Y., Huang, C. W., and Chen, J. P. (2009). Aerosol impact on the South China Sea biogeochemistry: an early assessment from remote sensing. *Geophys. Res. Lett.* 36:L17605. doi: 10.1029/2009GL037484

Liu, J., Clift, P. D., Yan, W., Chen, Z., Chen, H., Xiang, R., et al. (2014). Modern transport and deposition of settling particles in the northern South China Sea: sediment trap evidence adjacent to Xisha Trough. *Deep Sea Res.* 93, 145–155. doi: 10.1016/j.dsr.2014.08.005

Liu, K. K., Chao, S. Y., Shaw, P. T., Gong, G. C., Chen, C. C., and Tang, T. Y. (2002). Monsoon-forced chlorophyll distribution and primary production in the South China Sea: observations and a numerical study. *Deep Sea Res.* 49, 1387–1412. doi: 10.1016/S0967-0637(02)00035-3

Lu, Z., Gan, J., Dai, M., and Cheung, A. (2010). The influence of coastal upwelling and a river plume on the subsurface chlorophyll maximum over the shelf of the northeastern South China Sea. *J. Mar. Syst.* 82, 35–46. doi: 10.1016/j.jmarsys.2010.03.002

McGillicuddy, D. J., Robinson, A. R., Siegel, D. A., Jannasch, H. W., Johnsonk, R., Dickel, T. D., et al. (1998). Influence of mesoscale eddies on new production in the Sargasso Sea. *Nature* 394, 263–266. doi: 10.1038/28367

Mortlock, R. A., and Froelich, P. N. (1989). A simple method for the rapid determination of biogenic opal in pelagic marine sediments. *Deep Sea Res.* 36, 1415–1426. doi: 10.1016/0198-0149(89)90092-7

Moutin, T., and Prieur, L. (2012). Influence of anticyclonic eddies on the biogeochemistry from the oligotrophic to the ultraoligotrophic mediterranean (BOUM) cruise. *Biogeosciences* 9, 3827–3855. doi: 10.5194/bg-9-3827-2012

Nair, R. R., Ittekkot, V., Manganini, S. J., Ramaswamy, V., Haake, B., Degens, E. T., et al. (1989). Increased particle flux to the deep ocean related to monsoons. *Nature* 338, 749–751. doi: 10.1038/338749a0

Ning, X., Chai, F., Xue, H., Cai, Y., and Shi, J. (2004). Physical-biological oceanographic coupling influencing phytoplankton and primary production in the South China Sea. *J. Geophys. Res.* 109:C10005. doi: 10.1029/2004JC002365

Passow, U., Dunne, J., Murray, J. W., Balistrieri, L., and Alldredge, A. L. (2006). Organic carbon to 234Th ratios of marine organic matter. *Mar. Chem.* 100, 323–336. doi: 10.1016/j.marchem.2005.10.020

Priyadarshani, W. N. C., Ran, L., Wiesner, M. G., Chen, J., and Ling, Z. (2019). Seasonal and interannual variability of coccolithophore flux in the northern South China Sea. *Deep Sea Res. Oceanogr. Res. Pap.* 145, 13–30. doi: 10.1016/j.dsr.2019.01.004

Ran, L., Chen, J., Wiesner, M. G., Ling, Z., Lahajnar, N., Yang, Z., et al. (2015). Variability in the abundance and species composition of diatoms in sinking particles in the northern South China Sea: results from time-series moored sediment traps. *Deep Sea Res.* 122, 15–24. doi: 10.1016/j.dsr2.2015.07.004

Roemmich, D., and Gilson, J. (2001). Eddy transport of heat and thermocline waters in the North Pacific: a key to interannual/decadal climate variability? *J. Phys. Oceanogr.* 31, 675–687. doi: 10.1175/1520-0485(2001)031<0675:etohat>2.0.co;2

Salter, I., Kemp, A. E. S., Lampitt, R. S., and Gledhill, M. (2010). The association between biogenic and inorganic minerals and the amino acid composition of settling particles. *Limnol. Oceanogr.* 55, 2207–2218. doi: 10.4319/lo.2010.55.5.2207

Samuelsen, A., Honjo, S., Johannessen, J. A., and Patel, R. (2012). Particle aggregation at the edges of anticyclonic eddies and implications for distribution of biomass. *Ocean Sci.* 8, 389–400. doi: 10.5194/os-8-389-2012

Shaw, P. T., and Chao, S. Y. (1994). Surface circulation in the South China Sea. *Deep Sea Res.* 41, 1663–1683. doi: 10.1016/0967-0637(94)90067-1

Sigman, D. M., and Boyle, E. A. (2000). Glacial/interglacial variations in atmospheric carbon dioxide. *Nature* 407, 859–869. doi: 10.1038/35038000

Sweeney, E. N., McGillicuddy, D. J., and Buesseler, K. O. (2003). Biogeochemical impacts due to mesoscale eddy activity in the Sargasso Sea as measured at the bermuda atlantic time-series study (BATS). *Deep Sea Res.* 50, 3017–3039. doi: 10.1016/j.dsr2.2003.07.008

Thunell, R., Benitez-Nelson, C., Varela, R., Astor, Y., and Muller-Karger, F. (2007). Particulate organic carbon fluxes along upwelling-dominated continental margins: rate and mechanisms. *Glob. Biogeochem. Cycle* 21:GB1022. doi: 10.1029/2006GB002793

Tseng, C. M., Gong, G. C., Wang, L. W., Liu, K. K., and Yang, Y. (2009). Anomalous biogeochemical conditions in the northern South China Sea during the El-Niño events between 1997 and 2003. *Geophys. Res. Lett.* 36:14.

Tseng, C. M., Wong, G. T. F., Lin, I. I., Wu, C. R., and Liu, K. K. (2005). A unique seasonal pattern in phytoplankton biomass in low-latitude waters in the South China Sea. *Geophys. Res. Lett.* 32, 487–500. doi: 10.1029/2004GL02 2111

Volk, T., and Hoffert, M. I. (1985). "Ocean carbon pumps: analysis of relative strengths and efficiencies in ocean-driven atmospheric CO2 changes," in *The Carbon Cycle and Atmospheric CO2: Natural Variations Archean to Present*, eds E. T. Sundquist and W. S. Broecker (Washington, DC: Wiley), 99–110. doi: 10.1029/GM032p0099

Wang, L., Huang, B., Chiang, K. P., Liu, X., Chen, B., Xie, Y., et al. (2016). Physical-biological coupling in the western South China Sea: the response of phytoplankton community to a mesoscale cyclonic eddy. *PLoS One* 11:e0153735. doi: 10.1371/journal.pone.0153735

Wang, S. H., Tsay, S. C., Lin, N. H., Hsu, N. C., Bell, S. W., Li, C., et al. (2011). First detailed observations of long-range transported dust over the northern South China Sea. *Atmos. Environ.* 45, 4804–4808. doi: 10.1016/j.atmosenv.2011. 04.077

Wiesner, M. G., Zheng, L. F., Wong, H. K., Wang, Y., and Chen, W. (1996). "Fluxes of particulate matter in the South China Sea," in *Particle Flux in the Ocean*, eds V. Ittekkot, P. Schäfer, S. Honjo, and P. J. Depetris (New York: John Wiley & Sons Ltd), 293–312.

Wong, G. T. F., Chung, S. W., Shiah, F. K., Chen, C. C., Wen, L. S., and Liu, K. K. (2002). Nitrate anomaly in the upper nutricline in the northern South China Sea - evidence for nitrogen fixation. *Geophys. Res. Lett.* 29:2097. doi: 10.1029/2002GL015796

Wong, G. T. F., Ku, T. L., Mulholland, M., Tseng, C. M., and Wang, D. P. (2007). The SouthEast Asian Time-series Study (SEATS) and the biogeochemistry of the South China Sea – an overview. *Deep Sea Res.* 54, 1434–1447. doi: 10.1016/ j.dsr2.2007.05.012

Xie, S. P., Xie, Q., Wang, D., and Liu, W. T. (2003). Summer upwelling in the South China Sea and its role in regional climate variations. *J. Geophys. Res.* 108, 32–61. doi: 10.1029/2003JC001867

Xiu, P., and Chai, F. (2011). Modeled biogeochemical responses to mesoscale eddies in the South China Sea. *J. Geophys. Res.* 116:C10006. doi: 10.1029/ 2010JC006800

Xiu, P., Chai, F., Shi, L., Xue, H., and Chao, Y. (2010). A census of eddy activities in the South China Sea during 1993-2007. *J. Geophys. Res. Oceans* 115:C03012. doi: 10.1029/2009JC005657

Xue, H., Chai, F., Pettigrew, N., Xu, D., Shi, M., and Xu, J. (2004). Kuroshio intrusion and the circulation in the South China Sea. *J. Geophys. Res.* 109:C02017. doi: 10.1029/2002JC001724

Zhang, J., Li, H., Xuan, J., Wu, Z., Yang, Z., Wiesner, M. G., et al. (2018). Enhancement of mesopelagic sinking particle fluxes due to upwelling, aerosol deposition, and monsoonal influences in the northwestern South China Sea. *J. Geophys. Res. Oceans* 124, 1–14. doi: 10.1029/2018JC014704

Conflict of Interest: The authors declare that the research was conducted in the absence of any commercial or financial relationships that could be construed as a potential conflict of interest.

frontiers in Earth Science

ORIGINAL RESEARCH
published: 19 May 2020
doi: 10.3389/feart.2020.00144

Influence of Sediment Resuspension on the Biological Pump of the Southwestern East Sea (Japan Sea)

Minkyoung Kim[1†], Young-Il Kim[2], Jeomshik Hwang[1*], Ki Young Choi[3], Chang Joon Kim[3], Yeongjin Ryu[1], Ji-Eun Park[4], Kyung-Ae Park[4], Jae-Hyoung Park[1], SungHyun Nam[1], Negar Haghipour[5,6] and Timothy I. Eglinton[5]*

[1] School of Earth and Environmental Sciences/Research Institute of Oceanography, Seoul National University, Seoul, South Korea, [2] East Sea Research Institute, Korea Institute of Ocean Science and Technology, Ansan-si, South Korea, [3] Korea Institute of Ocean Science and Technology, Busan, South Korea, [4] Department of Earth Science Education, Seoul National University, Seoul, South Korea, [5] Geological Institute, Swiss Federal Institute of Technology in Zürich (ETHZ), Zurich, Switzerland, [6] Laboratory of Ion Beam Physics, ETH Zürich, Zurich, Switzerland

OPEN ACCESS

Edited by:
Makio Honda, Japan Agency for Marine-Earth Science and Technology (JAMSTEC), Japan

Reviewed by:
Shigeyoshi Otosaka, The University of Tokyo, Japan
Ting Hsuan Huang, National Sun Yat-sen University, Taiwan

***Correspondence:**
Young-Il Kim
yikim@kiost.ac
Jeomshik Hwang
jeomshik@snu.ac.kr

†Present address:
Minkyoung Kim, Geological Institute, ETH Zürich, Zurich, Switzerland

Specialty section:
This article was submitted to Biogeoscience, a section of the journal Frontiers in Earth Science

Received: *27 February 2020*
Accepted: *17 April 2020*
Published: *19 May 2020*

Citation:
Kim M, Kim Y-I, Hwang J, Choi KY, Kim CJ, Ryu Y, Park J-E, Park K-A, Park J-H, Nam S, Haghipour N and Eglinton TI (2020) Influence of Sediment Resuspension on the Biological Pump of the Southwestern East Sea (Japan Sea). Front. Earth Sci. 8:144. doi: 10.3389/feart.2020.00144

The biological carbon pump in the southwestern East Sea (Japan Sea, EJS hereafter) was investigated based on examination of sinking particulate matter samples intercepted by bottom-tethered sediment traps deployed on a mooring at three depths (500, 1000, and 2000 m) between 2011 and 2017. The total particle flux increased as the sampling depth increased, while particulate organic carbon (POC) flux was greatest at 500 m. The lithogenic material content was high at all depths, and accounted for an average of ∼42% of the particulate matter. The total particle flux at all sampling depths consistently shifted toward much higher values in 2014–2016. During this period, the POC flux at 500 m increased by 32% while net primary production (NPP) increased only slightly. Consequently, the POC flux/NPP ratio increased significantly, indicating greater biological pump efficiency than in earlier years of the study. The flux of lithogenic material derived primarily from sediment resuspension was much greater at 500 m in 2014−2016 compared with previous years, implying its potential role as a ballast mineral in enhancing particle export and transfer to the deep sea interior. The radiocarbon isotope ratio of POC was higher, and the excess Mn content values were lower at 500 m in 2014–2016, suggesting that the resuspended sediment at 500 m likely originated from a shallow region during this period, and differed in provenance from the lithogenic material intercepted at 2000 m. The period of enhanced particle flux coincided with the 2015/16 El Niño and a mesoscale warm (anticyclonic) eddy that persisted for 2 years in the study region. The East Korean Warm Current and the eddy may have facilitated the transport of resuspended particles entrained in the Korea Strait and/or the western shelf and upper slope of the basin to the study site.

Keywords: biological carbon pump, particulate organic carbon, sediment resuspension, sediment trap, lithogenic material, ENSO

INTRODUCTION

The East Sea (also known as the Japan Sea, the EJS hereafter) is a marginal sea that is connected to the northwest Pacific Ocean through straits shallower than 150 m (**Figure 1**). The Tsushima Warm Current (TWC), which is a branch of the Kuroshio Current, flows into the EJS through the Korea Strait. The East Korea Warm Current (EKWC), a branch of the TWC, flows north along the east

coast of the Korean Peninsula. Upon detachment from the coast, the EKWC forms a subpolar front at 38–40°N joining with the North Korea Cold Current (NKCC). In the southwestern part of the subpolar front lies the Ulleung Basin, where net primary production (NPP) is reportedly the highest in the entire EJS (Yamada et al., 2005; Kwak et al., 2013).

Chen et al. (2017) reported rapid acidification of the interior of the EJS between 1965 and 2015. The deep waters of the EJS are vulnerable to acidification because of high levels of dissolved inorganic carbon (DIC) from organic matter decomposition, and low levels of carbonate alkalinity (Na et al., 2019). Therefore, improved understanding of the functioning of the biological carbon pump is necessary to inform projections of acidification of the deep waters of the EJS.

Changes in the physical and biological characteristics of surface waters including the vertical temperature profile, and the phytoplankton community structure, can affect the biological carbon pump in the Ulleung Basin (Yoo and Kim, 2004; Chiba et al., 2008). For example, when the surface water temperature rose and the inflow from the TWC strengthened, the contribution of small phytoplankton to NPP increased (Li et al., 2009; Lee et al., 2013; Joo et al., 2017). In their study of the monthly NPP in the Ulleung Basin, using Moderate Resolution Imaging Spectroradiometer (MODIS-aqua) satellite observations and the Vertically Generalized Productivity Model (VGPM, Behrenfeld and Falkowski, 1997), Joo et al. (2014) reported a decline of ∼17% in the annual NPP from 2006 to 2013. This was hypothesized to reflect the effect of sea surface warming and the negative phase of the Pacific Decadal Oscillation (PDO). The effects of the El Niño Southern Oscillation (ENSO) on the sinking particle flux in the tropical Pacific have been relatively well studied (Honjo et al., 1995; Kawahata et al., 2000; Kim et al., 2011, 2014, 2019). However, the relationship between the sinking particle flux and its composition and high and low frequency climate variability is not well understood because of the lack of long-term data.

The sinking particle flux in the EJS has been studied over periods of 1–2-years (Otosaka et al., 2004, 2008; Kim et al., 2017). A study based on 1 year's data from March 2011 to February 2012 in the Ulleung Basin showed that the particulate organic carbon (POC) flux at a depth of 1000 m was bimodal, and mainly reflected the variations in the NPP. The ratio of the POC flux at 1000 m to the NPP (i.e., e-ratio at 1000 m) was ∼3%, which is similar to the values obtained for other basins in the EJS (Otosaka et al., 2008). Another finding was that, the sinking particles in the EJS contained high levels of lithogenic material from aeolian dust deposition and resuspended sediment (Otosaka et al., 2008; Kim et al., 2017), reflecting its location in a marginal sea.

In this study, we present quasi-continuous time-series data from 2011 to 2017 on the flux and composition of sinking particles at three depths at a site in the Ulleung Basin. We investigated the biological pump in the EJS, and paid particular attention to the marked increase in the particle flux that occurred in 2014–2016, and its relationship with climate variability.

MATERIALS AND METHODS

Sample Collection

Samples of sinking particulate matter were collected from July 2011 to September 2017 (**Supplementary Table S1**) using conical-type sediment traps (aperture diameter 80 cm, height/diameter ratio = 2; model SMC26S-6000, Nichiyu Giken Kogyo Co., Ltd., Japan), deployed at 500 m (changed to 300 m in March 2017), 1000 m, and 2000 m on a bottom-tethered mooring at station ES (37.63°N, 131.36°E; ∼2370 m water depth) in the Ulleung Basin (**Figure 1**). The sampling interval for each cup of the sediment traps was programmed for 6–10 days. Sample collection was interrupted several times because of mooring turnaround and trap malfunctioning. Detailed information regarding the sampling times is presented in **Supplementary Table S1**. The mooring was equipped with RCM-type current meters at 550 m and 2050 m. The sampling cups of the traps were filled with artificial seawater, prepared using distilled water and sea salts (Sigma-Aldrich) and adjusted to the approximate salinity at the deployment depths. Sodium borate-buffered 10% formalin solution was added as a preservative. The study site is approximately 34 km northwest of station EC1 (37.33°N, 131.45°E; 2300 m water depth), which has mainly been used for physical oceanographic studies since 1996 (Chang et al., 2002; Noh and Nam, 2018), although the sinking particle flux and composition at station EC1 were reported for a 1-year period by Kim et al. (2017).

Seafloor sediment samples were collected using a box corer during two cruises (**Figure 1** and **Supplementary Table S3**), the first in August 2011 aboard the survey vessel *Haeyang 2000* involving three sampling locations: TEB1 (37.00°N, 129.50°E), TEB5 (37.00°N, 131.00°E), and TEE5 (35.18°N, 129.80°E); and the second in May 2014 aboard the R/V *Eardo* involving sampling at DE2 (36.71°N, 129.81°E), DE3 (36.73°N, 129.86°E), DE4 (36.71°N, 130.02°E), and ES (37.65°N, 131.35°E). These sites lie under the path of the surface currents leading toward the trap mooring sites and therefore were chosen as potential sources of resuspended sediment particles.

Sample Analyses

Particulate matter samples were filtered using a 1-mm teflon mesh to remove swimmers and any large particles, centrifuged, and freeze-dried. The freeze-dried samples were weighed for gravimetric determination of the total particle flux. For POC content measurement, ∼0.5 g of each homogenized particle sample was weighed and decarbonated by soaking in 10 ml of 1 N HCl (ACS grade, Merck) for 30 min. The decarbonated sample was dried in an oven for 3 days at 80°C, then desiccated for 2 h at room temperature. The POC content of each sample (5–7 mg, wrapped in a tin cup) was measured with an elemental analyzer (Thermo Flash EA 1112 series). The mean measured value of a standard reference material (SRM 1941b) provided by the National Institute of Standards and Technology (NIST, United States) was 2.98 ± 0.18% (certified value = 2.99 ± 0.24%).

For radiocarbon isotope analysis of POC, each particle sample was finely ground, weighed in a silver cup, fumigated

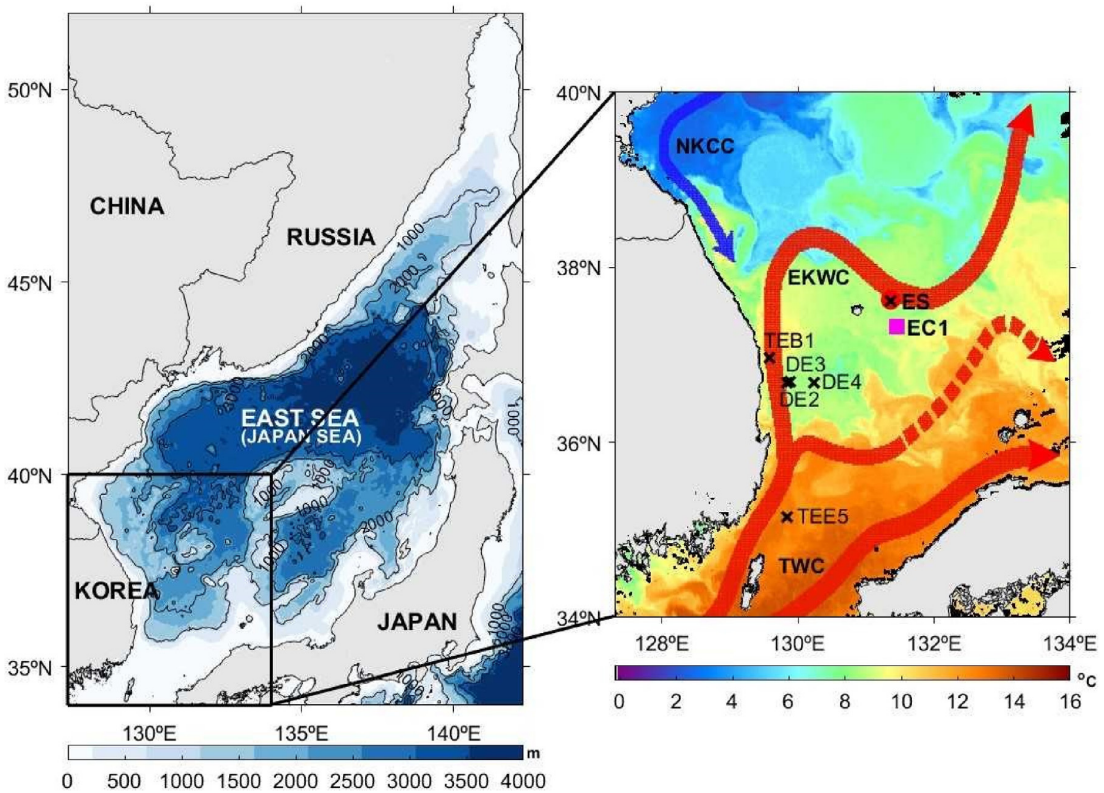

FIGURE 1 | Bathymetry **(left panel)** of the East Sea (Japan Sea) and the sea surface temperature (**right panel**, the image was taken by satellite NOAA-19 on 30 March, 2011). The locations of the mooring sites, ES and EC1, and the surface sediment sampling sites are indicated (X marks). A schematic of major surface currents is also shown (NKCC: North Korea Cold Current, EKWC: East Korea Warm Current, TWC: Tsushima Warm Current).

with HCl in a desiccator for 3 days at 70°C to remove inorganic carbon, then stored in a desiccator with NaOH pellets (Fischer Scientific; analytical reagent grade) at 70°C for 3 days to remove residual HCl. Radiocarbon isotope ratios were measured using a gas-ion source MICADAS (Mini Carbon Dating System) accelerator mass spectrometer in the Laboratory for Ion Beam Physics at ETH Zürich (Christl et al., 2013; McIntyre et al., 2017). Radiocarbon data were normalized using an oxalic acid II standard (NIST SRM 4990C), and measurements were corrected for constant contamination introduced during fumigation using in-house shale and soil reference materials according to Haghipour et al. (2019). We assign ±5‰ as a conservative uncertainty for $\Delta^{14}C$ measurements of POC samples although a precision of ±2‰ is routinely achievable for the modern standard oxalic acid II (McIntyre et al., 2017) and duplicate analysis results of a POC sample were within 3‰. After rinsing the samples with ultra-pure water three times and freeze-drying, the effect of formalin as a preservative on radiocarbon analysis is considered insignificant (Honda et al., 2000; Otosaka et al., 2008).

For metal analyses, ∼20 mg of each dry sample was digested in an acid mixture (HNO_3, $HClO_4$, and HF; Merck, Suprapur) for 12 h on a hot plate at 180°C, and the concentrations of Al and Mn in the digested sample were measured using inductively coupled plasma mass spectrometry (ICP-MS; Thermo X-Series). A standard material (MESS-3, National Research Council of Canada) was used for calibration. A subset of the sinking particle samples was analyzed for Al, Si, and Ca using inductively coupled plasma atomic emission spectrometry (ICP-AES; Optima 8300; PerkinElmer) at the Korea Basic Science Institute. Two standard materials (SRM 1646a, and SRM 2702, NIST, United States) were analyzed for calibration purposes. The lithogenic material content has been estimated to be 12.15-fold that of the Al content (Taylor and McLennan, 1985). For our set of samples, the $CaCO_3$ content was estimated by multiplying the biogenic Ca content by a factor of 2.5; the biogenic Ca content was estimated by subtracting the lithogenic Ca content (= 0.5 × Al) from the total Ca content. The opal content was estimated by multiplying the content of biogenic Si by a factor of 2.4; the biogenic Si content was estimated by subtracting the lithogenic Si content (= 3.5 × Al) from the total Si content (Honjo et al., 1995).

Determination of Net Primary Production Based on Satellite Observations

The NPP in the study period was estimated using the VGPM (Behrenfeld and Falkowski, 1997) and the optimal carbon fixation rate (Kameda, 2003; Kameda and Ishizaka, 2005). Satellite data for the area of 2-km radius around Station ES were obtained using

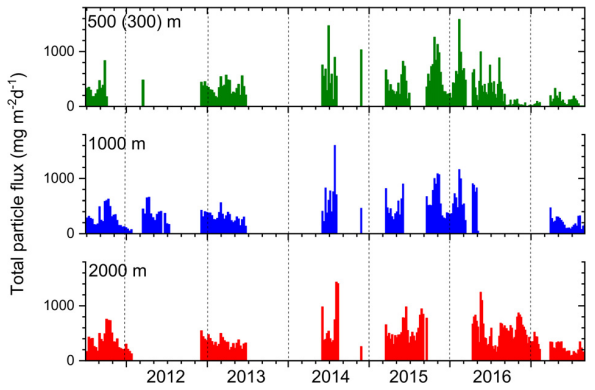

FIGURE 2 | The total particle flux at the three sampling depths from July 2011 to September 2017 (No bar indicates no data).

the MODIS Aqua level-2 chlorophyll-*a* concentration, the level-3 sea surface temperature (SST), the level-3 photosynthetically available radiation (PAR), and the level-3 diffuse attenuation coefficient for downwelling irradiance at 490 nm. A mean monthly map of the level-2 daily chlorophyll-*a* concentration was developed using an optimal interpolation technique after removing any speckles (Chae and Park, 2009; Park et al., 2013).

RESULTS

Particle Flux and Composition

The total particle flux over the entire sampling period varied from 0.8 to 1586 mg $m^{-2}d^{-1}$, 48 to 1606 mg $m^{-2}d^{-1}$, and 89 to 1432 mg $m^{-2}d^{-1}$ at 500 m, 1000 m, and 2000 m, respectively (**Supplementary Table S1**). Because of interruptions in the data collection, no seasonal variation was detected, but the interannual variability was high. In general, the particle flux values were higher for 2014–2016 than in the preceding and following years. The total particle flux increased as the depth increased: the sampling period-weighted average particle fluxes at 500 m, 1000 m, and 2000 m were 344, 393, and 432 mg $m^{-2}d^{-1}$, respectively (**Figure 2** and **Table 1**). Conspicuous peaks in the flux occurred coincidentally at all depths without any time lag. However, the particle fluxes at different depths were not tightly coupled. In particular, the correlation between particle fluxes at 500 m and 2000 m was very weak ($R^2 = 0.12$).

The POC content varied widely at 500 m (0.4—29%; **Supplementary Figure S1**), and was particularly high in July 2011. Unlike the total particle flux, the POC content generally decreased with increasing depth; the arithmetic mean of the POC content throughout the study period was 8.2 ± 4.2 at 500 m, 6.0 ± 1.7 at 1000 m, and 5.7 ± 1.3% at 2000 m (**Supplementary Figure S1** and **Table 1**; note: unless otherwise stated, the ±values throughout the paper indicate the standard deviation of the observed results, not measurement uncertainty). The temporal variation in the POC flux was in phase with the total particle flux (**Figure 3**). The POC flux ranged from 0.05 to 187 mgC $m^{-2}d^{-1}$ at 500 m (sampling duration-weighted average = 28), 0.9 to 84 mgC $m^{-2}d^{-1}$ at 1000 m (ave. = 25), and 6.8 to 95 mgC $m^{-2}d^{-1}$ (ave. = 26) at 2000 m (**Figure 3** and **Table 1**). Because the POC content and total particle flux varied inversely with depth, the POC flux was highest at 500 m, while the values at 1000 m and 2000 m were similar, especially during the high flux period in 2014/16.

The content of lithogenic material varied widely from 11 to 75% at 500 m (mean = 42 ± 15%), from 12 to 73% at 1000 m (mean = 42 ± 14%), and from 14 to 80% (mean = 47 ± 11%) at 2000 m (**Supplementary Figure S2** and **Table 1**). The lithogenic material flux was also very high at 500 m, where it varied from 5 to 765 mg $m^{-2}d^{-1}$ (**Figure 4**), and at this depth there was a distinct difference prior to and after June 2014. Before this time, the flux of lithogenic material increased considerably from 500 to 1000 m but showed only a small increase as the depth increased for 2014–2016. During the entire study period, the sampling duration-weighted average lithogenic material fluxes were 199, 161, and 241 mg $m^{-2}d^{-1}$ at 500, 1000, and 2000 m, respectively. Therefore, averaged over the entire period, both the content and the flux of lithogenic material was smallest at intermediate depth (1000 m). The increase in the flux of lithogenic material was largely responsible for the increase in the total particle flux in 2014–2016.

Biogenic opal accounted for 33–40% of the particulate matter. There was no clear trend in the vertical opal content (**Supplementary Figure S3**). The opal flux was greater at 500 m (204 mg $m^{-2}d^{-1}$) than at the other depths (160 and 159 mg $m^{-2}d^{-1}$, at 1000 m and 2000 m, respectively) (**Supplementary Figure S3** and **Table 1**). At all depths, $CaCO_3$ accounted for the smallest fraction of the particulate matter (**Supplementary Figure S4**). Both the $CaCO_3$ content and flux decreased with increasing depth: 6.1 ± 4.1% (27 mg $m^{-2}d^{-1}$), 5.3 ± 3.6% (21 mg $m^{-2}d^{-1}$), and 3.3 ± 3.1% (11 mg $m^{-2}d^{-1}$) at 500 m, 1000 m, and 2000 m, respectively (**Supplementary Figure S4** and **Table 1**).

Comparison Between Strong El Niño and Non-El Niño Periods

The particle flux was considerably higher in the period from June 2014 to September 2016 than in earlier years of the study or during the first 8 months 2017 (**Figure 2**). This period coincided with the occurrence of a super El Niño, as evidenced by a strong positive ONI (oceanic niño index) around 2015 (**Figure 3**); the period from 2011 to 2013 represented a negative phase of the ONI. For convenience, we refer to the former (2014–2016) and the latter periods (2011–2013) as the "EN" and the "non-EN" periods, respectively. Because the particle fluxes in these two periods were quite distinct, the properties of the two periods were compared (**Figure 5** and **Table 1**). We performed *t*-test to examine whether each property between the two periods was significantly different, although it is acknowledged that this comparison between the EN and the non-EN periods may suffer from bias caused by sampling hiatuses.

At 500 m, the POC flux averaged over each period was 32% higher for the EN period (2014–2016) than the non-EN period (2011–2013; **Table 1**), with a considerably greater discrepancy as the depth increased (the EN period being 96% and 113% higher

TABLE 1 | Values of observed parameters averaged over the entire study period (July 2011-September 2017), the non-El Niño period (July 2011-March 2014), and the El Niño period (June 2014-September 2016).

Parameters	Whole period Average ± σ	Non-El Niño period Average ± σ	El Niño period Average ± σ
Primary production	794 ± 267	774 ± 231	841 ± 316
Dust deposition	3.4 ± 2.3	4.1 ± 2.7	2.7 ± 1.7
		500 *m*(300 *m*)	
Particle flux (<1 mm)	338 ± 293	351 ± 137(n = 39)	509 ± 311(n = 78)
POC flux	28 ± 24	27 ± 15(n = 39)	36 ± 26(n = 78)
POC content	8.2 ± 4.2	8.4 ± 5.6	7.3 ± 3.0
POC flux/NPP (%)	3.5 ± 2.1	3.6 ± 1.9	4.1 ± 2.0
Lithogenic flux	201 ± 166	66 ± 61(n = 18)	232 ± 168(n = 78)
Lithogenic content	42 ± 15	34 ± 10	44 ± 16
Biogenic opal flux	208 ± 199	143 ± 90(n = 18)	261 ± 245(n = 22)
Biogenic opal content	38 ± 17	35 ± 11	41 ± 21
Biogenic $CaCO_3$ flux	27 ± 21	28 ± 16(n = 18)	26 ± 25(n = 20)
Biogenic $CaCO_3$ content	6 ± 4	8 ± 5	4 ± 3
$\Delta^{14}C$ (‰)	–	−14 ± 38(n = 7)	16 ± 18(n = 14)
Excess Mn flux	–	212 ± 238(n = 9)	147 ± 136(n = 71)
		1000 *m*	
Particle flux (<1 mm)	400 ± 258	311 ± 141(n = 65)	600 ± 290(n = 54)
POC flux	26 ± 16	18 ± 8(n = 65)	36 ± 19(n = 54)
POC content	6.0 ± 1.7	6.1 ± 1.7	5.9 ± 1.6
POC flux/NPP (%)	3.3 ± 1.7	2.5 ± 1.0	4.4 ± 1.8
Lithogenic flux	169 ± 135	123 ± 63(n = 65)	272 ± 189(n = 29)
Lithogenic content	42 ± 14	41 ± 13	43 ± 16
Biogenic opal flux	164 ± 142	128 ± 67(n = 61)	285 ± 237(n = 18)
Biogenic opal content	39 ± 14	39 ± 12	40 ± 18
Biogenic $CaCO_3$ flux	21 ± 14	24 ± 10(n = 14)	19 ± 17(n = 17)
Biogenic $CaCO_3$ content	5 ± 4	8 ± 3	3 ± 2
$\Delta^{14}C$ (‰)	–	−20 ± 22[1)]	8 ± 26(n = 13)
Excess Mn flux	–	157 ± 127(n = 65)	171 ± 138(n = 21)
		2000 *m*	
Particle flux (<1 mm)	440 ± 241	350 ± 140(n = 52)	573 ± 275(n = 63)
POC flux	28 ± 16	17 ± 8(n = 52)	37 ± 19(n = 62)
POC content	5.7 ± 1.3	5.0 ± 1.0	6.5 ± 1.3
POC flux/NPP (%)	3.6 ± 1.8	2.5 ± 1.0	4.2 ± 2.0
Lithogenic flux	249 ± 160	175 ± 63(n = 19)	272 ± 174(n = 61)
Lithogenic content	47 ± 11	49 ± 9	47 ± 12
Biogenic opal flux	165 ± 99	108 ± 54(n = 19)	220 ± 101(n = 20)
Biogenic opal content	33 ± 13	30 ± 13	36 ± 12
Biogenic $CaCO_3$ flux	13 ± 11	16 ± 14(n = 17)	11 ± 6(n = 17)
Biogenic $CaCO_3$ content	3 ± 3	5 ± 4	2 ± 2
$\Delta^{14}C$ (‰)	–	−48 ± 24[1)]	−26 ± 19(n = 6)
Excess Mn flux	–	1038 ± 217(n = 7)	236 ± 122(n = 52)

The number of samples analyzed for opal and $CaCO_3$ are provided because results are only available for only a subset of samples. Net primary production and all the flux values are expressed in mg $m^{-2}d^{-1}$, whereas the contents are expressed as %, with the exception of the excess Mn, the flux and content of which are expressed in μg $m^{-2}d^{-1}$and ppm, respectively. [1)] these results at 1000 m and 2000 m for the non-EN period (March 2011–February 2012) at Station EC1 are from Kim et al. (2017).

at 1000 m and 2000 m, respectively). Small vertical changes in the POC flux during the EN period were responsible for this vertical difference. At all depths, p-values were <0.05 for POC flux between the non-EN and the EN periods. The opal flux in the EN period was consistently greater (by 83–123%) at all depths than in the non-EN period (**Table 1**). By comparison, the $CaCO_3$ flux in the non-EN period was either similar to (at 500 m) or slightly higher (at 1000 and 2000 m) than in the EN period.

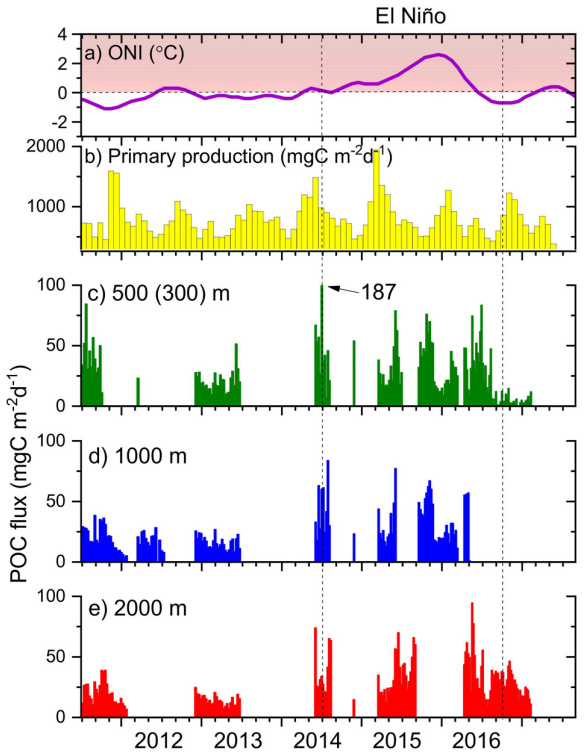

FIGURE 3 | (a) ONI (Oceanic Nino Index; upper panel); **(b)** net primary production determined from MODIS-aqua satellite observations and the Vertically Generalized Productivity Model (middle panel); and **(c–e)** the POC flux at 500 m, 1000 m, and 2000 m, respectively. Where there is no bar, there were no data.

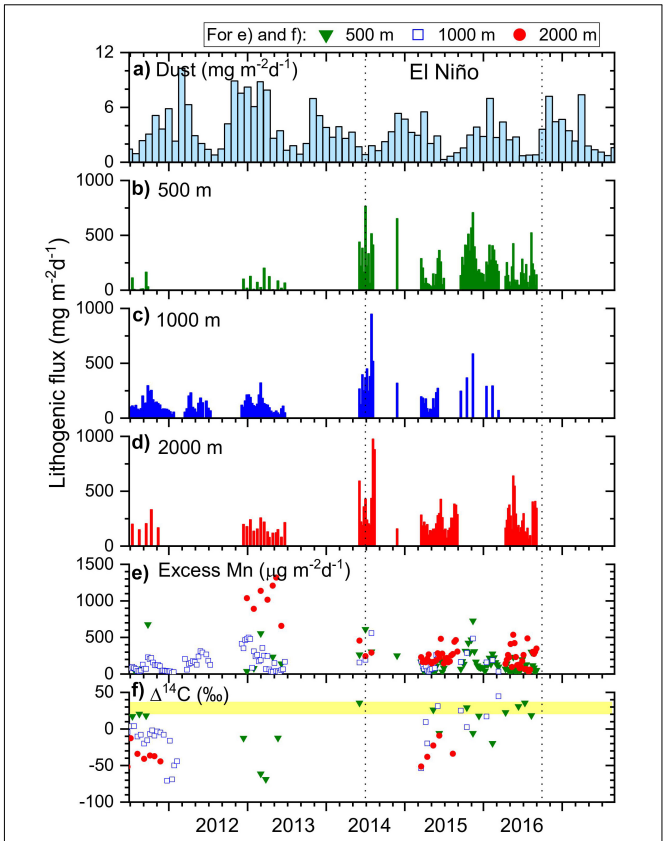

FIGURE 4 | (a) Dust deposition to the sea surface based on a MERRA 2 model; **(b–d)** lithogenic material flux at 500 m, 1000 m, and 2000 m, respectively; **(e)** excess Mn flux at the three sampling depths; and **(f)** $\Delta^{14}C$ (‰) values. To facilitate comparison, the $\Delta^{14}C$ results at 1000 m and 2000 m of Station EC1 in 2011–2012 are also included (Kim et al., 2017). Yellow horizontal bar indicates the range of the $\Delta^{14}C$ values of dissolved inorganic carbon (DIC) in the surface waters at nearby sites (30 ± 12‰, n = 7; Kim et al., 2017).

The differences between the two periods were also evident in the lithogenic material flux (p-values < 0.01). In the non-EN period, the lithogenic material fluxes were significantly lower at 500 m and 1000 m than at 2000 m, while these fluxes were similar at all depths during the EN period. Correspondingly, the relative increase in the lithogenic material flux from the non-EN period to the EN periods was much greater at 500 m (254%) and 1000 m (121%) than at 2000 m (56%; **Table 1**).

During the non-EN period, the particle composition changed with depth (**Figure 5** and **Table 1**), with decreasing POC content and increasing lithogenic material content with increasing depth, and a maximum opal content at 1000 m. In contrast, the particle composition did not change substantially and showed no systematic trends during the EN period. The particle composition was similar at 500 m and 1000 m, but had a higher lithogenic material content and a lower opal content at 2000 m. However, these vertical changes were all much smaller than the temporal variation at each depth.

DISCUSSION

Biological Carbon Pump in the EJS

We first evaluated whether the increase in POC flux at 500 m in the EN period was accompanied by a commensurate increase in the NPP. Although the existence of the SCM (subsurface chlorophyll maximum) may increase the uncertainty in the satellite-derived NPP, Joo et al. (2014) found that the MODIS-derived NPP using the regional primary production algorithm for the EJS correlated strongly with *in situ* measurements by Kwak et al. (2013). This lends confidence in the use of satellite-derived NPP values, at least with respect to temporal variability. The average of the NPP in the EN period was approximately 9% higher than in the non-EN period (841 and 774 gC $m^{-2}d^{-1}$, respectively). However, the relationship between the NPP and the ENSO indexes of the ONI and the MEI (multivariate ENSO index) was weak ($R = 0.23$). Next, we investigated the correlations between the variations in NPP and the POC flux. Monthly data for the NPP were interpolated to match the period when the sinking particles were sampled. While the two parameters appeared to co-vary, the highest correlation coefficient, between the $\log_{10}$(NPP) and $\log_{10}$(POC flux), was low (R = 0.42; not shown). The average change in POC flux at 500 m is greater between the two periods (by 32%) than the average difference in NPP (by 9%). Based on an empirical model in which export

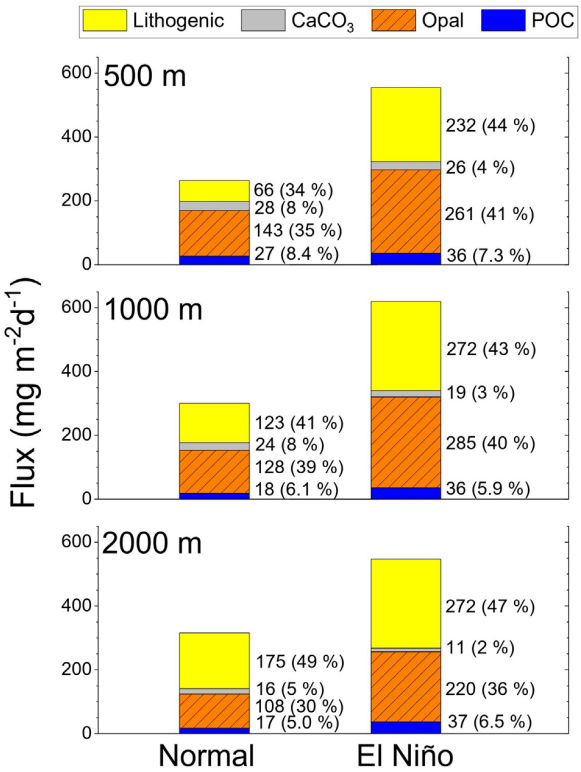

FIGURE 5 | Stacked bar plots of the biogenic and lithogenic material fluxes at the three sampling depths for the normal (non-EN) and EN periods (see **Table 1** for delineation of these periods). The proportions (as%) of each component are included (in parentheses). Note that the height of the stacked bar is not exactly equal to the total particle flux.

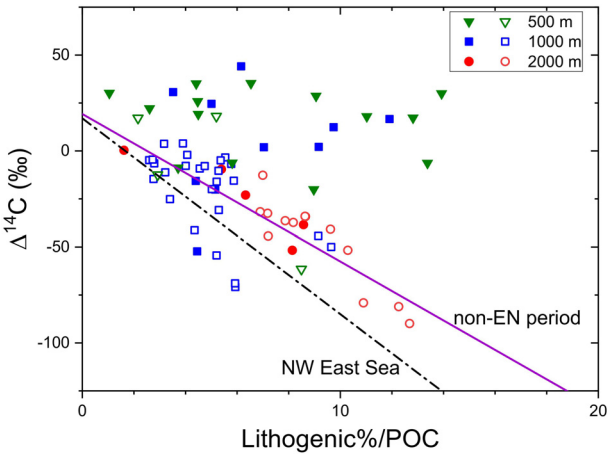

FIGURE 6 | $\Delta^{14}C$ values (‰) against the ratio of the content of lithogenic material to the POC of sinking particles. Open and closed symbols denote the non-EN and EN periods, respectively. Data from Station EC1 are included as non-EN period samples (Kim et al., 2017). The solid line denotes the linear fit of the non-EN period data and the dashed line denotes the linear fit of Japan Basin (Northwest East Sea; Otosaka et al., 2008; Kim et al., submitted).

from the euphotic zone scales to NPP with a power of 1.3 (Laws et al., 2011), an increase of 9% in NPP would correspond to a 17% increase in the export flux. Therefore, the observed 32% increase in POC flux was likely caused by other factors in addition to the increase in the NPP.

The ratio of POC flux at 500 m (which accounts for the majority of flux attenuation; Na et al., 2019) to NPP was generally higher in the EN period than in the non-EN period (**Table 1**), and this pattern was even clearer when the POC flux at 1000 m was considered. The POC flux/NPP ratio remained elevated with increasing depth in the EN period (4.1, 4.4, and 4.2% at 500, 1000, and 2000 m, respectively), whereas it decreased between 500 m and the two deeper trap depths (1000 m and 2000 m) during the non-EN period (3.6 and 2.5%, respectively), implying enhanced carbon sequestration efficiency during the EN period. High opal and lithogenic material fluxes appear to have boosted particle transfer efficiency in the EN period. Because $CaCO_3$ flux is always low in the EJS, opal and lithogenic material presumably have acted as ballast minerals (Armstrong et al., 2001).

Sources of Lithogenic Material and Its Influences on Particle Flux

The lithogenic material flux showed greatest relative difference between the two periods in both magnitude and vertical distribution (**Figures 4**, **5**). In the non-EN period, the lithogenic material flux was considerably greater at 2000 m, although was also significant at 1000 m. In the EN period, the lithogenic material flux was similar at each of the three depths, primarily as a consequence of increased lithogenic material flux at 500 m during this period. We used monthly aeolian dust deposition data obtained from a MERRA2 (Modern-Era Retrospective analysis for Research and Applications) model[1] to investigate whether dust deposition levels were higher and thus could be responsible for the increased lithogenic material flux during the EN period. Over the study period, the dust deposition reached a maximum in 2011, and did not increase significantly during the EN period (**Figure 4**). The dust deposition averaged 4.1 ± 2.7 and 2.7 ± 1.7 mg $m^{-2}d^{-1}$ during the non-EN and EN periods, respectively. The low levels of dust deposition observed during the EN period are consistent with the observations of Yumimoto and Takemura (2015), who found that there was more Asian dust occurrence in the source region during the La Niña years than in other years. The dust flux was estimated to account for only 1-3% of the observed lithogenic material flux at 500 m. We conclude, therefore, that dust deposition was not the major source of the lithogenic material flux.

Since we exclude dust deposition as a significant contributor to the lithogenic material flux, marine processes (i.e., sediment resuspension) must have been responsible for the observed difference in the lithogenic material flux between the two periods. However, despite the higher lithogenic material content, $\Delta^{14}C$ values of POC in the EN period were similar to those in the non-EN period (**Figure 4** and **Supplementary Table S2**). This finding is not consistent with the negative relationship between $\Delta^{14}C$ values of POC and the lithogenic material content or the

[1]https://giovanni.sci.gsfc.nasa.gov/giovanni

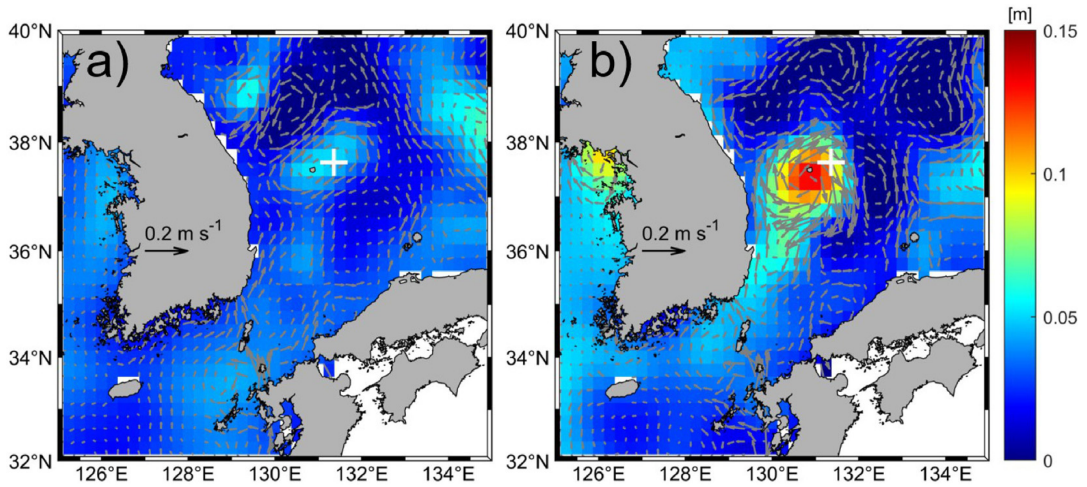

FIGURE 7 | Mean sea surface height (colors) and corresponding geostrophic surface currents (arrows) averaged over **(a)** the non-EN period from July 2011 to March 2014 and **(b)** the EN period from June 2014 to September 2016, estimated from the multi-mission altimeter-based gridded sea surface height data (horizontal resolution of 0.25° grid with error variance of 1.4 cm^2) of the Copernicus Marine Environment Monitoring Service (Taburet et al., 2019).

lithogenic material/POC ratio commonly observed in various environmental settings in the ocean (Hwang et al., 2010; Kim et al., submitted). Notably, higher $\Delta^{14}C$ values accompanied higher lithogenic material flux in the 500 m and 1000 m samples from the EN period (**Figure 6**), suggesting a different provenance for resuspended sediments from the two periods. Specifically, the higher $\Delta^{14}C$ values in the EN period implies an origin from of resuspended sediment entraining more modern POC (e.g., the continental shelf rather than the central basins). The Korea Strait and the southwestern shelf/slope of the Ulleung Basin represent potential sources where energetic semi-diurnal tides and internal waves can stimulate sediment resuspension (Chae et al., 2018). Surface sediments in this region have relatively high $\Delta^{14}C$ values (−100 to −144‰; **Supplementary Table S3**) compared to those from central regions of the Japan and Yamato basins (−173 to ca. −375‰; Otosaka et al., 2008).

The content and flux of excess Mn [i.e., Mn in excess of the Mn/Al ratio of the continental crust; excess Mn = $Mn_{observed} - Al_{observed} \times (Mn/Al)_{crust}$] were also consistent with the possible different sediment source areas noted above (**Figure 4**). The surface sediment in the central basin is reddish brown and enriched with Mn oxide, while the sediment of the slope are gray-brown (Hyun, 2016). The Mn content in the Ulleung Basin was up to 15,000 ppm, but was significantly lower (∼500 ppm) on shelf and slope. The lowest Mn content (∼250 ppm) was reported near the Korea Strait (Cha et al., 2007). Sediments in the central regions of the Japan Basin and the Yamato Basin also have significantly higher Mn contents than surrounding shelf/slope sediments (Otosaka et al., 2004). Consequently, the low excess Mn values in the EN period compared with the non-EN period imply that the lithogenic material at 500 m and 1000 m originated from resuspension of shelf/slope sediments rather than those underlying the central basin during the EN period.

Quantification of the relative contribution of autochthonous versus allochthonous (resuspended) POC based on $\Delta^{14}C$ mass balance is challenging because of the uncertainty in the provenance of advected material. We used the $\Delta^{14}C$ values of the Korea Strait region and the southwestern shelf/slope of the Ulleung Basin (−108‰, which is an average of 4 values obtained from this region) as the putative source for the 500 m and 1000 m samples in the EN period, and a lower $\Delta^{14}C$ value of the western Japan Basin (−375‰; Otosaka et al., 2008) as the source of the 2000 m samples in the EN period as well as those at all depths in the non-EN period. A $\Delta^{14}C$ value of 30‰ was used for freshly produced POC in the surface water (Kim et al., 2017). Using the mean $\Delta^{14}C$ value at each trap depth in the two periods, we estimate the contribution of resuspended sediment to sinking POC to be ca. 11, 12, and 19% for the 500 m, 1000 m, and 2000 m samples in the non-EN period, and ca. 10, 16, and 14% for the corresponding depths in the EN period. These estimates are heavily dependent on the selected value for the allochthonous end-member, which remains highly uncertain. For example, adopting the $\Delta^{14}C$ value of surface sediments from the central Ulleung Basin instead of the western Japan Basin, the estimated contribution from resuspended sediment increases to 50% for the 2000 m samples in the non-EN period. The actual contribution of resuspended sediment to sinking particles is likely between these two extreme cases. Additional $\Delta^{14}C$ and geochemical measurements to constrain sediment provenance, together with improved knowledge of the currents that entrain and transport resuspended particles are needed for more robust assessment of the contribution of resuspended sedimentary POC to sinking particles.

Potential Connection Between the Particle Flux and the Regional Climate in the EJS

Connections and the underlying mechanisms linking ENSO and biophysical properties such as temperature, sea surface height,

and primary production in the Ulleung Basin are not fully understood. Some studies have suggested a potential impact of ENSO on the NPP in the Ulleung Basin via cascading influence of this tropical phenomenon on the strength of the Kuroshio Current that in turn influences volume transport through the Korea Strait and mixed layer thickness (Toba et al., 2001; Yoo and Kim, 2004). However, these linkages need to be elucidated. Our results suggest that the El Niño may exert a strong influence on the efficiency of particle mobilization and export, with sediment resuspension and lateral transport potentially serving as a stronger vector than biogenic particle production in the Ulleung Basin.

A noteworthy feature in the Ulleung Basin during the 2015/16 El Niño was the development of a warm core eddy that persisted in the study region for protracted period of time (from September 2014 to August 2016; Jin et al., 2019; **Figure 7**). Enhanced biological activity and export flux associated with warm-core eddies have been well reported (e.g., Mahadevan et al., 2008; Shih et al., 2015). Eddy-driven subduction may have enhanced the export of biological particles (Boyd et al., 2019; Resplandy et al., 2019). Mesoscale eddy has also been invoked in sediment mobilization and transport (Zhang et al., 2014). Observations from 1993 to 2017 showed that up to 81% of the warm eddies in the Ulleung Basin were related to the EKWC (Shin et al., 2019). A strong EKWC could have entrained sediment during its passage along the western shelf of the Ulleung Basin, and these resuspended particles could have been further transported along the northern rim of the eddy to the mooring site (**Figure 7**). Further studies are needed to evaluate whether persistent eddies are characteristic of El Niño years in the Ulleung Basin (Yun et al., 2016), and if they are responsible for transporting resuspended sediments.

DATA AVAILABILITY STATEMENT

All datasets generated for this study are included in the article/**Supplementary Material**.

AUTHOR CONTRIBUTIONS

Y-IK and JH designed the study. MK, KC, CK, YR, NH, and TE did sample analyses and/or data interpretation. J-EP, J-HP, K-AP, and SN provided satellite-based data and interpretation. MK and JH lead manuscript writing. All authors contributed to the manuscript writing through discussion on the manuscript.

FUNDING

This research was partly supported by the project titled "Biogeochemical cycling and marine environmental change studies (PE99821)." This research was also partly supported by the project titled "Deep Water Circulation and Material Cycling in the East Sea (20160040)," funded by the Ministry of Oceans and Fisheries, Korea. MK was partly supported by the National Research Foundation of Korea grant funded by the Korean Government (Young Researchers' Exchange Programme between Korea and Switzerland 2017–2018: NRF-2017K1A3A1A14092122).

ACKNOWLEDGMENTS

We thank Yun-Bae Kim and Suyun Noh for providing current data and discussion on the draft of the manuscript. We also thank captains and crews of the survey vessel Haeyang 2000 and the R/V Eardo and the Laboratory of Ion Beam Physics at ETHZ for support with the AMS measurements.

SUPPLEMENTARY MATERIAL

The Supplementary Material for this article can be found online at: https://www.frontiersin.org/articles/10.3389/feart.2020.00144/full#supplementary-material

REFERENCES

Armstrong, R. A., Lee, C., Hedges, J. I., Honjo, S., and Wakeham, S. G. (2001). A new, mechanistic model for organic carbon fluxes in the ocean based on the quantitative association of POC with ballast minerals. *Deep Sea Res. II* 49, 219–236.

Behrenfeld, M. J., and Falkowski, P. G. (1997). Photosynthetic rates derived from satellite-based chlorophyll concentration. *Limnol. Oceanogr.* 42, 1–20.

Boyd, P. W., Claustre, H., Levy, M., Siegel, D. A., and Weber, T. (2019). Multi-faceted particle pumps drive carbon sequestration in the ocean. *Nature* 568, 327–335.

Cha, H. J., Choi, M. S., Lee, C. B., and Shin, D. H. (2007). Geochemistry of surface sediments in the southwestern East/Japan Sea. *J. Asian Earth Sci.* 29, 685–697. doi: 10.1016/j.jseaes.2006.04.009

Chae, H. J., and Park, K. (2009). Characteristics of speckle errors of SeaWiFS chlorophyll-α concentration in the East Sea. *J. Korean Earth Sci. Soc.* 30, 234–246. doi: 10.5467/jkess.2009.30.2.234

Chae, J. Y., Jeon, C., Park, S. J., and Park, J. H. (2018). Behavior of Diurnal Internal Waves in the Southwestern East/Japan Sea. *J. Coastal Res.* 85, 486–490. doi: 10.2112/SI85-098.1

Chang, K. I., Hogg, N. G., Suk, M. S., Byun, S. K., Kim, Y. G., and Kim, K. (2002). Mean flow and variability in the southwestern East Sea. *Deep Sea Res. I.* 49, 2261–2279.

Chen, C. T. A., Lui, H.-K., Hsieh, C. H., Yanagi, T., Kosugi, N., Ishii, M., et al. (2017). Deep oceans may acidify faster than anticipated due to global warming. *Nat. Clim. Change* 7, 890–894. doi: 10.1038/s41558-017-0003-y

Chiba, S., Aita, M. N., Tadokoro, K., Saino, T., Sugisaki, H., and Nakata, K. (2008). From climate regime shifts to lower-trophic level phenology: synthesis of recent progress in retrospective studies of the western North Pacific. *Prog. Oceanogr.* 77, 112–126. doi: 10.1016/j.pocean.2008.03.004

Christl, M., Vockenhuber, C., Kubik, P. W., Wacker, L., Lachner, J., Alfimov, V., et al. (2013). The ETH Zürich AMS facilities: performance parameters and reference materials. *Nucl. Instrum. Methods Phys. Res.* 294, 29–38. doi: 10.1016/j.nimb.2012.03.004

Haghipour, N., Ausin, B., Usman, M. O., Ishikawa, N., Wacker, L., Welte, C., et al. (2019). Compound-specific radiocarbon analysis by elemental analyzer–accelerator mass spectrometry: precision and limitations. *Anal. Chem.* 91, 2042–2049. doi: 10.1021/acs.analchem.8b04491

Honda, M. C., Kusakabe, M., Nakabayashi, S., and Katagiri, M. (2000). Radiocarbon of sediment trap samples from the Okinawa trough: lateral transport of 14C-poor sediment from the continental slope. *Mar. Chem.* 68, 231–247.

Honjo, S., Dymond, J., Collier, R., and Manganini, S. J. (1995). Export production of particles to the interior of the equatorial Pacific Ocean during the 1992 EqPac experiment. *Deep Sea Res. II*. 42, 831–870. doi: 10.1016/0967-0645(95)00034-N

Hwang, J., Druffel, E. R., and Eglinton, T. I. (2010). Widespread influence of resuspended sediments on oceanic particulate organic carbon: insights from radiocarbon and aluminum contents in sinking particles. *Glob. Biogeochem. Cycles* 24:GB4016.

Hyun, J. H. (2016). "Microbial ecology and biogeochemical processes in the Ulleung Basin," in *Oceanography of the East Sea (Japan Sea)*, eds K. I. L. Chang, C. I. K. Zhang, C. Park, D. J. Kang (Cham: Springer), 247–296.

Jin, H., Park, Y. G., Pak, G., and Kim, Y. H. (2019). On the Persistence of Warm Eddies in the East Sea. *Sea* 24, 318–331. doi: 10.7850/JKSO.2019.24.2.318

Joo, H., Park, J. W., Son, S., Noh, J. H., Jeong, J. Y., Kwak, J. H., et al. (2014). Long-term annual primary production in the Ulleung Basin as a biological hot spot in the East/Japan Sea. *J. Geophys. Res.* 119, 3002–3011.

Joo, H., Son, S., Park, J. W., Kang, J. J., Jeong, J. Y., Kwon, J. I., et al. (2017). Small phytoplankton contribution to the total primary production in the highly productive Ulleung Basin in the East/Japan Sea. *Deep Sea Res. II* 143, 54–61. doi: 10.1016/j.dsr2.2017.06.007

Kameda, T. (2003). Studies on oceanic primary production using ocean color remote sensing data. *Bull. Fish. Res. Agency* 9, 118–148.

Kameda, T., and Ishizaka, J. (2005). Size-fractionated primary production estimated by a two-phytoplankton community model applicable to ocean color remote sensing. *J. Oceanogr.* 61, 663–672. doi: 10.1007/s10872-005-0074-7

Kawahata, H., Suzuki, A., and Ohta, H. (2000). Export fluxes in the western Pacific warm pool. *Deep Sea Res. I* 47, 2061–2091. doi: 10.1016/S0967-0637(00)00025-X

Kim, H. J., Hyeong, K., Park, J. Y., Jeong, J. H., Jeon, D., Kim, E., et al. (2014). Influence of Asian monsoon and ENSO events on particle fluxes in the western subtropical Pacific. *Deep Sea Res. I* 90, 139–151. doi: 10.1016/j.dsr.2014.05.002

Kim, H. J., Kim, D., Yoo, C. M., Chi, S. B., Khim, B. K., Shin, H. R., et al. (2011). Influence of ENSO variability on sinking-particle fluxes in the northeastern equatorial Pacific. *Deep Sea Res. I* 58, 865–874.

Kim, H. J., Kim, T. W., Hyeong, K., Yeh, S. W., Park, J. Y., Yoo, C. M., et al. (2019). Suppressed CO2 outgassing by an enhanced biological pump in the Eastern Tropical Pacific. *J. Geophys. Res.* 124, 7962–7973. doi: 10.1029/2019JC015287

Kim, M., Hwang, J., Rho, T., Lee, T., Kang, D. J., Chang, K. I., et al. (2017). Biogeochemical properties of sinking particles in the southwestern part of the East Sea (Japan Sea). *J. Mar. Syst.* 167, 33–42.

Kim, M., Hwang, J., Druffel, E. R., and Eglinton, T. I. (submitted). Lateral particle supply as a key vector in the oceanic carbon cycle. *Glob. Biogeochem. Cycles*

Kwak, J. H., Lee, S. H., Park, H. J., Choy, E. J., Jeong, H. D., Kim, K. R., et al. (2013). Monthly measured primary and new productivities in the Ulleung Basin as a biological "hot spot" in the East/Japan Sea. *Biogeosciences* 10, 4405–4417. doi: 10.5194/bg-10-4405-2013

Laws, E. A., D'Sa, E., Naik, P. J. L., and Methods, O. (2011). Simple equations to estimate ratios of new or export production to total production from satellite-derived estimates of sea surface temperature and primary production. *Limnol. Oceanogr. Meth.* 9, 593–601. doi: 10.4319/lom.2011.9.593

Lee, S. H., Yun, M. S., Kim, B. K., Joo, H., Kang, S. H., Kang, C. K., et al. (2013). Contribution of small phytoplankton to total primary production in the Chukchi Sea. *Cont. Shelf Res.* 68, 43–50. doi: 10.1016/j.csr.2013.08.008

Li, W. K., McLaughlin, F. A., Lovejoy, C., and Carmack, E. C. (2009). Smallest algae thrive as the Arctic Ocean freshens. *Science* 326:539. doi: 10.1126/science.1179798

Mahadevan, A., Thomas, L. N., and Tandon, A. (2008). Comment on "eddy/wind interactions stimulate extraordinary mid-ocean plankton blooms". *Science* 320:448. doi: 10.1126/science.1152111

McIntyre, C. P., Wacker, L., Haghipour, N., Blattmann, T. M., Fahrni, S., Usman, M., et al. (2017). Online 13 C and 14 C Gas measurements by EA-IRMS–AMS at ETH Zürich. *Radiocarbon* 59, 893–903. doi: 10.1017/RDC.2016.68

Na, T., Hwang, J., Kim, S., Jeong, S., Rho, T., and Lee, T. (2019). Acidification -vunerable carbonate system of the East Sea (Japan Sea). *Biogeosci. Discuss* doi: 10.5194/bg-2019-474

Noh, S., and Nam, S. (2018). Data from: EC1, mooring time-series since 1996. *SEANOE* doi: 10.17882/58134

Otosaka, S., Tanaka, T., Togawa, O., Amano, H., Karasev, E. V., Minakawa, M., et al. (2008). Deep sea circulation of particulate organic carbon in the Japan Sea. *J. Oceanogr.* 64, 911–923.

Otosaka, S., Togawa, O., Baba, M., Karasev, E., Volkov, T. N., Omata, N., et al. (2004). Lithogenic flux in the Japan Sea measured with sediment traps. *Mar. Chem.* 91, 143–163.

Park, K. A., Chae, H. J., and Park, J. E. (2013). Characteristics of satellite chlorophyll-a concentration speckles and a removal method in a composite process in the East/Japan Sea. *Int. J. Remote Sens.* 34, 4610–4635.

Resplandy, L., Lévy, M., and McGillicuddy, D. J. Jr. (2019). Effects of eddy-driven subduction on ocean biological carbon pump. *Glob. Biogeochem. Cycles* 33, 1071–1084. doi: 10.1029/2018GB006125

Shih, Y. Y., Hung, C. C., Gong, G. C., Chung, W. C., Wang, Y. H., Lee, I. H., et al. (2015). Enhanced particulate organic carbon export at eddy edges in the oligotrophic Western North Pacific Ocean. *PLoS One* 10:e0131538. doi: 10.1371/journal.pone.0131538

Shin, H. R., Kim, I., Kim, D., Kim, C. H., Kang, B., and Lee, E. (2019). Physical characteristics and classification of the Ulleung Warm Eddy in the East Sea (Japan Sea). *Sea* 24, 298–317. doi: 10.7850/jkso.2019.24.2.298

Taburet, G., Sanchez-Roman, A., Ballarotta, M., Pujol, M. I., Legeais, J. F., Fournier, F., et al. (2019). DUACS DT-2018: 25 years of reprocessed sea level altimeter products. *Ocean Sci.* 15, 1207–1224. doi: 10.5194/os-2018-150

Taylor, S. R., and McLennan, S. M. (1985). *The Continental Crust: Its Composition and Evolution*. Oxford: Blackwell Sci.

Toba, Y., Kimura, J., Murakami, H., Kim, M., Yoshikawa, Y., and Shimada, K. (2001). Unusual behavior of the kuroshio current system from Winter 1996 to Summer 1997 Revealed by ADEOS-OCTS and other Data (continued): a study from broad external conditions with bottom topography. *J. Oceanogr.* 57, 141–154. doi: 10.1023/A:1011187023116

Yamada, K., Ishizaka, J., and Hagata, H. (2005). Spatial and temporal variability of satellite primary production in the Japan Sea from 1998 to 2002. *J. Oceanogr.* 61, 857–869.

Yoo, S., and Kim, H. C. (2004). Suppression and enhancement of the spring bloom in the southwestern East Sea/Japan Sea. *Deep Sea Res. II* 51, 1093–1111. doi: 10.1016/j.dsr2.2003.10.008

Yumimoto, K., and Takemura, T. (2015). Long-term inverse modeling of Asian dust: interannual variations of its emission, transport, deposition, and radiative forcing. *J. Geophys. Res.* 120, 1582–1607. doi: 10.1002/2014JD022390

Yun, J. Y., Chang, K. I., Kim, K. Y., Cho, Y. K., Park, K. A., and Magaard, L. (2016). ENSO teleconnection to the isopycnal depth fluctuations of the East/Japan Sea Intermediate Water in the Ulleung Basin during 1968-2002. *J. Phys. Oceanogr.* 46, 2675–2694. doi: 10.1175/JPO-D-15-0225.1

Zhang, Y., Liu, Z., Zhao, Y., Wang, W., Li, J., and Xu, J. (2014). Mesoscale eddies transport deep-sea sediments. *Sci. Rep.* 4:5937. doi: 10.1038/srep05937

Conflict of Interest: The authors declare that the research was conducted in the absence of any commercial or financial relationships that could be construed as a potential conflict of interest.

frontiers in Earth Science

ORIGINAL RESEARCH
published: 08 July 2020
doi: 10.3389/feart.2020.00266

Molecular Nature of Marine Particulate Organic Iron-Carrying Moieties Revealed by Electrospray Ionization Fourier-Transform Ion Cyclotron Resonance Mass Spectrometry (ESI-FTICRMS)

Chen Xu[1], Peng Lin[1], Luni Sun[1], Hongmei Chen[2], Wei Xing[1], Manoj Kamalanathan[3], Patrick G. Hatcher[2], Maureen H. Conte[4], Antonietta Quigg[3] and Peter H. Santschi[1]*

[1] Department of Marine Science, Texas A&M University at Galveston, Galveston, TX, United States, [2] Department of Chemistry and Biochemistry, Old Dominion University, Norfolk, VA, United States, [3] Department of Marine Biology, Texas A&M University at Galveston, Galveston, TX, United States, [4] Bermuda Institute of Ocean Sciences, St. George's, Bermuda

OPEN ACCESS

Edited by:
Gilad Antler, Ben-Gurion University of the Negev, Israel

Reviewed by:
Martha Gledhill, GEOMAR Helmholtz Center for Ocean Research Kiel, Germany
Mina Bižic, Leibniz-Institute of Freshwater Ecology and Inland Fisheries (IGB), Germany

***Correspondence:**
Chen Xu
xuchen66@tamu.edu

Specialty section:
This article was submitted to Biogeoscience, a section of the journal Frontiers in Earth Science

Received: *22 February 2020*
Accepted: *15 June 2020*
Published: *08 July 2020*

Citation:
Xu C, Lin P, Sun L, Chen H, Xing W, Kamalanathan M, Hatcher PG, Conte MH, Quigg A and Santschi PH (2020) Molecular Nature of Marine Particulate Organic Iron-Carrying Moieties Revealed by Electrospray Ionization Fourier-Transform Ion Cyclotron Resonance Mass Spectrometry (ESI-FTICRMS). Front. Earth Sci. 8:266. doi: 10.3389/feart.2020.00266

Marine sinking particulate organic matter (POM), acting as a link between surface primary production and burial of organic matter in marine sediments, undergoes a variety of physical and biochemical alterations on its way to the deep ocean, resulting in an increase in its un-characterizable proportion with diagenesis. Further, the binding ligands in POM for iron, an essential nutrient to marine life and tightly coupled with organic matter, has rarely been studied. In the current study, we employed an approach combining sequential extraction with ultrahigh resolution mass spectrometry (ESI-FTICRMS), in order to explore and unravel the chemical characteristics of organic matter compounds relevant to marine particle flux within the mesopelagic and deep ocean, with a focus on the potential iron-carrying molecules. With increasing depth, POM increases in aliphaticity, and decreases in intensity-normalized O/C ratios, aromatics, and carboxylic-rich alicyclic molecules (CRAM)-like compounds. The potential iron-carrying molecules account for ∼14% of total identified molecules, and appear to have been incorporated into the marine particles via ion complexation, hydrophobic interaction, and/or interlayered "occlusion." The relative abundance of iron-binding organic molecules in these three operationally-defined categories changes with depth: "surficially-complexed" fraction decreases with depth, the "interlayered-occluded" fraction increases to a comparable extent and "hydrophobic interaction" fraction occurs at all depths. Collectively, the potential iron-carrying organic molecules exhibit a set of unique molecular characteristics: a relatively lower average H/C ratio and a higher O/C ratio compared to bulk POM, a dominance of aromatics, black carbon-like compounds and CRAM-like compounds, and minor amounts of aliphatics. These molecules exhibit partial similar molecular features as precursors formed from photochemical reactions in the surface ocean, but they have been greatly modified by flux processes. Noticeably, a minor fraction of these iron-carrying molecules (<1%)

was identified to contain hydroxamate-like moieties [N(OH)-COOH], the key functionality of one of the strongest iron-binding ligands in the dissolved phase. This agrees with improved spectrophotometric results and corroborates their presence in the POM. These hydroxamate-like moieties play an important role in controlling the distributions and fluxes of Fe and particle-reactive radionuclides with similar chemical complexing properties as Fe (e.g., thorium) in the ocean.

Keywords: particulate organic matter, ESI-FTICR mass spectrometry, iron-carrying molecules, marine particles, hydroxamate-like molecules

INTRODUCTION

Sinking particles, composed of organic (sinking particulate organic matter, POM) and inorganic material, are the critical conduit for delivering photosynthetically-fixed organic carbon, food and energy from the surface ocean to the deep sea (Verdugo et al., 2004; Boeuf et al., 2019). They vary in size and shape, consisting of a suit of dead phytoplankton, zooplankton carcasses, larvacean houses, fecal pellet, etc. (Omand et al., 2020). Typically accounting for <20% of the surface primary production, sinking POM forms through a variety of biological, physical and chemical processes that alter its composition and attenuate the flux on its way to the sea floor (Volkman and Tanoue, 2002). Despite its paramount role in global carbon cycling, sinking POM is still a poorly understood organic matter pool in terms of the physical and chemical processes it undergoes while sinking (Lee, 2002).

Iron, as a trace element in the dissolved phase (dFe: 0.02–1.0 nmol L^{-1}; Bruland et al., 1991) at the surface ocean, is tightly coupled with organic carbon in both of their biogeochemical cycles and also regulates the export of POM flux from the euphotic zone to the deep ocean. For example, in high-nutrient, low-chlorophyll (HNLC) regions, the low surface ocean dFe concentration can limit primary productivity by as much as 30–40% (Marchetti and Maldonado, 2016). In response to the scarcity of Fe, microorganisms produce a variety of low-molecular-weight (LMW, <1 kDa) organic compounds, i.e., siderophores, with strong binding affinity to metals, especially Fe(III) (Reid et al., 1993; Neilands, 1995; Butler, 1998, 2005; Winkelmann, 2002; Vraspir and Butler, 2009; Butler and Theisen, 2010). Siderophores are typically multidentate, oxygen-donor ligands that include hydroxamate, catecholate and α-hydroxy-carboxylate types. Out of these three types of siderophores, hydroxamate has been the focus of many studies on marine dFe binding ligands (Macrellis et al., 2001; Mawji et al., 2008; Velasquez et al., 2011; Boiteau et al., 2016). First, dissolved hydroxamate siderophores (300–1000 Da) are ubiquitous in oceanic systems. For example, in surface waters and water below the photic zone of the Central California upwelling, more than half of the Fe-binding compounds have been characterized as either hydroxamate type or catecholate type siderophores (Macrellis et al., 2001). In contrast, in the non-Fe-limiting regions (e.g., the North Atlantic Ocean), the characterizable siderophores exclusively consist of hydroxamate siderophores, which are produced by heterotrophic bacteria and fungi (Raines et al., 2015) in the concentration range of 3–20 pM (Mawji et al., 2008). In the eastern Pacific Ocean, two types of hydroxamate siderophores (hydrophilic siderophore Ferrioxamine B and amphiphilic amphibactins) dominate the siderophore pool and alternate in their abundance across a transect from coastal waters to the HNLC region to the oligotrophic ocean (Boiteau et al., 2016). Second, dissolve hydroxamate siderophores have the highest stability constants (as logK) that range from 16 to 62 at 25°C for complexation of $Fe(H_2O)_6^{3+}$ with the fully deprotonated ligand of hydroxamate functionality (N(OH)-COOH) (Boukhalfa and Crumbliss, 2002). The tri-hydroxamate siderophores have an average conditional stability constant for Fe of 30.6 (Kraemer et al., 2005; Ahmed and Holmstrom, 2014). Third, hydroxamate siderophores are hydrophilic or amphiphilic, and they have relatively higher resistance towards photolysis compared to other types of Fe-binding ligands (Barbeau et al., 2001, 2003). These properties likely enhance their transport and stability in the upper ocean.

Most current studies have focused on the iron-carrying ligands in the dissolved phase (Macrellis et al., 2001; Hunter and Boyd, 2007; Vraspir and Butler, 2009; Bundy et al., 2016), and only recently it was suggested that hydroxamate-like moieties also existed in the particles/colloids (Chuang et al., 2013, 2015a). Yet the mechanisms by which these hydroxamate-like moieties are formed/incorporated in the particulate or colloidal phases, their molecular characteristics, their micro-molecular environment, and whether these potential Fe-binding sites play a significant role in Fe biogeochemical cycling remain largely unknown. The reason lies in the analytical difficulty of qualitatively and quantitatively assessing these iron-carrying ligands in the particulate phase, especially those hydroxamate-like moieties, the latter of which are a minor component of the particulate organic carbon (POC) pool [determined as <1.5% of POC in Chuang et al. (2013, 2015a)], and thus "masked" when applying techniques like NMR, FTIR or C K-edge X-ray absorption spectroscopy, and/or gas and liquid chromatography.

In the present study, electrospray ionization (ESI) Fourier-transform ion cyclotron resonance mass spectrometry (FTICRMS) was applied to elucidate the composition of organic matter from marine settling particles, using a sequential extraction method. Our objectives were to: (1) examine the overall molecular information of the settling particulate organic matter (POM) with depth, i.e., what the micro-molecular environment is like for the iron-complexing moieties; (2) characterize the molecular features of iron-complexing sites in fractions of the marine particles that were probed by different

extraction reagents, thus representing possible mechanisms for their incorporation into the settling particles; and (3) investigate their distributions at three depths (500, 1500, and 3200 m) in the northwestern Sargasso Sea, where there have been several studies in the particle and elemental fluxes with the Bermuda Time-Series Site (Conte et al., 2019).

MATERIALS AND METHODS

Here we apply an optimized sequential extraction method (Chuang et al., 2015b) followed by ESI-FTICRMS, to characterize the molecular features of the Fe-complexing sites in sinking particles (500, 1500, and 3200 m) in the northwestern Sargasso Sea near Bermuda. Using Fe(III) as the tracer, we identified potentially iron-complexing ligands in different operationally-defined fractions: an EDTA (Ethylenediaminetetraacetic acid disodium salt dihydrate) fraction of "surficial metal-complexed" POM (EDTA is used to chelate the surficial cations, dissociate the POM-metal complex, and thus the OM will be released into the solution); a SDS (sodium dodecyl sulfate) fraction of molecules that are bound to particles via hydrophobic interactions, i.e., "hydrophobically-sorbed POM;" and a HF (hydrofluoric acid) fraction of residual "interlayered and interstitial" mineral complexed/occluded POM.

Sample Collection

Particle flux material was collected by the Bermuda Oceanic Flux Program (OFP) time-series, located at 31°50′N, 64°10′W. The OFP mooring utilizes McLane Parflux sediment traps (0.5 m^2 surface area; McLane Labs, Falmouth, MA, United States) at 500, 1500, and 3200 m depths that are programmed at a nominal 2-week sampling interval. Sample cups are filled with high purity Sargasso Sea deep water (∼3000 m) brine (40 ppt) and amended with ultra-high purity $HgCl_2$ (200 mg/L) to minimize microbial degradation of the POM during sample collection. Details of sample collection and analytical methods are described elsewhere (Conte et al., 2019). Samples analyzed herein were collected in 2005 and 2006, and stored refrigerated. Additional sample information is provided in **Supplementary Table S1**.

Sequential Extraction of Marine Particles

The bulk hydroxamate concentration was determined using samples collected at different time points (n = 3 for each depth, see below section "Hydroxamate-Like Functionalities Determination in Marine Particles" and **Supplementary Table S1**). Due to the limited sample material, the sequential extraction required pooling of three discrete samples collected at different time points of the same depth (**Supplementary Table S1**). The sequential extraction procedure is shown in **Figure 1**. Briefly, ∼10 mg of particles from each depth were first incubated with 1 mL 100 mM EDTA solution (pH 8.0) at 4°C overnight on an end-to-end orbital shaker. The extractant soluble phase was separated from the particles via centrifugation and filtration with a syringe filter (PTFE membrane, diameter 25 mm, pore size 0.45 μm). The filtrate was extensively diafiltered (10–12 times) against ultrapure water with an Amicon Ultra-4 centrifugal filter unit with a membrane cutoff of 3 kDa. This retentate (>3 kDa and <0.45 μm) is defined as "EDTA extract." The residual particles were then re-suspended with 1 mL 1% SDS in 0.01 M Tris buffer (pH 6.8) at 95°C for 1 h. This extractant was processed the same way as described for "EDTA extract" and defined as the "SDS extract." The residual pellet from SDS extraction was then washed three times with ultrapure water and subsequently treated with 1 mL 52% HF on ice for 1 h. The slurry was evaporated to dryness under a N_2 stream. After this, the residual particle material was re-suspended in 1 mL Tris-HCl (250 mM, pH 8.0) and centrifuged at 5000 × g for 15 min to separate the particles from the solution, the latter of which was processed as described previously by ultrafiltration to isolate the "HF extract" (Chuang et al., 2015b).

In order to better understand the stepwise extraction efficiency of POM from the marine particles, particles collected at different time points from the three depths (**Supplementary Table S1**) were well mixed (∼5 mg each) with a spatula and four replicate particles were extracted in parallel to obtain the particles from each sequential step for elemental analysis, using a Perkin-Elmer CHNS/O 2400 analyzer. The mass loss and organic carbon contents of the residual particles after each extraction step were determined and the analytical error of these four replicates were reported. For elemental analysis, the pre-weighed sample was directly acidified in a silver capsule three times and was heated at 60°C overnight to remove any residual acid, prior to the analysis. Acetanilide (71.09% C, 6.71% H, 10.36% N) was used as the calibration standard.

Incubation of Fe (III) and Sequentially-Extracted POM Fractions

Sequential extractants, in the matrix of ultrapure water, from marine particles (section "Sequential Extraction of Marine Particles") were split into two aliquots, one amended with $FeCl_3$ (10 μM) and one without (control). The pH difference between these two treatments [i.e., Fe (+) and Fe (-)] were within 0.5 and both were around neutral. These were incubated at 4°C on an end-to-end orbital shaker in the dark for 3 days. After that, excess $FeCl_3$ was removed by extensively diafiltering the sample against ultrapure water with an Amicon Ultra-4 centrifugal filter unit with a membrane cutoff of 3 kDa (**Figure 1**), and the retentate (>3 kDa) was kept for further ESI-FTICRMS analysis. The sample of the Fe (-) treatment was processed the same manner (with diafiltration) for comparison purpose.

ESI-FTICRMS Analysis

Marine particle extracts were diluted with methanol (1:1, v/v) immediately before injection into a Bruker Daltonics 12 Tesla Apex Qe ESI-FTICRMS (College of Sciences Major Instrumentation Cluster, COSMIC, Old Dominion University, Virginia). Positive ion mode was used, as the molecules of interest are iron-carrying molecules, which have better ionization efficiency in this mode (Waska et al., 2016). Samples were continuously injected by a syringe pump (infusion rate of 120 μL/h), and electrospray voltages were optimized for each sample. Ions were accumulated in a hexapole for 2.0 s before being

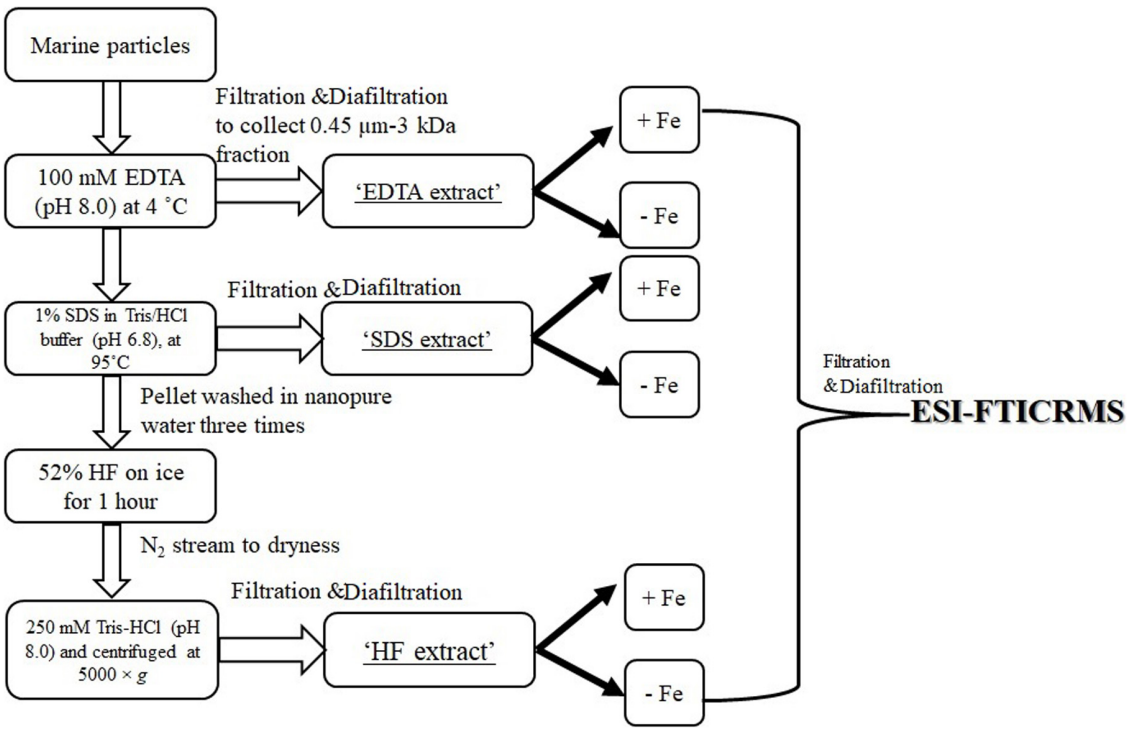

FIGURE 1 | Flow chart of sequential extraction and electrospray ionization (ESI) Fourier-transform ion cyclotron resonance mass spectrometry (FTICRMS) analysis.

transferred to the ICR cell and 300 transients were co-added. Fourier transformation and magnitude calculation of the free induction decay signal (FID) was accomplished using the Bruker Daltonics Data Analysis software (Version 4.0 SP 2). A total of 18 samples (three depths × three extractions × two treatments), as well as six procedure blanks (three extractions × two treatments) following the same steps as the samples (one for Fe addition and the other for no Fe addition), were included for FTICRMS analysis. Selected samples were analyzed multiple times to ensure the analytical reproducibility and all samples were analyzed within the same week to ensure stable instrumentation parameters and conditions for all samples (Sleighter et al., 2012).

Mass spectra were externally calibrated with a polyethylene glycol standard and then internally calibrated using a set of m/z values within the samples. Several criteria were met for picking out the calibration peak list: (1) peaks have a signal-to-noise (S/N) ratio $\geq$5, (2) peaks that have intermediate intensities to minimize instrumental artifacts that yield peaks with too high or too low intensities, (3) peaks have an error (i.e., the difference between the exact mass of calculated formula and the measured m/z) of $<$0.5 ppm, and (4) peaks can generate only one possible formula containing only C, H, O and/or Na elements, and all formulas have their corresponding structures found in Pubchem database. There was at least one calibration point every 15–20 m/z units (i.e., every other CH_2), across the entire m/z region (200–1400 m/z). Linear mode calibration was performed on each dataset.

All m/z lists, with an S/N $\geq$ 4, were first searched for ^{13}C peaks and confirmed they were mostly singly-charged. Those ^{13}C peaks were not included in the formula calculations. Moreover, the m/z values present in the procedure blank spectra were excluded from the sample mass list. A molecular formula calculator (Molecular Formula Calc Version 1.2.3 NHMFL, 2016) generated empirical formula matches within 1.0 ppm using elemental ranges of $C_{(\geq 5)}H_{(\geq 5)}N_{(0-10)}O_{(\geq 0)}S_{(0-2)}Na_{(0-1)}Fe_{(0-1)}$. All formulas were screened to eliminate those that are unlikely to occur in OM, according to a list of selection criteria (Neubert et al., 2002; Kind and Fiehn, 2007; Stubbins et al., 2010; Walker et al., 2016). Kendrick mass defect (KMD) analyses were then performed to look for homologous series of CH_2, CH_2O, COO, O, H_2O, H_2, etc., respectively, formed by at least two unique formulas (i.e., only one possible formula corresponds to a single m/z value after the formula rule's screening). If there are multiple possible formulas for a single m/z value (usually those with m/z values $>$400 Da), the one that fell within a homologous series was kept as the more likely formula (Sleighter and Hatcher, 2007). Subsequently, multiple formulas of one m/z value were screened by searching chemical structures in the Pubchem database. Formulas with no chemical structures identified were excluded from the final formula assignment. Fe-carrying molecules were also examined if their ^{54}Fe isotopic peak could be found (i.e., the singly-charged ^{56}Fe and ^{54}Fe-carrying peak m/z difference is 1.99533 $\pm$ 0.00070 and the isotopic ratio of $^{54}Fe/^{56}Fe$ as 0.063 $\pm$ 0.030) (Boiteau and Repeta, 2015; Walker et al., 2016). Adduct of iron hydroxide with methanol is likely irrelevant, since the mass list of the procedure blank (with the addition of $FeCl_3$ yet without the addition of particle extracts) had been subtracted

from the sample mass lists. Besides, this issue should occur much less likely at μM $FeCl_3$ concentrations (Waska et al., 2016).

Molecules in each sample were categorized by both elemental classes and compound classification. The double bond equivalent (DBE) was calculated as DBE = 1+ 0.5 (2C-H+N). Aliphatic compounds were assigned to formulas with DBE: C < 0.3 and H:C = 1.0–3.0. Aromatic compounds and condensed aromatic compounds were assigned to formulas with aromaticity indices [AI, calculated by (1+C-O-S-0.5(N+H))/(C-O-S-N)] >0.5 and >0.67, respectively. A modified AI, which was suggested to be more inclusive by dividing the possible number of carbonyl unsaturation by two: AI_{mod} = (1+C-0.5O-S-0.5(H+N))/(C-0.5O-S-N) (Stubbins et al., 2010; Koch and Dittmar, 2016), was also calculated. Black carbon was defined as molecules with O:C 0.3–0.6, H:C 0.5–0.8 (Kim et al., 2004). Carboxylic-rich alicyclic molecules (CRAM) were defined as molecules having DBE: C 0.30–0.68, H 0.20–0.95, and O 0.77–1.75 (Hertkorn et al., 2006).

To unambiguously identify a specific functional group, a tandem mass spectrometry analysis (MS/MS) would be required (Sleighter and Hatcher, 2007, 2008). However, MS/MS analysis would have great difficulty to identify a trace component, i.e., a hydroxamate functional group (<1% of POC, see section "Bulk Hydroxamate Concentrations in Marine Particles") using the bulk OM without any extensive pre-separation and concentration. Instead, a KMD (Kendrick Mass Defect) analysis was conducted to search the whole mass list for molecules that fall in some homologous series of the key functionality of hydroxamate, N(OH)-COOH (with the formula total H number being corrected for Na adducts or Fe complexation). A homologous series of N(OH)-COOH was formed, if at least two formulas differ only by $[N(OH)\text{-}COOH]_n$.

Hydroxamate-Like Functionalities Determination in Marine Particles

Bulk hydroxamate concentration of the particles was quantified using the classical "Csaky" spectrophotometric method (Gillam et al., 1981), which required a hydrolysis step to first release the bound hydroxamic acid. The un-hydrolyzed particle yielded no response to the reactions, suggesting it is hydroxamic acid rather than hydroxylamine that is being detected. We noticed a rapid "browning" effect of this method when analyzing particle samples, likely caused by sulfuric acid. This effect was corrected by subtracting the absorbance of a control sample without the addition of the final coloring reagent from that of a sample aliquot with the addition of the final coloring reagent. The net absorbance was used to calculate hydroxamate concentration from the calibration curve using acetohydroxamic acid (AHA) as the standard. This modified method was validated with siderophore standards added to marine particles or soil particles (Xu et al., 2015). In addition, we also critically scrutinized if there could be any other interferences by the following biomolecule classes: (1) neutral polysaccharides (e.g., dextran); (2) acidic polysaccharides and monosaccharides (e.g., alginic acid and glucuronic acid); (3) proteins/amino acid (e.g., cytochrome c and phenylalanine); (4) fatty acids (e.g., palmitic acid); (5) humic acid (e.g., 1S104H from IHSS); (6) fulvic acid (2S101F from IHSS); (7) deoxyribonuclease. We verified that none of these compounds caused any significant interferences to this method (i.e., their absorbance is the same as in ultrapure water) (Xu et al., data not shown).

The presence of N(OH)-COOH in the marine particles, either detected as "positive" with the "Csaky" method, or calculated by KMD analysis to fall in the homologous N(OH)-COOH series, are defined as "hydroxamate-like" molecules below.

RESULTS

Bulk Hydroxamate Concentrations in Marine Particles

The average hydroxamate concentration of the settling particles at 500, 1500, and 3200 m depth was 19.4 (± 12.4), 8.7 (± 1.4), and 7.3 (± 0.1) μM-AHA eq./g-particle (n = 3 for each depth, **Supplementary Table S1** and **Figure 2A**). While particulate hydroxamate decreased with water depth, the POC-normalized hydroxamate concentrations decreased only slightly or remained steady (**Figure 2B**, ∼0.2–0.6% POC).

Relative Distribution of POM in Sequential Extracts With Depth

The mass and organic carbon changes after each sequential extraction step are shown in **Supplementary Table S2**. The organic carbon (%, residual mass) generally increased with each extraction step, from the original value of (5.55% ± 0.05) to (45.48% ± 1.90) after HF extraction. EDTA extraction released (67% ± 2) of the particle mass and (39.74% ± 7.52) of the total original organic carbon into the solution. SDS and HF extraction released similar amounts of the original mass (13% ± 2) and (17% ± 3), yet quite different amounts of original organic carbon: (30.17% ± 2.35) and (7.46% ± 0.95), respectively. Their respective extraction efficiencies, which were calculated as the loss of particulate mass or organic carbon (the part being extracted into the solution) to those in the previous particles/residues being extracted, change in the following order: HF (86% ± 3) > EDTA (67% ± 2) > SDS (41% ± 7) by mass, and SDS: (49.92% ± 2.34) > EDTA (39.74% ± 7.52) > HF (24.68% ± 2.74) based on organic carbon. These rankings are likely to be different if one changes the sequential extraction order, which is not the focus of the current study. These three consecutive steps removed substantial amounts of original mass (98%) and of original organic carbon (77%) from the marine sinking particles, supporting the idea that ESI-FTICRMS analysis of these fractions represents the overall composition of OM in the marine particles.

The ESI-FTICRMS intensity percentages of the three extracts with depth is given in **Figure 3**. For each depth, the mass lists of the three extract (EDTA, SDS and HF) of the non-$FeCl_3$-amended samples were combined. If there are common m/z values shared by different samples within the same depth, the average intensity was adopted. At 500 m, the POM consists mostly of SDS-extractable material (87%), followed by EDTA-extractable compounds (12%), and the HF-extractable material

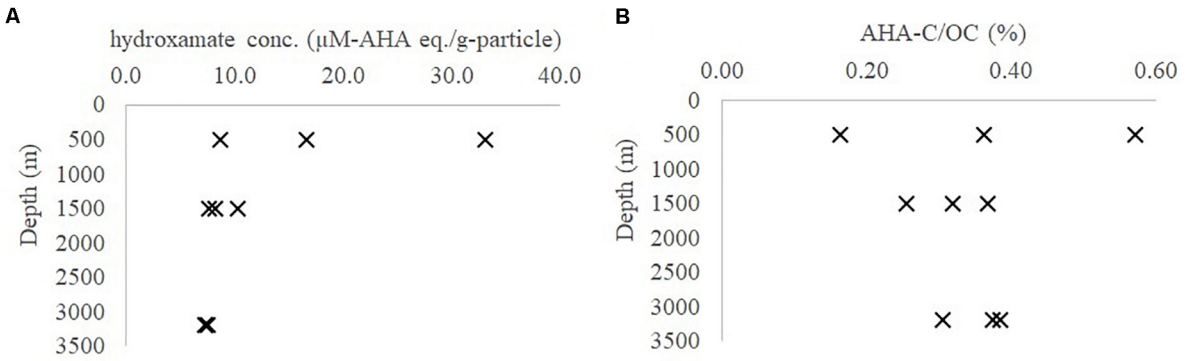

FIGURE 2 | Hydroxamate concentration in **(A)** μM-AHA eq./g-particle; **(B)** AHA-C/OC (%) in marine particles from the northern Atlantic Ocean at different seasons (AHA, acetohydroxamic acid; OC, organic carbon).

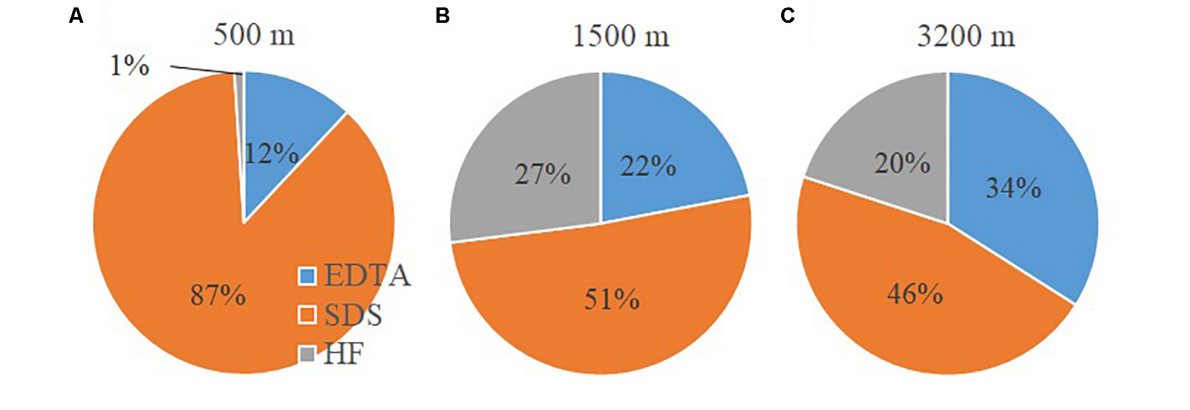

FIGURE 3 | Intensity percentages of the three sequential fractions determined by electrospray ionization (ESI) Fourier-transform ion cyclotron resonance mass spectrometry (FTICRMS) in the settling particles: **(A)** 500 m; **(B)** 1500 m; **(C)** 3200 m.

is only a very minor fraction (1%). At 1500 m depth, the SDS fraction decreases to 51% of the total extractable POM, while the EDTA and HF fractions increase (22 and 27%, respectively). At 3200 m, POM compounds are more evenly distributed and comprise 34, 46, and 20% for the EDTA, SDS and HF fractions, respectively.

Molecular Characteristics of Sequential Extracts of Marine Particles

Each sequential extractant (the non-$FeCl_3$-amended) recovered a distinct set of compounds (in terms of elemental groupings and compound classifications) from the particles. The formula elemental groupings are listed in **Table 1**. CHO, CHON, and CHONS formulas are three major groups, all together accounting for 96, 91, and 85% of the total formulas for 500, 1500, and 3200 m, respectively. The number of peaks shared among POM at the different depths is shown in **Supplementary Table S3** (773 formulas between 500 and 1500 m; 790 formulas between 1500 and 3200 m; 877 formulas between 500 and 3200 m). CHO formulas increased with depth, from 27% at 500 m to 35% at 1500 m, and to 41% at 3200 m. In contrast, the CHON formulas slightly decreased with depth, from 38% at 500 m to 39% at 1500 m, and to 34% at 3200 m. CHONS formulas decreased more rapidly with depth, from 31% at 500 m to 17% at 1500 m, and to 9% at 3200 m. CHOS, a minor fraction of the total identified formulas (within 5%) increased by twofold from 1.5% at 500 m to 3.7% at 1500 m, and stayed steady as 3.4% at 3200 m. Notably, deoxy-compounds increased from 2% at 500 m to 5% at 1500 m, and to 12% at 3200 m.

TABLE 1 | Elemental grouping of assignable peaks at different depths.

# of formulas	500		1500		3200	
	2184		1127		1354	
	Number	%, total intensity	Number	%, total intensity	Number	%, total intensity
CHO	1013	27.0	418	35.3	547	41.4
CHON	722	38.1	433	39.4	502	34.0
CHONS	344	31.3	198	16.7	224	9.4
CHOS	48	1.5	38	3.7	37	3.4
Deoxy-compounds	57	2.1	40	4.9	44	11.9

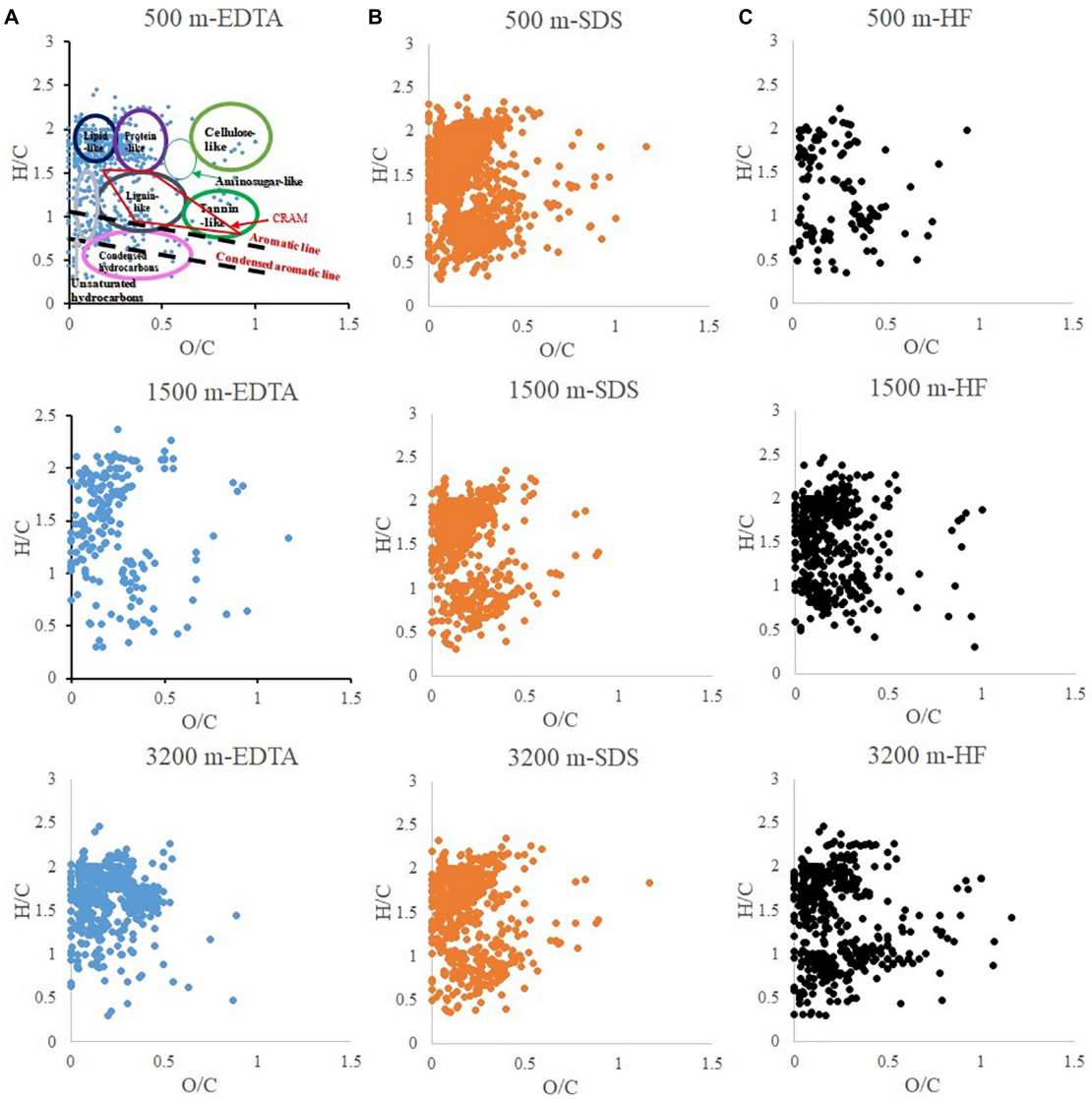

FIGURE 4 | van-Krevelen diagram of particulate organic matter extracted by different reagents: **(A)** EDTA (ethylenediaminetetraacetic acid disodium salt dihydrate); **(B)** SDS (sodium dodecyl sulfate); **(C)** HF (hydrofluoric acid).

The compound classifications are displayed in van Krevelen diagrams (**Figure 4**) and also listed in **Table 2**. From 500 to 3200 m, aliphatics steadily increased from 41.8 to 67.9%, while the N-containing aliphatics, which mostly consist of protein, peptides, and amino sugars, first increased from 15.4% at 500 m to 33.1% at 1500 m, and then decreased to 17.6% at 3200 m. Aromatics, condensed aromatics and black-carbon-like compounds decreased from 27.2 to 8.6%, 7.5 to 3.7%, and 3.1 to 0.7%, respectively. Similarly, with increasing depth the intensity-normalized H/C values (Sleighter and Hatcher, 2008) (calculated by summing up the product of individual intensity and the corresponding H/C ratio of each formula, and then being divided by the total intensity) increased from 1.31 to 1.62 whereas O/C values decreased from 0.20 to 0.16. CRAM-like compounds were only a minor fraction (5.0% at 500 m to 4.4% at 3200 m).

Iron-Carrying Molecules

In total, 745 iron-carrying molecules were identifiable, accounting for ∼14% of total assignable molecules including all depths, $FeCl_3$-amended and non-$FeCl_3$-amended treatments (**Figure 5A**). The majority of the Fe-carrying molecules were found in the $FeCl_3$-amended samples, and only 33 formulas were found in the non-$FeCl_3$-amended samples. These iron-carrying molecules could have been corroborated by adding another trivalent metal (e.g., Ga) at the same concentration (10 μM) and identifying if the same apo molecule forms the similar complex with the other metal, which can be applied in future study.

The absolute number of iron-carrying molecules in the "EDTA extract" increased from 103 at 500 m to 587 at 1500 m and then dropped to 101 at 3200 m; those in the "SDS extract" increased

TABLE 2 | Compound classification of assignable peaks at different depths (CRAMs were defined as molecules having DBE: C 0.30–0.68, DBE: H 0.20–0.95, and DBE: O 0.77–1.75; average H/C and O/C are calculated as intensity-normalized average values).

Molecular class	500 m		1500 m		3200 m	
	Peak no.	Intensity (%, total intensity)	Peak no.	Intensity (%, total intensity)	Peak no.	Intensity (%, total intensity)
All identified formulas	2184	100	1127	100	1354	100
Aliphatics	1235	41.8	621	51.8	739	67.9
Aromatics (AI > 0.5)	238	27.2	134	17.2	174	8.6
Aromatics ($AI_{modified}$ > 0.5)	325	38.6	180	22.7	230	10.9
Condensed aromatics (AI ≥ 0.67)	89	7.5	49	7.3	64	3.7
Black carbon (O/C 0.3–0.6; H/C 0.5–0.58)	46	3.1	23	1.8	22	0.7
CRAM	149	5.0	83	5.1	116	4.4
N-containing CRAM	105	4.1	57	3.6	76	3.3
N-containing aliphatics	308	15.4	227	33.1	252	17.6
Average H/C	1.31		1.47		1.62	
Average O/C	0.20		0.18		0.16	

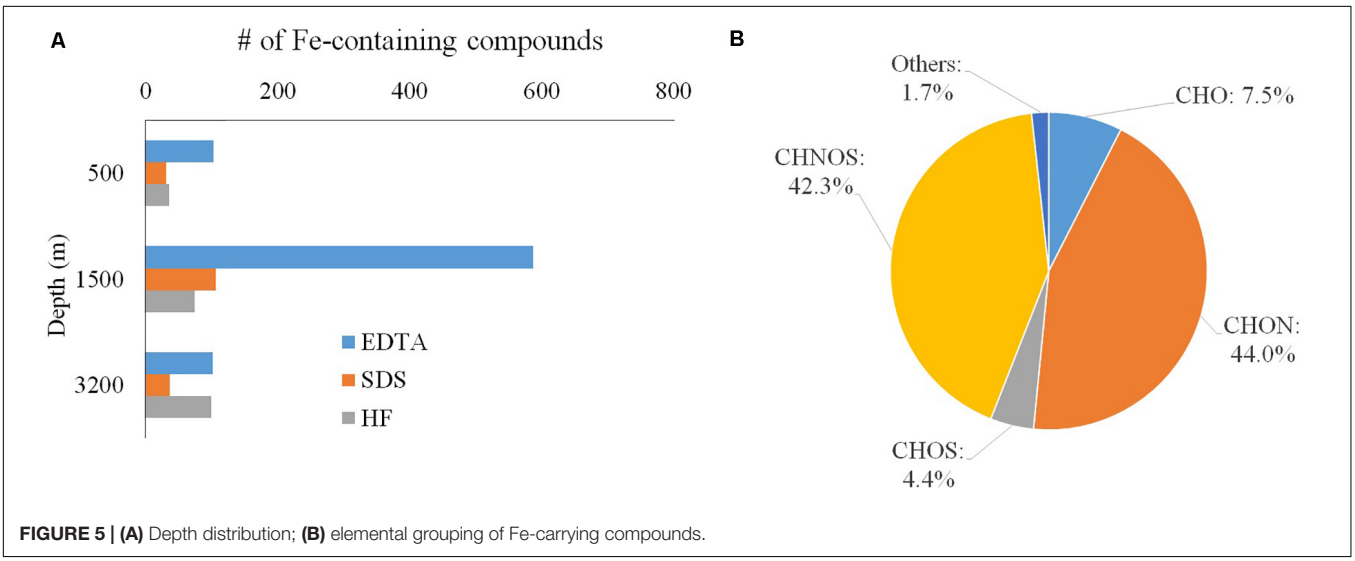

FIGURE 5 | (A) Depth distribution; **(B)** elemental grouping of Fe-carrying compounds.

from 31 at 500 m to 106 at 1500 m and then dropped to 37 at 3200 m; those in the "HF extract" increased from 35 at 500 m to 74 at 1500 m and to 99 at 3200 m (**Figure 5A**). The EDTA fraction ranked highest in the number of iron-carrying molecules at both the 500 m and 1500 m depths, while at 3200 m depth the EDTA and HF fractions have a similar number of Fe-carrying molecules.

CHON and CHONS were the dominant elemental groups and accounted for 86.3% of total assignable Fe-carrying formulas (**Figure 5B**). CHO and CHOS were both minor elemental groups, and accounted for 7.5 and 4.4% of total assignable Fe-carrying formulas, respectively. The compound classification of the Fe-carrying formulas is distinct from that of the bulk POM in that these Fe-carrying molecules consist mainly of aromatics (57.6% if using AI, and 61.7% if using modified AI), black carbon (14.8%), CRAM-like compounds (11.5%), and very minor amount of aliphatics (1.7%) (**Table 3** and **Figure 6**). The intensity-normalized H/C and O/C ratios are 0.75 and 0.44 (**Figure 6**), respectively, indicating an unsaturated/aromatic and highly-oxygenated composition.

Direct Evidence for the Presence of Hydroxamate-Like Molecules

Eleven formulas were found that belong to some N(OH)-COOH homologous series (**Supplementary Table S4**). Their m/z ranged from 431.98069 to 684.99753, mostly falling into the regions of aromatics and condensed aromatics (**Figure 6**). All these hydroxamate-like molecules accounted for 0.20 and 0.41% of all the assignable formulas in number and intensity, respectively, and 1.48 and 0.95% of the total Fe-carrying formulas in number and intensity, respectively (**Table 3**). These values provide a lower limit of hydroxamate-like moieties because not all these molecules may necessarily fall into any N(OH)-COOH homologous series. In the CH_2-Kendrick-Mass-Defect (KMD)-Kendrick-Mass (KM) plot, which categorizes the molecules according to their mass defect (or the elemental

TABLE 3 | Compound classification of assignable Fe-containing peaks at all depths (CRAMs were defined as molecules having DBE: C 0.30–0.68, DBE: H 0.20–0.95, and DBE: O 0.77–1.75, percentage is calculated by number of each class to the total number of formulas, i.e., 745).

Compound class	No. of peaks	% total Fe-carrying compounds
Aliphatic (DBE:C < 0.3, H:C 1.0–3.0)	13	1.7
Aromatics (AI > 0.5 or AI_{mod} > 0.5)	429 or 460	57.6 or 61.7
Condensed aromatics (AI > 0.67)	334	44.8
Condensed aromatic ring structures (DBE:C > 0.7)	505	67.8
Black carbon-like (O:C 0.3–0.6; H:C 0.5–0.8)	110	14.8
Carboxylic-rich alicyclic molecules (CRAM)	86	11.5
N(OH)-COOH kendrick mass defect analysis ($n \geq 2$)	27	1.48 (and 0.95 in intensity percentage)

composition), Kendrick mass defect of the Fe-containing molecules shifted below that of their corresponding apo molecules, the latter of which were found in the Fe (-) treatment (**Supplementary Figure S1**).

DISCUSSION

Characteristics of the Molecular Micro-Environment of the Iron-Carrying Molecules in the Settling Particles

The changing molecular characteristics of the sinking particles with depth can be contrasted with trends observed for dissolved organic matter (DOM) (Chen et al., 2014b; Timko et al., 2015). First, higher average H/C values of DOM have been reported for the surface water of both North Pacific and Atlantic oceans, compared to those values of their respective deep water (Chen et al., 2014b; Timko et al., 2015), whereas the sinking particles exhibit an opposite trend with depth in our study (i.e., increasing H/C values with depth, **Table 2**). Second, the contents of aliphatic and carbohydrate-like compounds in DOM decrease with depth, likely due to the selective biodegradation of these molecules with increasing depth (Chen et al., 2014b). In samples collected at the same Sargasso Sea location, Timko et al. (2015) found higher concentrations of aliphatic compounds in the surface DOM pool than deep waters, while conversely those of aromatic/unsaturated and polyphenolic-like compounds were higher in deep waters. In contrast, we observe that particulate aliphatics (**Figure 4** and **Table 2**) contents increased with depth. In addition, though carbohydrates are not well ionized in ESI (Shen and Perreault, 1998; Chen et al., 2011), spectrophotometric measurements by Chuang et al. (2013) provide evidence for the carbohydrate preservation in the sinking particles: 30% of OC at 500 m, 33% at 1500 m, and 26% at 3200 m, compared to the percentage of POC in particle mass as 11% at 500 m, 7% at 1500 m, and 5% at 3200 m. Third, higher percentages of CRAM-like formulas were observed in the intermediate and deep waters compared to surface water DOM in both North Pacific and Atlantic oceans, generally accounting for a substantial portion of the total mass spectrum intensity (40–65%) (Chen et al., 2014b). However, the particulate CRAM-like compounds are not a significant component of the POM (<6%) (**Figure 4** and **Table 2**).

The results show that aliphatic compounds, and carbohydrate-like molecules become more predominant in sinking particles with increasing depth while aromatics, condensed aromatics, black carbon-like molecules, and CRAM-like compounds are preferentially "removed." One hypothetical explanation for this pattern is the microbial community attached on particles actively modifies POM and thus produces labile material (Boeuf et al., 2019; Omand et al., 2020). The other alternative explanation is these compounds might be condensation products resulting from a Maillard-type reaction (Brandes et al., 2004) and thus become less biodegradable (Hedges et al., 2001). The differences in the molecular data for the three sequential extraction fractions provide some hints for understanding the molecular interactions within the organic phase of the sinking particles. Hydrophobic interactions (as probed by SDS extraction) appear to be the dominant mechanism for surface-active organic materials to associate with particles at mesopelagic depths (500 m) (**Figure 3**). With increasing depth there is, however, a greater importance of metal complexation and cation bridging. It could be due to the fact that more intact (dead or senescent) cells are present in the sinking particles at the 500 m than the other two deeper depths (1500 and 3200 m), and thus more cellular and membrane material became available for SDS extraction. However, at the other two depths, the cells could have mostly broken down, and the resulting OM either has been degraded or resulted in the metal complexed fraction. Lastly, more organic materials appear to partition into particle interstices (as probed by HF extraction) with depth (1500 and 3200 m vs. 500 m, **Figure 3**), which could provide a physical protective mechanism for organic molecules to become less accessible to microbial activity.

Refractory Nature of Particulate Hydroxamate-Like Moieties Revealed by Their Depth Distribution

In general, the absolute hydroxamate concentration in the settling particles decreased with depth in the Sargasso Sea while the POC-normalized concentration did not. This could indicate that hydroxamate-like moieties in the settling particles might be relatively less labile, compared to the bulk POC (**Figures 2A,B**). These hydroxamate concentrations are 10 to 20-fold lower than what was reported by Chuang et al. (2013). The source of this discrepancy is likely because Chuang et al. (2013) did not correct for the "browning effect" caused by the sulfuric acid step (see above).

The particulate hydroxamate concentrations determined at different seasons in the upper mesopelagic depth (500 m) has a larger variation compared to those in the intermediate (1500 m) and bathypelagic (3200 m) depths (**Figure 2** and **Supplementary Table S1**). This suggests that abundances of iron and microbially-derived iron-binding ligands are more seasonally-driven in upper mesopelagic (e.g., seasonality of atmospheric dust input to surface waters) than at the intermediate and deep depths (Sedwick et al., 2005; Bundy et al., 2016). Once incorporated into the settling

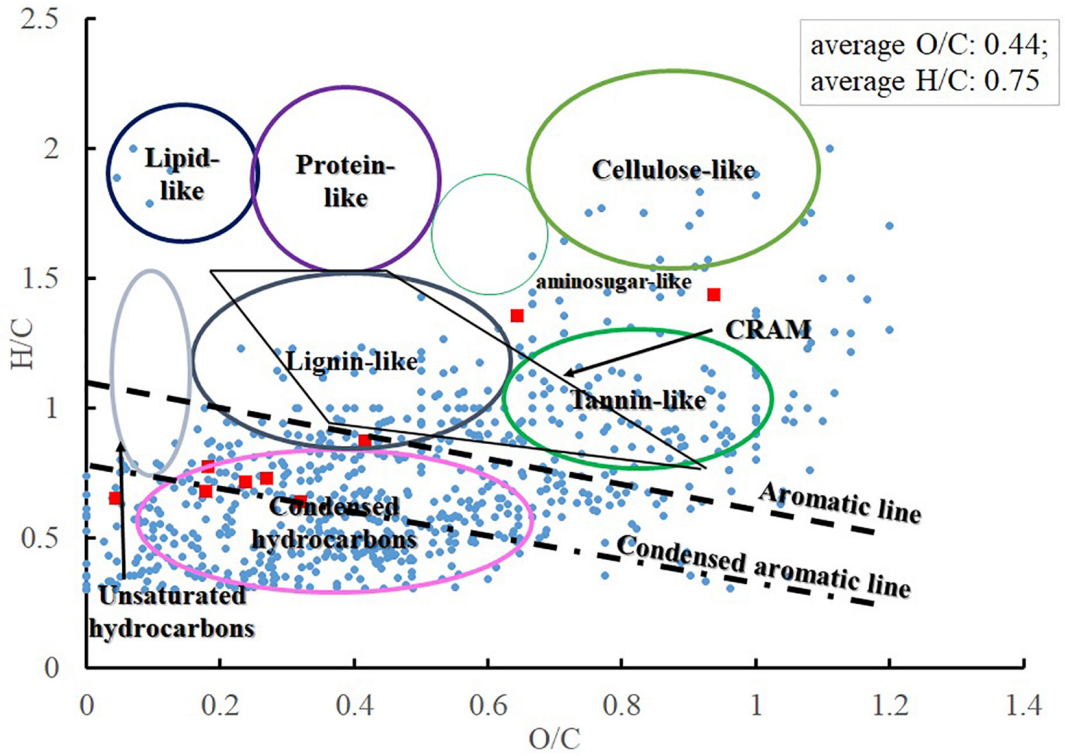

FIGURE 6 | Compound classification of Fe-carrying compounds from three extractants (blue circle, Fe-containing formulas; red square, Fe, hydroxamate-like containing formulas).

particles and transported to depth, hydroxamate-like molecules could have been stabilized via metal complexation (as probed by EDTA) (Iskrenova-Tchoukova et al., 2010), or hydrophobic sorption (as probed by SDS) or mineral interlayered occlusion (as probed by HF), and thus they may have been protected against enzymatic reaction (see below discussion).

While one needs to be cautious about applying the ESI-FTICRMS data for any quantitative purpose given the ionization efficiencies of ESI are variable for different types of compound groups, our results are in good agreement with the spectrophotometric results (a range of 0.2–0.6% of POC contributed by the carbon of N(OH)-COOH, in a comparison to 0.41% of total peak intensity contributed by hydroxamate-like molecules, **Table 3** and **Supplementary Table S1**). Both results show that the N(OH)-COOH functionality is only a trace component compared to the bulk POM. These two independent lines of evidence collectively support the presence of N(OH)-COOH functional group in the sinking particles of the open ocean, at a level < 1% of the POC.

Using the lower limit of particle mass concentration and flux [10 μg/L and 10 mg/m^2/d reported in Chuang et al. (2013)] and a median value of 10 μM-AHA eq./g-particle for particulate hydroxamate concentration, the particulate hydroxamate concentration (in overall volume) and flux at the studied site can be estimated to be 100 pM and 0.1 μmol-AHA eq./m^2/d, respectively. This is on the same order of magnitude as the dissolved equivalent hydroxamate flux in the same area which is estimated to be 0.2 μmol-AHA eq./m^2/d, assuming a dissolved organic carbon flux of 15 mg/m^2/d (Giering et al., 2014) and a hydroxamate-C to dissolved organic carbon ratio of 10^{-6}. Meanwhile, Mawji et al. (2008) reported the dissolved hydroxamate siderophore in the surface water of the Atlantic Ocean was 3–20 pM. Thus, our results indicate that while hydroxamate-like moieties appear to be a trace component of POM, they could be comparable to their dissolved counterparts in the concentrations and fluxes. However, one has to be cautious that a direct comparison between the hydroxamate-like moieties in the particulate phase and the dissolved hydroxamate siderophores deserves more scrutiny. The reason is that there are still quantitative uncertainties based on the assumptions of relative concentrations of hydroxamate moieties and organic carbon in particles and water, and lack of evidence to connect dissolved hydroxamate siderophore as the source of the hydroxamate-like moieties in the particulate phase.

Possible Mechanisms for Incorporation and Preservation of Iron-Carrying Molecules and the Subset Hydroxamate-Like Molecules

We observed distinct molecular differences between Fe-carrying molecules with likely Fe-chelating properties and the bulk POM. This could reflect differences in biogeochemical sources and respective biosynthetic pathways. For example,

Chen et al. (2014a) showed that POM produced from photo-flocculated DOM was enriched with both aliphatic and aromatic components, yet no direct evidence supported whether the co-precipitated Fe was complexed with both types of compounds or preferentially complexed with one or the other. This Fe-rich photo-produced black carbon pool (~10% of the POC) was estimated to be nearly equivalent to the estimated global flux of dissolved black carbon from land to the ocean (Chen et al., 2014a). In a study that was not conducted in the oceanic context, plutonium (an A-type or hard metal (i.e., ion with low polarizability) that was often referred to having similar chemical complexing properties as Fe due to their similar ionic potential Z/r) (Chuang et al., 2013) was found to be predominantly associated with nitrogen-enriched, low average H/C (~0.64), high DBE (~16), aromatic and condensed aromatic compounds (DiDonato et al., 2017). In the present study, we did observe the Fe-carrying molecules are enriched in aromatic and condensed aromatics, and also contain black carbon with a content similar to what was reported in Chen et al. (2014a), however, these particulate Fe-carrying molecules were deplete in aliphatic (only 1.7%, **Table 3**), and also distinctly different from the bulk POM (41.8–67.9%, **Table 2**). A hypothetical explanation is as follows: Below 500 m where photochemical reactions are minor, the aliphatic moieties of these molecules are preferentially removed via microbial activity. Meanwhile, both the black carbon-like and CRAM-like compounds are preserved, compared to the bulk of the POM, and the latter exhibit a totally opposite pattern (i.e., aliphatic-enriched, aromatic and CRAM-depleted and deoxygenation) with increasing depth (**Table 2** vs. **Table 3**).

While the hydroxamate-like moieties are only a minor fraction of the potential Fe-binding ligands of the POM, they may play an important role in both carbon and Fe cycling. As shown here, a substantial portion of the POM (~77% of POC) can be removed by our sequential extraction method and saturated with dissolved Fe^{3+}, which would otherwise not likely be exposed and accessible to Fe^{3+} under natural conditions. Furthermore, the flux of the hydroxamate-like moieties in the sinking particles is the same order of magnitude as their dissolved counterparts. We adopt here the hydroxamate flux of 0.1 μmol-AHA eq./m^2/d as we calculated in section "Refractory Nature of Particulate Hydroxamate-Like Moieties Revealed by Their Depth Distribution." Considering hydroxamate and Fe usually forms hexadentate or octahedral complexes via three bidentate ligands, this particulate hydroxamate flux has a theoretical maximum capacity of carrying an Fe flux of 0.03 μmol-Fe/m^2/d. This is to be compared to an average particulate Fe flux of 4 μmol-Fe/m^2/d (Chuang et al., 2013). Uncertainties in this assessment are possibly large, yet these rough calculations suggest that particulate hydroxamate could be one of the strongest organic Fe-binding ligands in natural sinking particles, considering their high binding affinity to Fe(III) over other known ligands (Reid et al., 1993; Neilands, 1995; Winkelmann, 2002; Butler, 2005; Butler and Theisen, 2010).

In addition to the above mentioned general molecular features of the iron-carrying molecules (**Figure 6** and **Table 3**), the prevalence of sulfur with these hydroxamate-like functionalities (**Supplementary Table S4**) is noticeable, as dissolved S-containing hydroxamates were previously reported

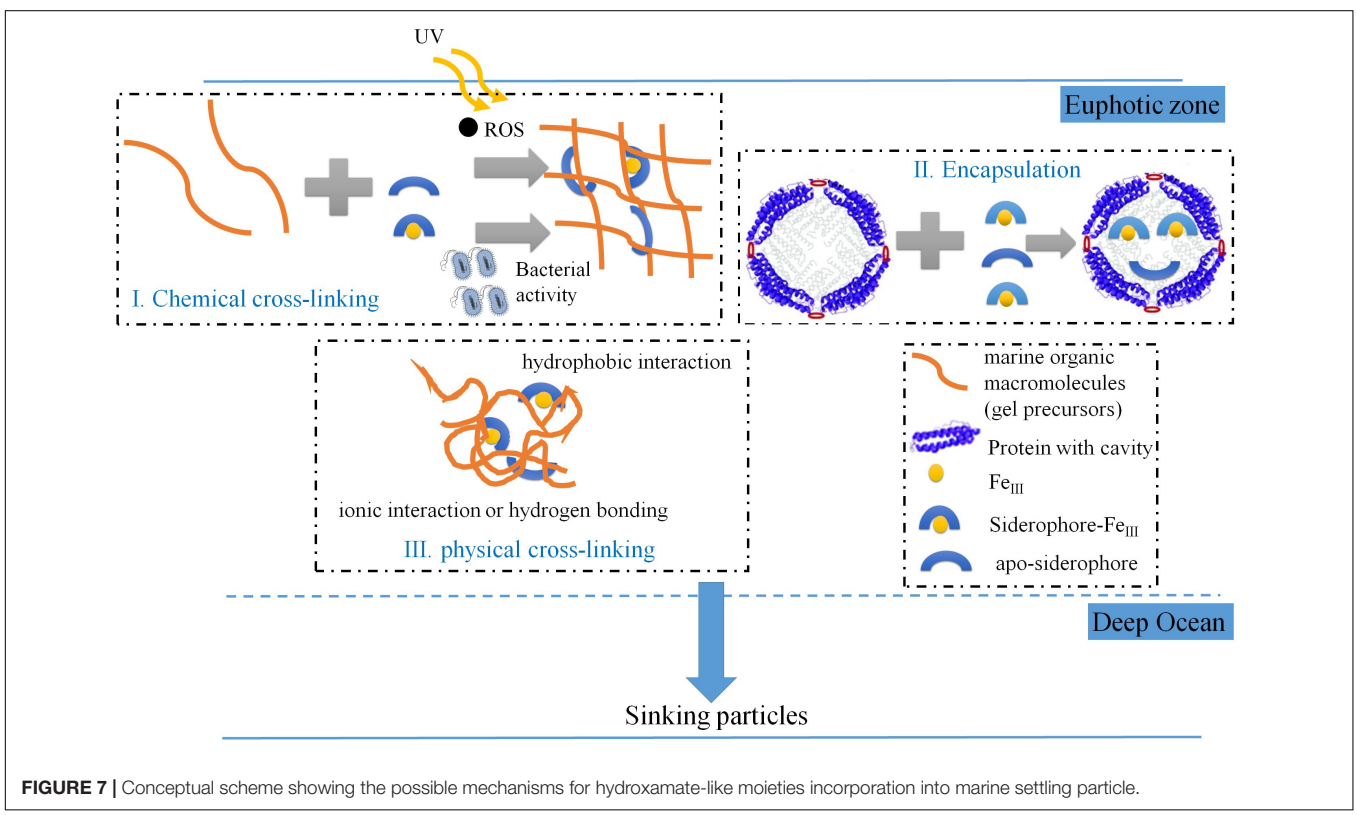

FIGURE 7 | Conceptual scheme showing the possible mechanisms for hydroxamate-like moieties incorporation into marine settling particle.

yet in a low proportion to the total dissolved hydroxamate siderophores in natural environments (Gledhill et al., 2019). How sulfur was incorporated into these hydroxamate-like moieties in the marine particles is equivocal, with one option being via abiotic pathways (Sleighter and Hatcher, 2008; Raven et al., 2016; Pohlabeln et al., 2017), or biological processes (Boeuf et al., 2019). Another molecular feature is that these hydroxamate-like molecules have relatively low H/C ratio (average H/C as 0.83, **Supplementary Table S4**) compared to those of the dissolved hydroxamate siderophores which usually exceed 1.0 (e.g., average H/C in the dissolved hydroxamate siderophore is 1.49; Gledhill et al., 2019). It is possible that dissolved hydroxamate siderophores produced by particle-attached bacteria or fungi are a direct source to be incorporated into the particles. However, these molecular characteristics suggest that these hydroxamate-like moieties are by no means similar in chemical composition or structure to their dissolved counterparts, thus they likely have experienced complex biogeochemical processes yet to be defined (**Figure 7**).

First, hydroxamate-like moieties might be incorporated into the particles via sunlight-induced reactive oxygen species (ROS) mediated protein aggregation (Sun et al., 2017, 2018, 2019) in surface waters. In support of this mechanism, many previous studies have shown, although indirectly, that more nitrogen than carbon could accumulate into particles during irradiation (Helms et al., 2013; Chen et al., 2014a; Sun et al., 2019). We have observed N-containing aliphatics, consisting mostly of proteins, peptides, and amino sugars (Chen et al., 2018), accounting for 15.4–33.1% of the POM (in intensity %, **Table 2**). In comparison Chuang et al. (2013) found that about 45% of POC in particles consisted of protein (Chuang et al., 2013). Thus, it is compelling to believe that proteinaceous components are a significant component of the settling particles. The photo-reaction-induced and ROS-mediated crosslinking process in surface waters would generate precursors including aliphatic and condensed aromatic-like molecules (Chen et al., 2014a) that would be further modified as particles are processed in the water column (see above in this section).

A protein encapsulating mechanism could be an alternative pathway for hydroxamate-like moieties incorporation into marine particles. For example, ferritin, a large protein primarily storing iron mineral internally (Frankel, 1991) by marine microbes (Marchetti et al., 2009; Shire and Kustka, 2015), has been demonstrated to also encapsulate siderophores into cavity-like structures within the apoferritin (Dominguez-Vera, 2004). This ferritin-encapsulating mechanism has been exploited in health sciences to design slow-release drugs (Dominguez-Vera, 2004; Zhang et al., 2006; He and Marles-Wright, 2015).

Finally, some labile organic molecules, e.g., amino acids or simple sugars, have been shown to be preserved in marine sediments via sorption mechanisms (Keil et al., 1994; Barber et al., 2017). This likely involves relatively "weak" forces such as hydrophobic, ionic interactions or hydrogen bonding that are associated with mineral phases. Some bacteria (e.g., *Pseudomonas aeruginosa*) have been shown to utilize pyoverdine (a siderophore that contains both catecholate- and hydroxamate-like ligands) to complex the metal oxide surface for attachment (Upritchard et al., 2007). Thus, it is possible that some hydroxamate-like moieties in particles might be located with bacteria. In addition, the apparent LMW hydroxamate-like moieties observed in ESI-FTICRMS (**Supplementary Table S4**) could also be ionically bound as they were reversibly desorbed by the EDTA reagent. LMW molecules that are held together via hydrophobic interactions, hydrogen bonding and ionic interactions (complexation) can form supramolecular ("physical cross-linking") associations (Sutton and Sposito, 2005) with an apparent molecular weight over 3 kDa (either present in the marine particles captured by sediment trap or a 0.45 μm membrane, or an ultrafiltration membrane). These supramolecular associations can dissociate within the electrospray interface, releasing LMW molecules.

Regardless of the exact mechanism of incorporation, it is clearly evident from our work that hydroxamate-like moieties exist in the particulate phase, potentially equivalent in concentrations and fluxes to their counterparts in the dissolved phase. The Fe-carrying compounds which represent all the potential organic Fe-binding ligands of the settling particles, have molecular features in a contrast to the bulk POM, the latter of which is then different from the vast DOM pool. The next step would be to identify the exact mechanism of hydroxamate-like molecule formation/incorporation, as this would be of great value for better understanding of the cycling of Fe, organic matter and organic nitrogen in the ocean. While our study only analyzed particulate Fe-carrying molecules in the oligotrophic North Atlantic gyre, our results strongly suggest the relative importance of hydroxamate-like molecules, which possibly have been incorporated via various physical and chemical mechanisms. These, along with the major fractions of Fe-binding compounds identified here, likely play an important role in controlling Fe and other A-type particle-reactive radionuclides (e.g., thorium) distributions and flux in the ocean.

DATA AVAILABILITY STATEMENT

All datasets generated for this study are included in the article/**Supplementary Material**.

AUTHOR CONTRIBUTIONS

CX and PS conceived and designed the experiment. CX and WX performed the particle extraction experiment. CX performed the iron amendment incubation experiment. PL, CX, and HC performed the ESI-FTICRMS experiment. CX, PL, LS, HC, WX, and MK performed the ESI-FTICRMS data analysis. CX, PL, HC, WX, MK, PH, MC, AQ, and PS wrote the manuscript. All authors contributed to the article and approved the submitted version.

FUNDING

The early part of our work was funded by the NSF-OCE Grant No. 1356453. The OFP time-series was funded by the NSF-OCE Grant No. 0623505 to MC.

ACKNOWLEDGMENTS

We thank the crew of the R/V Weatherbird II and R/V Atlantic Explorer for assistance with OFP ship operations, and JC Weber, S. Huang, and J. Barkman for assistance with sample processing. We greatly appreciate two reviewers for their very constructive comments.

SUPPLEMENTARY MATERIAL

The Supplementary Material for this article can be found online at: https://www.frontiersin.org/articles/10.3389/feart.2020.00266/full#supplementary-material

REFERENCES

Ahmed, E., and Holmstrom, S. J. M. (2014). The effect of soil horizon and mineral type on the distribution of siderophores in soil. *Geochim. Cosmochim. Acta* 131, 184–195. doi: 10.1016/j.gca.2014.01.031

Barbeau, K., Rue, E. L., Bruland, K. W., and Butler, A. (2001). Photochemical cycling of iron in the surface ocean mediated by microbial iron(III)-binding ligands. *Nature* 413, 409–413. doi: 10.1038/35096545

Barbeau, K., Rue, E. L., Trick, C. G., Bruland, K. T., and Butler, A. (2003). Photochemical reactivity of siderophores produced by marine heterotrophic bacteria and cyanobacteria based on characteristic Fe(III) binding groups. *Limnol. Oceanogr.* 48, 1069–1078. doi: 10.4319/lo.2003.48.3.1069

Barber, A., Brandes, J., Leri, A., Lalonde, K., Balind, K., Wirick, S., et al. (2017). Preservation of organic matter in marine sediments by inner-sphere interactions with reactive iron. *Scie. Rep.* 7:366.

Boeuf, D., Edwards, B. R., Eppley, J. M., Hu, S. K., Poff, K. E., Romano, A. E., et al. (2019). Biological composition and microbial dynamics of sinking particulate organic matter at abyssal depths in the oligotrophic open ocean. *Proc. Natl. Acad. Sci. U.S.A.* 116, 11824–11832. doi: 10.1073/pnas.1903080116

Boiteau, R. M., Mende, D. R., Hawco, N. J., McIlvin, M. R., Fitzsimmons, J. N., Saito, M. A., et al. (2016). Siderophore-based microbial adaptations to iron scarcity across the eastern Pacific Ocean. *Proc. Natl. Acad. Scie. U.S.A.* 113, 14237–14242. doi: 10.1073/pnas.1608594113

Boiteau, R. M., and Repeta, D. J. (2015). An extended siderophore suite from Synechococcus sp PCC 7002 revealed by LC-ICPMS-ESIMS. *Metallomics* 7, 877–884. doi: 10.1039/c5mt00005j

Boukhalfa, H., and Crumbliss, A. L. (2002). Chemical aspects of siderophore mediated iron transport. *Biometals* 15, 325–339. doi: 10.1023/A:1020218608266

Brandes, J. A., Lee, C., Wakeham, S., Peterson, M., Jacobsen, C., Wirick, S., et al. (2004). Examining marine particulate organic matter at sub-micron scales using scanning transmission X-ray microscopy and carbon X-ray absorption near edge structure spectroscopy. *Mar. Chem.* 92, 107–121. doi: 10.1016/j.marchem.2004.06.020

Bruland, K. W., Donat, J. R., and Hutchins, D. A. (1991). Interactive influences of bioactive trace-metals on biological production in oceanic waters. *Limnol. Oceanogr.* 36, 1555–1577. doi: 10.4319/lo.1991.36.8.1555

Bundy, R. M., Jiang, M., Carter, M., and Barbeau, K. A. (2016).). Iron-binding ligands in the Southern California current system: mechanistic studies. *Front. Mar. Sci.* 3:27. doi: 10.3389/fmars.2016.00027

Butler, A. (1998). Acquisition and utilization of transition metal ions by marine organisms. *Science* 281, 207–210. doi: 10.1126/science.281.5374.207

Butler, A. (2005). Marine Siderophores and microbial iron mobilization. *Biometals* 18, 369–374. doi: 10.1007/s10534-005-3711-0

Butler, A., and Theisen, R. M. (2010). Iron(III)–siderophore coordination chemistry: reactivity of marine siderophores. *Coord. Chem. Rev.* 254, 288–296. doi: 10.1016/j.ccr.2009.09.010

Chen, H., Stubbins, A., and Hatcher, P. G. (2011). A mini-electrodialysis system for desalting small volume saline samples for Fourier transform ion cyclotron resonance mass spectrometry. *Limnol. Oceanogr. Methods* 9, 582–592. doi: 10.4319/lom.2011.9.582

Chen, H. M., Abdulla, H. A. N., Sanders, R. L., Myneni, S. C. B., Mopper, K., and Hatcher, P. G. (2014a). Production of black carbon-like and aliphatic molecules from terrestrial dissolved organic matter in the presence of sunlight and Iron. *Environ. Sci. Technol. Lett.* 1, 399–404. doi: 10.1021/ez5002598

Chen, H. M., Stubbins, A., Perdue, E. M., Green, N. W., Helms, J. R., Mopper, K., et al. (2014b). Ultrahigh resolution mass spectrometric differentiation of dissolved organic matter isolated by coupled reverse osmosis-electrodialysis from various major oceanic water masses. *Mar. Chem.* 164, 48–59. doi: 10.1016/j.marchem.2014.06.002

Chen, H. M., Yang, Z. M., Chu, R. K., Tolic, N., Liang, L. Y., Graham, D. E., et al. (2018). Molecular Insights into arctic soil organic matter degradation under warming. *Environ. Sci. Technol.* 52, 4555–4564. doi: 10.1021/acs.est.7b05469

Chuang, C. Y., Ho, Y. F., Conte, M. H., Guo, L. D., Schumann, D., Ayranov, M., et al. (2013). Role of biopolymers as major carrier phases of Th, Pa, Po, Pb and Be radionuclides in settling particles from the Atlantic Ocean. *Mar. Chem.* 157, 131–143. doi: 10.1016/j.marchem.2013.10.002

Chuang, C. Y., Santschi, P. H., Wen, L. S., Guo, L., Xu, C., Zhang, S., et al. (2015a). Binding of Th, Pa, Pb, Po and Be radionuclides to marine colloidal macromolecular organic matter. *Mar. Chem.* 173, 320–329. doi: 10.1016/j.marchem.2014.10.014

Chuang, C. Y., Santschi, P. H., Xu, C., Jiang, Y. L., Ho, Y. F., Quigg, A., et al. (2015b). Molecular level characterization of diatom-associated biopolymers that bind Th-234, Pa-233, Pb-210, and Be-7 in seawater: a case study with Phaeodactylum tricornutum. *J. Geophys. Res. Biogeosci.* 120, 1858–1869. doi: 10.1002/2015jg002970

Conte, M. H., Carter, A. M., Koweek, D. A., Huang, S., and Weber, J. C. (2019). The elemental composition of the deep particle flux in the Sargasso Sea. *Chem. Geol.* 511, 279–313. doi: 10.1016/j.chemgeo.2018.11.001

DiDonato, N., Xu, C., Santschi, P. H., and Hatcher, P. G. (2017). Substructural components of organic colloids from a pu-polluted soil with implications for pu mobilization. *Environ. Sci. Technol.* 51, 4803–4811. doi: 10.1021/acs.est.6b04955

Dominguez-Vera, J. M. (2004). Iron(III) complexation of Desferrioxamine B encapsulated in apoferritin. *J. Inorganic Biochem.* 98, 469–472. doi: 10.1016/j.jinorgbio.2003.12.015

Frankel, R. B. (1991). "Iron biominerals: an overview," in *Iron Biominerals*, eds R. B. Frankel and R. P. Blakemore (Boston, MA: Springer), 1–6. doi: 10.1007/978-1-4615-3810-3_1

Giering, S. L. C., Sanders, R., Lampitt, R. S., Anderson, T. R., Tamburini, C., Boutrif, M., et al. (2014). Reconciliation of the carbon budget in the ocean's twilight zone. *Nature* 507, 480–483. doi: 10.1038/nature13123

Gillam, A. H., Lewis, A. G., and Andersen, R. J. (1981). Quantitative determination of hydroxamic acids. *Anal. Chem.* 53, 841–844. doi: 10.1021/ac00229a023

Gledhill, M., Basu, S., and Shaked, Y. (2019). Metallophores associated with Trichodesmium erythraeum colonies from the Gulf of Aqaba. *Metallomics* 11, 1547–1557. doi: 10.1039/c9mt00121b

He, D. D., and Marles-Wright, J. (2015). Ferritin family proteins and their use in bionanotechnology. *New Biotechnol.* 32, 651–657. doi: 10.1016/j.nbt.2014.12.006

Hedges, J. I., Baldock, J. A., Gelinas, Y., Lee, C., Peterson, M., and Wakeham, S. G. (2001). Evidence for non-selective preservation of organic matter in sinking marine particles. *Nature* 409, 801–804. doi: 10.1038/35057247

Helms, J. R., Mao, J., Schmidt-Rohr, K., Abdulla, H., and Mopper, K. (2013). Photochemical flocculation of terrestrial dissolved organic matter and iron. *Geochim. Cosmochim. Acta* 121, 398–413. doi: 10.1016/j.gca.2013.07.025

Hertkorn, N., Benner, R., Frommberger, M., Schmitt-Kopplin, P., Witt, M., Kaiser, K., et al. (2006). Characterization of a major refractory component of marine dissolved organic matter. *Geochim. Cosmochim. Acta* 70, 2990–3010. doi: 10.1016/j.gca.2006.03.021

Hunter, K. A., and Boyd, P. W. (2007). Iron-binding ligands and their role in the ocean biogeochemistry of iron. *Environ. Chem.* 4, 221–232.

Iskrenova-Tchoukova, E., Kalinichev, A. G., and Kirkpatrick, R. J. (2010). Metal cation complexation with natural organic matter in aqueous solutions: molecular dynamics simulations and potentials of mean force. *Langmuir* 26, 15909–15919. doi: 10.1021/la102535n

Keil, R. G., Montluçon, D. B., Prahl, F. G., and Hedges, J. I. (1994). Sorptive preservation of labile organic matter in marine sediments. *Nature* 370, 549–552. doi: 10.1038/370549a0

Kim, S. W., Kaplan, L. A., Benner, R., and Hatcher, P. G. (2004). Hydrogen-deficient molecules in natural riverine water samples - evidence for the existence of black carbon in DOM. *Mar. Chem.* 92, 225–234. doi: 10.1016/j.marchem.2004.06.042

Kind, T., and Fiehn, O. (2007). Seven golden rules for heuristic filtering of molecular formulas obtained by accurate mass spectrometry. *BMC Bioinformatics* 8:105. doi: 10.1186/1471-2105-8-105

Koch, B. P., and Dittmar, T. (2016). From mass to structure: an aromaticity index for high-resolution mass data of natural organic matter (vol 20, pg 926, 2006). *Rapid Commun. Mass Spectrom.* 30, 250–250. doi: 10.1002/rcm.7433

Kraemer, S. M., Butler, A., Borer, P., and Cervini-Silva, J. (2005). Siderophores and the dissolution of iron-bearing minerals in marine systems. *Rev. Mineral. Geochem.* 59, 53–84. doi: 10.1515/9781501509551-008

Lee, C. (2002). "Particulate organic matter composition and fluxes in the Sea," in *Chemistry of Marine Water and Sediments*, eds A. Gianguzza, E. Pelizzetti, and S. Sammartano (Berlin: Springer), 125–146. doi: 10.1007/978-3-662-04935-8_5

Macrellis, H. M., Trick, C. G., Rue, E. L., Smith, G., and Bruland, K. W. (2001). Collection and detection of natural iron-binding ligands from seawater. *Mar. Chem.* 76, 175–187. doi: 10.1016/s0304-4203(01)00061-5

Marchetti, A., and Maldonado, M. T. (2016). Iron. *Physiol. Microal.* 6, 233–279. doi: 10.1007/978-3-319-24945-2_11

Marchetti, A., Parker, M. S., Moccia, L. P., Lin, E. O., Arrieta, A. L., Ribalet, F., et al. (2009). Ferritin is used for iron storage in bloom-forming marine pennate diatoms. *Nature* 457, 467–470. doi: 10.1038/nature07539

Mawji, E., Gledhill, M., Milton, J. A., Tarran, G. A., Ussher, S., Thompson, A., et al. (2008). hydroxamate siderophores: occurrence and importance in the Atlantic Ocean. *Environ. Sci. Technol.* 42, 8675–8680. doi: 10.1021/es801884r

Neilands, J. B. (1995). Siderophores - structure and function of microbial iron transport compounds. *J. Biol. Chem.* 270, 26723–26726. doi: 10.1074/jbc.270.45.26723

Neubert, H., Hider, R. C., and Cowan, D. A. (2002). Speciation of Fe(III)-chelate complexes by electrospray ionization ion trap and laser desorption/ionization Fourier transform ion cyclotron resonance mass spectrometry. *Rapid Commun. Mass Spectrom.* 16, 1556–1561. doi: 10.1002/rcm.756

Omand, M. M., Govindarajan, R., He, J., and Mahadevan, A. (2020). Sinking flux of particulate organic matter in the oceans: sensitivity to particle characteristics. *Sci. Rep.* 10:5582. doi: 10.1038/s41598-020-60424-5

Pohlabeln, A. M., Gomez-Saez, G. V., Noriega-Ortega, B. E., and Dittmar, T. (2017). Experimental evidence for abiotic sulfurization of marine dissolved organic matter. *Front. Mar. Sci.* 4:364. doi: 10.3389/fmars.2017.00364

Raines, D. J., Sanderson, T. J., Wilde, E. J., and Duhme-Klair, A. K. (2015). *Siderophores, Reference Module in Chemistry, Molecular Sciences and Chemical Engineering*. Amsterdam: Elsevier.

Raven, M. R., Sessions, A. L., Adkins, J. F., and Thunell, R. C. (2016). Rapid organic matter sulfurization in sinking particles from the Cariaco Basin water column. *Geochim. Cosmochim. Acta* 190, 175–190. doi: 10.1016/j.gca.2016.06.030

Reid, R. T., Live, D. H., Faulkner, D. J., and Butler, A. (1993). A siderophore from a marine bacterium with an exceptional ferric Ion Affinity Constant. *Nature* 366, 455–458. doi: 10.1038/366455a0

Sedwick, P. N., Church, T. M., Bowie, A. R., Marsay, C. M., Ussher, S. J., Achilles, K. M., et al. (2005). Iron in the Sargasso Sea (Bermuda Atlantic Time-series Study region) during summer: eolian imprint, spatiotemporal variability, and ecological implications. *Global Biogeochem. Cycles* 19:GB4006. doi: 10.1029/2004gb002445

Shen, X., and Perreault, H. (1998). Characterization of carbohydrates using a combination of derivatization, high-performance liquid chromatography and mass spectrometry. *J. Chromatogr. A* 811, 47–59. doi: 10.1016/S0021-9673(98)00238-6

Shire, D. M., and Kustka, A. B. (2015). Luxury uptake, iron storage and ferritin abundance in *Prochlorococcus marinus* (*Synechococcales*) strain MED4. *Phycologia* 54, 398–406. doi: 10.2216/14-109.1

Sleighter, R. L., Chen, H. M., Wozniak, A. S., Willoughby, A. S., Caricasole, P., and Hatcher, P. G. (2012). Establishing a measure of reproducibility of ultrahigh-resolution mass spectra for complex mixtures of natural organic matter. *Anal. Chem.* 84, 9184–9191. doi: 10.1021/ac3018026

Sleighter, R. L., and Hatcher, P. G. (2007). The application of electrospray ionization coupled to ultrahigh resolution mass spectrometry for the molecular characterization of natural organic matter. *J. Mass Spectrom.* 42, 559–574. doi: 10.1002/jms.1221

Sleighter, R. L., and Hatcher, P. G. (2008). Molecular characterization of dissolved organic matter (DOM) along a river to ocean transect of the lower chesapeake bay by ultrahigh resolution electrospray ionization Fourier transform ion cyclotron resonance mass spectrometry. *Mar. Chem.* 110, 140–152. doi: 10.1016/j.marchem.2008.04.008

Stubbins, A., Spencer, R. G. M., Chen, H., Hatcher, P. G., Mopper, K., Hernes, P. J., et al. (2010). Illuminated darkness: molecular signatures of Congo River dissolved organic matter and its photochemical alteration as revealed by ultrahigh precision mass spectrometry. *Limnol. Oceanogr.* 55, 1467–1477. doi: 10.4319/lo.2010.55.3.1467

Sun, L., Chin, W.-C., Chiu, M.-H., Xu, C., Lin, P., Schwehr, K. A., et al. (2019). Sunlight induced aggregation of dissolved organic matter: role of proteins in linking organic carbon and nitrogen cycling in seawater. *Sci. Total Environ.* 654, 872–877. doi: 10.1016/j.scitotenv.2018.11.140

Sun, L., Chiu, M.-H., Xu, C., Lin, P., Schwehr, K. A., Bacosa, H., et al. (2018). The effects of sunlight on the composition of exopolymeric substances and subsequent aggregate formation during oil spills. *Mar. Chem.* 203, 49–54. doi: 10.1016/j.marchem.2018.04.006

Sun, L. N., Xu, C., Zhang, S. J., Lin, P., Schwehr, K. A., Quigg, A., et al. (2017). Light-induced aggregation of microbial exopolymeric substances. *Chemosphere* 181, 675–681. doi: 10.1016/j.chemosphere.2017.04.099

Sutton, R., and Sposito, G. (2005). Molecular structure in soil humic substances: the new view. *Environ. Sci. Technol.* 39, 9009–9015. doi: 10.1021/es050778q

Timko, S., Maydanov, A., Pittelli, S., Conte, M., Cooper, W., Koch, B., et al. (2015). Depth-dependent photodegradation of marine dissolved organic matter. *Front. Mar. Sci.* 2:66. doi: 10.3389/fmars.2015.00066

Upritchard, H. G., Yang, J., Bremer, P. J., Lamont, I. L., and McQuillan, A. J. (2007). Adsorption to metal oxides of the *Pseudomonas aeruginosa* siderophore pyoverdine and implications for bacterial biofilm formation on metals. *Langmuir* 23, 7189–7195. doi: 10.1021/la7004024

Velasquez, I., Nunn, B. L., Ibisanmi, E., Goodlett, D. R., Hunter, K. A., and Sander, S. G. (2011). Detection of hydroxamate siderophores in coastal and Sub-Antarctic waters off the South Eastern Coast of New Zealand. *Mar. Chem.* 126, 97–107. doi: 10.1016/j.marchem.2011.04.003

Verdugo, P., Alldredge, A. L., Azam, F., Kirchman, D. L., Passow, U., and Santschi, P. H. (2004). The oceanic gel phase: a bridge in the DOM–POM continuum. *Mar. Chem.* 92, 67–85. doi: 10.1016/j.marchem.2004.06.017

Volkman, J. K., and Tanoue, E. (2002). Chemical and biological studies of particulate organic matter in the ocean. *J. Oceanogr.* 58, 265–279.

Vraspir, J. M., and Butler, A. (2009). Chemistry of marine ligands and siderophores. *Annu. Rev. Mar. Sci.* 1, 43–63. doi: 10.1146/annurev.marine.010908.163712

Walker, L. R., Hoyt, D. W., Walker, S. M., Ward, J. K., Nicora, C. D., and Bingol, K. (2016). Unambiguous metabolite identification in high-throughput metabolomics by hybrid 1D H-1 NMR/ESI MS1 approach. *Magn. Reson. Chem.* 54, 998–1003. doi: 10.1002/mrc.4503

Waska, H., Koschinsky, A., and Dittmar, T. (2016). Fe- and cu-complex formation with Artificial ligands investigated by ultra-high resolution fourier-transform ion cyclotron resonance mass spectrometry (FT-ICR-MS): implications for natural metal-organic complex studies. *Front. Mar. Sci.* 3:119. doi: 10.3389/fmars.2016.00119

Winkelmann, G. (2002). Microbial siderophore-mediated transport. *Biochem. Soc. Trans.* 30, 691–696. doi: 10.1042/bst0300691

Xu, C., Zhang, S. J., Kaplan, D. I., Ho, Y. F., Schwehr, K. A., Roberts, K. A., et al. (2015). Evidence for hydroxamate siderophores and other n-containing organic compounds controlling (PU)-P-239,240 immobilization and remobilization in a wetland sediment. *Environ. Sci. Technol.* 49, 11458–11467. doi: 10.1021/acs.est.5b02310

Zhang, B., Watt, R. K., Galvez, N., Dominguez-Vera, J. M., and Watt, G. D. (2006). Rate of iron transfer through the horse spleen ferritin shell determined by the rate of formation of Prussian Blue and Fe-desferrioxamine within the ferritin cavity. *Biophys. Chem.* 120, 96–105. doi: 10.1016/j.bpc.2005.10.005

Conflict of Interest: The authors declare that the research was conducted in the absence of any commercial or financial relationships that could be construed as a potential conflict of interest.

frontiers in Earth Science

ORIGINAL RESEARCH
published: 14 July 2020
doi: 10.3389/feart.2020.00280

Long-Term Changes of Particle Flux in the Canary Basin Between 1991 and 2009 and Comparison to Sediment Trap Records Off Mauritania

Gerhard Fischer[1,2], Susanne Neuer[3], Simon Ramondenc[2,4], Thomas J. Müller[5], Barbara Donner[2], Götz Ruhland[2], Volker Ratmeyer[2], Gerrit Meinecke[2], Nico Nowald[2], Marco Klann[2] and Gerold Wefer[2]*

[1] Department of Geosciences, University of Bremen, Bremen, Germany, [2] MARUM, Center of Marine and Environmental Sciences, University of Bremen, Bremen, Germany, [3] School of Life Sciences, Arizona State University, Tempe, AZ, United States, [4] Alfred Wegener Institute for Polar and Marine Research, Bremerhaven, Germany, [5] GEOMAR Helmholtz Centre for Ocean Research Kiel, Kiel, Germany

OPEN ACCESS

Edited by:
Rut Pedrosa Pàmies, Marine Biological Laboratory (MBL), United States

Reviewed by:
Anna Sanchez-Vidal, University of Barcelona, Spain
Cathryn Ann Wynn-Edwards, University of Tasmania, Australia
Weifeng Yang, Xiamen University, China

***Correspondence:**
Gerhard Fischer
gfischer@marum.de

Specialty section:
This article was submitted to Biogeoscience, a section of the journal Frontiers in Earth Science

Received: *12 March 2020*
Accepted: *17 June 2020*
Published: *14 July 2020*

Citation:
Fischer G, Neuer S, Ramondenc S, Müller TJ, Donner B, Ruhland G, Ratmeyer V, Meinecke G, Nowald N, Klann M and Wefer G (2020) Long-Term Changes of Particle Flux in the Canary Basin Between 1991 and 2009 and Comparison to Sediment Trap Records Off Mauritania. Front. Earth Sci. 8:280. doi: 10.3389/feart.2020.00280

Eastern Boundary Upwelling Ecosystems (EBUEs) are associated with high biological productivity, high fish catch and they highly contribute to marine carbon sequestration. Whether coastal upwelling has intensified or weakened under climate change in the past decades is controversially discussed and different approaches (e.g., time-series of chlorophyll, wind, sea surface temperature, modeling experiments) have been considered. We present a record of almost two decades of particle fluxes (1991–2009) from ca. 600 to 3100 m water depth in the Canary Basin at site ESTOC (European Station for Time series in the Ocean Canary Islands; ca. 29°N, 15°30.W, ca. 3600 m water depth), located in the offshore transition zone of the northern Canary Current-EBUE. We compare these flux records with those measured at a mesotrophic sediment trap site further south off Cape Blanc (Mauritania, ca. 21°N). The deep ocean fluxes at ESTOC in ca. 3 km recorded the evolution of the coastal Cape Ghir filament (30–32°N, 10–12°W) due to lateral advection of particles, whereas the upper water column sediment traps in ca. 1 km reflected the oligotrophic conditions in the overlying waters of ESTOC. We observed an increased emphasis in spring-time fluxes since 2005, associated with a change in particle composition, while satellite chlorophyll biomass did not show this pattern. Due to its northern location in the CC-EBUEs, spring biogenic fluxes at ESTOC provide a better relationship to the forcing of the North Atlantic Oscillation than those recorded further south off Cape Blanc. Off Cape Blanc, deep fluxes showed the best overlap with the deep ESTOC fluxes during the spring season before 2005. On the long-term, both chlorophyll and particle fluxes showed an increasing trend at ESTOC which was not observed further south at the mesotrophic Cape Blanc site. This might indicate that, depending on their location along the NW African margin, coastal upwelling systems react differently to global change.

Keywords: particle flux, sediment traps, Canary Current, ESTOC, Cape Blanc, biological pump, seasonality, climate change

INTRODUCTION

Eastern Boundary Upwelling Ecosystems (EBUEs) are among the most productive ecosystems in the world oceans and are economically important. The nutrient-rich upwelled waters along the coastal shelves sustain large phytoplankton blooms that play a crucial role in the marine carbon cycle and sequestration. Therefore, EBUEs are discussed also in the context of global warming. Bakun (1990) and Bakun et al. (2010, 2015) proposed a scenario of a general intensification of coastal upwelling due to increasing pressure gradients and wind fields associated with global warming. This hypothesis is under discussion and differing findings were recently summarized by Garcìa-Reyes et al. (2015); Bonino et al. (2019), and Sylla et al. (2019). Bonino et al. (2019) stressed that each EBUEs is unique in terms of forcings and climate variability and that the Canary Current (CC) system reveals a negative trend in upwelling intensity. Even the various sub-systems of the EBUEs defined by Cropper et al. (2014; **Figure 1**) could react differently to global warming (Lathuilière et al., 2008; Arístegui et al., 2009; Sydeman et al., 2014; Garcìa-Reyes et al., 2015; Bonino et al., 2019). A progressive warming and decreasing productivity over the last two decades was suggested for the CC-EBUEs as a whole (Arístegui et al., 2009).

Over decadal time scales, the NW African coastal upwelling can be influenced by the North Atlantic Oscillation (NAO, e.g., González-Dávila et al., 2007; Narajan et al., 2010; Cianca et al., 2012), the Atlantic Meridional Overturning (AMO, Bonino et al., 2019), the AMOC (e.g., Vélez-Belchí et al., 2017) and the El Niño Southern Oscillation (ENSO). ENSO related teleconnections have been discussed by e.g., Behrenfeld et al. (2001) and Pradhan et al. (2006) and can be illustrated by the negative correlation of sea level pressure (SLP) with eastern tropical Pacific SST (Fischer et al., 2016). According to Fischer et al. (2016), correlations during winter show that NAO and ENSO may have opposite effects on the NW African/eastern Atlantic region for coastal upwelling. A positive phase of the NAO is associated with anomalously high pressure in the Azores region and stronger northeasterly winds along the NW African coast, and *vice versa*. However, the correlation is larger for the NAO than for ENSO as shown by modeling approaches (Fischer et al., 2016).

The times series site ESTOC is located in the eastern subtropical North Atlantic about 110 km north of Gran Canaria (Canary Basin, ca. 29°N/15°30.W, ca. 4 km water depth) and about 255 km off the African shelf. A sediment trap station to which results from ESTOC will be compared lies further south off Cape Blanc ca. 550 km off the shelf (CB mesotrophic, ca. 21°N/21° W, ca. 4 km water depth; **Figure 1A**). Both, the ESTOC and CB stations are within the influence of the Canary Current-EBUEs. In the depth range from the surface down to ca. 800 m, the Canary Current (CC) carries North Atlantic Central Water (NACW) southwards and dominates the geostrophic contribution to the wind-driven subtropical gyre (see Neuer et al., 2007, for a seasonally repeated survey along 29°N via ESTOC). To a large part, it is fed in the north at ca 34°N by the eastward flowing Azores Current. The CC closes the North Atlantic's subtropical gyre in the east off the West African shelf, and starts to leave the shelf edge further south with a more westward component at about 21°N (e.g., Stramma, 1984; **Figure 1A**).

The trade winds and the seasonal signal dominate the directly wind-driven contribution to the subtropical gyre's flow pattern. The wind is directed southward, almost parallel to the general coastline, and is strongest over the annual mean off Cape Blanc with a maximum in July. Further north at Cape Ghir at 30°N, it is weaker in the annual mean, but with a late spring to August summer maximum (Mittelstaedt, 1991). The component parallel to the coast with its maximum in spring and summer creates the strongest coastal upwelling, with maxima depending regionally on the wind maxima in summer (Van Camp et al., 1991). The offshore Ekman transport is confined to the near surface and has two further effects. First, it may create thin filaments of nutrient-rich upwelled water observed by satellites that reach from the coast toward southwest up to several hundred kilometers far into the oligotrophic open ocean. Permanently and strongest, these filaments occur at coastal capes, e.g., Cape Ghir at ca. 30°N and Cape Blanc at ca. 21°N (Nykjaer and Van Camp, 1994; Davenport et al., 1999). They vary seasonally with the wind system, and they may contribute to particle transport to more oligotrophic regions like ESTOC and the mesotrophic Cape Blanc site through lateral advection (Neuer et al., 2002b; Helmke et al., 2005; Fischer et al., 2009). Secondly, the offshore Ekman transport induces a geostrophic poleward undercurrent (PUC) along the shelf edge (Mittelstaedt, 1991). North of 25°N and during the wind maximum in summer and fall, this undercurrent is confined to 500–1050 m water depth (Knoll et al., 2002). On the shelf edge, the PUC supports the enrichment of lithogenic and biogenic particles through erosion and interaction with the Canary Current. The associated meso-scale eddy field also supports the horizontal dispersion of suspended materials further offshore.

The ESTOC site has phytoplankton biomass typical for oligotrophic conditions of the subtropical gyre (Davenport et al., 2002) with satellite-derived and *in situ* chlorophyll concentrations ranging from 0.03 to 0.20 mg m^{-3}, sometimes reaching 0.4 mg m^{-3} (Neuer et al., 2007). Neuer et al. (1997, 2002b) found a clear seasonality in biomass with maxima following the breakup of the seasonally stratified mixed layer in winter. The historical CZCS data from 1979 to 1985 showed maximal pigment concentrations in December and January, declining in February (Davenport et al., 1999).

Deep ocean fluxes generally follow the seasonal signal of phytoplankton biomass with a high mineral (ballast) component from mostly coccolithophore sedimentation (Abrantes et al., 2002; Sprengel et al., 2002). Roughly one third of the flux is due to non-biogenic (lithogenic) particles mostly from Saharan dust. Biogenic silica (BSi) is of minor importance due to low silicate availability in the upwelling waters of the ENACW (=Eastern North Atlantic Central Water; ca. 200–800 m water depth) (Ragueneau et al., 2000). Neuer et al. (1997) observed an increase of particulate fluxes with depth at ESTOC and attributed the increased flux to the productive Cape Ghir filament to the northeast as a potential particle source region; this hypothesis was supported by CZCS

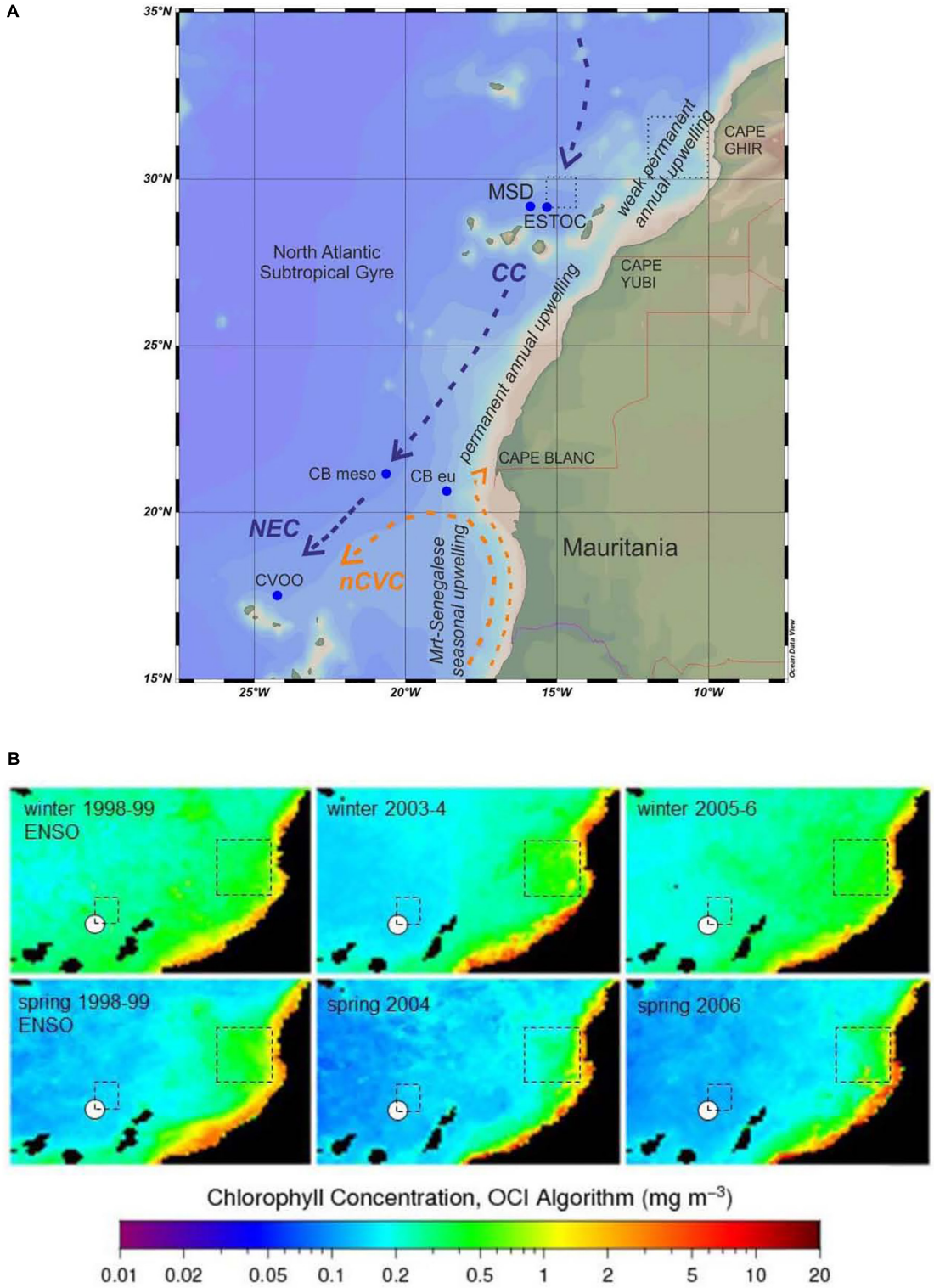

FIGURE 1 | (A) Location of ESTOC and MSD traps in the Canary Basin and other relevant time series flux sites [Cape Blanc (CBmeso, CBeu), CVOO (Cape Verde Ocean Observatory, GEOMAR)] within the Canary Current system. General currents and the upwelling zones defined by Cropper et al. (2014) are indicated. Boxes at ESTOC and Cape Ghir where environmental data have been extracted from GIOVANNI are shown as well (stippled lines). CC, Canary Current; NEC, North Equatorial Current; nCVC, northern Cape Verde Current; the northward moving coastal current is the Mauritanian Current. **(B)** Examples of winter and spring surface chlorophyll from SeaWiFs and MODIS (9 km resolution) for the extreme ENSO year 1999 (La Niña phase), the years 2004 and 2006 (as examples for the years before and after 2005). The ESTOC study site is marked with a white dot, the ESTOC and Cape Ghir boxes are shown.

satellite imagery (Davenport et al., 1999, 2002) and by nitrogen isotope studies carried out by Freudenthal et al. (2001). Satellite derived chlorophyll concentration is more than twice as high (0.4 ± 0.18 mg m^{-3}; SeaWifs 1997–2009) in that filament compared to the ESTOC area (**Figure 2**).

Here, we present a synthesis of the existing particle flux data collected between ca. 600 and ca. 3 km water depth at the ESTOC time series site [1991–2009, ESTOC (1–22), ca. 3600 m water depth]. We further add high-resolution trap data from the nearby site MSD 1–5 (2002–2005; **Figure 1A**). We strongly build on studies conducted by Neuer et al. (1997, 2002a,b, 2004, 2007) on upper ocean flux data from Oct 1992 to April 2001 (CI-2 to CI-13). We use the ESTOC fluxes to evaluate potential long-term changes and trends of the strength of the biological carbon pump within the CC-EBUEs. Secondly, we will provide a synchronous overlap of deep ocean fluxes at ESTOC with the mesotrophic Cape Blanc study site in the southern part of the CC-EBUEs (Fischer et al., 2016, 2019). Both sites are located in similar settings offshore the coastal upwelling and influenced by larger upwelling filaments (Pelegrí et al., 2005).

MATERIALS AND METHODS

Sediment Traps Moorings

We deployed Kiel-type time-series sediment traps (Kremling et al., 1996) at sites ESTOC and MSD (**Figure 1A**) in meso- and bathypelagic depths between ca. 600 and ca. 3 km (**Supplementary Material**). The average sampling depths of the traps were ca. 750 m (upper), 1050 m (middle), and 3060 m (lower). Mooring site MSD slightly to the west of ESTOC (**Figure 1**) was equipped with high-resolution sediment traps (40 cups). Detailed mooring and sampling dates for the sediment traps are listed in the **Supplementary Material**. Mooring data from Cape Blanc are given in Fischer et al. (2016, 2019). Prior to the deployments, the sampling cups were poisoned with $HgCl_2$ and pure NaCl was used to increase the salinity and density in the sampling cups to 40‰. Upon recovery, samples were stored at 4°C and wet-splitted in the home laboratory. All flux data here refer to the size fraction of <1 mm. For a more detailed description of materials and methods we refer to Fischer et al. (2016). Analysis of the fraction <1 mm, using 1/4 or 1/5 wet splits, was performed according to Fischer and Wefer (1991). Samples were freeze-dried and the homogenized samples were analyzed for bulk (total mass), organic carbon, total nitrogen, carbonate and biogenic opal (BSi = biogenic silica). Organic carbon, nitrogen and calcium carbonate were measured by combustion with a CHN-Analyzer (HERAEUS). Carbonate was obtained from non-acidified and organic carbon from acidified (1N HCl) samples through CHN measurements. BSi was determined with a sequential leaching technique with 1 M NaOH at 85°C (Müller and Schneider, 1993), measuring SiO_2 (biogenic opal) without including the variable water content of biogenic opal (around 5–10%). For a detailed table of standard deviations for various samples we refer to Müller and Schneider (1993). Lithogenic fluxes or the non-biogenic material was estimated by the difference between the biogenic fluxes (organic matter, BSi, carbonate) and total material flux. Organic matter was estimated by multiplying organic carbon by a factor of two (Hedges et al., 2002). The lithogenic fluxes were estimated by subtracting the biogenic fluxes from total fluxes. We attribute the lithogenic flux to dust-derived material (=mineral dust flux) as no large rivers supply suspended material to the Canary Basin. Due to partly low sample amounts (low fluxes), only total and BSi/organic carbon fluxes were available for the entire period of study.

The sediment trap collections were carried out with different time resolutions (4.3–22 days, see **Supplementary Material**) which limit comparisons between seasons and years. Therefore, average daily fluxes for the seasons and years were calculated according to Fischer et al. (2016). Seasons were defined using the dates of opening and closure of the individual sampling cups closest to the start of the astronomical seasons (March 21, June 21, September 23, December 21). The annual fluxes refer to the period of ca. 21 December to about the same date of the following year.

Moored Current Measurements

During September 1994 to March 2002, current meters were moored in seven settings at ESTOC in safe distance of ca. 20 km to the ESTOC sediment trap deployments. The first four settings carried an upward looking 150 kHz Acoustic Doppler Profiler (ADCP, made by RDI) to resolve the upper layer between 200 m depth and the surface. The ADCP, for logistic reasons, later was replaced by an Aanderaa RCM-8, which were also used to cover the deeper major water masses in the water column: North Atlantic Central Water (NACW, nominal RCM-8 depths 300 m, 500 m, 800 m), the Mediterranean Outflow Water (MW, 1250 m), and the North Atlantic Deep Water (NADW, 2000, 3550 m). Data processing followed the procedures described by Müller and Waniek (2013) for a different site, in particular determining best estimates of instrumental depths. The instruments' sampling frequency was at least every 2 h to allow resolving the semi-diurnal tide and inertial motions. For this study, we used a low-pass filter and calculated 1-day averaged values to remove high frequency signals. The daily values then were interpolated in the vertical to common depths close to measuring depths: 50, 100, 150, 200, 250, 350, 500, 1250, 2000, and 3500 m, and in time to close the gaps between recovery and follow-up deployment. Vector averaging over 30 days provided current speeds and directions making them comparable to the seasonal description of particle flux data. Note that current meter data at ESTOC were measured only between 1994 and 2002, thus covering only part of the period of the trap measurements (1991–2009). There are no current meter measurements available at the MSD site.

Environmental Data

We used several observational time-series datasets from the GIOVANNI website (chlorophyll, MLD). Due to earlier findings on particle transport and lateral advection of particles and chlorophyll (e.g., Neuer et al., 1997; Davenport et al., 1999), we extracted these additional data from an ESTOC particle source box (29–30°N/14°30′–15°30′W; **Figure 1A**) located to the northeast of the mooring due to the general current direction in the surface and subsurface waters. We used another source box

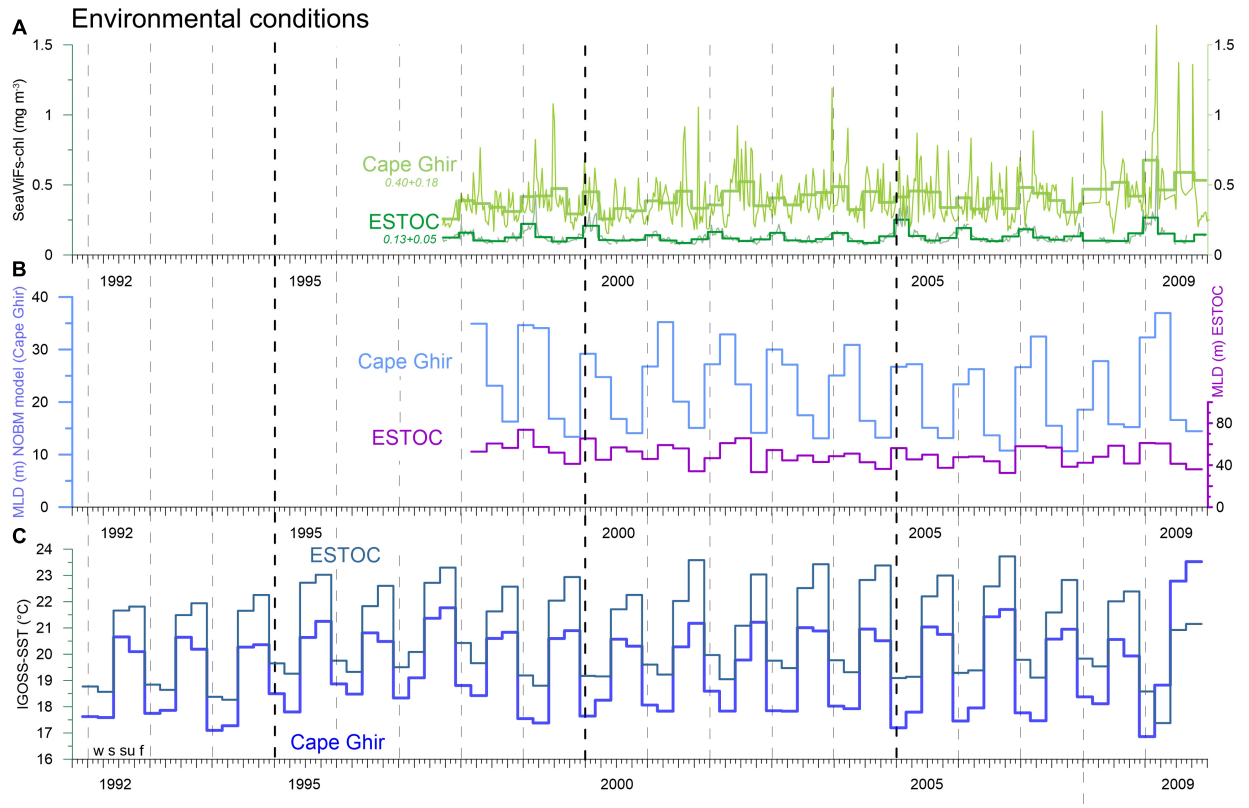

FIGURE 2 | Time series of major environmental variables. **(A)** Weakly and seasonal (DJF) SeaWiFs-chlorophyll (mg m^{-3}); seasonal (DJF), model-based MLD (m) **(B)** (NASA Ocean Biological Model, NOBM, from GIOVANNI); seasonal (DJF) IGOSS-SST (°C) **(C)**. Note the long-term increasing trend for chlorophyll at the coastal Cape Ghir filament box which is statistically significant. Vertical hatched lines indicate years (with the four seasons winter = w, spring = s, summer = su, fall = f; starting on Jan. 1), thick hatched lines indicate a 5-year mark.

of the Cape Ghir filament (30–32°N, 10–12°W) which is known to supply material laterally, mainly to the deeper ESTOC traps (e.g., Neuer et al., 1997; Davenport et al., 1999). The concept of particle source boxes above moored sediment traps and the statistical funnels above them are primarily based on studies by Siegel et al. (2008).

Data on chlorophyll, sea surface temperature (SST), mixed-layer depth (MLD, modeled), NAO winter (DJFM) station-based Hurrell North Atlantic Oscillation (NAO) Index were obtained using the following sources:

https://oceancolor.gsfc.nasa.gov/l3/

https://giovanni.gsfc.nasa.gov/giovanni/#service=TmAvMp&starttime=&endtime=&bbox=-19,20,-18,21

http://climatedataguide.ucar.edu/guidance/hurrell-north-atlantic-oscillation-nao-index-station-based (Hurrell, 1995)

https://crudata.uea.ac.uk/cru/data/nao/ (Jones et al., 1997)

https://iridl.ldeo.columbia.edu/SOURCES/.IGOSS/.nmc/.Reyn_SmithOIv2/.monthly/.sst/index.html?Set-Language=en

Statistics

The chlorophyll time series recorded by satellites were regularized and interpolated. The global trends were tested by applying the seasonal Mann-Kendall test (Hirsch et al., 1982), which estimate a single pattern on each month, separately. In addition, the correlation between environmental variables and the winter BSi fluxes or winter NAO Hurrell Indices and spring BSi fluxes were analyzed by parametric Pearson tests or non-parametric Spearman tests following the normality and the homoscedasticity of the measurements.

RESULTS

Our results span observations over nearly 20 years. In a first step, we investigated the relationships between the environmental data (e.g., SSTs, chlorophyll, modeled MLD), around ESTOC and Cape Ghir and the particle fluxes at ESTOC. A major focus was the investigation of the seasonal and interannual variability of environmental variables (e.g., chlorophyll) and the flux signals in the meso- and bathypelagic. During the observation period, several NAO cycles and ENSO events could be identified, and we will present the time-series also in the context of those events in the following paragraph. Particularly noticeable was the ENSO event during 1997–1999 (**Figure 1B**). Finally, we will compare synchronous fluxes from the bathypelagic at ESTOC and off Cape Blanc (mesotrophic site) from the southern CC system.

Environmental Changes and Trends at ESTOC and the Cape Ghir Box

The weekly chlorophyll time series from 1997 to 2009 provided by SeaWiFs for the ESTOC (14°30′–15°30′W, 29–30°N) and the Cape Ghir (30–32°N, 10–12°W) boxes (**Figure 1A**) reveal distinct peaks in March to April reaching almost 1.5 mg m^{-3} within the Cape Ghir box (**Figure 2A**). Partly, summer and fall maxima were found in the coastal box as well. In addition, there is a tendency of a chlorophyll biomass increase from 1997 to 2009 at the coastal upwelling at Cape Ghir but not for the ESTOC box (**Figure 2A**, $p < 0.05$ and $p = 0.08$ Mann-Kendall test). There, SeaWiFs chlorophyll values were about 2–3-fold lower with distinct seasonal maxima in winter providing highest values in 2005 and 2009 (**Figure 2A**). No chlorophyll summer peaks were observed in the ESTOC box. Mean SeaWiFs-derived chlorophyll values in the Cape Ghir box were 0.40 ± 0.18 mg m^{-3} and 0.13 ± 0.05 for the ESTOC box. For comparison, we show satellite-derived chlorophyll time series obtained by the CZCS sensor (1979–1985, Davenport et al., 1999) for almost similar areas that reveal lower mean values (0.06 at ESTOC and 0.14 mg m^{-3} at Cape Ghir) compared to the SeaWiFs data which show maxima in January in both areas (**Figure 3**). Compared to *in situ* values, these lower values seem to better match the measured chlorophyll data (Neuer et al., 2007). Using monthly SST values from IGOSS, we observed a SST increase both inshore at Cape Ghir and offshore at ESTOC between 1991 and 2009 in the order of 1°C (**Figure 2C**). Simultaneously, we observed a shallowing of the mean winter and spring modeled mixed layer depths (MLD) from ca. 35 to ca. 25 m from 1997 to 2005 at Cape Ghir, which then increased again (**Figure 2B**).

Current Strength and Directions in the Water Column

Current strengths are crucial to evaluate particle collection efficiencies of sediment traps (see Buesseler et al., 2007, for a review). Current speeds in the trap depths at ESTOC of 1 and 3 km were mostly below the critical values, around 10–12 cm s^{-1} (sampling interval of 2 h, data not shown). The available 8-year record (1994–2002) from GEOMAR shows that currents averaged over 30 days rarely exceeded 10 cm s^{-1}; and in such cases generally were confined to depths shallower than 500 m (**Figure 4**). In very few cases, Mediterranean water lenses (Mediterranean Outflow Water) at around 1250 m depth (Siedler et al., 2005) may pass the mooring site as indicated by extremely high current anomalies (**Figure 4A**) accompanied by positive temperature anomalies around that depth, e.g., in early 1995 (not shown here). Also, current directions were more or less uniform over the water column, but changing rather regularly with time between all four 90-degree directional sectors (**Figure 4B**).

Amplitudes and Timings of Major Flux Peaks and Particle Composition

The cup-by-cup total particle fluxes in the upper (ca. 600–900 m, average ca. 750 m) and middle-depth traps (900–1300 m, average ca. 1050 m) and in the deeper water column (ca. 3060 m) showed a distinctive seasonality of fluxes with maxima mainly in winter and partly in spring, reaching almost 200 mg m^{-2} d^{-1} in the mesopelagic and slightly higher values in the bathypelagic (**Figure 5**). Fluxes at the nearby MSD site (**Figure 6**) largely followed the flux pattern of the deep ESTOC-traps (**Figure 5**) but were slightly lower in the bathypelagic as expected due to the greater distance to the coastal upwelling of the Cape Ghir filament (**Figure 1A**). Fluxes at site MSD decreased continuously from 2002 to 2004, then increased rather abruptly with a high and broad flux maximum in winter 2005 (**Figure 6**). The BSi fluxes as one indicator (e.g., besides organic carbon) of the efficiency of the biological pump (Dugdale et al., 1995) mirror the total flux patterns both at MSD and ESTOC. The average fraction of BSi of total flux was generally below 5% with the exception of

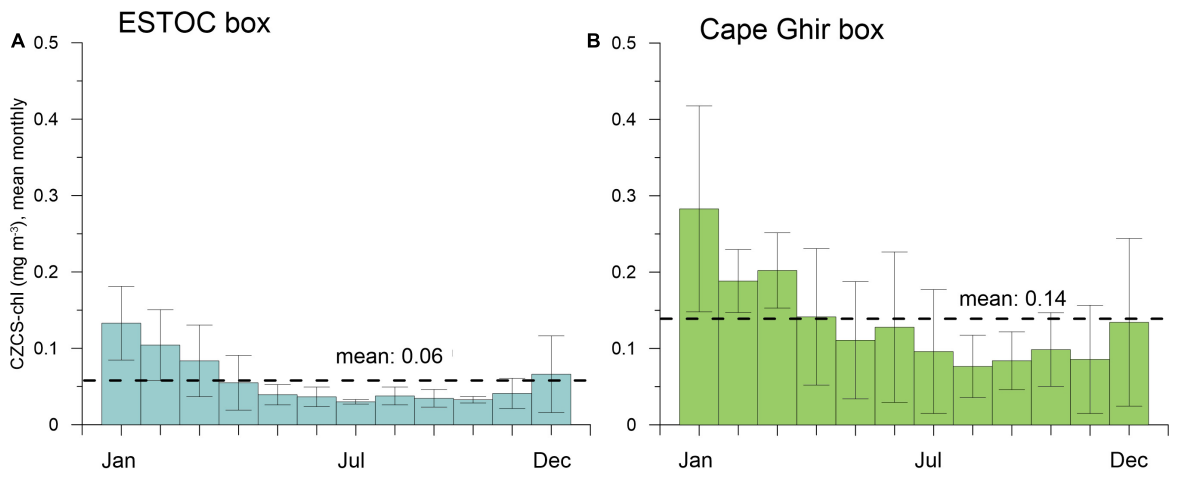

FIGURE 3 | Mean monthly chlorophyll (mg m^{-3}) from the satellite-CZCS sensor from 1979 to 1985 [Davenport et al. (1999) for (**A**) the ESTOC box and (**B**)] the Cape Ghir box. Annual means are shown by stippled lines. Values decline thereafter to a minimum in summer and increase again at the end of the year. Annual means are given as well. A distinct summer maximum at the Cape Ghir box (from SeaWiFs, **Figure 2**) cannot be found in these old CZCS records **(B)**.

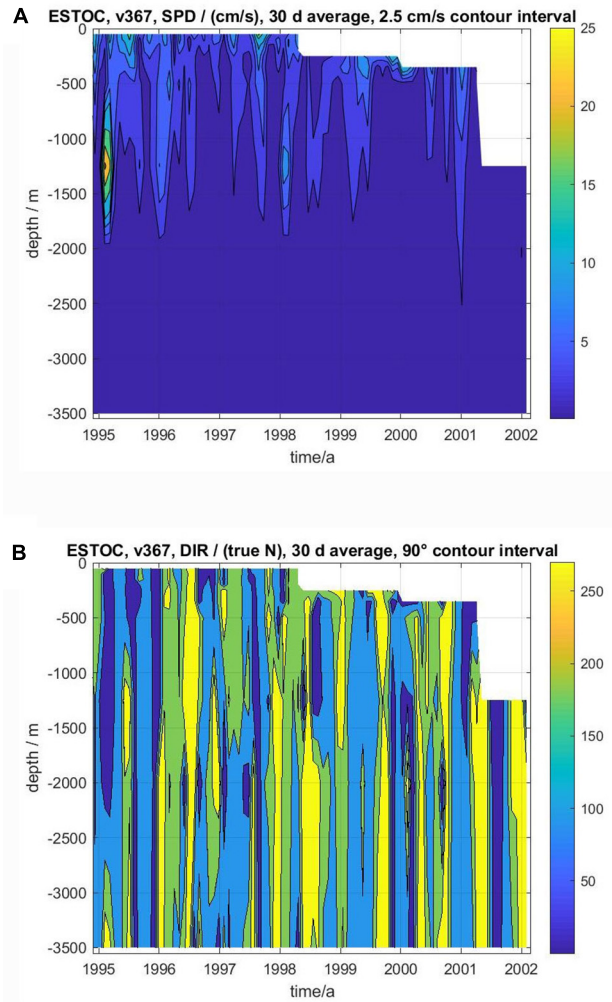

FIGURE 4 | Vector averaged (30 days) current speeds (**A**, cm s^{-1}) and directions (**B**, degree direction true north) at ESTOC from November 1994 to February 2002. Contour interval for current speed is 2.5 cm/s between 0 and 10 cm s^{-1}, and 10 cm s^{-1} above. For direction, contour interval is 90 degrees between 0° and 360°, thus resolving average current directions toward the four sectors North-East NE (dark blue), SE (light blue), SW (green), and NW (yellow). Note that current meter data at ESTOC were measured only between 1994 and 2002, thus covering only part of the period of the trap measurements (1991–2009).

the prominent peak in mid-March 2005 (MSD trap, ca. 10%, **Figure 6B**).

Peak particles fluxes may be almost twice as high in the deeper compared to the upper water column which was attributed previously to lateral advection of particles from the Cape Ghir filament (**Figure 1**; Neuer et al., 1997, 2002a; Davenport et al., 1999; Freudenthal et al., 2001). The overall correspondence of upper and lower water column fluxes indicates that the deeper traps obtain their material not only from the coastal environment of the Cape Ghir filament but from the oligotrophic setting above ESTOC as well, or that sinking particles from the two different source regions interact. Secondary flux maxima occurred in the summer season, e.g., in 1994, 2000, and 2002, and less clear in 2007 and 2008 (**Figure 5**). Before 2005, highest fluxes in winter during the major bloom were observed during the strongest ENSO event 1997–1999, but high values were also found during 1992–1993 at both depths levels. Within the time-series, 1992–1994 constituted the second most important ENSO event (**Figure 5**), all other ENSO events during the period of observation were less important.

Mostly, elevated fluxes in the upper water column and in the deep water appear without any cup/time delay, pointing to high particle settling velocities (200–430 m d^{-1}, Fischer and Karakas, 2009). A time delay of about 1.5 months between surface ocean biomass peaks (chlorophyll-CZCS) and the timing of major winter peaks in the deep water column (Neuer et al., 1997) can be translated into particle settling rates of around 70 m d^{-1} for the entire water column. Considering the bathypelagic sinking rates of ca. 200–430 m d^{-1} (between ca. 1 and 3 km; Fischer and Karakas, 2009), this observation could indicate an increase of sinking rates with depths (Berelson, 2002; Fischer et al., 2016).

Using the high-resolution MSD flux record (**Figure 6**) nearby ESTOC (**Figure 1A**), we can define a detailed timing of the peak fluxes in the winter season with highest fluxes in February to March 2003 and 2004 in the deep traps and, slightly later, in mid-March in 2005 in the upper trap in the Canary Basin. Additionally, we may identify secondary summer peaks in September 2002 and July 2005 (**Figure 6**). In the ESTOC record, major peaks in winter were found from January to March (mostly in March) in ca. 1 km and from February to March in ca. 3 km water depths (**Figure 5**). Later, in 2007 and 2008, maxima occurred from March to April and from April to May in the ca. 3 km traps (**Figure 5**). During the strong ENSO cycle 1997–1999, maxima in both depth levels were identified in January 1999 and February/March (**Figure 5**). An unusual major peak occurred in November 2005 (**Figure 5**), this year was attributed by Fischer et al. (2016, 2019) to an exceptional year of coastal upwelling in the CC-EBUEs further south at Cape Blanc.

Particle Flux Patterns Before and After 2005

Considering the entire ESTOC record, we can observe a clear seasonality and interannual variability of BSi (and organic carbon) fluxes in both the mesopelagic (ca. 1 km) and the bathypelagic (ca. 3 km) water column with major flux peaks in winter and spring (**Figures 5–8**). In ca. 1 km, the record may be separated into the periods from 1992 to 2004 and 2005 to 2009, when winter flux maxima can be found during the first winter period, while spring maxima occurred thereafter (**Figure 7A**). This change in the pattern of the seasonal flux maxima from winter to spring was less clear in the 3 km depth level (**Figure 7B**). At 3 km, mean seasonal BSi fluxes showed winter (1992–2004) and spring maxima (2005–2009) and minima in fall (**Figure 8**). Note that the described changes of seasonality of fluxes from winter to spring in both depths and the standard deviations in the second period (2005–2009) as a measure for flux variability for each season is based on 4–5 values only and therefore on a lower level of statistical reliability (**Figures 8D,H**). For comparison to

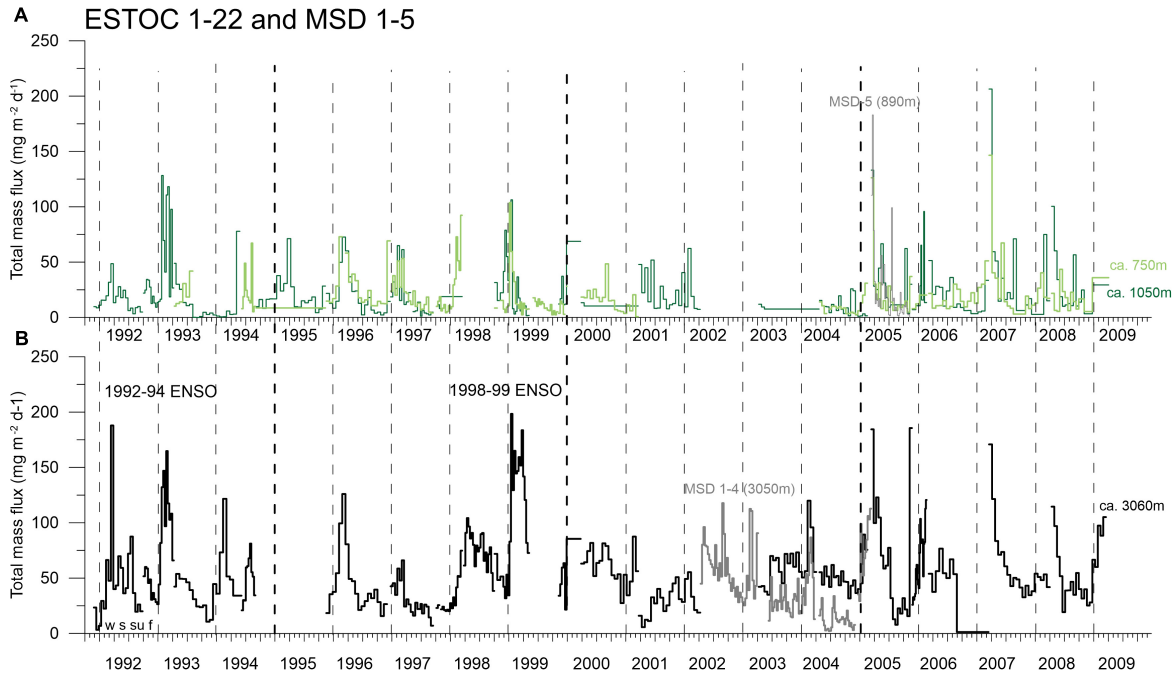

FIGURE 5 | Cup-by-cup data of total particle flux (mg m^{-2} d^{-1}) at ESTOC (1–22) and the MSD-site 1–5 (see **Supplementary Material** and **Figure 1**) for the mesopelagic (**A:** ca. 750 and 1050 m) and bathypelagic (**B:** ca. 3060 m). Fluxes in ca. 750 m are only shown here to fill the gaps in the upper water column but will not be used later on for the discussion of flux seasonality. Vertical hatched lines indicate the years (with the four seasons winter = w, spring = s, summer = su, fall = f, starting on Jan. 1), and bold hatched lines indicates the 5-year mark.

the period of 2005–2009, we showed the fluxes and standard deviations for the period directly before (2000–2004) as well, with a comparable number of observations (**Figures 8C,G**). The summer and fall variability remained almost the same in 2005–2009 compared to the first period of observation (1992–2004).

DISCUSSION

Long-term biogeochemical observations of the oceans are crucial to understand different marine ecosystems and the impacts of natural climate variability and climate change. EBUEs are potential hotspots for observing climate change impacts on oceanic systems (e.g., Garcìa-Reyes et al., 2015). However, distinguishing between natural climate variabilities such as the NAO and trends due to global change requires time series observations in the order of ca. 4 decades. Such observations are available for e.g., SSTs and wind data which are essential to analyze and understand coastal upwelling and test for instance the Bakun upwelling intensification hypothesis (Bakun, 1990; Bakun et al., 2010, 2015; Cropper et al., 2014). However, computed upwelling intensities (Bonino et al., 2019) do not necessarily result in increased primary production, elevated carbon export and deep carbon sequestration. Hence, in order to study the potential changes of the biological carbon pump over decades and over a larger area, time- and space-integrating flux measurements with sediment traps are a useful tool. Studies on interannual to decadal variations of particle fluxes from coastal upwelling areas (EBUEs) or locations influenced by coastal upwelling (i.e., ESTOC) are rare. Even more, research on the relationship of particle fluxes and deep ocean carbon sequestration to low frequency climate variability and climate change is lacking due to the limited observations of most flux studies and the complex forcings on the respective EBUEs (e.g., Bonino et al., 2019).

A long-term flux record (1989–2017) at ca. 4000 m from the northern Californian Current shows increasing POC flux events during the last decade (Smith et al., 2018). Additionally, a warming trend during the past 100 years can be observed influenced by ENSO and associated with an increasing importance of harmful algal blooms since 1985 (Checkley and Barth, 2009). In the southern CC-EBUEs off Cape Blanc (Mauritania), the biogenic flux records show no indications of a coastal upwelling intensification (Fischer et al., 2016, 2019) and the biogenic flux relationships to the NAO turned out to be biased by short-term episodic flux changes (Fischer et al., 2016). We will discuss in the following the two-decade long flux record of ESTOC in the offshore region of the northern CC-EBUEs (in comparison to the CB records in the southern part) with a focus on the development of the biological carbon pump which is strongly influenced by the coastal Cape Ghir filament and its environmental changes.

Influence of Chlorophyll SSTs and MLD on Particle Fluxes at ESTOC

The SeaWiFs time-series of chlorophyll point to a more distinct and different seasonality at ESTOC than at the coastal site Cape Ghir site (**Figures 2**, **9**). A co-maximum in seasonal

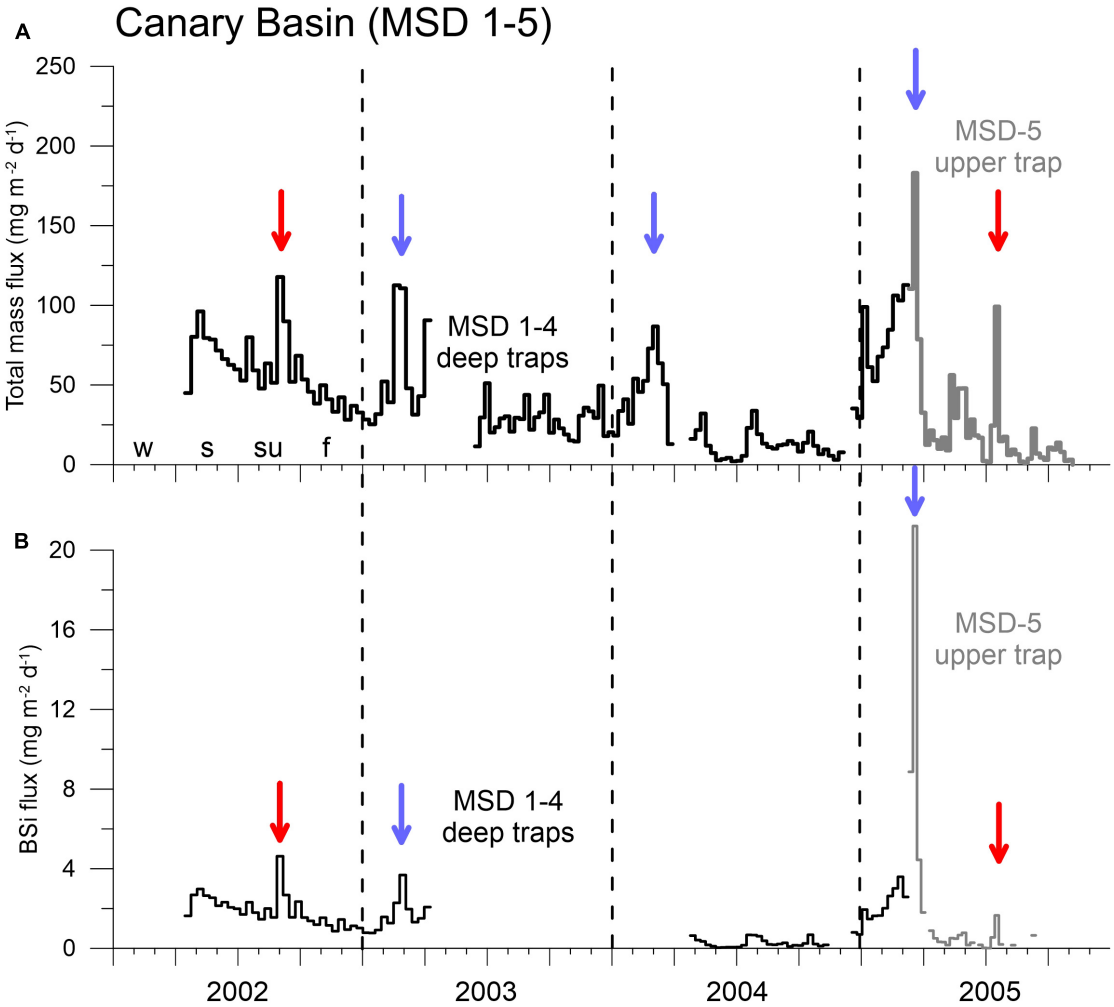

FIGURE 6 | High resolution total mass (**A**, mg m^{-2} d^{-1}) and BSi flux (**B**, mg m^{-2} d^{-1}) record at the MSD site (MSD1–4 lower traps, MSD-5 upper trap, **Supplementary Material**) between 2002 and 2005, revealing regular winter peaks in February-March (blue arrows) and unusual high fluxes in winter 2005. Red arrows mark high summer fluxes. Vertical hatched lines indicate the years (with the four seasons winter = w, spring = s, summer = su, fall = f; starting on Jan. 1).

chlorophyll of both boxes can be seen during the major production seasons in winter (**Figure 9**). This suggests a connection between ESTOC and the Cape Ghir filament, either due to lateral advection of water masses with higher phytoplankton biomass or a coincidence of the occurrence of the spring bloom following deep winter mixing of the surface ocean. Lateral advection of chlorophyll (as a proxy of phytoplankton biomass) is evident in similar coastal upwelling filament settings such as the giant Cape Blanc filament (e.g., Helmke et al., 2005) or in other EBUEs (e.g., in the California Current; Barth et al., 2002). However, ESTOC is outside the direct impact of the Cap Ghir filament, as seen by the minima in chlorophyll at ESTOC in summer (ca. 0.1 mg chl m^{-3}) but varied strongly in the Cape Ghir box with highest summer values of ca. 0.6 mg chl m^{-3} (**Figure 2**), indicative of episodic upwelling and filament activity in summer (Davenport et al., 1999). From 2005 on, chlorophyll peaks at ESTOC became increasingly higher and broader (**Figure 2**). In the ESTOC-chlorophyll time series (**Figure 2**), significant monthly trends were not observed ($p > 0.05$). However, concerning the Cape Ghir chlorophyll time series (**Figure 2A**), the overall trend was significant ($p < 0.05$) and was mainly driven by a positive trend in September ($p < 0.05$).

Neuer et al. (2007) found a clear seasonality in phytoplankton development at ESTOC with winter maxima, coinciding with the time of deepest winter MLD. We found the highest correlation coefficients between MLD and the strength of the biological carbon pump represented by the deep BSi fluxes (Dugdale et al., 1995) in winter (**Table 1**). However, these relationships are statistically insignificant ($p > 0.05$). We have to consider, that the modeled MLDs at ESTOC in winter (DJF) is shallower than the observed MLD at ESTOC (c.f. Neuer et al., 2007), in particular during the overlapping winters DJF 1997/1998, DJF 1998/1999, and DJF 1999/2000. We have no detailed explanation for this discrepancy. However, it is known that the present global

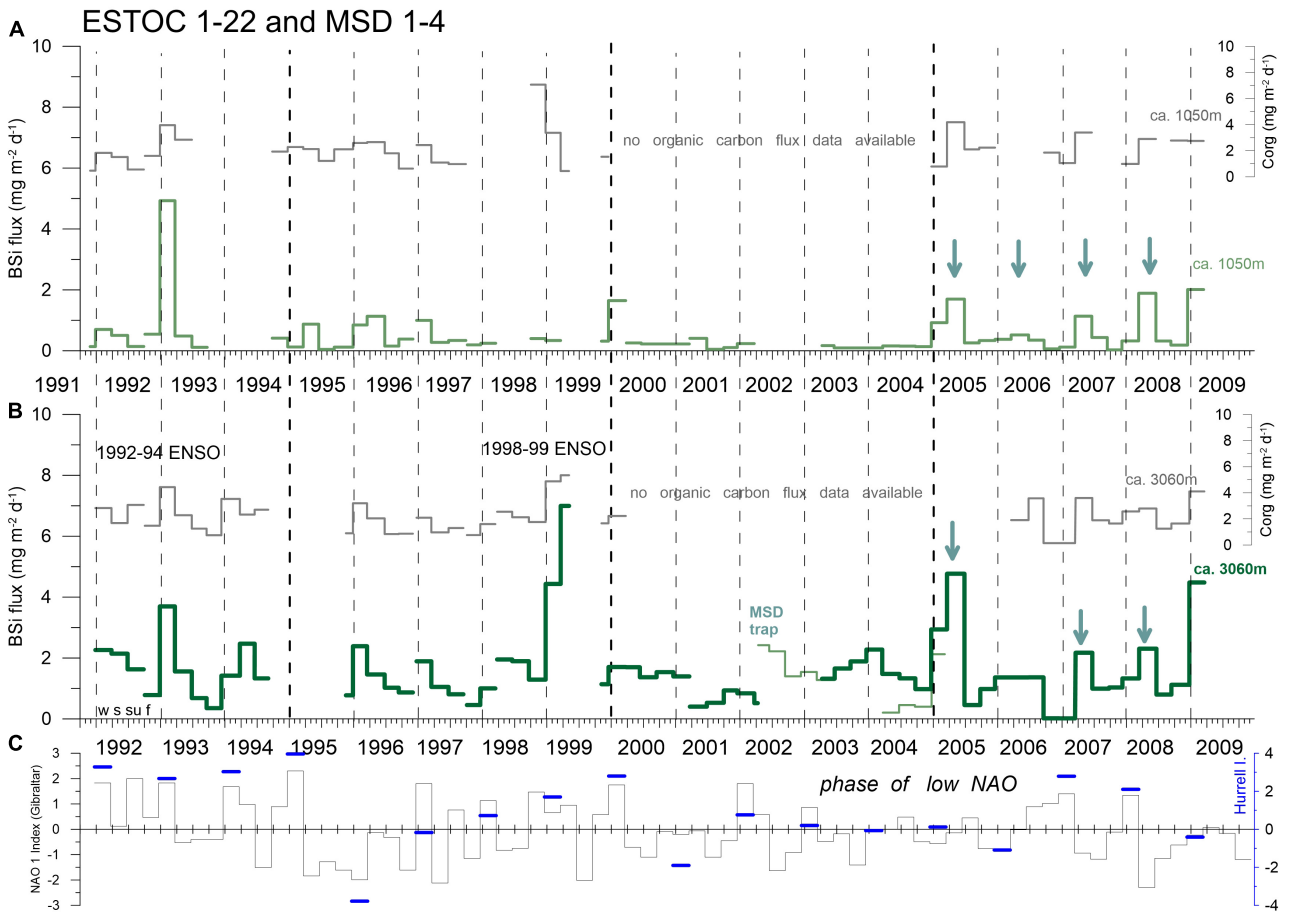

FIGURE 7 | Seasonal fluxes of BSi (mg m^{-2} d^{-1}) at ESTOC and MSD in the upper (**A**, ca. 1050 m) and lower water column (**B**, ca. 3060 m) together with two NAO indices **(C)**. Available organic carbon fluxes are shown as well. Major spring peaks after 2005 are marked with green arrows. Vertical hatched lines indicate years (with the four seasons winter = w, spring = s, summer = su, fall = f; starting on Jan. 1), thick hatched lines indicate a 5-year mark.

and ocean scale models still lack accurate outputs, the more difficult the underlying physical processes (i.e., in a filamental zone with eddies) are to be described and the finer the scales the model has to resolve.

Compared to the CZCS-chlorophyll time series (1979–1985; **Figure 3**), the SeaWiFs-chlorophyll (1997–2009; **Figure 2**) record points to an increasing importance of summer maxima since the 1980s in the Cape Ghir filament (**Figure 9**). CZCS- chlorophyll show clear winter maxima, mostly at the turn of the year or in January/February (**Figure 3**), whereas SeaWiFs-chlorophyll reveals major peaks in March to April (**Figure 2**). Further, there is a tendency of a biomass increase from 1997 to 2009 in the coastal Cape Ghir filament (**Figures 2**, **9**) which is consistent with trends shown by Arístegui et al. (2009). A significant relationship is provided between the SST at ESTOC and the BSi fluxes in both depth levels ($p < 0.05$, Spearman Test, **Table 1**) which has implications for climate change scenarios with increasing temperatures.

For the 1 km traps, we observed a significant correlation ($p < 0.05$) between BSi and SeaWiFs-chlorophyll for the ESTOC box (**Table 1**). This suggests that the biogenic fluxes recorded in the bathypelagic at ESTOC were also determined by the area above ESTOC, in addition to the influence from the more remote coastal upwelling filament of Cape Ghir (Neuer et al., 1997; Davenport et al., 1999; Freudenthal et al., 2001). However, this lateral contribution could be more important during the winter-spring seasons with increasing wind fields as observed for the Cape Blanc area (Fischer et al., 2009). In a new modeling study conducted in this region of the Cape Ghir filament, Santana-Falcón et al. (2020) obtained highest lateral advection of POC and DOC in spring and summer. However, the distinct summer chlorophyll peaks observed at Cape Ghir (**Figure 9**) resulted only in a small increase in fluxes peaks in the deep ESTOC traps (**Figure 10**), pointing to reduced lateral advection of particles during this season when considering the particle flux records.

NAO Controls and an Increased Emphasis in Spring-Time Fluxes at ESTOC Since 2005

We observed increasing trends in the total and the BSi fluxes at both depth levels, which could point to an increase of

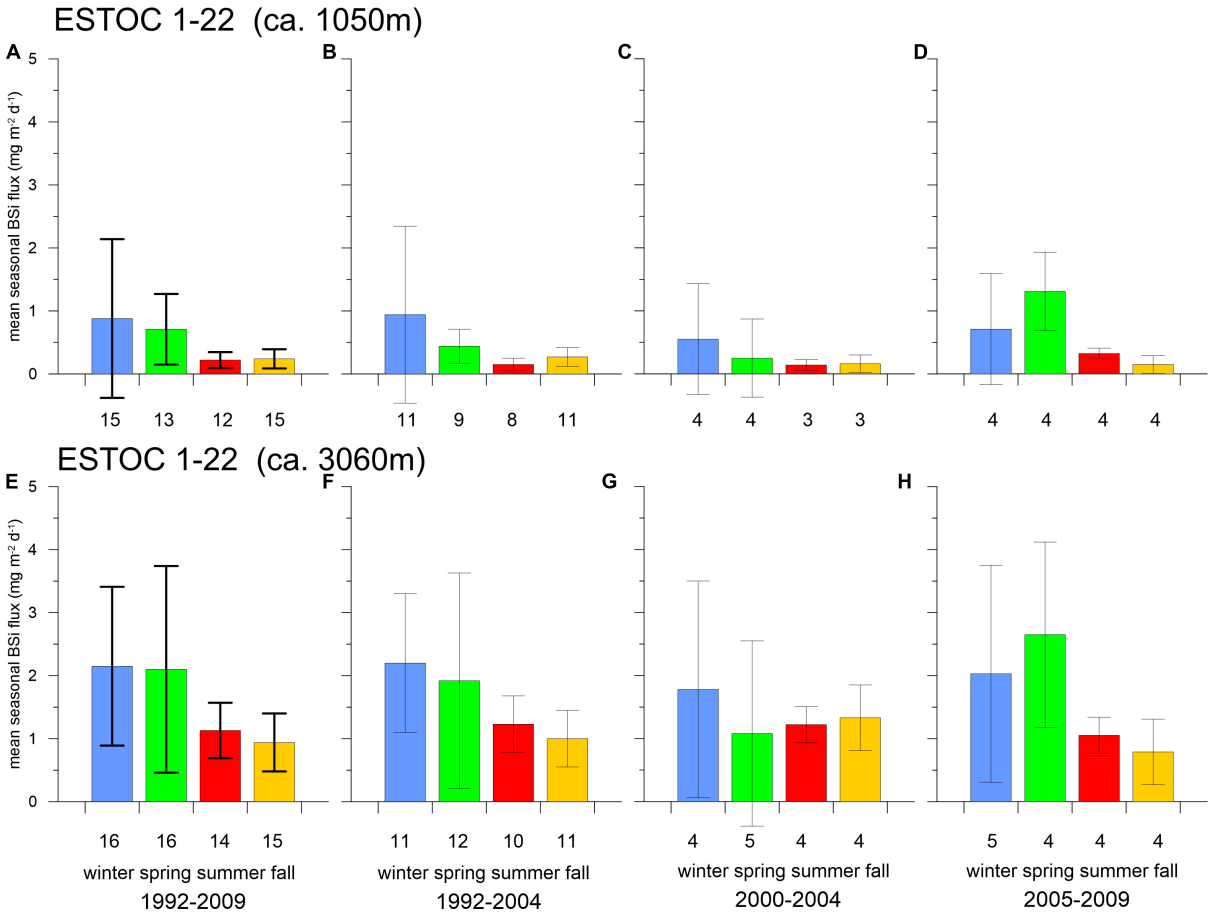

FIGURE 8 | Seasonal means of BSi (mg m^{-2} d^{-1}) and standard deviations (SD) for the total sampling period, for 1992–2004, 2000–2004, and 2005–2009 derived from the 1 km **(A–D)** and 3 km **(E–H)** ESTOC traps. The BSi flux patterns change from winter to spring since 2005. Number of observations are given in numbers below the x-axis; note the low numbers of observations (4–5) for fluxes since 2005.

coastal upwelling in the Cape Ghir and an increase at the oligotrophic ESTOC region (**Figure 10**). These trends can be seen in the chlorophyll as well (**Figure 9**). These overall changes in the Canary Basin could support the Bakun coastal upwelling intensification hypothesis (e.g., Bakun, 1990). However, these trends could be also due to the high NAO index (**Figure 7C**), resulting in intensified upwelling at the end of the sampling period in 2007 and 2008. In the region further south at Cape Blanc, Mauritania, there was no indication supporting the Bakun coastal upwelling intensification hypothesis (Bakun, 1990; Bakun et al., 2015; Cropper et al., 2014) when considering the deep ocean fluxes at the mesotrophic and the eutrophic study site (Fischer et al., 2016, 2019). Meanwhile, evidence increases pointing rather to upwelling relaxation or no variations due to climate change in the CC-EBUEs (e.g., Arístegui et al., 2009; Barton et al., 2013; Gómez-Letona et al., 2017; Sylla et al., 2019).

There is a statistically significant relationship between the spring BSi fluxes of the deeper sediment traps with the NAO-DJFM Hurrell Index (Hurrell, 1995) (excluding the extreme years 1999 (ENSO) and 2005) which we interpret to reflect the influence of the Cape Ghir coastal upwelling ($R^2 = 0.38$, $N = 14$, $p < 0.05$, Spearman Test). The year 2005 was discussed by Fischer et al. (2016, 2019) as an exceptional year with high fluxes despite a low NAO. Romero and Fischer (2017) and Romero et al. (2020) found a change in diatom fluxes and composition at the coastal Cape Blanc site (CB eu) starting in 2005/2006. Unusually high particle fluxes in 2005 in the bathypelagic were also observed far offshore at site Kiel 276 (ca. 33°N/22°W; Fründt and Waniek, 2012). There are also indications of an overall change in circulation in the North Atlantic (i.e., the AMOC) and in the intensity and/or timing of coastal upwelling since 2005 (e.g., Haine, 2016).

In contrast, the relationship between winter NAO and winter BSi flux was weak. This suggests some delay between the NAO wind forcing and the biological response and/or the transport time of particles advected from the Cape Ghir filament to ESTOC. According to Pradhan et al. (2006), the biological response to changing alongshore wind stress is immediate. Therefore, we attribute the time lag between increased upwelling/high standing stock of chlorophyll at Cape Ghir and the arrival of this signal in the deep ESTOC fluxes to lateral particle advection.

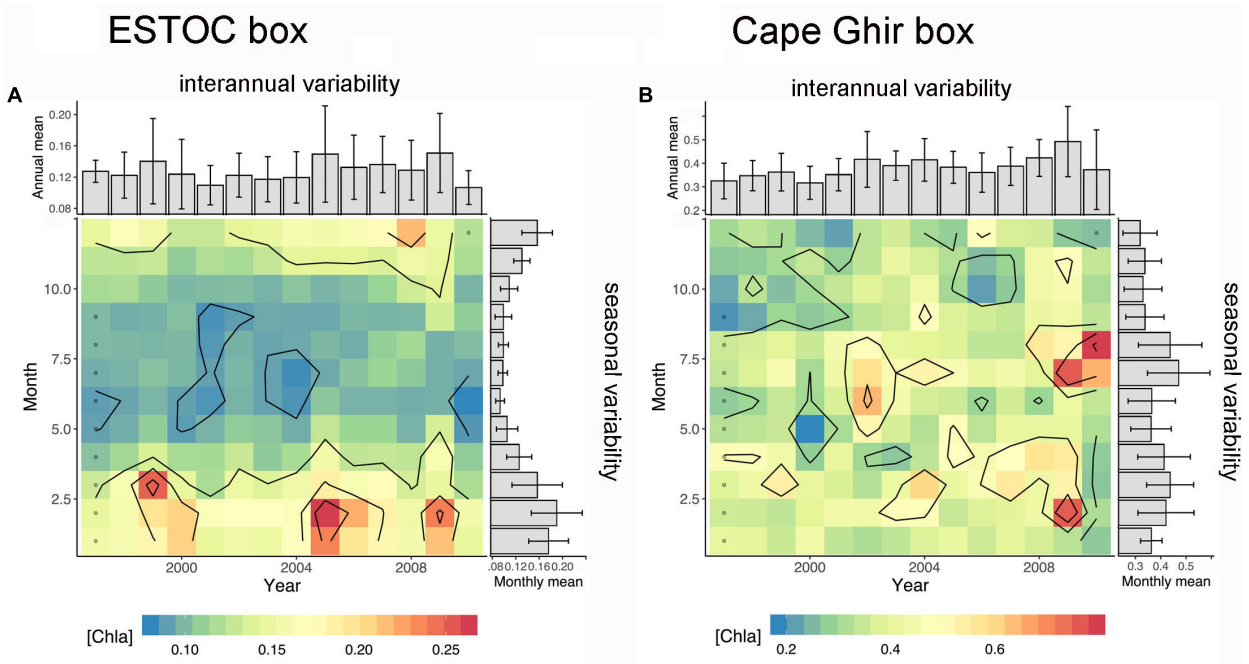

FIGURE 9 | Seasonal vs. interannual variability of SeaWiFs-chlorophyll for the ESTOC **(A)** and the Cape Ghir box **(B)**. Note the difference in seasonality between both boxes (summer maximum at Cape Ghir) and the long term increasing trend in chlorophyll from 1997 to 2010 mainly off Cape Ghir. Gray dots represent the squares interpolated by the Barnes method.

The winter or spring biogenic fluxes of the mesopelagic traps (ca. 1 km), reflecting the oligotrophic area above ESTOC, do not reveal a connection to the NAO (e.g., Cianca et al., 2012). The extreme 1997–1999 ENSO might however impact on chlorophyll biomass (Pradhan et al., 2006) and on particle fluxes in the CC-EBUEs as described by Fischer et al. (2016, 2019) for the Cape Blanc coastal upwelling. Helmke et al. (2005) found 2.5 times higher organic carbon fluxes due to the 1997–1999 ENSO, compared to the regular/normal years. A similar increase in chlorophyll standing stock was observed by Pelegrí et al. (2005) for the same ENSO cycle 1997–1999 within the Mauritanian upwelling off Cape Blanc.

The most interesting feature at ESTOC is an increased emphasis in spring-time fluxes since 2005 (**Figures 7**, **8**, **10**, **11**). A long-term change was also found in the timing of major biomass peaks from winter (CZCS record, **Figure 3**, Davenport et al., 1999) to spring (SeaWiFs record, **Figures 2**, **9**). However, the pattern of SeaWiFs chlorophyll peaks at Cape Ghir and ESTOC did not reveal a change since 2005 in our record (**Figure 9**). Instead, when studying the available individual images of satellite-based chlorophyll from SeaWiFs and MODIS for the winter and spring seasons, we found no significant change in the spring chlorophyll patterns (**Figure 1B**), but an expansion of the high-chlorophyll (ca. 0.5–1 mg m^{-3}) area in winter since 2005 (**Figure 1B**) and thereafter. Analyzing the major peaks of total and biogenic fluxes (e.g., for BSi and organic carbon) in detail using the original high resolution cup-by-cup data of the individual deployments, we found a small displacement of the BSi maxima between 1992–2004 and 2005–2009, mainly for the 1 km traps (**Figure 11**). However, these flux patterns are mainly driven by individual years [e.g., 1993 (ENSO), 2005]. Interestingly, the BSi flux pattern (and organic carbon as well, not shown) of the extreme 1997–1999 ENSO resembles the 2005–2009 picture recorded by the deep traps (**Figure 11B**), reflecting the Cape Ghir filament. However, applying statistical tests using the biogenic fluxes before and after 2005 revealed no significant change in the patterns.

The reasons for the observed long-term changes of the timing of meso- and bathypelagic flux peaks remain elusive. Considering the unchanged chlorophyll patterns in spring since 2005 (**Figure 1B**), we hypothesize that this scenario implies a changing settling behavior of particles originated from the expanded winter blooms which almost reached ESTOC (**Figure 1B**). Lower particle settling rates of particles originating from the winter bloom could have resulted in delayed flux peaks in the 1 and 3 km traps, causing the change to higher spring-time fluxes since 2005. The changing BSi:Corg and C:N ratios in winter and spring discussed in the following paragraph underline this scenario and could point to a longer particle transport of a more diatom-enriched winter bloom leading to elevated spring-time fluxes.

An alternative scenario to explain the increase in the spring-time fluxes recorded in the traps might also be the increase in wet and dry dust deposition reflected by direct measurements on Gran Canaria (López-García et al., 2013). These authors found a marked seasonality of dry and wet dust deposition in spring during 2009–2012. However, if we analyze available satellite-derived AOT (from GIOVANNI: 2000–2015), we observe no

TABLE 1 | Regression parameters of mean winter BSi fluxes measured at 1 km and 3 km depth vs. the environmental variables from both boxes.

		Chlorophyll	SSTs	MLD	N-wind
ESTOC box					
BSi winter	R^2 =	**0.62**	0.18	0.21	0.01
(ca. 1 km)	*N* =	10	15	9	15
	Slope =	13.9	−0.9	0.03	−0.1
	Intercept =	−2.0	19.1	−1.1	0.6
Cape Ghir box					
B Si winter	R^2 =	**0.49**	0.05	0.20	0.004
(ca. 1 km)	*N* =	10	15	9	15
	slope =	5.1	−0.5	0.1	0.05
	intercept =	−1.7	9.2	−1.3	1.0
ESTOC box					
BSi winter	R^2 =	**0.57**	0.32	**0.45**	0.18
(ca. 3 km)	*N* =	11	16	10	16
	Slope =	26.1	−1.3	0.09	−0.4
	Intercept =	−2.9	27.5	−3.2	0.96
Cape Ghir box					
BSi winter	R^2 =	0.29	0.21	**0.45**	0.07
(ca. 3 km)	*N* =	11	16	10	16
	Slope =	8.6	−1.0	0.1	−0.21
	Intercept =	−1.7	19.9	−3.2	1.41

High correlation coefficients (95% confidence level) are in bold. Statistically relevant relationships are gray-shaded ($p < 0.05$, Pearson and Spearman tests). Mesopelagic BSi fluxes at ESTOC are mainly driven by chlorophyll and SSTs around ESTOC.

long-term trend of the available dust nor is there any evidence of a change in seasonality (with normal peaks in late summer) in dust availability. On the other hand, these data only provide the potential dust availability in the lower atmosphere rather than the dust deposition at the ocean surface that is relevant for particle ballasting or fertilization processes in the surface waters.

Interestingly, we observed increasing summer flux peaks since 2005 at ESTOC but only for the upper traps, representing the oligotrophic conditions at ESTOC. However, this feature is only seen in the increasing dominance of chlorophyll peaks in summer at the Cape Ghir, but not in the ESTOC box (**Figure 9**). Summer flux peaks recorded by the 1 km-ESTOC traps might therefore be explained by lateral advection of biomass and particles within the Cape Ghir box and associated eddies via the ESTOC site (e.g., Davenport et al., 1999) as outlined by Helmke et al. (2005) for the Cape Blanc filament. An increase of lateral advection due to increasing winds and due to global change (e.g., Bakun, 1990) was suggested by Lluch-Cota et al. (2014). Alternatively, summer flux peaks at ESTOC might be explained by a nitracline uplift which might be responsible for episodic short term peaks in organic carbon during summer (Neuer et al., 2007).

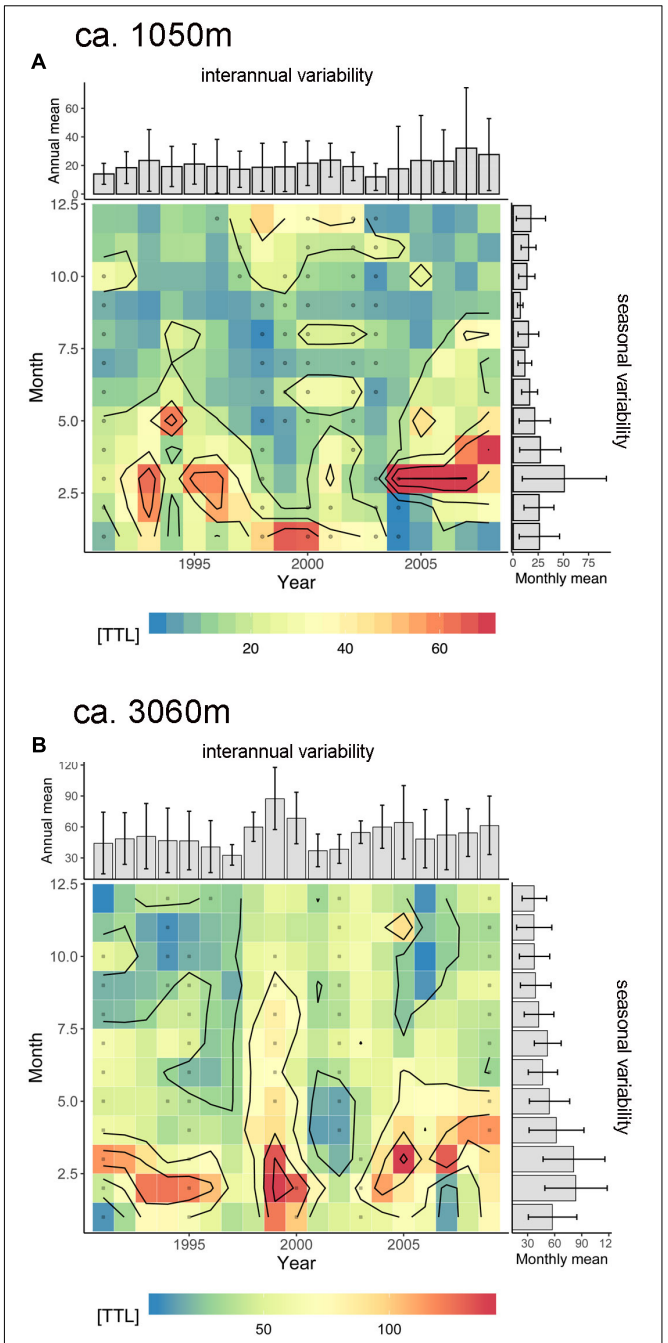

FIGURE 10 | Seasonality vs. long-term variability of total mass flux (TTL, mg m^{-2} d^{-1}) in the upper (**A:** ca. 1 km) and deeper (**B:** ca. 3 km) trap level. Note a change in seasonality from late winter to early spring (Feb/Mar to Mar/Apr) on the long-term (mainly in the 1 km trap) and the increasing fluxes. Extraordinary high fluxes from 1998 to 2000 in ca. 3 km **(B)** are hypothesized to be caused by the extreme ENSO event and its effect on coastal upwelling. Gray dots represent the squares interpolated by the Barnes method.

Lateral Particle Advection From the Cape Ghir Filament and Changes of Flux Composition at ESTOC

The lithogenic fraction of particle flux can be used as a refractory component in the water column to estimate the amount of laterally contributed material to the deep ESTOC traps by comparing the bathypelagic to the mesopelagic trap data. We estimate a relative lateral contribution in the deep water column at 3 km between 52 and 81% with some seasonal variability (not shown). Using the total flux data (**Table 2**) which provide a more complete record, we estimate between 43 and 65%

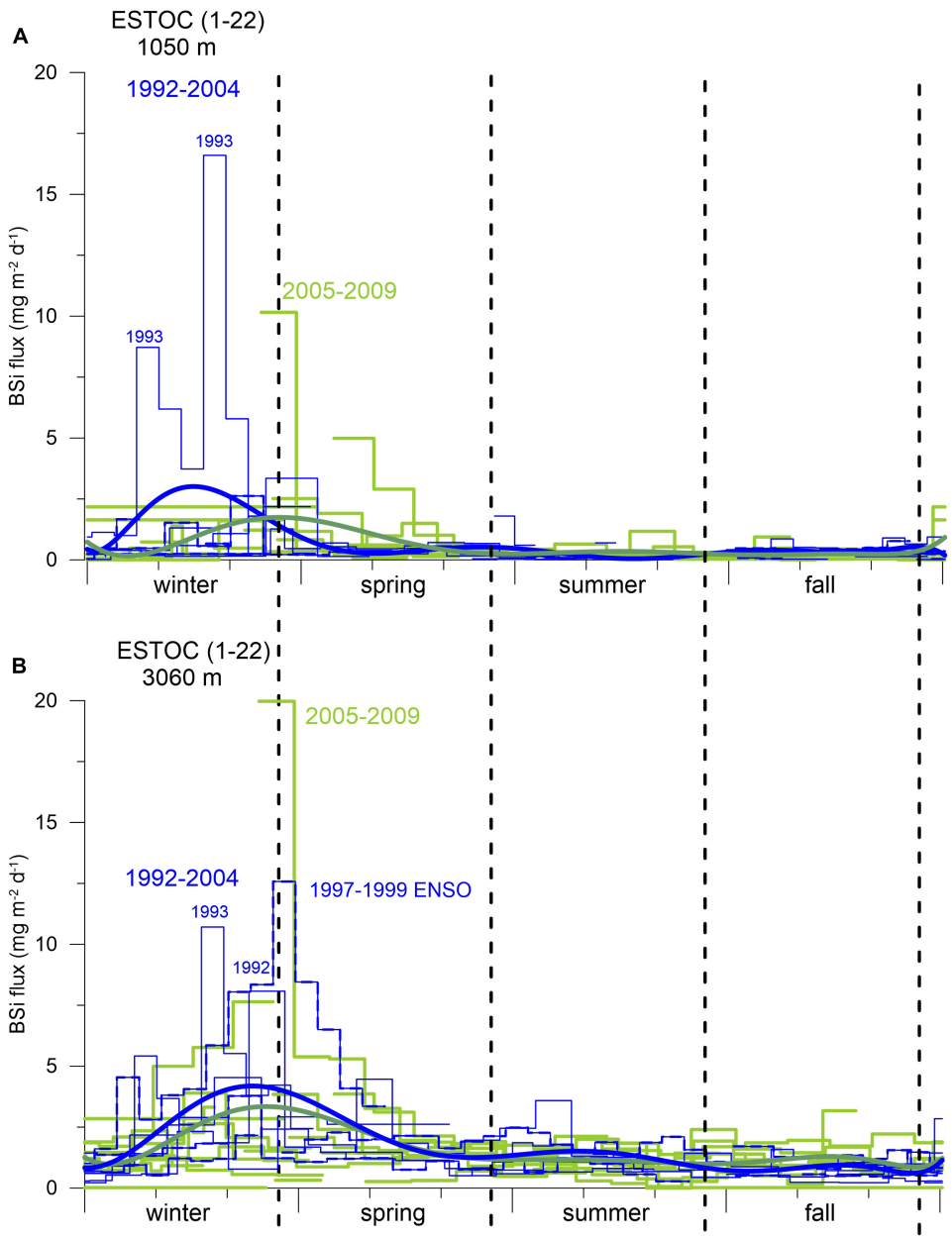

FIGURE 11 | Annual cycles of BSi fluxes from the individual cup-by-cup data for the 1 km **(A)** and 3 km **(B)** traps from 1992 to 2004 (blue line) and for 2005–2009 (green line). The extreme 1997–1999 ENSO cycle is additionally marked with a stippled blue line. A polynomial fit (thick blue line for 1992–2004; thick green line for 2005–2009) indicates small displacements of the BSi flux maxima from winter to spring. Seasons are indicated by vertical hatched lines.

lateral advection with a slightly higher contribution in winter. The highest lateral contribution (65%) was measured in the winters 2005–2009. The calculated values for the lateral fluxes assume no flux changes with depth, in fact, fluxes decrease due to degradation, e.g., of organic matter. Therefore, our values are assumed to underestimate the true advective fluxes. Our values from the lithogenic component and the total material are within the range of estimates of lateral advection from stable nitrogen isotopes (Freudenthal et al., 2001) which indicate a lateral contribution between 50 and 75% at 3 km depth.

The distance between the southwestern edge of the Cape Ghir and the ESTOC box is ca. 350 km (**Figure 1A**). Thus, without eddy field and considering a simple advective particle transport path, particles would reach the deep ESTOC trap in ca. 40 days, assuming an average horizontal current speed of 10 cm s^{-1} and an average particle settling rate of 75 m d^{-1}. Such a delay matches the observed delay of ca. 1.5 months in the occurrence of chlorophyll peaks at Cape Ghir and the arrival of the flux signal in the deep ESTOC traps (e.g., Neuer et al., 1997; Davenport et al., 1999). However, while the required average

TABLE 2 | Daily mean total fluxes (in mg m^{-2} d^{-1} with the standard deviations) for traps deployed in the Canary Basin for winter and spring seasons averaged over different yearly intervals.

Trap (depth, km) (Duration)	Mean winter flux (mg m^{-2} d^{-1}) 1992–2009	Mean winter flux (mg m^{-2} d^{-1}) 1992–2004	Mean winter flux (mg m^{-2} d^{-1}) 2005–2009
Winter			
1 km	27.2 ± 16.4	30.6 ± 18.5	19.6 ± 7.0
(87 ± 8 days)			
3 km	66.0 ± 29.8	70.6 ± 28.5	55.9 ± 33.1
(88 ± 9 days)			
Flux increase	**38.8**	**40.0**	**36.3**
Rel. Increase	**59%**	**57%**	**65%**
Trap (depth, km) (Duration)	**Mean spring flux (mg m^{-2} d^{-1}) 1992–2009**	**Mean spring flux (mg m^{-2} d^{-1}) 1992–2004**	**Mean spring flux (mg m^{-2} d^{-1}) 2005–2009**
Spring			
1 km	28.7 ± 19.4	22.7 ± 15.6	47.0 ± 19.9
(81 ± 26 days)			
3 km	59.0 ± 30.5	51.2 ± 29.7	82.4 ± 21.6
(82 ± 22 days)			
Flux increase	**30.3**	**28.5**	**35.4**
Rel. Increase	**51%**	**56%**	**43%**

Flux increase calculated as difference between the flux at 3 km minus the flux at 1 km depths (bold numbers).

particle settling rate corresponds to values estimated earlier (70 to a few 100 m d^{-1}, Neuer et al., 1997), the required average horizontal advective speed in the order of ca. 10 cm s^{-1} does not match the generally much lower 30-day averaged currents observed at ESTOC (**Figure 4**). The slow settling velocities that Alonso-González et al. (2010) reported from a location just south of Gran Canaria, were measured at 260 m depth close to or within the production area, i.e., under conditions different from the ESTOC-Cape Ghir system. However, slowly settling particles could play a major role at ESTOC as well, besides the fast sinking particle pool (210–430 m day^{-1}, between 1 and 3 km), estimated from particle flux patterns at ESTOC (Fischer and Karakas, 2009). In the Cape Blanc area, we were able to model (ROMS, Regional Ocean Modeling System) particle nepheloid layers using particle settling rates between 5 and 10 m per day (e.g., Fischer et al., 2009). These particles of the smaller size fraction constitute different nepheloid layers but may participate in the downward flux as well. The settling speeds applied at Cape Blanc were in the range of particle sizes discussed by Alonso-González et al. (2010) for the southern Canary Island region. It is reasonable to assume similar transport processes and particle characteristics in the ESTOC area, considering different particle pools with different particle settling rates, which constitute the sediment trap material.

The available 8-year record (1994–2002) of current speeds and directions (**Figure 4**) indicates that the flow at ESTOC is dominated by deep reaching coupled barotropic and first baroclinic mode meso-scale eddies, as it was observed earlier in other parts of the eastern subtropical North Atlantic (Müller and Siedler, 1992). Assuming that meso-scale eddy activity in the region north of ESTOC toward Cape Ghir may be of comparable intensity as at ESTOC, we follow Neuer et al. (2002b) that meso-scale eddy diffusion could explain the Cape Ghir filament as a long distance source for the observed increase in fluxes in the deep ESTOC sediment traps. Combining field observations and a statistical funnel model at ESTOC, e.g., similar to that of Siegel et al. (2008) for the ALOHA station near Hawaii would be needed for further confirmation, however, this is beyond the scope of this study.

Other comparable ocean areas with similar advective processes (e.g., in the Benguela Current; Inthorn et al., 2006) reveal lateral advection in the same order of magnitude as described above of the NW African continental slope (McCave et al., 2001; Hwang et al., 2009; Lovecchio et al., 2017). A high particulate organic carbon offshore transport of ca. 1050 km by mesoscale eddies is observed in other EBUEs such as the California Current (Amos et al., 2019). The estimated advective fluxes from ESTOC also fall in the range of values from the Cape Blanc area (Fischer et al., 2009, 2016, 2019), where winter was the most prominent season for lateral advection of particles. In a recent modeling study conducted in the region of the Cape Ghir filament, Santana-Falcón et al. (2020) obtained highest lateral advection of POC and DOC in spring and summer.

We found changes not only in the seasonality of fluxes since 2005 but also in the composition of sinking materials between the beginning (1992–2004) and the end of the ESTOC record (2005–2009; **Table 3**). The deep ESTOC traps showed highest lithogenic fluxes for the winter and spring seasons between 8.1 and 35 mg m^{-2} d^{-1}, which are attributed to dust minerals and amount between 18 and 50% of the total flux (**Table 3**). Upper trap fluxes for the lithogenic fraction are clearly lower on average. The overall proportion of about one third of lithogenic material of total flux is comparable to estimates from the coastal upwelling off Cape Blanc, Mauritania (Fischer et al., 2016, 2019). A clear coupling between atmospheric dust occurrences and lithogenic particle fluxes at 2000 m water depth was suggested by Brust et al. (2011) for site Kiel 276 (33°N/22°W), an almost similar latitude but more offshore than ESTOC. The lithogenic component at site Kiel 276, however, amounts only about 15% on average and individual lithogenic flux peaks ranged between 0.2 and 42.5 mg m^{-2} d^{-1} (Brust et al., 2011). The individual values ranged from almost zero to ca. 181 mg m^{-2} d^{-1} in the bathypelagic at ESTOC. The individual maxima exceeded the values at Kiel 276 by more than a factor of four due to a much closer location of ESTOC to the African source regions of dust and the clear decline of dust deposition observed from the coast to the open ocean (e.g., Kaufman et al., 2005).

The trap collections at ca. 1 and 3 km show a decrease of all biogenic fluxes (BSi, organic carbon and carbonate) in winter, accompanied by an increase of most fluxes in spring-time since 2005 (**Table 3**). In the 1 km trap collections, BSi increased 2–3-fold in spring-time between 1992–2004 and 2005–2009 (**Table 3**) while the winter fluxes decreased. In the deep traps, these changes were less clear. Additionally, increasing BSi:Corg ratios in spring-time (**Table 3**) may point to some change in the composition of sinking detritus, with a likely increase in diatoms since 2005.

TABLE 3 | Mean seasonal winter and spring fluxes (in mg m^{-2} d^{-1}) and ratios and their seasonal changes since 2005 (bold numbers) measured at 1 km and 3 km depths in the Canary Basin.

Time period	1 km TRAPS	Fluxes					Fluxes						Ratios		
	Season	Total mass mg m^{-2} d^{-1}	SD	B Si mg m^{-2} d^{-1}	SD		Total mass mg m^{-2} d^{-1}	B Si mg m^{-2} d^{-1}	Corg mg m^{-2} d^{-1}	Ntot mg m^{-2} d^{-1}	Carbonate mg m^{-2} d^{-1}	Lithogenic mg m^{-2} d^{-1}	B Si/ Corg	Corg/ Ccarb	C/N Molar
1992–2004	Winter	30.64	18.5	0.94	1.4	1992–2000	36.03	1.32	2.74	0.45	18.75	10.28	0.5	1.2	7.1
	Spring	22.66	15.6	0.44	0.3		26.87	0.60	2.05	0.31	11.48	9.09	0.3	1.5	7.7
2005–2009	Winter	19.64	7.0	0.71	0.9	2005–2009	18.84	0.82	1.60	0.19	9.01	4.00	0.5	1.5	10.0
	Spring	46.97	19.9	1.31	0.6		54.31	1.57	3.49	0.45	26.09	19.65	0.5	1.1	9.0
Changes since 2005	**Winter**	**−11.0**		**−0.2**			**−17.2**	**−0.5**	**−1.1**	**−0.3**	**−9.7**	**−6.3**	**0.0**	**0.3**	**2.9**
	Spring	**24.3**		**0.9**			**27.4**	**1.0**	**1.4**	**0.1**	**14.6**	**10.6**	**0.2**	**−0.4**	**1.4**
Time period	**3 km TRAPS**	**Fluxes**					**Fluxes**						**Ratios**		
	Season	**Total mass mg m^{-2} d^{-1}**	**SD**	**B Si mg m^{-2} d^{-1}**	**SD**		**Total mass mg m^{-2} d^{-1}**	**B Si mg m^{-2} d^{-1}**	**Corg mg m^{-2} d^{-1}**	**Ntot mg m^{-2} d^{-1}**	**Carbonate mg m^{-2} d^{-1}**	**Lithogenic mg m^{-2} d^{-1}**	**B Si/ Corg**	**Corg/ Ccarb**	**C/N Molar**
1992–2004	Winter	70.63	28.6	2.20	1.1	1992–2000	76.03	2.46	3.16	0.38	31.37	35.18	0.8	0.8	9.6
	Spring	51.18	29.7	1.92	1.7		59.44	2.52	2.46	0.29	22.10	29.90	0.8	0.9	10.0
2005–2009	Winter	55.93	33.1	2.03	1.7	2005–2009	44.58	1.94	2.27	0.29	29.91	8.05	0.9	0.6	9.1
	Spring	82.35	21.6	2.65	1.5		78.07	1.95	2.77	0.28	34.56	22.85	1.0	0.7	12.0
Changes since 2005	**Winter**	**−14.7**		**−0.2**			**−31.5**	**−0.5**	**−0.9**	**−0.1**	**−1.5**	**−27.1**	**0.1**	**−0.2**	**−0.5**
	Spring	**31.2**		**0.7**			**18.6**	**−0.6**	**0.3**	**0.0**	**12.5**	**−7.1**	**0.2**	**−0.3**	**2.0**

Note that organic carbon flux was not available for 2000 to 2004. Therefore, the right part shows fluxes and ratios for the periods 1992–2000 and 2005–2009. SD, Standard Deviations.

The increase of the C:N ratios by two molar units in the deeper trap collections in spring since 2005 (**Table 3**) points to a longer particle transport and, thus, a higher degradation of organic matter before arriving in the deep offshore traps. This scenario is in accordance with the assumption of a more diatom-enriched winter bloom, which settles with decreased rates and constitutes a higher spring signal in the sediment traps since 2005. It is known from laboratory and field studies that particles with higher BSi (more diatoms) may sink at lower rates (Ploug et al., 2008; Fischer and Karakas, 2009; Iversen and Ploug, 2010).

Total carbonate flux which constitutes roughly one half of the total flux (**Table 3**) increased in spring as well by more than 2-fold (1 km traps). However, as total carbonate is mainly constituted by planktonic foraminifera, pteropods, and coccolithophores, we do not know which fraction is most important in the entire record. An estimation of the contribution of coccolithophores to total carbonate flux revealed a value of about one third at ESTOC for individual deployments (Sprengel et al., 2002). Roughly three quarters of the yearly coccolithophore-carbonate settles in winter, indicating their importance for the seasonal bloom. Abrantes et al. (2002) associated 93% of the microplankton to coccolithophore cells in the northern Canary Islands region. Short term episodic sedimentation pulses (hours to days) with fecal pellets packed tightly with coccolithophores were found to be characteristic for the ESTOC site (deployments 1–2, Fischer et al., 1996), suggesting carbonate as an important ballast mineral (e.g., Klaas and Archer, 2002). More recent studies on the polysaccharide contents of coccolithophores indicate high organic carbon contents (Anderson et al., 2014; Lee et al., 2016) which might explain the tight correlations between coccolithophores and organic carbon at ESTOC (Fischer et al., 1996). The almost perfect coupling between organic carbon and carbonate sedimentation (Fischer et al., 1996; Neuer et al., 1997, 2007), however, did change during the sampling period, leading to different Carbon Rain Ratios (CRR = $C_{org}/C_{carbonate}$) in the ESTOC trap samples (**Table 3**). During the exceptional ENSO 1997–1999 event for instance, deep organic carbon fluxes were much higher during the La Niña phase 1999, whereas carbonate fluxes were relatively low, resulting in an exceptional CRR of about 6.3. Overall, upper trap values were higher (CRR = 1.1–1.5) than the lower trap samples (CRR = 0.8–1.0), the latter show a decreasing tendency between 1992–2004 and 2005–2009 (**Table 3**). This could result in a lower efficiency to sequester CO_2 by the biological pump. Increasing coccolithophore abundance in the euphotic zone of the western subtropical North Atlantic (BATS) between 1990 and 2014 was observed by Krumhardt et al. (2016) and was attributed to global change. A basin-wide increase in coccolithophore growth and biomass was found for the North Atlantic by Rivero-Calle et al. (2015) and could match our findings from ESTOC.

Synchronous Particle Flux Records at ESTOC and off Cape Blanc and Long Term Changes

As pointed out by Lluch-Cota et al. (2014), poleward coastal upwelling sites and the more equatorward locations (e.g., Cape Blanc upwelling) might react differently to climate change. ESTOC generally provides a more distinct seasonality of particle fluxes with regular winter peaks on the long term (see also Neuer et al., 2007) compared to the Cape Blanc study sites (Fischer et al., 2016, 2019). At the offshore site CBmeso, characterized by permanent annual upwelling (**Figure 1**; Cropper et al., 2014), seasonality of fluxes is less clear with winter peaks and additional late summer peaks occurring during certain years (e.g., 2002, **Figure 12**) due to the influence from northward flowing warm water Mauritanian Current (**Figure 1A**; Fischer et al., 2016, 2019). **Figure 12** shows the deep mass fluxes at CBmeso compared to the synchronous deep ESTOC record as both sites were influenced by coastal upwelling, large filaments and eddies reaching far offshore (Davenport et al., 1999; Neuer et al., 2002b; Fischer et al., 2009, 2016, 2019). Both time series reveal some similarities in the overall variability of fluxes due to the overall NAO forcing of the Canary Current coastal upwelling (e.g., González-Dávila et al., 2007; Narajan et al., 2010; section "NAO Controls and an Increased Emphasis in Spring-Time Fluxes at ESTOC Since 2005"). Further, the strong 1997–99 ENSO appears to influence particle flux patterns at both sites and resulted in elevated fluxes in 1998–1999 during the La Niña cold phase (**Figures 5**, **7**; Fischer et al., 2016, 2019). The best coincidence of particle flux variability at ESTOC and CBmeso is observed for the spring season, however, the correlation coefficient for the entire period is very low (R^2 = 0.13, N = 10) (**Figure 12**). A detailed look shows that before 2005, major flux peaks occur earlier at ESTOC (winter, e.g., **Figure 11**), thus coinciding with the major peaks (in winter) at CBmeso (**Figure 12**; insert, N = 6, R^2 = 0.66). However, statistical tests revealed no significant relationship ($p > 0.05$, Spearman Test). Due to a stronger emphasis of spring fluxes at ESTOC since 2005 (section "NAO Controls and an Increased Emphasis in Spring-Time Fluxes at ESTOC Since 2005"), we observed a large scatter of data points for the second sampling period between 2005 and 2009 (**Figure 12**).

Romero and Fischer (2017), Fischer et al. (2019), and Romero et al. (2020) found a change in particle fluxes and composition at the coastal Cape Blanc site (CB eu) starting in 2005/2006. This could point to an overall change in circulation in the North Atlantic and in the intensity and/or timing of coastal upwelling. Such changes in the Atlantic are described for a major driver of the biogeochemistry and circulation in the North Atlantic Ocean, i.e., the AMOC (with an Ekman component) that could have decreased since 2005 in the eastern North Atlantic (Smeed et al., 2014; Srokosz and Bryden, 2015; Haine, 2016). Relaxation of Ekman upwelling might be responsible for the statistical significant decrease in carbon fluxes ($p < 0.05$) between 2003 and 2016 at the coastal Cape Blanc site CB eu (Fischer et al., 2019). However, an overall long-term decrease of the AMOC is doubted by many other oceanographers and climatologists and the observed circulation changes might be part of a natural climatic variability as well.

In summary, the time series of chlorophyll biomass (**Figures 2**, **9**) and particle fluxes from ESTOC (**Figures 5**, **7**, **10**) point to an increase of coastal upwelling and/or a change in the advective flux (as proposed by Lluch-Cota et al., 2014) in the northern CC-EBUEs. Additionally, we observed a long-term

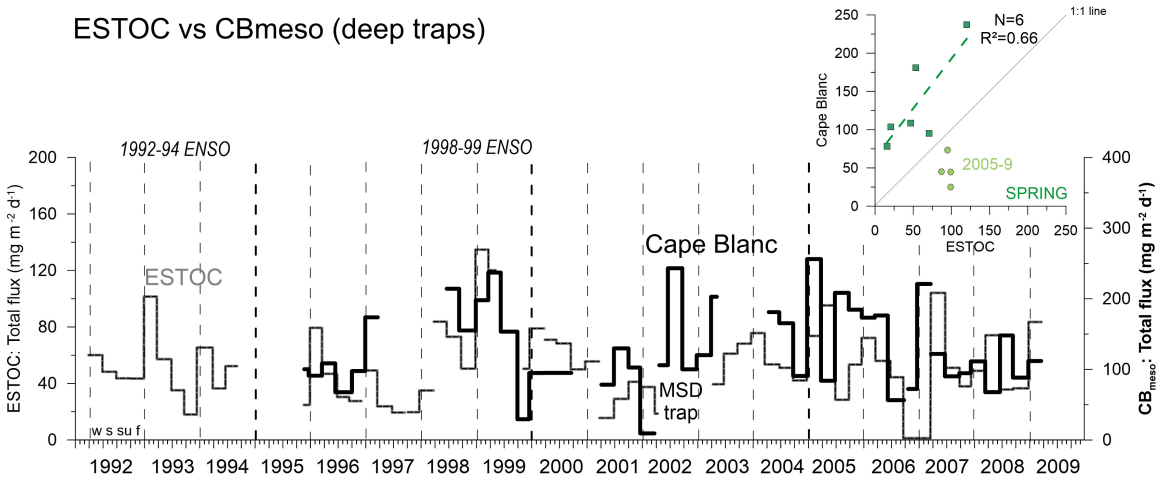

FIGURE 12 | Comparison of deep ocean total mass fluxes between the ESTOC site (including MSD traps) and the Cape Blanc mesotrophic site. Note the different scales for fluxes. The correlation coefficient between fluxes is highest for spring (upper right panel) for 1996–2004 (R^2 = 0.66, N = 6) but the relationship is not significant ($p > 0.05$). Between 2005 and 2009, data points show some scatter due to a shift in particle flux seasonality at ESTOC. Vertical hatched lines indicate years (with the four seasons winter = w, spring = s, summer = su, fall = f, starting on Jan. 1), thick hatched lines indicate the 5-year mark.

increase of chlorophyll (**Figure 2**) in the Cape Ghir filament, pointing to an intensification of coastal upwelling. However, the individual seasonal patterns of satellite chlorophyll in the ESTOC area reveal an expansion of the high chlorophyll area (ca. 0.5–1 mg m^{-3}) in the winter seasons since 2005 but no clear changes in spring (**Figure 1B**). Further, it seems that the summer chlorophyll peaks at the Cape Ghir filament became more prominent since 2005 (**Figure 9**) which is, however, not clearly reflected in the deep particle flux records at ESTOC (**Figure 10**). Increasing trends in chlorophyll and particle fluxes at ESTOC were not observed further south in the Mauritanian upwelling (Fischer et al., 2016, 2019).

CONCLUSION

An almost two-decade long flux record from ca. 1 and 3 km at the oligotrophic ESTOC site combined with environmental data and compared to the offshore flux record off Cape Blanc (Fischer et al., 2016, 2019) revealed the following major findings:

- SeaWiFs-chlorophyll from 1997 to 2009 showed an overall increasing trend at the Cape Ghir coastal upwelling box ($p < 0.05$) but not in the oligotrophic ESTOC region,
- over decadal time scales, satellite chlorophyll appeared to switch from peaks in winter (CZCS: 1979–1985, Davenport et al., 1999) to spring at ESTOC (SeaWiFs: 1997–2009),
- ESTOC is an oligotrophic time series station but bathypelagic fluxes were influenced by lateral advection of particles (between 43 and 65%) from the coastal Cape Ghir filament (Davenport et al., 1999). Mesopelagic fluxes revealed the more oligotrophic conditions at ESTOC with ca. 2–3-fold lower particle fluxes compared to the bathypelagic fluxes,
- SeaWiFs-chlorophyll from ESTOC shows a significant relationship to the mesopelagic BSi fluxes in winter,
- we found a stronger emphasis in spring-time fluxes since 2005 and BSi fluxes increased by 3-fold (1 km traps). However, this change in fluxes from 1992–2004 to 2005–2009 was statistically not significant,
- in association with the higher spring-time fluxes, the composition of the sinking material changed (e.g., BSi:Corg and C:N increased) between 1992–2004 and 2005–2009, which might point to a change in plankton composition and particle transport,
- the deep spring BSi fluxes (3 km, reflecting mainly the Cape Ghir filament) show a statistical significant relationship to the winter (DJFM) NAO Hurrell Index when excluding the extreme years 1999 (ENSO) and 2005,
- the best agreement between deep particle flux patterns at ESTOC (northern CC-EBUEs) and Cape Blanc (southern CC-EBUE, site CB mesotrophic) was during the spring season, but only before 2005.

The reasons for the observed higher spring-time fluxes since 2005 remain elusive. This change could be due to shift in productivity (and biomass), forced by upwelling favorable winds (in intensity or timing) in both the ESTOC and the Cape Ghir boxes. However, the stronger emphasis in spring-time fluxes since 2005 was not found in the satellite chlorophyll patterns. Instead, considering the larger winter bloom (satellite chlorophyll) and the compositional changes since 2005 in both traps, we conclude that lower particle settling rates of the winter bloom resulted in a higher spring-time signal recorded with the sediment traps.

There is an increasing trend of SeaWiFs-chlorophyll and particle fluxes in the oligotrophic ESTOC region which was not observed further south at the mesotrophic Cape Blanc site, located in the southernmost permanent upwelling zone close to the tropics (**Figure 1A**). At the eutrophic Cape Blanc site, we even observed statistically significant decreasing organic

carbon fluxes (Fischer et al., 2019), which contradict the Bakun coastal upwelling intensification hypothesis (e.g., Bakun, 1990). Our observations from ESTOC and Cape Blanc are more in accordance with the concept of Lluch-Cota et al. (2014), who argued that coastal upwelling due to global change may be intensified in the poleward parts of the EBUEs (e.g., at ESTOC) rather than in the equatorward regions (e.g., off Cape Blanc). However, the flux records both at ESTOC and Cape Blanc are still not long enough to disentangle natural low frequency variability from long-term trends of fluxes which might be due to climate change, like the potential intensification of coastal upwelling (e.g., Bakun, 1990; Bakun et al., 2010, 2015; Cropper et al., 2014).

DATA AVAILABILITY STATEMENT

The raw data supporting the conclusions of this article will be made available by the authors, without undue reservation, to any qualified researcher.

AUTHOR CONTRIBUTIONS

GF and SN collected the data. GF mainly wrote the article with the help of SN and TM. SR carried out the statistical analyses. BD contributed to the data collection. GR, VR, GM, NN, and MK carried out the mooring work and analysis of the sediment trap data. GW contributed with the ideas and writing. All authors contributed to the article and approved the submitted version.

ACKNOWLEDGMENTS

We dedicate this contribution to the memory of our friend Dr. Helge Meggers whose contributions to paleoceanography and microfossil observations off NW Africa have been invaluable. We acknowledge the guidance of the expeditions with RV Meteor and RV Poseidon, in the later years by Tim Freudenthal. We are indebted to ships' crews and masters of the relevant cruises (**Supplementary Material**). For discussion, we thank Oscar Romero, Holger Kuhlmann, and Gesine Mollenhauer. Thanks to colleagues from former ICBM in Telde, Gran Canaria (now PLOCAN) for the support during and before the ships' cruises. Establishing such a long time series of fluxes and water column studies at ESTOC and off Cape Blanc was only possible due to a long-term funding by the Deutsche Forschungsgemeinschaft through the SFB 261, the RCOM, and the MARUM Excellence Cluster "The Ocean in the Earth System" at Bremen University. Further, the long financial support for the technologicl innovations and current meter moorings by the BMBF (also through JGOFS) and the EU is greatly acknowledged. We thank the three reviewers for helpful comments and the editorial staff of "Frontiers."

SUPPLEMENTARY MATERIAL

The Supplementary Material for this article can be found online at: https://www.frontiersin.org/articles/10.3389/feart.2020.00280/full#supplementary-material

REFERENCES

Abrantes, F., Meggers, H., Nave, S., Bollman, J., Palma, S., Sprengel, C., et al. (2002). Fluxes of micro-organisms along a productivity gradient in the Canary Islands region (29°N): implications for paleoreconstructions. *Deep Sea Res. II* 49, 3599–3629. doi: 10.1016/s0967-0645(02)00100-5

Alonso-González, I. J., Arístegui, J., Lee, C., Sanchez-Vidal, A., Calafat, A., Fabrés, J., et al. (2010). Role of slowly settling particles in the ocean carbon cycle. *Geophys. Res. Lett.* 37:L13608. doi: 10.1029/2010GL043827

Amos, C. M., Castelao, R. M., and Medeiros, P. M. (2019). Offshore transport of particulate organic carbon in the California Current System by mesoscale eddies. *Nat. Commun.* 10:4940. doi: 10.1038/s41467-019-12783-5

Anderson, M. P., Hem, C. P., Schultz, L. N., Nielsen, J. W., Pedersen, C. S., Sand, K. K., et al. (2014). Infrared spectroscopy and density functional theory investigation of calcite, chalk, and coccoliths - do we observe the mineral surface? *J. Phys. Chem. A* 2014, 10720–10729. doi: 10.1021/jp5053858

Arístegui, J., Barton, E. C., Álvarez-Salgado, X. A., Santos, A. M. P., Figueiras, F. G., Kifani, S., et al. (2009). Sub-regional ecosystem variability in the Canary Current upwelling. *Prog. Oceanogr.* 83, 33–48. doi: 10.1016/j.pocean.2009.07.031

Bakun, A. (1990). Global climate change and intensification of coastal ocean upwelling. *Science* 247, 198–201.

Bakun, A., Black, B. A., Bograd, S. J., García-Reyes, M., Miller, A. J., Rykaczewski, R. R., et al. (2015). Anticipated effects of climate change on coastal upwelling ecosystems. *Curr. Clim. Change Rep.* 1, 85–93. doi: 10.1007/s40641-015-0008-4

Bakun, A., Field, D., Redondo-Rodriguez, A., and Weeks, S. (2010). Greenhouse gas, upwelling-favourable winds, and the future of coastal ocean upwelling ecosystems. *Glob. Change Biol.* 16, 1213–1228.

Barth, J. A., Cowles, T. J., Kosro, P. M., Shearman, R. K., Huyer, A., and Smith, R. L. (2002). Injection of carbon from the shelf to offshore beneath the euphotic zone in the California current. *J. Geophys. Res.* 107:3057.

Barton, E. D., Field, D. B., and Roy, C. (2013). Canary current upwelling: more or less? *Prog. Oceanogr.* 116, 167–178. doi: 10.1016/j.pocean.2013.07.007

Behrenfeld, M. J., Randerson, J. T., McClain, C. R., Feldman, G. C., Los, S. O., Tucker, C. J., et al. (2001). Biospheric primary production during an ENSO transition. *Science* 291, 2594–2597. doi: 10.1126/science.1055071

Berelson, W. M. (2002). Particle settling rates increase with depth in the ocean. *Deep Sea Res. II* 49, 237–251. doi: 10.1016/s0967-0645(01)00102-3

Bonino, G., Di Lorenzo, E., Masina, S., and Iovino, D. (2019). Interannual to decadal variability within and across the major Eastern boundary upwelling systems. *Sci. Rep.* 9:19949. doi: 10.1038/s41598-019-56514-8

Brust, J., Schulz-Bull, D. E., Leipe, T., Chavagnac, V., and Waniek, J. J. (2011). Descending particles: from the atmosphere to the deep ocean: a time series study in the subtropical NE Atlantic. *Geophys. Res. Lett.* 38:L06603. doi: 10.1029/2010GL045399

Buesseler, K. O., Antia, A. A., Chen, M., Fowler, S. W., Gardner, W. D., Gustafsson, O., et al. (2007). An assessment of the use of sediment traps for estimating upper ocean particle fluxes. *J. Marine Res.* 65, 345–416. doi: 10.1357/002224007781567621

Checkley, D. M. Jr., and Barth, J. A. (2009). Patterns and processes in the California current systems. *Prog. Oceanogr.* 83, 49–64. doi: 10.1016/j.pocean.2009.07.028

Cianca, A., Godoy, J. M., Martin, J. M., Perez-Marrero, J., Rueda, M. J., Llinás, O., et al. (2012). Interannual variability of chlorophyll and the influence of low-frequency climate modes in the North Atlantic subtropical gyre. *Glob. Biogeochem. Cycles* 26:GB2002. doi: 10.1029/2010GB004022

Cropper, T., Hanna, E., and Bigg, G. R. (2014). Spatial and temporal seasonal trends in coastal upwelling off Northwest Africa, 1981–2012. *Deep Sea Res. II* 86, 94–111. doi: 10.1016/j.dsr.2014.01.007

Davenport, R., Neuer, S., Helmke, P., Perez-Marrero, J., and Llinas, O. (2002). Primary productivity in the northern Canary Islands region as inferred from

SeaWiFS imagery. *Deep Sea Res. II Top. Stud. Oceanogr.* 49, 3481–3496. doi: 10.1016/S0967-0645(02)00095-4

Davenport, R., Neuer, S., Hernández-Guerra, A., Rueda, M. J., Linas, O., Fischer, G., et al. (1999). Seasonal and interannual pigment concentration in the Canary Islands region from CZCS data and comparison with observations from the ESTOC time-series station. *Int. J. Remote Sens.* 20, 1419–1433. doi: 10.1080/014311699212803

Dugdale, R. C., Wilkerson, F. P., and Minas, H. J. (1995). The role of a silicate pump in driving new production. *Deep Sea Res. I Oceanogr. Res. Pap.* 42, 697–719. doi: 10.1016/0967-0637(95)00015-X

Fischer, G., and Karakas, G. (2009). Sinking rates and ballast composition of particles in the Atlantic Ocean: implications for the organic carbon fluxes to the deep ocean. *Biogeosciences* 6, 85–102. doi: 10.5194/bg-6-85-2009

Fischer, G., Krause, G., Neuer, S., and Wefer, W. (1996). Short-term sedimentation pulses recorded with a chlorophyll sensor and sediment traps in 900 m water depth in the Canary Basin. *Limnol. Oceanogr.* 41, 1354–1359. doi: 10.4319/lo.1996.41.6.1354

Fischer, G., Reuter, C., Karakas, G., Nowald, N., and Wefer, G. (2009). Offshore advection of particles within the Cape Blanc filament, Mauritania: results from observational and modelling studies. *Prog. Oceanogr.* 83, 322–330. doi: 10.1016/j.pocean.2009.07.023

Fischer, G., Romero, O., Toby, E., Iversen, M., Donner, B., Mollenhauer, G., et al. (2019). Changes in the dust-influenced biological carbon pump in the Canary Current System: implications from a coastal and an offshore sediment trap record off Cape Blanc, Mauritania. *Glob. Biogeochem. Cycl.* 33, 1100–1128. doi: 10.1029/2019GB006194

Fischer, G., Romero, O. E., Merkel, U., Donner, B., Iversen, M., Nowald, N., et al. (2016). Deep ocean mass fluxes in the coastal upwelling off Mauritania from 1988 to 2012: variability on seasonal to decadal timescales. *Biogeosciences* 13, 3071–3090. doi: 10.5194/bg-13-3071-2016

Fischer, G., and Wefer, G. (1991). "Sampling, preparation and analysis of marine particulate matter," in *The Analysis and Characterization of Marine Particles*, eds D. C. Hurd, and D. W. Spencer (Washington DC: American Geophysical Union), 391–397. doi: 10.1029/gm063p0391

Freudenthal, T., Neuer, S., Meggers, H., Davenport, B., and Wefer, G. (2001). Influence of lateral particle advection and organic matter degradation on sediment accumulation and stable nitrogen isotope ratios along a productivity gradient in the Canary Islands region. *Mar. Geol.* 177, 93–109. doi: 10.1016/s0025-3227(01)00126-8

Fründt, B., and Waniek, J. (2012). Impact of the Azores front propagation on deep ocean particle flux. *Cen. Eur. J. Geosci.* 4, 531–544. doi: 10.2478/s13533-012-0102-2

Garcìa-Reyes, M., Sydeman, W. J., Schoeman, D. S., Rykaczewski, R. R., Black, B. A., Smit, A. J., et al. (2015). Under pressure: climate change, upwelling, and Eastern Boundary upwelling ecosystems. *Front. Mar. Sci.* 2:109. doi: 10.3389/fmars.2015.00109

Gómez-Letona, M., Ramos, A. G., Coca, J., and Arístegui, J. (2017). Trends in primary production in the Canary Current upwelling system-a regional perspective comparing remote sensing models. *Front. Mar. Sci.* 4:370. doi: 10.3390/fmars.2017.00370

González-Dávila, M., Santana-Casiano, J. M., and González-Dávila, E. F. (2007). Interannual variability of the upper ocean carbon cycle in the northeast Atlantic Ocean. *Geophys. Res. Lett.* 34:L07608. doi: 10.1029/2006GL028145

Haine, T. W. N. (2016). Vagaries of Atlantic overturning. *Nat. Geosci.* 9, 479–480. doi: 10.1038/ngeo2748

Hedges, J. I., Baldock, J. A., Gelinas, Y., Lee, C., Peterson, M. L., and Wakeham, S. G. (2002). The biochemical and elemental compositions of marine plankton: a NMR perspective. *Mar. Chem.* 78, 47–63. doi: 10.1016/s0304-4203(02)00009-9

Helmke, P., Romero, O., and Fischer, G. (2005). Northwest African upwelling and its effect on off-shore organic carbon export to the deep sea. *Glob. Biogeochem. Cycl.* 19:GB4015. doi: 10.1029/2004GB002265

Hirsch, R. M., Slack, J. R., and Smith, R. A. (1982). Techniques of trend analysis for monthly water quality data. *Water Resour. Res.* 18, 107–121. doi: 10.1029/WR018i001p00107

Hurrell, J. W. (1995). *NAO Index Data provided by the Climate Analysis Section*. Boulder: NCAR.

Hwang, J., Manganini, S. J., Montlucaon, D. B., and Eglington, T. E. (2009). Dynamics of particle export on the Northwest Atlantic margin. *Deep Sea Res. I* 56, 1792–1803. doi: 10.1016/j.dsr.2009.05.007

Inthorn, M., Wagner, T., Scheeder, G., and Zabel, M. (2006). Lateral transport controls distribution, quality, and burial of organic matter along continental slopes in high-productivity areas. *Geology* 34, 205–208.

Iversen, M. H., and Ploug, H. (2010). Ballast minerals and the sinking carbon flux in the ocean: carbon-specific respiration rates and sinking velocities of marine snow aggregates. *Biogeosciences* 7, 2613–2624. doi: 10.5194/bg-7-2613-2010

Jones, P. D., Jónsson, T., and Wheeler, D. (1997). Extension to the North Atlantic Oscillation using early instrumental pressure observations from Gibraltar and South-West Iceland. *Int. J. Climatolol.* 17, 1433–1450. doi: 10.1002/(sici)1097-0088(19971115)17:13<1433::aid-joc203>3.0.co;2-p

Kaufman, Y. J., Koren, I., Remer, L. A., Tanré, D., Ginoux, P., Fan, S., et al. (2005). Dust transport and deposition from the Terra-Moderate Resolution Imaging Spectroradiometer (MODIS) spacecraft over the Atlantic Ocean. *J. Geophys. Res.* 110:D10S12. doi: 10.1029/2003/JD004436

Klaas, C., and Archer, D. E. (2002). Association of sinking organic matter with various types of ballast in the deep sea: implications for the rain ratio. *Glob. Biogeochem. Cycle* 16:1116. doi: 10.1029/2001GB001765

Knoll, M., Hernández-Guerra, A., Lenz, B., López Laatzen, F., Machín, F., Müller, T. J., et al. (2002). The Eastern Boundary Current system between the Canary Islands and the African Coast. *Deep Sea Res. II Top. Stud. Oceanogr.* 49, 3427–3440. doi: 10.1016/S0967-0645(02)00105-104

Kremling, K., Lentz, U., Zeitzschell, B., Schulz-Bull, D. E., and Duinker, J. C. (1996). New type of time-series sediment trap for the reliable collection of inorganic and organic trace chemical substances. *Rev. Sci. Instrument.* 67, 4360–4363. doi: 10.1063/1.1147582

Krumhardt, K. M., Lovenduski, N. S., Freeman, N. M., and Bates, N. R. (2016). Apparent increase in coccolithophore abundance in the subtropical North Atlantic from 1990 to 2014. *Biogeosciences* 13, 1163–1177. doi: 10.5194/bg-13-1163-2016

Lathuilière, C., Echevin, V., and Levy, M. (2008). Seasonal and intraseasonal surface chlorophyll-a variability along the northwest African coast. *J. Geophys. Res. Oceans* 13:C05007. doi: 10.1029/2007/JC004433

Lee, R. B. Y., Mavridou, D. A. I., Papadakos, G., McClelland, H. L. O., and Rickaby, R. E. M. (2016). The uronic acid content of coccolith-associated polysaccharides provides insight into coccolithogenesis and past climate. *Nat. Comm.* 7:13144. doi: 10.1038/ncomms13144

Lluch-Cota, S. E., Hoegh-Guldberg, O., Karl, D., Pörtner, H.-O., Sundby, S., and Gattuso, J. P. (2014). "Cross-chapter box on uncertain trends in major upwelling ecosystems, in Impacts, Adaptation, and Vulnerability," in *Part A: Global and Sectoral Aspects. Contribution of Working Group II to the Fifth Assessment Report of the Intergovernmental Panel on Climate Change*, ed. C. B. Field (Cambridge, MA: Cambridge University Press), 149–151.

López-García, P., Gelado-Caballero, M. D., Santana-Castellano, D., Suárez, de Tangil, M., Collado-Sánchez, C., et al. (2013). A three-year time-series of dust deposition flux measurements in Gran Canaria, Spain: a comparison of wet and dry surface deposition samplers. *Atmos. Environ.* 79, 689–694. doi: 10.1016/j.atmosenv.2013.07.044

Lovecchio, E., Gruber, N., Münnich, M., and Lachkar, Z. (2017). On the long-range offshore transport of organic carbon from the Canary Upwelling System to the open North Atlantic. *Biogeosciences* 14, 3337–3369. doi: 10.5194/bg-14-3337-2017

McCave, I. N., Halla, I. R., Antia, A. N., Chou, L., Dehairs, F., Lampitt, R. S., et al. (2001). Distribution, composition and flux of particulate material over the European margin at 47–50N. *Deep Sea Res. II* 48, 3107–3139. doi: 10.1016/s0967-0645(01)00034-0

Mittelstaedt, E. (1991). The ocean boundary along the northwest African coast: circulation and oceanographic properties at the sea surface. *Prog. Oceanogr.* 26, 307–355. doi: 10.1016/0079-6611(91)90011-a

Müller, P. J., and Schneider, R. (1993). An automated leaching method for the determination of opal in sediments and particulate matter. *Deep Sea Res. I* 40, 425–444. doi: 10.1016/0967-0637(93)90140-x

Müller, T. J., and Siedler, G. (1992). Multi-year current time series in the eastern North Atlantic Ocean. *J. Mar. Res.* 50, 63–98. doi: 10.1357/002224092784797755

Müller, T. J., and Waniek, J. J. (2013). KIEL276 time series data from moored current meters madeira abyssal plain 33°N, 22°W, 5285 m water depth March 1980 – April 2011 background information and data compilation. *GEOMAR Rep. N. Ser.* 13:65. doi: 10.3289/GEOMAR_REP_NS_13_2013

Narajan, N., Paul, A., and Schulz, M. (2010). Trends in coastal upwelling intensity during the late 20th century. *Ocean Sci.* 6, 815–823. doi: 10.5194/os-6-815-2010

Neuer, S., Cianca, A., Helmke, P., Freudenthal, T., Davenport, R., Meggers, H., et al. (2007). Biogeochemistry and hydrography in the eastern subtropical North Atlantic gyre. Results from the European time-series station ESTOC. *Prog. Oceanogr.* 72:1. doi: 10.1016/j.pocean.2006.08.001

Neuer, S., Davenport, R., Freudenthal, T., Wefer, G., Llinás, O., Rueda, M.-J., et al. (2002a). Differences in the biological carbon pump at three subtropical ocean sites. *Geophys. Res. Lett.* 29, 32/1–32/4.

Neuer, S., Freudenthal, T., Davenport, R., Llinás, O., and Rueda, M.-J. (2002b). Seasonality of surface water properties and particle flux along a productivity gradient off NW Africa. *Deep Sea Res. II Top. Stud. Oceanogr.* 49, 3561–3576. doi: 10.1016/S0967-0645(02)00098-X

Neuer, S., Ratmeyer, V., Davenport, R., Fischer, G., and Wefer, G. (1997). Deep water particle flux in the Canary Island region: seasonal trends in relation to long-term satellite derived pigment data and lateral sources. *Deep Sea Res.* 44, 1451–1466. doi: 10.1016/s0967-0637(97)00034-4

Neuer, S., Torres-Padron, M. E., Gelado-Caballeo, M. D., Rueda, M. J., Hernández-Brito, J., Davenport, R., et al. (2004). Dust deposition to the eastern subtropical North Atlantic gyre: does ocean's biogeochemistry respond?. *Glob. Biogeochem. Cycle* 18:GB4020. doi: 10.1029/2004GB002228

Nykjaer, L., and Van Camp, L. (1994). Seasonal and interannual variability of coastal upwelling along northwest Africa and Portugal from 1981 to 1991. *J. Geophys. Res.* 99, 14197–14207. doi: 10.1029/94JC00814

Pelegrí, J. L., Arístegui, J., Cana, L., González-Dávila, M., Hernández-Guerra, A., Hernández-León, S., et al. (2005). Coupling between the open-ocean and coastal upwelling region off northwest Africa: water circulation and offshore pumping of organic matter. *J. Mar. Syst.* 54, 3–7.

Ploug, H., Iversen, M. H., and Fischer, G. (2008). Ballast, sinking velocity, and apparent diffusivity within marine snow and zooplankton fecal pellets: implications for substrate turnover by attached bacteria. *Limnol. Oceanogr.* 53, 1878–1886. doi: 10.4319/lo.2008.53.5.1878

Pradhan, Y., Lavender, S. J., Hardman-Mountford, N. J., and Aiken, J. (2006). Seasonal and inter-annual variability of chlorophyll-a concentration in the Mauritanian upwelling: observation of an anomalous event during 1998–1999. *Deep Sea Res. II* 53, 1548–1559. doi: 10.1016/j.dsr2.2006.05.016

Ragueneau, O., Tréguer, P., Anderson, R. F., Brzezinski, M. A., DeMaster, D. J., Dugdale, R. C., et al. (2000). A review of the Si cycle in the modern ocean: recent progress and missing gaps in the application of biogenic opal as a paleoproductivity proxy. *Glob. Planet. Change* 26, 317–365. doi: 10.1016/s0921-8181(00)00052-7

Rivero-Calle, S., Gnanadesikan, A., Del Castillo, C. E., Balch, W. B., and Guikema, S. D. (2015). Multidecadal increase in North Atlantic coccolithophores and the potential role of rising CO2. *Science* 350, 1533–1537. doi: 10.1126/science.aaa8026

Romero, O., and Fischer, G. (2017). Shift in the species composition of the diatom community in the eutrophic Mauritanian coastal upwelling: results from a multi-year sediment trap experiment from 2003 to 2010. *Prog. Oceanogr.* 159, 31–44. doi: 10.1016/j.pocean.2017.09.010

Romero, O. E., Baumann, K.-H., Zonneveld, K. A. F., Donner, B., Hefter, J., Hamady, B., et al. (2020). Flux variability of phyto- and zooplankton communities in the Mauritanian coastal upwelling between 2003 and 2008. *Biogeosciences* 17, 187–214. doi: 10.5194/bg-17-187-2020

Santana-Falcón, Y., Mason, E., and Arístegui, J. (2020). Offshore transport of organic carbon by upwelling filaments in the Canary Current system. *Prog. Oceanogr.* doi: 10.1016/j.pocean.2020.102322 [Epub ahead of print].

Siedler, G., Armi, L., and Müller, T. J. (2005). Meddies and decadal changes at the Azores front from 1980 to 2000. *Deep Sea Res. II Top. Stud. Oceanogr.* 52, 583–604. doi: 10.1016/j.dsr2.2004.12.010

Siegel, D. A., Fields, E., and Buesseler, K. O. (2008). A bottom-up view of the biological pump: modeling source funnels above ocean sediment traps. *Deep Sea Res. I* 55, 108–127. doi: 10.1016/j.dsr.2007.10.006

Smeed, D. A., Josey, S. A., Beaulieu, C., Johns, W. E., Moat, B. I, Frajka-Williams, E., et al. (2014). The North Atlantic Ocean is in a state of reduced overturning. *Geophys. Res. Lett.* 45, 1527–1533. doi: 10.1002/2017GL076350

Smith, K. L., Ruhl, H. A., Huffard, C. L., Messié, M., and Kahru, M. (2018). Episodic organic carbon fluxes from surface ocean to abyssal depths during long-term monitoring in NE Pacific. *Proc. Nat. Acad. Sci. U.S.A.* 48, 12235–12240. doi: 10.1073/pnas.1814559115

Sprengel, C., Baumann, K.-H., Henderiks, J., Henrich, R., and Neuer, S. (2002). Modern coccolithophore and carbonate sedimentation along a productivity gradient in the Canary Islands region: seasonal export production and surface accumulation rates. *Deep Sea Res. II* 49, 3577–3598. doi: 10.1016/s0967-0645(02)00099-1

Srokosz, M. A., and Bryden, H. L. (2015). Observing the Atlantic Meridional Overturning Circulation yields a decade of inevitable surprises. *Science* 348:6241.

Stramma, L. (1984). Geostrophic transport in the Warm Water Sphere of the eastern subtropical North Atlantic. *J. Mar. Res.* 42, 537–558. doi: 10.1357/002224084788506022

Sydeman, W. J., Garcìa-Ryes, M., Schoeman, D. S., Rykaczewski, R. R., Thompson, S. A., Black, B. A., et al. (2014). Climate change and wind intensification in coastal upwelling systems. *Science* 345, 77–80. doi: 10.1126/science.1251635

Sylla, A., Mignot, J., Capet, X., and Gaye, A. T. (2019). Weakening of the Senegalo-Mauritanian upwelling system under climate change. *Clim. Dyn.* 53, 4447–4473. doi: 10.1007/s00382-019-04797-y

Van Camp, L., Nykjær, L., Mittelstaedt, E., and Schlittenhardt, P. (1991). Upwelling and boundary circulation off Northwest Africa as depicted by infrared and visible satellite observations. *Prog. Oceanogr.* 26, 357–402. doi: 10.1016/0079-6611(91)90012-b

Vélez-Belchí, P., Pérez-Hernández, M. D., Casanova-Masjoan, M., Cana, L., and Hernáandez-Guerra, A. (2017). On the seasonal variability of the Canary Current and the Atlantic meridional overturning circulation. *J. Geophys. Res. Oceans* 122, 4518–4538. doi: 10.1002/2017JC012774

Conflict of Interest: The authors declare that the research was conducted in the absence of any commercial or financial relationships that could be construed as a potential conflict of interest.

frontiers in Earth Science

ORIGINAL RESEARCH
published: 06 August 2020
doi: 10.3389/feart.2020.00329

Particle Fluxes at the Australian Southern Ocean Time Series (SOTS) Achieve Organic Carbon Sequestration at Rates Close to the Global Median, Are Dominated by Biogenic Carbonates, and Show No Temporal Trends Over 20-Years

Cathryn A. Wynn-Edwards[1,2,3], Elizabeth H. Shadwick[1,2,3], Diana M. Davies[1,2,3], Stephen G. Bray[3], Peter Jansen[1,2,3], Rebecca Trinh[4] and Thomas W. Trull[1,2,3]*

[1] Australian Antarctic Program Partnership, Institute for Marine and Antarctic Studies, University of Tasmania, Hobart, TAS, Australia, [2] Oceans and Atmosphere, Commonwealth Scientific and Industrial Research Organisation, Hobart, TAS, Australia, [3] Antarctic Climate and Ecosystems Cooperative Research Centre, University of Tasmania, Hobart, TAS, Australia, [4] Department of Earth and Environmental Sciences and Lamont-Doherty Earth Observatory, Columbia University, Palisades, NY, United States

OPEN ACCESS

Edited by:
Gerhard Josef Herndl,
University of Vienna, Austria

Reviewed by:
Alexandra Gogou,
Hellenic Centre for Marine Research (HCMR), Greece
Eric Pieter Achterberg,
GEOMAR Helmholtz Centre for Ocean Research Kiel, Germany

***Correspondence:**
Cathryn A. Wynn-Edwards
Cathryn.WynnEdwards@utas.edu.au

Specialty section:
This article was submitted to Biogeoscience, a section of the journal Frontiers in Earth Science

Received: 22 April 2020
Accepted: 15 July 2020
Published: 06 August 2020

Citation:
Wynn-Edwards CA, Shadwick EH, Davies DM, Bray SG, Jansen P, Trinh R and Trull TW (2020) Particle Fluxes at the Australian Southern Ocean Time Series (SOTS) Achieve Organic Carbon Sequestration at Rates Close to the Global Median, Are Dominated by Biogenic Carbonates, and Show No Temporal Trends Over 20-Years. Front. Earth Sci. 8:329. doi: 10.3389/feart.2020.00329

Particle fluxes at the Southern Ocean time series (SOTS) site in the Subantarctic Zone (SAZ) south of Australia (~47°S, ~142°E, 4600 m water depth) were collected from 1997 – 2017 using moored sediment traps at nominal depths of 1000, 2000, and 3800 m. Annually integrated mass fluxes showed moderate variability of 14 ± 6 g m^{-2} yr^{-1} at 1000 m, 20 ± 6 g m^{-2} yr^{-1} at 2000 m and 21 ± 4 g m^{-2} yr^{-1} at 3800 m. Particulate organic carbon (POC) fluxes were similar to the global median, indicating that the Subantarctic Southern Ocean exports considerable amounts of carbon to the deep sea despite its high-nutrient, low chlorophyll characteristics. The interannual flux variations were larger than those of net primary productivity as estimated from satellite observations. Particle compositions were dominated by carbonate minerals (>60% at all depths), opal (~10% at all depths), and particulate organic matter (~17% at 1000 m, decreasing to ~10% at 3800 m), with seasonal and interannual variability much smaller than for their flux magnitudes. The carbonate counter-pump effect reduced carbon sequestration by ~8 ± 2%. The average seasonal cycle at 1000 m had a two-peak structure, with a larger early spring peak (October/November) and a smaller late summer (January/February) peak. At the two deeper traps, these peaks became less distinct with a greater proportion of the fluxes arriving in autumn. Singular value decomposition (SVD) shows that this temperate seasonal structure accounts for ~80% of the total variance (SVD Mode 1), but also that its influence varies significantly relative to Modes 2 and 3 which describe changes in seasonal timings. This occurrence of significant interannual variability in seasonality yet relatively constant annual fluxes, is likely to be useful in selecting appropriate models for the simulation of environmental-ecological

coupling and its role in controlling the biological carbon pump. No temporal trends were detected in the mass or component fluxes, or in the time series of the SVD Modes. The SOTS observations provide an important baseline for future changes expected to result from warming, stratification, and acidification in this globally significant region.

Keywords: particle flux, Subantarctic Zone, Southern Ocean, time series, seasonal variability, ocean acidification, biological carbon pump

INTRODUCTION

The constant sinking of particles from the euphotic zone moves carbon away from the atmosphere and connects the surface and deep sea on shorter timescales than achieved by advection (Agassiz, 1888; Boyd and Trull, 2007; Buesseler et al., 2007a). This downward export of biogenic material has become colloquially known as "the biological pump" (Volk and Hoffert, 1985), and more recently defined as the gravitational component of the biological carbon pump (gBCP) to distinguish it from particulate carbon transfers mediated by advection, mixing, or biological migrations (Boyd et al., 2019). The biological pumps redistribute carbon and nutrients within the ocean and thereby play a significant role in controlling atmospheric carbon dioxide (CO_2) concentrations (e.g., Shaffer, 1993; Sarmiento and LeQuere, 1996; Lee et al., 1998; Sarmiento et al., 1998; Archer et al., 2000; Trull et al., 2001b; DeVries et al., 2012; Boyd et al., 2019). Estimates of the modern biological pump for organic carbon to the deep sea remain rather uncertain at 5–15 Pg C yr^{-1} or ∼14–42 g C m^{-2} yr^{-1} (Ducklow, 1995; Falkowski et al., 1998, 2000; Boyd and Trull, 2007; Boyd et al., 2019), and it is not yet understood how the strength of the biological pump will be impacted by global climate change (Falkowski et al., 2000; Sigman and Boyle, 2000; Bopp et al., 2001; Feely et al., 2004; Boyd et al., 2019).

The Southern Ocean has been estimated to account for ∼30% of the global annual oceanic carbon export, i.e., about 3 Pg C yr^{-1} (Arteaga et al., 2018), even though it accounts for less than 20% of the global ocean surface area. Given this large contribution, and the status of the Southern Ocean as the largest region with unused surface ocean macro-nutrients and thus the greatest capacity for increased biological carbon pump strength (e.g., Boyd et al., 2000; Trull et al., 2001a), it is paramount to resolve the question of how global climate change will alter this region's ability and efficiency to take up atmospheric CO_2 (Falkowski et al., 2000; Cram et al., 2018). Long-term time series observations of the sinking particle flux are one important step toward assessing the efficiency and strength of the biological pump, and thus the scope and propensity for change. Sediment traps are widely used for this purpose and although they have their limitations in terms of providing quantitative flux estimates, especially at shallow depths, as extensively reviewed by Yu et al. (2001) and Buesseler et al. (2007a), they are currently the best available tool for collecting year round particle flux data.

Abbreviations: BSi, biogenic silicon; DOC, dissolved organic carbon; FSI, Flux Stability Index; NCP, net community production; NPP, net primary production; PIC, particulate inorganic carbon; POC, particulate organic carbon; POM, particulate organic matter; PN, particulate nitrogen; SAZ, subantarctic zone; SOTS, Southern Ocean Time Series; SVD, singular value decomposition.

Here we present a 20-year time series of particle fluxes collected by deep ocean sediment traps in the Subantarctic Zone (SAZ) of the Southern Ocean south of Australia, in terms of dry mass and three main chemical components: particulate organic matter (POM), expressed as particulate organic carbon (POC), and two main biogenic ballasting materials, calcium carbonate, expressed as particulate inorganic carbon (PIC), and opal, expressed as biogenic silica (BSi). The POC fluxes provide direct quantification of the gBCP at the trap depths, and because multiple mechanisms (settling, advection, migration) may have contributed to the transfer through the overlying water column, we hereafter refer to the measured values simply as BCP estimates. Biogenic calcium carbonate is precipitated by calcifiers, most prominently foraminifera and coccolithophores, along with other zooplankton such as pteropods. The PIC fluxes allow us to address the opposing role of calcium carbonate as ballast to enhance particle sinking and thus the BCP versus alkalinity loss through production of CO_2 during calcium carbonate precipitation, which reduces CO_2 solubility and thus weakens the ocean CO_2 sink (known colloquially as the carbonate counter-pump, e.g., Rost and Riebesell, 2004; Manno et al., 2018). The BSi fluxes provide a gauge on the importance of diatoms, a phytoplankton functional group that forms silica frustules and has the ability to rapidly bloom and achieve high biomass and thus mediate strong export from the surface ocean (e.g., Dugdale et al., 1995). However, diatoms are limited in their overall impact in the Subantarctic Southern Ocean by the availability of silicic acid, which is sufficient over winter and spring but currently nearly completely consumed during summer, in contrast to the excess abundances of phosphate and nitrate (e.g., Trull et al., 2001c).

The sediment traps have been deployed at the Southern Ocean Time Series (SOTS) site (∼47°S, ∼142°E) approximately annually since inception of the program in 1997 (Trull et al., 2001b,c). The SOTS site is located ∼530 km southwest of Tasmania, in the Indian/Australian sector of the SAZ and has been suggested to be representative of a broader region of the SAZ from ∼90 to 145°E, based on regional oceanography and remote sensing (Trull et al., 2001c). The SAZ covers the area between Subtropical and Subantarctic Fronts (**Figure 1**) and is characterized by high (macro) nutrient, low-chlorophyll (HNLC) waters, with abundant phosphate and nitrate concentrations year-round, and summertime depletion of silicate concentrations. The phytoplankton community is dominated numerically by *Phaeocystis antarctica* and in terms of bio-volume by a mixture of haptophytes, flagellates, and small diatoms (Eriksen et al., 2018). Surface ocean pCO_2 values are below atmospheric equilibrium in summer (Metzl et al., 1999;

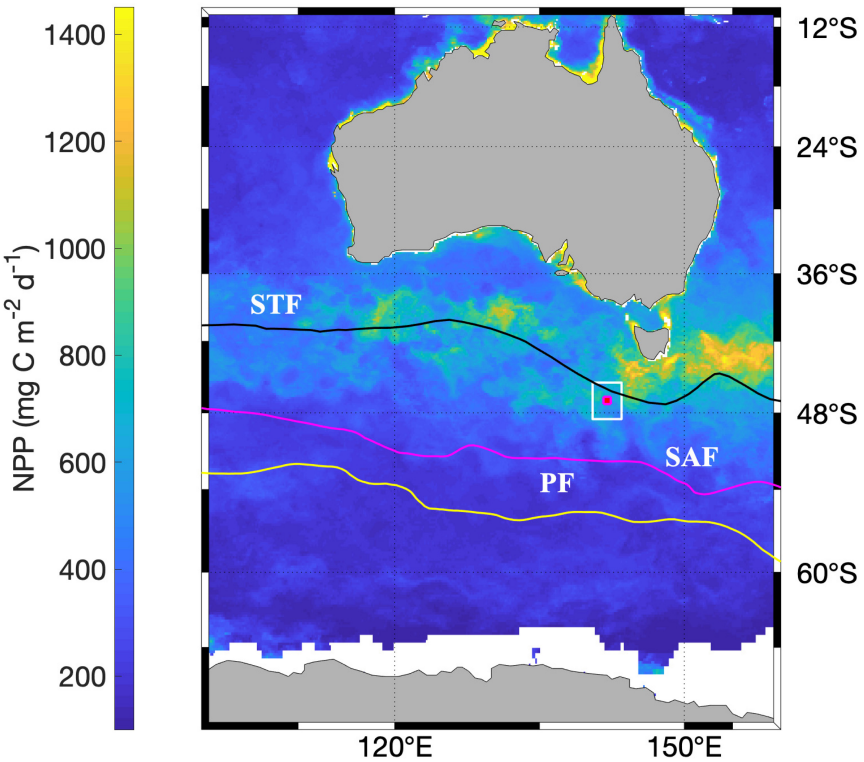

FIGURE 1 | Location of the SOTS site (red dot) relative to average frontal positions (solid lines): Subtropical Front (STF), Subantarctic Front (SAF), Polar Front (PF). Background is Net Primary Production (illustrated for January 2012) as estimated from satellite remote sensing (see section "Materials and Methods"). The white square indicates the area used for NPP comparisons with SOTS particle fluxes.

Shadwick et al., 2015). Deep mixing to >400 m in winter (Rintoul and Trull, 2001), replenishes surface nutrients and supplies oxygen to the subsurface southern hemisphere subtropical gyre waters via Subantarctic Mode Waters (Helm et al., 2011). Limitation of productivity by iron is thought to be the main driver of the region's HNLC status (Bowie et al., 2009; Lannuzel et al., 2011).

Our goals in examining the long time series are:

1. to obtain a representative decadal estimate of the SAZ biological carbon pump (BCP),
2. to examine inter-annual variability in the BCP, including the possibility of a trend that might arise from anthropogenic impacts,
3. to characterize the seasonality of the total and component fluxes, as indicators of the probable environmental and ecological mechanisms that control the BCP strength in the Subantarctic Southern Ocean.

MATERIALS AND METHODS

The Southern Ocean Time Series (SOTS) and Sample Collection

The Southern Ocean time series is a Sub-Facility of the Australian Integrated Marine Observing System (IMOS), which currently consists of two deep ocean moorings: the Southern Ocean Flux Station (SOFS) and the SAZ sediment trap mooring.

The SAZ moorings were deployed at ∼47°S, 140°E on the abyssal plain in the central SAZ in water depth of ∼4600 m. The sediment traps were McLane PARFLUX time-series conical sediment traps, with a 0.5 m^2 baffled funnel (2.5 cm baffle cell diameter) at the top and a carousel underneath that moved a series of cups under the funnel over the course of the deployment. The number of cups per trap and deployment varied between 13 and 21. Typically, the mooring was deployed with three sediment traps at nominal depths of 1000, 2000, and 3800 m except in years 2000 and 2005 (1000 and 2000 m) and 2003 (500, 1000, and 2000 m). For some of the deployments the controllers of the top two sediment traps contained tilt meters. In addition, the moorings were instrumented with current meters. Details of mooring designs, deployment voyages (and ancillary data such as CTD casts) are given in the SOTS Annual Reports (Wynn-Edwards et al., 2019). Long time series particle flux observations are particularly sparse for the Southern Ocean (but see Ducklow et al., 2008) and this time series covers nearly a full decade (from 2009–2017) and a partial decade in the late 1990s. The moorings were first deployed in September 1997 (Trull et al., 2001b) and maintained with some gaps until the present. With a few exceptions the moorings were deployed for 12 months, and trap cup sampling times ranged from 4 to 60 days. The time series has several data gaps (**Figures 2A–C**) due to sediment trap

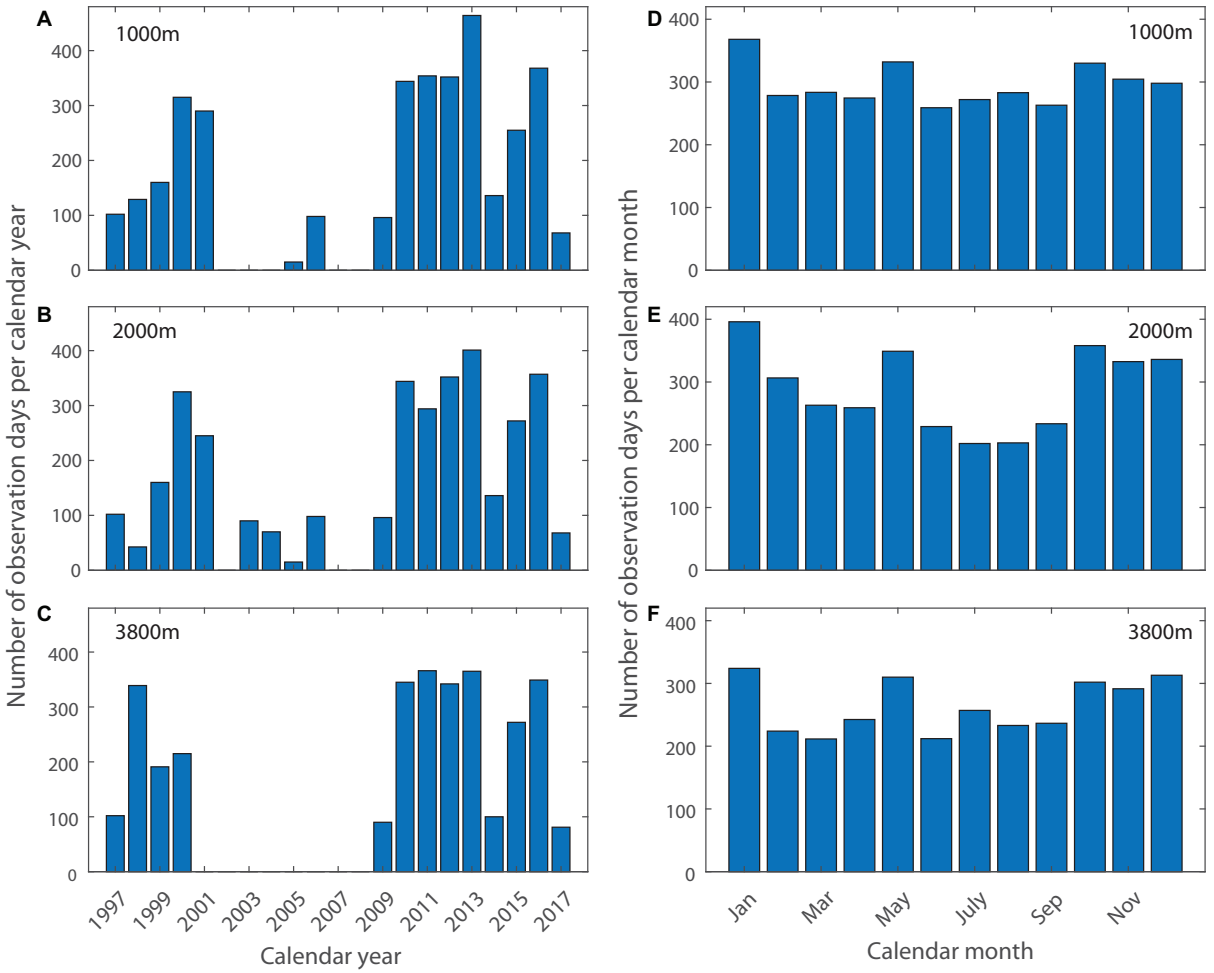

FIGURE 2 | Statistics of 47°S sediment trap data per calendar year [**(A)** 1000 m, **(B)** 2000 m, **(C)** 3800 m] and month [**(D)** 1000 m, **(E)** 2000 m, **(F)** 3800 m]. During the calendar year 2013, two moorings were in the water at the same time for a short period, leading to observation days that exceed 365.

failures (deployment year 2005, partial data recovery), mooring loss (deployment years 2001, 2004, and 2006), vessel availability and insufficient trap sample material. The mooring was not deployed at 47°S in 2007, 2008, 2014, and 2017, owing to its use elsewhere, lack of ship time, or lack of funding. The 1000 m dataset for 2003/2004 was excluded due to suspected compromise of the mooring dynamics induced by the 500 m trap above.

Assessment of the trap samples as a function of month of collection reveals a slight sample bias against winter, with highest sample numbers in austral summer in January across all three depths (**Figures 2D–F**).

Sediment Trap Preparation and Post Recovery Handling

Sediment trap cups were filled with a brine solution made up of 0.8 μm GF/F filtered seawater, collected close to the SOTS site. Typically, 5 g L^{-1} NaCl was added to increase density and improve particle retention in the cups, as well as 2 g L^{-1} $Na_2B_4O_7$ 10 H_2O to buffer pH and reduce carbonate dissolution, 0.22 g L^{-1} $SrCl_2$ 6 H_2O for preservation of $SrCO_4$ acantharians and 3 g L^{-1} $HgCl_2$ as a biocide.

After recovery of the mooring the sediment traps were hosed down with fresh water and allowed to settle for several days. Any unusual conditions, such as missing cups or trap failure (e.g., cups in position under the collection funnel on recovery) were recorded. Each cup had ∼20% of supernatant removed with a syringe via the fill hole to reduce the risk of spillage of poisoned brine on removing the cups from the trap carousel. The sample cups were then capped and stored refrigerated in the dark until transport to the onshore laboratory.

Sample Processing

The cups were allowed to settle for at least 3 days after transport to the onshore laboratory refrigerator. Samples were typically processed to dry matter within the following 2–3 months.

Photos of the cup collection were generally taken prior to any processing. The height of the solids in each cup was recorded after settling. Samples that had a noticeable foul odor or excessive organic material, e.g., large zooplankton (swimmers),

were poisoned again with 100 μl of saturated mercuric chloride solution ($HgCl_2$). The sample cup supernatant was sampled for pH and salinity measurements and the remaining supernatant removed carefully and discarded. Particles in the cups were re-suspended and quantitatively transferred onto a 1 mm nylon sieve to remove swimmers. Where fecal pellets were present, they were photographed and rinsed through the sieve with a stream of buffered (1 g L^{-1} $Na_2B_4O_7$ 10 H_2O), filtered seawater, followed by another photograph. The >1 mm fraction, mostly zooplankton, was stored in the buffered, filtered rinse seawater, re-poisoned if a foul odor indicated its necessity, and archived. The <1 mm fraction was split 10 ways using a McLane wet sample divider (McLane, WSD-10). Three splits were archived, and the remaining seven splits were re-combined, filtered onto 0.4 μm 47 mm polycarbonate membrane filters and dried over several days at 60°C to constant weight. The dried material was weighed and then scraped off the filter and homogenized by grinding to a powder using a mortar and pestle. Samples smaller than 10 mg dry matter were insufficient for further analysis and were left on their filters and archived. Quality assurance (QA) and assessment procedures, quality control (QC) tests and flagging decisions, as well as estimated measurement uncertainties are detailed in Wynn-Edwards et al. (2020).

Chemical Analyses

Only <1 mm dry material was analyzed for biogenic silica (BSi), PIC, particulate total carbon (PC), particulate total nitrogen (PN) and POC composition. Over the course of the programme, analytical methods have changed, and are described briefly here; for additional detail see Trull et al. (2001b) and the SOTS Annual Reports (Wynn-Edwards et al., 2019). From 1997 – 2000, total silicon was determined after digestion in HNO_3/HF closed Teflon bomb under heat and pressure in a digesting microwave oven, then analyzed by inductively coupled plasma/atomic emission spectroscopy (ICP-AES) (Bray et al., 2000). Between 2001 and 2013, BSi was determined by alkaline digestion and colorimetric analysis via segmented flow analysis (SFA) using an Alpkem model 3590 autoanalyser. Since 2015, BSi has been determined by the same alkaline digestion, followed by analysis at CSIRO's hydrochemistry lab using similar segmented flow spectrometric methods (Rees et al., 2018). PIC was analyzed by conversion to CO_2 through addition of phosphoric acid, followed by coulometry, at the Woods Hole Oceanographic Institution, in the United States, between 1997 and 2000 and thereafter at CSIRO, in Australia. PC and PN were determined by combustion using a CHN Thermo Finnigan EA 1112 Series Flash Elemental Analyser at the Central Science Laboratory of the University of Tasmania. POC was calculated from PC by subtraction of PIC. No corrections were made for potential particle dissolution (Antia, 2005). Notably, these particle dissolution contributions can be significant, e.g., Trull et al. (2001b) estimated silica dissolution to represent 20–30% of the total silica flux and phosphate dissolution to range as widely as 10–80% with shallower traps usually around 20% and deep traps around 40%. No corrections were made for potential under- or over-collection during high tilt or current events, although ^{230}Th observations from the 1997–1998 deployment suggested annual average under-collection of 30–40% was possible. The choice to make no corrections represents the uncertainties of these processes and their assessment, specifically that estimation of the dissolution component from the retained brine cannot assess the possibility of brine loss, and corrections based on radio-nuclide inventories are hampered by the likelihood that ^{230}Th is associated with small surface-rich particles in contrast to the bulk components (mass, PIC, POC, BSi) which are delivered by large particles and accordingly correction was not recommended by the SCAR Working Group assembled report on trap methodologies (Buesseler et al., 2007a).

Data Processing

Mass and component flux data were evaluated and flagged according to Wynn-Edwards et al. (2020) and only data with QC flags 1 and 2 (good and probably good, respectively) were included in subsequent analyses. Across the deployment, cups were open for varying number of days, the midpoint date was used as the date of the cup result. Data gaps within deployments due to missing cup data were linearly interpolated from neighboring cups. The cup-by-cup data sets were then linearly interpolated on daily time steps for mass and component flux calculations per year. Due to the typical seasonality with peak particle flux in austral spring and summer (mid-September to mid-March, see **Figure 7** and section "Possible Role of Seasonality in Control of Flux: Singular Value Decomposition"), and to avoid fragmenting these major flux events, the annual cycle was defined as 21st June to 20th June, rather than by calendar year. Daily interpolated data were only constructed for periods with data that covered a full annual cycle.

Data gaps between deployments were filled onto daily time steps via either of the following two ways, but only if the data gap fell outside of the main flux periods:

1. linear interpolation in six cases for the 1000 m, four cases for the 2000 m and six cases for the 3800 m data set; these gaps were no longer than 85 days;
2. extrapolation of the nearest data point to complete an annual cycle was used six times for the 1000 m, four times for the 2000 m, and five times for the 3800 m data set; these gaps were no longer than 117 days.

Based on cumulative annual flux calculations used in evaluating flux stability (see below) these duration gaps represent less than 10% of the average annual mass flux. If large data gaps fell within the main flux periods the data set was excluded for annual calculations.

In 2013, the deployment and recovery schedule resulted in two moorings sampling at the same time in close proximity. For the 1000 m traps there was an overlap between 26/05/2013 and 05/09/2013. Due to trap failure, the overlap was only one cup at 2000 m, between 26/05/2013 and 12/06/2013 and there was no overlap for the 3800 m traps. The overlapping mass and component flux results were averaged.

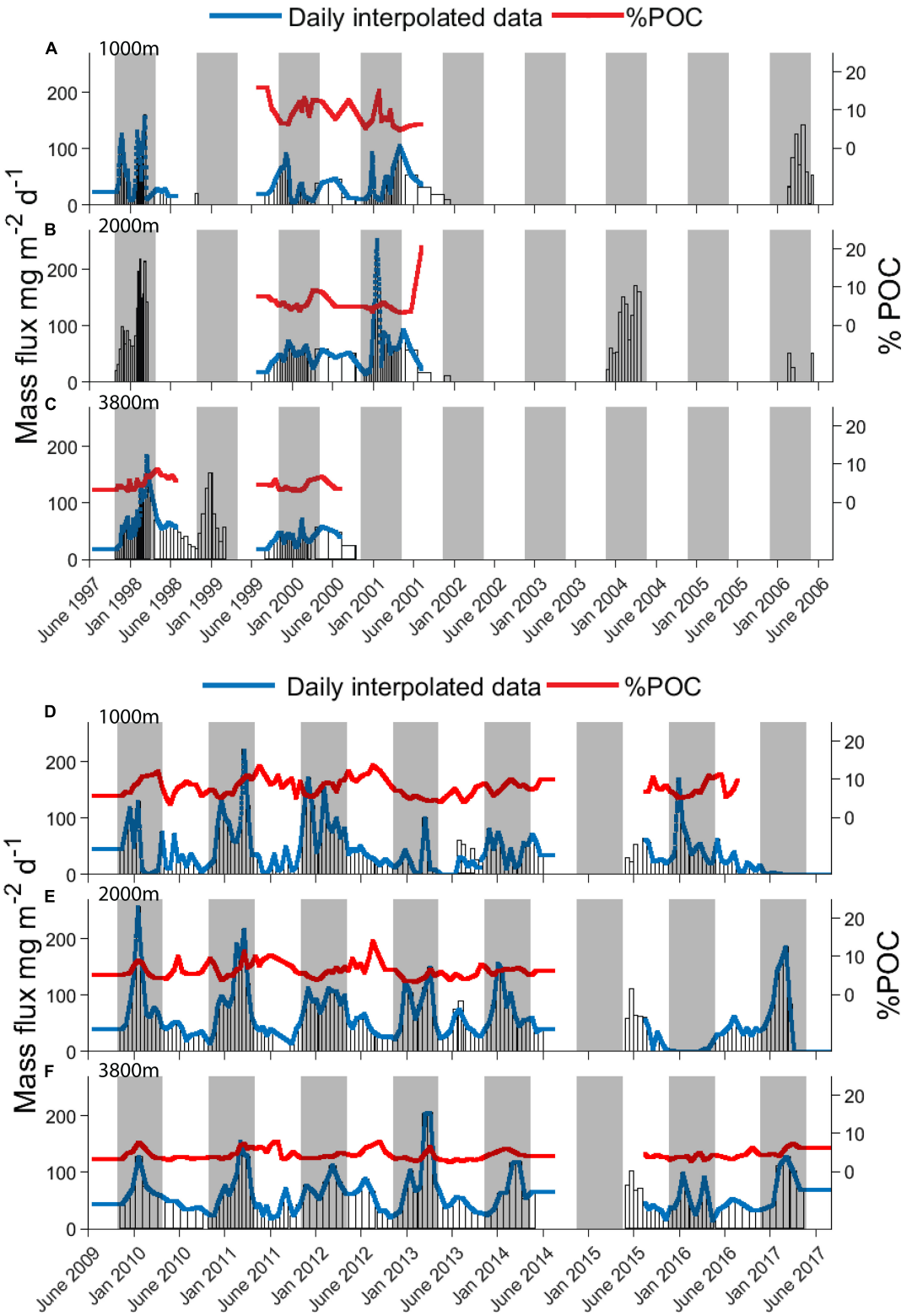

FIGURE 3 | Multi-year record of mass fluxes at SOTS showing interannual variability in timing and amplitude of peak mass flux periods. Collection cup durations are represented by bar widths, with interpolated daily fluxes overlaid in blue and % POC (w/w) compositions in red. **(A–C)** Are for the first decade (June 1997 – June 2008) and **(D–F)** for the second decade (June 2008 to June 2017). Gray shaded areas represent the 6 months that cover the main flux period during early spring and summer, 21th September to 21th March, as shown by average fluxes discussed in section "Possible Role of Seasonality in Control of Flux: Mean Seasonal Cycles" and **Figure 7**.

RESULTS AND DISCUSSION

To address our goals as listed in the Introduction, we first present the average characteristics of the deep particle fluxes over the 20-year record and their attenuation with depth, and then examine their interannual, seasonal, and higher frequency variability. Our evaluation emphasizes potential controls on POC fluxes, including:

1. the influence of biogenic minerals, including the magnitude of the carbonate counter-pump,
2. the seasonal stability of the flux as an indication of possible decoupling of production and grazing,
3. the magnitude of surface productivity.

We begin with information gained directly from the flux measurements, and then compare to other observations.

Our analysis treats the observations as a time series of local processes in a 1-dimensional framework of settling particles, without explicit consideration of advective particle inputs from outside the region. We base this simplification on the location of SOTS within a small gyre lying between the eastward flowing Antarctic Circumpolar Current and westward flow to its north (Herraiz-Borreguero and Rintoul, 2011), low surface velocities estimated from satellite altimetry (∼20 cm s^{-1} with occasional excursions to 50 cm s^{-1} in mesoscale eddies Meijers et al., 2011), and currents as measured on the SOTS moorings (∼12 cm s^{-1} with short excursions to <35 cm s^{-1} at 1200 m, and decreasing further with depth; Bray et al., 2000 and the SOTS Annual Reports Wynn-Edwards et al., 2019 available on the AODN portal). These velocities suggest that most particles derive from sources close to SOTS. At 20 cm s^{-1} (equivalent to 17 km d^{-1}) fast sinking particles (100 m d^{-1}) arrive at the 1000 m deep trap from no further than 170 km away. The source region to the deeper trap is only ∼50% larger, because current velocities decrease with depth. Moreover, as shown using a circulation model, the dominance of mesoscale eddies in the region confines the particle source regions to within a few

TABLE 1 | SOTS average particle fluxes and compositions for the years with full records, minimum and maximum values in brackets, relative standard deviation expressed as percentage in square brackets.

	1000 m	2000 m	3800 m
Mean ± SD [RSD](min, max)			
Mass flux (g m^{-2} y^{-1})	13.7 ± 6.1 [45%] (1.4, 23.4)	20.0 ± 6.1 [31%] (6.4, 25.0)	21.0 ± 3.7 [18%] (14.3, 25.4)
Component fluxes expressed as the most likely molecular forms, and for the atom of interest (all in g m^{-2} yr^{-1})			
$CaCO_3$	8.5 ± 2.8 [33%] (4.8, 14.7)	14.8 ± 1.9 [13%] (10.6, 16.2)	14.4 ± 2.6 [18%] (10.6, 18.5)
PIC	1.1 ± 0.3 [27%] (0.6, 1.8)	1.8 ± 0.3 [17%] (1.3, 1.9)	1.7 ± 0.3 [18%] (1.2, 2.2)
POM	2.6 ± 0.9 [35%] (1.1, 4.2)	3.0 ± 0.6 [20%] (2.2, 3.9)	2.2 ± 0.5 [23%] (1.3, 3.0)
POC	1.2 ± 0.4 [33%] (0.5, 1.9)	1.4 ± 0.3 [21%] (1.0, 1.8)	1.0 ± 0.2 [20%] (0.6, 1.4)
Opal	1.6 ± 0.7 [44%] (0.6, 2.7)	2.7 ± 0.8 [30%] (1.7, 3.9)	2.6 ± 0.9 [35%] (1.1, 4.1)
BSi	0.7 ± 0.3 [43%] (0.3, 1.1)	1.1 ± 0.3 [27%] (0.7, 1.6)	1.1 ± 0.4 [36%] (0.4, 1.7)
Components expressed as percentage (w/w) of the most likely molecular forms			
% POM	17.1 ± 2.1 [12%] (14.7, 21.1)	13.3 ± 1.6 [12%] (11.1, 15.8)	10.4 ± 1.5 [14%] (8.2, 12.5)
% $CaCO_3$	62.7 ± 4.2 [7%] (53.6, 67.4)	66.0 ± 4.1 [6%] (59.9, 71.7)	68.8 ± 4.1 [6%] (61.2, 72.6)
% Opal	10.3 ± 2.7 [26%] (6.8, 15.8)	11.8 ± 2.4 [20%] (8.9, 15.8)	12.2 ± 3.2 [26%] (7.4, 17.2)
Atomic ratios (mol/mol)			
PIC/POC	1.0 ± 0.2 [20%] (0.8, 1.2)	1.3 ± 0.2 [15%] (1.1, 1.7)	1.7 ± 0.3 [18%] (1.3, 2.3)
BSi/POC	0.25 ± 0.08 [32%] (0.17, 0.44)	0.27 ± 0.07 [26%] (0.19, 0.40)	0.27 ± 0.09 [33%] (0.16, 0.42)
PIC/BSi	4.0 ± 1.2 [30%] (2.3, 5.9)	3.7 ± 1.0 [27%] (2.5, 5.4)	3.8 ± 1.2 [32%] (2.4, 6.4)
POC/PN	7.2 ± 0.3 [4%] (6.6, 7.7)	7.8 ± 0.4 [5%] (7.5, 8.5)	8.2 ± 0.8 [10%] (7.8, 10.4)

Actual trap depths varied across deployments within ±100 m of these nominal values; No corrections were made for depth variations. Material masses based on opal: SiO_2.0.4 H_2O; carbonate: $CaCO_3$, POM: 2.2 POC (Klaas and Archer, 2002). Lithogenic fluxes were considered negligible based on previous work – see section "Results and Discussion."

degrees of latitude and longitude of the SOTS site for sinking rates greater than 30 m d^{-1} (Hamilton, 2006). Further, this region is largely homogeneous in satellite ocean color images, and evaluation of statistical funnel effects (as described by Siegel et al., 1990) suggests local surface variations may add noise to seasonal records but do not bias their average seasonal cycle (Hamilton, 2006). While direct measurements of particle sinking rates are not available, gel trap analysis of sinking particles in the SAZ showed that most of the particles are large and therefore presumably fast sinking (Ebersbach et al., 2011). There are, however, some observations that suggest slowly sinking small particles may also influence the trap records. In particular, silicon isotopic variations suggest that slowly sinking small diatoms produced in summer do not arrive in the traps until winter (Closset et al., 2015), and study of suspended particles filtered from the top 600 m along a northward transect found rare earth element signatures suggesting inputs of small lithogenic clays from the Tasmanian shelf (Cardinal et al., 2001). Thus, while our 1-dimensional homogeneous source analysis seems appropriate for the major component fluxes, it comes with the caveat that allochthonous advective inputs may also occur, especially for small particles.

Average Particle Fluxes and Their Composition

The 20-year record of mass fluxes is shown in **Figure 3**, for both the cup-by-cup observed intervals and the interpolated daily resolution. The top three panels show the results for the first decade (**Figures 3A–C**), and the second three panels for the second decade (**Figures 3D–F**), during which higher data returns were achieved as the moorings became more durable and the deployment and recovery procedures more reliable. There is both considerable seasonal variability and interannual variability in the seasonality. Some summers have single peaks, others multiple events. Some winters have very low fluxes; others do not. Analysis of this variability is important to assess its causes and the associated implications for appropriate descriptions of ecosystem and export dynamics (as addressed in the sections below). As shown in **Table 1**, annual average fluxes (computed by breaking the records at 21st June each year to yield 7–9 years with full annual records, depending on the component and depth under consideration- see section "Materials and Methods") are less variable, with a relative standard deviation of ∼45% at 1000 m depth, which tightens to ∼30% at 2000 m depth and less than 20% at 3800 m depth. This sense of relatively small interannual variability in the integrated annual fluxes (in contrast to strong seasonality and its interannual variability as mentioned above) implies that our determination of representative decadal average flux estimates (as listed in **Table 1**) is robust, but also requires the caveat that the full range of integrated annual flux values is quite large, decreasing with depth from ∼17-fold to 4-fold to 2-fold.

The flux composition is more stable than its magnitude. This is seen readily by comparing the mass flux and %POC data in **Figure 3**, and by the average compositions in **Table 1**. The total mass flux at 1000 m depth is dominated by carbonate minerals (>60%), accompanied by opal (∼10%), and POM (∼17%). The contribution of POM decreases steadily with depth to ∼10% at

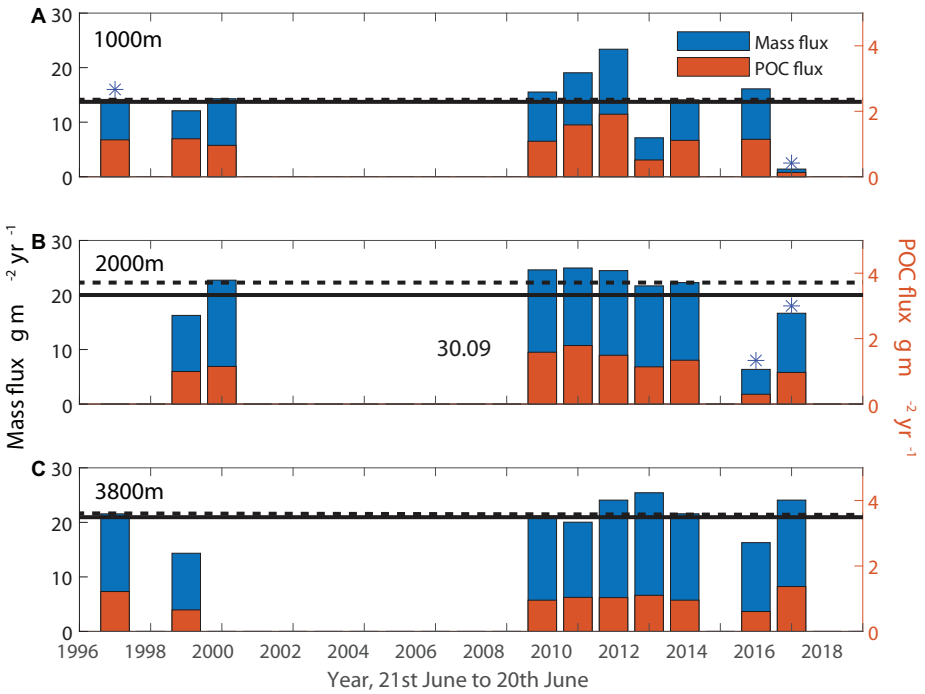

FIGURE 4 | Annual mass and POC fluxes in g m^{-2} yr^{-1}. POC fluxes for years marked with * had gaps filled with average %POC values to complete an annual cycle for this figure. Median (dashed line) and average (solid line) mass fluxes do not include the years marked with *. **(A)** 1000 m, **(B)** 2000 m, **(C)** 3800 m.

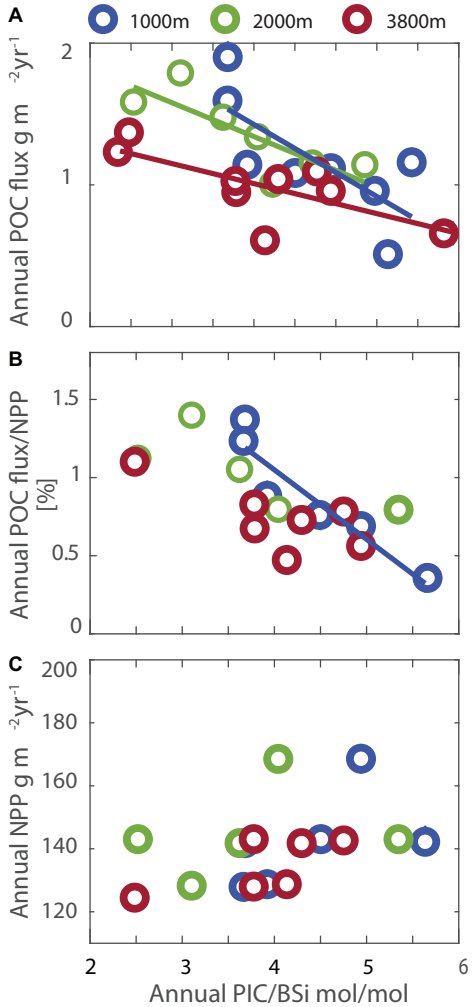

FIGURE 5 | Relationships between the two major ballasting components of sinking particles (expressed as their ratio PIC/BSi on the *x*-axes) and POC flux **(A)**, NPP **(B)**, and the transfer efficiency (expressed as POC flux/NPP, **C**). Trend lines are shown only for statistically significant correlations.

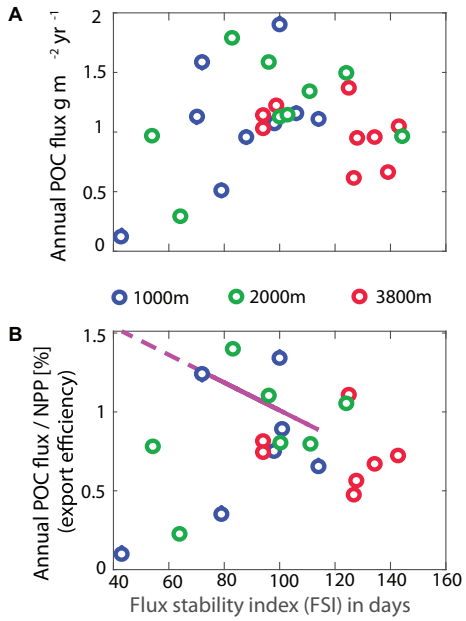

FIGURE 6 | Comparisons of POC flux **(A)** and transfer efficiency **(B)** with the flux stability index (FSI) revealed no significant correlations. The pink dashed line shows the relationship between transfer efficiency and FSI proposed for non-polar regions by Lampitt and Antia (1997).

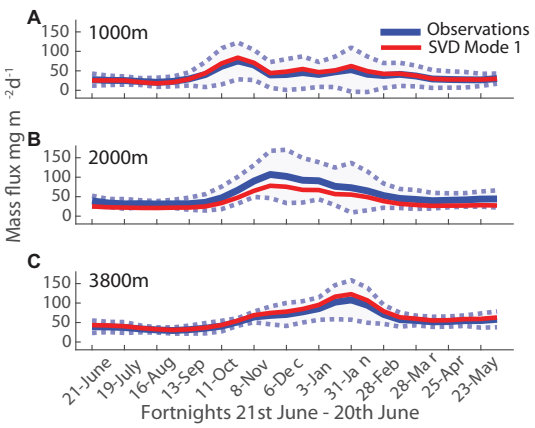

FIGURE 7 | Mass flux seasonality at each depth: **(A)** 1000 m, **(B)** 2000 m, **(C)** 3800 m. Fortnightly averages in blue, with blue shaded area representing 1 SD. The first mode from the SVD analysis is shown in red.

3800 m, with the other components showing smaller changes. Variability in the percent composition is small at all depths, well under 10% for the carbonate component, approximately twice this for POM, and slightly more for opal with the highest variability at 3800 m reaching 26%.

On a molar basis, inorganic carbon (PIC) is 4-fold more abundant than BSi and of similar abundance than organic carbon (POC) at 1000 m. Thus, the SOTS site is well-characterized as a "carbonate ocean" in the terminology of Honjo (Honjo et al., 2008), with secondary influence from biogenic opal, derived primarily from diatoms (Rigual-Hernández et al., 2015; Eriksen et al., 2018). The average POC flux of 1.4 ± 0.3 g m^{-2} $year^{-1}$ at 2000 m is similar both to the first estimate made at the site in 1998 and to the global median (Trull et al., 2001b). Lithogenic fluxes have not been measured regularly, and previous work has suggested they are negligible (Trull et al., 2001b). However, the sum of the masses of the measured component fluxes is on average only ∼90% of the total measured mass fluxes, leaving open the possibility of lithogenic fluxes contributing up to 10% of the total flux. Comparing estimates of coccolithophore calcite (Rigual Hernández et al., 2019; Rigual-Hernández et al., 2020) and foraminifera shell weights (King and Howard, 2003; Moy et al., 2009) to total PIC fluxes suggests roughly equal contributions from these phytoplankton and zooplankton sources to the sediment trap collected carbonate fluxes (Trull et al., 2019). The POM had

average POC/PN ratios that increased with depth (**Table 1**) and were above those expected for phytoplankton (Redfield, 1963; Copin-Montegut and Copin-Montegut, 1983), presumably as a result of preferential nitrogen remineralization (Honjo and Manganini, 1993; Conte et al., 2001; Schneider et al., 2003).

In summary, annual average fluxes at SOTS are close to the global median for POC, which is accompanied dominantly by PIC. Interannual variability is moderate (as represented by the standard deviations over 10 years for 1000 m and 9 years for 2000 and 3800 m). No long-term trends were present in any of the annual averages over the observational period (**Figure 4** and additional analyses of the time series). The presence of PIC has important implications: it adds ballast to sinking aggregates which can enhance their delivery of POC to the ocean interior (Klaas and Archer, 2002). It also reduces the impact of the POC fluxes on the partitioning of CO_2 between the atmosphere and ocean, via the effect known as the carbonate counter-pump, in which each mole of carbonate precipitated increases seawater aqueous CO_2 by ∼0.6 mole (Frankignoulle and Gattuso, 1993), countering its removal by photosynthesis and the biological carbon pump. The importance of this counter-pump is usually assessed for the surface mixed layer, where the aqueous CO_2 content affects air-sea exchange, by assuming that deep trap PIC fluxes represent carbonate losses from the surface and back-extrapolating the deep trap POC fluxes to the mixed layer depth (e.g., Salter et al., 2014) assuming an attenuation function for the intervening depths, typically a canonical power law (Martin et al., 1987). That is, the effective carbon sequestration flux leaving the mixed layer can be written:

$$Effective\_Flux = Flux\_POC\_mld - 0.6 Flux\_PIC\_mld$$

with

$$Flux\_PIC\_mld = Flux\_PIC\_1000\,m$$

$$Flux\_POC\_mld = Flux\_POC\_1000\,m(mld/1000)^{-b}$$

Using 100 m for the summer mixed layer depth when production is significant (Trull et al., 2019), $b = 0.858$ (Martin et al., 1987), and the average PIC/POC at 1000 m of 1.0 ± 0.2 (**Table 1**) suggests the presence of PIC reduces the effectiveness of the biological organic carbon pump by 8 ± 2%. This is similar to previous Southern Ocean estimates (Salter et al., 2014). Clearly this efficiency estimate is approximate and dependent on many assumptions. Notably, the attenuation of POC flux with depth at SOTS may be higher than expected from the Martin et al. (1987) formulation, as discussed in the next section, and this would reduce the impact of the carbonate counter-pump on carbon sequestration.

Finally, the importance of PIC at SOTS implies that the ecosystem and its biological pump are likely to be susceptible to ocean acidification. In this regard, previous work has suggested that foraminifera shell weights at SOTS are lower than during the pre-industrial Holocene, by amounts consistent with expectations from ocean acidification (Moy et al., 2009). In contrast, study of recent decadal variations in pteropod fluxes at SOTS showed both increases and decreases over time, depending on the species examined (Roberts et al., 2014). Carbonate mineral saturation states are currently still relatively high in the SAZ (Trull et al., 2018), but are expected to diminish strongly by the end of the century at which time impacts may increase (Orr et al., 2005), and the present SOTS observations provide a well determined baseline and an archived set of samples for later comparisons.

Flux Variations With Depth: Observations

On average sediment traps at 1000 m recorded a lower mass flux than the two deeper traps. This apparent under-collection has been reported previously (Honjo and Manganini, 1993; Yu et al., 2001; Berelson, 2002) and tentatively attributed to a combination of stronger currents at shallower depths that reduce trapping efficiency and mesopelagic processes that lead to increased compacting and aggregation of sinking particles below 1000 m which lead to improved trapping efficiency at greater depth. Since there is currently no consensus on the magnitude that currents and tilt might have on trapping efficiency (Gardner, 1985; Buesseler et al., 2007a), we did not correct our flux data (see section "Materials and Methods").

The range of mass fluxes was largest at 1000 m and decreased with depth. Interestingly, the largest fluxes measured at all three depths over the time series were similar, while the smallest fluxes which occurred at 3800 m were vastly greater than those at 1000 and 2000 m. The highest cup flux measured was 222 mg m^{-2} d^{-1} at 1000 m, 256 mg m^{-2} d^{-1} at 2000 m and 205 mg m^{-2} d^{-1} at 3800 m. The lowest cup mass flux measured at 1000 m was 0.2 mg m^{-2} d^{-1} and 0.1 mg m^{-2} d^{-1} at 2000 m but never less than 13.9 mg m^{-2} d^{-1} at 3800 m. POC fluxes at SOTS ranged between 4 and 2298 mg m^{-2} d^{-1} at 1000 m, 67 and 2457 mg m^{-2} d^{-1} at 2000 m and 54 and 1312 mg m^{-2} d^{-1}, which may seem large but is in line with other time series and smaller than that reported for the upper 500 m at the BATS time series station at 32°N, 64°W (0.1–311 mg POC m-2 d-1 between 1998 and 2016, Johnson and Pacheco, 1998-2016)[1]. The average attenuation of POC flux in g m^{-2} d^{-1} from 2000 to 3800 m was 29%, similar to previously reported attenuations between 1500 and 3200 m of 25% in the western Sargasso Sea (Conte et al., 2001).

As noted in the previous section, the standard deviation of annual mass fluxes decreased with depth. This was broadly speaking also true for POC, with relative standard deviations of 35, 21, and 24% at 1000, 2000, and 3800 m, respectively. Decreases in the variability of BSi and PIC fluxes with depth were smaller (**Table 1**). Overall, the compositional information is consistent with the view that flux composition becomes more homogeneous with depth, either as a result of removal of labile components from all particles (Conte et al., 2001), or the ability of only a limited class of particles to reach the deep sea (Boyd and Trull, 2007; Trull et al., 2008). Reduced flux variability could also be due to the increased spatial and temporal statistical funnel at greater depth (Siegel et al., 1990). The statistical funnel refers to the theoretical surface area from which particles most likely originated, which depends on the particle sinking

[1] http://bats.bios.edu/bats-data/

speed and the three-dimensional fluid velocity acting on the particle as it sinks.

Flux Variations With Depth: Comparisons to Common Algorithms

The most commonly used algorithm for C export attenuation is the empirical formulation of Martin et al. (1987)

$$C_{flux(z)} = C_{export} \left(\frac{z}{z_0}\right)^{-0.858}$$

where $C_{flux(z)}$ represents carbon flux at depth z and C_{export} the carbon exported from the surface ocean at depth z_o, typically taken as the mixed layer depth. C_{export} is equivalent to net community production (NCP) in a steady-state system (assuming negligible DOC export). NCP at the SOTS site has been estimated using a range of techniques: mixed layer O_2/N_2 budgets (Weeding and Trull, 2014), nitrogen depletion in the surface layer (Lourey and Trull, 2001), ^{234}Th surface water deficit measurements (Jacquet et al., 2011) and a dissolved inorganic carbon budget (Shadwick et al., 2015), and reported values range from 3 to 6 mol C m^{-2} yr^{-1}. POC fluxes at the SOTS site thus represent 2–3% of NCP at 1000 m, 2–4% at 2000 m and 1–3% at 3800 m. In comparison, using z_0 of 100 m and the *b* value of −0.858 proposed by Martin et al. (1987) based on limited observations from the Pacific Ocean, ∼8% of NCP would arrive at 2000 m. A wide range of b values from 0.5 to 2 have been shown to occur globally (Boyd and Trull, 2007 and ref. therein), in which case 0.3 – 22% of NCP can be expected to arrive at 2000 m, and the POC fluxes at 2000 m over the 20-year time series place the *b* value at 1.1 to 1.3 for z_0 100 m, i.e., higher than the canonical Martin *b* value but well within the global range of power-law attenuation coefficients.

An earlier algorithm for POC flux at depth related it directly to Net Primary Production (NPP) (Suess, 1980)

$$C_{flux(z)} = {}^{C_{NPP}}/_{(0.0283z + 0.212)}$$

where $C_{flux(z)}$ represents carbon flux at depth z and C_{NPP} is the rate of NPP in carbon units. The dependence on depth is equivalent to a power law *b* value of 1, and thus the attenuation is similar; while the expression in terms of NPP convolves the attenuation with depth with the fraction of NPP that escapes the surface layer, commonly described by the e-ratio, and taken as equivalent to the fraction of new production known as the f-ratio over the annual mean (see Boyd and Trull, 2007 for discussion).

Satellite ocean color-based estimates using the VGPM algorithm (see section "Possible Role of Net Primary Production in Control of Flux" for details) place the average annual NPP between 2009 and 2016 at 138 ± 14 g C m^{-2} yr^{-1} at SOTS. There are several sources of potential bias in this estimate of NPP in the Southern Ocean, including that phytoplankton chlorophyll-a is likely underestimated by standard ocean color algorithms (e.g., Johnson et al., 2013) and large variations among productivity models have been reported (e.g., Carr et al., 2006). Putting those caveats aside, comparing the SOTS sediment trap POC fluxes to this annual NPP estimate suggests ∼0.8 ± 0.4% of surface NPP arrives at 1000 m depth (0.9 ± 0.4% at 2000 m and 0.7 ± 0.2% at 3800 m), which is less than half of the 1.8% expected from the Suess algorithm.

The SOTS trap-based fluxes at 2000 m of 2–4% of NCP are also low compared to estimates of ∼15% from Weber et al. (2016) and DeVries and Weber (2017) based on large-scale ocean nutrient distributions, and the estimate of <5% from Henson et al. (2012) for the Southern Ocean (euphotic zone to 2000 m) based on satellite productivity and ^{234}Th measurements. In summary, POC transfer efficiency at SOTS seems to be lower than expected from commonly used export models but within the ranges of values observed globally and elsewhere within the Southern Ocean (Boyd and Trull, 2007; Buesseler et al., 2007b; Maiti et al., 2013).

Can We Explain the Interannual Variability of Mass or POC Fluxes?

Broadly speaking, interannual flux variability should derive from differences in surface primary productivity (stage 1), the component of this production exported from surface waters (stage 2), and/or attenuation at mesopelagic depths (stage 3), with each of these stages considered to contribute similarly to flux variations at global scale (Boyd and Trull, 2007). Previous conceptions of important controls on these processes have included the ballast hypothesis (Armstrong et al., 2001) in which the presence of biogenic minerals increases sinking rates and reduces remineralization rates thereby enabling more POC to reach the deep sea (influencing stage 3), and the flux-stability hypothesis (Lampitt and Antia, 1997) in which systems with strong seasonality are considered to achieve decoupling of production and grazing thereby enabling greater export (influencing stage 2). We investigate each stage of the BCP by considering the mechanisms that influence the three stages outlined above. The influence of stages 3 and 2 can be gauged using our time series observations, and the possible role of stage 1, primary production, by comparison to satellite-derived productivity estimates. We first examine the role of ballast (see section "Possible Role of Particle Ballast in POC Flux Magnitude") and then seasonality via the flux stability metric [see section "Possible Role of Seasonality in Control of Flux – The Flux Stability Index (FSI)"], mean seasonal cycles (see section "Possible Role of Seasonality in Control of Flux: Mean Seasonal Cycles"), and SVD to derive seasonal modes (see section "Possible Role of Seasonality in Control of Flux: Singular Value Decomposition"). Finally, we compare the annual mean fluxes to annual mean NPP (see section "Possible Role of Net Primary Production in Control of Flux").

Possible Role of Particle Ballast in POC Flux Magnitude

The importance of ballast minerals for POC flux to depth has been widely explored, and there is a growing understanding that the magnitude of POC export from the surface might be less important than the composition of the particles and site specific mesopelagic processes (Buesseler et al., 2007b). Independent of the magnitude of NPP, how particles sink and what happens to them on the way down, i.e., attenuation mechanisms, play an

important role in determining the magnitude of flux at depth. Flux attenuation is a function of sinking velocity and how well the particles can be remineralized or how likely they are to be grazed on their path down. It has been proposed that plankton community structure influences both the exported fraction (i.e., the f-ratio) and the flux attenuation mechanisms. A NPP with a high percentage of diatoms may to lead to high export ratios but low transfer efficiency due to the labile state of the POC associated with diatom-dominated particle export (Lima et al., 2014). Conversely, particle fluxes dominated by calcifiers can have a higher transfer efficiency, due to faster sinking velocities and reduced particle porosity (Guidi et al., 2009; Lima et al., 2014; Bach et al., 2016, 2019; Mouw et al., 2016), although Honda and Watanabe (2010) found a higher POC carrying capacity for BSi than PIC in the sub-arctic northwest Pacific.

At SOTS, the annual POC flux was positively correlated with PIC flux only at 1000 m (adjusted $R^2 = 0.8$, $p = 0.0009$), and not at the two depths below ($p > 0.1$) whereas annual POC fluxes were positively correlated with annual BSi fluxes at all three depths (adjusted $R^2 = 0.7$, $p = 0.006$, adjusted $R^2 = 0.8$, $p = 0.004$ and adjusted $R^2 = 0.8$, $p = 0.0006$ for 1000–3800 m, respectively). This could indicate that the presence of diatoms increases POC transfer to depth in the Subantarctic, as found in the sub-arctic (Honda and Watanabe, 2010). Expressing the particle composition as a ratio of the two ballasting components (PIC and BSi, **Figure 5A**), also shows that on an annual basis lower PIC/BSi molar composition of sinking particles is weakly associated with higher POC fluxes (1000 m adjusted $R^2 = 0.5$, $p = 0.04$; 2000 m adjusted $R^2 = 0.6$, $p = 0.03$; 3800 m adjusted $R^2 = 0.5$, $p = 0.03$), challenging the notion that diatom-dominated POC export is more labile and therefore has a lower transfer efficiency (Lima et al., 2014). The correlation between PIC/BSi molar ratio and transfer efficiency (expressed as the percentage of NPP carbon arriving at depth) is much weaker and only statistically significant at 1000 m (adjusted $R^2 = 0.9$, $p = 0.004$, 2000 m $p = 0.2$ and 3800 m $p = 0.06$, **Figure 5B**). This is consistent with the finding in section "Possible Role of Net Primary Production in Control of Flux" below that annual POC fluxes were independent of NPP. The molar ratio of PIC to BSi was also not correlated with annual NPP (**Figure 5C**). In combination, these observations suggest that biogeochemically defined phytoplankton functional types (diatoms, coccolithophores) influence either the fraction of NPP that is exported, or its subsequent attenuation (or both together) as it transits the mesopelagic zone, while the magnitude of NPP is not a useful predictor for POC fluxes beyond 1000 m.

Possible Role of Seasonality in Control of Flux – The Flux Stability Index (FSI)

A conventional view (e.g., Lampitt and Antia, 1997) of particulate fluxes is that large annual mass fluxes are the result of short-duration, but large magnitude events (in high latitude and temperate systems), while smaller annual fluxes are the result of smaller magnitude events occurring consistently through the year (in tropical/oligotrophic systems). To quantitatively distinguish between these two flux behaviors, Lampitt and Antia (1997) devised the Flux Stability Index (FSI), in which measured fluxes are sorted by decreasing magnitude, irrespective of their seasonal timing, and the FSI is given by the number of days required to accumulate 50% of the annual flux.

The average FSI computed at each trap depth (**Figure 6**) were not statistically different from each other and ranged from 87 ± 21 days at 1000 m, to 98 ± 28 at 2000 m, to 120 ± 19 at 3800 m. These values are at the higher end of the global range reported by Lampitt and Antia (1997), and accordingly relatively low annual POC fluxes would be anticipated. However, as noted in section "Average Particle Fluxes and Their Composition," the SOTS POC fluxes are close to the global median. The FSI values at the site varied interannually over much of the global range, but there was no statistically significant correlation between FSI and annual POC fluxes (**Figure 6A**), nor between the FSI and the transfer efficiency expressed as percentage of NPP arriving at depth (**Figure 6B**). This lack of significant relationship between FSI and mass flux was also observed by Lampitt and Antia (1997) for polar regions and may be due to significant fluxes during non-peak seasons, which have also been observed at SOTS (**Figure 3**). A closer look at the seasonality at SOTS is provided in the next section.

Possible Role of Seasonality in Control of Flux: Mean Seasonal Cycles

Given that annual POC flux is correlated with particle composition, and thus likely with ecosystem structure, a closer look at flux seasonality might help shed some light on the source of this correlation. This is also motivated by the long-standing recognition that organic matter available from the euphotic zone arises from the small imbalance between autotrophic production and its heterotrophic consumption, and this imbalance may be larger when there is strong seasonality owing to the generally longer life cycles of heterotrophs (e.g., Evans and Parslow, 1985; Morel et al., 1991; Lutz et al., 2007; Lindemann and St John, 2014). To construct a mean flux seasonality, daily interpolated mass flux data was averaged over fortnightly intervals (**Figure 7**, blue line, shaded area). The resulting mean seasonal cycle is best described by a temperate, early spring and late summer, two-peak pattern at all three depths. This is most clearly distinct at 1000 m, with the peaks overlapping at 2000 and 3800 m (where their distinct nature is mainly discernible via the compositional variations (**Figure 8**). Variability during peak flux periods is reduced with depth, as seen in the reduced standard deviation envelope around the mean flux in **Figure 7**. The largest standard deviation falls into the summer period of December and January, indicating that the timing and magnitude of the summer flux peak is variable across years. Looking at individual years (**Figure 3**), the large standard deviation for the 1000 m flux data in January is due to the varying timing of the secondary peak (**Figure 7A**). At 2000 m, the standard deviation of the mass flux data in December is large since half of the analyzed years had no peak flux in December (**Figure 7B**). Explanations for the change in seasonal pattern with depth include a time shift in the observed peak flux from October to January moving from 1000 to 3800 m due to slow sinking particles, and the possibility that the late summer peak at 1000 m does not penetrate to depth. It is also possible to view the background flux at 3800 m during winter as a result of slow sinking particles originating from the late

summer peak at 1000 m (Closset et al., 2015). Fluxes during winter at 3800 m never reach zero and are far greater than those measured at 1000 and 2000 m during the same period (as stated in section "Flux Variations With Depth: Observations"). An alternative explanation could be that particles from the spring peak at 1000 m are attenuated more quickly, and this explains the near absence of the first peak at 3800 m – in this view the main peak at 3800 m would be derived from the late summer peak observed at 1000 m, via very rapid particle sinking (Conte et al., 2001). Cross-covariance calculations with daily interpolated mass flux data (as described by Conte et al., 2001) and with component ratios of particles across depth (modified after Berelson, 2002) indicated that particle sinking speeds are in the order of days, i.e., hundreds of meters per day (data not shown).

Figure 8 shows the seasonal variations in the component fluxes of PIC, POC, and BSi, which deviate slightly from the pattern of mass fluxes. The PIC flux has a similar two-peak shape at all three depths, with the same shape and timing as total mass flux, unsurprising due to its dominant role in particle composition. The BSi flux at 1000 m appears more diffuse across a broad time frame, from spring to summer (October to February), with three possible minor peak flux events. This is in line with diatom fluxes found in sediment trap material from 1999–2001 (Rigual-Hernández et al., 2015). At 2000 and 3800 m biogenic silica flux was similar to that of the mass flux in its overlapping two peak seasonality. The concept of multiple episodes of BSi export is consistent with seasonal surface phytoplankton community observations via autonomous water sample collection during the 2010/2011 deployment, which

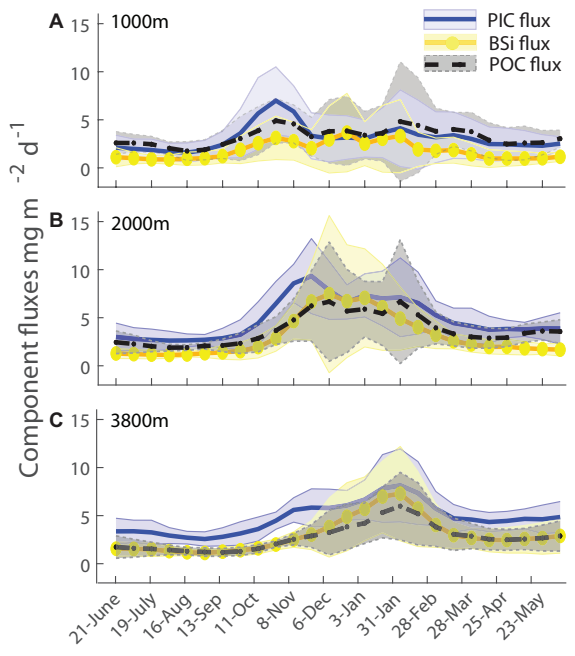

FIGURE 8 | Seasonal component flux variations at each depth: **(A)** 1000 m, **(B)** 2000 m, **(C)** 3800 m. Lines show average values; shaded envelopes show 1 SD.

indicated that diatom biovolume peaked in late September, with contributions from large diatoms highest in early December, and the late summer community exhibiting more weakly silicified frustules (Eriksen et al., 2018). The average POC flux was highest in the spring to summer period, again with three possible peak flux events at 1000 m, two peaks at 2000 m and two overlapping peaks at 3800 m. Average POC fluxes were largest in late January, when interannual standard deviations were also largest.

Possible Role of Seasonality in Control of Flux: Singular Value Decomposition

Calculating average fortnightly total mass and component fluxes and their associated standard deviations helps to describe the mean seasonality and how much it varies between years, but is in itself not an explanation for the interannual variability in mass or POC flux. To help us quantify whether the seasonality of fluxes and its variability influences total annual POC flux we used the results of a Singular Value Decomposition (SVD) as explained in the next section.

SVD offers an objective way to elucidate underlying patterns in time series, via least-squares minimization to deconvolve them into a reduced set of orthogonal modes that are ranked in order of the fraction of variance they explain (e.g., Cadzow et al., 1983; Yoder and Kennelly, 2003; Kim et al., 2016; Trinh and Ducklow, 2018). To do this, our time series was divided into annual cycles (at 21st June of each year, see section "Materials and Methods") with fortnightly resolution, providing 10 records for 1000 m, and 9 records for the deeper depths (2000 and 3800 m). The first 3 modes captured nearly all the variance (at all depths), and we focus our discussion accordingly. The first mode of the SVD analysis is overlaid on the fortnightly mass flux averages in **Figure 7** (red line), and has very similar seasonality to the average fluxes, i.e., it exhibits spring and late summer peaks. It explained 79% of the variability in mass fluxes at 1000 m, 85% at 2000 m and 93% at 3800 m.

The first three modes for the 1000 m mass fluxes are compared in **Figure 9A**. Mode 1 describes the dominant temperate seasonal pattern of a spring bloom (in October) and secondary late summer (late January) peak. Mode 2 shows that a relatively strong summer peak is associated with a late start to the spring peak (and vice versa). Mode 3 indicates that a short duration spring peak is associated with an early and short duration secondary peak (and vice versa). Modes 2 and 3 each explain similarly small portions of interannual variance of 8 and 5%, respectively. The majority of interannual variation in mass fluxes is therefore explained by a typical seasonality (Mode 1) with varying contributions to the flux magnitudes each year, as shown by seasonal representation of Mode 1 for the 10 years at 1000 m in **Figure 10A**, i.e., high and low flux years therefore share a common seasonality of two peaks. **Figures 9B**, **10** also show that Modes 2 and 3 vary in their sign across the time series, and that there is no overall trend in any of the three Modes. While Mode 1 dominates the other two modes, individual years stand out, e.g., in 2010 when the influence of Mode 2 is similar to Mode 1 in other years (**Figure 10B**). Despite this variation in the strength of Mode 2 and 3 for individual years, their annual coefficients do not correlate with annual mass flux (not shown) and so the timing of total mass

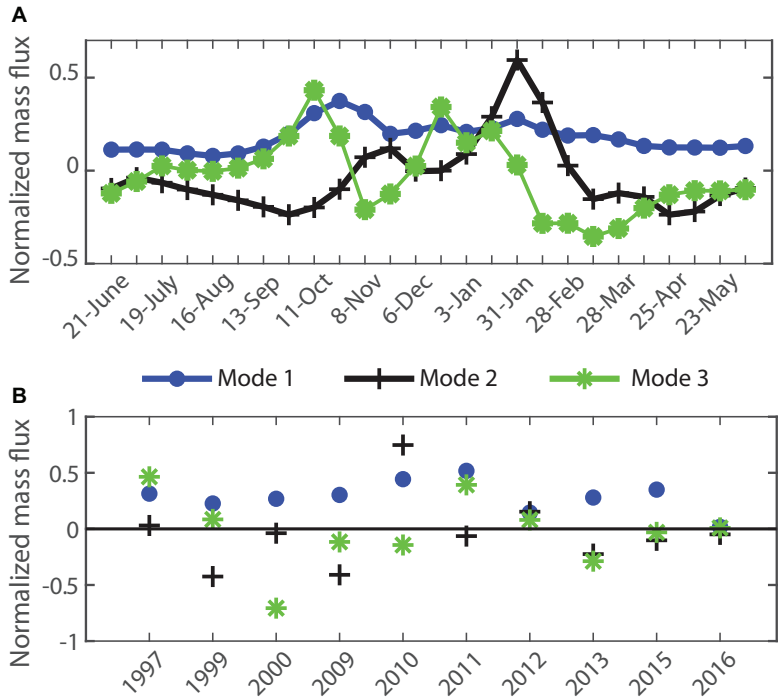

FIGURE 9 | Singular Value Decomposition for mass flux at 1000 m **(A)** Seasonal structure of Modes 1 – 3. **(B)** Interannual time series of the principal component coefficients of Modes 1–3. The % variance explained by these Modes was 79, 8, and 5%, respectively.

peak flux events does not explain interannual variability in total mass flux. This has important ramifications for the evaluation of ecological hypotheses based on decoupling of production and grazing in the control of POC fluxes, as discussed below.

Mode 1 for mass fluxes at 2000 and 3800 m explains an even larger percentage of the interannual variances, 85 and 93%, respectively. Again, most of the interannual variation in mass fluxes is explained by the differences in Mode 1 mass flux magnitudes and to a lesser extent by the timing of the peak flux events. The seasonality of mass fluxes at 2000 m is best described by a broad, possibly overlapping double-peak in late November (**Figure 7B**). At 2000 m, Mode 2 explains more than twice as much of the interannual variability than Mode 3 (7 and 3%, respectively). Mode 2 represents a change in the timing of the peak flux events at 2000 m by a few weeks from year to year and Mode 3 shows that for years with smaller fluxes during summer, mass fluxes occur later in the year and vice versa (data not shown). The seasonality of mass fluxes at 3800 m is also best described by an overlapping double peak, however, much later than at 2000 m, in late January (**Figure 7C**). Mode 2 explains 4% of the variability and with only 1% Mode 3 is not considered further here. Mode 2 indicates that years with relatively small peak mass flux in January exhibit increased mass fluxes throughout the rest of the year (1997/1998, 2010/2011, and 2012/2013, data not shown). The larger statistical funnel for particle collection at 3800 m depth likely explains the high percentage of variability accounted for by Mode 1. This deepest trap collects particles over a larger spatial range and slow sinking particles originating in high flux periods during summer can arrive at greater depths during later low flux periods, smoothing out the seasonal variation at greater depth (Closset et al., 2015).

In summary, variations in the timing of peak flux events (characterized by Modes 2 and 3) explain a small proportion of interannual flux variability and as such do not help to explain interannual variability in total flux. That variability is dominated by the changing intensity of Mode 1. Analysis of the time series of mode coefficients did not reveal any trends, and thus there is not yet evidence of change in the spring initiation of productivity or the duration of the production season, as expected from century timescale coupled climate change and ocean biogeochemistry simulations (e.g., Bopp et al., 2001; Gehlen et al., 2006; but see Ducklow et al., 2008).

This analysis of the role of seasonality in interannual flux variations has been built on the Modes of mass flux. It is possible to also estimate Modes for each major component (PIC, BSi and POC) separately (as shown in **Figure 11** for 1000 m depth). Again, the first Mode explains most of the variance of each of the flux constituents. For PIC Mode 1 has a very similar shape to that of mass flux, with somewhat greater influence of the first spring peak relative to the summer peak. BSi Mode 1 exhibits an intervening December peak, and thus less distinct separation into two separate flux events. POC Mode 1 combines aspects from both of these other components, with spring and especially summer peaks and a smaller intervening flux component. This explains 78% of interannual variability. The difference in timing of component peaks, with the PIC in

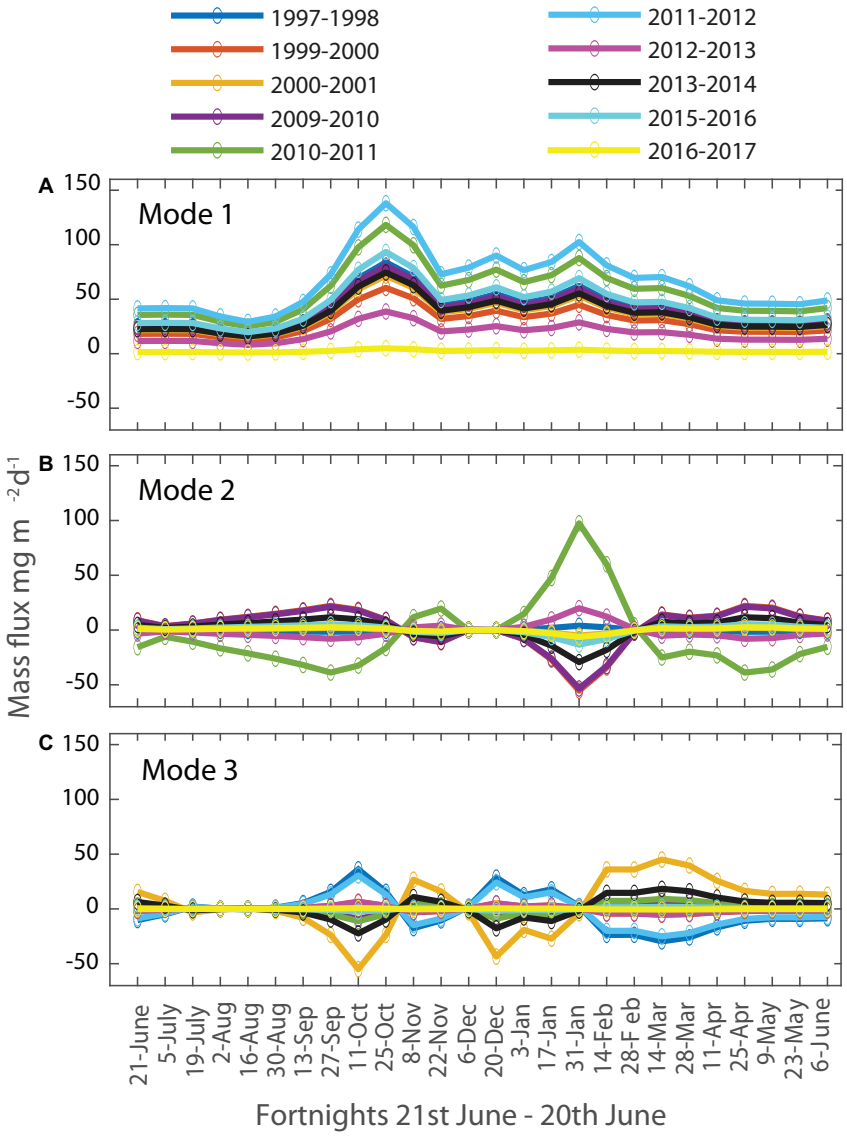

FIGURE 10 | Interannual variations in the seasonal 1000 m mass flux contributions of the Singular Value Decomposition Modes. **(A)** Mode 1: 79%, **(B)** Mode 2: 8%, **(C)** Mode 3: 5%.

late October and the BSi in late December, in comparison to peak POC fluxes in late January, seem to place more emphasis on opal forming plankton as POC carriers. Seasonally varying processes in the mesopelagic that might lead to stronger POC flux attenuation in spring *versus* late summer, however, cannot be ruled out. Modes 2 and 3 of component fluxes at all three depths do not correlate with annual POC flux, again indicating that the timing of peak flux events, whether it be total or that of any particular component, does not explain interannual variability of POC flux. There was also no temporal trend in the coefficients of Modes 1–3 for the components at any of the three depths.

With the SVD perspectives on seasonality in mind, we reconsider the FSI at SOTS. The interannual range in FSI of 43–144 days (43–114 at 1000 m, 54–144 at 2000 m, 94–143 at 3800 m) was similar to the global range reported by Lampitt and Antia (1997), and thus to the expectation of significant interannual variability in transfer efficiency. **Figure 6** shows that interannual variation does occur, but is not correlated with FSI. The SVD shows that an overwhelming portion of the interannual flux variance is accounted for by the intensity of Mode 1, and thus that changes in the intra-seasonal temporal structure of the flux (as captured by the FSI) are not the most important driver of the interannual flux variations. In other words, results for all three depths indicate that the shape of the seasonal cycle is relatively consistent. This is consistent with the results that Modes 2 and 3, that describe changes in the seasonality, explain only small proportions

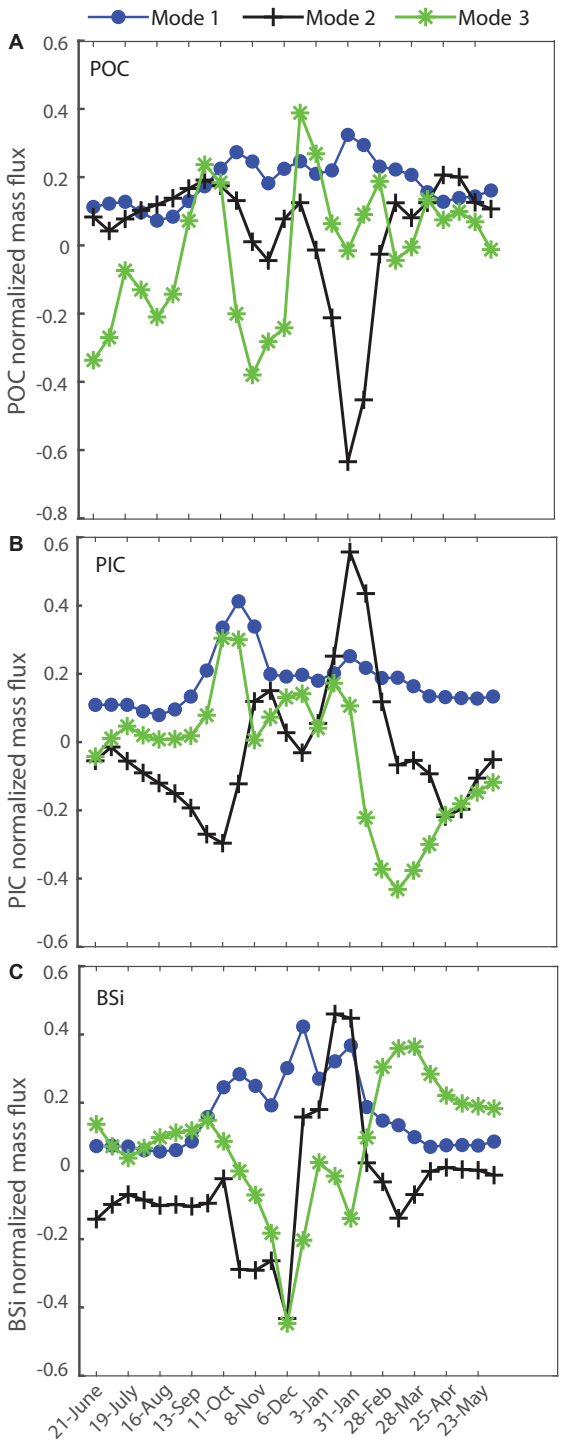

FIGURE 11 | Singular Value Decomposition Modes for the particle component fluxes at 1000 m **(A)** POC, **(B)** PIC, **(C)** BSi.

of the interannual flux variance. In combination, the FSI and SVD analyses suggest that if trophic decoupling is a major driver of exported flux, then it must occur without changes in seasonality.

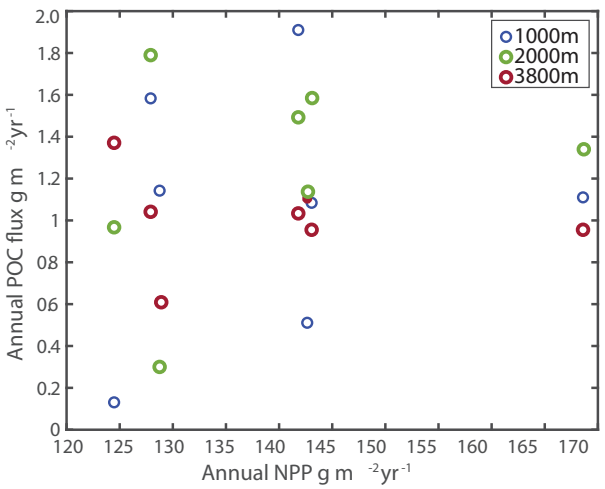

FIGURE 12 | Comparison of Annual POC flux and Annual NPP at SOTS. No statistical correlation was observed at any depth.

Possible Role of Net Primary Production in Control of Flux

A possible source of variability in annual flux is variability in NPP at the surface. Monthly estimates of NPP around the SOTS site (47°S and 142°E, with a square box around it of 1.5 degrees in both latitude and longitude, **Figure 1**) were obtained from the satellite-derived Vertically Generalized Production Model (VGPM, Behrenfeld and Falkowski, 1997) via the Oregon State University Ocean Productivity website[2], and assembled to provide integrated annual estimates of production. **Figure 12**, however, shows that there is no correlation between integrated annual production at the surface and integrated annual flux arriving at depth. Relative standard deviation of annual NPP between 2009 and 2016 was 10% compared to annual POC flux variability of 39% at 1000 m and 20% at 2000 m, which implies that export and/or attenuation may be more important controls than NPP. Recent assessments of satellite ocean color records have shown no statistically significant trends in either chlorophyll or derived NPP estimates in the SOTS region over the period 2003–2019, in keeping with the lack of trends in our observed fluxes at depth (Thompson and McDonald, 2020; Thompson et al., 2020).

CONCLUSION AND PERSPECTIVES

After 20 years, SOTS is now one of the longest duration particle flux time series, particularly in the sparsely sampled Southern Ocean. Average POC fluxes across the three depths of 1.0 to 1.4 g m^{-2} yr^{-1} (1000–3800 m) recorded over the 20-year time series are comparable to previously measured values at the SOTS site (Trull et al., 2001b), other Subantarctic sites (Honjo et al., 2000; Nodder et al., 2016), the North Atlantic (Conte et al., 2001), the northeastern Subarctic Pacific (Wong

[2]http://www.science.oregonstate.edu/ocean.productivity/index.php

et al., 1999) and the global median (Lampitt and Antia, 1997; Mouw et al., 2016). In contrast, the SOTS POC fluxes are lower than those of 2.5 g m^{-2} yr^{-1} for the polar North Pacific Ocean, 3.8 g m^{-2} yr^{-1} for the Pacific Sector of the Southern Ocean, 1.7 g m^{-2} yr^{-1} for the Atlantic Sector of the Southern Ocean, but larger than 0.6 g m^{-2} yr^{-1} for the Indian Sector of the Southern Ocean, as compiled by Lutz et al. (2007). The moderate interannual variability in total mass flux and the range in fluxes are similar to that of other long standing sediment trap time series (e.g., Ocean Station Papa in the Northeast Pacific, Wong et al., 1999).

No long-term trends in mass or POC fluxes can yet be seen beyond natural variability, which was also true for the 20-year time-series at BATS (Conte et al., 2001). This is consistent with expectations from a recent modeling study. Schlunegger et al. (2019) calculated the emergence time scales of anthropogenic impacts for a range of physical and biological processes, including a reduction in the strength of the soft-tissue pump as a consequence of reduced supply of nutrients to the surface ocean caused by changes in ocean circulation and stratification. The emergence timescale of this reduction is expected to be on the order of 23–50 years globally and up to 76 years locally. Schlunegger et al. (2019) also predicted a reduction in the calcium carbonate counter-pump to emerge in 10 years globally and 9-18 years regionally, but this depends on a strong response of biogenic carbonate production to carbonate saturation state (which has not been observed in field data in the Southern Ocean south of Australia, Trull et al., 2018).

Surface seasonality at SOTS is moderate, with no major autotrophic blooms (Eriksen et al., 2018) and small interannual variability in NPP (VGPM, Behrenfeld and Falkowski, 1997). The magnitude of NPP did not predict POC flux magnitude at depth on an annual timescale, possibly indicating that the mechanisms that affect export production and flux attenuation are more important than surface production. The lack of correlation between satellite derived surface productivity and POC flux at depth highlights the value of long-term direct measurements. In order to assess the importance of processes that link upper ocean productivity with carbon export versus remineralization during particle sinking on seasonal and interannual time scales, additional physical and biogeochemical water column parameters, are required. Some of these are available already from the SOTS program, and construction and validation of multiyear records are underway.

Interannual changes in flux seasonality were also moderate with a highly preserved seasonal structure and with most of the interannual variation explained by differences in flux magnitude that was not correlated with changes in seasonality. POC flux at depth was between 1 and 4% of NCP, at the lower end of values expected from commonly used attenuation models. The characteristic of moderate seasonality with significant interannual variations in the seasonal pattern but not the integrated annual fluxes, yet relatively constant annual fluxes is likely to be useful in selecting appropriate models for the simulation of environmental-ecological coupling and its role in controlling the biological carbon pump. Carbon export models for the SAZ need to be able to mechanistically reproduce the amplification of variability from ∼10% in surface NPP to 21–35% in POC flux at depth.

The Southern Ocean is a globally significant region for carbon export. The findings of this 20 year record, including the lack of any identifiable trends, will serve as an important baseline against which to measure future changes. Given the high proportion of biogenic carbonate minerals in the particle export, SOTS will be an important sentinel for the effects of both climate change and ocean acidification. The lack of correlation between satellite derived results of surface productivity and POC flux at depth may emphasize the importance of processes that control export production and flux attenuation. Our sediment trap based particle export time series is embedded in a wealth of data produced by the moorings, associated instruments, and service voyages at SOTS (see Eriksen et al., 2018; Trull et al., 2019 for further information on the diversity of observations). It is hoped that future work connecting our findings to locally measured environmental and biological parameters will shed additional light on the processes that control particle fluxes in the Southern Ocean.

DATA AVAILABILITY STATEMENT

The raw data supporting the conclusions of this article will be made available by the authors, without undue reservation. Particle flux data is available through the IMOS AODN portal (https://portal.aodn.org.au/).

AUTHOR CONTRIBUTIONS

All authors except ES, PJ, and RT performed the processing and chemical analyses of sediment trap samples. All authors except RT participated in voyage preparations and support during mooring servicing voyages. CW-E, ES, and TT analyzed and interpreted the time series results. RT provided the expertise on the singular value decomposition technique. CW-E, TT, and ES wrote the manuscript, with refinements contributed by all other authors.

FUNDING

This project has received grant funding from the Australian Government via many sources over the past two decades, including ship support from the Marine National Facility and Australian Antarctic Division, mooring equipment support from CSIRO and the Antarctic Climate and Ecosystems Cooperative Research Centre, and research staff support via all these agencies as well as the University of Tasmania and Australian Antarctic Program Partnership. RT was supported by a US NSF Graduate Research Fellowship. Support contributed by the USA National Science Foundation via the Woods Hole Oceanographic Institution was important to the initiation of the time series in 1997.

ACKNOWLEDGMENTS

We acknowledge support from the agencies Antarctic Climate and Ecosystems Cooperative Research Centre (ACE CRC), Integrated Marine Observing System (www.imos.org.au), University of Tasmania (UTAS), Bureau of Meteorology (BoM), Marine National Facility (MNF) and Australian Antarctic Division (AAD). Australia's Integrated Marine Observing System (IMOS) is enabled by the National Collaborative Research Infrastructure Strategy (NCRIS). It is operated by a consortium of institutions as an unincorporated joint venture, with the University of Tasmania as Lead Agent. We also acknowledge the support of the CSIRO Marine and Atmospheric Research Moorings Group and Dr. Thomas Rodemann of Central Science Lab, UTAS for elemental analysis. SOTS is a member of the OceanSITES global network of time series observatories (www.OceanSITES.org). Thanks to Edward Doddridge for help with evaluation of singular value decomposition results, and Hugh Ducklow and Tyler Rohr for providing helpful comments that improved an earlier version of the manuscript.

REFERENCES

Agassiz, A. (1888). Three cruises of the United States coast and Geodetic survey steamer Blake in the Gulf of Mexico, in the Caribbean sea, and along the Atlantic coast of the United States from 1877 to 1880. *Bull. Museum Comp. Zool. Harvard* 1, 1–314.

Antia, A. N. (2005). Solubilization of particles in sediment traps: revising the stoichiometry of mixed layer export. *Biogeosciences* 2, 189–204. doi: 10.5194/bg-2-189-2005

Archer, D., Winguth, A., Lea, D., and Mahowald, N. (2000). What caused the glacial/interglacial atmospheric pCO2 cycles? *Biogeosciences* 11, 1177–1198.

Armstrong, R. A., Lee, C., Hedges, J. I., Honjo, S., and Wakeham, S. G. (2001). A new, mechanistic model for organic carbon fluxes in the ocean based on the quantitative association of POC with ballast minerals. *Deep Sea Res. Part II Top. Stud. Oceanogr.* 49, 219–236. doi: 10.1016/s0967-0645(01)00101-1

Arteaga, L., Haentjens, N., Boss, E., Johnson, K. S., and Sarmiento, J. L. (2018). Assessment of export efficiency equations in the southern ocean applied to satellite-based net primary production. *J. Geophys. Res. Oceans* 123, 2945–2964. doi: 10.1002/2018jc013787

Bach, L. T., Boxhammer, T., Larsen, A., Hildebrandt, N., Schulz, K. G., and Riebesell, U. (2016). Influence of plankton community structure on the sinking velocity of marine aggregates. *Global Biogeochem. Cycles* 30, 1145–1165. doi: 10.1002/2016gb005372

Bach, L. T., Stange, P., Taucher, J., Achterberg, E. P., Alguero-Muniz, M., Horn, H., et al. (2019). The influence of plankton community structure on sinking velocity and remineralization rate of marine aggregates. *Global Biogeochem. Cycles* 33, 971–994. doi: 10.1029/2019gb006256

Behrenfeld, M. J., and Falkowski, P. G. (1997). Photosynthetic rates derived from satellite-based chlorophyll concentration. *Limnol. Oceanogr.* 42, 1–20. doi: 10.4319/lo.1997.42.1.0001

Berelson, W. M. (2002). Particle settling rates increase with depth in the ocean. *Deep Sea Res. II* 49, 237–251. doi: 10.1016/s0967-0645(01)00102-3

Bopp, L., Monfray, P., Aumont, O., Dufresne, J. L., Le Treut, H., Madec, G., et al. (2001). Potential impact of climate change on marine export production. *Global Biogeochem. Cycles* 15, 81–99. doi: 10.1029/1999gb001256

Bowie, A. R., Lannuzel, D., Remenyi, T. A., Wagener, T., Lam, P. J., Boyd, P. W., et al. (2009). Biogeochemical iron budgets of the Southern Ocean south of Australia: decoupling of iron and nutrient cycles in the subantarctic zone by the summertime sypply*Global Biogeochem. Cycles* 23:GB4034. 128.

Boyd, P. W., Claustre, H., Levy, M., Siegel, D. A., and Weber, T. (2019). Multi-faceted particle pumps drive carbon sequestration in the ocean. *Nature* 568, 327–335. doi: 10.1038/s41586-019-1098-2

Boyd, P. W., and Trull, T. W. (2007). Understanding the export of biogenic particles in oceanic waters: Is there consensus? *Progr. Oceanogr.* 72, 276–312. doi: 10.1016/j.pocean.2006.10.007

Boyd, P. W., Watson, A. J., Law, C. S., Abraham, E. R., Trull, T., Murdoch, R., et al. (2000). A mesoscale phytoplankton bloom in the polar Southern Ocean stimulated by iron fertilization. *Nature* 407, 695–702. doi: 10.1038/35037500

Bray, S. G., Trull, T. W., and Manganini, S. J. (2000). *SAZ Project Moored Sediment Traps: Results of the 1997-1998 Deployments*. Hobart, TAS: Antarct Coop. Res. Cent, 128.

Buesseler, K. O., Antia, A. N., Chen, M., Fowler, S. W., Gardner, W. D., Gustafsson, O., et al. (2007a). An assessment of the use of sediment traps for estimating upper ocean particle fluxes. *J. Mar. Res.* 65, 345–416. doi: 10.1357/002224007781567621

Buesseler, K. O., Lamborg, C. H., Boyd, P. W., Lam, P. J., Trull, T. W., Bidigare, R. R., et al. (2007b). Revisiting carbon flux through the ocean's twilight zone. *Science* 316, 567–570.

Cadzow, J. A., Baseghi, B., and Hsu, T. (1983). "Singular-value decomposition approach to time series modelling," in *IEE Proceedings F (Communications, Radar and Signal Processing)*, London: IET.

Cardinal, D., Dehairs, F., Cattaldo, T., and André, L. (2001). Geochemistry of suspended particles in the Subantarctic and Polar Frontal Zones south of Australia: constraints on export and advection processes. *J. Geophys. Res. Oceans* 106, 31637–31656. doi: 10.1029/2000jc000251

Carr, M.-E., Friedrichs, M. A., Schmeltz, M., Aita, M. N., Antoine, D., Arrigo, K. R., et al. (2006). A comparison of global estimates of marine primary production from ocean color. *Deep Sea Res. Part II Top. Stud. Oceanogr.* 53, 741–770.

Closset, I., Cardinal, D., Bray, S. G., Thil, F., Djouraev, I., Rigual-Hernandez, A. S., et al. (2015). Seasonal variations, origin, and fate of settling diatoms in the Southern Ocean tracked by silicon isotope records in deep sediment traps. *Global Biogeochem. Cycles* 29, 1495–1510. doi: 10.1002/2015gb005180

Conte, M. H., Ralph, N., and Ross, E. H. (2001). Seasonal and interannual variability in deep ocean particle fluxes at the Oceanic Flux Program (OFP)/Bermuda Atlantic Time Series (BATS) site in the western Sargasso Sea near Bermuda. *Deep-Sea Res. II* 48, 1471–1505. doi: 10.1016/s0967-0645(00)00150-8

Copin-Montegut, C., and Copin-Montegut, G. (1983). Stoichiometry of carbon, nitrogen, and phosphorus in marine particulate matter. *Deep Sea Res. Part A Oceanogr. Res. Pap.* 30, 31–46. doi: 10.1016/0198-0149(83)90031-6

Cram, J. A., Weber, T., Leung, S. W., McDonnell, A. M. P., Liang, J.-H., et al. (2018). The role of particle size, ballast, temperature, and oxygen in the sinking flux to the deep sea. *Global Biogeochem. Cycles* 858–876. doi: 10.1029/2017gb005710

DeVries, T., Primeau, F., and Deutsch, C. (2012). The sequestration efficiency of the biological pump. *Geophys. Res. Lett.* 39:5.

DeVries, T., and Weber, T. (2017). The export and fate of organic matter in the ocean: new constraints from combining satellite and oceanographic tracer observations. *Global Biogeochem. Cycles* 31, 535–555. doi: 10.1002/2016gb005551

Ducklow, H. W. (1995). Ocean biogeochemical fluxes: new production and export of organic matter from the upper ocean. *Rev. Geophys.* 33, 1271–1276. doi: 10.1029/95rg00130

Ducklow, H. W., Erickson, M., Kelly, J., Montes-Hugo, M., Ribic, C. A., Smith, R. C., et al. (2008). Particle export from the upper ocean over the continental shelf of the west Antarctic Peninsula: a long-term record, 1992–2007. *Deep Sea Res. Part II Top. Stud. Oceanogr.* 55, 2118–2131. doi: 10.1016/j.dsr2.2008.04.028

Dugdale, R. C., Wilkerson, F. P., and Minas, H. J. (1995). The role of a silicate pump in driving new production. *Deep Sea Res. Part I Oceanogr. Res. Pap.* 42, 697–719. doi: 10.1016/0967-0637(95)00015-x

Ebersbach, F., Trull, T. W., Davies, D. M., and Bray, S. G. (2011). Controls on mesopelagic particle fluxes in the Sub-Antarctic and Polar Frontal Zones in the Southern Ocean south of Australia in summer—Perspectives from free-drifting sediment traps. *Deep Sea Res. Part II Top. Stud. Oceanogr.* 58, 2260–2276. doi: 10.1016/j.dsr2.2011.05.025

Eriksen, R., Trull, T. W., Davies, D., Jansen, P., Davidson, A. T., Westwood, K., et al. (2018). Seasonal succession of phytoplankton community structure from

autonomous sampling at the Australian Southern Ocean Time Series site. *Mar. Ecol. Progr. Ser.* 589, 13–31. doi: 10.3354/meps12420

Evans, G. T., and Parslow, J. S. (1985). A model of annual plankton cycles. *Biol. Oceanogr.* 3, 327–347.

Falkowski, P., Scholes, R., Boyle, E., Canadell, J., Canfield, D., Elser, J., et al. (2000). The global carbon cycle: a test of our knowledge of earth as a system. *Science* 290, 291–296. doi: 10.1126/science.290.5490.291

Falkowski, P. G., Barber, R. T., and Smetacek, V. (1998). Biogeochemical controls and feedbacks on ocean primary production. *Science* 281, 200–206. doi: 10.1126/science.281.5374.200

Feely, R. A., Sabine, C. L., Lee, K., Berelson, W., Kleypas, J., Fabry, V. J., et al. (2004). Impact of anthropogenic CO2 on the CaCO3 system in the oceans. *Science* 305, 362–366. doi: 10.1126/science.1097329

Frankignoulle, M., and Gattuso, J. (1993). "Air-sea CO2 exchange in coastal ecosystems," in *Interactions of C, N, P and S Biogeochemical Cycles and Global Change. NATO ASI Series (Series I: Global Environmental Change)*, eds R. Wollast, F. T. Mackenzie, and L. Chou (Heidelberg: Springer), 4.

Gardner, W. D. (1985). The effect of tilt on sediment trap efficiency. *Deep-Sea Res.* 32, 349–361. doi: 10.1016/0198-0149(85)90083-4

Gehlen, M., Bopp, L., Emprin, N., Aumont, O., Heinze, C., and Ragueneau, O. (2006). Reconciling surface ocean productivity, export fluxes and sediment composition in a global biogeochemical ocean model. *Biogeosciences* 3, 521–537. doi: 10.5194/bg-3-521-2006

Guidi, L., Stemmann, L., Jackson, G. A., Ibanez, F., Claustre, H., Legendre, L., et al. (2009). Effects of phytoplankton community on production, size and export of large aggregates: a world-ocean analysis. *Limnol. Oceanogr.* 54, 1951–1963. doi: 10.4319/lo.2009.54.6.1951

Hamilton, K. M. (2006). *Evaluating the Consistency of Satellite and Deep Sediment Trap Carbon Export Data in the Southern Ocean. Institute of Antarctic and Southern Ocean Studies (IASOS)*. Hobart: University of Tasmania. Bachelor of Science.

Helm, K. P., Bindoff, N. L., and Church, J. A. (2011). Observed decreases in oxygen content of the global ocean. *Geophys. Res. Lett.* 38, L23602.

Henson, S. A., Sanders, R., and Madsen, E. (2012). Global patterns in efficiency of particulate organic carbon export and transfer to the deep ocean. *Global Biogeochem. Cycles* 26:GB1028.

Herraiz-Borreguero, L., and Rintoul, S. R. (2011). Regional circulation and its impact on upper ocean variability south of Tasmania (Australia). *Deep-Sea Res. II* 58, 2071–2081. doi: 10.1016/j.dsr2.2011.05.022

Honda, M. C., and Watanabe, S. (2010). Importance of biogenic opal as ballast of particulate organic carbon (POC) transport and existence of mineral ballast-associated and residual POC in the Western Pacific Subarctic Gyre. *Geophys. Res. Lett.* 37:L02605.

Honjo, S., Francois, R., Manganini, S., Dymond, J., and Collier, R. (2000). Particle fluxes to the interior of the Southern Ocean in the Western Pacific sector along 170°W. *Deep Sea Res. II* 47, 3521–3548. doi: 10.1016/s0967-0645(00)00077-1

Honjo, S., and Manganini, S. J. (1993). Annual biogenic particle fluxes to the interior of the North Atlantic Ocean; studied at 34°N 21°W and 48°N 21°W. *Deep Sea Res. I* 40, 587–607. doi: 10.1016/0967-0645(93)90034-k

Honjo, S., Manganini, S. J., Krishfield, R. A., and Francois, R. (2008). Particulate organic carbon fluxes to the ocean interior and factors controlling the biological pump: a synthesis of global sediment trap programs since 1983. *Progr. Oceanogr.* 76, 217–285. doi: 10.1016/j.pocean.2007.11.003

Jacquet, S., Lam, P., Trull, T., and Dehairs, F. (2011). Carbon export production in the subantarctic zone and polar front zone south of Tasmania. *Deep Sea Res. Part II Top. Stud. Oceanogr.* 58, 2277–2292. doi: 10.1016/j.dsr2.2011.05.035

Johnson, R., Strutton, P. G., Wright, S. W., McMinn, A., and Meiners, K. M. (2013). Three improved satellite chlorophyll algorithms for the Southern Ocean. *J. Geophys. Res. Oceans* 118, 3694–3703.

Johnson, R., and Pacheco, F. (1998-2016). Bermuda atlantic time-series study (BATS) sediment trap data. *Retrieved* 1:2020.

Kim, H., Doney, S. C., Iannuzzi, R. A., Meredith, M. P., Martinson, D. G., and Ducklow, H. W. (2016). Climate forcing for dynamics of dissolved inorganic nutrients at Palmer Station, Antarctica: an interdecadal (1993–2013) analysis. *J. Geophys. Res. Biogeosci.* 121, 2369–2389. doi: 10.1002/2015jg003311

King, A. L., and Howard, W. R. (2003). Planktonic foraminiferal flux seasonality in Subantarctic sediment traps: a test for paleoclimate reconstructions. *Paleoceanography* 18:1019.

Klaas, C., and Archer, D. E. (2002). Association of sinking organic matter with various types of mineral ballast in the deep sea: implications for the rain ratio. *Global Biogeochem. Cycles* 16:14.

Lampitt, R. S., and Antia, A. N. (1997). Particle flux in deep seas: regional characteristics and temporal variability. *Deep Sea Res. I* 44, 1377–1403. doi: 10.1016/s0967-0637(97)00020-4

Lannuzel, D., Bowie, A. R., Lam, P., Townsend, A., Ibisanmi, E., Butler, E., et al. (2011). Distribution of dissolved and particulate iron in the sub-Antarctic and Polar Frontal Southern Ocean (astralian sector). *Deep Sea Res. II* 58, 2094–2112. doi: 10.1016/j.dsr2.2011.05.027

Lee, K., Wanninkhof, R., Takahashi, T., Doney, S. C., and Feely, R. A. (1998). Low interannual variability in recent oceanic uptake of atmospheric carbon dioxide. *Nature* 396, 155–159. doi: 10.1038/24139

Lima, I. D., Lam, P. J., and Doney, S. C. (2014). Dynamics of particulate organic carbon flux in a global ocean model. *Biogeosciences* 11, 1177–1198. doi: 10.5194/bg-11-1177-2014

Lindemann, C., and St John, M. A. (2014). A seasonal diary of phytoplankton in the North Atlantic. *Front. Mar. Sci.* 1:37. doi: 10.3389/fmars.2014.00037

Lourey, M. J., and Trull, T. W. (2001). Seasonal nutrient depletion and carbon export in the subantarctic and polar frontal zones of the Southern Ocean south of Australia. *J. Geophys. RES.* 106, 31463–31487. doi: 10.1029/2000jc000287

Lutz, M. J., Caldeira, K., Dunbar, R. B., and Behrenfeld, M. J. (2007). Seasonal rhythms of net primary production and particulate organic carbon flux to depth describe the efficiency of biological pump in the global ocean. *J. Geophys. Res.* 112:C10011.

Maiti, K., Charette, M. A., Buesseler, K. O., and Kahru, M. (2013). An inverse relationship between production and export efficiency in the Southern Ocean. *Geophys. Res. Lett.* 40, 1557–1561. doi: 10.1002/grl.50219

Manno, C., Giglio, F., Stowasser, G., Fielding, S., Enderlein, P., and Tarling, G. (2018). Threatened species drive the strength of the carbonate pump in the northern Scotia Sea. *Nat. Commun.* 9, 1–7.

Martin, J. H., Knauer, G. A., Karl, D. M., and Broenkow, W. W. (1987). VERTEX: carbon cycling in the northeast Pacific. *Deep-Sea Res.* 34, 267–285. doi: 10.1016/0198-0149(87)90086-0

Meijers, A., Bindoff, N., and Rintoul, S. (2011). Estimating the four-dimensional structure of the Southern Ocean using satellite altimetry. *J. Atmos. Oceanic Technol.* 28, 548–568. doi: 10.1175/2010jtecho790.1

Metzl, N., Tilbrook, B., and Poisson, A. (1999). The annual fCO2 cycel and the air-sea CO2 flux in the sub-Antarctic Ocean. *Tellus Ser. B.* 51, 849–861. doi: 10.1034/j.1600-0889.1999.t01-3-00008.x

Morel, F. M., Rueter, J. G., and Price, N. M. (1991). Iron nutrition of phytoplankton and its possible importance in the ecology of ocean regions with high nutrient and low biomass. *Oceanography* 4, 56–61. doi: 10.5670/oceanog.1991.03

Mouw, C. B., Barnett, A., McKinley, G. A., Gloege, L., and Pilcher, D. (2016). Global ocean particulate organic carbon flux merged with satellite parameters. *Earth Syst. Sci. Data* 8, 531–541. doi: 10.5194/essd-8-531-2016

Moy, A. D., Howard, W. R., Bray, S. G., and Trull, T. W. (2009). Reduced calcification in modern Southern Ocean planktonic foraminifera. *Nat. Geosci.* 2, 276–280. doi: 10.1038/ngeo460

Nodder, S. D., Chiswell, S. M., and Northcote, L. C. (2016). Annual cycles of deep-ocean biogeochemical export fluxes in subtropical and subantarctic waters, southwest Pacific Ocean. *J. Geophys. Res.* 121, 2405–2424. doi: 10.1002/2015jc011243

Orr, J. C., Fabry, V. J., Aumont, O., Bopp, L., Doney, S. C., and Feely, R. A. (2005). Anthropogenic ocean acidification over the twenty-first century and its impact on calcifying organisms. *Nature* 437, 681–696.

Redfield, A. C. (1963). The influence of organisms on the composition of seawater. *Sea* 2, 26–77.

Rees, C., Lindsay, P., Sherrin, K., Schwanger, C., Hughes, P., Tibben, S., et al. (2018). Methods for reproducible shipboard SFA nutrient measurement using RMNS and automated data processing. *Limnol. Oceanogr. Methods* 17, 25–41.

Rigual Hernández, A. S., Trull, T. W., Nodder, S. D., Flores, J. A., Bostock, H., Abrantes, F., et al. (2019). Coccolithophore biodiversity controls carbonate export in the Southern Ocean. *Biogeosci. Discuss.* 17, 245–263. doi: 10.5194/bg-17-245-2020

Rigual-Hernández, A., Trull, T., Bray, S., Cortina, A., and Armand, L. (2015). Latitudinal and temporal distributions of diatom populations in the pelagic waters of the Subantarctic and Polar Frontal zones of the Southern Ocean and

their role in the biological pump. *Biogeosciences* 12, 5309–5337. doi: 10.5194/bg-12-5309-2015

Rigual-Hernández, A., Trull, T., Flores, J., Nodder, S., Eriksen, R., Davies, D., et al. (2020). Full annual monitoring of Subantarctic Emiliania huxleyi populations reveals highly calcified morphotypes in high-CO2 winter conditions. *Sci. Rep.* 10, 1–14.

Rintoul, S. R., and Trull, T. W. (2001). Seasonal evolution of the mixed layer in the Subantarctic Zone south of Australia. *J. Geophys. Res. Oceans* 106, 31447–31462. doi: 10.1029/2000jc000329

Roberts, D., Hopcroft, R. R., and Hosie, G. W. (2014). "6.4. southern ocean pteropods," in *Biogeographic Atlas of the Southern Ocean*, Vol. XII, eds C. De Broyer, P. Koubbi, H. J. Griffiths, et al. (Cambridge: Scientific Committee on Antarctic Research), 276–283.

Rost, B., and Riebesell, U. (2004). *Coccolithophores and the Biological Pump: Responses to Environmental Changes. Coccolithophores*. Berlin: Springer, 99–125.

Salter, I., Schiebel, R., Ziveri, P., Movellan, A., Lampitt, R., and Wolff, G. A. (2014). Carbonate counter pump stimulated by natural iron fertilization in the Polar Frontal Zone. *Nat. Geosci.* 7, 885–889. doi: 10.1038/ngeo2285

Sarmiento, J. L., Hughes, T. M. C., Stouffer, R. J., and Manabe, S. (1998). Simulated response of the ocean carbon cycle to anthropogenic climate warming. *Nature* 393, 245–249. doi: 10.1038/30455

Sarmiento, J. L., and LeQuere, C. (1996). Oceanic carbon dioxide uptake in a model of century-scale global warming. *Science* 274, 1346–1350. doi: 10.1126/science.274.5291.1346

Schlunegger, S., Rodgers, K. B., Sarmiento, J. L., Frölicher, T. L., Dunne, J. P., Ishii, M., et al. (2019). Emergence of anthropogenic signals in the ocean carbon cycle. *Nat. Clim. Change* 9, 719–725. doi: 10.1038/s41558-019-0553-2

Schneider, B., Schlitzer, R., Fischer, G., and Nöthig, E. M. (2003). Depth-dependent elemental compositions of particulate organic matter (POM) in the ocean. *Global Biogeochem. Cycles* 17, 1–16.

Shadwick, E. H., Trull, T. W., Tilbrook, B., Sutton, A. J., Schulz, E., and Sabine, C. L. (2015). Seasonality of biological and physical controls on surface ocean CO2 from hourly observations at the Southern Ocean Time Series site south of Australia . *Global Biogeochem. Cycles* 29, 1–16.

Shaffer, G. (1993). *Effects of the Marine Carbon Biota on Global Carbon Cycling. The Global Carbon Cycle*, *eds M. Heimann*. New York, NY: Springer-Verlag, 431–435.

Siegel, D. A., Granata, T. C., Michaels, A. F., and Dickey, T. D. (1990). Mesoscale eddy diffusion, particle sinking, and the interpretation of sediment trap data. *J. Geophys. Res. Oceans* 95, 5305–5311.

Sigman, D. M., and Boyle, E. A. (2000). Glacial/Interglacial variations in atmospheric carbon dioxide. *Nature* 407, 859–869. doi: 10.1038/35038000

Suess, E. (1980). Particulate organic carbon flux in the oceans—surface productivity and oxygen utilization. *Nature* 288, 260–263. doi: 10.1038/288260a0

Thompson, P., and McDonald, K. (2020). "Spatial and seasonal trends in net primary production," in *State and Trends of Australia's Ocean Report*, eds A. J. Richardson, R. Eriksen, T. Moltmann, I. Hodgson-Johnston, and J. R. Wallis (Hobart: Integrated Marine Observing System), 1–5.

Thompson, P., Antoine, D., and King, E. (2020). "Spatial and seasonal trends in chlorophyll *a*," in *State and Trends of Australia's Ocean Report*, eds A. J. Richardson, R. Eriksen, T. Moltmann, I. Hodgson-Johnston, and J. R. Wallis (Hobart: Integrated Marine Observing System), 1–5.

Trinh, R., and Ducklow, H. (2018). "Years of particle export in west antarctic peninsula coastal waters," in *Proceedings from Polar 2018 A SCAR & IASC Conference*, Davos.

Trull, T., Rintoul, S. R., Hadfield, M., and Abraham, E. R. (2001a). Circulation and seasonal evolution of polar waters south of Australia: implications for iron fertilization of the Southern Ocean. *Deep Sea Res. Part II Top. Stud. Oceanogr.* 48, 2439–2466. doi: 10.1016/s0967-0645(01)00003-0

Trull, T. W., Bray, S. G., Manganini, S. J., Honjo, S., and Francois, R. (2001b). Moored sediment trap measurements of carbon export in the Subantarctic and Polar Frontal Zones of the Southern Ocean, south of Australia. *J. Geophys. Res.* 106, 31489–31506.

Trull, T. W., Sedwick, P. N., Griffiths, F. B., and Rintoul, S. R. (2001c). Introduction to special edition: SAZ Project. *J. Geophys. Res.* 106, 31425–31429. doi: 10.1029/2001jc001008

Trull, T. W., Bray, S. G., Buesseler, K. O., Lamborg, C. H., Manganini, S. J., Moy, C., et al. (2008). In situ measurements of mesopelagic particle sinking rates and the control of carbon transfer to the ocean interior during the Vertical Flux in the Global Ocean (VERTIGO) voyages in the North Pacific. *Deep-Sea Res. II* 55, 1684–1695. doi: 10.1016/j.dsr2.2008.04.021

Trull, T. W., Jansen, P., Schulz, E., Weeding, B., Davies, D. M., and Bray, S. G. (2019). Autonomous multi-trophic observations of productivity and export at the Australian Southern Ocean Time Series (SOTS) reveal sequential mechanisms of physical-biological coupling. *Front. Mar. Sci.* 6:525. doi: 10.3389/fmars.2019.00525

Trull, T. W., Passmore, A., Davies, D. M., Smit, T., Berry, K., and Tilbrook, B. (2018). Distribution of planktonic biogenic carbonate organisms in the Southern Ocean south of Australia: a baseline for ocean acidification impact assessment. *Biogeosciences* 15, 31–49. doi: 10.5194/bg-15-31-2018

Volk, T., and Hoffert, M. I. (1985). *Ocean Carbon Pumps: Analysis of Relative Strengths and Efficiencies in Ocean-Driven Atmospheric CO2 Changes. The Carbon Cyclen and Atmospheric CO2: Natural variations archean to present, eds E. Sundquist and W.S. Broecker*. Washington, DC: AGU, 99–110.

Weber, T., Cram, J. A., Leung, S. W., DeVries, T., and Deutsch, C. (2016). Deep ocean nutrients imply large latitudinal variation in particle transfer efficiency. *Proc. Natl. Acad. Sci. U.S.A.* 113, 8606–8611. doi: 10.1073/pnas.1604414113

Weeding, B., and Trull, T. W. (2014). Hourly oxygen and total gas tension measurements at the Southern Ocean Time Series site reveal winter ventilation and spring net community production. *J. Geophys. Res. Oceans* 119, 348–358. doi: 10.1002/2013jc009302

Wong, C., Whitney, F., Crawford, D., Iseki, K., Matear, R., Johnson, W., et al. (1999). Seasonal and interannual variability in particle fluxes of carbon, nitrogen and silicon from time series of sediment traps at Ocean Station P, 1982–1993: relationship to changes in subarctic primary productivity. *Deep Sea Res. Part II Top. Stud. Oceanogr.* 46, 2735–2760. doi: 10.1016/s0967-0645(99)00082-x

Wynn-Edwards, C. A., Davies, D. M., Jansen, P., Bray, S. G., Eriksen, R., and Trull, T. W. (2019). *Southern Ocean Time Series. SOTS Annual Reports: 2012/2013. Report 2. Samples. IMOS – ABOS Southern Ocean Time Series (SOTS) – Annual Reports*. Canberra: CSIRO. Available online at: https://catalogue-imos.aodn.org.au/geonetwork/srv/api/records/afc166ce-6b34-44d9-b64c-8bb10fd43a07

Wynn-Edwards, C. A., Davies, D. M., Shadwick, E. H., and Trull, T. W. (2020). *Southern Ocean Time Series. SOTS Quality assessment and control report. Sediment trap particle fluxes Version* 1.0. *IMOS – Integrated Marine Observing System*. Canberra: CSIRO.

Yoder, J. A., and Kennelly, M. A. (2003). Seasonal and ENSO variability in global ocean phytoplankton chlorophyll derived from 4 years of SeaWiFS measurements. *Global Biogeochem. Cycles* 17:1112.

Yu, E.-F., Francois, R., Bacon, M. P., Honjo, S., Fleer, A. P., Manganini, S. J., et al. (2001). Trapping efficiency of bottom-tethered sediment traps estimated from the intercepted fluxes of 230Th and 231Pa. *Deep-Sea Res. Part* 1, 865–889. doi: 10.1016/s0967-0637(00)00067-4

Conflict of Interest: The authors declare that the research was conducted in the absence of any commercial or financial relationships that could be construed as a potential conflict of interest.

frontiers in Earth Science

ORIGINAL RESEARCH
published: 26 August 2020
doi: 10.3389/feart.2020.00349

Variability in Water-Column Respiration and Its Dependence on Organic Carbon Sources in the Canary Current Upwelling Region

Javier Arístegui[1], María F. Montero[1], Nauzet Hernández-Hernández[1], Iván J. Alonso-González[2], Federico Baltar[3], Maria Ll. Calleja[4] and Carlos M. Duarte[5]*

[1] Instituto de Oceanografía y Cambio Global, IOCAG, Universidad de Las Palmas de Gran Canaria, Las Palmas de Gran Canaria, Spain, [2] OCEOMIC, Marine Bio and Technology S.L., Parque Tecnológico de Fuerteventura, Puerto del Rosario, Spain, [3] Department of Functional and Evolutionary Ecology, University of Vienna, Vienna, Austria, [4] Department of Climate Geochemistry, Max Planck Institute for Chemistry, Mainz, Germany, [5] Red Sea Research Center and Computational Bioscience Research Center, King Abdullah University of Science and Technology, Thuwal, Saudi Arabia

OPEN ACCESS

Edited by:
Rut Pedrosa Pàmies, Marine Biological Laboratory (MBL), United States

Reviewed by:
Dennis Arthur Hansell, University of Miami, United States
Craig Alexander Carlson, University of California, Santa Barbara, United States

***Correspondence:**
Javier Arístegui
javier.aristegui@ulpgc.es

Specialty section:
This article was submitted to Biogeoscience, a section of the journal Frontiers in Earth Science

Received: *28 April 2020*
Accepted: *27 July 2020*
Published: *26 August 2020*

Citation:
Arístegui J, Montero MF, Hernández-Hernández N, Alonso-González IJ, Baltar F, Calleja ML and Duarte CM (2020) Variability in Water-Column Respiration and Its Dependence on Organic Carbon Sources in the Canary Current Upwelling Region. Front. Earth Sci. 8:349. doi: 10.3389/feart.2020.00349

Plankton respiration (R) is a key factor governing the ocean carbon cycle. However, although the ocean supports respiratory activity throughout its entire volume, to our knowledge there are no studies that tackle both the spatial and temporal variability of respiration in the dark ocean and its dependence on organic carbon sources. Here, we have studied the variability of epipelagic and mesopelagic R via the enzymatic activity of the electron transport system (ETS) in microbial communities, along two zonal sections (21°N and 26°N) extending from the northwest African coastal upwelling to the open-ocean waters of the North Atlantic subtropical gyre, during the fall 2002 and the spring 2003. Overall, integrated R in epipelagic (R_{epi}; 0–200 m) waters, was similar during the two periods, while integrated mesopelagic respiration (R_{meso}; 200–1000 m) was >25% higher in the fall. The two seasons, however, exhibited contrasting zonal and meridional patterns of ETS distribution in the water column, largely influenced by upwelling effects and associated mesoscale variability. Multiple linear regression between average R and average concentrations of dissolved organic carbon (DOC) and slow-sinking (suspended) particulate organic carbon (POC_{sus}) indicates that POC_{sus} is the main contributor to R_{meso}, supporting previous results in the same area. R_{meso} exceeded satellite-derived net primary production (NPP) at all stations except at the most coastal ones, with the imbalance increasing offshore. Moreover, the export flux of sinking POC collected at 200 m with sediment traps, represented on average less than 6% of the NPP. All this indicates that R_{meso} depends largely on small particles with low sinking rates, which would be laterally advected at mid water depths from the continental margin toward the open ocean, or transported by mesoscale features from the surface to the mesopelagic ocean, providing support to inferences from modeling studies in the region.

Keywords: mesopelagic respiration variability, ETS activity, suspended and sinking particulate organic carbon, dissolved organic carbon, Canary Current upwelling region

INTRODUCTION

Microplankton (<200 μm) respiration is one of the main metabolic processes controlling the organic carbon cycle in the ocean. The classical view of the biological pump considers that organic matter synthesized in the ocean is mostly respired by microplankton within surface waters, leaving a small surplus of organic matter to be transported vertically into the dark ocean. However, in contrast to this prevailing 1D conceptualization of organic carbon supply to the dark ocean, several studies have shown that lateral particulate organic carbon (POC) inputs from the ocean margins to the ocean interior could be more than an order of magnitude greater than inputs of vertically transported organic carbon derived from the surface (e.g., Bauer and Druffel, 1998; Alonso-González et al., 2009). These lateral inputs of organic matter would be particularly intense within eastern boundary currents (EBC), because of the high productivity of the nearby upwelling regions (Lovecchio et al., 2017) and the importance of horizontal advective processes in upwelling systems.

The Canary Current (CanC) is one of the four main EBC. Past studies in the coastal transition zone of this EBC have shown that upwelling filaments may transport offshore up to 50% of the carbon originated by primary production in the coastal upwelling (García-Muñoz et al., 2004, 2005; Santana-Falcón et al., 2017, 2020), accounting for 2.5–4.5 times the offshore carbon export driven by Ekman transport (Álvarez-Salgado et al., 2007) and up to 80% of the total offshore carbon flux (Lovecchio et al., 2018). Most of this exported carbon takes place at surface as semi-labile dissolved material (DOC). Nevertheless, it has been estimated that <20% of this DOC is respired in the coastal transition zone waters (Álvarez-Salgado et al., 2007), the remainder being transported and accumulated in the subtropical gyre (Hansell, 2002). In the mesopelagic zone, however, the off-shelf carbon transport is thought to be mainly supported by suspended particles transported in a prevailing horizontal direction along density gradients (e.g., Alonso-González et al., 2009; Vilas et al., 2009), except in regions of water mass subduction (Santana-Falcón et al., 2017), since the strong surface stratification limits semi-labile DOC mixing from surface waters to the deep ocean. Indeed, Alonso-González et al. (2009) estimated, through a box-model approach, that slow-sinking POC in the mesopelagic zone of the CanC may account for up to 60% of the total mesopelagic respiration during a low productivity period of the annual cycle. They suggested that a large fraction of this POC may originate in the nearby coastal upwelling region or be transported to depth by mesoscale eddies, being respired in the upper 1000 m of the CanC. However, limited information on the temporal and spatial variability of water-column respiration and its dependence on carbon sources in this EBC, as well as in any other EBC, have precluded empirical testing of the inferences derived from models.

We hypothesize that a significant fraction of the R_{meso} will be supported by laterally advected POC due to the intense mesoscale activity characteristic of this and other EBC. To test this hypothesis, we characterized the spatial and temporal variability of microplankton respiration (R) in the CanC region, and quantify the contribution of both DOC and POC to R in the water column. We do so on the basis of results from two cruises that took place in the CanC from September 10 to October 1, 2002 (COCA I) and from May 21 to June 7, 2003 (COCA II), in a region affected by a strong mesoscale activity (Arístegui et al., 2004, 2009; Baltar et al., 2009a). We measured microplankton respiratory activity (ETS activity), as well as dissolved (DOC) and slow-sinking (suspended) particulate organic carbon (POC_{sus}) down to 1000 m, at 10 stations placed along two sections extending from the African coast to the open ocean. Moreover, sinking POC was collected with free-floating sediment traps at the same stations.

MATERIALS AND METHODS

Data Sources

The study was conducted along two zonal sections (21°N and 26°N) extending from the coastal upwelling to the open ocean at 26°W (**Figure 1**), and focused on the epipelagic (0–200 m) and mesopelagic (200–1000 m) zones, where microplankton contributes on a global average to > 90% of water column respiration (Arístegui et al., 2005). The cruises consisted of a total of 31 hydrographic stations and 10 biogeochemical stations, half of them along each section, which were roughly equidistant. At each station, conductivity, temperature and depth were determined by means of a Seabird 911 + CTD, mounted on a General Oceanics rosette sampler equipped with 24 10L-Niskin bottles, lowered down to 1000 m. Seawater samples were collected at fixed depths in the biogeochemical stations every 50 m for POC_{sus}, DOC and ETS activity. Free-drifting sediment traps were deployed for 24 h at each biogeochemical station to collect sinking particles at 200 m depth.

DOC Analysis

Water samples for dissolved organic carbon (DOC) were passed through an online acid-cleaned polycarbonate filter cartridge, holding a pre-combusted (500°C, 12 h) GF/F filter. The initial filtrate was discarded and the subsequent filtrate was dispensed into 10 ml glass ampoules pre-combusted likewise. 50 μL of H_3PO_4 was added immediately to the sample, sealed and stored at 4°C until analyzed with a Shimadzu TOC-5000 analyzer (Sharp et al., 1993). Before analysis, samples were sparged with CO_2-free air for several minutes to remove inorganic carbon. DOC concentrations were determined from standard curves (30–200 μM) of potassium hydrogen phthalate produced every day (Thomas et al., 1995). To check accuracy and precision, reference material of deep-sea water (DSW, 42–45 μmol C L^{-1}) and low carbon water (LCW, 1–2 μmol C L^{-1}) provided by D. A. Hansell laboratory (University of Miami) was analyzed daily.

POC Analysis for Water Samples (POC_{sus}) and Particles Collected With Sediment Traps

Water samples (2–4 L) for the analysis of POC_{sus} were filtered onto pre-combusted (450°C, 12 h), 25-mm Whatman GF/F

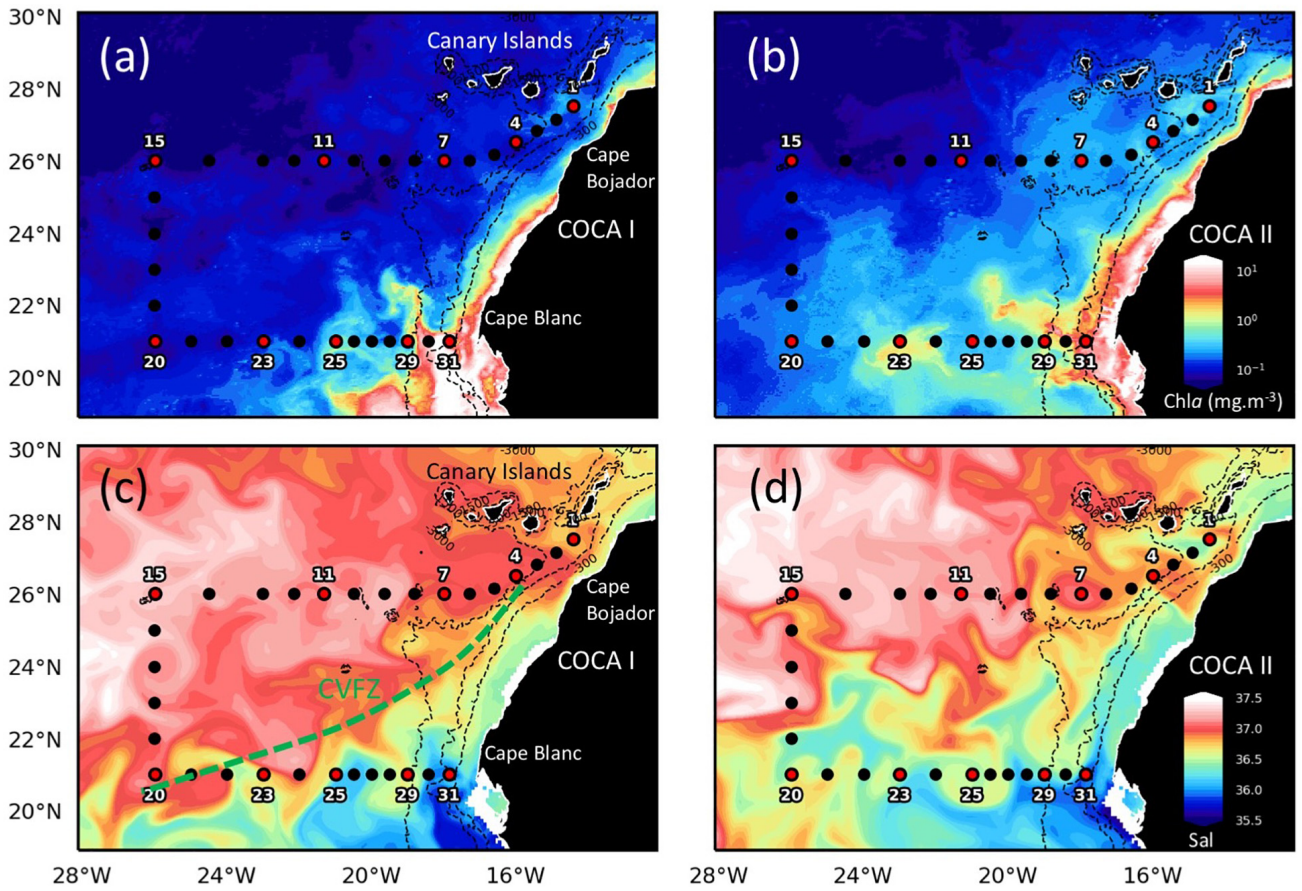

FIGURE 1 | Maps of surface chlorophyll (**a,b**; Chl*a*, mg m^{-3}) and salinity at 25 m depth (**c,d**; Sal) indicating stations' location along two sections (21°N and 26°N), extending from the NW African coast to the open ocean, during cruises COCA I (fall, 2002) and COCA II (spring, 2003). Black dots indicate CTD stations. Red dots with numbers indicate biogeochemical stations. The dashed green line represents the Cape Verde Frontal Zone (CVFZ), the boundary between North and South Atlantic Central Waters. Notice the northward displacement of the coastal upwelling and the CVFZ during the spring. Chlorophyll satellite observations for September 27, 2002 (COCA I) and May 31, 2003 (COCA II) were obtained from Global Ocean Satellite Observations. The images are based on the merging of the sensors SeaWiFS, MODIS, MERIS, VIIRS-SNPP&JPSS1 and OLCI-S3A&S3B. Salinity maps were plotted for the same dates, from numerical reanalysis, model NEMO (resolution 8 km), obtained from Copernicus Marine Environment Monitoring Services (CMEMS).

filters. For the measurement of sinking POC, particles were collected using a free-drifting multi-trap array holding eight cylinders (9 cm diameter: 50 cm length and 0.005 m^2 collection area), similar to the model described by Knauer et al. (1979). NaCl (∼45 g L^{-1}; analytical reagent-grade) was added to increase the salinity inside the traps in order to reach a high-density water. No poisons were used to retard bacterial decomposition. Upon recovery 24 h after deployment, samples were filtered onto pre-combusted (450°C, 12 h), 25 mm Whatman GF/F filters. Large swimming organisms were removed by wet sieving through a 1 mm nylon mesh, while organisms <1 mm were hand- picked under a microscope with fine-tweezers after filtration. All the filters for POC were wrapped in pre-combusted aluminum foil and frozen at −20°C until processed. In the laboratory the filters were thawed and dried overnight at 60°C, then placed overnight in a desiccator saturated with HCl fumes, dried again in a new desiccator with silica gel and packed in pre-combusted nickel sleeves. The carbon analyses were carried out on a Perkin–Elmer 2400 CHN elemental analyzer (UNESCO, 1994). The DOC adsorption onto GF/F filters (<12% of the POC signal) was subtracted from the samples to avoid overestimation of POC (Turnewitsch et al., 2007). For this, we analyzed blank filters in which water filtered by 0.4 μm pore was re-filtered through a pre-combusted 25 mm GF/F filter.

Respiratory Electron Transport System (ETS) Activity and Conversions to Actual Respiration Rates

Pre-filtered (<200 μm) seawater samples (10–20 L) were filtered through 47-mm Whatman GF/F glass-fiber filters at a low vacuum pressure (<0.3 atm). The filters were immediately stored in liquid nitrogen until being assayed in the laboratory within a few weeks. ETS determinations were carried out according to the Kenner and Ahmed (1975) modification of the tetrazolium reduction technique proposed by Packard (1971)

as described in Arístegui and Montero (1995). The frozen filters were mechanically ground for 2 min by means of a drill equipped with a teflon bit in 5 ml of a cold homogenization buffer. The homogenate was centrifuged at 14,000 r.p.m. for 15 min at 0–3°C. An incubation time of 20 min at 18°C was selected from an earlier time and temperature kinetic study. ETS activities measured at 18°C were converted to activities at *in situ* temperatures by using the Arrhenius equation. A calculated mean activation energy of 16 kcal mol^{-1} was used. This activation energy value is similar to those obtained from other studies in oceanic regions (Arístegui and Montero, 1995).

Respiration rates in the epipelagic (R_{epi}) were derived from temperature-corrected ETS activity applying the regression equation between R and ETS obtained by Arístegui and Montero (1995) for the global surface ocean. Respiration rates in the mesopelagic zone (R_{meso}) were estimated by applying a R:ETS of 0.68, as obtained by Arístegui et al. (2005) in experiments performed with mesopelagic communities during COCA II. This ratio lies in the range of the ratios (R:ETS = 1.1, range = 0.6–1.7) observed by Christensen et al. (1980) for bacteria cultures during their exponential growth phase, being about 7–8 times higher that the ratio observed for the same cultures when reaching the senescent phase. This gives evidence that bacteria in the mesopelagic waters of the CanC were actively growing. To convert oxygen to carbon units we used respiratory quotients (RQ = CO_2 per O_2 by moles) of 0.719 and 0.645, estimated for the epipelagic and mesopelagic zones of this region, respectively (Fernández-Castro et al., 2019).

Satellite-Derived Net Primary Production (NPP)

Net primary production estimates at each station were obtained from the Eppley modified version of the Vertically Generalized Production Model (VGPM-Eppley; Behrenfeld and Falkowski, 1997). Eight-day averaged estimation with a 1/12° spatial resolution provided by the Oregon State University (OSU)[1] were used. MODIS-aqua satellite-derived chlorophyll was selected as model input.

Data Analysis

In order to determine which source of organic matter (POC_{sus} or DOC) present higher influence over R in the different zones (epipelagic and mesopelagic), multiple linear regression analysis was applied. Residuals from every model were tested for normality (Shapiro-Wilk test), homoscedasticity (Q-Q plots) and multicollinearity (Variance Inflation Factors, VIF). Following, the relative importance contribution (RI,%) of each predictor to the total explained variance (R^2) of each model was calculated using the Lindeman, Merenda and Gold method (LMG; Lindeman et al., 1980). All paired comparisons were statistically tested by means of a Welch's *t*-test. The confidence level was set at 95% ($p = 0.05$). All statistical analyses were performed with R-software[2].

[1]http://www.science.oregonstate.edu/ocean.productivity/

[2]http://www.r-project.org

RESULTS

Regional Oceanographic Settings

The two surveyed sections stretched across an area of high mesoscale variability, spanning from the NW Africa coastal upwelling region to >500 miles offshore into the subtropical open ocean waters of the CanC (**Figure 1**). The 21°N section intersected the Cape Verde Frontal Zone (CVFZ), the inner boundary of the CanC, characterized by the presence of numerous meanders and eddies, resulting from the interaction of high-salinity (>36.5) North Atlantic Central Water (NACW) and low-salinity (<36.5) South Atlantic Central Water (SACW). As a result, patches of high and low temperature and salinity waters are observed across this section in the upper 500 m (**Figures 1–3**). The 26°N section was placed north of the CVFZ and hence was entirely affected by NACW. Several upwelling filaments and mesoscale eddies were observed stretching off the coastal jet of the upwelling region, with the most intense at Cape Blanc (**Figure 1**). During the spring, the location of the CVFZ shifted to the north with respect to the fall, and the coastal upwelling was displaced and intensified northwards. Moreover, surface chlorophyll *a* (Chl*a*) was higher in the spring than in the fall, particularly in open ocean waters (**Figures 1a,b**). A detailed description on the hydrography, circulation and mass transport in the region of study during the two cruises is described in Burgoa et al. (2020).

Spatial and Temporal Variability in Respiratory Activity

Coastal-offshore sections of ETS activity for the two periods are shown in **Figure 4**. The epipelagic waters exhibited contrasting meridional and zonal patterns of distribution. ETS activity presented high values in the epipelagic waters (consuming 32.3 ± 26.0 and 36.4 ± 23.3 μmol O_2 m^{-3} h^{-1} in the fall and the spring, respectively). ETS activity decreased with depth, although relative peaks were frequently observed in the mesopelagic zone, exceeding 10 μmol O_2 m^{-3} h^{-1}. At 21°N (**Figures 4b,d**), epipelagic ETS was highest at the two most coastal stations, due to the intense upwelling at the Cape Blanc region, decreasing toward the open ocean, although zonal variability across the CVFZ favored patchiness of lower and higher ETS associated with intrusions of water from the Cape Blanc filament. In contrast, at 26°N the surface open-ocean waters of the most distant stations presented a two to fivefold higher ETS activity (in the spring and the fall, respectively) compared to the two stations closer to the upwelling region (**Figures 4a,c**). The averaged integrated values in the epipelagic zone were always higher at 21°N than at 26°N (**Table 1**), but the differences were not significant due to the large zonal variability.

In contrast to the epipelagic, ETS activity in the mesopelagic zone did not display a clear meridional trend, in contrast to the epipelagic layer (**Figure 4**). However, averaged integrated ETS rates for the mesopelagic showed significantly ($p < 0.01$) higher values in the fall than in the spring at

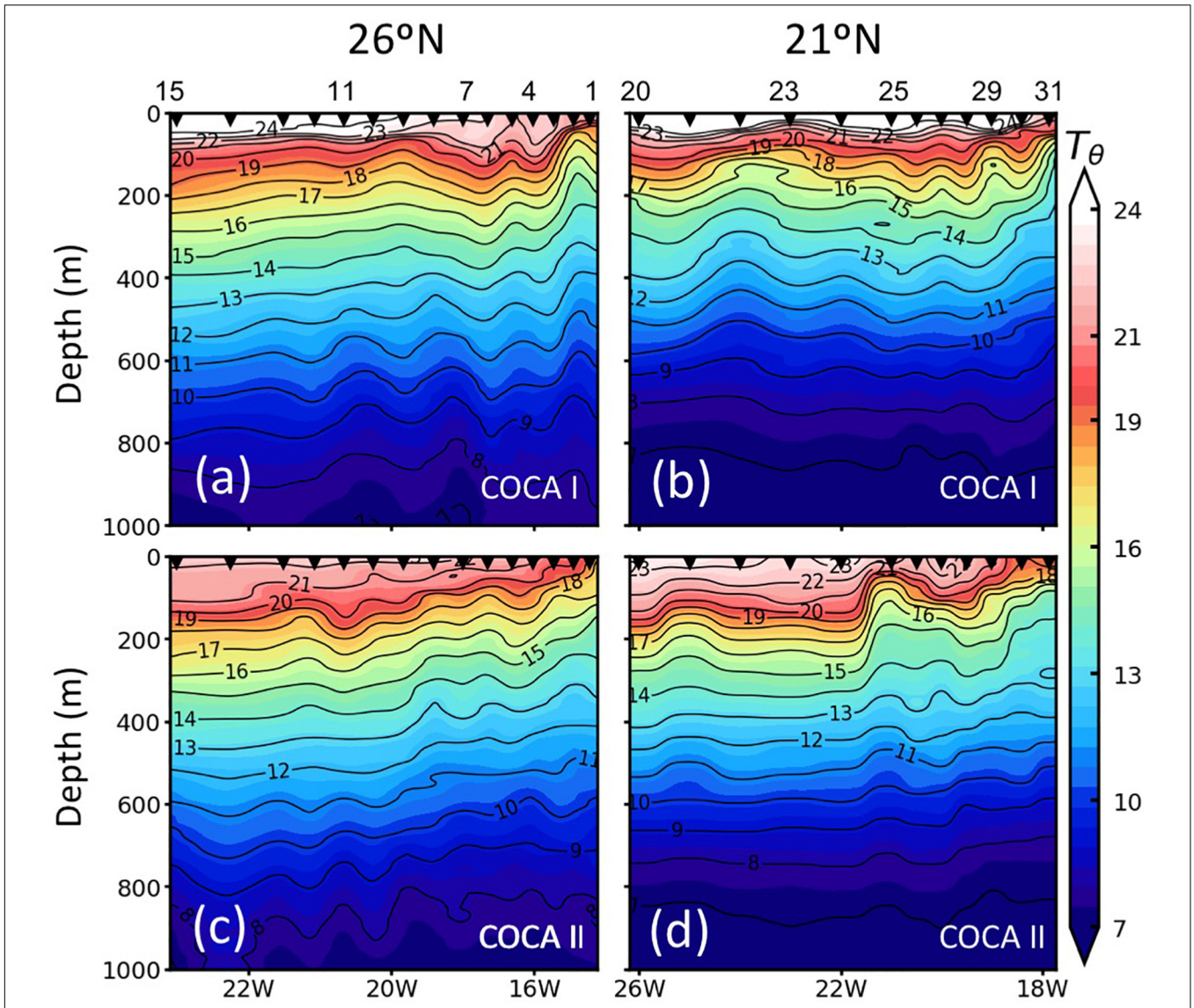

FIGURE 2 | Vertical distribution (0–1000 m) of potential temperature (Tθ;°C) along the two sections (21°N and 26°N), during cruises COCA I **(a,b)** and COCA II **(c,d)**.

21°N (**Table 1**), coinciding also with significantly higher DOC concentrations (see below).

DOC and POC Distribution and Contribution to Water Column Respiration

The depth distribution of average POC_{sus} concentrations in the mesopelagic followed a similar pattern as the ETS activity, suggesting that this pool of organic matter was a main substrate supporting respiratory activity (**Figure 5**). Nevertheless, POC_{sus} did not decrease exponentially with depth, as would be expected due to carbon remineralization of sinking material under the conventional assumption of 1D (vertical) dominance of transport, but rather showed similar high concentrations (>5 μM) across the mesopelagic zone; sometimes even higher than in the epipelagic zone (**Figure 5**). Average integrated values of POC_{sus} presented meridional and temporal variability (**Table 2**). In the epipelagic zone POC_{sus} was significantly higher at 21°N during the fall, while at 26°N it was higher in the spring than in the fall. In the mesopelagic zone POC_{sus} was however significantly higher at 21°N during the spring.

DOC concentrations generally decreased with depth, although average integrated values (0–200 m and 200–1000 m) were significantly higher at 21°N during the fall than at 26°N in the same period, and higher than at the two sections in the spring (**Table 2**). Nevertheless, despite these differences in DOC concentrations between the two cruises (>8 mmol C m^{-2} d^{-1} for the epipelagic and >25 mmol C m^{-2} d^{-1} for the mesopelagic), multiple regression analyses of R, POC_{sus} and DOC (**Table 3**) indicate that the relative importance (RI,%) of POC_{sus} to R

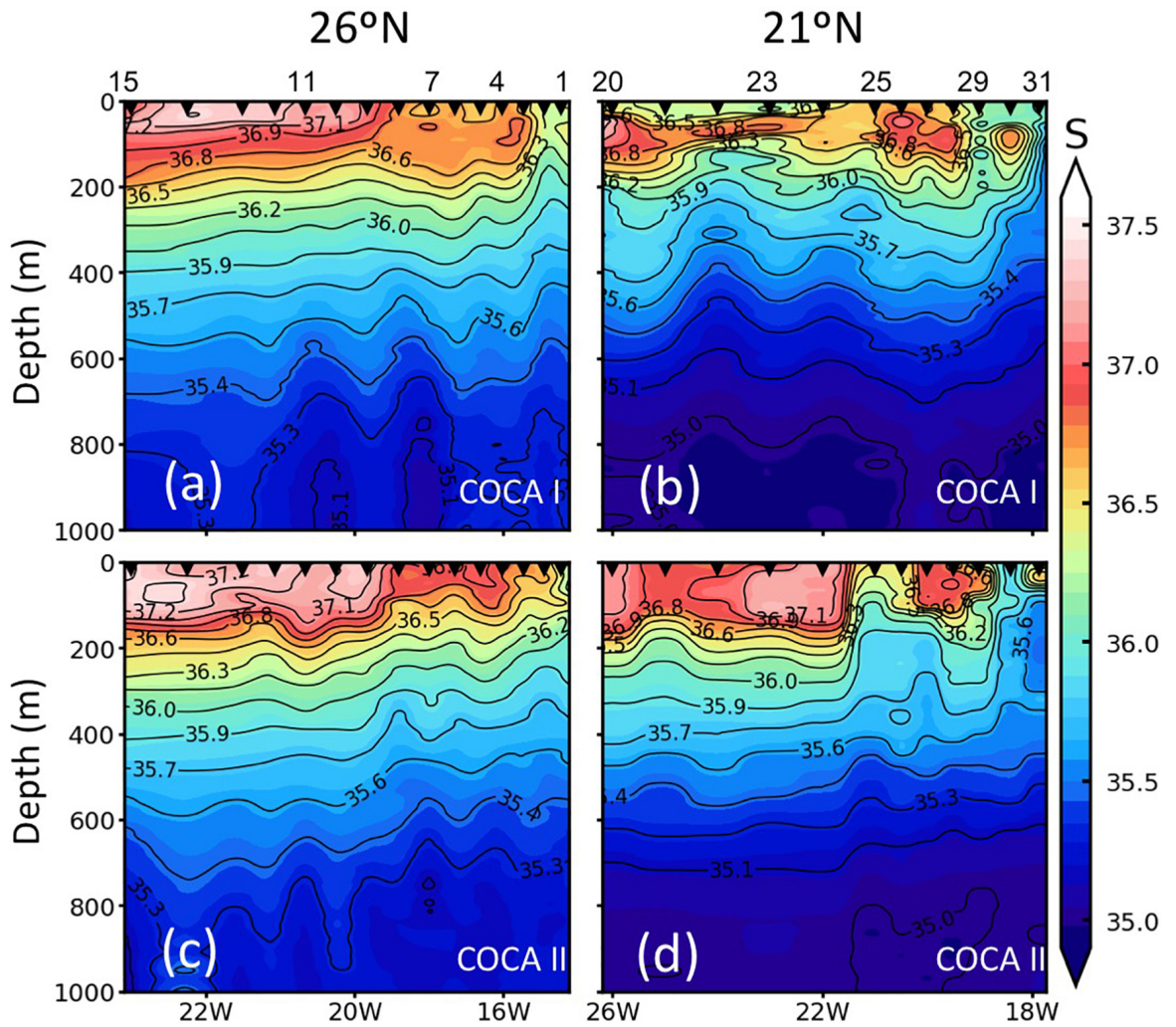

FIGURE 3 | Vertical distribution (0–1000 m) of salinity (S) along the two sections (21°N and 26°N), during the COCA I **(a,b)** and COCA II **(c,d)**.

was always higher than of DOC, both in the epipelagic and mesopelagic zones.

DISCUSSION

Epipelagic Respiration

Average integrated epipelagic R rates in this study (75–125 mmol C m^{-2} d^{-1}) are higher than those reported from open ocean waters of the CanC north of the Canary Islands (<60 mmol C m^{-2} d^{-1}; Arístegui and Harrison, 2002; Fernández-Castro et al., 2016), but similar to those previously estimated for the coastal transition zone of the CanC (60–120 mmol C m^{-2} d^{-1}; Arístegui et al., 2003b). The high epipelagic R coincides with high POC concentrations in the two studies south of the islands (**Table 2**; Arístegui et al., 2003b). The epipelagic average integrated values of POC_{sus} in these two studies (>1 mol C m^{-2}) are also significantly higher than values observed in previous studies at the ESTOC station, north of the Canary Archipelago (Neuer et al., 2007), or in the more oceanic sector of the CanC (Alonso-González et al., 2009).

POC inputs to the epipelagic zone in our region of study can be due to local primary production or lateral advection from the coast. Stations closer to the coastal upwelling present NPP values up to 10 times higher than in the open ocean (**Table 4**), although epipelagic R is sometimes higher in the open ocean and clearly exceeds NPP (**Figure 4**). Therefore, in addition to the *in situ* production rates, the high respiratory activity needs be supported by horizontal inputs of coastal organic matter, consistent with existing modeling predictions. Indeed, offshore POC and DOC transports from the continental margin by upwelling filaments in this region have been reported, from both observational (Gabric et al., 1993; García-Muñoz et al., 2004, 2005; Santana-Falcón et al., 2017) and modeling (Lovecchio et al., 2017, 2018; Santana-Falcón et al., 2020) studies, representing an important carbon source to the open ocean, reaching up to 50% of the NPP in the coastal upwelling (Álvarez-Salgado et al., 2007). This offshore export would explain former studies carried out in this same area

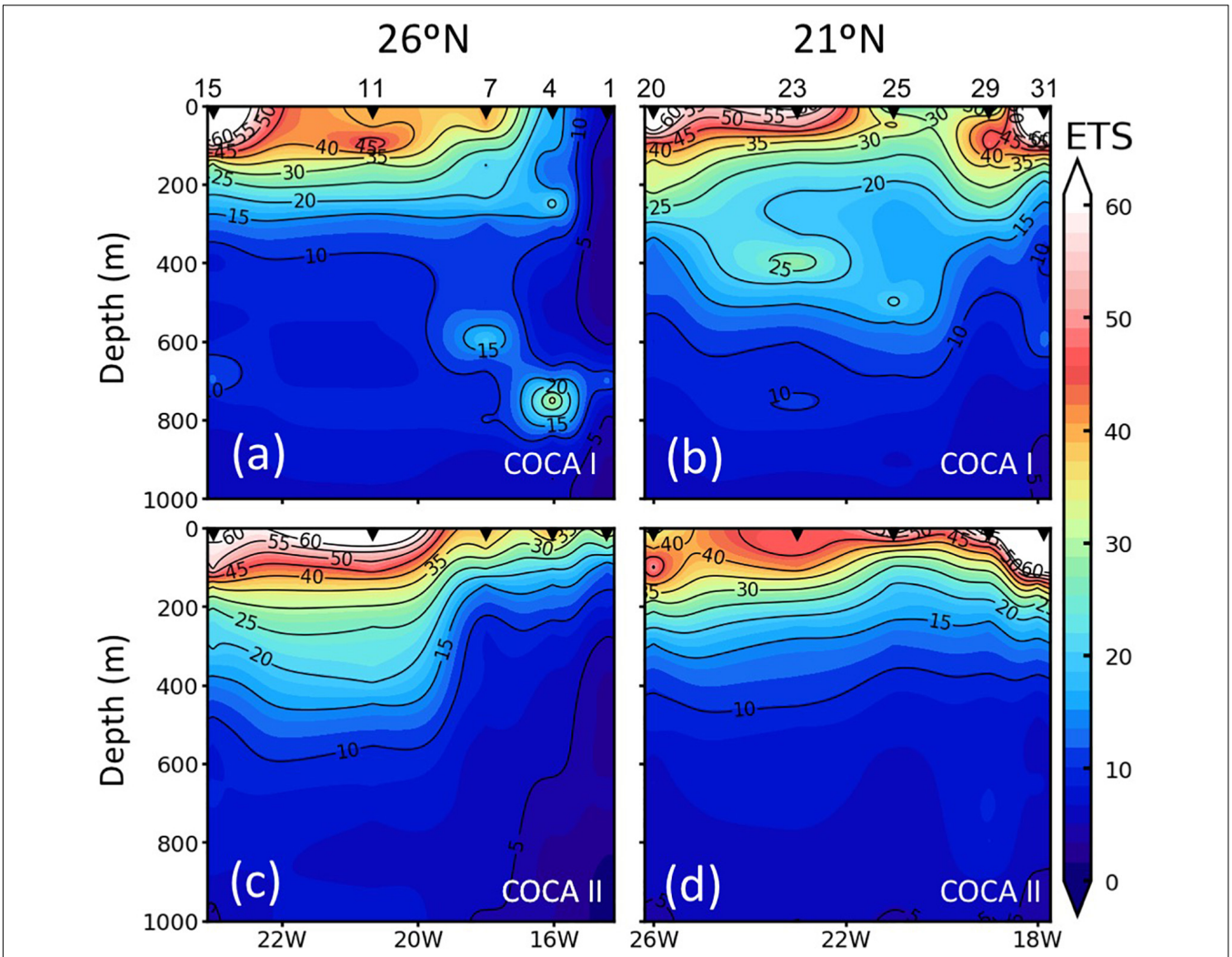

FIGURE 4 | Vertical distribution (0–1000 m) of enzymatic respiratory activity (ETS; μmol O_2 m^{-3} h^{-1}) along the two sections (21°N and 26°N), during cruises COCA I **(a,b)** and COCA II **(c,d)**.

TABLE 1 | Average integrated enzymatic respiratory activity (ETS) and actual respiration (R) in the epipelagic and mesopelagic zones for cruises COCA I (fall 2002) and COCA II (spring 2003).

		COCA I		COCA II	
Depth (m)	**Section (latitude)**	**ETS (mmol C m^{-2} d^{-1})**	**R (mmol C m^{-2} d^{-1})**	**ETS (mmol C m^{-2} d^{-1})**	**R (mmol C $m^{-2}d^{-1}$)**
Epipelagic (0–200 m)	26°N	99.42 ± 70.38	74.56 ± 52.79	122.48 ± 59.65	91.92 ± 44.77
	21°N	155.50 ± 46.86	116.62 ± 35.15	165.86 ± 78.34	124.47 ± 58.79
Mesopelagic (200–1000 m)	26°N	125.64 ± 50.38	85.43 ± 34.26	96.25 ± 46.69	65.47 ± 31.76
	21°N	134.90 ± 23.59	91.73 ± 16.04	97.62 ± 8.56	66.40 ± 5.82

describing a metabolic imbalance in the balance between primary production and microplankton respiration in the epipelagic zone (Duarte et al., 2001; Robinson et al., 2002; Arístegui et al., 2003b; Fernández-Castro et al., 2016). Indeed, assuming data that NPP in the coastal upwelling ranged approximately from 100 to 300 mmol C m^{-2} d^{-1} and that average epipelagic R ranged from 75 to125 mmol C m^{-2} d^{-1} (**Table 4**), a 50% export of NPP would suffice in excess to explain the metabolic imbalance, summing up the local NPP at each station.

Mesopelagic Respiration

The mesopelagic layer supports intense organic matter remineralization (Arístegui et al., 2003a, 2005). Indeed, the major decrease in molecular-characterized material occurs in the

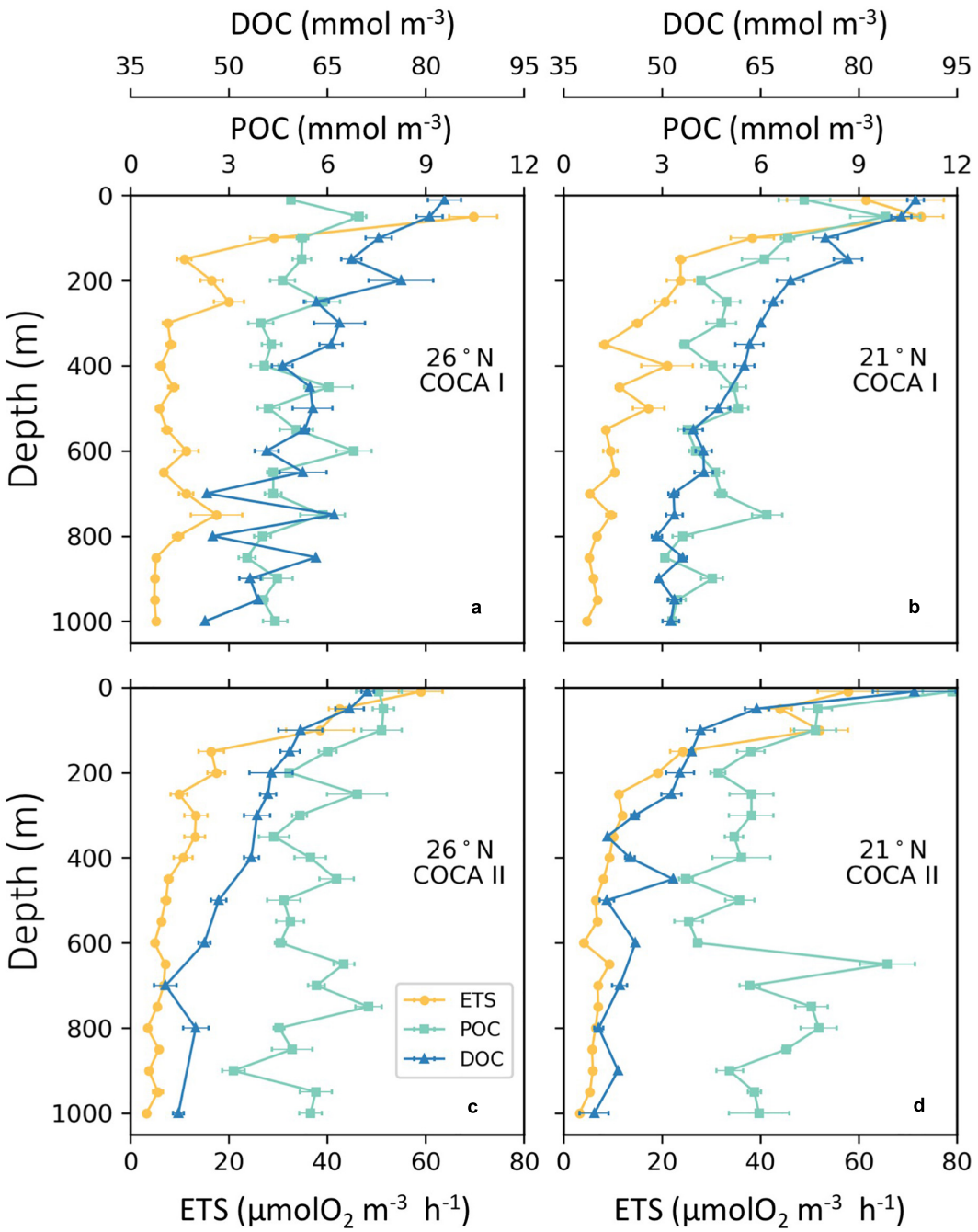

FIGURE 5 | Vertical average distributions of enzymatic respiratory activity (ETS; µmol O_2 m^{-3} h^{-1}), dissolved organic carbon (DOC; µM) and suspended particulate organic carbon (POC; µM) of the two sections (21°N and 26°N), during cruises COCA I **(a,b)** and COCA II **(c,d)**.

mesopelagic zone, even though the larger relative decrease in POC flux of sinking particles is in the euphotic zone (Lee et al., 2004). However, in spite of the key role of the mesopelagic waters as the site where the bulk of exported matter from the epipelagic zone is remineralized (Arístegui et al., 2005; Burd and Jackson, 2009), to our knowledge there are no studies that tackle both the spatial and temporal variability of respiration in the dark ocean, which has been hitherto assumed to be rather invariant.

In our study, the mesopelagic waters did not reveal any clear meridional or zonal trend in respiratory activity for the two cruises, although on average there was >25% increase in R in the fall with respect to the spring (**Figure 4** and **Table 1**). This difference could be partly explained by significantly higher DOC concentrations in the fall, particularly at 21°N (**Table 2**), when the relative importance of DOC to R accounts for up to 35% (**Table 3**). In any case, POCsus contributes more than DOC to

TABLE 2 | Average integrated suspended particulate organic carbon (POC_{sus}) and dissolved organic carbon in the epipelagic and mesopelagic zones for cruises COCA I (fall 2002) and COCA II (spring 2003).

		COCA I		COCA II	
Depth (m)	**Section (latitude)**	**POC_{sus} (mol C m^{-2})**	**DOC (mol C m^{-2})**	**POC_{sus} (mol C m^{-2})**	**DOC (mol C m^{-2})**
Epipelagic (0–200 m)	26°N	0.99 ± 0.27	17.56 ± 1.75	1.67 ± 0.18	17.37 ± 4.99
	21°N	1.56 ± 0.51	19.51 ± 1.10	1.73 ± 0.36	14.63 ± 0.88
Mesopelagic (200–1000 m)	26°N	3.51 ± 0.91	32.81 ± 10.59	3.93 ± 0.50	31.62 ± 4.09
	21°N	2.56 ± 1.07	41.52 ± 5.34	4.02 ± 1.10	29.87 ± 3.77

TABLE 3 | Multiple linear regression statistics between actual respiration rates and suspended particulate organic carbon (POC_{sus}) and dissolved organic carbon (DOC), for the epipelagic and mesopelagic zones in cruises COCA I and COCA II.

	COCA I					COCA II				
	X_i	**R^2**	**RI (%)**	**VIF**	**n**	**X_i**	**R^2**	**RI (%)**	**VIF**	**n**
Epipelagic (0–200 m)	POC_{sus}	0.51	84.9	1.00	32	POC_{sus}	0.65	54.8	1.13	39
	DOC		15.1			DOC		45.2		
Mesopelagic (200–1000 m)	POC_{sus}	0.46	65.3	1.01	78	POC_{sus}	0.64	70.3	1.03	58
	DOC		34.7			DOC		29.7		

X_i, predictor variables; R^2, correlation coefficient; RI, relative importance in percentage; VIF, Variance Inflation Factors; n, number of data.

R in all cases (**Table 3**). This agrees with the results obtained by Alonso-González et al. (2009) from a box-model approach in the more oceanic section of our region of study. It coincides also with the estimations obtained from a tracer conservation model at the ESTOC station north of Gran Canaria, where lateral supply of POC_{sus} would be the main carbon source to explain mesopelagic R (Fernández-Castro et al., 2016). Baltar et al. (2009b), also found significant correlations between POC_{sus} and ETS in bathypelagic waters (1000–3000 m) of the subtropical North Atlantic. All these findings, together with our results, indicate that microbial metabolism in the mesopelagic waters of the CanC region is largely supported by suspended organic particles. These finding are also consistent with a recent global ocean multi-omics study suggesting that organic matter cleavage is mediated mainly by particle-associated prokaryotes releasing their extracellular enzymes into diffusion-limited particles in the meso- and bathypelagic realm (Zhao et al., 2020).

The correlation between the particulate fraction of the organic matter pool and ETS activity of planktonic communities (and hence R) may be expected beforehand, taking into account that ETS activity also represents a living biomass (enzyme) measurement. However, total prokaryote abundances in the sampled mesopelagic waters represented only a small fraction of total POC_{sus}. Free living prokaryote abundances ranged from 1 to 3×10^8 cells l^{-1} (Gasol et al., 2009). Assuming an average carbon conversion factor of 20 fg $cell^{-1}$ (Fukuda et al., 1998) the maximum prokaryote abundance (3×10^8 cells l^{-1}) yields a prokaryotic carbon content of 0.5 μmol C l^{-1}. This value represents less than 10% of total POC_{sus} and suggests that the correlation between ETS activity and POC_{sus} is independent on the living biomass fraction.

Overall, average integrated estimates of R in the mesopelagic zone (65–98 mmol C m^{-2} d^{-1}) are of the same order as in the epipelagic, indicating that prokaryotes are metabolically active in the dark ocean, as evidenced in a former study from COCA II (Arístegui et al., 2005). The upper average integrated range of R_{meso} in our study is however up to 10 times higher than the upper range of R_{meso} inferred from physical-biogeochemical models at ESTOC (Fernández-Castro et al., 2016) and the more oceanic waters of our region of study (Alonso-González et al., 2009). *A priori*, one would expect R_{meso} to be higher in our region of study, due to enhanced offshore export of organic matter from the coastal upwelling and the higher POC_{sus} values observed in the water column compared with the other studies. However, differences in methodological approaches (biogeochemical modeling vs. ETS activity) preclude direct comparison of the magnitude of R determined between these studies.

We must have, however, some precautions with regards to our R estimations from ETS activity in the two cruises. Contrary to other studies that assume a theoretical R:ETS, we measured actual R by oxygen consumption in 29 experiments with water collected from 600 and 1000 m depth, but only during COCA II. We also measured at the same stations and depths ETS activity, obtaining an average R:ETS ratio of 0.68 ± 0.11 (Arístegui et al., 2005). This ratio is 7.5 times higher than the R:ETS obtained from senescent bacteria cultures (R:ETS = 0.09; Christensen et al., 1980), that was used in the past to derive a lower-threshold R for the global ocean (Arístegui et al., 2003a). Nevertheless, during COCA II, other proxies for metabolic activity gave evidence that mesopelagic prokaryotic assemblages were activity growing, rather than in senescent phase. We cannot be sure however that the same conditions applied also for cruise COCA I. If prokaryotic activity were lower during the fall than the spring, then the R:ETS could be lower,

as well as the mesopelagic R. In any case, even assuming that the R:ETS ratio was two times lower during the fall, mesopelagic R would exceed by far the export production measured by gravitational flux (EP: sinking POC flux at 200 m depth).

Synthesis: Carbon Fluxes and Metabolic Balance

Table 4 collates the integrated plankton metabolic rates (NPP and R) and compare them with the EP at each station during the two cruises. Only at the very coastal stations of the two sections does NPP exceed R_{meso}. In offshore waters, R_{meso} is up to five times higher than NPP, suggesting that much of the organic carbon respired must originate in the more productive coastal upwelling region. Moreover, the e-ratio (% EP/NPP) ranges from 2 to 14%, being <3% at most of the stations, indicating that only a small fraction of the NPP is exported from the surface by local gravitational flux.

If we sum up the average gravitational flux ($EP = 4.2 \pm 4.6$) with the active flux mediated by migrant zooplankton (0.8 ± 1.5 mmol C m^{-2} d^{-1}) estimated for COCA I (Hernández-León et al., 2019), both fluxes fail short of accounting for the respiratory rates in the mesopelagic at any of the stations, with the respiratory imbalance being up to > 90 times higher in one of the most oceanic stations.

The average EP in the fall (4.2 ± 4.6 mmol C m^{-2} d^{-1}) and the spring (3.1 ± 3.0 mmol Cm^{-2} d^{-1}) are significantly lower than previous EP reported for late winter (8.3–28.5 mmol C m^{-2} d^{-1}) and summer (5.5–13–1 mmol C m^{-2} d^{-1}) in open ocean waters of the CanC (Alonso-González et al., 2010). However, in any case the EP can account for the high R_{meso} in the region. This must be maintained by lateral export of organic carbon from the coastal upwelling region. Indeed, Lovecchio et al. (2017), by means of a coupled physical-ecosystem model, described a strong offshore flux of organic carbon from the NW Africa coastal upwelling, that would be particularly efficient near Cape Blanc, transporting as nearly 60% of the local NPP.

The offshore transport is largely mediated by the numerous upwelling filaments (Gabric et al., 1993; García-Muñoz et al., 2004, 2005; Santana-Falcón et al., 2016, 2020) and filament-eddy interactions, produced particularly south of the Canaries Archipelago (Arístegui et al., 2004, 2009). Mesoscale eddies would transport organic carbon to the mesopelagic zone, by means of physical processes (e.g., Omand et al., 2015; Resplandy et al., 2019), explaining the high concentrations and irregular peaks of POC_{sus} (and ETS activity) in deep layers observed at most of the stations. Recently, Amos et al. (2019) used satellite-derived measurements of POC to show that mesocale eddies generated from meanders in the California Current, trap organic carbon and transport it as far as 1000 km offshore, greatly enriching the open ocean waters. Lovecchio et al. (2018) ran simulations with a coupled physical-ecosystem model to show that both filaments and eddies contribute to the offshore flux of organic carbon in the CanC upwelling system, although in a

TABLE 4 | Integrated plankton metabolic rates (NPP, R; see methods for calculations) and export production (EP: sinking POC flux collected with sediment traps at 200 m depth) at each station during the two cruises.

Cruise	Section	Station	NPP (mmolC $m^{-2}d^{-1}$)	EP (mmolC $m^{-2}d^{-1}$)	R_{epi} (mmolC $m^{-2}d^{-1}$)	R_{meso} (mmolC $m^{-2}d^{-1}$)	R_{meso}/NPP	R_{meso}/EP	e-ratio (%) (EP/NPP)
COCA I	26°N	1	186.88	16.60	10.36	23.37	0.13	1.41	8.88
		4	33.74	4.88	39.50	56.54	1.68	11.60	14.45
		7	28.62	3.70	80.16	54.96	1.92	14.85	12.93
		11	19.39	2.40	95.18	105.71	5.45	44.05	12.38
		15	24.01	2.60	147.63	86.76	3.61	33.37	10.83
	21°N	20	31.54	0.70	139.60	67.91	2.15	97.02	2.22
		23	84.29	2.30	105.15	72.76	0.86	31.63	2.73
		25	30.15	0.80	70.58	59.59	1.98	74.49	2.65
		29	104.93	2.60	105.93	70.65	0.67	27.17	2.48
		31	204.66	5.60	161.87	61.07	0.30	10.91	2.74
COCA II	26°N	1	87.19	–	47.14	6.68	0.08	–	–
		4	41.37	1.30	64.10	25.48	0.62	19.60	3.14
		7	35.92	0.70	68.37	51.72	1.44	73.88	1.95
		11	23.72	1.10	145.55	61.41	2.59	55.82	4.64
		15	21.29	2.10	134.42	95.24	4.47	45.35	9.86
	21°N	20	27.85	1.90	109.17	90.06	3.23	47.40	6.82
		23	41.43	1.10	114.60	67.84	1.64	61.67	2.66
		25	55.45	3.70	82.36	45.53	0.82	12.31	6.67
		29	332.89	9.80	89.35	68.34	0.21	6.97	2.94
		31	306.68	6.10	226.88	104.43	0.34	17.12	1.99

NPP: satellite-derived (VGPM) net primary production; R_{epi} and R_{meso}: microplankton respiration in the epipelagic and mesopelagic zones; e-ratio: export ratio.

different way. Filaments would transport organic carbon offshore in a very intense way but near the coast, while at distances beyond 500 km from the shore eddies would dominate the mesoscale offshore transport.

CONCLUSION

The estimated integrated mesopelagic respiratory activity was comparable in magnitude to that in the epipelagic zone, and higher than in other reported studies from more open-ocean waters in the North Atlantic. This finding provides evidence of the importance of the dark waters of the CanC EBC (and probably of other EBC) as a sink of organic carbon in the ocean. The epipelagic waters revealed a clear meridional variability with the highest respiratory rates along the 21°N section, closer to the intense upwelling filament off Cape Blanc. Mesopelagic waters, however, did not show clear zonal or meridional patterns of variability, although integrated respiration rates were significantly different during the two periods of study. Water-column respiration was largely supported by suspended POC, which presented concentrations in depth comparable to the epipelagic zone. Our results suggest that microbial respiratory activity in this area is likely controlled by seasonal fluctuations in suspended particulate organic carbon advected from productive coastal waters, rather than by sinking particles from the euphotic zone or the active flux by migrants, which together represented a very small fraction of the carbon respired by microorganisms. The main source of the respired POC is through offshore export from the coastal upwelling, mostly mediated by filaments, mesoscale eddies and the interaction among them. This study also underlines the fact that respiration in the mesopelagic zone does not occur uniformly over time and space in the ocean. Hence, the urgent need to expand our database on mesopelagic respiration at regional and basin scales, reconciling ecological, biogeochemical and model estimates, to gain a better understanding of the global carbon cycle in the ocean.

DATA AVAILABILITY STATEMENT

The raw data supporting the conclusions of this article will be made available by the authors, without undue reservation, to any qualified researcher.

AUTHOR CONTRIBUTIONS

JA and CD designed the field work. JA, MC, and CD participated in the sampling. JA wrote the manuscript with inputs from all co-authors. All authors contributed to samples' analyses.

FUNDING

This work was a contribution to projects COCA (REN2000 1471-C02-01-MAR), FLUXES (CTM2015- 69392-C3-1-R), and e-IMPACT (PID2019-109084RB-C2), funded by the Spanish "Plan Nacional de I+D" and to projects SUMMER (AMD-817806-5) and TRIATLAS (AMD-817578-5) funded from the European Union's Horizon 2020 Research and Innovation Programme.

ACKNOWLEDGMENTS

We thank the captain, crew, and technical staff of the B.I.O Hespérides for their support at sea, and to J. C. Vilas and M. Espino for their help in sampling and data analyses. Some of the contents of this manuscript formed part of the Ph.D. thesis of Alonso-González (2011).

REFERENCES

Alonso-González, I. J. (2011). *New Insights into POC Dynamics in the Subtropical Northeast Atlantic Ocean*. Ph.D. Thesis, Universidad de Las Palmas de Gran Canaria Las Palmas.

Alonso-González, I. J., Arístegui, J., Lee, C., and Calafat, A. (2010). Regional and temporal variability of sinking organic matter in the subtropical northeast Atlantic Ocean: a biomarker diagnosis. *Biogeosciences* 7, 2101–2115. doi: 10.5194/bg-7-2101-2010

Alonso-González, I. J., Arístegui, J., Vilas, J. C., and Hernández-Guerra, A. (2009). Lateral POC transport and consumption in surface and deep waters of the Canary Current region: a box model study. *Glob. Biogeochem. Cycles* 23, 1–12. doi: 10.1029/2008GB003185

Álvarez-Salgado, X. A., Arístegui, J., Barton, E. D., and Hansell, D. A. (2007). Contribution of upwelling filaments to offshore carbon export in the subtropical Northeast Atlantic Ocean. *Limnol. Oceanogr.* 52, 1287–1292. doi: 10.4319/lo.2007.52.3.1287

Amos, C. M., Castelao, R. M., and Medeiros, P. M. (2019). Offshore transport of particulate organic carbon in the California Current System by mesoscale eddies. *Nat. Commun.* 10:4940. doi: 10.1038/s41467-019-12783-12785

Arístegui, J., Agustí, S., and Duarte, C. M. (2003a). Respiration in the dark ocean. *Geophys. Res. Lett.* 30:1041. doi: 10.1029/2002GL016227

Arístegui, J., Barton, E. D., Álvarez-Salgado, X. A., Santos, A. M. P., Figueiras, F. G., Kifani, S., et al. (2009). Sub-regional ecosystem variability in the Canary Current upwelling. *Prog. Oceanogr.* 83, 33–48. doi: 10.1016/j.pocean.2009.07.031

Arístegui, J., Barton, E. D., Montero, M. F., García-Muñoz, M., and Escánez, J. (2003b). Organic carbon distribution and water column respiration in the NW Africa-Canaries Coastal Transition Zone. *Aquat. Microb. Ecol.* 33, 289–301. doi: 10.3354/ame033289

Arístegui, J., Barton, E. D., Tett, P., Montero, M. F., García-Muñoz, M., Basterretxea, G., et al. (2004). Variability in plankton community structure, metabolism, and vertical carbon fluxes along an upwelling filament (Cape Juby, NW Africa). *Prog. Oceanogr.* 62, 95–113. doi: 10.1016/j.pocean.2004.07.004

Arístegui, J., Duarte, C. M., Gasol, J. M., and Alonso-Sáez, L. (2005). Active mesopelagic prokaryotes support high respiration in the subtropical northeast Atlantic Ocean. *Geophys. Res. Lett.* 32, 1–4. doi: 10.1029/2004GL021863

Arístegui, J., and Harrison, W. G. (2002). Decoupling of primary production and community respiration in the ocean: implications for regional carbon studies. *Aquat. Microb. Ecol.* 29, 199–209. doi: 10.3354/ame029199

Arístegui, J., and Montero, M. F. (1995). The relationship between community respiration and ETS activity in the ocean. *J. Plankton Res.* 17, 1563–1571. doi: 10.1093/plankt/17.7.1563

Baltar, F., Arístegui, J., Gasol, J. M., Sintes, E., and Herndl, G. J. (2009a). Evidence of prokaryotic metabolism on suspended particulate organic matter in the

dark waters of the subtropical North Atlantic. *Limnol. Oceanogr.* 54, 182–193. doi: 10.4319/lo.2009.54.1.0182

Baltar, F., Arístegui, J., Montero, M. F., Espino, M., Gasol, J. M., and Herndl, G. J. (2009b). Mesoscale variability modulates seasonal changes in the trophic structure of nano- and picoplankton communities across the NW Africa-Canary Islands transition zone. *Prog. Oceanogr.* 83, 180–188. doi: 10.1016/j.pocean.2009.07.016

Bauer, J. E., and Druffel, E. R. M. (1998). Ocean margins as a significant source of organic matter to the deep open ocean. *Nature* 392, 482–485. doi: 10.1038/33122

Behrenfeld, M. J., and Falkowski, P. G. (1997). Photosynthetic rates derived from satellite-based chlorophyll concentration. *Limnol. Oceanogr.* 42, 1–20. doi: 10.4319/lo.1997.42.1.0001

Burd, A. B., and Jackson, G. A. (2009). Particle aggregation. *Ann. Rev. Mar. Sci.* 1, 65–90. doi: 10.1146/annurev.marine.010908.163904

Burgoa, N., Machín, F., Marrero-Díaz, Á., Rodríguez-Santana, Á., Martínez-Marrero, A., Arístegui, J., et al. (2020). Mass, nutrients and dissolved organci carbon (DOC) lateral transports off northwest Africa during fall 2002. *Ocean Sci.* 16, 483-511. doi: 10.5194/os-16-483-2020

Christensen, J. P., Owens, T. G., Devol, A. H., and Packard, T. T. (1980). Respiration and physiological state in marine bacteria. *Mar. Biol.* 55, 267–276. doi: 10.1007/bf00393779

Duarte, C. M., Agustí, S., Arístegui, J., González, N., and Anadón, R. (2001). Evidence for a heterotrophic subtropical northeast Atlantic. *Limnol. Oceanogr.* 46, 425–428. doi: 10.4319/lo.2001.46.2.0425

Fernández-Castro, B., Arístegui, J., Anderson, L., Montero, M. F., Hernández-León, S., Marañón, E., et al. (2016). Mesopelagic respiration near the ESTOC (European Station for Time-Series in the Ocean, 15.5°W, 29.1°N) site inferred from a tracer conservation model. *Deep Sea Res. I Oceanogr. Res. Pap.* 115, 63–73. doi: 10.1016/J.DSR.2016.05.010

Fernández-Castro, B., Mouriño-Carballido, B., and Álvarez-Salgado, X. A. (2019). Non-redfieldian mesopelagic nutrient remineralization in the eastern North Atlantic subtropical gyre. *Prog. Oceanogr.* 171, 136–153. doi: 10.1016/j.pocean.2018.12.001

Fukuda, R., Ogawa, H., Nagata, T., and Koike, I. I (1998). Direct determination of carbon and nitrogen contents of natural bacterial assemblages in marine environments. *Appl. Environ. Microbiol.* 64, 3352–3358. doi: 10.1128/aem.64.9.3352-3358.1998

Gabric, A. J., Garcia, L., Van Camp, L., Nykjaer, L., Eifler, W., and Schrimpf, W. (1993). Offshore export of shelf production in the Cape Blanc (Mauritania) giant filament as derived from coastal zone color scanner imagery. *J. Geophys. Res. Ocean.* 98, 4697–4712. doi: 10.1029/92JC01714

García-Muñoz, M., Arístegui, J., Montero, M. F., and Barton, E. D. (2004). Distribution and transport of organic matter along a filament-eddy system in the Canaries - NW Africa coastal transition zone region. *Prog. Oceanogr.* 62, 115–129. doi: 10.1016/j.pocean.2004.07.005

García-Muñoz, M., Arístegui, J., Pelegrí, J. L., Antoranz, A., Ojeda, A., and Torres, M. (2005). Exchange of carbon by an upwelling filament off Cape Ghir (NW Africa). *J. Mar. Syst.* 54, 83–95. doi: 10.1016/j.jmarsys.2004.07.005

Gasol, J. M., Alonso-Sáez, L., Vaqué, D., Baltar, F., Calleja, M. L., Duarte, C. M., et al. (2009). Mesopelagic prokaryotic bulk and single-cell heterotrophic activity and community composition in the NW Africa–Canary Islands coastal-transition zone. *Prog. Oceanogr.* 83, 189–196. doi: 10.1016/J.POCEAN.2009.07.014

Hansell, D. A. (2002). "DOC in the global ocean carbon cycle," in *Biogeochemistry of Marine Dissolved Organic Matter*, eds D. A. Hansell and C. A. Carlson (San Diego: Academic Press), 685–715. doi: 10.1016/b978-012323841-2/50017-8

Hernández-León, S., Putzeys, S., Almeida, C., Bécognée, P., Marrero-Díaz, A., Arístegui, J., et al. (2019). Carbon export through zooplankton active flux in the Canary Current. *J. Mar. Syst.* 189, 12–21. doi: 10.1016/j.jmarsys.2018.09.002

Kenner, R. A., and Ahmed, S. I. (1975). Measurements of electron transport activities in marine phytoplankton. *Mar. Biol.* 33, 119–127. doi: 10.1007/BF00390716

Knauer, G. A., Martin, J. H., and Bruland, K. W. (1979). Fluxes of particulate carbon, nitrogen, and phosphorus in the upper water column of the northeast Pacific. *Deep Sea Res. A. Oceanogr. Res. Pap.* 26, 97–108. doi: 10.1016/0198-0149(79)90089-X

Lee, C., Wakeham, S., and Arnosti, C. (2004). Particulate organic matter in the sea: the composition conundrum. *Ambio* 33, 565–575. doi: 10.1579/0044-7447-33.8.565

Lindeman, R. H., Merenda, P. F., and Gold, R. Z. (1980). *Introduction to Bivariate and Multivariate Analysis*. Glenview, IL: Scott, Foresman and Company.

Lovecchio, E., Gruber, N., and Münnich, M. (2018). Mesoscale contribution to the long-range offshore transport of organic carbon from the Canary Upwelling System to the open North Atlantic. *Biogeosciences* 15, 5061–5091. doi: 10.5194/bg-15-5061-2018

Lovecchio, E., Gruber, N., Münnich, M., and Lachkar, Z. (2017). On the long-range offshore transport of organic carbon from the Canary Upwelling System to the open North Atlantic. *Biogeosciences* 14, 3337–3369. doi: 10.5194/bg-14-3337-2017

Neuer, S., Cianca, A., Helmke, P., Freudenthal, T., Davenport, R., Meggers, H., et al. (2007). Biogeochemistry and hydrography in the eastern subtropical North Atlantic gyre. Results from the European time-series station ESTOC. *Prog. Oceanogr.* 72, 1–29. doi: 10.1016/J.POCEAN.2006.08.001

Omand, M. M., D'Asaro, E. A., Lee, C. M., Perry, M. J., Briggs, N., Cetini, I., et al. (2015). Eddy-driven subduction exports particulate organic carbon from the spring bloom. *Science* 348, 22–25. doi: 10.1126/science.1260062

Packard, T. T. (1971). The measurement of respiratory electron-transport activity in marine phytoplankton. *J. Mar. Res.* 29, 235–144.

Resplandy, L., Lévy, M., and McGillicuddy, D. J. Jr. (2019). Effects of eddy-driven subduction on ocean biological carbon pump. *Glob. Biogeochem. Cycles* 33, 1071–1084. doi: 10.1029/2018GB006125

Robinson, C., Serret, P., Tilstone, G., Teira, E., Zubkov, M. V., Rees, A. P., et al. (2002). Plankton respiration in the Eastern Atlantic Ocean. *Deep Sea Res. I Oceanogr. Res. Pap.* 49, 787–813. doi: 10.1016/S0967-0637(01)00083-88

Santana-Falcón, Y., Álvarez-Salgado, X. A., Pérez-Hernández, M. D., Hernández-Guerra, A., Mason, E., and Arístegui, J. (2017). Organic carbon budget for the eastern boundary of the North Atlantic subtropical gyre: major role of DOC in mesopelagic respiration. *Sci. Rep.* 7, 1–12. doi: 10.1038/s41598-017-10974-y

Santana-Falcón, Y., Benavides, M., Sangrá, P., Mason, E., Barton, E. D., Orbi, A., et al. (2016). Coastal-offshore exchange of organic matter across the Cape Ghir filament (NW Africa) during moderate upwelling. *J. Mar. Sys.* 154, 233–242. doi: 10.1016/j.jmarsys.2015.10.008

Santana-Falcón, Y., Mason, E., and Arístegui, J. (2020). Offshore transport of organic carbon by upwelling filaments in the Canary Current System. *Prog. Oceanogr.* 186:102322. doi: 10.1016/J.POCEAN.2020.102322

Sharp, J. H., Peltzer, E. T., Alperin, M. J., Cauwet, G., Farrington, J. W., Fry, B., et al. (1993). Procedures subgroup report. *Mar. Chem.* 41, 37–49. doi: 10.1016/0304-4203(93)90104-V

Thomas, C., Cauwet, G., and Minster, J.-F. (1995). Dissolved organic carbon in the equatorial Atlantic Ocean. *Mar. Chem.* 49, 155–169. doi: 10.1016/0304-4203(94)00061-H

Turnewitsch, R., Springer, B. M., Kiriakoulakis, K., Vilas, J. C., Arístegui, J., Wolff, G., et al. (2007). Determination of particulate organic carbon (POC) in seawater: the relative methodological importance of artificial gains and losses in two glass-fiber-filter-based techniques. *Mar. Chem.* 105, 208–228. doi: 10.1016/J.MARCHEM.2007.01.017

UNESCO (1994). *Protocols for the Joint Global Ocean Flux Study (JGOFS) Core Measurement*. Paris: UNESCO.

Vilas, J. C., Arístegui, J., Kiriakoulakis, K., Wolff, G. A., Espino, M., Polo, I., et al. (2009). Seamounts and organic matter—Is there an effect? The case of sedlo and seine seamounts: part 1. Distributions of dissolved and particulate organic matter. *Deep Sea Res. II Top. Stud. Oceanogr.* 56, 2618–2630. doi: 10.1016/J.DSR2.2008.12.023

Zhao, Z., Baltar, F., and Herndl, G. J. (2020). Linking extracellular enzymes to phylogeny indicates a predominantly particle-associated lifestyle of deep-sea prokaryotes. *Sci. Adv.* 6:eaaz4354. doi: 10.1126/sciadv.aaz4354

Conflict of Interest: The authors declare that the research was conducted in the absence of any commercial or financial relationships that could be construed as a potential conflict of interest.

frontiers in Earth Science

ORIGINAL RESEARCH
published: 04 September 2020
doi: 10.3389/feart.2020.00376

Efficient Particle Transfer to Depth in Oxygen Minimum Zones of the Pacific and Indian Oceans

Thomas Weber[1]* *and Daniele Bianchi*[2]

[1] Department of Earth and Environmental Science, University of Rochester, Rochester, NY, United States, [2] Department of Atmospheric and Oceanic Sciences, University of California, Los Angeles, Los Angeles, CA, United States

The remineralization depth of sinking organic particles controls the efficiency of the biological carbon pump by setting the sequestration timescale of remineralized carbon in the ocean interior. Oxygen minimum zones (OMZs) have been identified as regions of elevated particle transfer and efficient carbon sequestration at depth, but direct measurements remain sparse in these regions and only provide snapshots of the particle flux. Here, we use remineralization tracers to reconstruct time-mean particle flux profiles in the OMZs of the Eastern Tropical Pacific and the Arabian Sea. Compared to the surrounding tropical waters, both OMZs exhibit slow flux attenuation between 100 and 1000 m where suboxic waters reside, and sequester carbon beneath 1000 m more than twice as efficiently. Using a mechanistic model of particle sinking, remineralization, and disaggregation, we show that three different mechanisms might explain the shape of the OMZ flux profiles: (i) a significant slow-down of remineralization when carbon oxidation transitions from aerobic to anaerobic respiration (e.g., denitrification); (ii) the exclusion of zooplankton that mediate disaggregation of large particles from suboxic waters, and (iii) the limitation of remineralization by the diffusive supply of oxidants (oxygen and nitrate) into large particles. We show that each mechanism leaves a unique signature in the size distribution of particles, suggesting that observations with optical instruments such as Underwater Vision Profilers hold great promise for understanding the drivers of efficient carbon transfer though suboxic water columns. In turn, this will allow more accurate prediction of future changes in carbon sequestration as the ocean loses oxygen in a warming climate.

Keywords: biological pump, ocean carbon sequestration, particle flux, oxygen minimum zones, remineralization, disaggregation, particle size spectra

OPEN ACCESS

Edited by:
Makio Honda,
Japan Agency for Marine-Earth Science and Technology (JAMSTEC), Japan

Reviewed by:
Morgan Reed Raven,
University of California, Santa Barbara, United States
Frank Pavia,
California Institute of Technology, United States

***Correspondence:**
Thomas Weber
t.weber@rochester.edu

Specialty section:
This article was submitted to Biogeoscience, a section of the journal Frontiers in Earth Science

Received: *30 May 2020*
Accepted: *11 August 2020*
Published: *04 September 2020*

Citation:
Weber T and Bianchi D (2020) Efficient Particle Transfer to Depth in Oxygen Minimum Zones of the Pacific and Indian Oceans. Front. Earth Sci. 8:376. doi: 10.3389/feart.2020.00376

INTRODUCTION

The biological pump sequesters carbon out of contact with the atmosphere in deep ocean waters, owing to the formation of organic particles in the surface ocean followed by their sinking and remineralization at depth (Passow and Carlson, 2012). The depth of particle remineralization determines the "efficiency" of the biological pump, quantified as the amount of time remineralized carbon dioxide (CO_2) remains sequestered in the ocean interior before returning to the surface (DeVries et al., 2012; Boyd et al., 2019). Recently, systematic large-scale patterns in particle remineralization depth have been identified from sediment trap data (Buesseler et al., 2007;

Marsay et al., 2014) and confirmed by geochemical flux reconstructions, which provide a more spatially and temporally integrated view than the snapshots provided by sediment traps (Weber et al., 2016). Particles remineralize shallowest in the subtropics and deepest in high latitudes, which can be explained by a combination of temperature-sensitive remineralization rates and the effects of particle size and ballasting on particle sinking speed (Weber et al., 2016; DeVries and Weber, 2017; Laufkötter et al., 2017; Cram et al., 2018).

In addition to this large-scale pattern, sediment trap observations indicate that tropical oxygen minimum zones (OMZs) are regions of particularly efficient particle transfer to depth (Devol and Hartnett, 2001; Van Mooy et al., 2002; Keil et al., 2016), although this has not yet been confirmed by geochemical reconstructions based on dissolved tracer distributions. The mechanisms explaining efficient particle transfer through OMZs are not well understood, but multiple hypotheses have been advanced which fall into three broad categories, referred to here as Hypotheses 1–3.

Hypothesis 1 states that particle attenuation slows because the microbial community transitions from aerobic to anaerobic respiration – mostly denitrifying metabolisms – in oxygen deficient water (Devol, 1978), resulting in significantly slower organic carbon oxidation (Devol and Hartnett, 2001; Van Mooy et al., 2002). Hypothesis 2 states that the exclusion of zooplankton from oxygen deficient waters (Wishner et al., 2013; Wishner et al., 2018), or the suppression of zooplankton activity at low oxygen (O_2) concentrations (Seibel, 2011; Kiko et al., 2016), prevents the disaggregation of large aggregates during zooplankton feeding, allowing more efficient transfer through the mesopelagic (Cavan et al., 2017). Hypothesis 3 revises Hypothesis 1 to state that organic carbon oxidation is governed by the physico-chemical "microenvironment" within sinking particles (Wright et al., 2012), rather than the ambient seawater chemistry. In oxygen deficient water columns, aerobic respiration and denitrification can exhaust O_2 and nitrate (NO_3) inside large particles faster than it is supplied diffusively (Ploug, 2001), preventing further carbon oxidation or slowing it significantly as the microbial community transitions to inefficient metabolisms such as sulfate reduction (Bianchi et al., 2018). Unlike Hypothesis 1, Hypothesis 3 does not invoke a substantial slowdown of carbon oxidation during denitrification relative to aerobic respiration, consistent with the similar free energy yield of the two pathways (Froelich et al., 1979).

Accurately quantifying particle fluxes through OMZs, and identifying their driving mechanisms, is critical for robust prediction of ocean carbon in a warming and deoxygenating ocean (Bopp et al., 2013; Laufkötter et al., 2017; Schmidtko et al., 2017), and for understanding the interaction of ocean oxygen content and carbon storage during past climate transitions (Lu et al., 2016). This paper serves two primary purposes. First, it presents new geochemical reconstructions that confirm and more firmly quantify efficient particle transfer through oxygen minimum zones (Section "Reconstruction of OMZ Particle Fluxes"). Second, it employs a mechanistic particle flux model (Section "Mechanistic Particle Size Spectrum Model") to test which of the three hypotheses outlined above can explain the reconstructed flux profiles (Section "Simulated Particle Fluxes in the OMZs"), while demonstrating that each mechanism makes different predictions about particle size spectra within the OMZs (Section "Particle Size Spectra Distinguish Between Attenuation Mechanisms"). It is our hope that this will allow each hypothesis to be further scrutinized using burgeoning particle spectra datasets from Underwater Vision Profilers (UVPs) (Stemmann et al., 2012) in future work.

RECONSTRUCTION OF OMZ PARTICLE FLUXES

Previous work that reconstructed organic particle fluxes using dissolved geochemical tracers found that flux profiles averaged across tropical ocean regions exhibit intermediate attenuation over depth, sitting halfway between the fast-attenuating subtropics and slow-attenuating high latitudes (Weber et al., 2016). For this study, we repeated the geochemical reconstruction approach, but divided the Tropical Pacific and Indian oceans into suboxic OMZs (defined as $[O_2] < 5$ μM at 400 m) and surrounding oxygenated waters (**Figure 1A**).

The method for flux reconstruction is fully described in Weber et al. (2016). Briefly, an observationally constrained ocean circulation model is used to diagnose the accumulation rate of PO_4 in the ocean interior (>100 m) due to particle remineralization, and the particulate organic phosphorus (POP) flux through a given depth horizon is estimated by integrating the remineralization that occurs beneath that horizon. Finally, fluxes are averaged into profiles across large ocean regions to minimize gridpoint-scale noise and identify large scale patterns in the particle flux. We note that in our interpretations, we implicitly assume that the shape of POP flux profiles is representative of all organic particle constituents, including particulate organic carbon (POC). This is a necessary limitation of our approach, given that POC flux profiles cannot be reconstructed more directly (Weber et al., 2016).

Four averaging regions are used here (**Figure 1A**). In the Indian Ocean, waters north of 2.5°S are integrated into the Tropical Indian (TI) region, with the exception of the Arabian Sea (AS) OMZ (**Figure 1A**), which houses a thick layer of suboxic water between ∼250 and 900 m (**Figure 1B**). In the Pacific, waters between 30°S and 30°N with a shallow nutricline [see (Weber et al., 2016)] are integrated into the Tropical Pacific (TP) region, with the exception of two OMZ regions at the eastern boundary (**Figure 1A**). To the north, the Eastern Tropical North Pacific (ETNP) is the world's most expansive OMZ, where suboxic waters spread westward between 300 and 800 m (**Figure 1C**). To the south, the Eastern Tropical South Pacific (ETSP) is more coastally confined, and covers too few gridcells on our coarse model grid to allow for reliable flux reconstruction. This OMZ is not incorporated into the broader TP region, but is also not considered as a separate region in our analysis. The only further modification made here to the method of Weber et al. (2016) is that we use an updated ocean circulation model (DeVries and Holzer, 2019), and twelve model configurations with slightly different diffusive parameterizations are used to propagate circulation uncertainty into the flux reconstructions.

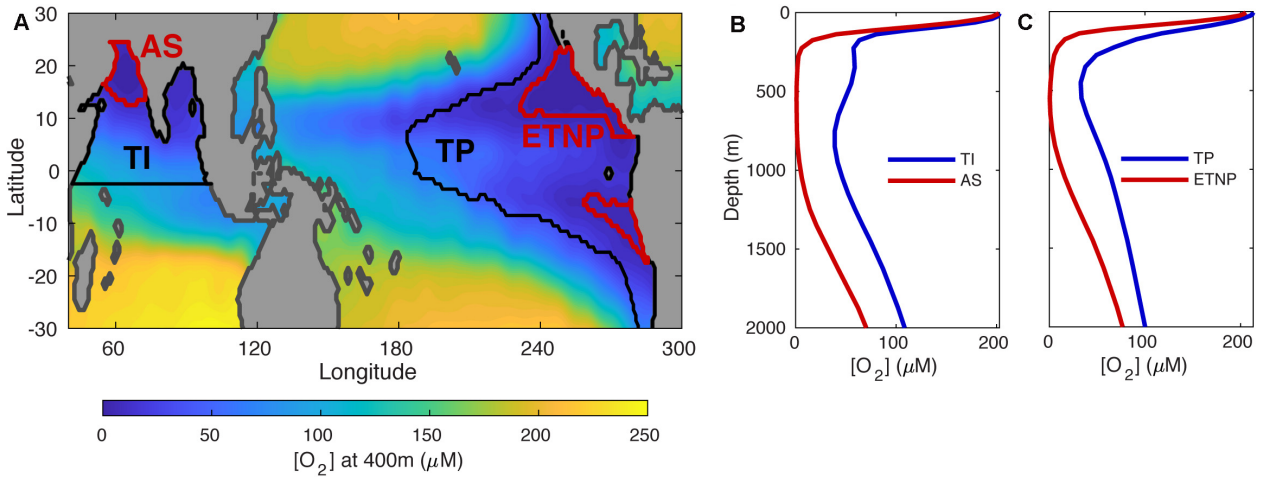

FIGURE 1 | Regions used in our flux reconstruction analysis. **(A)** Contour map of annual-mean oxygen concentration at 400 m depth in the low latitude ocean, from the World Ocean Atlas 2013 (Garcia et al., 2013). Black and red contours delineate the regions over which reconstructed particle flux profiles are averaged. The areas inside of the black contours in the Indian and Pacific Oceans are defined as the oxygenated Tropical Indian (TI) and Tropical Pacific (TP) averaging regions, respectively, with the exception of the areas inside of the red contours, which enclose suboxic waters with $[O_2] < 5$ μM at 400 m. These are defined as the OMZ averaging regions – Arabian Sea (AS) and Eastern Tropical North Pacific (ETNP). In the South Pacific, the area inside of the red contour is not incorporated into the TP region, but is not defined as independent averaging region because it spans too few gridcells on our model grid. **(B)** Depth profiles of annual-mean $[O_2]$ averaged across the TI and AS regions. **(C)**, same as **(B)** but for the TP and ETNP regions.

In the oxygenated TP and TI regions, reconstructed POP fluxes (**Figures 2A,D**) are very similar to those presented in Weber et al. (2016) for tropical regions. When normalized to the flux at ∼100 m (actually 114 m on our model grid), these flux profiles exhibit a similar shape to the canonical "Martin curve" (Martin et al., 1987), which attenuates over depth following a power-law relationship. At a depth of 1000 m, 15 ± 3% of the 100 m flux remains in the TP, and 18 ± 2% remains in the TI (**Figures 2C,F**), both similar to the 14% predicted by the Martin curve with canonical attenuation exponent of 0.858 (Martin et al., 1987).

Flux profiles in the ETNP and AS OMZ regions differ from the surrounding tropical waters in two ways. First, the export flux at the base of the euphotic zone is ∼30% higher in the OMZs than the oxygenated tropics in both ocean basins (**Figures 2B,E**), which can be attributed to the fact that OMZs are located in productive coastal upwelling regions. Second, and more importantly, the normalized flux profiles do not follow the same simple power-law shape over depth (**Figures 2C,F**). In the shallow subsurface (100–200 m), OMZ particle fluxes attenuate almost as quickly in the OMZs as in the surrounding tropics, but the attenuation slows significantly beneath 200 m, and the ETNP and AS profiles begin to diverge from the TP and TI profiles, respectively (**Figures 2C,F**). This divergence reaches its maximum at 1000 m, where 37 ± 4% of the 100 m flux remains in the ETNP, and 40 ± 8% remains in the AS. In both Pacific and Indian Oceans, particle transfer through the mesopelagic zone (100–1000 m) is therefore more than twice as efficient in OMZs than in oxygenated tropical waters. In the lower oxyclines beneath 1000 m, the ETNP and AS particle fluxes attenuate more rapidly again, re-converging with the TP and TI profiles, respectively. This provides strong evidence that the slow particle attenuation is specifically linked to water column suboxia, and not caused by unrelated differences such as larger particles or lower temperatures in the OMZs.

The results presented here are consistent with sediment trap observations, which also find particle transfer efficiency of ∼40% to 1000 m in OMZs (Devol and Hartnett, 2001; Van Mooy et al., 2002), and confirm that slow flux particle attenuation is a systematic and time-mean feature of OMZs. Our finding that slow attenuation is specifically associated with the suboxic layer is consistent with a recent study using thorium isotopes to reconstruct particle fluxes in the ETSP (Pavia et al., 2019), but our results do not support their finding that fluxes attenuate faster in the upper oxycline of the OMZ than in oxygenated water columns.

MECHANISTIC PARTICLE SIZE SPECTRUM MODEL

To investigate the mechanisms driving differences in flux attenuation between OMZs and oxygenated tropical waters, we employed the size-resolved particle spectrum model developed by DeVries et al. (2014) and updated by Bianchi et al. (2018). In this model, particles are produced in the surface euphotic zone (<100 m) following a power-law size spectrum, in which $\log_{10}$ (particle number density) declines linearly with $\log_{10}$ (diameter), and the relative abundance of large and small particles is controlled by the "slope" of the spectrum. The spectrum is discretized into ∼200 size classes between limits of 50 μm and 5 mm, and the organic carbon mass of each particle class is related to its diameter (d, in mm) by $POC = c_m d^{\alpha}$, where c_m (μgC) is the reference carbon mass of a 1 mm particle and α (unitless) is an

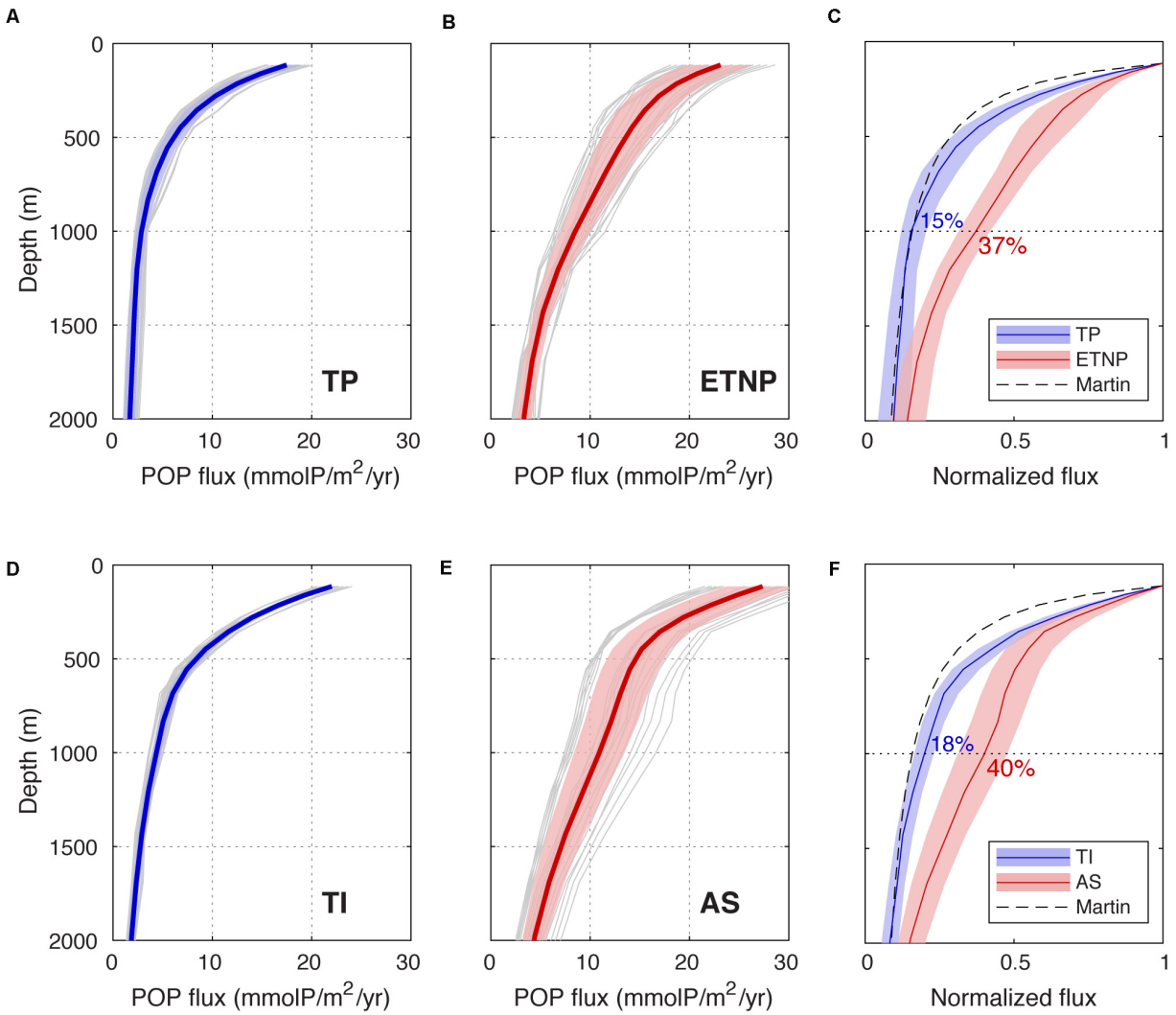

FIGURE 2 | Reconstructed particle flux profiles. **(A,B,D,E)**, Flux profiles of particulate organic phosphorus (POP) averaged across the TP, ETNP, TI and AS regions, respectively, reconstructed by diagnosing PO_4 accumulation in an ocean circulation model. Gray lines show the individual profiles derived from an ensemble of different ocean circulation models. Central red and blue lines show the ensemble-means, and shaded envelopes delineate $\pm$ 1σ from the mean. **(C)**, Ensemble-mean flux profiles and uncertainty envelopes from the TP and ETNP regions are normalized to the flux at the base of the euphotic zone, facilitating comparison between profile shapes in the oxygenated tropics and the OMZ. The fraction of the flux remaining at 1000 m is labeled for each region, and the canonical Martin curve (dashed black line) is shown for reference. **(F)** Same as **(C)** but for TI and AS regions.

exponent that accounts for the fractal nature of marine organic particles (Alldredge, 1998).

The simulated particle size spectrum then evolves through the water column due to remineralization, disaggregation, and size-dependent sinking, which are each parameterized based on empirically derived relationships and observed particle properties (Bianchi et al., 2018). Remineralization is represented by first-order mass loss from each particle at carbon-specific rate c_r (day^{-1}), which means that each particle shrinks and its sinking speed slows over depth, resulting in attenuation of the particle flux. When particles shrink beneath the lower size limit of 50 μm they are assumed to stop sinking and are transferred to a suspended particle class that remineralize *in situ*. Disaggregation is represented as first order mass loss from each size class at rate k_d (day^{-1}), which can be thought of as the probability of a given particle fragmenting in a unit time. Particles are assumed to fragment into a spectrum of smaller sized particles, which means their mass is re-apportioned among all smaller size classes (Bianchi et al., 2018). Because disaggregation transfers mass from large, fast-sinking size classes to small, slow-sinking classes, it also results in significant attenuation of the particle flux over depth, consistent with observations (Briggs et al., 2020).

The default model configuration used here (referred to as Model 0, see **Table 1**) is the same as that described in Bianchi et al. (2018), with two modifications. First, the model of Bianchi et al. (2018) simulates internal particle chemistry,

TABLE 1 | Summary of O_2 effects on the particle flux in each model configuration, and the hypothesis that is tested by the model.

	O_2 effect on particle flux	Hypothesis tested	Regions applied (RMSE)
Model 0	None (default model)	Null	TP (0.022), TI (0.025) ETNP (0.15), AS (0.18)
Model 1	Slow carbon oxidation following switch from aerobic respiration to denitrification	Hypothesis 1	ETNP (0.036) AS (0.057)
Model 2	Slow fragmentation of large particles at low O_2 due to reduced zooplankton activity	Hypothesis 2	ETNP (0.025) AS (0.027)
Model 3	Diffusion limitation of aerobic respiration and denitrification in large particles.	Hypothesis 3	ETNP (0.019) AS (0.033)

The final column lists the regions in which each model is applied, and in parentheses gives the root-mean-square error between the model-predicted normalized flux profiles (unitless) between 100 and 2000 m, and the "observed" profiles reconstructed from geochemical tracers.

allowing remineralization to be partitioned between different redox pathways. In Model 0, this behavior is "deactivated", and particles are assumed to remineralize homogeneously due to aerobic respiration. Second, we reformulate the remineralization rate constant c_r as function of temperature, to be consistent with laboratory cultures (Iversen and Ploug, 2013) and other recent modeling efforts (DeVries and Weber, 2017; Laufkötter et al., 2017; Cram et al., 2018):

$$c_r = c_{ref} Q_{10}^{(T-T_{ref})/10} \quad (1)$$

In Eq.1, c_{ref} is the carbon-specific oxidation rate at the reference temperature T_{ref} (here 20°C), and Q_{10} is the factor by which this rate increases/decreases for each 10°C of warming/cooling.

We developed three further configurations of the model (Models 1–3, **Table 1**), designed to formalize the three different effects of O_2 on particle fluxes proposed in Hypotheses 1–3 (see Section "Introduction"). Each of these configurations makes a single modification to Model 0, independently of one another. While a combination of the O_2 effects may operate in real OMZs, our "end-member" simulations serve to explore the flux profiles and particle spectra that would be produced when each mechanism operates in isolation.

Model 1 imposes a simple O_2 threshold effect on the c_r, representing slower carbon oxidation following a transition from aerobic respiration to denitrification as the sole remineralization pathway in suboxic waters (Hypothesis 1):

$$c_r = c_{ref} Q_{10}^{(T-T_{ref})/10} \left(\varepsilon_d + (1-\varepsilon_d) f_{O_2}\right), \text{ where}$$
$$f_{O_2} = .5 + .5\ tanh\ (O_2 - O_{2,crit}) \quad (2)$$

In Eq 2, ε_d is the ratio of the carbon oxidation rate achieved during denitrification to the rate achieved during aerobic respiration, and the transition between metabolisms occurs sharply when O_2 drops below $O_{2,crit}$ (Devol, 1978).

Model 2 represents the slowing of particle disaggregation in OMZs due to declining zooplankton activity at low [O_2] (Cavan et al., 2017) (Hypothesis 2). In Bianchi et al. (2018), the disaggregation rate constant k_d was chosen to ensure that large particle classes lose mass due to remineralization and disaggregation at relatively even rates, consistent with constraints from thorium isotopes (Lam and Marchal, 2015), and new evidence suggesting that fragmentation is responsible for up to 50% of the particle flux attenuation (Briggs et al., 2020). In Model 2, we redefine:

$$k_d = k_d^{\infty} \left(\varepsilon_f + (1-\varepsilon_f) f_{O_2}\right), \text{ where}$$
$$f_{O_2} = O_2/(O_2 + K_{O_2}) \quad (3)$$

In Eq. 3, $k_d{}^{\infty}$ is the fragmentation rate constant when O_2 is abundant, ε_f is the fraction of this rate that is maintained under anoxic conditions (which can be thought of as the fraction of disaggregation attributed to processes other zooplankton feeding) and K_{O2} is the half-saturation O_2 concentration for zooplankton activity.

Finally, Model 3 "reactivates" the full simulation of internal particle chemistry described in Bianchi et al. (2018), to represent the diffusion-limitation of carbon oxidation in suboxic water columns (Hypothesis 3). Briefly, this model represents the diffusive supply of oxidants into each particle, and their stepwise consumption in the particle interior by carbon oxidation. O_2 is consumed first, and if the demand exceeds the O_2 supply a denitrifying microenvironment is formed where NO_3 is reduced and carbon oxidation proceeds at ∼99% of the aerobic rate, reflecting the relative free energy yields of the pathways (Froelich et al., 1979). If NO_3 also becomes exhausted, a final internal microenvironment is formed in which Bianchi et al. (2018) assumed that carbon is oxidized extremely slowly by sulfate reduction. For simplicity, we instead assume that organic carbon oxidation cannot proceed at all in this NO_3-free zone.

Our goal is to determine which of the three mechanisms formalized in Models 1–3 can adequately explain the differences in reconstructed particle flux profiles between OMZs and the surrounding tropical waters (**Figures 2C,F**). To achieve this, we first fit Model 0 to the reconstructed flux profiles from the TP and TI regions, by optimizing c_{ref} and Q_{10} to minimize the root-mean-square error (RMSE) between the model prediction and the mean normalized flux profile from our ensemble of 12 different reconstructions (central blue line in **Figures 2C,F**). All other model parameters are left unchanged from Bianchi et al. (2018). The values of c_{ref} and Q_{10} determined for the TP region were propagated into all simulations of the ETNP, and the values

determined for TI were propagated into all simulations of the AS. In the ETNP and AS regions, Model 0 was first applied to test the null hypothesis that OMZ flux profiles can simply be explained by differences in water column temperature relative to the surrounding tropics, with no O_2 effect. Then, Models 1–3 were applied and optimized to assess Hypotheses 1–3.

In each optimization, a small number of parameters that control the strength of the O_2 effect on particle flux attenuation were adjusted to minimize the RMSE between the model and the reconstructed flux profiles (central red line in **Figures 2C,F**): In Model 1, ε_d and $O_{2,crit}$ were adjusted; in Model 2, ε_f and K_{O2} were adjusted; in Model 3, a single free parameter (c_m) was adjusted, which controls the carbon content of particles and therefore determines how quickly diffusion-limitation of carbon oxidation is reached (see Bianchi et al., 2018). Following model optimization, Hypotheses 1–3 can be assessed based on how well Models 1–3 reproduce the reconstructed OMZ flux profiles, and whether this can be achieved without violating prior constraints on the parameter values (see Section "Simulated Particle Fluxes in the OMZs").

All water column data required for these simulations (temperature for remineralization, O_2 and NO_3 for boundary conditions in Model 3) are taken from the World Ocean Atlas 2013 climatology (Garcia et al., 2013) and averaged across the regions shown in **Figure 1**. The particle spectrum slope at the base of the euphotic zone of all regions is set to −3.4, which was identified as characteristic value for low latitude systems in Bianchi et al. (2018).

SIMULATED PARTICLE FLUXES IN THE OMZS

Following parameter optimization, Model 0 accurately reproduced the time-mean particle flux profiles that we reconstructed for the oxygenated TP and TI regions (**Figures 3A,C**, **Table 1**). To achieve this, the model required carbon oxidation rate constants at 20°C of ∼0.6 day^{-1} and ∼0.5 day^{-1} in the TP and TI regions, respectively, which fall within the range of rates measured by particle-interceptors in warm low latitude regions (McDonnell et al., 2015). It also required Q_{10} of ∼2.4 and ∼2.1 in TP and TI, respectively, similar to the values selected by other data-constrained models (DeVries and Weber, 2017; Cram et al., 2018).

Reconstructed flux profiles in the ETNP and AS could not be reproduced by Model 0, which predicts flux profiles that attenuate far too rapidly over depth, demonstrating that temperature is not an important factor driving efficient particle transfer through OMZs (**Figures 3B,D**, **Table 1**). However, Models 1–3 could all reproduce the reconstructed OMZ flux profiles reasonably well following the parameter optimizations outlined in Section "Mechanistic Particle Size Spectrum Model" (**Figures 3B,D**, **Table 1**). Of the three configurations, Model 2 fit the reconstructed flux profile best in the AS region (RMSE≈0.03, unitless) and Model 3 fit best in the ETNP region (RMSE≈0.02), whereas Model 1 was least skillful in both regions (∼0.06 in AS; ∼0.04 in ETNP). This is because Model 1 predicts that the particle flux attenuates slightly faster than observed in the lower oxycline beneath the suboxic layer (**Figures 3B,D**). However, all three models can largely fit the reconstructed fluxes within their uncertainty envelopes, suggesting the shape of the particle flux profiles does not place a strong constraint on the mechanism driving slow attenuation in the OMZs.

In Model 1, our optimization process selects ε_d of ∼0.19 and ∼0.17 in ETNP and AS, suggesting that carbon oxidation must slow down more than 80% following the transition from aerobic respiration to denitrification, in order to best explain the reconstructed fluxes. This is not consistent with the difference in free energy yield between the two process, which is only ∼1% (Froelich et al., 1979), but might be explained by lag time associated with particle colonization by the denitrifying microbial community, which remains poorly quantified to date (Bristow, 2018), or other processes that limit the efficiency of anaerobic metabolisms. The optimization also selects $O_{2,crit}$ of 15 μM and 20 μM in ETNP and AS, respectively, which is much higher than the range of 2–5 μM observed to select for denitrifying metabolisms in cultures (Devol, 1978). Taken together, these parameter selections cast doubt on the idea that slow carbon oxidation during denitrification is the primary driver of slow flux attenuation in OMZs (Hypothesis 1).

In Model 2, our optimization selects ε_f of ∼0.02 in both ETNP and AS regions, which means that disaggregation must be almost entirely curtailed in suboxic water in order to explain the reconstructed flux profiles, requiring that very little disaggregation occurs due to processes other than zooplankton feeding. It also selects K_{O2} of ∼22 μM in ETNP and ∼40 μM in AS, consistent with observations that zooplankton generally adjust their migration depth to avoid hypoxic ($[O_2] < 60$ μM) regions of the water column, not just suboxic waters (Bianchi et al., 2013).

Finally, in Model 3 our optimization process selects c_m (carbon content of a 1 mm particle) of 6.8 μgC in ETNP and 7.2 μgC in AS, which both fall within the observationally constrained range of 5.5–8 μgC defined in Bianchi et al. (2018). This model predicts that large NO_3-depleted microenvironments develop in the interior of particles >0.5 mm in the suboxic layers of the ETNP and AS, and particles >1 mm also harbor these microenvironments in the upper and lower oxyclines, dramatically curtailing remineralization of large particles through the water column.

PARTICLE SIZE SPECTRA DISTINGUISH BETWEEN ATTENUATION MECHANISMS

Even though Models 1–3 achieve relatively similar flux profiles (**Figures 3B,D**), they make very different predictions about how the particle size spectrum evolves through the OMZ, and how it diverges from the spectra generated in oxygenated water columns (**Figure 4**). Here, we analyze particle spectra only from simulations of the TP and ETNP regions for brevity, although similar conclusions can be drawn from the TI and AS regions.

In our model, changes in the size spectrum over depth are largely driven by the balance of remineralization, disaggregation,

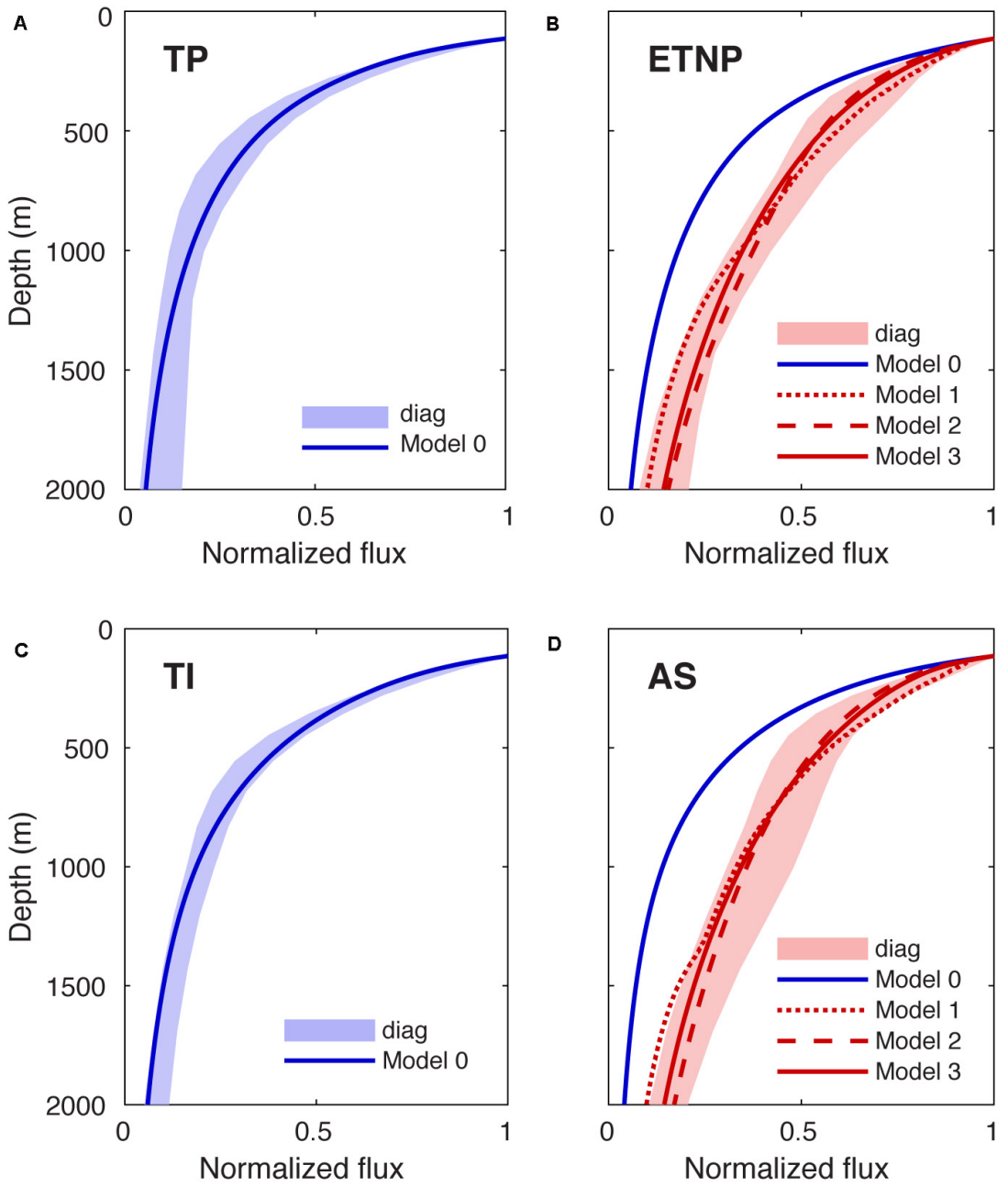

FIGURE 3 | Particle flux profiles predicted by a mechanistic size-resolved model. **(A)** Normalized particle flux predicted by the default Model 0 configuration (blue line) in the TP region, compared to the uncertainty envelope of the reconstructed flux (blue shading, repeated from **Figure 2C**). **(B)** Predicted particle fluxes in the ETNP region from Model 0 (blue line) and Models 1–3 (red lines), which simulate different O_2 effects on particle flux attenuation, compared to the reconstructed profile (red shading). **(C,D)** Same as **(A,B)** but for the TI and AS regions, respectively.

and sinking. While all particles remineralize at the same first-order rate, smaller particles spend a longer time within each depth interval due to their slower sinking speed, and so remineralize shallower in the water column. The effect of remineralization is therefore a "flattening" of the particle spectrum over depth, due to the preferential loss of particles from the small end of the spectrum. Disaggregation has the opposite effect: by redistributing mass from large to small particle size classes, it tends to "steepen" the particle size spectrum. In the default configuration of our model (Model 0), the relatively even rates of disaggregation and remineralization means their opposing effects on the particle size spectrum largely balance one another, and the particles are lost evenly from all size classes over depth (**Figure 4A-upper**) in the TP region, causing little variation in the size spectrum slope (**Figures 4A-lower**, **5A**). This is consistent with a compilation of UVP particle observations from

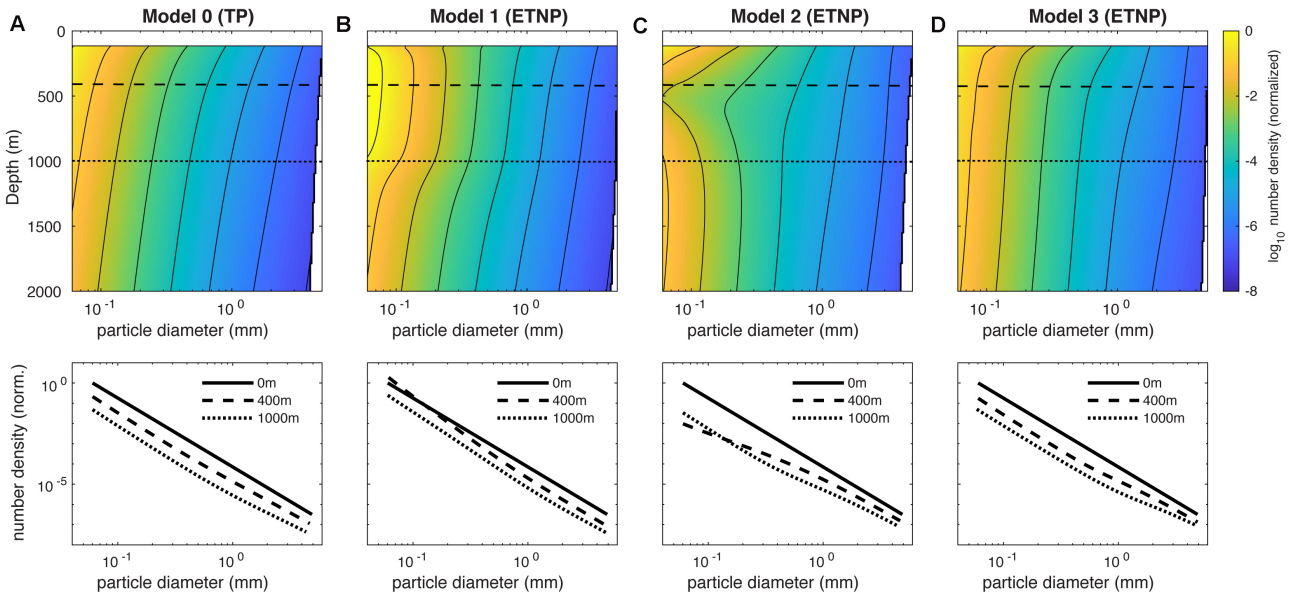

FIGURE 4 | Predicted particle size spectra in our mechanistic model. **(A)**, Upper panel shows the particle number density predicted in the TP region by Model 0, as a function of depth and particle diameter. Number density in $\#mm^{-1}$ is normalized to the abundance of the smallest size class in the surface ocean, yielding a dimensionless size spectrum. Lower panel shows the surface size spectrum (solid line, slope = –3.4) and "slices" through the spectrum at depths of 400 m (oxygen minimum) and 1000 m (lower oxycline), which are indicated on the upper panel as dashed and dotted lines, respectively. **(B–D)**, Same as **(A)**, but showing the size spectra predicted by Models 1–3 in the ETNP region. Each of these models predicts unique differences in the OMZ size spectra relative to the oxic water column.

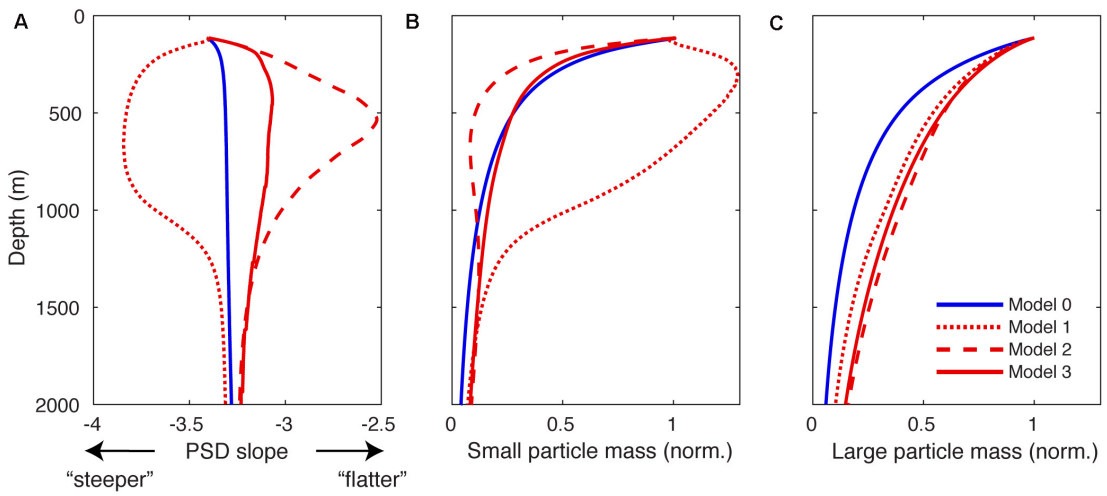

FIGURE 5 | Summary statistics of simulated particle spectra. **(A)**, Slope of the particle spectrum as a function of depth predicted by Model 0 in the TP region and by Models 1–3 in the ETNP region, derived by fitting a straight line through the simulated spectrum at each model depth horizon. More negative numbers indicate a "steeper" spectrum that is more dominated by small particles, and less negative numbers indicate a "flatter" spectrum that is more dominated by large particles. **(B)** Mass of particulate organic matter (POM) integrated across small particle size classes, defined here as < 0.5 mm, and normalized to the mass at 100 m. **(C)** Same as **(B)** but for large aggregate particles >0.5 mm.

the oxic Tropical Atlantic Ocean, which revealed no systematic variations over depth (Bianchi et al., 2018).

Models 1–3 each predict particle spectra in the OMZ that diverge from this simple behavior in unique ways. In Model 1, particles smaller than ∼100 μm actually increase in abundance moving from the surface into the suboxic layer, while large particle abundance declines (**Figure 4B-upper**). This is because when remineralization is suppressed at $O_2 < O_{2,crit}$ (Eq. 2), the transfer of mass from large to small size classes by disaggregation becomes the primary mechanism shaping the particle size spectrum. The spectrum slope therefore steepens moving into the core of suboxic layer (**Figures 4B-lower**, **5A**), before flattening again toward the original value of −3.4 in the lower oxycline (**Figure 5A**).

In Model 2, small particles are lost very rapidly moving into the OMZ (**Figure 4C-upper**), compared to their loss rate over the same depth interval in the oxygenated water column (**Figure 4A-upper**). With disaggregation suppressed at low O_2 (Eq. 3), the preferential loss of small particles due to remineralization becomes the dominant process shaping the particle spectrum, and the spectral slope sharply flattens moving into the suboxic layer (**Figure 4C-lower**), reaching a value of −2.5 at ∼500 m (**Figure 5A**). The spectrum then steepens again in the lower oxycline (**Figures 4C-lower**, **5A**) where disaggregation resumes in waters that become habitable for zooplankton once more (Wishner et al., 1998).

In Model 3, particles larger than 0.5 mm are preferentially preserved through the suboxic layer due to the diffusion-limitation of carbon oxidation (**Figure 4D-upper**), resulting in flattening of the particle flux, followed by a gradual steepening through the lower oxycline (**Figures 4D-upper**, **5A**). Although Models 2 and 3 both predict flattening size spectra over depth in the OMZ, indicating that large particles become more abundant relative to small particles, the two mechanisms can be distinguished based on a closer analysis of the spectra. Model 3 predicts a much subtler flattening of the spectrum than Model 2, reaching a minimum slope of −3.1 compared to −2.5 in Model 2 (**Figure 5A**). In Model 3, even though small particles are preferentially lost due to remineralization in the OMZ, they are rapidly replenished through disaggregation. Therefore, in comparison to an oxygenated water column, Hypothesis 3 predicts a relatively similar concentration profile of small particles (<0.5 mm) in the OMZ, whereas Hypothesis 2 predicts a much more rapid decline in small particle concentration in the suboxic layer (**Figure 5B**). By contrast, Hypothesis 1 uniquely predicts that the concentration of small particles actually increases over the same depth interval (**Figure 5B**). This analysis suggests that the smaller end of the particle spectrum contains the most important clues for distinguishing between different mechanisms of slow flux attenuation through OMZs, whereas all mechanisms predict higher concentrations of large particles relative to the oxic water column (**Figure 5C**).

Identifying the unique particle size spectrum signatures of O_2 effects on remineralization and disaggregation opens a promising new pathway for understanding the mechanisms driving the efficient biological pump of OMZ regions, through analysis of UVP size spectrum observations. These instruments allow accurate enumeration of particles between the size limits of 100 μm−2.6 mm (Picheral et al., 2010), spanning most of the size range simulated in our model, and therefore provide ideal datasets for evaluating our model formalizations of Hypotheses 1–3.

A compilation 6 UVP size spectrum profiles from the ETSP (Bianchi et al., 2018), found that the spectral slope increased slightly between 100 and 1000 m, largely driven by increased abundance of large particles relative to an oxic water column, rather than decreased abundance of small particles. This is not consistent with Hypothesis 1 (slow remineralization during denitrification) and is most consistent with the predictions of Hypothesis 3 (diffusion limitation of carbon oxidation in large particles). However, this analysis was far too limited to draw firm conclusions, and further analysis of UVP observations from all three of the ocean's major OMZs is required in order to assess systematic patterns in their particle size spectra.

Because each UVP image serves only as a snapshot of the particle flux, and can be strongly influenced by pulses of organic matter, compilation of numerous UVP profiles from a single location or region will be critical to identify coherent features of the particle spectrum. The new Ecotaxa repository for UVP images (Picheral et al., 2017) may now contain sufficient data to construct meaningful composites for comparing OMZs to oxic tropical regions, but this analysis is beyond the scope of the current study. By showing that different flux attenuation mechanisms leave an imprint in particle size spectra, we hope to motivate further work scrutinizing the existing UVP archives, and new field campaigns that collect targeted UVP data across oxygen gradients in the ocean.

Given that a combination of oxygen effects likely operates in the OMZs (with different mechanisms potentially dominating in the upper and low oxyclines and the OMZ core) size spectra from these regions may exhibit a complex blend of the end-member patterns shown in **Figure 4**. In this case, UVP data alone may be insufficient to adequately determine the relative importance of each mechanism, and future work will greatly benefit from collecting additional particulate data alongside UVP profiles. Because disaggregation can produce particles smaller than the lower UVP detection limit of ∼100 μm (Lam and Marchal, 2015), extending the spectral range using alternative particle-counting instruments (Stemmann and Boss, 2012) or microscopy (Durkin et al., 2015) would help quantify the difference in disaggregation rates between OMZs and oxygenated waters. Additionally, measuring trace-metal (Janssen et al., 2014) and genomic (Ganesh et al., 2015) indicators of particle interior redox conditions would further elucidate the degree to which diffusion-limited microenvironments impede carbon oxidation in OMZs. When supplied with this broad range of observational constraints, our mechanistic particle model will be better equipped to assess the balance of processes that control particle fluxes through OMZs.

It is also worth noting that while our model includes the main processes that contribute to particle flux attenuation with depth, it does not consider other processes that may contribute to weaker flux attenuation in OMZ. These include particle formation at depth (e.g., by autotrophy or zooplankton vertical migration), zooplankton detritivory, and various effects of ballasting material, among others (Keil et al., 2016). For completeness, these processes should be considered in future modeling of OMZ particle fluxes.

CONCLUSION

The key contribution of this study is the new constraints we have placed on the efficiency of the biological pump in OMZ regions, by reconstructing time-mean particle flux profiles for the Eastern Tropical North Pacific and the Arabian Sea

from geochemical tracer data. These reconstructions revealed slow particle flux attenuation over depth in the suboxic water column, consistent with previous evidence from sediment trap "snapshots" (Devol and Hartnett, 2001; Keil et al., 2016) and confirming that this is a systematic feature of OMZ particle fluxes. Compared to surrounding tropical waters, the fraction of organic matter sinking from the euphotic zone that penetrates the mesopelagic zone to 1000 m is more than twice as large in OMZs. The convergence of OMZ flux profiles toward those from oxic water columns revealed in our reconstructions beneath 1000 m providers compelling new evidence that suboxia itself is the factor driving slow flux attenuation (**Figures 2C,F**).

Using a mechanistic particle flux model we showed that the shape of OMZ flux profiles can be explained by any of three oxygen effects: (i) very slow carbon oxidation during denitrification (Devol and Hartnett, 2001; Van Mooy et al., 2002); (ii) dramatically reduced fragmentation in suboxic waters due to exclusion of zooplankton (Cavan et al., 2017); (iii) diffusion limitation of carbon oxidation in large particles (Bianchi et al., 2018). However, each of these mechanisms makes unique predictions about changes in particle size spectra through the water column, opening the possibility to extract mechanistic information from UVP observations. The idealized end-member cases presented here serve as a starting point for interpreting patterns in UVP spectral data from OMZ regions.

We suggest that combining existing UVP archives, new targeted observations across oxygen gradients, and mechanistic models like the one used here is a promising approach for unraveling the processes driving efficient biological pump of OMZs. In turn, this will allow for improved prediction of carbon sequestration in the future ocean, where continued warming and deoxygenation are likely to reshape the efficiency of the biological pump (Laufkötter et al., 2017; Cram et al., 2018).

DATA AVAILABILITY STATEMENT

The datasets presented in this study can be found in online repositories. The names of the repository/repositories and accession number(s) can be found below: 10.6084/m9.figshare.12401000.

AUTHOR CONTRIBUTIONS

TW and DB designed the study and analyzed the results. TW conducted the flux reconstruction analysis, implemented the mechanistic particle flux model, and wrote the manuscript, with input from DB. Both authors contributed to the article and approved the submitted version.

FUNDING

This work was supported by NSF grants OCE-1635414 awarded to TW and OCE-1635632 awarded to DB.

ACKNOWLEDGMENTS

We thank Tim DeVries for providing access to the updated version of the Ocean Circulation Inverse Model (OCIM) used in our flux reconstructions, and Jacob Cram for discussions that helped motivate this study.

REFERENCES

Alldredge, A. (1998). The carbon, nitrogen and mass content of marine snow as a function of aggregate size. *Deep Sea Res. Part I Oceanogr. Res. Papers* 45, 529–541. doi: 10.1016/s0967-0637(97)00048-4

Bianchi, D., Galbraith, E. D., Carozza, D. A., Mislan, K. A. S., and Stock, C. A. (2013). Intensification of open-ocean oxygen depletion by vertically migrating animals. *Nat. Geosci.* 6, 545–548. doi: 10.1038/ngeo1837

Bianchi, D., Weber, T. S., Kiko, R., and Deutsch, C. (2018). Global niche of marine anaerobic metabolisms expanded by particle microenvironments. *Nat. Geosci.* 11, 263–268. doi: 10.1038/s41561-018-0081-0

Bopp, L., Resplandy, L., Orr, J. C., Doney, S. C., Dunne, J. P., Gehlen, M., et al. (2013). Multiple stressors of ocean ecosystems in the 21st century: projections with CMIP5 models. *Biogeosciences* 10, 3627–3676. doi: 10.5194/bgd-10-3627-2013

Boyd, P. W., Claustre, H., Levy, M., Siegel, D. A., and Weber, T. (2019). Multi-faceted particle pumps drive carbon sequestration in the ocean. *Nature* 568, 327–335. doi: 10.1038/s41586-019-1098-2

Briggs, N., Dall'olmo, G., and Claustre, H. (2020). Major role of particle fragmentation in regulating biological sequestration of CO⁢sub>2⁢/sub> by the oceans. *Science* 367:791. doi: 10.1126/science.aay1790

Bristow, L. A. (2018). Anoxia in the snow. *Nat. Geosci.* 11, 226–227. doi: 10.1038/s41561-018-0088-6

Buesseler, K. O., Lamborg, C. H., Boyd, P. W., Lam, P. J., Trull, T. W., Bidigare, R. R., et al. (2007). Revisiting Carbon Flux Through the Ocean ' s Twilight Zone. *Science* 316, 567–570.

Cavan, E. L., Trimmer, M., Shelley, F., and Sanders, R. (2017). Remineralization of particulate organic carbon in an ocean oxygen minimum zone. *Nat. Commun.* 8:14847.

Cram, J. A., Weber, T., Leung, S. W., McDonnell, A. M. P., Liang, J.-H., and Deutsch, C. (2018). The Role of Particle Size, Ballast, Temperature, and Oxygen in the Sinking Flux to the Deep Sea. *Glob. Biogeochem. Cycles* 32, 858–876. doi: 10.1029/2017gb005710

Devol, A. H. (1978). Bacterial oxygen uptake kinetics as related to biological processes in oxygen deficient zones of the oceans. *Deep Sea Res.* 25, 137–146. doi: 10.1016/0146-6291(78)90001-2

Devol, A. H., and Hartnett, H. E. (2001). Role of the oxygen-deficient zone in transfer of organic carbon to the deep ocean. *Limnol. Oceanogr.* 46, 1684–1690. doi: 10.4319/lo.2001.46.7.1684

DeVries, T., and Holzer, M. (2019). Radiocarbon and Helium Isotope Constraints on Deep Ocean Ventilation and Mantle-3He Sources. *J. Geophys. Res.* 124, 3036–3057. doi: 10.1029/2018jc014716

DeVries, T., Liang, J.-H., and Deutsch, C. (2014). A mechanistic particle flux model applied to the oceanic phosphorus cycle. *Biogeosciences* 11, 5381–5398. doi: 10.5194/bg-11-5381-2014

DeVries, T., Primeau, F., and Deutsch, C. (2012). The sequestration efficiency of the biological pump. *Geophys. Res. Lett.* 39, 1–5.

DeVries, T., and Weber, T. (2017). The export and fate of organic matter in the ocean: new constraints from combining satellite and oceanographic tracer observations. *Glob. Biogeochem. Cycles* 31, 535–555. doi: 10.1002/2016gb005551

Durkin, C. A., Estapa, M. L., and Buesseler, K. O. (2015). Observations of carbon export by small sinking particles in the upper

mesopelagic. *Mar. Chem.* 175, 72–81. doi: 10.1016/j.marchem.2015.02.011

Froelich, P. N., Klinkhammer, G., Bender, M. A. A., Luedtke, N., Heath, G. R., Cullen, D., et al. (1979). Early oxidation of organic matter in pelagic sediments of the eastern equatorial Atlantic: suboxic diagenesis. *Geochim. Cosmochim. Acta* 43, 1075–1090. doi: 10.1016/0016-7037(79)90095-4

Ganesh, S., Bristow, L. A., Larsen, M., Sarode, N., Thamdrup, B., and Stewart, F. J. (2015). Size-fraction partitioning of community gene transcription and nitrogen metabolism in a marine oxygen minimum zone. *ISME J.* 9, 2682–2696. doi: 10.1038/ismej.2015.44

Garcia, H. E., Locarnini, R. A., Boyer, T. P., Antonov, J. I., Baranova, O. K., Zweng, M. M., et al. (2013). "World Ocean Atlas 2013, Volume 4: dissolved Inorganic Nutrients (phosphate, nitrate, silicate), in *NOAA Atlas NESDIS 68*, Ed. S. Levitus (Washington, DC: U.S. Government Printing Office).

Iversen, M., and Ploug, H. (2013). Temperature effects on carbon-specific respiration rate and sinking velocity of diatom aggregates–potential implications for deep ocean export processes. *Biogeosciences* 10, 4073–4085. doi: 10.5194/bg-10-4073-2013

Janssen, D. J., Conway, T. M., John, S. G., Christian, J. R., Kramer, D. I., Pedersen, T. F., et al. (2014). Undocumented water column sink for cadmium in open ocean oxygen-deficient zones. *Proc. Natl. Acad. Sci. U.S.A.* 111, 6888–6893. doi: 10.1073/pnas.1402388111

Keil, R. G., Neibauer, J. A., Biladeau, C., Elst, K. V. D., and Devol, A. H. (2016). A multiproxy approach to understanding the " enhanced " flux of organic matter through the oxygen-deficient waters of the Arabian Sea. *Biogeosciences* 13, 2077–2092. doi: 10.5194/bg-13-2077-2016

Kiko, R., Hauss, H., Buchholz, F., and Melzner, F. (2016). Ammonium excretion and oxygen respiration of tropical copepods and euphausiids exposed to oxygen minimum zone conditions. *Biogeosciences* 13, 2241–2255. doi: 10.5194/bg-13-2241-2016

Lam, P. J., and Marchal, O. (2015). Insights into particle cycling from thorium and particle data. *Ann. Rev. Mar. Sci* 7, 159–184. doi: 10.1146/annurev-marine-010814-015623

Laufkötter, C., John, J. G., Stock, C. A., and Dunne, J. P. (2017). Temperature and oxygen dependence of the remineralization of organic matter. *Glob. Biogeochem. Cycles* 31, 1038–1050. doi: 10.1002/2017gb005643

Lu, Z., Hoogakker, B. A. A., Hillenbrand, C.-D., Zhou, X., Thomas, E., Gutchess, K. M., et al. (2016). Oxygen depletion recorded in upper waters of the glacial Southern Ocean. *Nat. Commun.* 7:11146.

Marsay, C. M., Sanders, R. J., Henson, S. A., Pabortsava, K., and Achterberg, E. P. (2014). Attenuation of sinking particulate organic carbon flux through the mesopelagic ocean. *PNAS* 112, 1089–1094. doi: 10.1073/pnas.1415311112

Martin, J. H., Knauer, G. A., Karl, D. M., and Broenkow, W. W. (1987). VERTEX: carbon cycling in the northeast Pacific. *Deep Sea Res. Part A Oceanogr. Res. Papers* 34, 267–285. doi: 10.1016/0198-0149(87)90086-0

McDonnell, A. M. P., Boyd, P. W., and Buesseler, K. O. (2015). Effects of sinking velocities and microbial respiration rates on the attenuation of particulate carbon fluxes through the mesopelagic zone. *Glob. Biogeochem. Cycles* 29, 175–193. doi: 10.1002/2014gb004935

Passow, U., and Carlson, C. (2012). The biological pump in a high CO2 world. *Mar. Ecol. Progr. Ser.* 470, 249–271.

Pavia, F. J., Anderson, R. F., Lam, P. J., Cael, B. B., Vivancos, S. M., Fleisher, M. Q., et al. (2019). Shallow particulate organic carbon regeneration in the South Pacific Ocean. *Proc. Natl. Acad. Sci. U.S.A.* 116:9753. doi: 10.1073/pnas.1901863116

Picheral, M., Colin, S., and Irisson, J.-O. (2017). EcoTaxa, a tool for the taxonomic classification of images. Available online at: http://ecotaxa.obs-vlfr.fr

Picheral, M., Guidi, L., Stemmann, L., Karl, D. M., Iddaoud, G., and Gorsky, G. (2010). The Underwater Vision Profiler 5: an advanced instrument for high spatial resolution studies of particle size spectra and zooplankton. *Limnol. Oceanogr.* 8, 462–473. doi: 10.4319/lom.2010.8.462

Ploug, H. (2001). Small-scale oxygen fluxes and remineralization in sinking aggregates. *Limnol. Oceanogr.* 46, 1624–1631. doi: 10.4319/lo.2001.46.7.1624

Schmidtko, S., Stramma, L., and Visbeck, M. (2017). Decline in global oceanic oxygen content during the past five decades. *Nature* 542, 335–339. doi: 10.1038/nature21399

Seibel, B. A. (2011). Critical oxygen levels and metabolic suppression in oceanic oxygen minimum zones. *J. Exp. Biol.* 214:326. doi: 10.1242/jeb.049171

Stemmann, L., and Boss, E. (2012). Plankton and particle size and packaging: from determining optical properties to driving the biological pump. *Ann. Rev. Mar. Sci.* 4, 263–290. doi: 10.1146/annurev-marine-120710-100853

Stemmann, L., Picheral, M., Guidi, L., Lombard, F., Prejger, F., Claustre, H., et al. (2012). "Assessing the spatial and temporal distributions of zooplankton and marine particles using the Underwater Vision Profiler," in *Sensors for Ecology: Towards Integrated Knowledge of Ecosystems*, J.F Le Galliard, J.F Guarini, and F. Gaill (France: Institut Ecologie et Environnement), 119.

Van Mooy, B. A. S., Keil, R. G., and Devol, A. H. (2002). Impact of suboxia on sinking particulate organic carbon: enhanced carbon flux and preferential degradation of amino acids via denitrification. *Geochim. Cosmochim. Acta* 66, 457–465. doi: 10.1016/s0016-7037(01)00787-6

Weber, T., Cram, J. A., Leung, S. W., Devries, T., and Deutsch, C. (2016). Deep ocean nutrients imply large latitudinal variation in particle transfer efficiency. *Proc. Natl. Acad. Sci. U.S.A.* 113, 8606–8611. doi: 10.1073/pnas.1604414113

Wishner, K. F., Gowing, M. M., and Gelfman, C. (1998). Mesozooplankton biomass in the upper 1000m in the Arabian Sea: overall seasonal and geographic patterns, and relationship to oxygen gradients. *Deep Sea Res. Part II Top. Stud. Oceanogr.* 45, 2405–2432. doi: 10.1016/s0967-0645(98)00078-2

Wishner, K. F., Outram, D. M., Seibel, B. A., Daly, K. L., and Williams, R. L. (2013). Zooplankton in the eastern tropical north Pacific: boundary effects of oxygen minimum zone expansion. *Deep Sea Res. Part I Oceanogr. Res. Papers* 79, 122–140. doi: 10.1016/j.dsr.2013.05.012

Wishner, K. F., Seibel, B. A., Roman, C., Deutsch, C., Outram, D., Shaw, C. T., et al. (2018). Ocean deoxygenation and zooplankton: very small oxygen differences matter. *Sci. Adv.* 4:eaau5180. doi: 10.1126/sciadv.aau5180

Wright, J. J., Konwar, K. M., and Hallam, S. J. (2012). Microbial ecology of expanding oxygen minimum zones. *Nat. Rev. Microbiol.* 10, 381–394. doi: 10.1038/nrmicro2778

Conflict of Interest: The authors declare that the research was conducted in the absence of any commercial or financial relationships that could be construed as a potential conflict of interest.

frontiers in Earth Science

ORIGINAL RESEARCH
published: 08 September 2020
doi: 10.3389/feart.2020.00366

Effective Vertical Transport of Particulate Organic Carbon in the Western North Pacific Subarctic Region

*Makio C. Honda**

Japan Agency for Marine-Earth Science and Technology, Yokosuka, Japan

To quantify the biological carbon pump in the Northwestern Pacific and project future changes induced by multiple stressors, a comparative biogeochemistry study of subarctic-eutrophic and subtropical-oligotrophic regions, the K2S1 project, was conducted between 2010 and 2014. The present study uses data collected during the K2S1 project to re-examine the biological carbon pump in subarctic and subtropical regions of the northwestern Pacific with a focus on the factors governing the attenuation of the downward fluxes of particulate organic carbon (POC). Seasonal and time-series observations made during the K2S1 project revealed that primary productivity and the POC flux in the upper 200 m at subtropical-oligotrophic station S1 were comparable to or slightly higher than those at subarctic-eutrophic station K2, but the POC flux at a depth of ∼5000 m at K2 was 2–3 times that at S1. Based on these observations, the index of vertical attenuation (exponent *b* of the "Martin curve") was estimated to be 0.64 at K2 and 0.90 at S1. The downward transport of POC was therefore more efficient at the subarctic station than at the subtropical station. Sinking particles were ballasted mainly by biogenic opal (Opal) at K2 and by $CaCO_3$ at S1. The results of a multiple linear regression analysis of sediment trap data indicated that among potential ballast materials, Opal was most strongly correlated with POC at K2. Thus, Opal might contribute to the more effective vertical transport of POC in the western North Pacific Subarctic region. In addition, lower water temperatures and dissolved oxygen concentrations in the twilight zone (200–1000 m depth) at K2 likely slowed microbial decomposition of organic carbon and may also have contributed to the smaller attenuation of the downward POC flux. However, seasonal observations indicated that the carbon demand of zooplankton (prokaryotes) in the water column at K2 was ∼2.5 (1.5) times that at S1. These results were inconsistent with the lower rate of attenuation of POC fluxes at K2. Moreover, the carbon demand at the two stations inferred from the POC fluxes and the carbon fluxes associated with diurnal migration by zooplankton exceeded the carbon supply, especially at K2. Other sources of carbon, such as slowly sinking and suspended POC, might account for this mismatch.

Keywords: biological carbon pump, K2S1 project, sediment trap, vertical attenuation, biogenic opal, metabolism, mismatch between carbon supply and demand

OPEN ACCESS

Edited by:
Timothy Ferdelman, Max Planck Institute for Marine Microbiology (MPG), Germany

Reviewed by:
Frank Dehairs, Vrije University Brussel, Belgium
Joeran Maerz, Max Planck Institute for Meteorology, Germany

***Correspondence:**
Makio C. Honda
hondam@jamstec.go.jp

Specialty section:
This article was submitted to Biogeoscience, a section of the journal Frontiers in Earth Science

Received: *02 April 2020*
Accepted: *07 August 2020*
Published: *08 September 2020*

Citation:
Honda MC (2020) Effective Vertical Transport of Particulate Organic Carbon in the Western North Pacific Subarctic Region. Front. Earth Sci. 8:366. doi: 10.3389/feart.2020.00366

INTRODUCTION

The biological carbon pump (BCP) is a crucial mechanism by which atmospheric CO_2 is taken up by the ocean and transported to the ocean interior. Without the BCP, the pre-industrial atmospheric CO_2 concentration (∼280 ppm) would have risen to ∼460 ppm (Volk and Hoffert, 1985). At present, the particulate organic carbon (POC) flux from the surface layer of the ocean to the ocean interior has been estimated to be 4–13 Pg-C year^{-1} (Lima et al., 2014). To evaluate the efficiency of the BCP, it is necessary to quantify the vertical attenuation of the POC flux with depth because the deeper that POC is transported, the longer the CO_2 will be isolated from the atmosphere. Thus, an increase in the efficiency of the BCP has the potential to cause an increase of ocean carbon sequestration of atmospheric CO_2 that would result in a negative feedback on global warming. The vertical attenuation of the POC flux has been investigated since the 1980s (e.g., Suess, 1980; Betzer et al., 1984; Berger et al., 1987; Pace et al., 1987), and Martin et al. (1987) have proposed the following power law function to describe POC flux attenuation:

$$\mathrm{POCF_{(z)}} = \mathrm{POCF_{(100)}} \times (\mathrm{z}/100)^{-\mathrm{b}} \quad (1)$$

where z is water depth (m), and $\mathrm{POCF}_{(z)}$ and $\mathrm{POCF}_{(100)}$ are the POC fluxes at depths of z m and 100 m, respectively. Although other functions, such as an exponential curve, have also been proposed and validated (Gloege et al., 2017; Cael and Bisson, 2018 and references in these papers), this power law function, commonly known as the "Martin curve," has been used very frequently in discussions of the BCP, and the exponent b in this equation has been used as an index of BCP efficiency (e.g., Berelson, 2001): the larger the exponent b, the higher the vertical attenuation rate of the POC flux and the lower the BCP efficiency. Moreover, numerical simulations have shown that a change in the value of b would significantly change the atmospheric CO_2 concentration (Yamanaka and Tajika, 1996; Kwon et al., 2009; Wilson et al., 2019).

The vertical attenuation rate of the POC flux is very dependent on the sinking velocity and decomposition rate of POC in the water column. Because POC is labile and has little negative buoyancy, it must be aggregated with relatively heavy materials called ballast to settle gravitationally in the ocean. Materials that may serve as ballast include biogenic opal (hereinafter Opal), $CaCO_3$, and aluminosilicates. Ittekkot (1993) have hypothesized that the drastic decrease from ∼280 to ∼200 ppm of atmospheric CO_2 that occurred during the last glacial maximum (e.g., Lorius et al., 1990) was caused by an increase of the input of aeolian dust (aluminosilicate ballast) to the ocean, which strengthened the BCP. Francois et al. (2002); Klaas and Archer (2002), who compiled and analyzed global sediment trap data, have suggested that $CaCO_3$, which has the largest density among possible ballast materials, is globally the most important and effective facilitator of vertical POC transport, because the transfer efficiency (the ratio of the POC flux in the deep sea to that at the bottom of the surface mixed layer) is higher in subtropical and tropical areas where $CaCO_3$ is a major component of marine snow. Moreover, reported sinking velocities of $CaCO_3$-rich particles are high (Fisher and Karakas, 2009; Sukigara et al., 2019). Numerical simulations that take into account these findings have indicated that future ocean acidification will reduce the efficiency of the BCP by decreasing ocean calcification (Heinze, 2004). In addition, the POC export ratio (the ratio of the POC flux from an upper layer [a fixed depth such as 100 m, or the euphotic zone or mixed layer] to net primary productivity) in subtropical and tropical areas is low because high temperatures in the upper layer increase POC decomposition rates (e.g., Laws et al., 2000). The result might be a higher transfer efficiency and a strong positive correlation between POC and $CaCO_3$ in these low-latitude areas (Francois et al., 2002; Henson et al., 2012): labile POC, which is fresher and easier for microbes to break down, decomposes in the upper layer, and relatively refractory POC is transported to the ocean interior in low-latitude areas.

On the basis of observations that revealed a large increase of POC fluxes in high-latitude areas during diatom blooms and on the fact that diatoms are much bigger than coccolithophorids (Buesseler, 1998; Buesseler et al., 2007, 2008), Honda and Watanabe (2010) have proposed that Opal, rather than $CaCO_3$, is crucial as ballast for effective POC vertical transport in subarctic regions. Weber et al. (2016) have also reported a strong negative correlation between transfer efficiency and the picoplankton fraction of plankton as well as higher transfer efficiencies in high-latitude areas, where large phytoplankton such as diatoms predominate. They have also calculated that the fraction of vertically transported CO_2 that has been sequestered in the ocean interior for at least 100 years is higher in high-latitude (polar and subpolar) regions than in low-latitude regions.

In contrast, Bach et al. (2019) conducted a mesocosm experiment to study how the plankton community structure affected sinking velocities and reported that during more productive periods the sinking velocity of aggregated particles was not necessarily higher, because the aggregated particles produced then were very fluffy; rather, the settling velocity was higher when the phytoplankton were dominated by small cells. In addition, Henson et al. (2012) have revisited the global sediment trap data and have reported that the POC flux is negatively correlated with the Opal export flux and uncorrelated with the $CaCO_3$ export flux.

Key factors affecting the rate of biological decomposition of sinking POC in the water column are water temperature and the dissolved oxygen (DO) concentration: the lower the water temperature and the DO concentration, the slower the biological respiration rate and, consequently, the POC flux decomposition rate (e.g., Marsay et al., 2015; DeVries and Weber, 2017; Laufkötter et al., 2017; Pavia et al., 2019). For example, Marsay et al. (2015) have analyzed POC flux data from neutrally buoyant sediment traps in the upper 500 m of the water column and have found a significant positive correlation between the exponent b in Eq. (1) and water temperature (i.e., the POC flux was attenuated more rapidly when the water was warmer). In addition, Bach et al. (2019) have found that POC decomposition rates are high (low) when diatoms and *Synechococcus* (harmful algae) are the dominant phytoplankton because of increased (decreased) zooplankton

abundance and the consequent increase (decrease) in grazing pressure. Using radiochemical observations (^{234}Th-based POC flux observations), Pavia et al. (2019) found that the exponent *b* of the Martin curve was significantly smaller in the low-oxygen (hypoxic) eastern Pacific equatorial zone than in other areas; that is, vertical attenuation of the POC flux was smaller in the hypoxic area. They also pointed out that a more hypoxic ocean in the future would lead to a lower attenuation of the POC flux and therefore increased BCP efficiency and could thereby be a negative feedback on global warming. McDonnell et al. (2015) have reported that vertical transport of POC is more effective in the Antarctic, where the sinking velocity is higher and the biological respiration rate is lower than in the subtropical Atlantic. Henson et al. (2019) have also reported a high export ratio during the early bloom period, when primary productivity is low, and a low export ratio during the late bloom period, when primary productivity is high. They attributed the low export ratio during the late bloom to grazing pressure by microzooplankton and bacteria.

Despite these many investigations of the BCP, the factors governing the vertical attenuation of POC flux are still under debate. Observations in subarctic regions have shown that the transfer efficiency between depths of 1000 and 2000 m is relatively low and that between the bottom of the euphotic zone and a depth of 1000 m it is relatively high (Marsay et al., 2015). Marsay et al. (2015) have therefore proposed that the Martin curve does not appropriately express the vertical attenuation of POC flux in all regions and that a different equation should instead be developed for each region. Gloege et al. (2017) have discussed parameterization of the vertical attenuation of POC flux and have reported that vertical attenuation of the POC flux in the "twilight zone" (from the base of the euphotic zone to 1000 m) can be parameterized well not only by a power law model (Martin curve) but also by an exponential model (Banse, 1990) and a ballast model (Armstrong et al., 2002). However, the exponential model tends to underestimate the POC flux in the "midnight" zone (depths greater than 1000 m). Cael and Bisson (2018) have reported that the exponential model (power law model) tends to underestimate (overestimate) the POC flux in the upper layer, and vice versa in the deep layer. However, the abilities of both models to describe POC fluxes were comparable statistically when they were applied to the POC flux dataset from the eastern Pacific that was used to propose the "Martin curve" (Martin et al., 1987). In a long-term study in the northeastern Pacific, Smith et al. (2018) observed a sudden increase of the POC flux accompanied by an unusually high transfer efficiency; they have suggested that because the Martin curve cannot express such a sudden increase, it may sometimes underestimate BCP strength. In addition, contrary to previous findings, some studies have reported a significantly higher transfer efficiency, especially to the deep sea, in subtropical regions than in subarctic regions (Henson et al., 2012; Marsay et al., 2015; DeVries and Weber, 2017). This pattern may be attributable to small temperature and DO concentration differences in the deep sea between high-latitude and low-latitude regions, as well as to a higher sinking velocity in subtropical regions, where $CaCO_3$ is a major component of deep-sea marine snow. Moreover, it is also possible that POC is more refractory in low-latitude areas than in high-latitude areas (Henson et al., 2012; Marsay et al., 2015; DeVries and Weber, 2017).

The K2S1 project (Honda et al., 2017) was conducted between 2010 and 2014 to quantify the strength of the BCP in subarctic-eutrophic and subtropical-oligotrophic regions of the western North Pacific and to provide information that would enable the projection of future changes caused by multiple stressors, such as ocean warming, acidification, and hypoxia. In this study, the BCP in subarctic and subtropical regions of the western Pacific was revisited with a focus on the factors governing the vertical attenuation of POC fluxes.

K2S1 PROJECT

The time-series study, "Study of Change in Ecosystem and Material Cycles Caused by Climate Change and its Feedback: K2S1 Project," was designed to collect essential baseline data about marine ecosystems and the strength of the BCP to facilitate projection of changes of material cycles due to biological activity. This comparative study of the marine ecosystem and its biogeochemistry was conducted during 2010–2014 at two time-series stations, one in the western Pacific subarctic gyre (station K2: 47°N, 160°E) and the other in the subtropics (station S1: 30°N, 145°E), two oceanographic regions that differ physically, chemically, and biologically (**Figure 1**). In addition, during seasonal scientific cruises of the RV *Mirai* (Japan Agency for Marine-Earth Science and Technology) during 2010–2014, physical, chemical, and biological parameters were measured, and time-series observations were made with a mooring system. Analyses of satellite data and numerical simulations were also carried out as part of the K2S1 project.

The following major differences in the oceanography of the two regions were identified during the K2S1 project:

(a) Surface water temperature was usually ∼15°C lower at station K2 than at station S1.
(b) Surface waters at Station K2 were eutrophic, and those at station S1 were oligotrophic: at station K2, the nitrate + nitrite concentrations (NO_x) ranged from ∼10 μM in summer to ∼25 μM in winter, whereas at station S1, NO_x was at most ∼3 μM, even in winter, and it was less than 0.5 μM or undetectable in summer.
(c) Diatoms predominated among the phytoplankton at station K2, whereas at station S1, smaller phytoplankton such as *Prochlorococcus* predominated during most seasons.

Honda et al. (2017) have provided a detailed summary of the K2S1 project, including the physical, chemical, and biological settings of the sites. All data collected during the project are available online in the "K2S1 project database"[1].

[1]http://ebcrpa.jamstec.go.jp/k2s1/en/

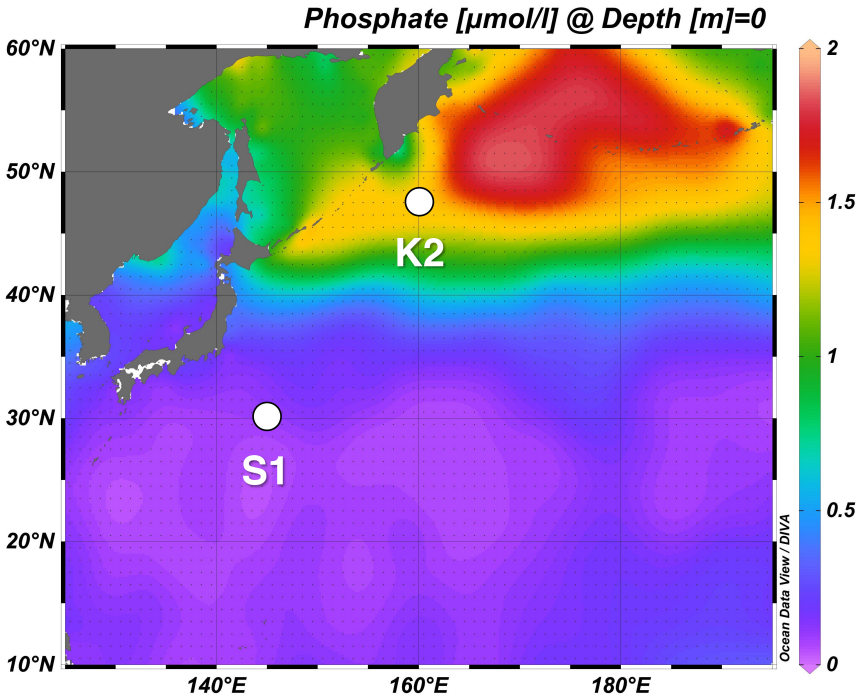

FIGURE 1 | Western North Pacific time-series stations K2 and S1. The background is the horizontal distribution of annual mean of surface phosphate concentration based on World Ocean Atlas data of Garcia et al. (2010) (https://www.nodc.noaa.gov/OC5/WOA09/pr_woa09.html).

MATERIALS AND METHODS

In this section, observations related to the biological carbon pump are described.

Primary Productivity Measurement

Primary productivity was estimated during seasonal cruises of the RV *Mirai* between 2010 and 2013 (Matsumoto et al., 2016; Honda et al., 2017) based on the incorporation of ^{13}C-labeled inorganic carbon into POC during 24-h incubations from dawn to the next dawn. Incubations were conducted either *in situ* or on-deck using water samples from eight depths that were selected at appropriate intervals between light levels of ∼100 and 0.1% of photosynthetically active radiation (PAR) at the surface. After the incubation, the water samples were filtered through a pre-combusted GF/F filter, and inorganic carbon was removed by fuming with HCl. The ^{13}C content of the particulate fraction was measured with an automatic nitrogen-and-carbon analyzer–mass spectrometer (EUROPA20-20, SerCon, Ltd., United Kingdom). Water-column-integrated values of primary production (IPP) were computed between the surface and the 0.1% light depth to facilitate comparison of settling particulate carbon fluxes measured with sediment traps (see section "Particle Flux Observations").

Particle Flux Observations

Settling particles in the upper 200 m were collected by using drifting sediment traps (DSTs: Honda et al., 2015). The sediment traps, which were traditional, surface-tethered cylindrical particle interceptor traps (Knauer et al., 1979), were deployed at nominal depths of 60, 100, 150, and 200 m for a few days during several cruises (**Figure 2**). After recovery, the water in the sample cups from each depth was filtered through pre-weighed Nuclepore filters for later determination of the total mass flux (TMF) and trace element contents, and through pre-combusted GF/F filters for later determination of particulate organic carbon, inorganic carbon, and nitrogen contents. Swimmers visible by the naked eye were removed from the filtered residues with tweezers. The Nuclepore filters and the GF/F filters were kept in a freezer (∼−10°C) until analysis in an on-shore laboratory.

Settling particles below 200 m were collected in bottom-tethered moored time-series sediment traps (MSTs). Conical, time-series sediment traps (Nichiyu-Giken-Kogyo SMD26S-6000, Saitama, Japan and McLane Mark VII-21, MA, United States) were deployed at 200, 500, and 4810 m and turned around annually between February 2010 and June 2014 (**Figure 1**). The sampling interval varied from 6 to 18 days. Before deployment, the collecting cups were filled with a seawater-based buffered 10% formalin solution as a preservative, and the salinity was adjusted to ∼39 by the addition of NaCl. After recovery of the sediment traps, the samples were stored in a refrigerator at 4°C until chemical and biological analysis in a shore-based laboratory. In the laboratory, the collected particles were water-sieved through 1-mm nylon mesh, and any remaining swimmers <1 mm were removed with tweezers.

The major components of the settling particles collected by the DSTs and MSTs were measured and analyzed as

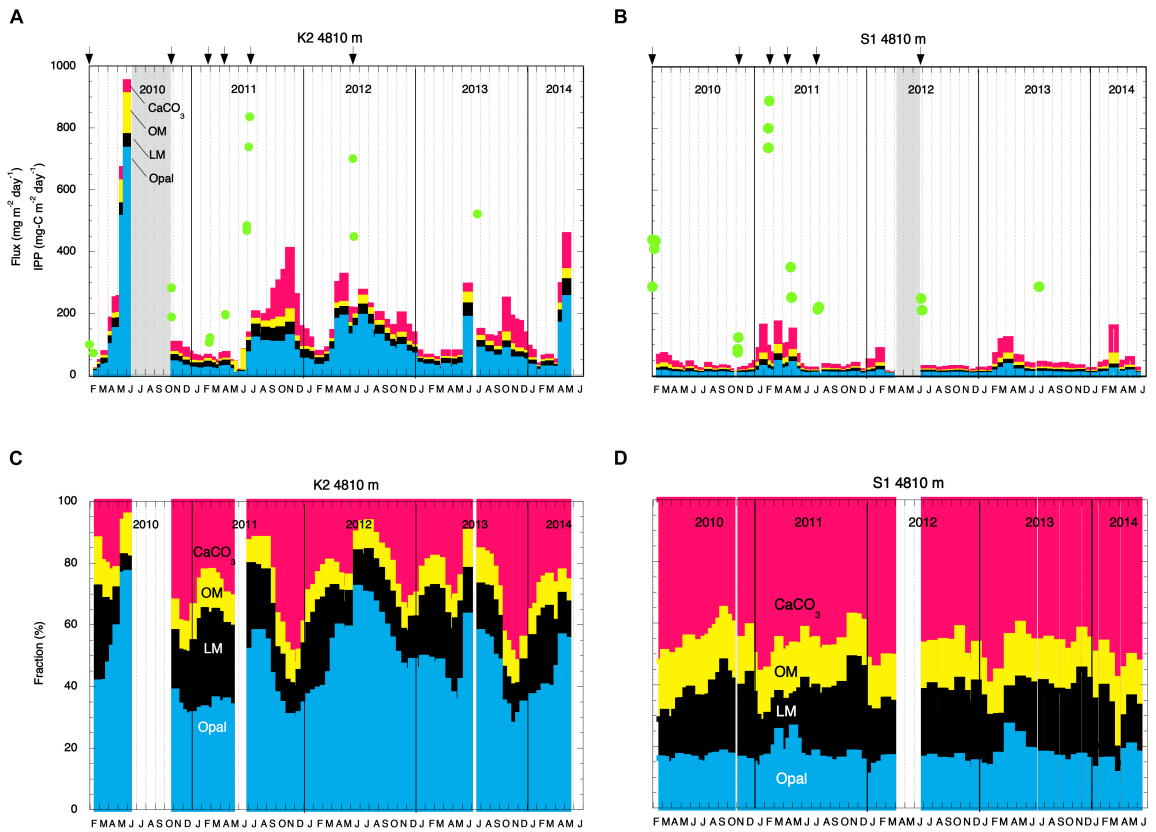

FIGURE 2 | Seasonal and interannual variability of the total mass flux at 4810 m and the chemical compositions of collected particles. Mass fluxes at panels **(A)** station K2 and **(B)** station S1 and chemical compositions of collected particles at panels **(C)** station K2 and **(D)** station S1 between February 2010 and May 2014. Red, yellow, black, and blue shading denotes $CaCO_3$, organic materials (OM), lithogenic materials (LM), and biogenic opal (Opal), respectively. In panels **(A,B)**, green circles indicate integrated primary productivity (IPP), and arrows indicate the dates of drifting sediment trap (DST) deployments.

follows: Concentrations of organic carbon, inorganic carbon, and nitrogen were measured with an elemental analyzer (Thermo Fisher Scientific Flash2000, Waltham, MA, United States). Concentrations of Al, Si, Ca, and trace elements such as Fe and Ti were measured with an inductively coupled plasma emission mass spectrometer (PerkinElmer Optima 3300DV, Waltham, MA, United States). Details of the sample pre-treatments and analyses are given by Honda et al. (2002, 2013). The following equations were used to estimate the concentrations of organic materials (OM), Opal ($SiO_2{\cdot}0.4H_2O$), $CaCO_3$, and lithogenic materials (LM). The coefficients in the equations are based on the Redfield ratio (Redfield et al., 1963) and the crustal ratio (Taylor, 1964):

$$\mathrm{OM}(\%) = \mathrm{organiccarbon}/0.36 \quad (2)$$

$$\mathrm{Opal}(\%) = (\mathrm{Si} - 3.42\mathrm{Al}) \times 67.2/28 \quad (3)$$

$$\mathrm{CaCO_3}(\%) = (\mathrm{Ca} - 0.5\mathrm{Al}) \times 100/40 \quad (4)$$

$$\mathrm{LM}(\%) = \mathrm{Al}/0.08 \quad (5)$$

The sum of OM, Opal, $CaCO_3$, and LM was generally within ± 15% of 100%. Therefore, the contents of these four components were summed and normalized to 100% to express the chemical composition of the settling particles. All flux data and chemical composition data are available online in the "K2S1 database" (see http://ebcrpa.jamstec.go.jp/k2s1/en/).

In this study, the fluxes and characteristics of settling particles collected by MSTs at 200 and 500 m were not included in the analysis. At both stations, sinking particles at 200 m were collected by both MSTs and DSTs, and the fluxes of POC collected by MSTs were several times lower than those collected by DSTs during the same period (Honda et al., 2015). However, POC fluxes based on DST data were comparable to POC flux estimated by a budget analysis of dissolved carbon and nutrients in the upper layer (Wakita et al., 2016). Laws et al. (1989) reported that conical sediment traps at a depth of 200 m underestimated fluxes (by a factor of 30–40) compared to cylindrical traps. Therefore, POC fluxes and other fluxes at 200 m collected by DSTs are likely to be realistic. Sinking particles collected at 500 m by the MSTs might also have been under-trapped. The trapping efficiency at 500 m at K2 has been estimated on the basis of excess ^{210}Pb flux measurements to be only ∼24%, although there is uncertainty because of the assumption of a steady state and the use of a one-dimensional model (Honda and Kawakami, 2014). In addition, sinking particles were collected at 500 m by DST in mid-June 2012, when the TMF was ∼360 mg m^{-2} day^{-1}; in

contrast, the TMFs before and after this period based on data collected at 500 m by MST were ∼127 and ∼230 mg m^{-2} day^{-1}, respectively (K2S1 database: see text footnote 1). In contrast, based on radiochemical analysis, it has been reported that the trapping efficiency of MSTs at depths greater than 1250 m, where external disturbances due to factors such as hydrodynamics and "swimmers" are weak, is close to 100% (Yu et al., 2001). Thus, to allow direct comparison of the K2 and S1 datasets, only data based on settling particles collected at 4810 m by MSTs and data based on settling particles collected in the upper 200 m by DSTs were used in this study on the assumption that the trapping efficiencies of the two types of sediment traps were close to 100% at those depths.

Because the sampling frequency differed between the DSTs and the MSTs, there is concern about the representativeness of the DST and MST data as metrics of annual means, especially at K2, because the DST observations there were limited, and the MST data indicated that there were large, interannual differences, such as an unusually high POC flux in 2010. It is likely, however, that the DST and MST data are representative of annual means for the following reasons:

(1) The annual mean of the observed POC flux at 150 m (∼49 mg-C m^{-2} day^{-1}) was very similar to the POC flux estimated from the dissolved carbon and nutrient budget (∼47 mg-C m^{-2} day^{-1}: Wakita et al., 2016; Honda et al., 2017).
(2) When the annual mean POC flux at 4810 m was estimated without the unusually high POC flux at 4810 m in 2010, the annual mean decreased by only 11% (from 5.5 to 4.9 mg-C m^{-2} day^{-1}), and the "exponent *b*" increased only from 0.64 to 0.67, which was still smaller than the corresponding value of ∼0.89 at S1 (described later).
(3) Comparison of my "exponent *b*" with previously reported values of the "exponent *b*" for POC flux in the western Pacific subarctic gyre (Honda et al., 2002; Buesseler et al., 2007) indicates that my data are comparable to those previously reported exponents (described later).

Because of the use of annual means at respective depths (**Table 1**), the time-lag problem (e.g., Giering et al., 2014; Henson et al., 2015) and seasonal and interannual differences do not affect the results.

RESULTS

Primary Productivity

Details of the primary-production observations have been reported elsewhere (Matsumoto et al., 2016; Honda et al., 2017). Briefly, at subarctic-eutrophic station K2, the maximum IPP of ∼850 mg-C m^{-2} day^{-1} was observed in early summer (July 2011), and the minimum IPP of ∼100 mg-C m^{-2} day^{-1} was observed in winter (February 2010) (**Figure 2A**). At subtropical-oligotrophic station S1, the IPP was higher in winter (late January 2010, ∼500 mg-C m^{-2} day^{-1}; February 2011, ∼900 mg-C m^{-2} day^{-1}) and lower in summer (∼250 mg-C m^{-2} day^{-1} in July of

TABLE 1 | Average fluxes and chemical compositions of settling particles during the K2S1 project.

Stn.	Trap type	Depth	TMF	POC	Flux (mg m^{-2} day^{-1})				Fraction (%)			Opal/$CaCO_3$	IPP	E-ratio	Org-C/Inorg-C	References
		(m)			Opal	$CaCO_3$	LM	OM	Opal	$CaCO_3$	LM	(mole ratio)	(mg m^{-2} day^{-1})	(%)	(mole ratio)	
K2	DST	60	631±124	97±34	202.3±99.8	135.9±54.4	16.6±12.9	43.8±8.3	32.1±12.5	22±8	2.6±3.0	2.2±0.2	315±39	30.7±9.4	5.9±1.9	Honda et al., 2015
	DST	100	483±63	63±11	167.2±76.4	121.6±59.8	15.0±11.6	37.1±4.5	34.6±13.6	25±13	3.1±2.6	2.0±0.2		19.9±6.1	4.3±1.4	Honda et al., 2015
	DST	150	317±140	49±23	103.3±99.6	61.0±47.2	13.2±11.6	44.0±5.0	32.6±13.6	19±11	4.2±7.8	2.5±0.2		15.5±4.8	6.7±2.1	Honda et al., 2015
	DST	200	327±184	45±21	105.1±73.5	77.8±67.3	14.5±12.0	39.6±6.5	32.2±14.4	24±14	4.4±6.8	2.0±0.2		14.3±4.4	4.8±1.6	Honda et al., 2015
	MST	4810	158±39	5.5±1.6	80.7±36.2	38.5±8.6	23.0±4.1	9.7±1.5	51.2±12.1	24±9	14.6±3	3.1±0.3		1.8±0.5	1.2±0.6	This study
S1	DST	60	670±328	150±102	34.4±31.9	193.1±135.4	13.9±16.4	64.0±5.9	5.1±2.5	29±5	2.1±3.2	0.3±0.0	369±47	40.7±12.5	6.5±2.1	Honda et al., 2015
	DST	100	324±267	56±46	21.9±22.3	128.4±128.9	12.8±13.9	49.6±5.2	6.8±4.9	40±6	4.0±6.2	0.3±0.0		15.2±4.7	3.6±1.2	Honda et al., 2015
	DST	150	287±236	48±36	16.1±17.6	115.4±134.0	17.2±14.1	48.1±10.2	5.6±4.2	40±13	6.0±5.0	0.2±0.0		13.1±4.0	3.5±1.1	Honda et al., 2015
	DST	200	301±238	42±28	24.8±21.2	136.4±135.4	20.0±16.6	39.9±8.5	8.2±5.5	45±12	6.6±11.0	0.3±0.0		11.4±3.5	2.6±0.8	Honda et al., 2015
	MST	4810	41±21	2.3±0.7	7.0±2.9	20.4±6.1	7.1±1.7	15.4±1.6	17.1±2.3	50±3	17.5±1.4	0.5±0.1		0.6±0.2	0.9±0.3	This study

Particles were collected at depths of 60, 100, 150, and 200 m by drifting sediment traps (DSTs) and at 4810 m by moored sediment traps (MSTs). TMF, total mass flux; POC, particulate organic carbon; Opal, biogenic opal; LM, lithogenic materials; IPP, integrated primary productivity; E-ratio, export ratio (POC flux at respective depths, expressed as a percentage of IPP).

both 2011 and 2012) and autumn (November 2010, ∼100 mg-C m^{-2} day^{-1}) (**Figure 2B**). One scientific highlight of the K2S1project is the discovery that the average IPP (± standard deviation) at S1, the oligotrophic station (369 ± 47 mg-C m^{-2} day^{-1}), was comparable to or slightly higher than that at K2, the eutrophic station (315 ± 39 mg-C m^{-2} day^{-1}) (**Table 1**). On the basis of observations and numerical simulations, Honda et al. (2018) have proposed that one of the "missing" nutrient sources that might account for the higher IPP at station S1 is upwelling driven by mesoscale cyclonic eddies.

Fluxes and Chemical Compositions of Settling Particles in the Upper 200 M

The seasonal variability of the fluxes of settling particles and their chemical composition in the upper 200 m based on DST data have been reported by Honda et al. (2015). Those data indicate that the average Opal fluxes during 2010–2012 at station K2 ranged from ∼105 mg m^{-2} day^{-1} at 200 m to ∼202 mg m^{-2} day^{-1} at 60 m, and they were about 5–7 times the fluxes at station S1 at comparable depths (**Table 1**). However, $CaCO_3$ fluxes at comparable depths were higher at station S1 (115–193 mg m^{-2} day^{-1}) than at station K2 (61–136 mg m^{-2} day^{-1}). As a result, the mole ratio of Opal to $CaCO_3$ ($Opal/CaCO_{3(mole)}$) was an order of magnitude higher at station K2 than at station S1. The TMF, POC flux, and export ratio (an index of BCP efficiency and equal to the POC flux at respective depths, expressed as a percentage of IPP), however, were comparable at comparable depths at both stations (K2: ∼14–31%, S1: ∼11–41%, see **Table 1**). The OM content of the settling particles was also comparable at the two stations; at both stations it accounted for ∼40–60% of the particles collected by DST. The similarity of the export fluxes and export ratios in the upper 200 m at stations K2 and S1 is inconsistent with previous reports of higher export fluxes and export ratios in subarctic regions (e.g., Henson et al., 2012).

Fluxes and Chemical Compositions of Settling Particles in the Deep Sea

The fluxes of settling particles and their chemical compositions based on data collected at 4810 m by MSTs showed remarkable seasonal and interannual variability (**Figure 2**). At station K2, the largest annual TMF maximum of ∼950 mg m^{-2} day^{-1} was observed in May 2010; in other years, the annual TMF maximum was at most 500 mg m^{-2} day^{-1} (**Figure 2A**). The TMF tended to increase in late spring (May and June) and in autumn at station K2. In contrast, at station S1, the annual TMF maximum was at most 200 mg m^{-2} day^{-1}, and the TMF tended to increase in late winter and in spring (**Figure 2B**). The earlier occurrence of the annual TMF maximum at station S1 (winter/spring at S1 versus late spring/summer at K2) is consistent with the earlier occurrence of the annual IPP maximum there (winter at S1 versus late spring at K2). The average TMF at station K2, ∼158 mg m^{-2} day^{-1}, was four times the average TMF at station S1 (∼41 mg m^{-2} day^{-1}) (**Table 1**). The POC flux at K2 averaged ∼6 mg-C m^{-2} day^{-1}, ∼3 times the average POC flux at station S1 (∼2 mg-C m^{-2} day^{-1}). The export ratio at 4810 m of K2 (1.8%) was also ∼3 times that at station S1. At station K2, although the Opal fraction varied seasonally (higher in summer and lower in winter) and the $CaCO_3$ fraction increased in winter, the dominant component of the settling particles was Opal (average, ∼51%) (**Figure 2C** and **Table 1**). In contrast, at station S1 the seasonal variability in the chemical composition of settling particles was small, and $CaCO_3$ was the dominant component year-round (average, ∼50%, **Figure 2D** and **Table 1**).

DISCUSSION

Vertical Changes in the Organic and Inorganic Carbon Fluxes

On the assumptions (1) that the DST trapping efficiency in the upper 200 m and the MST trapping efficiency at 4810 m were both 100% and (2) that the averaged organic carbon fluxes (**Table 1**) represented the average annual POC fluxes, we directly compared the POC fluxes in the upper 200 and at 4810 m between the sites (**Figure 3A**). Because the POC flux at 4810 m was higher at K2 than at S1, whereas the POC fluxes in the upper 200 m were comparable at both stations, the value of the exponent b estimated by fitting Eq. (1), the Martin curve, to the POC flux–depth relationship at each station was 0.64 (n = 5, r^2 = 0.99, $p < 0.001$) at K2 and 0.90 (n = 5, r^2 = 0.92, $p < 0.001$) at S1. When the exponent b was estimated with the upper POC flux (average flux +1σ) (the lower POC flux: average flux −1σ) at the respective depths at both stations, the exponent b was estimated to be 0.65 with an r^2 of 0.95 (0.63 with an r^2 of 0.94) at K2 and 0.97 with an r^2 of 0.95 (0.66 with an r^2 of 0.69) at S1. It is noteworthy that the effect of the choice of water depth for measuring the export flux of POC (e.g., a fixed depth such as 100 m, base of seasonal euphotic zone, or base of seasonal or annual maximum mixed layer) on the POC flux vertical attenuation or transfer efficiency has been a subject of debate (Buesseler and Boyd, 2009; Palevsky and Doney, 2018). The exponent b calculated using the MST-derived POC flux and the DST-derived POC flux at the base of the euphotic zone, at the depth of the seasonal mixed layer, at a fixed depth of 100 m, and at the annual maximum depth of the mixed layer (K2: 150 m, S1: 200 m) were also estimated separately. However, variations of the estimated exponent b were small: 0.64–0.67 for K2 and 0.86–0.93 for S1. The estimated exponent b for the POC flux at K2 in this study (∼0.64) is comparable to previous estimates: 0.51 ± 0.05 for POC fluxes observed with neutral buoyancy sediment traps at 150, 300, and 500 m in late spring and early summer at station K2 (Buesseler et al., 2007), and ∼0.63 for the POC fluxes observed with DSTs at 13 depths between 60 and 400 m, and with MSTs at 1000, 3000, and 5000 m in the middle of spring and late autumn at the former western North Pacific subarctic time-series station KNOT (Honda et al., 2002). It has also been reported that the exponent b is larger at the central Pacific subtropical station ALOHA (1.33 ± 0.15) than at station K2 (Buesseler et al., 2007). Thus, it can be said that the vertical attenuation of the POC flux was significantly smaller at station K2 than at station S1. In other words, POC was transported vertically more efficiently at station K2 than at station S1.

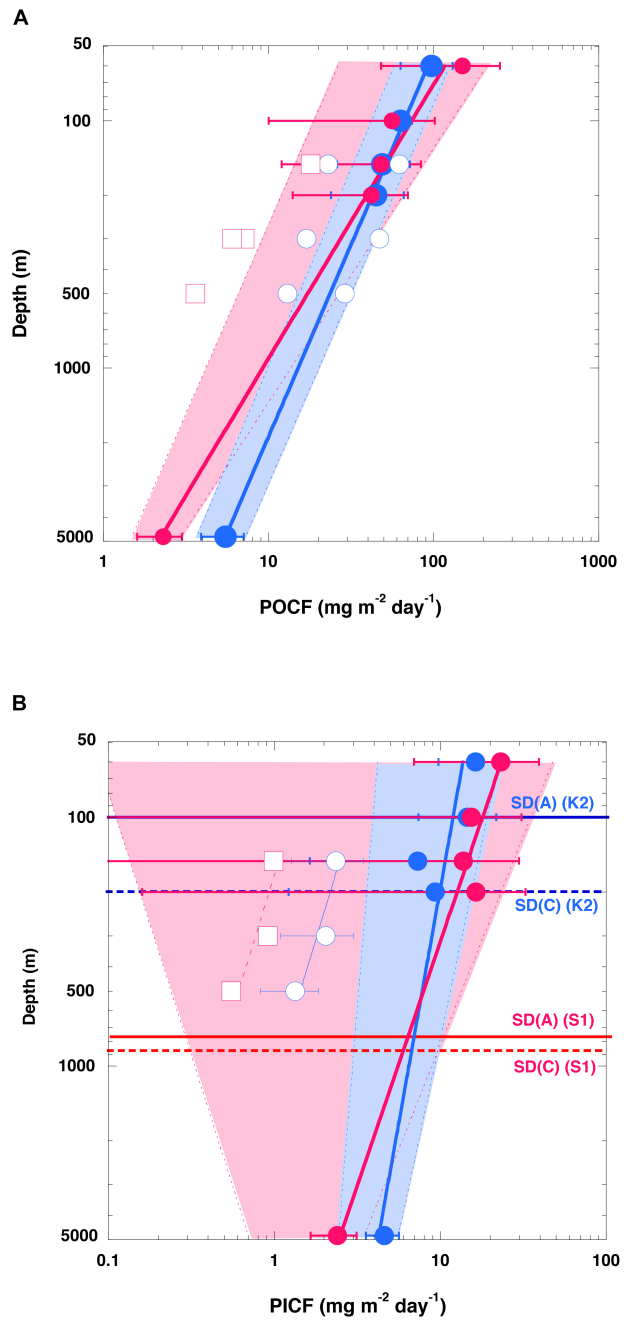

FIGURE 3 | Vertical profiles of carbon fluxes. **(A)** Particulate organic carbon (POC) fluxes (POCF) and **(B)** particulate inorganic carbon (PIC) fluxes (PICF) at K2 (blue) and S1 (red). Please note that the scale of both axes is logarithmic. Error bars show the standard deviation (1σ). The solid curves are regression curves (power law functions) fitted to upper-level flux data (at 60, 100, 150, and 200 m) and deep flux data (at 4810 m) at each station. Hatched areas for K2 (blue) and S1 (red) are deviations from regression curves fit to the lower flux (average −1σ) and the upper flux (average +1σ) of POC at respective depths. Open blue circles (red squares) are **(A)** POCFs and **(B)** PICFs observed by neutrally buoyant sediment traps at 150, 300, and 500 m at station K2 (ALOHA) previously reported by Buesseler et al. (2007) (data are based on their **Table 1**). The horizontal solid and dotted lines in panel **(B)** labeled SD(A) and SD(C), respectively, are the saturation depths of aragonite and calcite, respectively, at the respective stations.

As described in the introduction, the choice of which empirical equation (power law model, exponential model, and so on) to parameterize the vertical attenuation of POC fluxes has been a subject of debate. In this study, I also tried to parameterize the vertical attenuation of the POC flux with an exponential model. However, the r^2 statistic was lower for the exponential model than for the power law model: r^2 = ∼0.67 (K2) and ∼0.41 (S1) for the exponential model whereas $r^2 \geq 0.99$ (K2) and ∼0.91 (S1) for the power law model. Moreover, the exponential model results in a rate of vertical attenuation of POC fluxes that is constant throughout the water column. Based on the likely decrease of biological activity and/or increase of sinking velocity with increasing depth (see section "Effects of Lower Water Temperature and Lower Oxygen Concentration"), the constant rate of vertical attenuation of POC fluxes assumed by the exponential model seems unlikely. Thus, the power law model (Martin curve) is likely more appropriate for parameterizing the vertical attenuation of POC fluxes at K2 and S1, even though the lack of POC flux data in the deep ocean does not rule out the possibility that there are some deviations from the shape of the Martin curve in that part of the water column.

It is noteworthy that the value of the exponent b for the flux of particulate inorganic carbon (PIC) (i.e., carbon in $CaCO_3$) was also smaller at station K2 than at station S1 (K2: ∼0.19, r^2 = 0.76; S1: ∼0.51, r^2 = 0.91) (**Figure 3B**), even if the exponent b for the PIC flux, like that for the POC flux, was estimated in different ways and although its variability was slightly larger (0.17–0.28 for K2, 0.45–0.60 for S1). The saturation depths of the aragonite and calcite polymorphs of $CaCO_3$ (where the saturation state $\Omega = 1$) have been estimated to be at depths of around 100–200 m at station K2 and 600–800 m at station S1 (Honda et al., 2017; **Figure 3B**). The seawater at station K2 is therefore more corrosive with respect to $CaCO_3$. In addition, preservation of settling POC might be less efficient at station K2 because biological grazing pressure is higher there than at station S1 (*vide infra*). Nevertheless, the vertical attenuation of PIC was smaller at station K2 than at station S1. This higher export flux and higher transfer efficiency in the deep sea in the subarctic region (station K2) than in the subtropical region (station S1) are inconsistent with previous reports of higher transport efficiencies in subtropical regions (e.g., Francois et al., 2002; Henson et al., 2012). Instead, the here reported higher transfer efficiency for the subarctic region (K2) compared to the subtropical region (S1) supports former observational and modeling studies featuring the found pattern (Marsay et al., 2015; Weber et al., 2016; DeVries and Weber, 2017; Cram et al., 2018; Maerz et al., 2020). In the next section, mechanisms related to the preservation of the POC flux and settling particles in the water column are discussed.

Correlations Between POC and Ballast Materials

Because settling particles are, in general, aggregates of various kinds of particles, the POC flux is usually positively correlated with the Opal, $CaCO_3$, and LM fluxes (**Figures 4A,B**). However, which of these three materials plays the most important role in ballasting the vertical transport of light and labile POC is still being debated. By conducting multiple linear

regression analyses (MLRAs) of global sediment trap data, Francois et al. (2002); Klaas and Archer (2002) have determined that $CaCO_3$ is the dominant ballast material for POC on a global scale. In the western Pacific, including the Japan Sea, however, Otosaka and Noriki (2005) have reported that Opal is the dominant ballast material. Moreover, because the MLRA used a global sediment trap dataset consisting of annually averaged data, spatiotemporal variation of the Si/C ratio of primary production might have been missed; as a result, the conclusion that Opal is unimportant as ballast for POC transport might be inaccurate (Passow and De La Rocha, 2006; Boyd and Trull, 2007). Honda and Watanabe (2010), who conducted an MLRA of seasonal time-series of settling-particle data from individual sediment trap collecting cups, have reported that Opal is the dominant ballast material for vertical POC transport in the western Pacific subarctic gyre, including station K2. In accord with Honda and Watanabe (2010), we used an MLRA to fit the sediment trap data at a depth of 4810 m at K2 and S1 to the following equation to estimate the carrying coefficients (CCs) of Opal (A), $CaCO_3$ (B), and LM (C):

$$R_{OC} = A \times R_{Opal} + B \times R_{CaCO3} + C \times R_{LM} + D \quad (6)$$

where R_{OC}, R_{Opal}, R_{CaCO3}, and R_{LM} are the relative fluxes of OC, Opal, $CaCO_3$, and LM, respectively (i.e., the flux of each

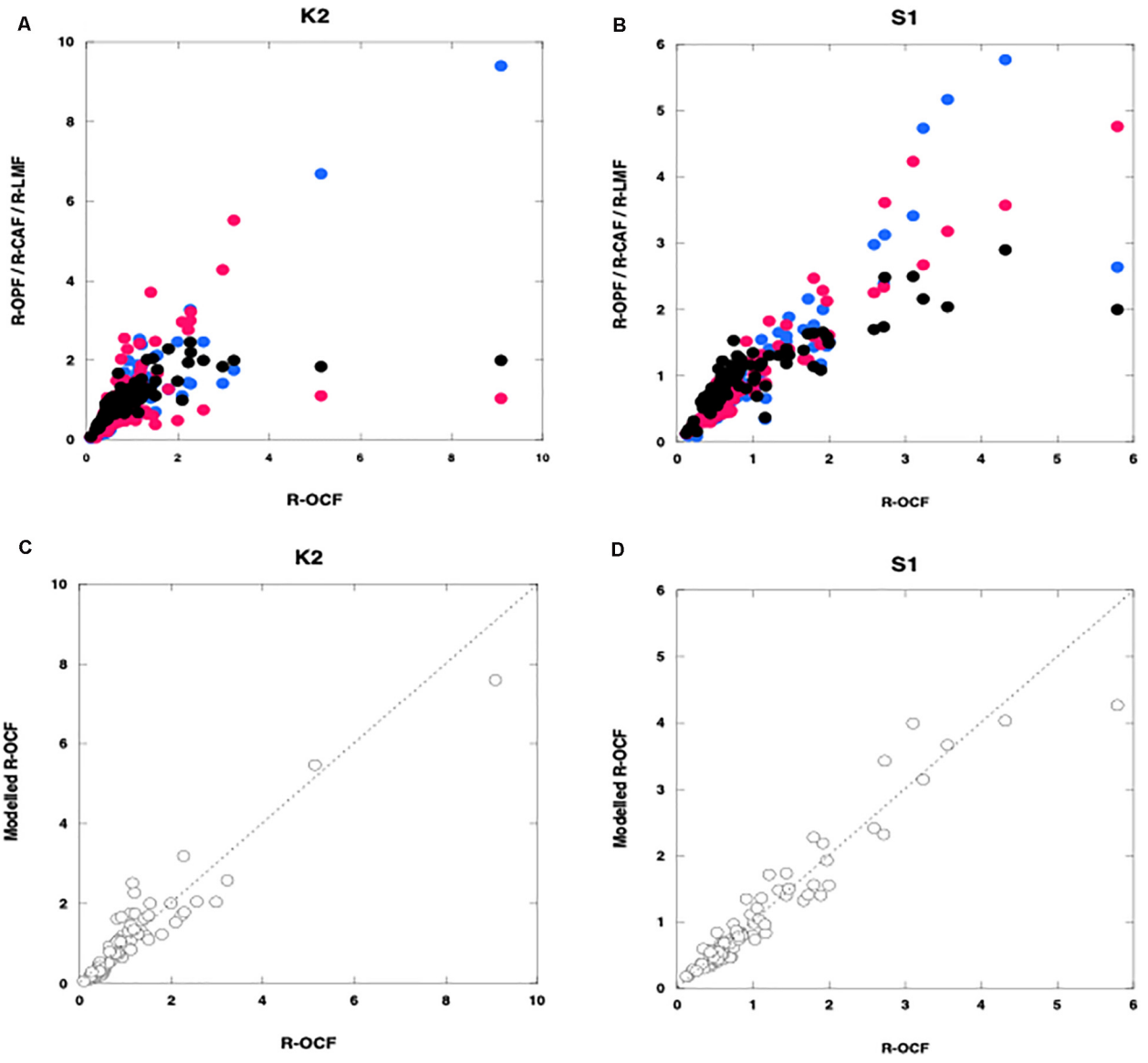

FIGURE 4 | Relationships between the relative organic carbon flux (R-OCF) and other variables. **(A,B)** are relative fluxes of Opal (R-OPF: blue), $CaCO_3$ (R-CAF: red), and lithogenic materials (R-LMF: black); **(C,D)** are modeled organic carbon: open circles) (obtained by using carrying coefficients estimated by multiple linear regression analysis) at K2 **(A,C)** and S1 **(B,D)**. Broken lines in panels **(C,D)** are regression lines for panel **(C)** K2 (n = 89, r^2 = 0.89, $p < 0.001$) and **(D)** S1 (n = 94, r^2 = 0.92, $p < 0.001$).

material relative to its average flux). Because we used relative fluxes in Eq. (6), each CC indicated the fraction of the POC flux carried by or associated with the corresponding ballast material ($A + B + C + D = 1$). The parameter D represents the residual R_{OC} flux, that is, the fraction of the R_{OC} not associated with any ballast material. The MLR equations at each site were as follows:

K2:

$$R_{OC} = 0.79 \times R_{Opal} + 0.23 \times R_{CaCO3} - 0.04 \times R_{LM} + 0.01$$

$$(n = 89, r^2 = 0.89, p < 0.001) \quad (7)$$

S1:

$$R_{OC} = 0.26 \times R_{Opal} + 0.79 \times R_{CaCO3} - 0.12 \times R_{LM} +$$

$$0.06\ (n = 94, r^2 = 0.92, p < 0.001) \quad (8)$$

Figures 4C,D shows the relationship between the observed relative POC fluxes (R-OCFs) and the modeled relative POC fluxes, that is, the relative fluxes calculated by using the MLRA equations. At K2, A was equal to 0.79. Thus, consistent with the results reported by Otosaka and Noriki (2005); Honda and Watanabe (2010), this result indicates that ∼80% of the POC was ballasted by or associated with Opal. It is thus likely that Opal plays a pivotal role in the vertical transport of POC flux to the ocean interior in the western Pacific subarctic gyre, even though $CaCO_3$, because it is denser than Opal, might be expected to function better as ballast. Although the composition of the collected Opal was not quantitatively determined, diatoms are likely the main source of the opal, because diatoms are the dominant phytoplankton group in the western Pacific subarctic gyre. Diatoms are among the producers of transparent exopolymer particles (TEP), which aggregate with small suspended particles to form macroscopic, settling particles (e.g., Passow et al., 2001; Simon et al., 2002 and references in their paper). Qualitatively speaking, a sediment trap sample containing many diatoms is very sticky or mushy. Thus, owing to their large size, their tendency to aggregate with small particles, and their stickiness, diatoms might surround labile materials such as POC and even $CaCO_3$ and could serve to protect them from biological degradation and chemical reactions, as reported previously (Mayer, 1994; Armstrong et al., 2002). Hansen et al. (1996) also found that fecal pellets formed from a diet of diatoms were more recalcitrant to microbial degradation.

At S1, B (= 0.79) was the largest CC. This result indicates that ∼80% of the POC was ballasted by or associated with $CaCO_3$, which is produced not only by phytoplankton such as coccolithophores but also by zooplankton such as foraminifera. Thus, in the western Pacific subtropical region, as in many other ocean regions (Francois et al., 2002; Klaas and Archer, 2002), $CaCO_3$ might function as ballast for POC. Observations of carbonate chemistry made during the K2S1 project have confirmed that ocean acidification is ongoing at both K2 and S1 but that the shoaling rate of the $CaCO_3$ saturation depth is higher at S1 than at K2 (Honda et al., 2017). Although the effects of ocean acidification on the ocean ecosystem and biogeochemistry are still being debated (e.g., Doney et al., 2009), ocean acidification might reduce the production of $CaCO_3$. Whereas a decrease in $CaCO_3$ production could increase alkalinity and decrease the production of CO_2 associated with calcification, a decrease in the supply of $CaCO_3$ ballast could cause the POC flux to decrease and surface pCO_2 to increase, especially in subtropical regions (e.g., Heinze, 2004; Kwon et al., 2009).

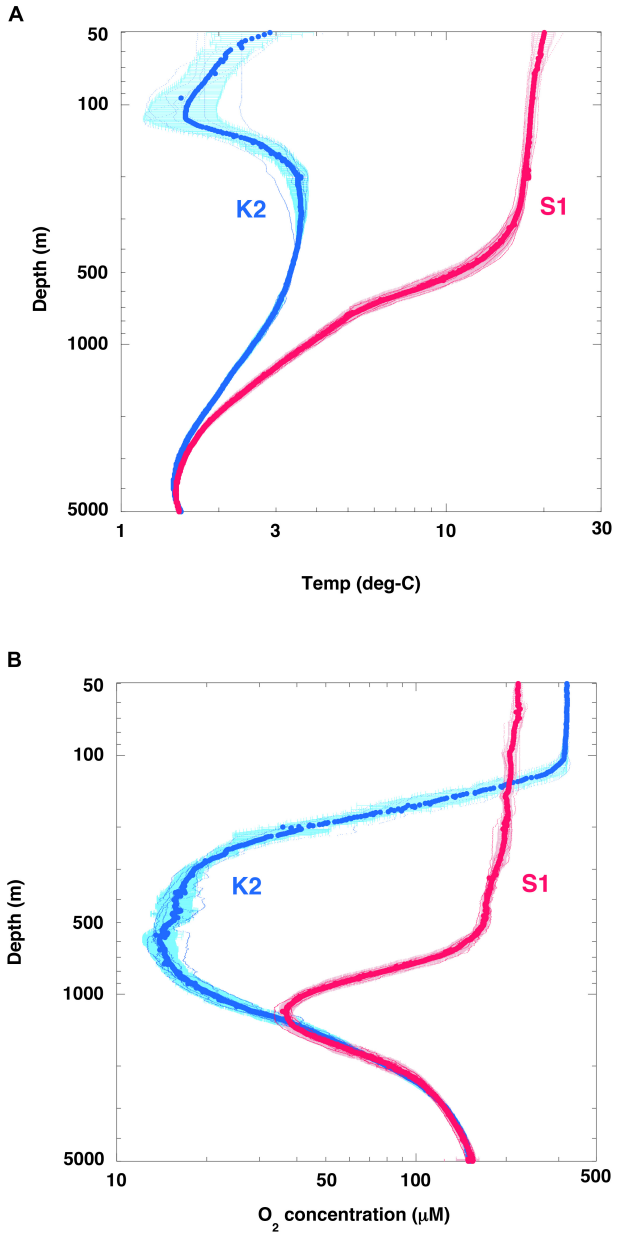

FIGURE 5 | Seasonal vertical profiles of temperature and dissolved oxygen. **(A)** Temperature and **(B)** dissolved oxygen (O_2) at stations K2 (small blue dots) and S1 (small red dots). Large circles for respective stations are averages of each 1-m interval with standard deviation (1σ). Note that the scales of both axes are logarithmic.

Effects of Lower Water Temperature and Lower Oxygen Concentration

Seasonal observations during the K2S1 project have shown that water temperatures were much lower at K2 than at S1: ∼15°C lower at the surface, ∼18°C lower at 100 m (the depth of the cold subsurface dicothermal layer at K2; Dodimead et al., 1963; Favorite et al., 1976), ∼8°C lower at 500 m, and ∼1.5°C lower at 1000 m (**Figure 5A**). The rates of metabolic processes, including the rates at which microbial organisms respire, consume oxygen, and decompose POC, generally decrease with decreasing temperature and vice versa. The Q_{10} is a well-known index used to express the sensitivity of metabolic processes to a temperature increase of 10°C, and the Q_{10} value of microbial metabolism typically ranges from 2 to 3 (Quinlan, 1981).

In addition, it is possible that the rate of POC decomposition was affected by dissolved oxygen (O_2) concentrations. The O_2 concentration in the upper 100 m was generally higher at station K2 than at station S1 (**Figure 5B**), because the solubility of atmospheric oxygen in the surface ocean layer is higher at low temperatures. In the twilight zone, however, the O_2 concentration was significantly lower at station K2 than at station S1. A sufficiently low O_2 concentration would be expected to cause rates of microbial respiration and POC decomposition to decrease. For example, DeVries and Weber (2017) have reported that the rate of POC decomposition decreases by 70% and 20% when the O_2 concentration is reduced to 50 μM and 20 μM, respectively. In addition, based on an on-deck incubation experiment in the Arabian Sea, Keil et al. (2016) have reported that an O_2 concentration of 20 μM is the threshold for O_2 effects on respiration; aerobic rates of POC decomposition in their experiments dropped to 0% for a few days at O_2 concentrations below 1 μM. Pavia et al. (2019) have reported that the exponent *b* of Eq. (1) is small (low rate of attenuation of POC flux) in the eastern tropical Pacific, an hypoxic area with $O_2 < 20$ μM, a finding supported by numerical simulation results (Cram et al., 2018). The oxygen sensitivity of the respiration rate thus has the potential to affect the rate of POC decomposition in water columns that include oxygen minimum zones, in which the O_2 concentration may become low enough to slow aerobic rates of particle degradation. A half-saturation constant, [KO_2], has been proposed as an index of the O_2 dependence of POC decomposition rates (e.g., DeVries and Weber, 2017), and [KO_2] values ranging from 4 to 30 μM have been suggested (Ploug, 2001; Kalvelage et al., 2015; Keil et al., 2016; DeVries and Weber, 2017; Laufkötter et al., 2017).

In this study, the rate of attenuation of the POC flux [$R_{(T,O)}$] due to remineralization was estimated at K2 and S1 by using the following equation proposed by Cram et al. (2018):

$$R_{(T,O)} = (Cr)(Q_{10}^{(T-Tref)/10})([O_2]/([KO_2] + [O_2])) \quad (9)$$

where T and O_2 are the observed water temperature and dissolved oxygen concentration, respectively (**Figures 5A,B**). Cr (day^{-1}) is the base remineralization rate of POC at a reference temperature (Tref). On the basis of incubation experiments, Iversen and Ploug (2013) have proposed that the carbon-specific respiration rates are 0.12 ± 0.03 day^{-1} at 15°C and 0.03 ± 0.01 day^{-1} at 4°C, and they applied these rates to an analysis of the vertical attenuation of POC fluxes observed by sediment traps in the world ocean. In this study, their carbon-specific respiration rate was used as the Cr at Tref: 0.12 ± 0.03 day^{-1} at 15°C or 0.03 ± 0.01 day^{-1} at 4°C. Use of these numbers indicated that the Q_{10} was 3.5 on average with a range from 2.1 to 6.2 (**Figure 6A**). The $[O_2]/([KO_2] + [O_2])$ ratio is a metric of the intensity of

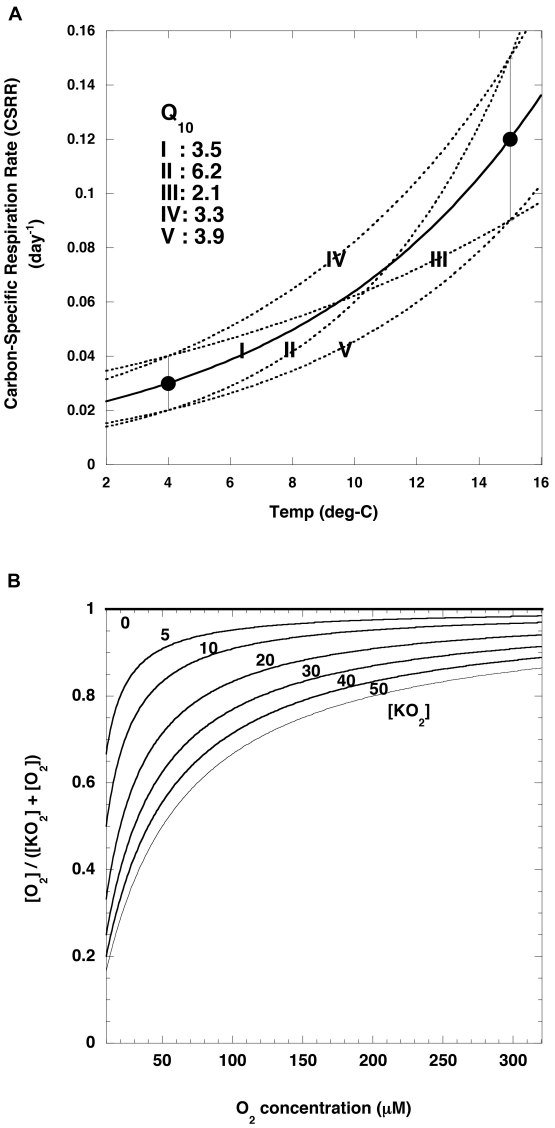

FIGURE 6 | Relationships between variables and temperature or oxygen concentrations. **(A)** Carbon-specific respiration rates (black circles) reported by Iversen and Ploug (2013) and temperature. Curves are regression curves (exponential functions) fit to various combinations of data (I: average-average, II: lower value (average −1σ)-upper value (average +1σ), III: upper value-lower value, IV: upper value-upper value, V: lower value-lower value). Based on these exponential curves, the following Q_{10} values were estimated for these datasets (I: 3.5, II: 6.2, III: 2.1, IV: 3.3, V: 3.9). Cr at reference temperature of 4°C in Eq (9) (see text) for I, II, III, IV and V are 0.03, 0.02, 0.04, 0.04 and 0.02 day^{-1}, respectively. **(B)** Relationship between O_2 concentration and $[O_2]/([KO_2] + [O_2])$ for various [KO_2] values (0–50 μM).

the dependence of the rate of POC remineralization on the O_2 concentration: the smaller $[KO_2]$, the smaller the O_2 dependence (**Figure 6B**). $[KO_2] = 0$ means that the O_2 concentration does not affect POC remineralization rates.

The estimated $(Cr)(Q_{10}^{(T-Tref)/10})$ (hereinafter $Cr_{(T)}$) at K2 was nearly constant (2–3% day^{-1} on average) throughout the water column (**Figure 7A**) (note: the original rate $[day^{-1}]$ was converted to [% day^{-1}] by multiplying the original rate by 100%). I attributed this small rate of change to the small change in water temperature throughout the water column at K2 (1–4°C, **Figure 5A**). In contrast, the $Cr_{(T)}$ at 100 m at S1 was estimated to be ∼19% day^{-1} on average, and it decreased with depth. At around 1000 m, the $Cr_{(T)}$ values at both stations were comparable, and they were nearly constant below 1000 m. The $[O_2]/([KO_2] + [O_2])$ ratio at around 100 m at K2 was about 0.9 (**Figure 7B**), and it decreased with depth. The minimum $[O_2]/([KO_2] + [O_2])$ ratio of 0.5 occurred at a depth of ∼600 m. This pattern is attributable to the O_2 minimum at that depth (∼12 μM, **Figure 5B**). The $[O_2]/([KO_2] + [O_2])$ ratio at S1 was estimated to be ∼0.9 in the upper 600 m and below 3000 m. Between these depths, the $[O_2]/([KO_2] + [O_2])$ ratio decreased (**Figure 5B**) and reached a minimum (∼0.7) at around 1000 m. A comparison of the $Cr_{(T)}$ values and $[O_2]/([KO_2] + [O_2])$ ratios between the two stations revealed that the $Cr_{(T)}$ was on average ∼8 times higher at around 100 m and more than twice as high in the upper 600 m at S1 than at K2, whereas the $[O_2]/([KO_2] + [O_2])$ ratio was slightly higher in the twilight zone (200–1000 m) and at most twice as high at around 600 m at S1 than at K2 (**Figure 7C**). These analyses indicated that the rate of respiration of POC in the upper ∼600 m was significantly higher at S1 than at K2. This difference could be attributed mainly to the higher water temperature at S1; the rates of respiration of POC below ∼1500 m were comparable at both stations.

Using these relationships, I estimated the vertical profiles of $R_{(T,O)}$ (note: the original rate $[day^{-1}]$ was converted to [% day^{-1}] by multiplying the original rate by 100%) at K2 and S1 (**Figure 8A**). The error bounds (1σ) of the $R_{(T,O)}$ values were large, ∼40%, because $Cr_{(Trefof\ 4°C)}$, Q_{10} and $[KO_2]$ ranged from 0.02 and 0.04, 2.1 to 6.5 and 0 to 50 μM, respectively (**Figures 6A,B**). The variation with depth of $R_{(T,O)}$ at K2 was small, and the average of $R_{(T,O)}$ throughout the water column was ∼2.5% day^{-1}. The small depth dependence could be attributed to the small range of temperatures throughout the water column (**Figure 5A**). At depths of 300–1000 m, where O_2 concentrations were less than 20 μM, $R_{(T,O)}$ decreased slightly to ∼1% day^{-1}. At S1, the $R_{(T,O)}$ between 100 and 200 m was estimated to be ∼16 (15–17)% day^{-1} on average, ∼8 times the corresponding rate at K2. This difference could be attributed mainly to the higher temperature at S1 versus K2. The $R_{(T,O)}$ at S1 decreased with increasing depth, and below 1500 m it became comparable to the corresponding $R_{(T,O)}$ at K2.

To determine whether these $R_{(T,O)}$ rates were reasonable, I compared them to the attenuation rate of the POC flux ($R_{(VA)}$:% m^{-1}). Although some deviations from the shape of the Martin curve could not be ruled out at depths below 200 m because of limited POC flux data, values of $R_{(VA)}$ at z m ($R_{(VA)\ (z)}$) were estimated using the Martin curve with the exponent b proposed

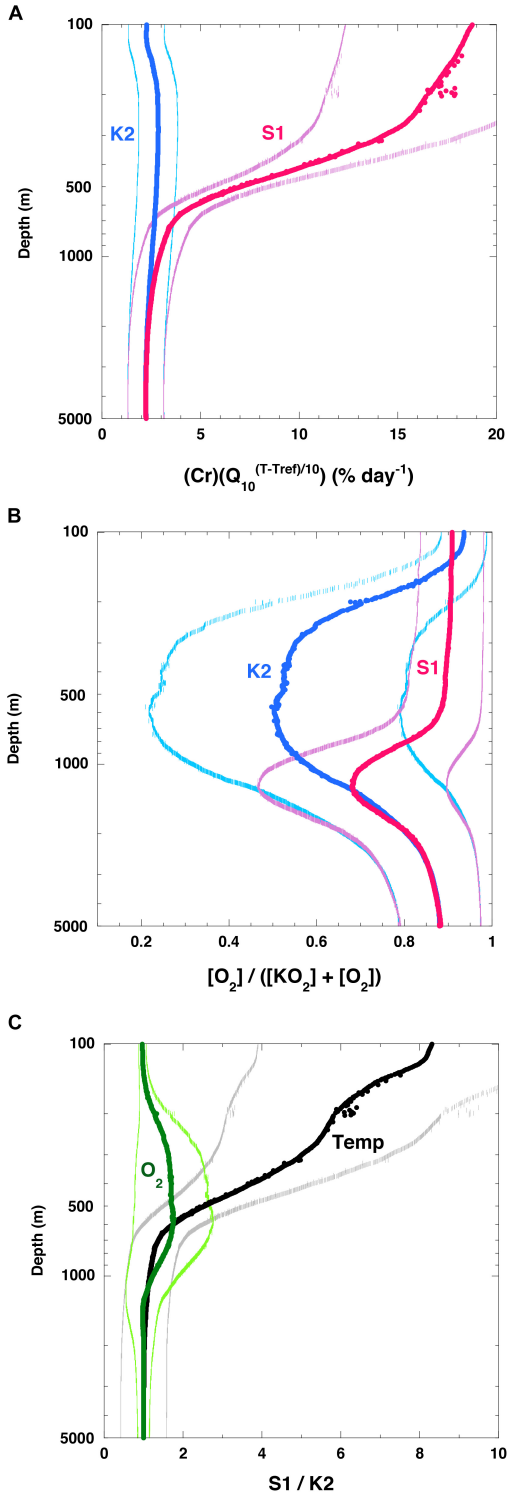

FIGURE 7 | Vertical profiles of variables related to respiration. **(A)** $(Cr)(Q_{10}^{(T-Tref)/10})$ (hereinafter $Cr_{(T)}$), **(B)** $([O_2]/[KO_2] + [O_2])$ at K2 (blue) and S1 (red). Values in panels **(A,B)** are averages of values estimated with various Q_{10} values and various $[KO_2]$ in **Figure 6** with standard deviation (1σ). **(C)** Vertical profiles of ratios at S1 and K2 of $Cr_{(T)}$ (label: Temp) and $([O_2]/([KO_2] + [O_2])$ (label: O_2). Note that only edge of error bars or standard deviation for respective values are shown in respective figures.

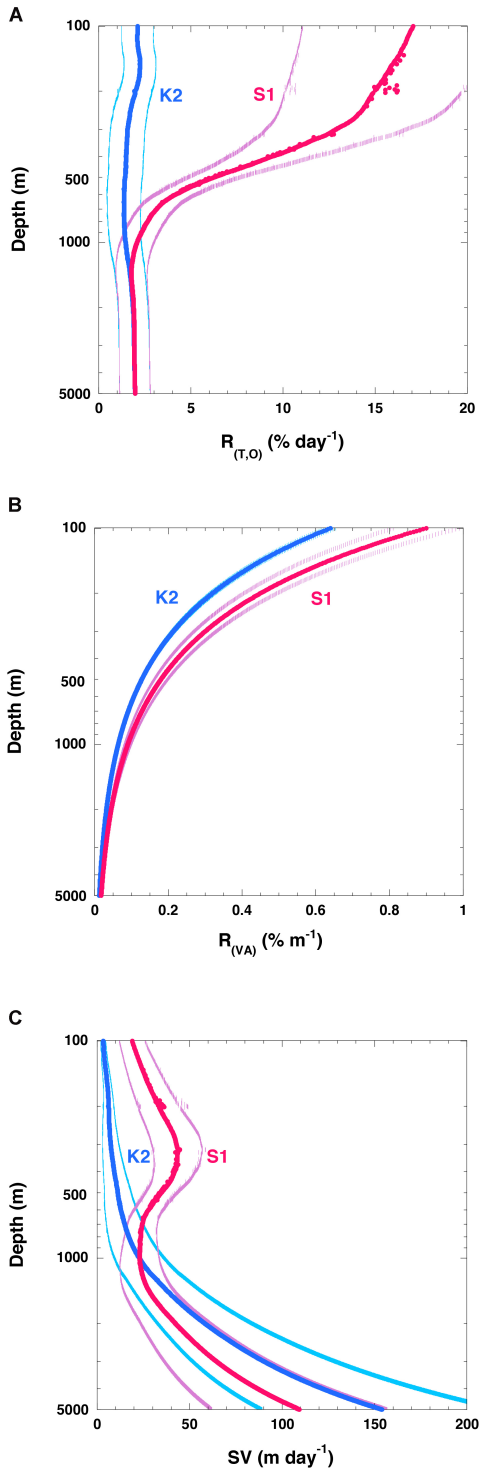

FIGURE 8 | Vertical profiles of variables related to attenuation of particle fluxes. **(A)** $R_{(T,O)}$ (rate of respiration of POC flux:% day^{-1}), **(B)** vertical attenuation rate of POC flux ($R_{(VA)}$:% m^{-1}) at K2 (blue) and S1 (red), and **(C)** POC sinking velocity (SV) at K2 (blue) and S1 (red). The values in panels **(A,C)** are averages for each 1-m interval with standard deviations (1σ). Error bars in panel **(B)** are 2% (10%) of respective values for K2 (S1) based on data in **Figure 3**. Note that only edge of error bars or standard deviation for respective values are shown in respective figures.

in this study (K2: 0.64, S1: 0.90) as follows:

$$R_{(VA)(z)}(\%\_m^{-1}) = -100/POCF_{(z)} \times \partial/\partial z \times POCF_{(z)} = 100 \times b \times z^{-1} \quad (10)$$

At K2 and S1, the $R_{(VA)}$ values at 200 m were ∼0.3 and ∼0.5% m^{-1}, respectively (**Figure 8B**), and they decreased with increasing depth. At 1000 (5000) m, the $R_{(VA)}$ values at K2 and S1 were ∼0.05 (0.02) and 0.1 (0.02)% m^{-1}, respectively:

The $R_{(VA)}$ rate was determined from the $R_{(T,O)}$ rates and the sinking velocity of the POC or particles (SV) as follows:

$$R_{(VA)}(\%m^{-1}) = R_{(T,O)}(\%day^{-1})/SV(mday^{-1}) \quad (11)$$

It should be noted that $R_{(VA)}/100$ is inversely related to the Remineralization Length Scale (RLS: RLS = $SV/R_{(T,O)}$), which has been used as an index of biological carbon pump efficiency (e.g., Cram et al., 2018).

I used $R_{(T,O)}$ (**Figure 8A**) and $R_{(VA)}$ (**Figure 8B**) to estimate SV (**Figure 8C**). At K2, the average SV at 200 m was estimated to be ∼6 m day^{-1}, and the SV increased with increasing depth. The SV became roughly 25 m day^{-1} at ∼1000 m and roughly 150 m day^{-1} at ∼5000 m. At S1, the average SV at 200 m was estimated to be ∼40 m day^{-1}, and the SV increased to roughly 45 m day^{-1} at ∼350 m. The SV then decreased with increasing depth, and at around 1000 m the SV was ∼25 m day^{-1}, comparable to the SV at the same depth at K2. At depths greater than 1000 m, the SVs at S1 were estimated to be smaller than those at K2, and they increased with depth again. This pattern is attributable to the fact that the $R_{(VA)}$ was still larger at S1 than at K2 at depths greater than 1000 m, whereas $R_{(T,O)}$ values were comparable at both stations. At 5000 m, the average SV was estimated to be ∼110 m day^{-1}. An increase of SV with depth has previously been reported (Berelson, 2002; Honda et al., 2009, 2013; Villa-Alfageme et al., 2016). My estimate that the SV was larger at S1 than at K2 in the upper 500 m is consistent with the results of previous studies (Honda et al., 2013; Sukigara et al., 2019) and thus seems reasonable. However, the absolute values of the SVs estimated in this study seem somewhat low compared to previous estimates: 72 m day^{-1} between 60 and 1000 m, and 136 m day^{-1} between 1000 and 4810 m at K2 (Honda et al., 2009); 26–71 m day^{-1} at K2 and 22–46 m day^{-1} at S1 in the upper 500 m, and >180 m day^{-1} below 500 m at both stations (Honda et al., 2013); and ∼30 m day^{-1} at K2 and ∼60 m day^{-1} at S1 at depths of 100–200 m (Sukigara et al., 2019). The low SVs estimated in this study might be attributable to the low Cr values used, 0.12 ± 0.03 day^{-1} at 15°C and 0.03 ± 0.01 day^{-1} at 4°C, based on the report of Iversen and Ploug (2013). For comparison, McDonnell et al. (2015) reported an average Cr of 0.5 (0.5–1.5) day^{-1} for POC flux at the Atlantic subtropical station BATS, and DeVries and Weber (2017) used a Cr of 0.32 ± 0.15 day^{-1} for fast-sinking POC and of 0.16 ± 0.06 day^{-1} for slow-sinking POC in their numerical simulation of the vertical attenuation of the global POC flux. In this study, metabolic rates were assumed to depend only on water temperature and O_2 concentration. Although many papers have discussed the hydraulic pressure effect on prokaryote production (reviewed by

TABLE 2 | Biomasses of metazoan zooplankton (ZP) and prokaryotes, estimated biological carbon demands of ZP and prokaryotes, and carbon supplies estimated from differences of POC fluxes, DOC fluxes, and ZP excretion.

		K2	S1	References
ZP biomass (mg m^{-2})		2250	300	Honda et al., 2017
Prokaryote biomass:(mg m^{-2})		1440	940	Honda et al., 2017
Carbon demand				
ZP (metazoan) carbon demand (mg m^{-2} day^{-1})	150 (or 200) to 1000 m	100 ± 4	40 ± 11	Kobari et al., 2016
Prokaryote carbon demand (mg m^{-2} day^{-1})	150 (or 200) to 1000 m	13.9 ± 1.8	9.6 ± 1.2	Honda et al., 2017
	200–4810 m	13.9 ± 0.9	10.6 ± 0.7	Uchimiya et al., 2018
Carbon supply				
ΔPOC flux (mg m^{-2} day^{-1})	200–4810 m	39.7	39.8	This study
DOC flux (mg m^{-2} day^{-1})	150 m (K2), 200 m (S1)	1.0	8.2	Wakita et al., 2016; Honda et al., 2017
ZP excretion (mg m^{-2} day^{-1})	150 m (K2), 200 m (S1)	0.9	1.1	Kobari et al., 2016; Honda et al., 2017

Nagata et al., 2010; Tamburini et al., 2013), I did not consider the hydraulic pressure effect on Cr and Q_{10} because no appropriate parameterization of its effect that could have been applied to this study has been proposed.

In addition, I did not take into account the biomass and rate of production of zooplankton and prokaryotes. The K2S1 project (Honda et al., 2017) has revealed that the biomasses of metazoan zooplankton (hereinafter ZP) and prokaryotes are ∼7 times and ∼1.5 times higher at K2 than at S1, respectively, and the carbon demands of ZP and prokaryotes at K2 were estimated to be ∼2.5 times and ∼1.4 times the corresponding demands at S1 (**Table 2**). This pattern is inconsistent with the smaller POC remineralization rate at K2 than at S1. The ZP carbon demand per unit biomass at S1 has been estimated to be ∼2.8 times (7/2.5) the corresponding demand at K2. In contrast, based on **Figure 8A**, the average $R_{(T,O)}$ at S1 in the twilight zone (100–1000 m) was estimated to be ∼4.4 times the average $R_{(T,O)}$ at K2. Thus, the estimated $R_{(T,O)}$ at K2, without consideration of the effect of ZP, might be underestimated relative to the $R_{(T,O)}$ at S1.

Moreover, it has been reported that the total carbon demands of ZP and prokaryotes tend to exceed the total carbon supply by remineralization of sinking POC and the excretion of dissolved organic carbon (DOC) by ZP, especially at K2 (**Table 2**). A similar mismatch between the carbon supply and demand has also been observed in other ocean basins. In a recent review, Boyd et al. (2019) proposed that, besides the particle flux due to gravitational settling, other carbon transport mechanisms may contribute to the carbon supply. They call such mechanisms "particle injection pumps": the supply of suspended particles to the ocean interior by, for example, eddy-induced subduction or the seasonal deepening of the mixed layer. In addition, slowly sinking particles (Giering et al., 2014) or suspended particles in the mesopelagic layer (Briggs et al., 2020), some of which are transported laterally (Lam and Bishop, 2008) and are difficult to observe with sediment trap measurements, might help to meet the biological carbon demand in the ocean interior. A discrepancy between the remineralization of sinking POC and biomass/carbon demand is therefore possible, and quantification of the relationship between these is strongly recommended in future studies.

CONCLUSION

Measurements of the fluxes of sinking particles at the western Pacific subarctic-eutrophic time-series station K2 and the subtropical-oligotrophic station S1 during the K2S1 project showed that the vertical attenuation of POC fluxes was smaller at subarctic station K2 than at subtropical station S1. In other words, POC was transported vertically more efficiently at station K2 than at station S1. The more efficient transport at K2 might be due to protection of the POC by diatoms from degradation and to the lower microbial metabolic rates in the twilight zone at K2 due to the lower temperatures and O_2 concentrations at K2. However, the carbon supplied by POC, DOC, and ZP to the ocean interior was insufficient to satisfy the observed biological carbon demand there, especially at station K2. The reason for this mismatch is still an open question.

DATA AVAILABILITY STATEMENT

Publicly available datasets were analyzed in this study. This data can be found here: http://ebcrpa.jamstec.go.jp/k2s1/en/.

AUTHOR CONTRIBUTIONS

MH designed the research and wrote the manuscript with great support from all concerned in the K2S1 project.

FUNDING

This work was financially supported by Grants-in-Aid for Scientific Research (KAKENHI JP18H04144 and JP19H05667)

funded by the Ministry of Education, Culture, Sports, Science, and Technology-Japan (MEXT).

ACKNOWLEDGMENTS

The author acknowledges all scientists, students, marine technicians, and ship crews who participated in the K2S1 project. Without their hard work, this research would never have been completed. Dr. Mario Uchimiya of the University of Georgia provided prokaryote data and valuable comments concerning the discussion of prokaryote biomass and production. The author deeply appreciate reviewers for their constructive and suggestive comments, TF as handling editor and guest editors of special issue, including Drs. Maureen H. Conte, Rut P. Pamies, and Gerhard J. Herndl.

REFERENCES

Armstrong, R. A., Lee, C., Hedges, J. I., Honjo, S., and Wakeham, S. G. (2002). A new, mechanistic model for organic carbon fluxes in the ocean based on the quantitative association of POC with ballast minerals. *Deep Sea Res. Part II* 49, 219–236. doi: 10.1016/S0967-0645(01)00101-1

Bach, L. T., Stange, P., Taucher, J., Achterberg, E. P., Algueró−Muñiz, M., Horn, H., et al. (2019). The influence of plankton community structure on sinking velocity and remineralization rate of marine aggregates. *Global Biogeochem. Cycles* 33, 971–994. doi: 10.1029/2019GB006256

Banse, K. (1990). New views on the degradation and disposition of organic particles as collected by sediment traps in the open ocean. *Deep Sea Res. Part A* 37, 1177–1195. doi: 10.1016/0198-0149(90)90058-4

Berelson, W. L. (2002). Particle settling rates increase with depth in the ocean. *Deep Sea Res. II* 49, 237–251. doi: 10.1016/s0967-0645(01)00102-3

Berelson, W. M. (2001). The flux of particulate organic carbon into the ocean interior.: a comparison of four U.S. JGOFS regional studies. *Oceanography* 14, 59–64.

Berger, W. H., Fischer, K., Lai, C., and Wu, G. (1987). "Ocean carbon flux: global maps of primary production and export production," in *Biogeochemical Cycling and Fluxes between the Deep Euphotic Zone and Other Oceanic Realms*, Vol. 3, ed. C. Agegian (Silver Spring, MD: NOAA), 87–30.

Betzer, P. R., Shower, W. L., Laws, E. A., Winn, C. D., Ditullio, G. R., and Kroopnick, P. M. (1984). Primary productivity and particle fluxes on a transect of the equator at 153°W in the Pacific Ocean. *Deep Sea Res.* 31, 1–11. doi: 10.1016/0198-0149(84)90068-2

Boyd, P. W., Claustre, H., Levy, M., Siegel, D. A., and Weber, T. (2019). Multi-faceted particle pumps drive carbon sequestration in the ocean. *Nature* 568, 327–335. doi: 10.1038/s41586-019-1098-2

Boyd, P. W., and Trull, T. W. (2007). Understanding the export of biogenic particles in oceanic waters: is there consensus? *Prog. Oceanogr.* 72, 276–312. doi: 10.1016/j.pocean.2006.10.007

Briggs, N., Dall'Olmo, G., and Claustre, H. (2020). Major role of particle fragmentation in regulating biological sequestration of CO_2 by the oceans. *Science* 367, 791–793. doi: 10.1126/science.aay1790

Buesseler, K. O. (1998). The decoupling of production and particulate export in the surface ocean. *Global Biogeochem. Cycles* 12, 297–310. doi: 10.1029/97GB03366

Buesseler, K. O., and Boyd, P. W. (2009). Shedding light on processes that control particle export and flux attenuation in the twilight zone of the open ocean. *Limnol. Oceanogr.* 54, 1210–1232. doi: 10.4319/lo.2009.54.4.1210

Buesseler, K. O., Lamborg, C. H., Boyd, P. W., Lam, P. J., Trull, T. W., Bidigare, R., et al. (2007). Revisiting carbon flux through the ocean's twilight zone. *Science* 316, 567–570. doi: 10.1126/science.1137959

Buesseler, K. O., Trull, T. W., Steinberg, D. K., Silver, M. W., Siegel, D. A., Saitoh, S. I., et al. (2008). VERTIGO (VERtical Transport In the Global Ocean): a study of particle sources and flux attenuation in the North Pacific. *Deep Sea Res. Part II* 55, 1522–1539. doi: 10.1016/j.dsr2.2008.04.024

Cael, B. B., and Bisson, K. (2018). Particle flux parameterizations: quantitative and mechanistic similarities and differences. *Front. Mar. Sci.* 5:395. doi: 10.3389/fmars.2018.00395

Cram, J. A., Weber, T., Leung, S. W., McDonnell, A. M. P., Liang, J.-H., and Deutsch, C. (2018). The role of particle size, ballast, temperature, and oxygen in the sinking flux to the deep sea. *Global Biogeochem. Cycles* 32, 858–876. doi: 10.1029/2017GB005710

DeVries, T., and Weber, T. (2017). The export and fate of organic matter in the ocean: new constraints from combining satellite and oceanographic tracer observations. *Global Biogeochem. Cycles* 31, 535–555. doi: 10.1002/2016GB005551

Dodimead, A. J., Favorite, F., and Hirano, T. (1963). Winter oceanographic conditions in the central Subarctic Pacific. *Bull. Int. North Pacific Comm.* 13, 1–195.

Doney, S., Fabry, V. J., Feely, R. A., and Kleypas, J. A. (2009). Ocean acidification: the other CO_2 problem. *Annu. Rev. Mar. Sci.* 2009, 169–192.

Favorite, F., Dodimead, A. J., and Nasu, K. (1976). Oceanography of the subarctic Pacific region. *Bull. Int. North Pacific Comm.* 33, 1–187.

Fisher, G., and Karakas, G. (2009). Sinking rates and ballast composition of particles in the Atlantic Ocean: implications for the organic carbon fluxes to the deep ocean. *Biogeosciences* 6, 85–102. doi: 10.5194/bg-6-85-2009

Francois, R., Honjo, S., Krishfield, R., and Manganini, S. (2002). Factors controlling the flux of organic carbon to the bathypelagic zone of the ocean. *Global Biogeochem. Cycles* 16:1087. doi: 10.1029/2001GB001722

Garcia, H. E., Locarnini, R. A., Boyer, T. P., Antonov, J. I., Zweng, M. M., Baranova, O. K., et al. (2010). *World Ocean Atlas 2009, Volume 4: Nutrients (Phosphate, Nitrate, Silicate)*. ed. S. Levitus (Washington, DC: U.S. Government Printing Office), 398.

Giering, S. L. C., Sanders, R., Lampitt, R. S., Anderson, T. R., Tamburini, C., Boutrif, M., et al. (2014). Reconciliation of the carbon budget in the ocean's twilight zone. *Nature* 507, 480–483. doi: 10.1038/nature13123

Gloege, L., McKinley, G. A., Mouw, C. B., and Clochetto, A. R. (2017). Global evaluation of particulate organic carbon flux parameterizations and implications for atmospheric pCO2. *Global Biogeochemical Cycles* 31, 1192–1215. doi: 10.1002/2016GB005535

Hansen, B., Fotel, F. L., Jensen, N. J., and Madsen, S. D. (1996). Bacteria associated with a marine planktonic copepod in culture. II. Degradation of fecal pellets produced on a diatom, a nanoflagellate or a dinoflagellate diet. *J. Plankton Res.* 18, 275–288. doi: 10.1093/plankt/18.2.275

Heinze, C. (2004). Simulating oceanic $CaCO_3$ export production in the greenhouse. *Geophys. Res. Lett.* 31:6308. doi: 10.1029/2004GL020613

Henson, S., Le Moigne, F., and Giering, S. (2019). Drivers of carbon export efficiency in the global ocean. *Global Biogeochem. Cycles* 33, 891–903. doi: 10.1029/2018GB006158

Henson, S. A., Sanders, R., and Madsen, E. (2012). Global patterns in efficiency of particulate organic carbon export and transfer to the deep ocean. *Global Biogeochem. Cycles* 26:GB1028.

Henson, S. A., Yool, A., and Sanders, R. (2015). Variability in efficiency of particulate organic carbon export: a model study. *Global Biogeochem. Cycles* 29, 33–45. doi: 10.1002/2014GB004965

Honda, M. C., Imai, K., Nojiri, Y., Hoshi, F., Sugawara, T., and Kusakabe, M. (2002). The biological pump in the northwestern North Pacific based on fluxes and major components of particulate matter obtained by sediment trap experiments (1997–2000). *Deep Sea Res. II* 49, 5595–5625. doi: 10.1016/s0967-0645(02)00201-1

Honda, M. C., and Kawakami, H. (2014). Sinking velocity of particulate radiocesium in the northwestern North Pacific. *Geophys. Res. Lett.* 41, 3959–3965. doi: 10.1002/2014GL060126

Honda, M. C., Kawakami, H., Matsumoto, K., Wakita, M., Fujiki, T., Mino, Y., et al. (2015). Comparison of sinking particles in the upper 200 m between subarctic station K2 and subtropical station S1 based on drifting sediment trap experiments. *J. Oceanogr.* 72, 373–386. doi: 10.1007/s10872-015-0280-x

Honda, M. C., Kawakami, H., Watanabe, S., and Saino, T. (2013). Concentration and vertical flux of Fukushima-derived radiocesium in sinking particles from

two sites in the Northwestern Pacific Ocean. *Biogeoscience* 10, 3525–3534. doi: 10.5194/bg-10-3525-2013

Honda, M. C., Sasai, Y., Siswanto, E., Kuwano-Yoshida, A., Aiki, H., and Cronin, M. F. (2018). Impact of cyclonic eddies and typhoons on biogeochemistry in the oligotrophic ocean based on biogeochemical / physical / meteorological time-series at station KEO. *Prog. Earth Planet. Sci.* 5:42. doi: 10.1186/s40645-018-0196-3

Honda, M. C., Sasaoka, K., Kawakami, H., Matsumoto, K., Watanabe, S., and Dickey, T. (2009). Application of underwater optical data to estimation of primary productivity. *Deep Sea Res. I* 56, 2281–2292. doi: 10.1016/j.dsr.2009.08.009

Honda, M. C., Wakita, M., Matsumoto, K., Fujiki, T., Siswanto, E., Sasaoka, K., et al. (2017). Comparison of carbon cycle between the western Pacific subarctic and subtropical time-series stations: highlights of the K2S1 project. *J. Oceanogr.* 73, 647–667. doi: 10.1007/s10872-017-0423-3

Honda, M. C., and Watanabe, S. (2010). Importance of biogenic opal as ballast of particulate organic carbon (POC) transport and existence of mineral ballast-associated and residual POC in the Western Pacific Subarctic Gyre. *Geophys. Res. Lett.* 37:L02605. doi: 10.1029/2009GL041521

Ittekkot, V. (1993). The abiotically driven biological pump in the ocean and short-term fluctuations in the atmospheric CO_2 content. *Global Planet. Change* 8, 17–25. doi: 10.1016/0921-8181(93)90060-2

Iversen, M. H., and Ploug, H. (2013). Temperature effects on carbon-specific respiration rate and sinking velocity of diatom aggregates – potential implications for deep ocean export processes. *Biogeosciences* 10, 4073–4085. doi: 10.5194/bg-10-4073-2013

Kalvelage, T., Lavik, G., Jensen, M. M., Revsbech, N. P., Löscher, C., Schunck, H., et al. (2015). Aerobic microbial respiration in oceanic oxygen minimum zones. *PLoS One* 10:e0133526. doi: 10.1371/journal.pone.0133526

Keil, R. G., Neibauer, J. A., and Devol, A. H. (2016). A multiproxy approach to understanding the "enhanced" flux of organic matter through the oxygen-deficient waters of the Arabian Sea. *Biogeosciences* 13, 2077–2092. doi: 10.5194/bg-13-2077-2016

Klaas, C., and Archer, D. E. (2002). Association of sinking organic matter with various types of mineral ballast in the deep sea: implications for the rain ratio. *Global Biogeochem. Cycles* 16:1116. doi: 10.1029/2001GB001765

Knauer, G. A., Martin, J. H., and Bruland, K. W. (1979). Fluxes of particulate carbon, nitrogen, and phosphorus in the upper water column of the northeast Pacific. *Deep Sea Res.* 26, 97–108. doi: 10.1016/0198-0149(79)90089-x

Kobari, T., Nakamura, R., Unno, K., Kitamura, M., Yanabe, K., Nagafuku, H., et al. (2016). Seasonal variability in carbon demand and flux by mesozooplankton communities at subarctic and subtropical sites in the western North Pacific Ocean. *J. Oceanogr.* 72, 403–418. doi: 10.1007/s10872-015-0348-7

Kwon, E. Y., Primeau, F., and Sarmiento, J. L. (2009). The impact of remineralization depth on the air–sea carbon balance. *Nature Geosci.* 2, 630–635. doi: 10.1038/ngeo612

Lam, P. J., and Bishop, J. K. B. (2008). The continental margin is a key source of iron to the HNLC North Pacific Ocean. *Geophys. Res. Lett.* 35:L07608. doi: 10.1029/2008GL033294

Laufkötter, C., John, J. G., Stock, C. A., and Dunne, J. P. (2017). Temperature and oxygen dependence of the remineralization of organic matter. *Global Biogeochem. Cycles* 31, 1038–1050. doi: 10.1002/2017GB005643

Laws, E. A., DiTullio, G. R., Betzer, P. R., Karl, D. M., and Carder, K. L. (1989). Autrophic production and elemental fluxes at 26°N, 155°W in the North Pacific subtropical gyre. *Deep Sea Res.* 36, 103–120. doi: 10.1016/0198-0149(89)90021-6

Laws, E. A., Falkowski, P. G., Smith, W. O. Jr., Ducklow, H., and McCarthy, J. J. (2000). Temperature effects on export production in the open ocean. *Global Biogeochem. Cycles* 14, 1231–1246. doi: 10.1029/1999gb001229

Lima, I. D., Lam, P. J., and Doney, S. C. (2014). Dynamics of particulate organic carbon flux in a global ocean model. *Biogeosciences* 11, 1177–1198. doi: 10.5194/bg-11-1177-2014

Lorius, C., Jouzel, J., Raynaud, D., Hansen, J., and Treut, H. L. (1990). The Ice-core record: climate sensitivity and future greenhouse warming. *Nature* 347, 139–145. doi: 10.1038/347139a0

Maerz, J., Six, K. D., Stemmler, I., Ahmerkamp, S., and Ilyina, T. (2020). Microstructure and composition of marine aggregates as co-determinants for vertical particulate organic carbon transfer in the global ocean. *Biogeosciences* 17, 1765–1803. doi: 10.5194/bg-17-1765-2020

Marsay, C. M., Sanders, R. J., Henson, S. A., Pabortsava, K., Achterberg, E. P., and Lampit, R. C. (2015). Attenuation of sinking particulate organic carbon flux through the mesopelagic ocean. *Proc. Natl. Acad. Sci. U.S.A.* 112, 1089–1094. doi: 10.1073/pnas.1415311112

Martin, J. H., Knauer, G. A., Karl, D. M., and Broenkow, W. W. (1987). VERTEX: carbon cycling in the northeast Pacific. *Deep Sea Res.* 34, 267–285. doi: 10.1016/0198-0149(87)90086-0

Matsumoto, K., Abe, O., Fujiki, T., Sukigara, C., and Mino, Y. (2016). Primary productivity at the time-series stations in the northwestern Pacific Ocean: is the subtropical station unproductive? *J. Oceanogr.* 72, 359–371. doi: 10.1007/s10872-016-0354-4

Mayer, L. M. (1994). Surface area control of organic carbon accumulation in continental shelf sediments. *Geochim. Cosmochim. Acta* 58, 1271–1284. doi: 10.1016/0016-7037(94)90381-6

McDonnell, A. M. P., Boyd, P. W., and Buesseler, K. O. (2015). Effects of sinking velocities and microbial respiration rates on the attenuation of particulate carbon fluxes through the mesopelagic zone. *Global Biogeochem. Cycles* 29, d175–d193. doi: 10.1002/2014GB004935

Nagata, T., Tamburini, C., Aristegui, J., Baltar, F., Bochdansky, A. B., Fonda-Umani, S., et al. (2010). Emerging concepts on microbial processes in the bathypelagic ocean-ecology, biogeochemistry, and genomics. *Deep Sea Res II* 57, 1519–1536. doi: 10.1016/j.dsr2.2010.02.019

Otosaka, S., and Noriki, S. (2005). Relationship between composition of settling particles and organic carbon flux in the western North Pacific and the Japan Sea. *J. Oceanogr.* 61, 25–40. doi: 10.1007/s10872-005-0017-3

Pace, M. L., Knauer, G. A., Karl, D. M., and Martin, J. H. (1987). Primary production and vertical flux in the eastern Pacific Ocean. *Nature* 325, 803–804. doi: 10.1038/325803a0

Palevsky, H. I., and Doney, S. (2018). How choice of depth horizon influences the estimated spatial patterns and global magnitude of ocean carbon export flux. *Geophys. Res. Lett.* 45, 4171–4179. doi: 10.1029/2017GL076498

Passow, U., and De La Rocha, C. L. (2006). Accumulation of mineral ballast on organic aggregates. *Global Biogeochem. Cycles* 20:GB1013. doi: 10.1029/2005GB002579

Passow, U., Shipe, R. F., Murray, A., Pak, D. K., Brzezinski, M. A., and Alldredge, A. L. (2001). The origin of transparent exopolymer particles (TEP) and their role in the sedimentation of particulate matter. *Cont. Shelf Res.* 21, 327–346. doi: 10.1016/s0278-4343(00)00101-1

Pavia, F. J., Anderson, R. F., Lam, P. J., Cael, B. B., Vivancos, S. M., Fleisher, M. Q., et al. (2019). Shallow particulate organic carbon regeneration in the South Pacific Ocean. *Proc. Natl. Acad. Sci. U.S.A.* 116, 9753–9758. doi: 10.1073/pnas.1901863116

Ploug, H. (2001). Small-scale oxygen fluxes and remineralization in sinking aggregates. *Limnol. Oceanogr.* 46, 1624–1631. doi: 10.4319/lo.2001.46.7.1624

Quinlan, A. V. (1981). The thermal sensitivity of generic Michaelis-Menten processes without catalyst denaturation or inhibition. *J. Thermal Biol.* 6, 103–114. doi: 10.1016/0306-4565(81)90061-9

Redfield, A. C., Ketchum, B. H., and Richards, F. A. (1963). "The influence of organisms on the composition of seawater," in *The Sea*, Vol. 2, ed. M. N. Hill (New York, NY: Interscience), 26–77.

Simon, M., Grossart, H.-P., Schweitzer, B., and Ploug, H. (2002). Microbial ecology of organic aggregates in aquatic ecosystems. *Aquat. Microb. Ecol.* 28, 175–211. doi: 10.3354/ame028175

Smith, K. L. Jr., Ruhl, H. A., Huffard, C. L., Messie, M., and Kahru, M. (2018). Episodic organic carbon fluxes from surface ocean to abyssal depths during long-term monitoring in NE Pacific. *Proc. Natl. Acad. Sci. U.S.A.* 115, 12235–12240. doi: 10.1073/pnas.1814559115

Suess, E. (1980). Particle organic carbon flux in the ocean surface productivity and oxygen utilization. *Nature* 288, 260–263. doi: 10.1038/288260a0

Sukigara, C., Mino, Y., Kawakami, H., Honda, M. C., Fujiki, T., Matsumoto, K., et al. (2019). Sinking dynamics of particulate matter in the subarctic and subtropical regions of the western North Pacific. *Deep Sea Res. I* 144, 17–27. doi: 10.1016/j.dsr.2018.11.004

Tamburini, C., Boutrif, M., Garel, M., Colwell, R. R., and Deming, J. W. (2013). Prokaryotic responses to hydrostatic pressure in the ocean – review. *Environ. Microbiol.* 15, 1262–1274. doi: 10.1111/1462-2920.12084

Taylor, S. R. (1964). Abundance of chemical elements in the continental crust: a new table. *Geochim. Cosmochim. Acta* 28, 1273–1285. doi: 10.1016/0016-7037(64)90129-2

Uchimiya, M., Fukuda, H., Wakita, M., Kitamura, M., Kawakami, H., Honda, M. C., et al. (2018). Balancing organic carbon supply and consumption in the ocean's interior: evidence from repeated biogeochemical observations conducted in the subarctic and subtropical western North Pacific. *Limnol. Oceanogr.* 63, 2015–2027. doi: 10.1002/lno.10821

Villa-Alfageme, M., de Soto, F. C., Ceballos, E., Giering, L. C., Le Moigne, F. A. C., Henson, S., et al. (2016). Geographical, seasonal, and depth variation in sinking particle speeds in the North Atlantic. *Geophys, Res. Lett.* 43, 8609–8616. doi: 10.1002/2016GL069233

Volk, T., and Hoffert, M. I. (1985). "Ocean carbon pumps: analysis of relative strengths and efficiencies in ocean-driven atmospheric CO_2 changes," in *The Carbon Cycle and Atmospheric CO_2: Natural Variations Archean to Present, 32. Geophysical Monograph*, eds E. T. Sundquist and W. S. Broecker (Washington, DC: American Geophysical Union), 99–110. doi: 10.1029/gm032p0099

Wakita, M., Honda, M. C., Matsumoto, K., Fujiki, T., Kawakami, H., Yasunaka, S., et al. (2016). Biological organic carbon export estimated from carbon budget in the surface water of western subarctic and subtropical North Pacific Ocean. *J. Oceanogr.* 72, 665–685. doi: 10.1007/s10872-016-0379-8

Weber, T., Cram, J. A., Leung, S. W., DeVries, T., and Deutsch, C. (2016). Deep ocean nutrients imply large latitudinal variation in particle transfer efficiency. *Proc. Natl. Acad. Sci. U.S.A.* 31, 8606–8611. doi: 10.1073/pnas.1604414113

Wilson, J. D., Barker, S., Edwards, N., Holden, P. B., and Ridgwell, A. (2019). Sensitivity of atmospheric CO_2 to regional variability in particulate organic matter remineralization depths. *Biogeosciences* 16, 2923–2936. doi: 10.5194/bg-16-2923-2019

Yamanaka, Y., and Tajika, E. (1996). The role of the vertical fluxes of particulate organic matter and calcite in the oceanic carbon cycle: studies using an ocean biogeochemical general circulation model. *Global Biogeochem. Cycles* 10, 361–382. doi: 10.1029/96gb00634

Yu, E., Francois, R., Bacon, M., Honjo, S., Fleet, A., Manganini, S., et al. (2001). Trapping efficiency of bottom-tethered sediment traps estimated from the intercepted fluxes of ^{230}Th and ^{231}Pa. *Deep Sea Res. I* 48, 865–889. doi: 10.1016/s0967-0637(00)00067-4

Conflict of Interest: The author declares that the research was conducted in the absence of any commercial or financial relationships that could be construed as a potential conflict of interest.

frontiers in Earth Science

ORIGINAL RESEARCH
published: 24 September 2020
doi: 10.3389/feart.2020.560893

Relative Importance of Phosphodiesterase vs. Phosphomonoesterase (Alkaline Phosphatase) Activities for Dissolved Organic Phosphorus Hydrolysis in Epi- and Mesopelagic Waters

Blair Thomson[1], Jess Wenley[1,2], Scott Lockwood[1,2], Isla Twigg[1], Kim Currie[3], Gerhard J. Herndl[4,5], Christopher D. Hepburn[1] and Federico Baltar[4]**

[1] Department of Marine Science, University of Otago, Dunedin, New Zealand, [2] Department of Microbiology, University of Otago, Dunedin, New Zealand, [3] NIWA/University of Otago Research Centre for Oceanography, Dunedin, New Zealand, [4] Department of Functional and Evolutionary Ecology, University of Vienna, Vienna, Austria, [5] Department of Marine Microbiology and Biogeochemistry, NIOZ, Royal Netherlands Institute for Sea Research, Utrecht University, Utrecht, Netherlands

OPEN ACCESS

Edited by:
Timothy Ferdelman, Max Planck Institute for Marine Microbiology (MPG), Germany

Reviewed by:
Masahiro Suzumura, National Institute of Advanced Industrial Science and Technology (AIST), Japan
France Van Wambeke, Centre National de la Recherche Scientifique (CNRS), France

***Correspondence:**
Blair Thomson
blair.thomson@otago.ac.nz
Federico Baltar
federico.baltar@univie.ac.at

Specialty section:
This article was submitted to Biogeoscience, a section of the journal Frontiers in Earth Science

Received: *11 May 2020*
Accepted: *31 August 2020*
Published: *24 September 2020*

Citation:
Thomson B, Wenley J, Lockwood S, Twigg I, Currie K, Herndl GJ, Hepburn CD and Baltar F (2020) Relative Importance of Phosphodiesterase vs. Phosphomonoesterase (Alkaline Phosphatase) Activities for Dissolved Organic Phosphorus Hydrolysis in Epi- and Mesopelagic Waters. Front. Earth Sci. 8:560893. doi: 10.3389/feart.2020.560893

Marine microbes use extracellular phosphatases to hydrolyze phosphate from organic matter. Dissolved organic phosphorus (DOP) is typically present in higher concentrations than phosphate in oceanic surface waters. Yet, the fate and role of different DOP components, such as phosphomonoester and phosphodiester, are poorly understood. Most of the investigations on extracellular enzymatic hydrolysis of marine DOP have focused on phosphomonoesterase (MEA) activity (i.e., alkaline phosphatase), whereas phosphodiesterase (DEA) measurements are scarce. This limits our understanding of the ecological and biogeochemical role of DOP sources other than P-monoesters in the sea. We determined extracellular MEA and DEA activities including their cell-free fractions on a bimonthly basis over 14 months in surface and mesopelagic subantarctic waters, thus covering a wide range of phosphate availability levels (from <0.5 to 2.3 μM). We found that DEA and MEA exhibit similar hydrolysis rates in surface as well as in mesopelagic waters. The MEA:DEA ratio varied between 0.38 and 5.42 during the study period, indicating potential differences in function and/or expression among the two enzyme groups, potentially reflecting differences in the availability and/or utilization of P-monoester and P-diester pools. Interestingly, the MEA:DEA was negatively correlated to phosphate (r = −0.82, p = 0.02, R^2=0.67) and positively with the inorganic N:P ratio (r = 0.84, p = 0.02, R^2 = 0.67), suggesting that the relative importance of DEA *vs.* MEA is linked to inorganic P availability and the N:P ratio. DEA was also related to the N:P ratio, both at the surface and at depth, suggesting DEA alone is sensitive to changes in the N:P ratio. The majority (>70%) of extracellular MEA and DEA was found in the cell-free fraction, increasing with depth for MEA. Our results indicated that DOP hydrolysis mediated by DEA in the surface as well as in dark ocean is as important as the frequently measured MEA.

Keywords: extracellular enzymatic activity, phosphomonoesterase, phosphodiesterase, alkaline phosphatase activity, phosphorus

INTRODUCTION

Microbial communities are the main drivers of the global biogeochemical cycles (Falkowski et al., 2008). In contrast to terrestrial systems, the bulk of the organic matter pool available in the oceans is largely comprised of dissolved organic matter (DOM) (Arnosti et al., 2014). Microbes, due to their small size, have exclusive access to this DOM pool, recycling essential nutrients back into marine food webs (Azam et al., 1983; Fenchel 2008). Microbes utilize preferentially high molecular weight DOM as conceptualized by the "size-reactivity model" (Amon and Benner, 1996; Benner and Amon, 2015). High molecular weight DOM, however, needs to be enzymatically cleaved into small molecular weight compounds (<600 Da) outside the cell before they can be funnelled through the complex cell wall of heterotrophic bacteria (Nikaido and Vaara, 1987; Nakae, 1976; Weiss et al., 1991; Amon and Benner, 1996; Benner and Amon, 2015). This requirement for extracellular hydrolysis makes microbial extracellular enzymatic activity (EEA) a rate limiting step in the recycling of marine organic matter (Hoppe, 1991).

Although dissolved inorganic phosphate (P_i) is the preferred form of phosphorus for microbial growth, phosphorus in the epipelagic, and upper mesopelagic layers of the ocean is mainly present as dissolved organic phosphorus (DOP) (Björkman and Karl, 2003; Duhamel et al., 2010; Moore et al., 2013). Phosphate esters (including monoesters and diesters), along with phosphonates, are the main components of DOP (Kolowith et al., 2001). The limited number of studies available indicate that marine P-diesters exhibit similar concentrations as P-monoesters in oceanic waters (Suzumura et al., 1998; Monbet et al., 2009; Yamaguchi et al., 2019). Still, most of the research on the extracellular hydrolytic activity in the ocean has focused on P-monoesterase (MEA) (i.e., alkaline phosphatase), while very little is known about P-diesterase (DEA) activity. MEA and DEA can come from a variety of sources in the environment including phytoplankton as well as heterotrophic microbes (Hoppe, 2003; Yamaguchi et al., 2014). Published DEA research has largely been based on culture studies (Yamaguchi et al., 2014; Accoroni et al., 2017). Available environmental studies have indicated that both P-monoesters and P-diesters can act as phosphorus sources for marine microbes living in the epipelagic layer (Sato et al., 2013; Yamaguchi et al., 2019). However, there are no studies on the seasonal dynamics of DEA to date. Hence, the relative importance of MEA and DEA in DOP hydrolysis in the surface waters remains unknown. Even less is known about the relative importance of MEA vs. DEA in the meso- and bathypelagic ocean. There are some studies on mesopelagic MEAs, often reporting comparable MEA activities in surface and in deep waters (Koike and Nagata, 1997; Hoppe and Ullrich, 1999; Tamburini et al., 2002; Baltar et al., 2009), with cell-specific MEAs increasing with depth down to the bathypelagic zone (Hoppe and Ullrich, 1999; Baltar et al., 2010; Baltar et al., 2013). However, there are no measurements available of DEA in the meso- and bathypelagic waters.

Extracellular enzymes can either be associated to the cell surface or released into the environment, i.e., cell-free enzymes or dissolved enzymes (Hoppe et al., 2002; Baltar, 2018). It has been found that cell-free EEA represents a significant fraction of the total EEA (cell-associated plus cell-free EEA), often accounting for the majority of the total enzyme pool (Duhamel et al., 2010; Allison et al., 2012; Baltar et al., 2016b; Baltar et al., 2019). A large contribution of the cell-free EEA to the total EEA has important ecological and biogeochemical implications because cell-free enzymes can be temporally and/or spatially decoupled from the producing cell (Baltar et al., 2010; Arnosti, 2011; Baltar et al., 2016b). Since residence times for cell-free enzymes are on the scale of days to weeks (Li et al., 1998; Ziervogel et al., 2010; Arnosti, 2011; Steen and Arnosti, 2011; Baltar et al., 2013; Thomson et al., 2019), the history of the water mass may have more explanatory power than the *in situ* microbial community in understanding EEA dynamics (Kamer and Rassoulzadegan, 1995; Baltar et al., 2010; Arnosti 2011; Baltar et al., 2016b). It has been suggested that a high proportion of cell-free MEA might explain the paradox of "high alkaline phosphatase activity at high P_i concentration" (Thomson et al., 2019). Thus, to understand the role of a particular type of EEA it is important to determine the contribution of the cell-free to the total EEA, and how it changes in response to different environmental conditions. The contribution of cell-free to total DEA ranged from 13–49% in the only study where the cell-free fraction of DEA was studied (Sato et al., 2013). The percentage of cell-free to total MEA ranges from 12–100% throughout the water column (Hoppe, 1986; Li et al., 1998; Van Wambeke et al., 2002; Van Wambeke et al., 2009; Duhamel et al., 2011; Allison et al., 2012; Baltar et al., 2016b; Baltar et al., 2019; Thomson et al., 2019). The proportion of cell-free MEA (as well as of glucosidases and leucine aminopeptidase) tends to increase with depth from the epi- to bathypelagic waters (Baltar et al., 2010). This increase in the cell-free EEA with depth is consistent with a recent multi-omics study revealing a relative increase in the secretory peptidases and carbohydrate active enzymes (CAZymes) expression from the epi- to bathypelagic layers (Zhao et al., 2020). However, despite the importance of cell-free EEA in the dark ocean, there are no reports on the contribution of cell-free to total DEA and its relation to MEA in the dark ocean.

In this study, the seasonal dynamics of total and cell-free DEA and MEA are reported for epi- and mesopelagic waters. We hypothesized that the relative contribution of MEA and DEA varies from surface to mesopelagic waters and that the fraction of cell-free DEA covaries with the fraction of cell-free MEA.

METHODS

Study Site and Sampling

Sampling was conducted bimonthly between November 2017 and January 2019 as part of MOTS (Munida Microbial Observatory Time-Series, https://www.otago.ac.nz/mots/about/index.html). MOTS is part of the well-established Munida Time Series Transect, where samples across the subtropical and

subantarctic waters off the south east coast of New Zealand are taken for more than two decades (Currie and Hunter 1999; Currie et al., 2011; Baltar et al., 2015; Baltar et al., 2016a). For this study, samples were taken at the most offshore station (Station 8), located in subantarctic waters approximately 65 km off the Otago coast (−45.83°N, 171.54°E). Station 8 was chosen for this sampling as it is known to be subantarctic water consistently thought the year in the epi-and mesopelagic (Jones et al., 2013). Seawater samples were taken in triplicate for extracellular enzymatic activities from 2 m depth using an onboard continuous pump, and from the mesopelagic (500 and 1000 m) waters using Niskin bottles mounted on a rosette sampler. Temperature was logged on conductivity temperature depth profilers. Samples collected from 1000 m were only taken on the final two research cruises.

Nutrient and Chlorophyll-*a* Analyses

Nutrient analyses were performed on a SEAL AA3 HR auto-analyser (Seal Analytical, United States). All sampling equipment was rinsed three times with Milli-Q water before and after soaking in 10% HCl for > 6 h and oven dried at 60°C prior to collecting samples. Seawater samples were filtered (GF/F) then immediately frozen until analysis for dissolved reactive phosphorus and dissolved inorganic nitrogen. The detection limits were 0.1 mmol m^{-3} for dissolved inorganic nitrogen and 0.03 mmol m^{-3} for dissolved reactive phosphorus. Samples for chlorophyll-*a* analysis were filtered on-board using low vacuum (e.g., <200 mm Hg) through Whatman GF/F filters and frozen until analysis. Chlorophyll-*a* was extracted in 90% acetone for 16–24 h and measured using a calibrated Turner Designs Fluorometer following the procedures outlined by Parsons et al., (1984).

Bacterial Abundance

The bacterial abundance was determined by flow cytometry as described elsewhere (Gasol (1999), Gasol and Del Giorgio (2000) using a FACS Canto II (Becton & Dickinson) with a blue laser (488 nm wavelength). Samples (0.4 ml) preserved in 2% glutaraldehyde were stained with 1:10,000 final concentration of Sybr Green I in the dark for 15 min. Samples were analyzed at low speed for 2 min each and FL1 positive events counted on a FL1 vs. SSC plot using FlowJo10 software.

Extracellular Enzymatic Activity Assays

Extracellular enzymatic activities were assessed based on the hydrolysis of the fluorogenic substrate analogues (Hoppe, 1983). The fluorogenic substrates 4-methylumbelliferyl (MUF)-phosphate, and Bis(MUF)-phosphate were used to assess phosphomonoesterase (MEA, i.e., alkaline phosphatase) and phosphodiesterase (DEA) activities. DEA estimates using Bis(MUF)-phosphate can theoretically be overestimated because one molecule of Bis-MUP can release two molecules of 4-methylumbelliferone, the latter of which is catalyzed by monoesterase, although in practice it was shown that it was overestimated by at most 5–16% in a large transect extending from the North to the South Pacific Ocean (Sato et al., 2013). Saturating substrate concentrations of 100 μM were used based on pre-established kinetics for MEA with sample from this study site. Since P-diesters are usually at lower concentrations than P-monoesters in the ocean (Yamaguchi et al., 2019), and therefore what is saturating for MEA should also be so for DEA, we decided to use the same saturating concentration of 100 μM for DEA in order to compare MEA to DEA rates under the same conditions. These concentrations are saturating, and hence they only represent potential activity rates in the environment. The saturating concentrations we obtained in our preliminary test (which ranged between 50 and 100 μM) are consistent with those from many other previous marine studies (Baltar et al., 2010; Celussi and Del Negro, 2012; Steen et al., 2016; Celussi et al., 2019). Greiner Bio-one 96-well non-protein binding microplates were filled with six technical replicates of the fluorogenic substrates (10 μl) and seawater (290 μl) reaching final concentrations of 100 μM. Standards were prepared using 0.22 μm filtered seawater. Plates were read in a Spectramax M2 spectrofluorometer (Molecular Devices, United States) with excitation and emission wavelengths of 365 and 445 nm, respectively, both before and after an incubation time of 3 h. The wavelength bandwidth was 9 nm with a detection limit of 3.0 fmol/well in 200 μl FITC 96 wells. Six replicate samples without substrate addition served as blanks in each plate. Incubations were performed in the dark at the mean seawater temperature at the time of sampling. To separate the cell-free fraction from the total EEA pool, samples were gently filtered through low protein binding 0.22 μm PES Millex-GP syringe filters following published protocols (Kim et al., 2007; Baltar et al., 2010). Cell-specific extracellular enzymatic activities were calculated by dividing the EEA rates by the abundance of bacterial cells.

Statistical Analyses

Pearson's correlations were carried out using the software package Sigma Stat 2.03 (SPSS). When tests for normality (Kolmogorov-Smirnov) were not met, data were square root transformed prior to analysis. When transformations were not possible Spearman's correlations were applied.

RESULTS AND DISCUSSION

Temperatures ranged from 8.7 to 17.4°C in the epipelagic layer and around 7°C in the mesopelagic waters (500 m) during the study period (**Figure 1A**). There was a shift in the inorganic nutrient concentrations in July 2018 in the epi- and mesopelagic waters, which separated the study into two periods (pre- and post-July 2018) (**Figure 1A**). In the epipelagic waters, mean phosphate and nitrate concentrations increased in July 2018 (from 0.51–1.03 μM and 8.1–11.8 μM for phosphate and nitrate, respectively), remaining at about these levels for the rest of the study (**Figure 1A**). In contrast, in the mesopelagic layer phosphate and nitrate concentrations decreased from February 2018 to April 2018. This increase in surface waters and decrease in mesopelagic waters of inorganic nutrients might be due to the austral winter overturning and mixing of surface and mesopelagic waters, which would cause a relative dilution of

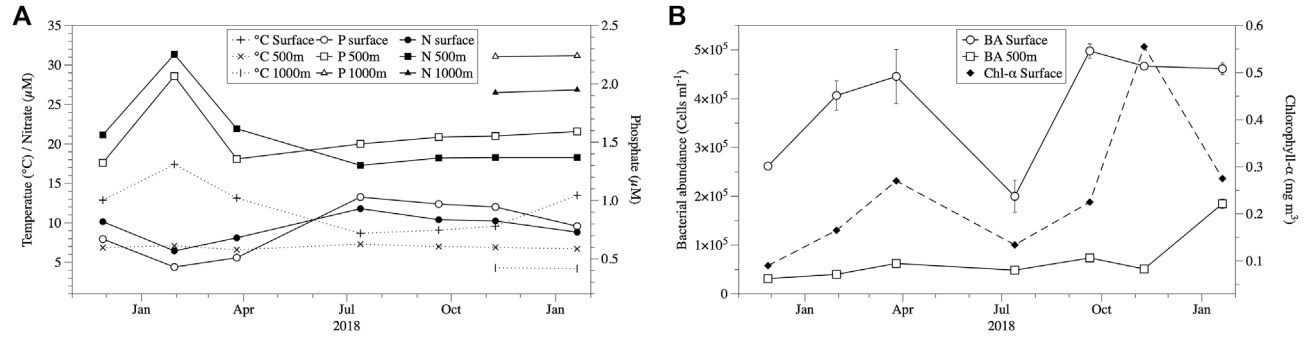

FIGURE 1 | Seasonal variability in temperature, phosphate, and nitrate **(A)**, and chlorophyll-*a* and mean (±SE) bacterial abundance **(B)** in the epi- and mesopelagic layer at the study site in subantarctic waters.

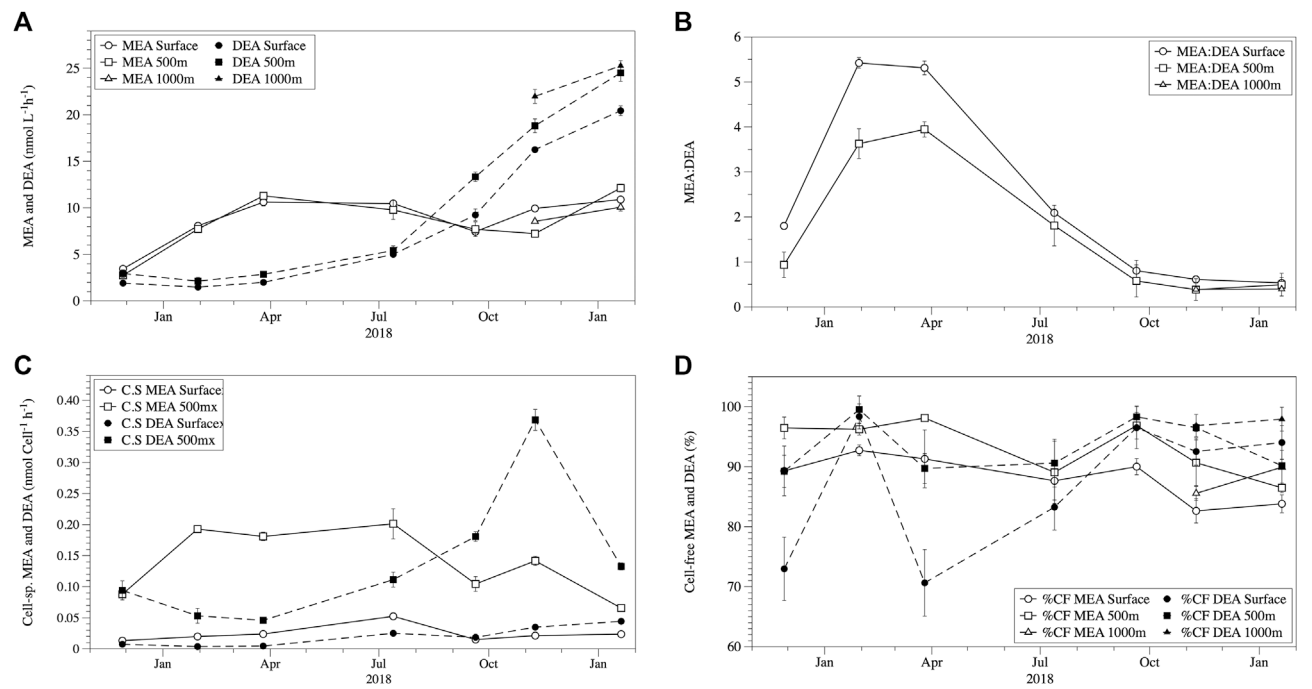

FIGURE 2 | Seasonal variation in mean (±SE) total phosphomonoesterase activity (MEA) and phosphodiesterase activity (DEA) **(A)**, the ratio of MEA to DEA (±SE) **(B)**, the mean (±SE) cell-specific MEA and DEA given in nmol/cell^{-1}/h^{-1} **(C)**, and the mean (±SE) cell-free (CF) fractions for MEA and DEA **(D)** in the epi- and mesopelagic layer at the study site.

deep water and an enrichment in surface waters. This is consistent with the seasonal characterisation of our study region/transect, in which the mixed layer of our Station 8 (SAW) varied from 20 m in summer to >200 m in winter (Jones et al., 2013). Chlorophyll-*a* concentrations indicated the presence of an austral autumn and spring-summer phytoplankton bloom in March-April and November 2018, respectively, coinciding with an increase in bacterial abundance (**Figure 1B**).

MEA and DEA activities were always detected throughout the study (both in the epi- and mesopelagic waters despite the observed differences in temperature and phosphate concentrations (**Figure 2**). MEA and DEA were in the same range in both epi- and mesopelagic waters (**Figure 2A**). MEA ranged between 2.75–12.23 nmol L^{-1} h^{-1} (mean ± SE: 8.6 ± 1.5 nmol L^{-1} h^{-1}), and DEA between 1.43–20.44 nmol L^{-1} h^{-1} (10.9 ± 4.7 nmol L^{-1} h^{-1}). The MEA rates measured in the subantarctic waters were similar to the MEA rates measured previously in this water mass (Thomson et al., 2019) and in the North Atlantic by Steen et al. (2016) but were frequently lower than some reports from the Mediterranean (Celussi and Del Negro, 2012; Celussi et al., 2019). In addition, our MEA rates were higher than those reported from the North Atlantic by (Baltar et al., 2009; Baltar et al., 2010; Baltar et al., 2013), North Pacific

TABLE 1 | Pearson's correlation coefficient (*r*) between the total, cell-free fractions (%) and ratios of phosphomonoesterase activity (MEA) and/to phosphodiesterase activity (DEA) and temperature, phosphate, nitrate, chlorophyll-*a*, and bacterial abundance.

	MEA		**DEA**		**MEA %**		**DEA %**		**MEA:DEA**	
	Surface		**Surface**		**Surface**		**Surface**		**Surface**	
	r	***p*-value**	***r***	***p*-value**	***r***	***p*-value**	***r***	***p*-value**	***r***	***p*-value**
Temp	–0.16	0.736	0.30	0.517	0.46	0.301	0.06	0.906	0.66	0.109
Phosphate	0.19	0.692	0.51	0.245	–0.62	0.140	0.24	0.612	**–0.82**	**0.025**
Nitrate	–0.06	0.893	0.20	0.665	–0.46	0.303	–0.18	0.701	–0.70	0.078
N:P	–0.26	0.578	**–0.84**	**0.018**	0.70	0.082	–0.61	0.148	**0.84**	**0.186**
Chlorophyll-*a*	0.49	0.269	0.65	0.114	–0.66	0.106	0.29	0.532	–0.32	0.489
Bacterial abundance	0.30	0.515	0.49	0.267	–0.13	0.785	0.48	0.278	–0.06	0.894
	500 m		**500 m**		**500 m**		**500 m**		**500 m**	
	r	***p*-value**	***r***	***p*-value**	***r***	***p*-value**	***r***	***p*-value**	***r***	***p*-value**
Temp	–0.23	0.615	–0.22	0.644	–0.14	0.757	0.40	0.375	0.03	0.946
Phosphate	0.10	0.825	–0.03	0.944	–0.05	0.911	0.73	0.0608	0.27	0.559
Nitrate	–0.17	0.724	–0.63	0.133	0.52	0.236	0.40	0.373	0.69	0.083
N:P*	–0.32	0.438	**–0.79**	**0.025**	**0.89**	**0.000**	–0.25	0.545	0.64	0.096
Bacterial abundance	0.65	0.116	0.74	0.058	–0.59	0.164	–0.21	0.658	–0.37	0.415

*Spearman correlations are indicated with an *. Values of* r *that are significant at* p > *0.05 are highlighted in bold.*

(Koike and Nagata, 1997), Indian Ocean (Tamburini et al., 2002) and Mediterranean Sea (Hoppe and Ullrich, 1999) which typically exhibit MEA rates < 4 nmol L^{-1} h^{-1}. The DEA rates measured in the subantarctic waters were comparable at times to values reported by Yamaguchi et al. (2019) from the North Pacific but were generally higher overall and were much higher (1–2 orders of magnitude) than those reported by Sato et al. (2013) for the North and South Pacific.

Prior to July 2018, MEA was higher than DEA, however, this was reversed after July 2018 (**Figure 2A**). The ratio MEA:DEA decreased from 5.3 to 2.1 in the epipelagic and from 4.0 to 1.8 in the mesopelagic waters by July 2018 and decreased to MEA: DEA ratios <1 from November 2018 onwards (**Figure 2B**). The shift in the MEA:DEA ratio also indicates potential changes in the availability of different P-esters and/or microbial enzyme groups. The distribution pattern for the two P-esters has been shown to differ latitudinally and with depth in the open ocean (Yamaguchi et al., 2019), which might explain the changes in the dominance from MEA prior to July to DEA after July (**Figure 2B**). Unfortunately, no measurements of phosphate esters are available from the study site. The shift in the MEA: DEA ratio coincides with the increase in inorganic P and N concentrations in July. Although no significant correlations were found for the MEA or DEA and any of the environmental parameters, a negative correlation between the MEA:DEA ratio and phosphate concentration was observed in surface waters (**Table 1**, Pearson's $R^2 = 0.67$, $p = 0.02$) along with a positive correlation between the N:P ratio and MEA:DEA (Pearson's $R^2 = 0.67$, $p = 0.02$). These relationships between the MEA:DEA ratio, phosphate, and the N:P ratio were not found in the mesopelagic, which is reasonable considering the fairly high phosphate concentration in the mesopelagic waters. The N:P ratio also showed negative correlations with total DEA in the epipelagic waters (**Table 1**, Pearson's $R^2 = 0.58$, $p = 0.02$) and in the mesopelagic layer (Spearman's $R^2 = 0.59$, $p = 0.03$). It is not clear why the negative correlations between DEA and the N:P ratio exist. Sato et al. (2013) found no relationship between phosphate concentration and total MEA and DEA in the South Pacific, but a negative relationship in the North Pacific. These findings from the South Pacific are consistent with the observations in this study, as we also did not find any relation between total MEA or DEA and phosphate. Collectively, these results show that DEA can, at times, be as important as MEA for DOP hydrolysis, indicating a key role of phosphate availability in the relative role of MEA vs. DEA.

Interestingly, the temporal patterns in MEA and DEA described above were detected in the epi- as well as in the mesopelagic waters, indicating a strong link between these two layers in DOP cycling. The cell-specific (i.e., total enzymatic activities per bacterial cell) MEA and DEA activities increased with depth (**Figure 2C**), mainly caused by the decreasing bacterial abundance with depth (**Figure 1B**). This is consistent with increases in cell-specific MEA from the epi- to the bathypelagic waters reported for the North Atlantic and Indian Ocean (Hoppe and Ullrich, 1999; Baltar et al., 2010; Baltar et al., 2013). As there are no previous cell-specific DEA rates available from mesopelagic waters, our results are the first to confirm hydrolysis of DOP in the mesopelagic waters by DEA. In our particular study, the key observation that almost all MEA and DEA was found in the cell-free fraction implies that the activity that we measured was in fact not associated with any particular group of organisms. The high (and comparable to surface) MEA and DEA rates in the mesopelagic (where phytoplankton should not be active) further indicates that if these extracellular enzymes would be associated with some organism it is most likely that it will be to heterotrophic prokaryotes (at least in the deep waters). The intention of normalizing the MEA and DEA rates to some biological source (in this case we selected heterotrophic prokaryotes because of the reasons just mentioned above) was to see

briefly how the relation was between the MEA and DEA rates and the presence of microorganisms with depth/time. However, this should be interpreted with some skepticism due to the complications arising from the cell-free fractions.

Cell-free enzymes accounted for the vast majority of both MEA and DEA in the epi- and mesopelagic waters throughout the study period (**Figure 2D**). In the epipelagic water, cell-free MEA contributed 88 ± 1.4% to total MEA and cell-free DEA 87 ± 4.3% to total DEA. Reports of the cell-free MEA proportion on total MEA vary widely ranging from as low as 12–100% of total MEA (Hoppe, 1986; Allison et al., 2012; Baltar et al., 2016b). Cell-free DEA contributed between 71 and 100% (91 ± 2%) to total DEA and was higher than reported in the only other published study (range: 13–49%, 38 ± 15%) in epipelagic waters (Sato et al., 2013). Possibly, the high cell-free DEA fraction in the present study might be associated with the low temperature characteristic of the subantarctic waters at our study site. The increase in the contribution of cell-free enzymes has been repeatedly linked to lower temperatures in the Atlantic Ocean (Baltar et al., 2010), in the Baltic Sea (Baltar et al., 2016b) and in laboratory experiments (Baltar et al., 2017). Lower temperatures are suggested to contribute to higher cell-free enzymatic activities due to the combined positive effects of cold preservation and reduced rates of heterotrophic consumption of dissolved proteins/enzymes (Baltar et al., 2016b; Baltar 2018).

In the mesopelagic layer, the contribution from cell-free MEA (92 ± 1.6%) was higher than in the epipelagic waters $t_{(12)} = -2.322$, $p = 0.039$*, DEA was also higher (93 ± 1.4%) but was not statistically significant $t_{(12)} = -1.413$, $p = 0.163$ (**Figure 2D**). This is consistent with previous studies reporting increasing cell-free proportions of MEA with depth (Baltar et al., 2010; Baltar et al., 2013). Although there are no other mesopelagic DEA estimates to make comparisons, the high contribution of cell-free MEA and DEA in the epi- and mesopelagic waters might explain the coupling observed between these two water layers, by transport of extracellular enzymes either via winter vertical overturning and mixing, and/or by fragmentation and dissolution of sinking particles (Koike and Nagata, 1997).

In conclusion, at the study site in South Pacific Antarctic waters, DEA rates can be comparable, at times, to the more frequently measured MEA. This suggests that DEA is relevant for the hydrolysis of DOP. The negative relationship between the MEA:DEA ratio and phosphate concentrations, and the positive relationship with the inorganic N:P ratio in epipelagic waters suggest that inorganic phosphorus availability along with the N:P ratio is the key parameter in controlling the relative importance of MEA vs. DEA in marine DOP hydrolysis. N:P ratios also showed negative relationships with DEA alone, both in the epi- and mesopelagic layer, suggesting DEA is sensitive to changes in the inorganic N:P ratio. Most of the DEA and MEA was found in the cell-free fraction and the contribution of the cell-free fractions to the total MEA and DEA was higher in the mesopelagic than in the epipelagic layer. These findings enhance our understanding of the marine ecological and biogeochemical mechanisms underpinning the cycling of phosphorus.

DATA AVAILABILITY STATEMENT

All datasets presented in this study are included in the article.

AUTHOR CONTRIBUTIONS

All authors contributed to the preparation of this manuscript

FUNDING

This research was supported by a University of Otago research grant and a Rutherford Discovery Fellowship (Royal Society of New Zealand) to FB.

ACKNOWLEDGMENTS

We thank the skipper of the RV Polaris II Bill Dickson and his crew for their help during the sampling events and the technical support by Dr. Doug Mackie, Linda Groenewegen, and Adam Brook at the Portobello Marine Laboratory.

REFERENCES

Accoroni, S., Tartaglione, L., Dello Iacovo, E., Pichierri, S., Marini, M., Campanelli, A., et al. (2017). Influence of environmental factors on the toxin production of Ostreopsis cf. ovata during bloom events. *Mar. Pollut. Bull.* 123, 261–268. doi:10.1016/j.marpolbul.2017.08.049

Allison, S., Chao, Y., Farrara, J., Hatosy, S., and Martiny, A. (2012). Fine-scale temporal variation in marine extracellular enzymes of coastal southern California. *Front. Microbiol.* 3, 301. doi:10.3389/fmicb.2012.00301

Amon, R. M. W., and Benner, R. (1996). Bacterial utilization of different size classes of dissolved organic matter. *Limnol. Oceanogr.* 41, 41–51. doi:10.4319/lo.1996.41.1.0041

Arnosti, C. (2011). Microbial extracellular enzymes and the marine carbon cycle. *Annu. Rev. Mar. Sci.* 3, 401–425. doi:10.1146/annurev-marine-120709-142731

Arnosti, C., Bell, C., Moorhead, D. L., Sinsabaugh, R. L., Steen, A. D., Stromberger, M., et al. (2014). Extracellular enzymes in terrestrial, freshwater, and marine environments: perspectives on system variability and common research needs. *Biogeochemistry* 117, 5–21. doi:10.1007/s10533-013-9906-5

Azam, F., Fenchel, T., Field, J., Gray, J., Meyer-Reil, L., and Thingstad, F. (1983). The ecological role of water-column microbes in the sea. *Mar. Ecol. Prog. Ser.* 10, 257–263. doi:10.3354/meps010257

Baltar, F. (2018). Watch out for the "living dead": cell-free enzymes and their fate. *Front. Microbiol.* 8, 2438. doi:10.3389/fmicb.2017.02438

Baltar, F., Arístegui, J., Gasol, J., Sintes, E., Van Aken, H., and Herndl, G. (2010). High dissolved extracellular enzymatic activity in the deep Central Atlantic Ocean. *Aquat. Microb. Ecol.* 58, 287–302. doi:10.3354/ame01377

Baltar, F., Arístegui, J., Gasol, J. M., Yokokawa, T., and Herndl, G. J. (2013). Bacterial versus archaeal origin of extracellular enzymatic activity in the northeast atlantic deep waters. *Microb. Ecol.* 65, 277–288. doi:10.1007/s00248-012-0126-7

Baltar, F., Arístegui, J., Sintes, E., Van Aken, H. M., Gasol, J. M., and Herndl, G. J. (2009). Prokaryotic extracellular enzymatic activity in relation to biomass production and respiration in the meso- and bathypelagic waters of the (sub)tropical Atlantic. *Environ. Microbiol.* 11, 1998–2014. doi:10.1111/j.1462-2920.2009.01922.x

Baltar, F., Currie, K., Stuck, E., Roosa, S., and Morales, S. E (2016a). Oceanic fronts: transition zones for bacterioplankton community composition. *Environ. Microbiol. Rep.* 8, 132–138. doi:10.1111/1758-2229.12362

Baltar, F., Legrand, C., and Pinhassi, J. (2016b). Cell-free extracellular enzymatic activity is linked to seasonal temperature changes: a case study in the Baltic Sea. *Biogeosciences* 13, 2815–2821. doi:10.5194/bg-13-2815-2016

Baltar, F., De Corte, D., Thomson, B., and Yokokawa, T. (2019). Teasing apart the differentsize pools of extracellular enzymatic activity in the ocean. *Sci. Total Environ.* 660, 690–696. doi:10.1016/j.scitotenv.2019.01.083

Baltar, F., Morán, X. A. G., and Lønborg, C. (2017). Warming and organic matter sources impact the proportion of dissolved to total activities in marine extracellular enzymatic rates. *Biogeochemistry* 133, 307–316. doi:10.1007/s10533-017-0334-9

Baltar, F., Stuck, E., Morales, S., and Currie, K. (2015). Bacterioplankton carbon cycling along the subtropical frontal zone off New Zealand. *Prog. Oceanogr.* 135, 168–175. doi:10.1016/j.pocean.2015.05.019

Benner, R., and Amon, R. M. W. (2015). The size-reactivity continuum of major bioelements in the ocean. *Annu. Rev. Mar. Sci.* 7, 185–205. doi:10.1146/annurev-marine-010213-135126

Björkman, K. M., and Karl, D. M. (2003). Bioavailability of dissolved organic phosphorus in the euphotic zone at Station ALOHA, North Pacific Subtropical Gyre. *Limnol. Oceanogr.* 48, 1049–1057. doi:10.4319/lo.2003.48.3.1049

Celussi, M., Zoccarato, L., Bernardi Aubry, F., Bastianini, M., Casotti, R., Balestra, C., et al. (2019). Links between microbial processing of organic matter and the thermohaline and productivity features of a temperate river-influenced Mediterranean coastal area. *Estuar. Coast Shelf Sci.* 228, 106378. doi:10.1016/j.ecss.2019.106378

Celussi, M., and Del Negro, P. (2012). Microbial degradation at a shallow coastal site: long-term spectra and rates of exoenzymatic activities in the NE Adriatic Sea. *Estuar. Coast Shelf Sci.* 115, 75–86. doi:10.1016/j.ecss.2012.02.002

Currie, K. I., and Hunter, K. A. (1999). Seasonal variation of surface water CO_2 partial pressure in the Southland Current, east of New Zealand. *Mar. Freshwater Res.* 50, 375–382. doi:10.1071/mf98115

Currie, K. I., Reid, M. R., and Hunter, K. A. (2011). Interannual variability of carbon dioxide drawdown by subantarctic surface water near New Zealand. *Biogeochemistry* 104, 23–34. doi:10.1007/s10533-009-9355-3

Duhamel, S., Björkman, K. M., Van Wambeke, F., Moutin, T., and Karl, D. M. (2011). Characterization of alkaline phosphatase activity in the North and South Pacific Subtropical Gyres: implications for phosphorus cycling. *Limnol. Oceanogr.* 56, 1244–1254. doi:10.4319/lo.2011.56.4.1244

Duhamel, S., Dyhrman, S. T., and Karl, D. M. (2010). Alkaline phosphatase activity and regulation in the North Pacific Subtropical Gyre. *Limnol. Oceanogr.* 55, 1414–1425. doi:10.4319/lo.2010.55.3.1414

Falkowski, P., Fenchel, T., and Delong, E. (2008). The microbial engines that drive earth's biogeochemical cycles. *Science* 320, 1034–1039. doi:10.1126/science.1153213

Fenchel, T. (2008). The microbial loop – 25 years later. *J. Exp. Mar. Biol. Ecol.* 366, 99–103. doi:10.1016/j.jembe.2008.07.013

Gasol, J. M. (1999). *How to count picoalgae and bacteria with the FACScalibur flow cytometer*. Barcelona, Spain: Institut de Ciències del Mar, 1–51.

Gasol, J. M., and Del Giorgio, P. A. (2000). Using flow cytometry for counting natural planktonic bacteria and understanding the structure of planktonic bacterial communities. *Sci. Mar.* 64, 197–224. doi:10.3989/scimar.2000.64n2197

Hoppe, H. G. (1983). Significance of exoenzymatic activities in the ecology of brackish water: measurements by means of methylumbelliferyl-substrates. *Mar. Ecol. Prog. Ser.* 11, 299–308. doi:10.3354/meps011299

Hoppe, H.-G. (1986). "Relations between bacterial extracellular enzyme activities and heterotrophic substrate uptake in a brackish water environment," in Proceeding of 2nd International Colloquium on Marine Bacteriology, Actes de Colloque 3, Brest, France, October 1–5, 1986.

Hoppe, H.-G. (1991). "Microbial extracellular enzyme activity: a new key parameter in aquatic ecology," in *Microbial enzymes in aquatic environments*. Editor Chróst, R. J. (New York, NY: Springer), 60–83.

Hoppe, H.-G. (2003). Phosphatase activity in the sea. *Hydrobiologia* 493, 187–200. doi:10.1023/A:1025453918247.

Hoppe, H.-G., Arnosti, C., and Herndl, G. F. (2002). "Ecological significance of bacterial enzymes in the marine environment," in *Enzymes in the environment*. Editors Burns, R. G., and Dick, R. P. (New York, NY: Marcel Dekker), 73–107.

Hoppe, H., and Ullrich, S. (1999). Profiles of ectoenzymes in the Indian Ocean: phenomena of phosphatase activity in the mesopelagic zone. *Aquat. Microb. Ecol.* 19, 139–148. doi:10.3354/ame019139

Jones, K. N., Currie, K. I., McGraw, C. M., and Hunter, K. A. (2013). The effect of coastal processes on phytoplankton biomass and primary production within the near-shore Subtropical Frontal Zone. Estuarine. *Estuar Coast Shelf Sci.* 124, 44. doi:10.1016%2Fj.ecss.2013.03.003

Kamer, M., and Rassoulzadegan, F. (1995). Extracellular enzyme activity: indications for high short-term variability in a coastal marine ecosystem. *Microb. Ecol.* 30, 143–156. doi:10.1007/BF00172570

Kim, C., Nishimura, Y., and Nagata, T. (2007). High potential activity of alkaline phosphatase in the benthic nepheloid layer of a large mesotrophic lake: implications for phosphorus regeneration in oxygenated hypolimnion. *Aquat. Microb. Ecol.* 49, 303–311. doi:10.3354%2Fame01137

Koike, I., and Nagata, T. (1997). High potential activity of extracellular alkaline phosphatase in deep waters of the central Pacific. *Deep Sea Res. Part II Top. Stud. Oceanogr.* 44, 2283–2294. doi:10.1016/S0967-0645(97)00025-8

Kolowith, L. C., Ingall, E. D., and Benner, R. (2001). Composition and cycling of marine organic phosphorus. *Limnol. Oceanogr.* 46, 309–320. doi:10.4319/lo.2001.46.2.0309

Li, H., Veldhuis, M., and Post, A. (1998). Alkaline phosphatase activities among planktonic communities in the northern Red Sea. *Mar. Ecol. Prog. Ser.* 173, 107–115. doi:10.3354%2Fmeps173107

Monbet, P., McKelvie, I. D., and Worsfold, P. J. (2009). Dissolved organic phosphorus speciation in the waters of the Tamar estuary (SW England). *Geochem. Cosmochim. Acta* 73, 1027–1038. doi:10.1016/j.gca.2008.11.024.

Moore, C. M., Mills, M. M., Arrigo, K. R., Berman-Frank, I., Bopp, L., Boyd, P. W., et al. (2013). Processes and patterns of oceanic nutrient limitation. *Nat. Geosci.* 6, 701. doi:10.1038%2FNGEO1765

Nakae, T. (1976). Identification of the outer membrane protein of *E. coli* that produces transmembrane channels in reconstituted vesicle membranes. *Biochem. Biophys. Res. Commun.* 71, 877–884. doi:10.1016/0006-291x(76)90913-x

Nikaido, H., and Vaara, M. (1987). *Escherichia coli and Salmonella typhimurium: cellular and molecular biology*. Washington, DC: American Society for Microbiology, Vol. 1, 7–22.

Parsons, T., Maita, Y., and Lalli, C. (1984). A manual of chemical and biological methods for seawater analysis. Pergamon, Oxford sized algae and natural seston size fractions. *Mar. Ecol. Prog. Ser.* 199, 43–53. doi:10.1016/C2009-0-07774-5

Sato, M., Sakuraba, R., and Hashihama, F. (2013). Phosphate monoesterase and diesterase activities in the North and South Pacific Ocean. *Biogeosciences* 10, 7677. doi:10.5194%2Fbg-10-7677-2013

Steen, A. D., and Arnosti, C. (2011). Long lifetimes of β-glucosidase, leucine aminopeptidase, and phosphatase in Arctic seawater. *Mar. Chem.* 123, 127–132. doi:10.1016%2Fj.marchem.2010.10.006

Steen, A. D., Quigley, L. N., and Buchan, A. (2016). Evidence for the priming effect in a planktonic estuarine microbial community. *Front. Mar. Sci.* 3, 6. doi:10.3389%2Ffmars.2016.00006

Suzumura, M., Ishikawa, K., and Ogawa, H. (1998). Characterization of dissolved organic phosphorus in coastal seawater using ultrafiltration and phosphohydrolytic enzymes. *Limnol. Oceanogr.* 43, 1553–1564. doi:10.4319/lo.1998.43.7.1553

Tamburini, C., Garcin, J., Ragot, M., and Bianchi, A. (2002). Biopolymer hydrolysis and bacterial production under ambient hydrostatic pressure through a 2000 m water column in the NW Mediterranean. *Deep Sea Res. Part II Top. Stud. Oceanogr.* 49, 2109–2123. doi:10.1016%2FS0967-0645(02)00030-9

Thomson, B., Wenley, J., Currie, K., Hepburn, C., Herndl, G. J., and Baltar, F. (2019). Resolving the paradox: continuous cell-free alkaline phosphatase activity despite high phosphate concentrations. *Mar. Chem.* 214, 103671. doi:10.1016%2Fj.marchem.2019.103671

Van Wambeke, F., Christaki, U., Giannakourou, A., Moutin, T., and Souvemerzoglou, K. (2002). Longitudinal and vertical trends of bacterial limitation by phosphorus and carbon in the Mediterranean Sea. *Microb. Ecol.* 43, 119. doi:10.1007%2Fs00248-001-0038-4

Van Wambeke, F., Ghiglione, J. F., Nedoma, J., Mével, G., and Raimbault, P. (2009). Bottom up effects on bacterioplankton growth and composition during summer-autumn transition in the open NW Mediterranean Sea. *Biogeosciences* 6, 705–720. doi:10.5194%2Fbg-6-705-2009

Weiss, M. S., Abele, U., Weckesser, J., Welte, W., Schiltz, E., and Schulz, G. E. (1991). Molecular architecture and electrostatic properties of a bacterial Porin. *Science* 254, 1627–1630. doi:10.1126/science.1721242

Yamaguchi, H., Arisaka, H., Otsuka, N., and Tomaru, Y. (2014). Utilization of phosphate diesters by phosphodiesterase-producing marine diatoms. *J. Plankton Res.* 36, 281–285. doi:10.1093%2Fplankt%2Ffbt091

Yamaguchi, T., Sato, M., Hashihama, F., Ehama, M., Shiozaki, T., Takahashi, K., et al. (2019). Basin-scale variations in labile dissolved phosphoric monoesters and diesters in the central North Pacific ocean. *J. Geophys. Res.* 124, 3058–3072. doi:10.1029/2018JC014763

Zhao, Z., Baltar, F., and Herndl, G. J. (2020). Linking extracellular enzymes to phylogeny indicates a predominantly particle-associated lifestyle of deep-sea prokaryotes. *Sci. Adv.* 6, eaaz4354. doi:10.1126%2Fsciadv.aaz4354

Ziervogel, K., Steen, A. D., and Arnosti, C. (2010). Changes in the spectrum and rates of extracellular enzyme activities in seawater following aggregate formation. *Biogeosciences* 7, 1007–1015. doi:10.5194%2Fbg-7-1007-2010

Conflict of Interest: The authors declare that the research was conducted in the absence of any commercial or financial relationships that could be construed as a potential conflict of interest.

frontiers in Earth Science

ORIGINAL RESEARCH
published: 28 October 2020
doi: 10.3389/feart.2020.567714

Barite Precipitation on Suspended Organic Matter in the Mesopelagic Zone

F. Martinez-Ruiz[1], A. Paytan[2], M. T. Gonzalez-Muñoz[3], F. Jroundi[3], M. M. Abad[4], P. J. Lam[2], T. J. Horner[5] and M. Kastner[6]*

[1]Instituto Andaluz de Ciencias de la Tierra (CSIC-UGR), Avda. de las Palmeras, Granada, Spain, [2]Institute of Marine Sciences, University of California Santa Cruz, Santa Cruz, CA, United States, [3]Department of Microbiology, Faculty of Science, University of Granada, Campus Fuentenueva, Granada, Spain, [4]Centro de Instrumentación Científica (CIC), University of Granada, Campus Fuentenueva, Granada, Spain, [5]Department of Marine Chemistry and Geochemistry, Woods Hole Oceanographic Institution, Woods Hole, MA, United States, [6]Scripps Institution of Oceanography, University of California, San Diego, La Jolla, CA, United States

Mechanisms underlying barite precipitation in seawater and the precise depths of barite precipitation in the water column have been debated for decades. Here we present a detailed study of water column barite distribution in the mesopelagic zone at diverse stations in the open ocean by analyzing samples collected using multiple unit large volume *in-situ* filtration systems in the Pacific, Atlantic and Indian oceans. Our results demonstrate that barite is an organo-mineral particularly abundant at intermediate depths throughout the world's ocean regardless of saturation state with respect to barite. This is confirming the notion of precipitation at depths of intense organic matter mineralization. Our observations further support the link between barite formation and microbial activity, demonstrated by the association of barite particles with organic matter aggregates and with extracellular polymeric substances. Evidence for microbial mediation is consistent with previous experimental work showing that in bacterial biofilms Ba binds to phosphate groups on cell surfaces and within extracellular polymeric substances. This organo-accumulation promotes high concentrations of Ba leading to saturated microenvironments and nucleation sites favoring precipitation. The distribution of Ba isotopes in the water column and in particulate matter is also consistent with the proposed precipitation mechanism.

Keywords: pelagic barite, organo-mineralization, barite saturation state, extracellular polymeric substances, bioaccumulation

OPEN ACCESS

Edited by:
Rut Pedrosa Pàmies, Marine Biological Laboratory (MBL), United States

Reviewed by:
Frank Dehairs, Vrije University Brussel, Belgium
Christophe Monnin, Géosciences Environnement Toulouse (GET), France

****Correspondence:***
F. Martinez-Ruiz
fmruiz@ugr.es

Specialty section:
This article was submitted to Biogeoscience, a section of the journal Frontiers in Earth Science

Received: *30 May 2020*
Accepted: *05 October 2020*
Published: *28 October 2020*

Citation:
Martinez-Ruiz F, Paytan A, Gonzalez-Muñoz MT, Jroundi F, Abad MM, Lam PJ, Horner TJ and Kastner M (2020) Barite Precipitation on Suspended Organic Matter in the Mesopelagic Zone. Front. Earth Sci. 8:567714. doi: 10.3389/feart.2020.567714

INTRODUCTION

Barium and barite are routinely used for reconstructing past export production in the ocean yet the processes linking barite formation to export production are still elusive. Since the early work of Chow and Goldberg (1960) who reported high Ba concentrations in marine sediments underlying regions of high biological productivity, a link between organic matter fluxes and Ba abundance has been broadly demonstrated (e.g., Dehairs et al., 1980; Dymond et al., 1992; Francois et al., 1995; Paytan et al., 1996; Paytan and Griffith 2007; Griffith and Paytan, 2012; Carter et al., 2020 and references therein). Studies using sediment traps have provided further evidence on the association of particulate Ba and particulate organic carbon (POC). It has been proposed that barite

precipitates in close association with aggregates of organic matter and sinking biological debris (e.g., Bishop, 1988; Dehairs et al., 1991). Different algorithms have been suggested to correlate export production and excess Ba (total Ba concentration corrected for the lithogenic phase) or barite accumulation (e.g., Dymond et al., 1992; Francois et al., 1995; Paytan et al., 1996; Eagle et al., 2003), allowing the reconstruction of past ocean productivity (e.g., Dymond et al., 1992; Gingele and Dahmke, 1994; Nürnberg et al., 1997; Eagle et al., 2003; Ma et al., 2015). Nevertheless, quantification of export production from Ba proxies is still hindered by poor understanding of the mechanisms and processes leading to barite (the main phase carrying excess Ba) formation in the oceanic water column. Moreover, barite distribution in the oceanic water column is variable in space, time, and depth and such variability is not yet fully understood (e.g., Hernandez-Sanchez et al., 2011; Bates et al., 2017).

Over decades of research, several hypotheses have been proposed to explain barite precipitation in the oceanic water column given that most of the world's ocean mesopelagic zone (200–1,000 m depth, Sutton et al., 2017) is undersaturated with respect to barite (Monnin et al., 1999; Rushdi et al., 2000). Hypotheses included precipitation in microenvironments formed within sinking biogenic particulate matter (e.g., Dehairs et al., 1980; Bishop, 1988), precipitation as a result of celestine ($SrSO_4$) dissolution from Acantharian tests (e.g., Bernstein et al., 1992; Bernstein et al., 1998) and by way of microbially mediated precipitation processes (Gonzalez-Muñoz et al., 2003; Gonzalez-Muñoz et al., 2012; Torres-Crespo et al., 2015). Specifically, Gonzalez-Muñoz et al. (2003) demonstrated in laboratory culture experiments the ability of soil bacteria to induce precipitation of barite, and later also highlighted the potential role of bacteria in barite precipitation in the ocean by using diverse marine strains in culture experiments (Gonzalez-Muñoz et al., 2012; Torres-Crespo et al., 2015). Bacterially mediated precipitation of barite is consistent with studies demonstrating the positive correlation between mesopelagic particulate Ba abundance and enhanced bacterial production in the North Pacific and the Southern Ocean as well as the relation between particulate Ba abundance and microbial oxygen consumption (Dehairs et al., 2008; Jacquet et al., 2011; Planchon et al., 2013). Moreover, mesocosm experiments inducing the decay of various phytoplankton species in the dark demonstrated that Ba is released during the decomposition of the phytoplankton, leading to barite precipitation (Ganeshram et al., 2003). Overall, several lines of evidence have supported the suggestion that the nutrient-like behavior of Ba is due to biological processes mediating barite precipitation. In particular, analyses of Ba isotopes of both water column and particulate matter at various sites in the ocean (e.g., Horner et al., 2015; Bates et al., 2017; Bridgestock et al., 2018) are also consistent with the formation of barite which preferentially incorporates the light Ba isotope at mesopelagic depths.

Additional experimental work (Martinez-Ruiz et al., 2018) demonstrated that bacterial biofilms, specifically, extracellular polymeric substances (EPS) may play a major role in barite precipitation by providing nucleation sites to locally enhance Ba concentration leading to barite precipitation. This work also showed that an amorphous P-rich phase is formed at the initial stages of Ba bioaccumulation eventually being replaced by sulfate and leading to the formation of barite crystals. The capacity of EPS to bind metal ions to negatively charged functional groups has been broadly demonstrated (e.g., Braissant et al., 2007; Tourney and Ngwenya, 2014) and the role of phospholipids acting as nucleation sites to incorporate diverse cations has been demonstrated for diverse metals such as U (e.g., Morcillo et al., 2014). Moreover, P-rich precursors have been described in the precipitation of several minerals such as aragonite apatite and iron oxides, both under experimental conditions (Rivadeneyra et al., 2010), and in the geological record (e.g., Sanchez-Navas and Martin-Algarra, 2001; Miot et al., 2009). In general, microbial precipitation through an amorphous precursor is a widespread process in natural environments (e.g., Weiner et al., 2005; Enyedi et al., 2020). Such crystallization path through an amorphous precursor phase is also associated with the inorganic precipitation of barite. For example, a metastable amorphous Ba sulfate phase that precedes barite formation has been recognized during the early stages of barium sulfate crystallization from aqueous solutions (Ruiz-Agudo et al., 2020), however, the binding of Ba to EPS in the open ocean has not been thoroughly investigated.

Mineralogical and crystallographic analyses of marine barite collected using multiple unit large volume *in-situ* filtration systems (MUL-VFS) at two stations in the North Atlantic and the Atlantic sector of the Southern Ocean demonstrated that barite formation in the open ocean also involves an amorphous precursor (Martinez-Ruiz et al., 2019). This initial amorphous precursor is a phosphorus-rich phase that evolves into barite when phosphate groups are substituted by sulfate. These crystallization pathways are similar to those reported to form within biofilms in laboratory based experiments (Martinez-Ruiz et al., 2018). These findings support the role of EPS in the precipitation of barite in the oceanic water column and the correlation between bacterial production and the abundance of Ba-rich particles. As our previous study (Martinez-Ruiz et al., 2019) focused only on two stations, from the North Atlantic and the Atlantic Sector of the Southern Ocean, the present work aims at providing new insights into the mechanisms of barite formation in the ocean water column by analyzing barite, also collected by MUL-VFS, at new stations representing additional ocean sectors with diverse barite saturation conditions. Stations within each sector were selected in high productivity settings. Barite crystallography, mineralogy and abundance in the water column have been investigated at different depths within the mesopelagic zone at the locations and sites described below.

SAMPLES AND METHODS

Oceanographic Setting

Locations for this study have been selected to represent four different ocean sectors (**Figure 1**; **Table 1**) where productivity is relatively high and hence barite is abundant in the upper water column however these sites represent different saturation states within the mesopelagic zone.

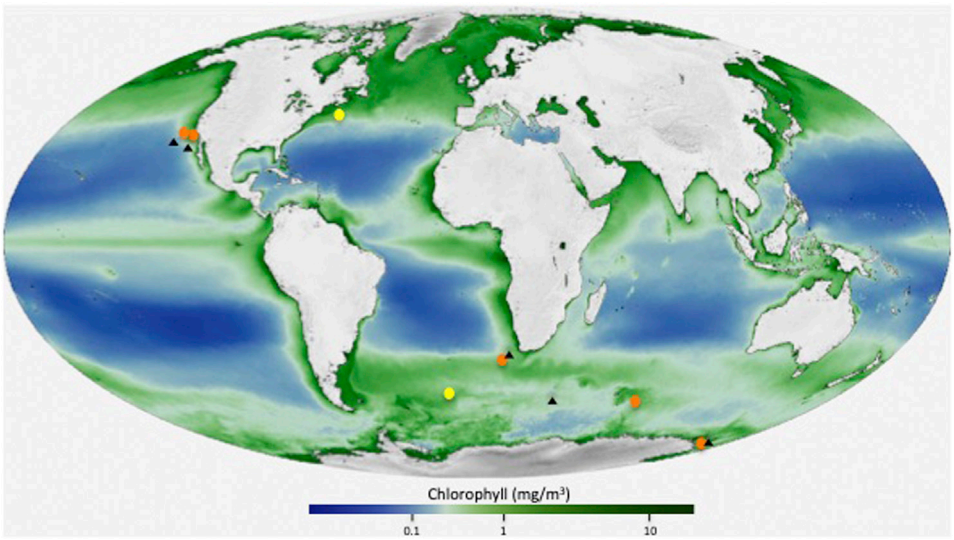

FIGURE 1 | Location map showing the analyzed stations (orange color), and two previously analyzed sites (yellow color) in the North Atlantic and in the Atlantic sector of the Southern Ocean (Martinez-Ruiz et al., 2019). Black triangles indicate the location of the stations with available Ba concentration depth profiles used for Ω_{barite} calculations. Base map modified from NASA/Goddard Space Flight Center, The SeaWiFS Project and GeoEye maps, https://svs.gsfc.nasa.gov/30801).

North Pacific: OC1608A, C-SNOW cruise, California current system, coastal North Pacific Station 1 (1,929 m water depth), and OC1608A, C-SNOW cruise, California current system, Santa Barbara basin, Station 2 (4,880 m water depth). These stations are at the edge of the North Pacific oligotrophic gyre. The North Pacific Subtropical Gyre harbors one of the largest biomas on Earth, it is a relatively stable oligotrophic environment, with low surface concentrations of nitrogen and phosphorus. Nutrients derived from advective transport from depth into the surface ocean stimulates primary production in this region (Karl and Church, 2017; Robidart et al., 2019). The two stations in the Santa Barbara basin are on the edge of this gyre and are characterized by relatively high productivity and high phytoplankton biomass that supports a productive pelagic ecosystem (Letelier, et al., 2019). The productivity is fueled by intensive coastal upwelling induced by northerly winds along the California margin (e.g., Brzezinski and Washburn, 2011; Abella-Gutiérrez and Herguera, 2016).

Atlantic: MV1101, Great Calcite Belt (GCB) 1, South Atlantic, Station 117 (Rosengard et al., 2015; Balch et al., 2016). During the GCB1 cruise the R/V Melville crossed the Atlantic sector from Punta Arenas, Chile, to Cape Town, South Africa, sampling between 39° S and 59° S. Station 92 from this cruise has been previously analyzed for marine barite (Martinez-Ruiz et al., 2018) and station 117 has been selected for this study (5,048 m water depth). Station GCB1-117 is located in the subtropical region of the South Atlantic Ocean and is dominated by seasonal coccolithophores and diatoms blooms (Smith et al., 2017).

Indian ocean: RR1202, Great Calcite Belt (GCB) 2, South Indian Ocean, Station 63 (Rosengard et al., 2015; Balch et al., 2016; Smith et al., 2017). During the GCB2 cruise, the R/V Revelle crossed the Indian sector from Durban, South Africa, to Perth, Australia, sampling between 37° S and 60° S. Station 63 has been selected for this study (1,310 m water depth). The region is characterized by elevated surface reflectance that is thought to result from high seasonal concentrations of coccolithophores. Data for multiple parameters sampled during the GCB cruises including chlorophyll, particulate inorganic carbon (PIC), POC, biogenic silica (BSi), coccolithophore concentration, calcification, photosynthesis, dissolved inorganic carbon (DIC), total alkalinity, iron limitation of phytoplankton and ^{234}Th-based vertical flux rates are available for these stations (Rosengard et al., 2015; Balch et al., 2016). Shipboard scientists reported dense coccolithophore populations that exported small, highly degraded, and compact particles out of the euphotic zone. Coccolithophore blooms are considered very efficient in transferring POC to the base of the mesopelagic zone, although the magnitude of exported POC is not as high as in diatom-rich regions (e.g., Henson et al., 2012).

South Pacific: NBP1101, Seafarers cruise, Ross Sea, Station 14. This station is located off the Ross Sea Shelf in the Pacific (1,887 m). Samples were collected between January 17, and February 13, 2011 aboard the R/V Nathaniel B (Hatta et al., 2017). The Ross Sea continental shelf is one of the most productive areas in the Southern Ocean (e.g., Smith, Jr. et al., 2014). Here a significant supply of dissolved Fe to surface waters is required to sustain high productivity (Sedwick et al., 2011; Hatta et al., 2017), and include dust, sea-ice, icebergs and upwelling of deeper waters as some of the main inputs (e.g., Measures et al., 2012; Marsay et al., 2014).

Particulate Ba Sampling, Particulate Organic Carbon Analyses, and Barite Saturation State (Ω_{barite})

Size-fractionated particulate material has been collected using multiple MUL-VFS (Bishop et al., 1985) and battery-operated McLane *in-situ* pumps (LV-WTS) (Rosengard et al., 2015). Analyzed samples and corresponding depths are indicated in **Table 1**. Particulate Ba concentrations (pBa) have been

TABLE 1 | Analyzed samples for this study.

Ocean (bottom depth)	Coordinates		Sample	Depth (m)	p[Ba] (pM)	POC (μM)
	Latitude	Longitude				
East Pacific (C-SNOW cruise)						
St 1—Santa Barbara basin (1,929 m)	33.75150	−119.4969	CS 1	30		
			CS 2	107		
			CS 3	160		
			CS 4	267		
			CS 5	535		
(1,927 m)	33.7500	−119.5001	CS 7	50		
			CS 8	70		
			CS 9	99		
			CS 10	149		
			CS 11	248		
St 2—edge of North Pacific oligotrophic gyre (4,880 m)	34.4167	−127.1667	CS 13	55		
			CS 14	101		
			CS 15	151		
			CS 16	251		
			CS 17	503		
(4,880 m)	34.4168	−127.1666	CS 19	25		
			CS 20	151		
			CS 21	251		
			CS 22	402		
			CS 23	603		
South Atlantic (Great calcite belt 1, MV1101) (5,048 m)	−38.9651	9.4866	GCM120	25	—	—
			GCM121	62	75	3.12
			GCM122	112	247	0.66
			GCM123	162	266	0.46
			GCM124	300	362	0.47
			GCM125	500	276	0.21
			GCM126	750	—	—
			GCM127	1,000	276	0.11
South Indian Ocean (great calcite belt 2, RR1202) (1,310 m)	−54.3995	74.5562	GCM 199	20		
			GCM 198	90		
			GCM 197	125		
			GCM 196	160		
			GCM 195	200		
			GCM 194	300		
			GCM 193	500		
			GCM 192	800		
South Pacific Ocean (Antarctic sector, SEAFARERS) (1,887 m)	−72.5835	178.5005	NBP 1016	50	26	3.66
			NBP 1017	100	99	0.61
			NBP 1018	150	197	0.29
			NBP 1019	250	279	0.18
			NBP 1020	400	256	0.13
			NBP 1021	600	291	0.10

determined at the South Atlantic (Great Calcite Belt) and South Pacific Ocean (Antarctic sector) stations, but these data are not available at other stations. *In situ* deployed filters were processed using the protocol described in Bishop and Wood (2008). Samples for pBa were collected on PES filters to ensure low blank and Ba concentrations in the particulate leachate was analyzed using an iCAP RQ inductively-coupled plasma mass spectrometer. Quantification was achieved via comparison of blank- and indium-normalized ion beam intensities in samples against those measured in a serially diluted multi-element standard that was prepared in house. Precision is generally better than ±3% relative standard deviation. POC samples were collected on pre-combusted QMA filters and concentrations were measured using a CHN elemental analyzer immediately on the ship during the cruises as described in Rosengard et al. (2015). Sampling details and complication associated with particles collected by MUL-VFS as well as retention efficiency are discussed in detail in Bishop et al. (2012). In the South Indian ocean station, both large (>51 μm) and small (1–51 μm) size particulates were analyzed. For the rest of stations, only filters retaining the 1–51 μm fraction were analyzed. The MUL-VFS sampling was found to be highly suitable for barite particles retention and QMA filters were ideal for barite microscopic detection and observation.

To place the p[Ba] data in context, we calculated the barite saturation state of seawater with respect to barite (Ω_{barite}) at the depths of sample collection Ω_{barite} is the ratio between the barium and sulfate ion activity product and the barite solubility product. Values of Ω <1, =1, and >1 indicate under-, perfect-, and super-saturation, respectively. For consistency with the literature, we consider water samples with Ω between 0.9 and 1.1 as being in saturation equilibrium (e.g., Monnin et al., 1999). Since co-located

TABLE 2 | Dissolved Ba, temperature, and calculated profiles of dissolved Ω_{barite} across depth in nearby stations to those analyzed in this work (co-located dissolved samples were generally not available for our study).

East Pacific (close to C-SNOW St. 1)

Cruise	GEOSECS Test
Station	Test
Location	28.483°N, 121.633°W
Collected	September 1969
Citation	Wolgemuth and Broecker, 1970
	doi:10.1029/JC075i036p07686

Depth (m)	[Ba] (nM)	Temperature (°C)	Ω_{barite}
1	50	18.07	0.29
30	43	17.85	0.25
150	50	11.66	0.39
255	57	8.71	0.50
400	67	6.9	0.65
700	85	5.07	0.89
1,000	93	4.01	1.02

Northeast Pacific (close to C-SNOW St. 2)

Cruise	KN195-08
Station	SAFe
Location	30°N, 140°W
Collected	May 2009
Citation	Geyman et al., 2019
	doi:10.1016/j.epsl.2019.115751

Depth (m)	[Ba] (nM)	Temperature (°C)	Ω_{barite}
25	35.0	19.01	0.20
75	37.8	18.20	0.22
110	35.0	18.18	0.20
150	35.3	16.76	0.22
200	37.1	12.81	0.27
250	37.5	11.23	0.30
300	39.4	9.92	0.33
350	43.5	8.85	0.38
400	48.9	7.95	0.45
500	59.4	6.32	0.59
600	68.3	5.19	0.71
700	77.9	4.64	0.83
850	89.4	4.08	0.98
1,000	98.1	3.72	1.10

South Atlantic (close to MV1101 St. 117)

Cruise	D357 (GA10E)
Station	3
Location	36°27.6′S, 13°23.4′E
Collected	October 2010
Citation	Bates et al., 2017
	doi:10.1016/j.gca.2017.01.043

Depth (m)	[Ba] (nM)	Temperature (°C)	Ω_{barite}
5	43.0	12.08	0.32
23	42.4	12.07	0.32
47	42.6	12.06	0.32
97	44.5	11.19	0.36
196	43.3	10.8	0.34
395	48.0	8.17	0.44
594	56.1	5.22	0.59
989	70.6	3.64	0.79

(Continued in next column)

TABLE 2 | (*Continued*) Dissolved Ba, temperature, and calculated profiles of dissolved Ω_{barite} across depth in nearby stations to those analyzed in this work (co-located dissolved samples were generally not available for our study).

South Indian Ocean (close to RR1202 St. 63)

Cruise	INDIGO 1
Station	18
Location	45°09′S, 72°20′E
Collected	March 1985
Citation	Jeandel et al., 1996
	doi:10.1016/0967-0637(95)00098-4

Depth (m)	d[Ba]	Temperature (°C)	Ω_{barite}
99	52.7	8.84	0.47
124	53.3	7.78	0.49
152	54.1	7.24	0.51
197	55.9	6.32	0.55
295	54.9	6.12	0.55
397	58.5	5.00	0.62
792	65.8	3.07	0.76
1,039	68.6	2.58	0.81

South Indian Ocean (close to RR1202 St. 63)

Cruise	INDIGO 3
Station	90
Location	55°01′S, 31°13′E
Collected	June 1987
Citation	Jeandel et al., 1996
	doi:10.1016/0967-0637(95)00098-4

Depth (m)	d[Ba]	Temperature (°C)	Ω_{barite}
52	76.6	2.06	0.93
76	76.1	1.44	0.96
100	77.7	1.22	0.98
151	77.6	0.95	0.98
198	77.6	1.10	0.98
303	80.8	1.91	0.98
400	82.2	1.70	1.00
496	81.6	1.93	1.00
745	88.1	1.82	1.12
891	87.2	1.79	1.07
1,289	91.0	1.45	1.15

Southern Ocean (close to NBP1101 St. 14)

Cruise	GEOSECS
Station	287
Location	−69.3°S, 186.5°E
Collected	February 1974
Citation	Ku et al., 1976
	doi:10.1016/0012-821X(76)90064-9

Depth (m)	d[Ba]	Temperature (°C)	Ω_{barite}
2	77.8	−1.07	1.10
21	77	−1.49	1.02
41	78.2	−1.40	1.12
81	78.1	−1.65	1.12
151	79.8	−0.31	1.07
201	83.1	0.87	1.07
272	84.7	1.43	1.05
352	85.7	1.43	1.07
449	92.6	1.37	1.15
598	89.8	1.27	1.12
797	92	1.12	1.18
996	94.5	0.97	1.20

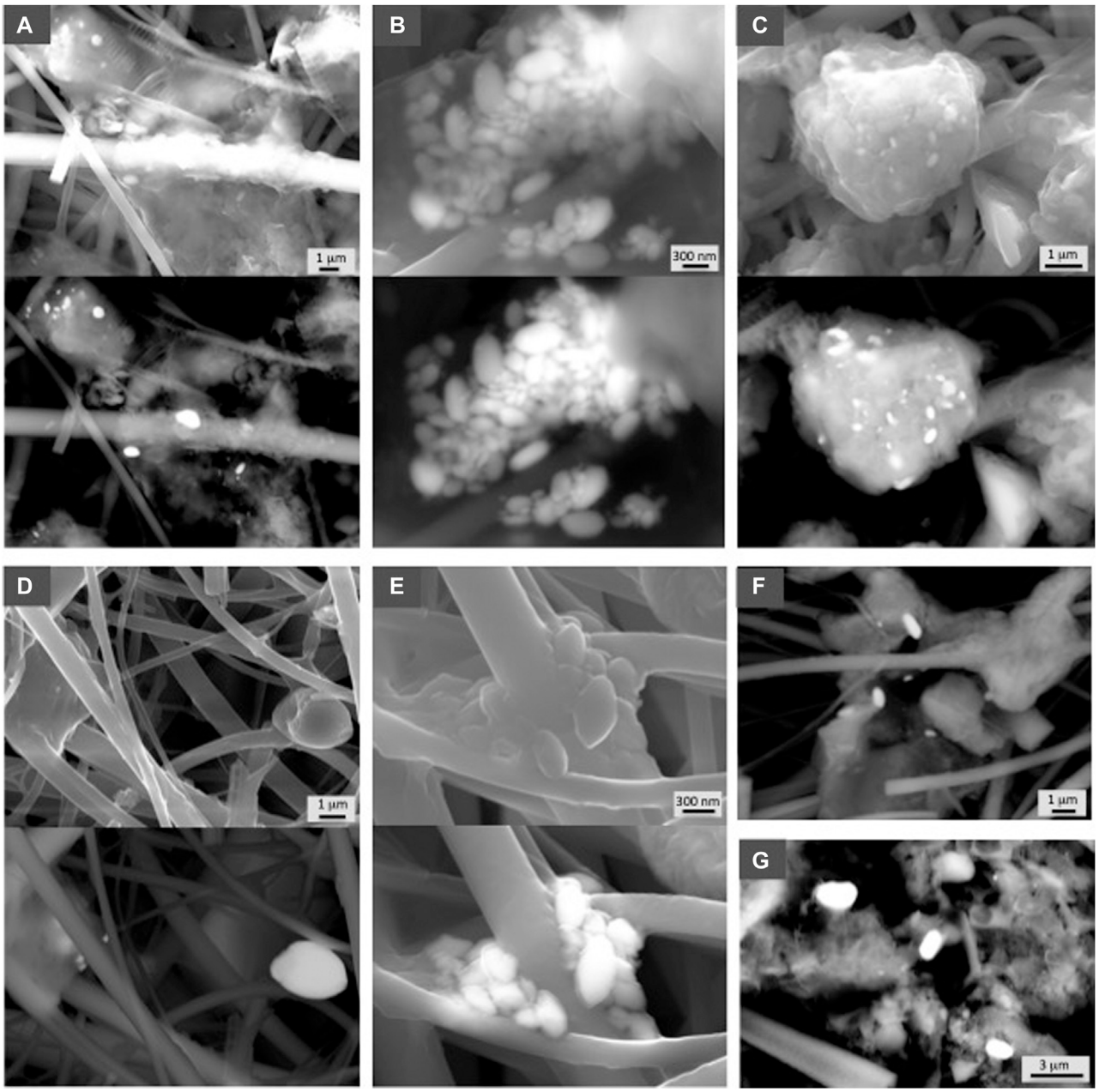

FIGURE 2 | SEM photographs showing representative examples of barite from the Pacific sector. Samples are indicated in **Table 1**. Both secondary electron and in backscattered electron (BSE) mode at 30 kV are shown in each sample. **(A)** CS4 (267 m), **(B)** CS9 (99 m), **(C)** CS10 (149 m), **(D)** CS20 (151 m), **(E)** CS 17 (503 m). **(F)** (CS 23) and **(G)** (CS 5) correspond to the deepest filter samples obtained at this ocean sector, 603 and 535 m, respectively.

samples for analysis of dissolved Ba and sulfate were generally not available for our study, we estimated Ω_{barite} from nearby stations with reliable published Ba concentration depth profiles (see **Table 2** for details and **Figure 1** for locations). Calculations were performed using PHREEQC version 3 (Parkhurst and Appelo, 2013). Values of Ω_{barite} were computed for each sample based on input parameters of *in situ* temperature, d [Ba], pressure (estimated from depth). Both pH and salinity were prescribed in all calculations at 8.1 and 35, respectively. The major ion composition of seawater in the calculations was based on that reported by Kester et al. (1967). We believe that using a fixed salinity in our calculations is a reasonable assumption given the relatively minor effect this property has on Ω_{barite} over the range of salinities encountered in open ocean seawater.

Electron Microscopy Observations

Quartz fiber filters (Whatman QMA) have been used for scanning electron microscopy (SEM) observation and analyses. Representative filter pieces were coated with

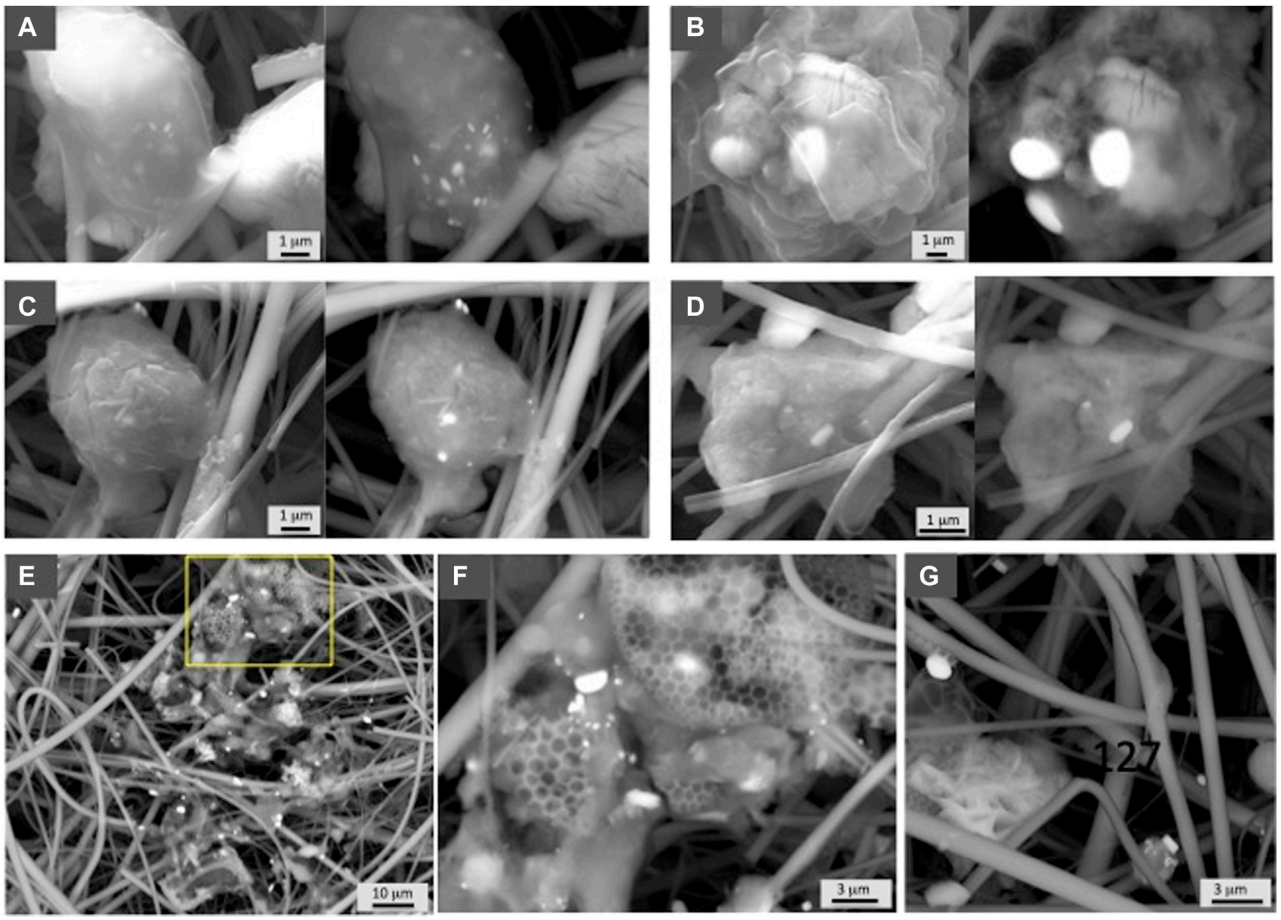

FIGURE 3 | SEM photographs showing representative examples of barite from the Atlantic sector analyzed in this study. Samples are indicated in **Table 1**. Both secondary electron and in backscattered electron (BSE) mode at 30 kV are shown in each sample. **(A)** GCM 122 (112 m), **(B)** GCM 123 (162 m), **(C)** GCM 124 (300 m), and **(D)** GCM 126 (750 m). **(E)** GCM 125 (500 m) shows the barite abundance at 500 m depth, and **(F)** GCM 127 (1,000 m) shows a detailed image of the square indicated in photograph e, in which different sizes of barite grains are shown in organic aggregates. **(G)** GCM 127 corresponds to the deepest filter sample obtained at this ocean sector, 1,000 m, in which barite is not abundant but still present.

carbon for observation under the SEM using an AURIGA FIB-FESEM Carl Zeiss SMT microscope equipped with an energy dispersive X-ray (EDX) detector system (Centre for Scientific Instrumentation, University of Granada). Filter pieces were grounded in an agate mortar and then dispersed in ethanol by sonication for approximately 3 min. Particulate matter released from the filter was deposited on carbon-film-coated copper grids for high-resolution transmission electron microscopy (HRTEM) observation by using a FEI TITAN G2 60–300 microscope with a high brightness electron gun (X-FEG) operated at 300 kV and equipped with a Cs image corrector CEOS (Centre for Scientific Instrumentation, University of Granada). For analytical electron microscopy (AEM), a SUPER-X silicon-drift windowless EDX detector was used. EDX maps and selected area electron diffraction (SAED) patterns were also collected on barite particles for crystallographic characterization and for determining major constituents composition.

RESULTS

Barite particles were observed in all the analyzed samples from all the locations and water depths (**Figures 2–6**). **Figure 2** shows representative examples of barite particles from the Coastal East Pacific water column. Barite shows typical rounded to oval morphologies ranging in size from nanometers to a few microns, and it is always associated with organic material, which in many cases has EPS-like morphology (**Figures 2A,C,E**). Aggregates of barite grains are commonly observed with grains of different sizes ranging from less than 100 nm to a few hundred nm (**Figure 2B**). Barite is also observed as individual barite grains of micron size (**Figure 2D**) present at all depth analyzed. **Figures 2F,G** show examples of the deepest samples analyzed at 603 and 535 m water depth at these stations.

Figure 3 shows examples from the South Atlantic sector demonstrating barite associated with organic aggregates, which in some cases show EPS-like morphologies (**Figure 2D**). SEM

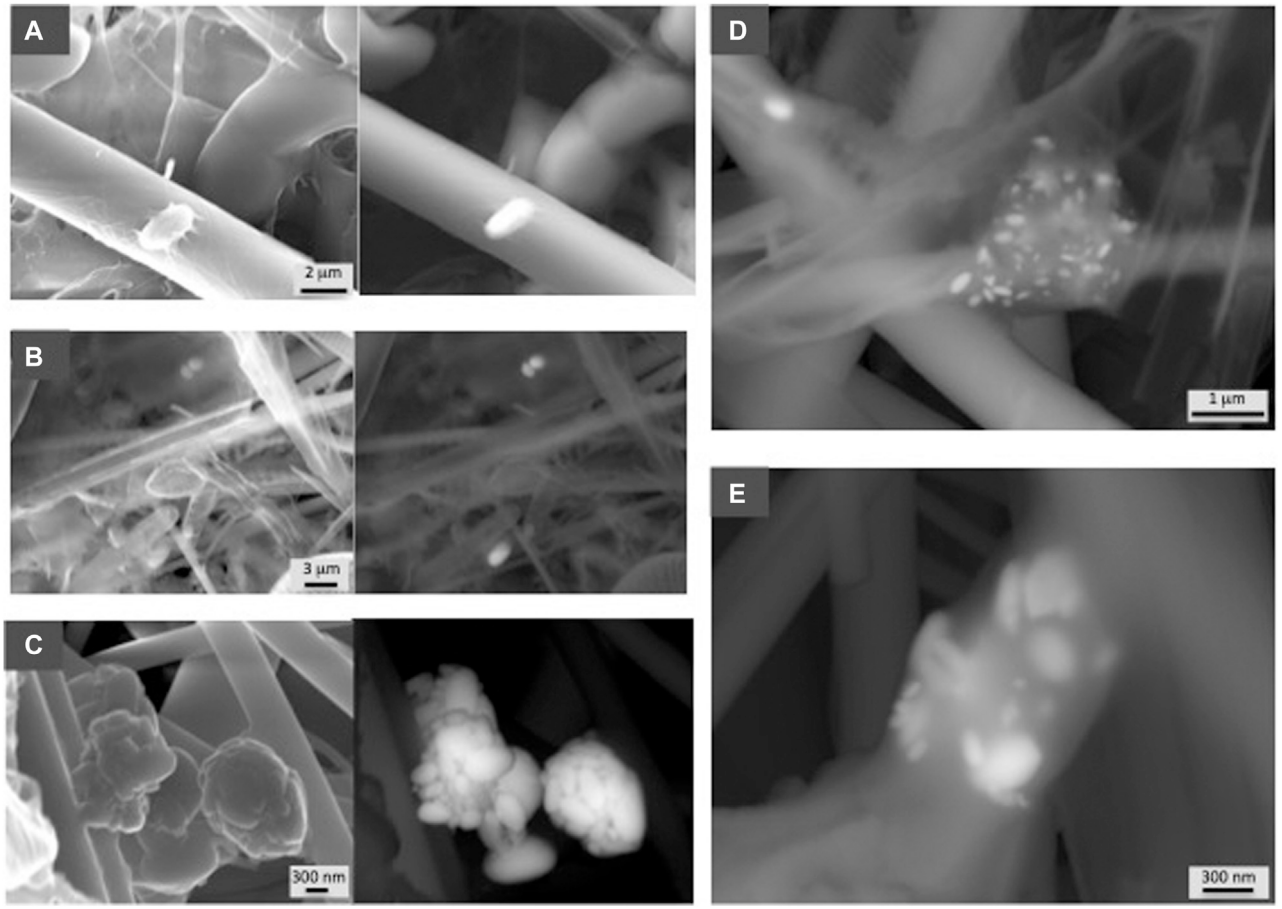

FIGURE 4 | SEM photographs showing representative examples of barite from the Indian sector of the Southern Ocean. Samples are indicated in **Table 1**. Both secondary electron and in backscattered electron (BSE) mode at 30 kV are shown in each sample. **(A)** GCM 199 (20 m), **(B)** GCM 197 (125 m), **(C)** GCM 193 (500 m). **(D)** and **(E)** GCM 194 (300 m) show a detail of the different size of barite grains formed within organic aggregates.

observations confirm the abundance of barite throughout this water column including the deepest sample at 1,000 m water depth (**Figure 3G**) and demonstrate that barite is particularly abundant in the intermediate mesopelagic zone (**Figures 3E,F**; sample GCM 125, 500 m). In the Indian sector of the Southern Ocean, a profile down to 800 m also shows higher barite abundance at depths corresponding to the upper mesopelagic zone (**Figure 7**). Crystals of different sizes are observed (**Figure 4**) as well as barite in organic aggregates (**Figures 4D,E**) at all depths. In the Antarctic sector of the South Pacific Ocean, barite shows similar morphologies and organic association as at the other sites (**Figure 5**). The particulate barite abundance at this station is slightly lower than at the studied station in the South Atlantic sector (**Figure 7**).

Electron microscopy observations demonstrate that morphology and composition of the barite particles are similar at all the studied ocean sectors and across depth in each station. The composition of the analyzed barite grains is similar to that previously reported in Martinez Ruiz et al. (2019), hence the EDX spectra are not shown in this work. EDX analyses show the expected barite composition, and in some cases, some barite grains also contain appreciable amounts of Sr and P. Although some variability among sites and depths in the P and Sr content is seen, a clear quantitative pattern of vertical or spatial variability in the content of P and Sr cannot be established with the EDX available data. However, qualitatively, at the South Atlantic and South Indian ocean stations, the number of barite grains enriched in Sr and P generally decreased with depth, suggesting that barite grains are more enriched in these elements at shallow depths. Acantharia shells have also been observed at the shallow depths in several stations (South Atlantic and South Indian oceans and East Pacific). It is important to note that the large Si peaks in EDX analyses from the quartz filter substrate overlap with the Sr L alfa (1.806 keV) peak, which may mask Sr when it is not in high enough abundance. However, at high concentrations Sr is easily detectable by the Sr K alfa 1 (14.165 keV) peak, and this has been carefully checked in SEM and HRTEM EDX spectra. As reported by Martinez Ruiz et al. (2019), Sr is clearly present in some of the analyzed barite grains but in other cases it is not detectable likely because of relatively low concentrations resulting in peaks

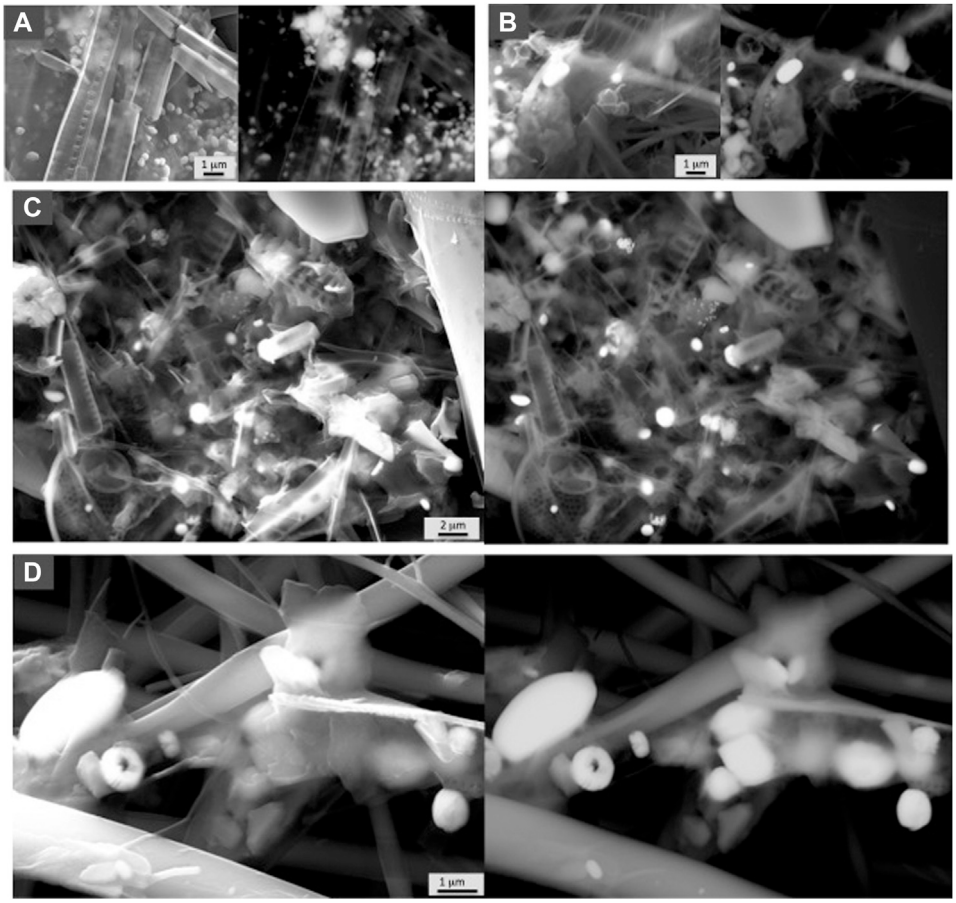

FIGURE 5 | SEM photographs showing representative examples of barite from the Southern Ocean edge Ross Sea sector. Samples are indicated in **Table 1**. Both secondary electron and in backscattered electron (BSE) mode at 30 kV are shown in each sample. **(A)** NBP 1017 (100 m), **(B)** NBP 1018 (150 m), **(C)** NBP 1019 (250 m) and **(D)** NBP 1021 (600 m). In all analyzed filter samples barite is particularly abundant.

obscured by the EDX Si spectra. HRTEM analyses also allow for Sr detection and indeed it is observed in many of the analyzed particles as shown in **Figure 6**. EDX maps also show that Sr content is variable at the nanometer scale and may vary even within the same particle (Martinez Ruiz et al., 2019).

Composition and crystallographic characteristics have been obtained by HRTEM. Representative examples are included in **Figure 6**. The analyses of organic aggregates indicate that barite crystallization starts with nanometer-sized amorphous precursors either P-rich (Martinez Ruiz et al., 2019) or with a barite-like composition and that the composition is variable even at this nano scale (**Figures 6A–F**). The amorphous nature of some of these particles is supported by SAED images and HRTEM diffraction data (**Figure 6A**). These analyses show crystals in which d-spaces corresponding to barite are clearly recognized (**Figure 6G**) as well as particles without a clear crystalline organization. High Angle Annular Dark Field (HAADF) STEM images and corresponding EDX map also demonstrate the high concentration of P and Sr in some of the barite grains (**Figures 6C–E**).

Particulate organic carbon (POC) and particulate Ba (pBa) profiles from the South Atlantic (Great Calcite Belt) Station 117 and the South Pacific Ocean (Antarctic sector) are shown in **Figure 7**. POC profiles are similar at both sites and show the typical POC profile with export out of the euphotic zone. At the Great Calcite Belt, Rosengard et al. (2015) argued that in this ocean region diatom-rich communities produce large and labile POC aggregates, which result in intense mineralization in the mesopelagic zone. The pBa profiles also support a significant increase in barite abundance at about 300 m, decreasing above and below that depth. At the Antarctic sector, the pBa profile show barite down to the deepest sample (600 m) analyzed at this station. Samples recovered from the top 1,000 m at low latitude sub/tropical locations exhibit undersaturation ($\Omega_{barite} < 1$) in the epipelagic and upper mesopelagic zones (e.g., east Pacific, southeast Atlantic). In contrast, water samples from the high-latitude Southern Ocean are generally close to saturation ($\Omega_{barite} = 1$) or even slightly supersaturated ($\Omega_{barite} > 1$), consistent with previous studies (e.g., Monnin et al., 1999; Rushdi et al., 2000).

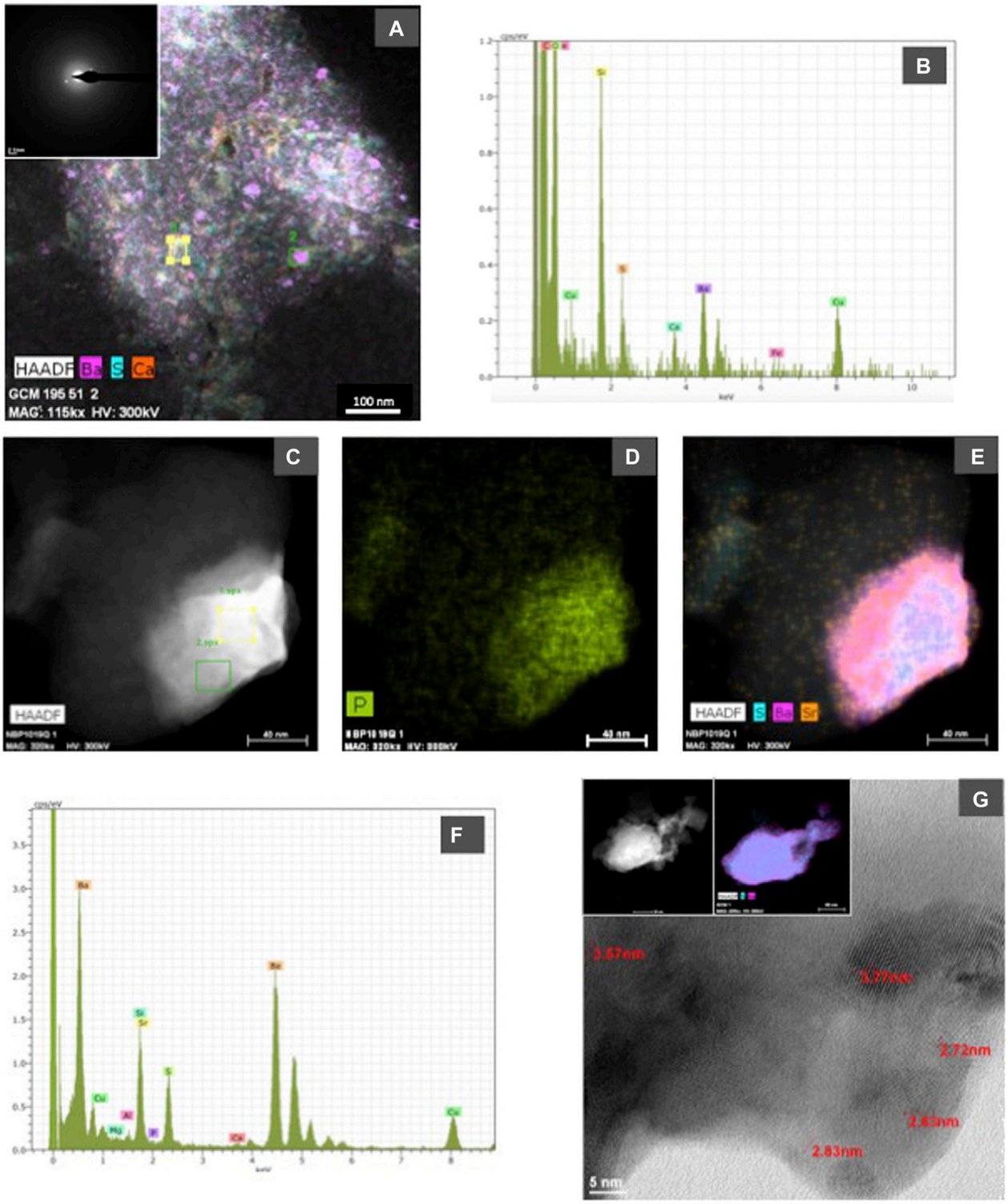

FIGURE 6 | (A) High Angle Annular Dark Field (HAADF) STEM image and corresponding EDX maps showing the distribution of S, Ba and Ca in an organic aggregate from sample GCM 195 (Indian sector of the Southern Ocean). In the upper left corner, a selected area electron diffraction (SAED) image obtained by HRTEM is included to show the poor crystallinity of the nanometer-sized particles with barite composition; **(B)** representative spectrum (indicated in the HAADF image as square 2) showing the barite composition of nanometer-sized particles; **(C)**, **(D)**, and **(E)** show HAADF-STEM images and corresponding EDX maps of P **(D)** and Sr, S, and Ba **(E)** in a barite particle from NBP 1019 sample; **(F)** representative EDX spectrum from the barite particle shown in photograph c. Analyzed area corresponds to square 2 in that photograph, the Sr peak shows its enrichment in this grain; **(G)** shows a lattice-fringe image from sample GCM 124 in which d-spaces characteristic of barite are indicated: 3.77 Å (201), 3.57 Å (002), 2.83 Å (112), and 2.72 Å (020). In upper left side, a HAADF-STEM image and corresponding EDX maps (S and Ba) of the analyzed particle are included.

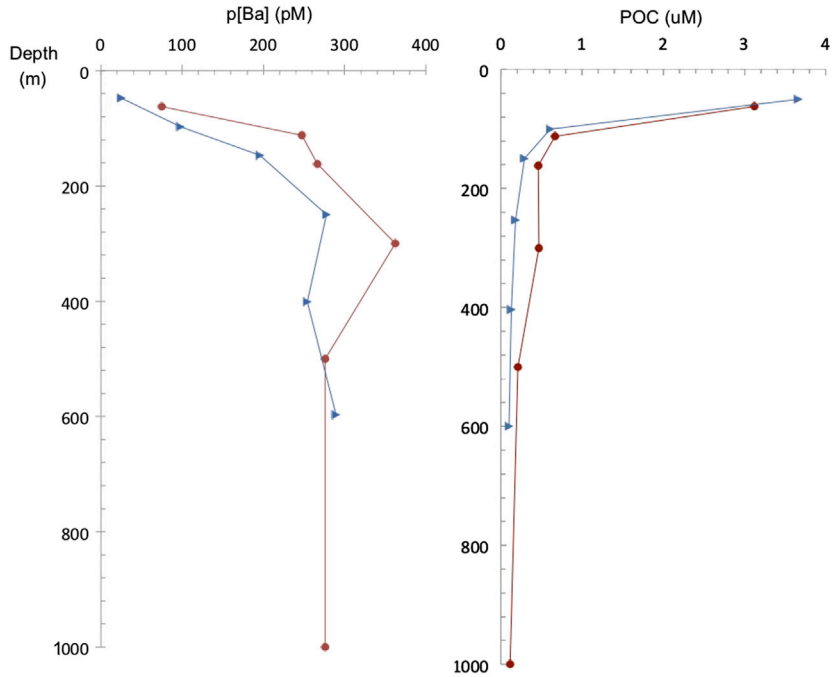

FIGURE 7 | Particulate Ba (pBa) concentration (1–51 μm size fraction) and POC profiles at the studied stations in the South Atlantic (Great Calcite Belt) (red dots) and South Pacific (Antarctic sector) (blue triangles).

DISCUSSION

Barite Distribution in the Open Ocean

To date, a large body of work from multiple oceanographic expeditions and sampling location has provided ample datasets of dBa and non-lithogenic pBa distribution in the ocean water column. In general, the GEOTRACES-era datasets exhibit similar depth-dependent patterns in pBa to those shown here; however, this study also adds novel results regarding the mechanisms behind these distributions. It has been demonstrated that barite abundance shows significant spatial differences mostly related to productivity. Also, significant differences are recognized with depth in the water column since processes involved in precipitation are occurring at certain depths and the barite may dissolve deeper in the water column. Since pBa is closely correlated with the flux of organic carbon, it is enriched in the mesopelagic zone and typically shows a maximum abundance at intermediate depths (200–600 m) (e.g., Dehairs et al., 1980; Bishop, 1988; Dehairs et al., 1991; Dymond and Collier, 1996; Dehairs et al., 1997; Dehairs et al., 2008; Stenberg et al., 2008; Jacquet et al., 2011; Planchon et al., 2013; Lemaitre et al., 2018; Conte et al., 2019). Overall, vertical pBa profiles are similar to those of calculated oxygen consumption rates, which supports the link between organic matter degradation and barite formation (e.g., Dehairs et al., 1997). Importantly, pBa has been correlated with rates of microbial degradation of organic matter, which further support the link to oxygen consumption and carbon respiration. Barium isotopes also support barite formation at mesopelagic depths as demonstrated by enrichment in the isotopically-heavy Ba in seawater (^{138}Ba) and depletion of the lighter Ba (^{134}Ba) due to the preferential incorporation of the lighter Ba isotopes in barite (Horner et al., 2015; Hsieh and Henderson, 2017; Bates et al., 2017; Bridgestock et al., 2018). Indeed a local maximum in δ^{138}Ba at depths between 200 and 600 m in diverse ocean basins indicates that barite precipitation mostly occurs at these depths (Horner et al., 2015; Bates et al., 2017). Our pBa data from the two analyzed stations at the South Atlantic (Great Calcite Belt) and South Pacific (Antarctic sector) stations are also consistent with the idea of enhanced barite formation at this depth the mesopelagic zone. Profiles show higher pBa concentrations below 200 m and down to 600 m with a maximum in at about 200–400 m. Though qualitative, SEM observations from all the analyzed stations similarly show higher barite abundance at these intermediate depths.

As discussed above, barite formation is linked to organic carbon mineralization and export production, however a notable spatial variability in the Ba:Corg ratio is found over ocean regions. For instance, sediment trap samples from the Western Atlantic have significantly lower Ba/Corg values than samples from the Pacific (e.g., Dymond and Collier, 1996). The causes for this spatial variability are still poorly understood. Differences in the Ba:Corg ratio have been related to the efficiency of mineralization of POC in the mesopelagic zone relative to the exported amount (e.g., Francois et al., 1995). Thus, using algorithms that relate Ba to carbon export may not be appropriate in regions of highly variable carbon flux. Moreover, barite formation may be affected by the rate at which particles sink, given that particles that are quickly removed from the water column by rapid sinking may reduce the likelihood for precipitation of particulate Ba phases (McManus et al., 2002).

This has also added uncertainty to sedimentary Ba interpretations and paleoproductivity reconstructions, particularly to the use of Ba content as a quantitative proxy for reconstructing productivity. In general, the poor understanding of barite distribution in the water column stems from our limited knowledge of the processes leading to barite saturation. A better knowledge of such processes may improve our ability to assess changes in past productivity. Results from experimental work and from the analyses of pBa phases in the water column have recently shed light into potential mechanisms leading to saturation and precipitation of barite in microenvironments within sinking particulate matter in the mesopelagic zone (Martinez-Ruiz et al., 2018; Martinez-Ruiz et al., 2019). Collectively this work emphasizes the role of biofilms as Ba-concentrating agents in a process that could be termed organo-mineralization. According to the Encyclopedia of Geobiology, organo-mineralization (Défarge, 2011) is a process of mineral formation mediated by organic matter (OM), independent of the living organisms which the OM derives from. The organic compounds may be excretion products or detached parts of living organisms, or relics and by-products of dead organisms that have been released into waters or incorporated into soils, sediments, or rocks. Our observations from suspended marine particulate matter agree with this process and further support previous findings. Our SEM and TEM observations at multiple stations also demonstrate that barite forms through a P-rich amorphous precursor phase, seen in the pBa composition, ranging from Ba-phosphate to Ba-sulfate consistent with previous studies from two Atlantic Ocean stations (Martinez-Ruiz et al., 2019). The present study adds further evidence in support of these findings. Moreover, although the Ω_{barite} (**Table 2**) in the epipelagic and upper mesopelagic zone at the newly studied ocean sectors differs from site to site, this does not seem to be a major control in barite precipitation as no relation between Ω_{barite} and pBa or barite abundance is evident. At all the studied stations, barite crystals show similar characteristics in terms of composition, size, distribution and association to organic material, prominently showing association with EPS-like morphologies, which further supports EPS production is a major factor in promoting barite formation (**Figures 2–5**) as well as organo-mineralization as a common process for barite formation throughout the ocean. Considering that the relation of pBa with export production depends on microbial processes related to organic matter degradation, barite formation is therefore linked to the suite of complex processes involved in the ocean biological carbon pump. Specifically, the fraction of primary production that leaves the upper ocean and is exported to depth, defined as export production is the fraction that "fuels" barite formation. Export production depends on diverse factors such as phytoplankton and zooplankton community structures, the formation of aggregates, sinking by ballasting, and bacterial mineralization rates (e.g., Francois et al., 2002; Cavan et al., 2015; Belcher et al., 2016; Le Moigne et al., 2016) and these factors change in space and time. For example, Henson et al. (2019) demonstrated that low primary production and high export efficiency regimes tend to occur when macro-zooplankton and bacterial abundances are low in the surface ocean. Thus, a large fraction of primary production is exported, likely as intact cells or phytoplankton-based aggregates. In contrast, when macro-zooplankton and bacterial abundances in the surface ocean are high, the export efficiency decreases. These results support that the whole ecosystem structure, rather than just the phytoplankton community, play a major role in export efficiency (Dehairs et al., 1992). All these factors not only depend on seasonality but can also be very different at regional and global scales. Hence, appropriate knowledge of the processes involved in carbon export fluxes, the formation of organic aggregates, and particle sinking is required for assessing the relationship between productivity and Ba proxies, and proper interpretative care and caution are required for using Ba as a proxy for export production. As the relation between export production and barite largely depends on microbial processes and EPS production, temperature, oxygen abundance, and the type of organisms involved may impact this relationship. Although the reason for Ba accumulation in bacteria and EPS or in other living organisms is not yet well understood, it is known that bioaccumulation of Ba occurs throughout the ocean. The nucleation and crystallization of barite results in the formation of a highly stable mineral that is hard to dissolve under oxygenated conditions, consequently a relatively large fraction of the particulate barite that forms reaches the sediments (Paytan and Kastner, 1996). Barite accumulation in the sediment would therefore represent a record of the combination of diverse processes including export productivity, organic matter degradation, bacterial activity, and EPS production. This complexity should be considered when interpreting temporal and spatial variability in the Ba:Corg ratios and in barite accumulation in marine sediments.

Role of Extracellular Polymeric Substances in Barite Precipitation

Understanding the microbial processes leading to the formation of the mineral barite in the oceanic water column is crucial to determining the utility of Ba proxies for paleo-productivity and paleo-chemistry reconstructions. How and why Ba associates with organic matter in microenvironments and how the rates of organic matter decomposition affect barite production are key questions that link primary productivity or export productivity to barite abundance in marine sediments. The important role that EPS and microbial cells may play in nucleation and crystallization in the ocean is still far from being well understood at the molecular scale. Even though the EPS in the ocean have been widely investigated, their role in mediating mineral precipitation remains mostly unknown, in particular as it pertains to barite formation. In seawater, these secretions facilitate attachment to surfaces leading to the formation of biofilms, organic colloids, and larger aggregations of cells (marine snow). Though difficult to measure accurately, EPS represent a significant portion of the bioavailable carbon pool in the ocean. These substances occur in a range of molecular sizes, with diverse physical and chemical properties, and their composition includes polysaccharides, proteins, lipids, and nucleic acids (Decho and Gutierrez, 2017). In general, the attachment of microbes to surfaces, or

to each other, provides higher environmental stability than being a free-living cell and may be favorable in the ocean (e.g., Flemming et al., 2016). The EPS matrix of biofilms provides a three-dimensional architecture framework (Decho, 2000) that is the building block of the aggregates suspended in the water column. These organic aggregates are known to be very rich in microbial communities with abundances up to two orders of magnitude higher than in the surrounding seawater environment (e.g., Alldredge et al., 1986; Herndl, 1988).

While both experimental work and observations in diverse natural environments have demonstrated that functional groups associated with EPS are able to bind different metal ions (e.g., Braissant et al., 2007; Tourney and Ngwenya, 2014), their precise role for the binding, trapping and concentrating metals in the open ocean has not been sufficiently investigated. For instance, in bioremediation, it has been demonstrated that the polyanionic nature of the EPS promotes the binding of heavy and toxic metal ions, and EPS use for detoxification of heavy metals is well known. Many examples have been described in the literature such as in the remediation of Cd, Cr, Pb, Ni, Cu, Al, and U (e.g., Beech and Cheung, 1995; Iyer et al., 2005; Bhaskar and Bhosle, 2006; Gerber et al., 2018). However, as many of these studies had commercial purposes, very few have addressed the ecological implications of marine EPS in metal biogeochemical cycles. Loaec et al. (1997, 1998) reported the heavy metal-binding capacity of EPS produced by hydrothermal vent bacteria and suggested that this could represent a survival strategy for the bacteria by reducing their exposure to toxic metals released from the hydrothermal vents. Major elements such as Na, Mg, Ca, K, Sr, and Si, have also been shown to be adsorbed by marine bacterial EPS (Gutierrez et al., 2008). Likewise, Fe uptake by EPS in eukaryotic phytoplankton has been investigated (Hassler et al., 2011; Gutierrez et al., 2012), and binding of Th to carboxylate, phosphate and sulfate groups in marine EPS has also been shown (Alvarado Quiroz et al., 2006). Nevertheless, the ecological implications of these binding processes are not well understood, and Ba has not been investigated yet in this regard. Thus, our data open an unexplored field and support the crucial role that EPS play not only for Ba bioaccumulation but also for mineral precipitation in the ocean, with important implications for paleo-oceanographic reconstructions. Although further investigations are required to elucidate precise nucleation and crystal growth processes, the available data strongly support that biofilm matrix is crucial for metal precipitation in the ocean. In this dynamic environment, with abundant microbial cells, polysaccharides and water, together with excreted cellular products (e.g., Sutherland, 2001), functional groups including sulfate and phosphate would contribute to the overall negative charge of the EPS, and these functional groups would interact with metals promoting precipitation.

The Microbial Pump and Future Perspectives

The use of barite as a proxy to gain insights into past microbial processes is a promising tool in paleoceanographic research. It is broadly known that microbial communities play a major role in biogeochemical cycles since they play a role both at the base of the oceanic food web and as decomposers (e.g., Falkowski et al., 2008; Robidart et al., 2019). Further knowledge of microbial productivity and structure of communities is required for predicting future marine ecosystem functions, and the impact of increasing environmental effects on ocean ecosystems. This is challenging at present because biogeochemical processes and microbial communities are very complex, but it is far more complex for the past because a record of microbial processes is not usually well preserved in marine sediments beyond the preservation of biomarkers and some minerals that form through direct or indirect association with microorganisms. Accordingly, although barite accumulation rates are closely correlated with carbon export to the deep ocean (Carter et al., 2020 and references therein), the occurrence of barite may also reflect Ba utilization in the surface ocean through microbial processes, EPS production and organic matter mineralization. Except in sulfate reducing environments, barite is well preserved in marine sediments, thus the presence of pelagic barite particles is an indication of past bacterial respiration processes. In fact, barite has been proposed as a good proxy reflecting average mineralization processes (e.g., Cardinal et al., 2005), which are in turn a major control in the global carbon cycle and atmospheric carbon sequestration (e.g., Cavan et al., 2017). Our observations at diverse ocean sectors and depths showing formation within organic aggregates commonly rich in EPS, further support that mineralization due to microbial respiration is responsible for barite formation and consequently barite is a bioindicator for such processes.

The occurrence of barite in marine particles may have additional effects that have so far not been thoroughly investigated. For example, the potential role of barite particles within marine snow in the ballasting and mineralization controls of carbon sedimentation. It has been demonstrated that particulate minerals, for instance eolian dust, can be incorporated into organic aggregates and act as ballast enhancing the marine carbon export hence the significant increase in the sinking velocities of aggregates (Van der Jagt et al., 2018). Although biological processes affecting the fragmentation and mineralization of large particles are the most important factors determining the POC profiles (e.g., Lam and Bishop, 2007), barite is a high-density mineral that could also affect export processes. Another important aspect that still requires further investigation is the distribution of barite at greater depths than the mesopelagic zone. To date most of the studies on barite distribution have focused on mesopelagic depths and little is known about distribution and potential precipitation or dissolution with depth since only very few data from deeper samples are available (Conte et al., 2019). Furthermore, in the bathypelagic ocean (depth >1,000 m), Archaea and Viruses are particularly important in the microbial loop, but they remain largely unexplored in deep waters, and interactions between microbes and minerals beyond bacterial precipitation is almost unknown, except some recent work on the role of viruses in carbonate precipitation (e.g., Lan et al., 2020; White III et al., 2020).

CONCLUSIONS

Comparisons of suspended marine particulate matter obtained from diverse ocean sectors indicate barite formation at intermediate depths (200–600 m) in the mesopelagic zone independent of barite saturation state. The formation of barite within organic aggregates in close association with EPS is a common process recognized in all the studied regions. Our results further confirm that microbial processes are mediating barite precipitation (organo-mineralization) within such aggregates as previously supported by experimental work showing that Ba binds to phosphate groups on cell surfaces and EPS in bacterial biofilms. Mineralogical and crystallographic characteristics of suspended barite particles in the ocean support the same crystallization path, from an amorphous P-rich phase to mineral barite. EPS play a crucial role in locally concentrating Ba and providing nucleation sites leading to saturation. The binding capacity of the functional groups associated with EPS, including phosphate groups, has been widely demonstrated in experimental conditions and diverse natural environments, and the interactions between Ba and the EPS is similarly occurring in the ocean leading to barite precipitation. The distribution of particulate Ba and Ba isotopes in the water column are consistent with this precipitation mechanism. Many processes are involved in barite precipitation including primary production, export production, organic matter degradation, bacterial respiration, EPS formation, aggregation and sinking, and all should be further investigated and taken into account when interpreting temporal and spatial variability in the Ba:Corg ratios and barite accumulation in sediments. In addition, EPS production by organisms other than bacteria, such as phytoplankton, may also play an important role in barite production. However, the ecological implications of these processes and interactions between diverse organisms have been poorly investigated. The strong link between organo-mineralization of pelagic barite and microbial processes could be used to gain insights into past microbial processes and the functioning of the microbial pump. This is of importance for reconstructing mineralization and microbial respiration, and their link to export production, which are key processes in the global carbon cycle and the ocean carbon sink.

DATA AVAILABILITY STATEMENT

The raw data supporting the conclusions of this article will be made available by the authors, without undue reservation.

AUTHOR CONTRIBUTIONS

All authors listed have made a substantial contribution to the work and approved it for publication. FM conceived and led this project and has written the manuscript with an active contribution by discussing the results and writing from AP, MK, and MG. MG and FJ also contributed to perform related culture experiments and to discuss microbiological aspects. PL provided the studied filter samples and corresponding information, and TH led the pBa analyses, and both contributed to the discussion. MA contributed TEM analytical data and corresponding discussion.

FUNDING

This study was supported by the European Regional Development Fund (ERDF) co-financed grants CGL2017-92600-EXP and PID2019-104624RB-I00 (Agencia Estatal de Investigación, Ministerio de Ciencia e Innovación, Spain), Research Groups RNM-179 and BIO 103, and Excellence Projects P18-RT-3804 and P18-RT-4074 (Junta de Andalucía), Unidad Científica de Excelencia UCE-PP2016-05 (University of Granada) and grant OCE-1443577.

ACKNOWLEDGMENTS

We thank the Center for Scientific Instrumentation (CIC, University of Granada) for electron microscopy analytical facilities, all the cruises supporting the sample collection, and laboratory assistance from C. W. Kinsley and H. V. Pryer for pBa analyses. We greatly acknowledge Frank Dehairs and Christophe Monnin whose constructive comments and suggestions helped improve and clarify this manuscript.

REFERENCES

Abella-Gutiérrez, J., and Herguera, J. C. (2016). Sensitivity of carbon paleoproductivity in the Southern California current system on different time scales for the last 2 ka. *Paleoceanogr. Paleoclimatol.* 31, 953–970. doi:10.1002/2015PA002872

Alldredge, A. L., Cole, J. J., and Caron, D. A. (1986). Production of heterotrophic bacteria inhabiting macroscopic organic aggregates (marine snow) from surface waters. *Limnol. Oceanogr.* 31, 68–78. doi:10.4319/lo.1986.31.1.0068

Alvarado Quiroz, N. G., Hung, C.-C., and Santschi, P. H. (2006). Binding of thorium(IV) to carboxylate, phosphate and sulfate functional groups from marine exopolymeric substances (EPS). *Mar. Chem.* 100, 337–353. doi:10.1016/j.marchem.2005.10.023

Balch, W. M., Bates, N. R., Lam, P. J., Twining, B. S., Rosengard, S. Z., Bowler, B. C., et al. (2016). Factors regulating the great calcite belt in the Southern Ocean and its biogeochemical significance. *Global Biogeochem. Cycles.* 30, 1124–1144. doi:10.1002/2016GB005414

Bates, S. L., Hendry, K. R., Pryer, H. V., Kinsley, C. W., Pyle, K. M., Woodward, E. M. S., et al. (2017). Barium isotopes reveal role of ocean circulation on barium cycling in the Atlantic. *Geochem. Cosmochim. Acta.* 204, 286–299. doi:10.1016/j.gca.2017.01.043

Beech, I. B., and Cheung, C. W. S. (1995). Interactions of exopolymers produced by sulphate-reducing bacteria with metal ions. *Int. Biodeterior. Biodegrad.* 35, 59–72. doi:10.1016/0964-8305(95)00082-G

Belcher, A., Iversen, M., Giering, S., Riou, V., Henson, S. A., Berline, L., et al. (2016). Depth-resolved particle-associated microbial respiration in the northeast Atlantic. *Biogeosciences.* 13 (17), 4927–4943. doi:10.5194/bg-13-4927-2016

Bernstein, R. E., Byrne, R. H., Betzer, P. R., and Greco, A. M. (1992). Morphologies and transformations of celestite in seawater: the role of acantharians in strontium and barium geochemistry. *Geochem. Cosmochim. Acta.* 56, 3273–3279. doi:10.1016/0016-7037(92)90304-2

Bernstein, R. E., Byrne, R. H., and Schijf, J. (1998). Acantharians: a missing link in the oceanic biogeochemistry of barium. *Deep Sea Res. Oceanogr. Res. Pap.* 45, 491–505. doi:10.1016/S0967-0637(97)00095-2

Bhaskar, P. V., and Bhosle, N. B. (2006). Bacterial extracellular polymeric substance (EPS): a carrier of heavy metals in the marine food-chain. *Environ. Int.* 32, 191–198. doi:10.1016/j.envint.2005.08.010

Bishop, J. K. B. (1988). The barite-opal-organic carbon association in oceanic particulate matter. *Nature.* 332, 341. doi:10.1038/332341a0

Bishop, J. K. B., Lam, P. J., and Wood, T. J. (2012). Getting good particles: accurate sampling of particles by large volume *in-situ* filtration. *Limnol Oceanogr. Methods.* 10, 681–710. doi:10.4319/lom.2012.10.681

Bishop, J. K. B., Schupack, D., Sherrell, R. M., and Conte, M. (1985). "A multiple-unit large-volume in situ filtration system for sampling oceanic particulate matter in mesoscale environments," in *Mapping strategies in chemical oceanography, Advances in chemistry*. Washington, DC: American Chemical Society, Vol. 9, 155–175.

Bishop, J. K. B., and Wood, T. J. (2008). Particulate matter chemistry and dynamics in the twilight zone at VERTIGO ALOHA and K2 sites. *Deep Sea Res. Oceanogr. Res. Pap.* 55, 1684–1706. doi:10.1016/j.dsr.2008.07.012

Braissant, O., Decho, A. W., Dupraz, C., Glunk, C., Przekop, K. M., and Visscher, P. T. (2007). Exopolymeric substances of sulfate-reducing bacteria: interactions with calcium at alkaline pH and implication for formation of carbonate minerals. *Geobiology.* 5, 401–411. doi:10.1111/j.1472-4669.2007.00117.x

Bridgestock, L., Hsieh, Y.-T., Porcelli, D., Homoky, W. B., Bryan, A., and Henderson, G. M. (2018). Controls on the barium isotope compositions of marine sediments. *Earth Planet Sci. Lett.* 481, 101–110. doi:10.1016/j.epsl.2017.10.019

Brzezinski, M. A., and Washburn, L. (2011). Phytoplankton primary productivity in the santa barbara channel: effects of wind-driven upwelling and mesoscale eddies. *J. Geophys. Res.* 116, C12013. doi:10.1029/2011JC007397

Cardinal, D., Savoye, N., Trull, T. W., André, L., Kopczynska, E. E., and Dehairs, F. (2005). Variations of carbon remineralisation in the Southern Ocean illustrated by the Baxs proxy. *Deep Sea Res. Oceanogr. Res. Pap.* 52, 355–370. doi:10.1016/j.dsr.2004.10.002

Carter, S. C., Paytan, A., and Griffith, E. M. (2020). Toward an improved understanding of the marine barium cycle and the application of marine barite as a paleoproductivity proxy. *Minerals.* 10, 421. doi:10.3390/min10050421

Cavan, E. L., Le Moigne, F. A. C., Poulton, A. J., Tarling, G. A., Ward, P., Daniels, C. J., et al. (2015). Attenuation of particulate organic carbon flux in the Scotia Sea, Southern Ocean, is controlled by zooplankton fecal pellets. *Geophys. Res. Lett.* 42, 821–830. doi:10.1002/2014GL062744

Cavan, E. L., Trimmer, M., Shelley, F., and Sanders, R. (2017). Remineralization of particulate organic carbon in an ocean oxygen minimum zone. *Nat. Commun.* 8, 14847. doi:10.1038/ncomms14847

Chow, T. J., and Goldberg, E. D. (1960). On the marine geochemistry of barium. *Geochem. Cosmochim. Acta.* 20, 192–198. doi:10.1016/0016-7037(60)90073-95

Conte, M. H., Carter, A. M., Koweek, D. A., Huang, S., and Weber, J. C. (2019). The elemental composition of the deep particle flux in the Sargasso Sea. *Chem. Geol.* 511, 279–313. doi:10.1016/j. chemgeo.2018.11.001

Decho, A. W. (2000). "Exopolymer microdomains as a structuring agent for heterogeneity with microbial biofilms," in *Microbial sediments.* Editors R. E. Riding and S. M. Awramik (Berlin, Germany: Springer-Verlag Press), 9–15.

Decho, A. W., and Gutierrez, T. (2017). Microbial extracellular polymeric substances (EPSs) in Ocean systems. *Front. Microbiol.* 8, 922. doi:10.3389/fmicb.2017.00922

Défarge, C. (2011). "Organomineralization," in *Encyclopedia of Geobiology*. Editors J. Reitner and V. Thiel (Dordrecht, Netherlands: Springer).

Dehairs, F., Baeyens, W., and Goeyens, L. (1992). Accumulation of suspended barite at mesopelagic depths and export production in the Southern Ocean. *Science.* 258, 1332–1335. doi:10.1126/science.258.5086.1332

Dehairs, F., Chesselet, R., and Jedwab, J. (1980). Discrete suspended particles of barite and the barium cycle in the open ocean. *Earth Planet Sci. Lett.* 49, 528–550. doi:10.1016/0012-821X(80)90094-1

Dehairs, F., Jacquet, S., Savoye, N., Van Mooy, B. A. S., Buesseler, K. O., Bishop, J. K. B., et al. (2008). Barium in twilight zone suspended matter as a potential proxy for particulate organic carbon remineralization: results for the North Pacific. *Deep Sea Res. Part II Top. Stud. Oceanogr.* 55, 1673–1683. doi:10.1016/j.dsr2.2008.04.020

Dehairs, F., Shopova, D., Ober, S., Veth, C., and Goeyens, L. (1997). Particulate barium stocks and oxygen consumption in the Southern Ocean mesopelagic water column during spring and early summer: relationship with export production. *Deep Sea Res. Part II Top. Stud. Oceanogr.* 44, 497–516. doi:10.1016/S0967-0645(96)00072-0

Dehairs, F., Stroobants, N., and Goeyens, L. (1991). Suspended barite as a tracer of biological activity in the Southern Ocean. *Mar. Chem.* 35, 399–410. doi:10.1016/S0304-4203(09)90032-9

Dymond, J., and Collier, R. (1996). Particulate barium fluxes and their relationships to biological productivity. *Deep Sea Res. Part II Top. Stud. Oceanogr.* 43, 1283–1308. doi:10.1016/0967-0645(96)00011-2

Dymond, J., Suess, E., and Lyle, M. (1992). Barium in deep-sea sediment: a geochemical proxy for paleoproductivity. *Paleoceanogr. Paleoclimatol.* 7, 163–181. doi:10.1029/92PA00181

Eagle, M., Paytan, A., Arrigo, K. R., van Dijken, G., and Murray, R. W. (2003). A comparison between excess barium and barite as indicators of carbon export. *Paleoceanogr. Paleoclimatol.* 18, 1021. doi:10.1029/2002PA000793

Enyedi, N. T., Makk, J., Kótai, L., Berényi, B., Klébert, S., Sebestyén, Z., et al. (2020). Cave bacteria-induced amorphous calcium carbonate formation. *Sci. Rep.* 10, 8696. doi:10.1038/s41598-020-65667-w

Falkowski, P. G., Fenchel, T., and DeLong, E. F. (2008). The microbial engines that drive Earth's biogeochemical cycles. *Science.* 320, 1034–1039. doi:10.1126/science.1153213

Flemming, H.-C., Wingender, J., Szewzyk, U., Steinberg, P., Rice, S. A., and Kjelleberg, S. (2016). Biofilms: an emergent form of bacterial life. *Nat. Rev. Microbiol.* 14, 563–575. doi:10.1038/nrmicro.2016.94

François, R., Honjo, S., Krishfield, R., and Manganini, S. (2002). Factors controlling the flux of organic carbon to the bathypelagic zone of the ocean. *Global Biogeochem. Cycles.* 16 (4), 1087. doi:10.1029/2001GB001722

François, R., Honjo, S., Manganini, S. J., and Ravizza, G. E. (1995). Biogenic barium fluxes to the deep sea: implications for paleoproductivity reconstruction. *Global Biogeochem. Cycles.* 9, 289–303. doi:10.1029/95GB00021

Ganeshram, R. S., François, R., Commeau, J., and Brown-Leger, S. L. (2003). An experimental investigation of barite formation in seawater. *Geochem. Cosmochim. Acta.* 67, 2599–2605. doi:10.1016/S0016-7037(03)00164-9

Gerber, U., Hübner, R., Rossberg, A., Krawczyk-Bärsch, E., and Merroun, M. L. (2018). Metabolism-dependent bioaccumulation of uranium by *Rhodosporidium toruloides* isolated from the flooding water of a former uranium mine. *PLoS One.* 13, e0201903. doi:10.1371/journal.pone.0201903

Geyman, B. M., Ptacek, J. L., LaVigne, M., and Horner, T. J. (2019). Barium in deep-sea bamboo corals: phase associations, barium stable isotopes, and prospects for paleoceanography. *Earth Planet Sci. Lett.* 525, 115751. doi:10.1016/j.epsl.2019.115751

Gingele, F., and Dahmke, A. (1994). Discrete barite particles and barium as tracers of paleoproductivity in South Atlantic sediments. *Paleoceanogr. Paleoclimatol.* 9, 151–168. doi:10.1029/93PA02559

González-Muñoz, M. T., Fernández-Luque, B., Martínez-Ruiz, F., Ben Chekroun, K., Arias, J. M., Rodríguez-Gallego, M., et al. (2003). Precipitation of barite by *Myxococcus xanthus*: possible implications for the biogeochemical cycle of barium. *Appl. Environ. Microbiol.* 69, 5722–5725. doi:10.1128/AEM.69.9.5722-5725.2003

Gonzalez-Muñoz, M. T., Martinez-Ruiz, F., Morcillo, F., Martin-Ramos, J. D., and Paytan, A. (2012). Precipitation of barite by marine bacteria: a possible mechanism for marine barite formation. *Geology.* 40, 675. doi:10.1130/G33006.1

Griffith, E. M., and Paytan, A. (2012). Barite in the ocean - occurrence, geochemistry and palaeoceanographic applications. *Sedimentology.* 59, 1817–1835. doi:10.1111/j.1365-3091.2012.01327.x

Gutierrez, T., Biller, D. V., Shimmield, T., and Green, D. H. (2012). Metal binding properties of the EPS produced by Halomonas sp. TG39 and its potential in enhancing trace element bioavailability to eukaryotic phytoplankton. *Biometals.* 25, 1185–1194. doi:10.1007/s10534-012-9581-3

Gutierrez, T., Shimmield, T., Haidon, C., Black, K., and Green, D. H. (2008). Emulsifying and metal ion binding activity of a glycoprotein exopolymer produced by *Pseudoalteromonas* sp. strain TG12. *Appl. Enivorn. Microbiol.* 74, 4867–4876. doi:10.1128/AEM.00316-08

Hassler, C. S., Schoemann, V., Nichols, C. M., Butler, E. C. V., and Boyd, P. W. (2011). Saccharides enhance iron bioavailability to Southern Ocean phytoplankton. *Proc. Natl. Acad. Sci. U.S.A.* 108, 1076–1081. doi:10.1073/pnas.1010963108

Hatta, M., Measures, C. I., Lam, P. J., Ohnemus, D. C., Auro, M. E., Grand, M. M., et al. (2017). The relative roles of modified circumpolar deep water and benthic sources in supplying iron to the recurrent phytoplankton blooms above Pennell and Mawson banks, Ross sea, Antarctica. *J. Mar. Syst.* 166, 61–72. doi:10.1016/j.jmarsys.2016.07.009

Henson, S., Le Moigne, F., and Giering, S. (2019). Drivers of carbon export efficiency in the global ocean. *Global Biogeochem. Cycles.* 33, 891–903. doi:10.1029/2018GB006158

Henson, S. A., Sanders, R., and Madsen, E. (2012). Global patterns in efficiency of particulate organic carbon export and transfer to the deep ocean. *Global Biogeochem. Cycles.* 26, a. doi:10.1029/2011GB004099

Hernandez-Sanchez, M. T., Mills, R. A., Planquette, H., Pancost, R. D., Hepburn, L., Salter, I., and FitzGeorge-Balfour, T. (2011). Quantifying export production in the Southern Ocean:implications for the Ba_{xs} proxy. *Paleoceanogr. Paleoclimatol.* 26, PA4222. doi:10.1029/2010PA002111

Herndl, G. (1988). Ecology of amorphous aggregations (marine snow) in the Northern Adriatic Sea. II. Microbial density and activity in marine snow and its implication to overall pelagic processes. *Mar. Ecol. Prog. Ser.* 48, 265–275. doi:10.3354/meps048265

Horner, T. J., Kinsley, C. W., and Nielsen, S. G. (2015). Barium-isotopic fractionation in seawater mediated by barite cycling and oceanic circulation. *Earth Planet Sci. Lett.* 430, 511–522. doi:10.1016/j.epsl.2015.07.027

Hsieh, Y.-T., and Henderson, G. M. (2017). Barium stable isotopes in the global ocean: tracer of Ba inputs and utilization. *Earth Planet Sci. Lett.* 473, 269–278. doi:10.1016/j.epsl.2017.06.024

Iyer, A., Mody, K., and Jha, B. (2005). Biosorption of heavy metals by a marine bacterium. *Mar. Pollut. Bull.* 50, 340–343. doi:10.1016/j.marpolbul.2004.11.012

Jacquet, S. H. M., Dehairs, F., Dumont, I., Becquevort, S., Cavagna, A.-J., and Cardinal, D. (2011). Twilight zone organic carbon remineralization in the polar front zone and subantarctic zone south of tasmania. *Deep Sea Res. Part II Top. Stud. Oceanogr.* 58, 2222–2234. doi:10.1016/j.dsr2.2011.05.029

Jeandel, C., Dupré, B., Lebaron, G., Monnin, C., and Minster, J.-F. (1996). Longitudinal distributions of dissolved barium, silica and alkalinity in the western and southern Indian Ocean. *Deep Sea Res. Oceanogr. Res. Pap.* 43, 1–31. doi:10.1016/0967-0637(95)00098-4

Karl, D. M., and Church, M. J. (2017). Ecosystem structure and dynamics in the North pacific subtropical gyre: new views of an old ocean. *Ecosystems.* 20, 433–457. doi:10.1007/s10021-017-0117-0

Kester, D. R., Duedall, I. W., Connors, D. N., and Pytkowicz, R. M. (1967). Preparation of artificial Seawater. *Limnol. Oceanogr.* 12, 176–179. doi:10.4319/lo.1967.12.1.0176

Ku, T.-L., and Lin, M.-C. (1976). ^{226}Ra distribution in the antarctic ocean. *Earth Planet Sci. Lett.* 32, 236–248. doi:10.1016/0012-821X(76)90064-9

Lam, P. J., and Bishop, J. K. B. (2007). High biomass, low export regimes in the Southern Ocean. *Deep Sea Res. Part II Top. Stud. Oceanogr.* 54, 601–638. doi:10.1016/j.dsr2.2007.01.013

Lan, Z., Zhang, S., Tucker, M., Li, Z., and Zhao, Z. (2020). Evidence for microbes in early Neoproterozoic stromatolites. *Sediment. Geol.* 398, 105589. doi:10.1016/j.sedgeo.2020.105589

Le Moigne, F. A. C., Henson, S. A., Cavan, E., Georges, C., Pabortsava, K., Achterberg, E. P., et al. (2016). What causes the inverse relationship between primary production and export efficiency in the Southern Ocean? *Geophys. Res. Lett.* 43, 4457–4466. doi:10.1002/2016GL068480

Lemaitre, N., Planquette, H., Planchon, F., Sarthou, G., Jacquet, S., García-Ibáñez, M. I., et al. (2018). Particulate barium tracing of significant mesopelagic carbon remineralisation in the North Atlantic. *Biogeosciences.* 15, 2289–2307. doi:10.5194/bg-15-2289-2018

Letelier, R. M., Björkman, K. M., Church, M. J., Hamilton, D. S., Mahowald, N. M., Scanza, R. A., et al. (2019). Climate-driven oscillation of phosphorus and iron limitation in the North Pacific subtropical gyre. *Proc. Natl. Acad. Sci. U.S.A.* 116 12720–12728. doi:10.1073/pnas.1900789116

Loaëc, M., Olier, R., and Guezennec, J. (1997). Uptake of lead, cadmium and zinc by a novel bacterial exopolysaccharide. *Water Res.* 31, 1171–1179. doi:10.1016/S0043-1354(96)00375-2

Loaëc, M., Olier, R., and Guezennec, J. (1998). Chelating properties of bacterial exopolysaccharides from deep-sea hydrothermal vents. *Carbohydr. Polym.* 35, 65–70. doi:10.1016/S0144-8617(97)00109-4

Ma, Z., Ravelo, A. C., Liu, Z., Zhou, L., and Paytan, A. (2015). Export production fluctuations in the eastern equatorial Pacific during the Pliocene-Pleistocene: reconstruction using barite accumulation rates. *Paleoceanogr Paleoclimatol.* 30, 1455. doi:10.1002/2015PA002860

Marsay, C. M., Sedwick, P. N., Dinniman, M. S., Barrett, P. M., Mack, S. L., and McGillicuddy, D. J. (2014). Estimating the benthic efflux of dissolved iron on the Ross Sea continental shelf. *Geophys. Res. Lett.* 41, 7576–7583. doi:10.1002/2014gl061684

Martinez-Ruiz, F., Jroundi, F., Paytan, A., Guerra-Tschuschke, I., Abad, M. M., and González-Muñoz, M. T. (2018). Barium bioaccumulation by bacterial biofilms and implications for Ba cycling and use of Ba proxies. *Nat. Commun.* 9, 1619. doi:10.1038/s41467-018-04069-z

Martinez-Ruiz, F., Paytan, A., Gonzalez-Muñoz, M. T., Jroundi, F., Abad, M. M., Lam, P. J., et al. (2019). Barite formation in the ocean: origin of amorphous and crystalline precipitates. *Chem. Geol.* 511, 441–451. doi:10.1016/j.chemgeo.2018.09.011

McManus, J., Dymond, J., Dymond, J., Dunbar, R. B., and Collier, R. W. (2002). Particulate barium fluxes in the Ross Sea. *Mar. Geol.* 184, 1–15. doi:10.1016/S0025-3227(01)00300-0

Measures, C., Hatta, M., and Grand, M. (2012). Bioactive trace metal distributions and biogeochemical controls in the Southern Ocean. *Oceanography.* 25, 122–133. doi:10.5670/oceanog.2012.85#sthash.KE78XEDj.dpuf

Miot, J., Benzerara, K., Morin, G., Kappler, A., Bernard, S., Obst, M., et al. (2009). Iron biomineralization by anaerobic neutrophilic iron-oxidizing bacteria. *Geochem. Cosmochim. Acta.* 73 (3), 696–711. doi:10.1016/j.gca.2008.10.033

Monnin, C., Jeandel, C., Cattaldo, T., and Dehairs, F. (1999). The marine barite saturation state of the world's oceans. *Mar. Chem.* 65, 253–261. doi:10.1016/S0304-4203(99)00016-X

Morcillo, F., González-Muñoz, M. T., Reitz, T., Romero-González, M. E., Arias, J. M., and Merroun, M. L. (2014). Biosorption and biomineralization of U(VI) by the marine bacterium *Idiomarina loihiensis* MAH_1: effect of background electrolyte and pH. *PLoS One.* 9, e91305. doi:10.1371/journal.pone.0091305

Nürnberg, C. C., Bohrmann, G., Schlüter, M., and Frank, M. (1997). Barium accumulation in the atlantic sector of the Southern Ocean: results from 190,000-year records. *Paleoceanogr Paleoclimatol.* 12, 594–603. doi:10.1029/97PA01130

Parkhurst, D. L., and Appelo, C. A. J. (2013). *Description of input and examples for PHREEQC version 3—a computer program for speciation, batch-reaction, one-dimensional transport, and inverse geochemical calculations*. Reston, CA: United States Geological Survey, 6-A43, 497.

Paytan, A., and Griffith, E. M. (2007). Marine barite: recorder of variations in ocean export productivity. *Deep Sea Res. Part II Top. Stud. Oceanogr.* 54, 687–705. doi:10.1016/j.dsr2.2007.01.007

Paytan, A., and Kastner, M. (1996). Benthic Ba fluxes in the central Equatorial Pacific, implications for the oceanic Ba cycle. *Earth Planet Sci. Lett.* 142, 439–450. doi:10.1016/0012-821x(96)00120-3

Paytan, A., Kastner, M., and Chavez, F. P. (1996). Glacial to interglacial fluctuations in productivity in the equatorial pacific as indicated by marine barite. *Science.* 274, 1355–1357. doi:10.1126/science.274.5291.1355

Planchon, F., Cavagna, A.-J., Cardinal, D., André, L., and Dehairs, F. (2013). Late summer particulate organic carbon export and twilight zone remineralisation in the Atlantic sector of the Southern Ocean. *Biogeosciences.* 10, 803–820. doi:10.5194/bg-10-803-2013

Rivadeneyra, M. A., Martín-Algarra, A., Sánchez-Román, M., Sánchez-Navas, A., and Martín-Ramos, J. D. (2010). Amorphous Ca-phosphate precursors for Ca-carbonate biominerals mediated by *Chromohalobacter marismortui*. *ISME J.* 4, 922–932. doi:10.1038/ismej.2010.17

Robidart, J. C., Magasin, J. D., Shilova, I. N., Turk-Kubo, K. A., Wilson, S. T., Karl, D. M., et al. (2019). Effects of nutrient enrichment on surface microbial community gene expression in the oligotrophic North Pacific subtropical gyre. *ISME J.* 13, 374–387. doi:10.1038/s41396-018-0280-0

Rosengard, S. Z., Lam, P. J., Balch, W. M., Auro, M. E., Pike, S., Drapeau, D., and Bowler, B. (2015). Carbon export and transfer to depth across the Southern Ocean great calcite belt. *Biogeosciences.* 12, 3953–3971. doi:10.5194/bg-12-3953-2015

Ruiz-Agudo, C., McDonogh, D., Avaro, J. T., Schuppa, D. J., and Gebauer, D. (2020). Capturing an amorphous $BaSO_4$ intermediate precursor to barite. *CrystEngComm.* 22, 1310–1313. doi:10.1039/C9CE01555H

Rushdi, A. I., McManus, J., and Collier, R. W. (2000). Marine barite and celestite saturation in seawater. *Mar. Chem.* 69, 19–31. doi:10.1016/S0304-4203(99)00089-4

Sánchez-Navas, A., and Martín-Algarra, A. (2001). Genesis of apatite in phosphate stromatolites. *Eur. J. Mineral.* 13 (2), 361–376. doi:10.1127/0935-1221/01/0013-0361

Sedwick, P. N., DiTullio, G. R., and Mackey, D. J. (1997). Regulation of algal blooms in Antarctic Shelf Waters by the release of iron from melting sea ice. *Geophys. Res. Lett.* 24, 2515–2518. doi:10.1029/2000jc000256

Sedwick, P. N., Marsay, C. M., Sohst, B. M., Aguilar-Islas, A. M., Lohan, M. C., Long, M. C., et al. (2011). Early season depletion of dissolved iron in the Ross Sea polynya: implications for iron dynamics on the Ant- arctic continental shelf. *J. Geophys. Res.* 116, C12019. doi:10.1029/2010JC006553

Smith, H. E. K., Poulton, A. J., Garley, R., Hopkins, J., Lubelczyk, L. C., Drapeau, D. T., et al. (2017). The influence of environmental variability on the biogeography of coccolithophores and diatoms in the great calcite belt. *Biogeosciences.* 14, 4905–4925. doi:10.5194/bg-14-4905-2017

Smith, W. O., Jr., Ainley, D. G., Arrigo, K. R., and Dinniman, M. S. (2014). The oceanography and ecology of the Ross Sea. *Annu. Rev. Mar. Sci.* 6, 469–487. doi:10.1146/annurev-marine-010213-135114

Sternberg, E., Jeandel, C., Robin, E., and Souhaut, M. (2008). Seasonal cycle of suspended barite in the Mediterranean Sea. *Geochem. Cosmochim. Acta.* 72, 4020–4034. doi:10.1016/j.gca.2008.05.043

Sutherland, I., (2001). The biofilm matrix—an immobilized but dynamic microbial environment. *Trends Microbiol.* 9, 222–227. doi:10.1016/S0966-842X(01)02012-1

Sutton, T. T., Clark, M. R., Dunn, D. C., Halpin, P. N., Rogers, A. D., Guinotte, J., et al. (2017). A global biogeographic classification of the mesopelagic zone. *Deep Sea Res. Oceanogr. Res. Pap.* 126, 85–102. doi:10.1016/j.dsr.2017.05.006

Torres-Crespo, N., Martínez-Ruiz, F., González-Muñoz, M. T., Bedmar, E. J., De Lange, G. J., and Jroundi, F. (2015). Role of bacteria in marine barite precipitation: a case study using Mediterranean seawater. *Sci. Total Environ.* 512-513, 562–571. doi:10.1016/j.scitotenv.2015.01.044

Tourney, J., and Ngwenya, B. T. (2014). The role of bacterial extracellular polymeric substances in geomicrobiology. *Chem. Geol.* 386, 115–132. doi:10.1016/j.chemgeo.2014.08.011

Van der Jagt, H., Friese, C., Stuut, J.-B. W., Fischer, G., and Iversen, M. H. (2018). The ballasting effect of Saharan dust deposition on aggregate dynamics and carbon export: aggregation, settling, and scavenging potential of marine snow. *Limnol. Oceanogr.* 63, 1386. doi:10.1002/lno.10779

Weiner, S., Sagi, I., and Addadi, L. (2005). Structural biology: choosing the crystallization path less traveled. *Science.* 309, 1027–1028. doi:10.1126/science.1114920

White, R. A., III, Visscher, P. T., and Burns, B. P. (Forthcoming, 2020). Between a rock and a soft place: the role of viruses in lithification of modern microbial mats. *Trends Microbiol.* doi:10.1016/j.tim.2020.06.004

Wolgemuth, K., and Broecker, W. S. (1970). Barium in sea water. *Earth Planet Sci. Lett.* 8, 372–378. doi:10.1016/0012-821X(70)90110-X

Conflict of Interest: The authors declare that the research was conducted in the absence of any commercial or financial relationships that could be construed as a potential conflict of interest.

frontiers in Earth Science

ORIGINAL RESEARCH
published: 18 November 2020
doi: 10.3389/feart.2020.558823

Late Summer Peak and Scavenging-Dominant Metal Fluxes in Particulate Export Near a Seamount in the Western North Pacific Subtropical Gyre

Kyoko Yamaoka[1], Atsushi Suzuki[1], Yuichiro Tanaka[1], Masahiro Suzumura[2], Ayumi Tsukasaki[2], Akifumi Shimamoto[3], Tatsuo Fukuhara[3], Takaaki Matsui[4†], Shogo Kato[4], Nobuyuki Okamoto[4] and Yoshiaki Igarashi[4]*

[1]Geological Survey of Japan, National Institute of Advanced Industrial Science and Technology, Tsukuba, Japan, [2]Environmental Management Research Institute, National Institute of Advanced Industrial Science and Technology, Tsukuba, Japan, [3]KANSO Co., Ltd., Osaka, Japan, [4]Japan Oil, Gas and Metals National Corporation, Tokyo, Japan

OPEN ACCESS

Edited by:
Makio Honda, Japan Agency for Marine-Earth Science and Technology (JAMSTEC), Japan

Reviewed by:
Jing Zhang, University of Toyama, Japan
Jonaotaro Onodera, Japan Agency for Marine-Earth Science and Technology (JAMSTEC), Japan

***Correspondence:**
Kyoko Yamaoka
k.yamaoka@aist.go.jp

†Present address:
Takaaki Matsui, Marine Biological Research Institute of Japan Co., Ltd., Tokyo, Japan

Specialty section:
This article was submitted to Biogeoscience, a section of the journal Frontiers in Earth Science

Received: *04 May 2020*
Accepted: *16 October 2020*
Published: *18 November 2020*

Citation:
Yamaoka K, Suzuki A, Tanaka Y, Suzumura M, Tsukasaki A, Shimamoto A, Fukuhara T, Matsui T, Kato S, Okamoto N and Igarashi Y (2020) Late Summer Peak and Scavenging-Dominant Metal Fluxes in Particulate Export Near a Seamount in the Western North Pacific Subtropical Gyre. Front. Earth Sci. 8:558823. doi: 10.3389/feart.2020.558823

We measured sedimentation fluxes around JA06 Seamount (Xufu Guyot; 19°30′N, 158°00′E) as part of an environmental baseline survey in Japan's exploration area for cobalt-rich crusts in the subtropical northwest Pacific. Sinking particles were collected at the flat top (sediment trap depths: 900 and 1,000 m) and northeastern base (sediment trap depths: 1,000 and 4,720 m) of the seamount from June 2016 to April 2017. Total mass fluxes were very low, with average values of 4.3–4.9 and 9.3 mg m^{-2} d^{-1} in the shallow traps at the flat top and base, respectively, which is consistent with an oligotrophic system. The lower fluxes at the flat top probably reflect lower productivity of siliceous microplankton, such as diatoms. However, we were unable to substantiate any potential mechanisms for this difference in productivity and cannot evaluate whether this is representative of typical conditions. When combined with previous observations at two adjacent seamounts, our results indicate widespread seasonality in sediment fluxes with a peak in late summer (August–September). However, satellite data indicate that summer is the season with the lowest primary production. This discrepancy could be explained either by phytoplankton blooms fueled by symbiotic nitrogen fixation that only cause minor increases in surface-ocean chlorophyll or short-lived blooms induced by passing typhoons under thick cloud cover. At the base site, we also analyzed material and element transport rates from shallow to deep waters. Half of the organic matter and >80% of the carbonate in sinking particles was not degraded in the water column, suggesting that most of the regeneration of these materials occurs near or on the sediment surface. Furthermore, four major processes appeared to control elemental fluxes in the area: lithogenic (Al, Ti, Fe), carbonate (Mg, Ca, Sr), biogenic (+scavenging) (Ni, Zn, Cd, Pb), and scavenging (V, Mn, Co, Cu, rare earth elements) processes. The estimation of excess flux based on the composition of upper continental crust demonstrated that >85% of total Mn, Co, Ni, Cu, Zn, Cd, and Pb fluxes were attributable to scavenging (+biogenic uptake). Scavenging-dominant metal fluxes are likely ubiquitous in the oligotrophic open ocean.

Keywords: seamount, sinking particle, sediment trap, trace element, scavenging

INTRODUCTION

Deep-sea mining has attracted increased interest in recent years due to rising demand for metallic elements that are crucial for cutting-edge and green technologies. One potential target for deep-sea mining is cobalt-rich ferromanganese crusts, which are marine polymetallic mineral deposits composed of hydrogenetic manganese oxide layers that slowly precipitate on seamount basement rocks. The subtropical Northwest Pacific is considered a prime area for exploration because of the presence of thick crusts on old seamount groups. On the high seas of the northwest Pacific, several countries including Japan, China, Korea, and Russia have already signed exploration contracts for cobalt-rich crusts with the International Seabed Authority (ISA). To minimize environmental impacts from any future deep-sea mining, careful environmental surveys, and assessments are essential. The ISA environmental guidelines (ISBA/25/LTC/6) mandate the study of six environmental baseline data groups: 1) physical oceanography, 2) chemical oceanography, 3) geological properties, 4) biological communities, 5) bioturbation, and 6) fluxes to the sediment.

The subtropical northwest Pacific is strongly oligotrophic. Since seamount ecosystems are mainly sustained by sinking organic matter, fluxes to the sediment are extremely important. Furthermore, a baseline assessment of fluxes and sinking particle compositions around the seamount is necessary to assess the impact of sediment plumes and discharge water from mining activities. Sediment traps are used to quantitatively study the seasonality and vertical transport of sinking particles in the ocean. Sediment trap observations are usually conducted in highly productive regions and have been used to improve marine carbon-cycle modeling (e.g., Ittekkot et al., 1991; Honjo, 1996; Kawahata, 2002). Observations in oligotrophic regions, however, are very limited (see the map compiled by Lutz et al., 2007). Seasonal variations in primary production and resulting export fluxes are generally small in the stratified north Pacific subtropical gyre (e.g., Field et al., 1998). However, enigmatic phytoplankton blooms have been recorded in the eastern north Pacific during the summer, which is the season when the ocean is most stratified (Karl et al., 2001; Wilson, 2003), and subsequent studies have revealed some of the unique mechanisms involving nitrogen fixation that support these blooms (e.g., Dore et al., 2008; Karl et al., 2012). Many knowledge gaps about fundamental processes in the oligotrophic open ocean remain unaddressed today, such as the influence of large seamounts on particulate fluxes, relationships between primary production and export fluxes, differences in particle composition between shallow and deep water, and particulate elemental fluxes from the shallow ocean to seafloor.

In 2016, four sediment traps were deployed and moored for a year on the flat top and base of JA06 seamount (Xufu Guyot) in the ISA-licensed area as part of an environmental baseline survey. In this paper, we discuss ISA baseline data group six (fluxes to the sediment) based on spatial/seasonal differences in flux rate and chemical compositions of sinking particles. Other environmental baseline data we obtained in the vicinity of the seamount have been reported elsewhere (Nagao et al., 2018; Sugishima et al., 2018; Iguchi et al., 2020; Yamaoka et al., submitted).

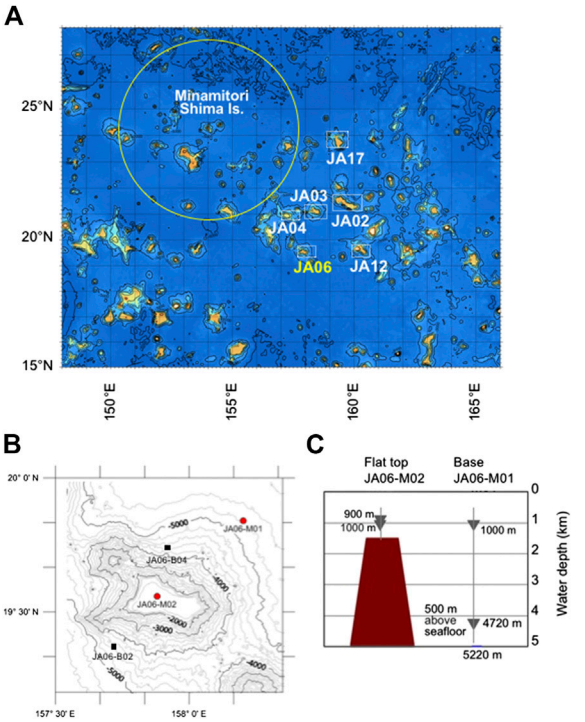

FIGURE 1 | (A) Map of Japan's exploration area for cobalt-rich ferromanganese crusts, covering six seamounts (JA02, 03, 04, 06, 12, and 17) southeast of Minamitori Shima Island (also known as Marcus Island) in the northwest Pacific. Yellow circle indicates Japan's exclusive economic zone (EEZ). **(B)** Bathymetry of JA06 Seamount showing locations of mooring sites JA06-M01 and M02 (red circles) and sampling sites for deep-sea sediments (pelagic clay) (black squares; JA06-B02 and B04). **(C)** Deployment depths of sediment traps used in our study.

MATERIALS AND METHODS

Sediment Trap Experiments

JA06 seamount (Xufu Guyot; 19°30′N, 158°00′E) is a large Guyot located in international waters in the northwest Pacific (**Figure 1**). The seamount summit has a depth of ~1,500 m, and the rise is located at >5,000 m. JA06 seamount is the southernmost of six seamounts located within Japan's exploration area for cobalt-rich ferromanganese crusts, and it is located within the oligotrophic subtropical gyre throughout the year. According to CTD measurements taken around the seamount in May 2016, surface water temperature and salinity are 27.7°C and 34.8, respectively; there were no marked differences between water column profiles taken at the flat top and base (Yamaoka et al., submitted).

Time-series sediment traps (SMD-26S, NiGK Corporation, Tokyo, Japan) comprising 22 sample bottles, each with a 0.5 m^2 inlet aperture, were moored to the seafloor at two sites. Site JA06-M01 was located on the northeastern side of the seamount at the seamount base (water depth, 5,220 m), and site JA06-M02 was located on the flat top (water depth, 1,270 m). Two traps were deployed at each site. At site JA06-M01, traps were deployed at depths of 1,000 m ("Shallow-3") and 4,720 m ("Deep-1"). The deep trap was located 500 m above the seafloor. At site JA06-M02, traps were deployed at 900 m ("Shallow-1") and 1,000 m ("Shallow-2"). According to the pressure data of sensors attached to the sediment traps, the actual water depths of Shallow-2, Shallow-3, and Deep-1 traps were 990, 839, and 4,792 m, respectively. Before deployment, all sample bottles were filled with filtered seawater (filter pore size: 0.45 μm). Formaldehyde was then added to produce a 3% solution buffered with sodium borate. Traps were deployed at site JA06-M01 from June 7, 2016 to April 20, 2017 (318 days) and at site JA06-M02 from June 7, 2016 to April 21, 2017 (319 days). Sampling interval (sampling period per one collecting cup) was 15 days. Upon recovery, sample bottles were immediately refrigerated at about 4°C onboard the vessel.

Analytical Procedures

The trapped material was carefully wet-sieved through a 1-mm sieve after all recognizable zooplankton swimmers were removed. The <1 mm fraction was freeze-dried and homogenized in preparation for bulk analysis. Carbonate and opal contents were determined by using modified versions of methods developed by Engleman et al. (1985) and Mortlock and Froelich (1989). For each sample, total carbon and nitrogen contents were measured with an elemental analyzer (Flash 2000, Thermo Scientific, Waltham, MA, USA), and then organic carbon content was calculated by subtracting carbonate content from total carbon content. The amount of lithogenic matter in each sample was calculated as follows: Lithogenic matter = total matter − carbonate − opal − organic matter (where organic matter was assumed to be 1.8 × organic carbon content, Kawahata et al., 2000). For elemental analysis, ~5 mg of the powdered sample was weighed in a Teflon vial and completely digested in an ultrapure HNO_3-HF-$HClO_4$ mixture. After the sample was dried down, the residue was dissolved in 2% HNO_3. Concentrations of major elements (Na, Mg, Al, P, K, Ca, Fe) were measured by using inductively coupled plasma atomic emission spectroscopy (ICP-AES SPS7800, Seiko Instruments, Chiba, Japan). Concentrations of trace elements were determined by using inductively coupled plasma mass spectroscopy (ICP-MS 7700x, Agilent Technologies, Santa Clara, CA, USA) combined with the indium internal standard technique. Analytical precision was better than 7% for each elemental analysis, except for the Na, K, and Ti analyses, which had an analytical precision of 10%.

Satellite Data Processing

Ocean color data, including chlorophyll *a* concentration, photosynthetically active radiation, and sea surface temperature were obtained from the Moderate Resolution Imaging Spectroradiometer (MODIS) mounted on the aqua satellite through NASA's ocean color Web. The Aqua satellite passes over the equator from south to north in the afternoon, and aqua MODIS views the entire surface of the Earth every 1 to 2 days, acquiring data in 36 spectral bands or wavelength groups. Further details on data collection are compiled in **Table S1**. To estimate depth-integrated monthly-averaged net primary production (NPP), defined as the difference between gross photosynthetic production rate and respiration rate, the Vertically Generalized Production Model (Behrenfeld and Falkowski, 1997) was used in combination with the two-phytoplankton community model of Kameda and Ishizuka (2005).

RESULTS AND DISCUSSION

Sinking Particles in the Shallow Traps on and Around the Seamount

At Site JA06-M02 (on the flat top), mean total mass fluxes were 4.3 and 4.9 mg m^{-2} d^{-1} for traps Shallow-1 (900 m) and Shallow-2 (1,000 m), respectively (**Table 1**). For Shallow-1, mean fluxes of organic matter, carbonate, biogenic opal, and lithogenic matter were 0.5, 3.7, 0.1, and 0.4 mg m^{-2} d^{-1}, respectively, and the corresponding mean contents were 11%, 78%, 2%, and 9%. C/N atomic ratios for most of the samples were about seven. Mean opal/carbonate and C_{org}/C_{inorg} ratios were 0.03 and 0.67, respectively. Samples from Shallow-2, which was deployed at a similar depth, had similar characteristics.

At Site JA06-M01 (on the northeastern side of the seamount base), mean total mass fluxes were 9.3 mg m^{-2} d^{-1} for trap Shallow-3 (1,000 m; **Table 1**). Mean fluxes of organic matter, carbonate, biogenic opal, and lithogenic matter for this trap were 1.7, 5.7, 0.7, and 1.2 mg m^{-2} d^{-1}. Mean contents of organic matter, carbonate, biogenic opal, and lithogenic matter were 18%, 62%, 7%, and 13%, respectively. C/N atomic ratios for most of the samples were about 8. Mean opal/carbonate and C_{org}/C_{inorg} ratios were 0.12 (mass ratio) and 1.4 (molar ratio), respectively.

These obtained total mass fluxes were the lowest among reported sediment trap observations in the global ocean and comparable to the mass flux of 4.8 mg m^{-2} d^{-1} obtained at 1,200 m water depth in the western Pacific below the north equatorial current (Kempe and Knaack, 1996), with similar mean percentage composition (15% organic matter, 70% carbonate, 9% biogenic opal, and 6% lithogenic matter). In the shallow traps at both sites around JA06 Seamount, seasonal variations in total mass fluxes showed similar patterns (**Figures 2A–C**, **Table S2**). However, average total mass fluxes at the base site were twice as large as those at the flat top site. One possible explanation is that the two sites have different rates of primary production; sinking fluxes roughly correspond to production rate in the surface ocean. Previous studies have posited the existence of a "seamount effect," in which local upwelling caused by circular currents at the seamount summit

TABLE 1 | Mean fluxes, average compositions, and ratios (C/N, opal/carbonate, and C_{org}/C_{inorg}) of sinking particles collected at JA06 seamount.

Trap site	Seafloor depth (m)	Trap depth (m)	Duration (days)	Fluxes (mg m^{-2} d^{-1})					% of total				C/N (mol/mol)	Opal/carbonate (wt./wt.)	C_{org}/C_{inorg}
				Total	Organic matter	Carbonate	Opal	Lithogenic	Organic matter	Carbonate	Opal	Lithogenic			
Shallow-1	1,270	900	319	4.3	0.5	3.7	0.1	0.4	11	78	2	9	7.0	0.03	0.67
Shallow-2	–	1,000	315[a]	4.9	0.5	4.3	0.1	0.5	9	79	2	10	6.8	0.03	0.53
Shallow-3	5,220	1,000	300[a]	9.3	1.7	5.7	0.7	1.2	18	62	7	13	7.9	0.12	1.4
Deep-1	–	4,720	318	8.6	0.9	4.9	1.5	1.4	11	55	17	17	9.9	0.32	0.96

[a]*The last one or two sample bottles were excluded due to contamination by swimmers.*

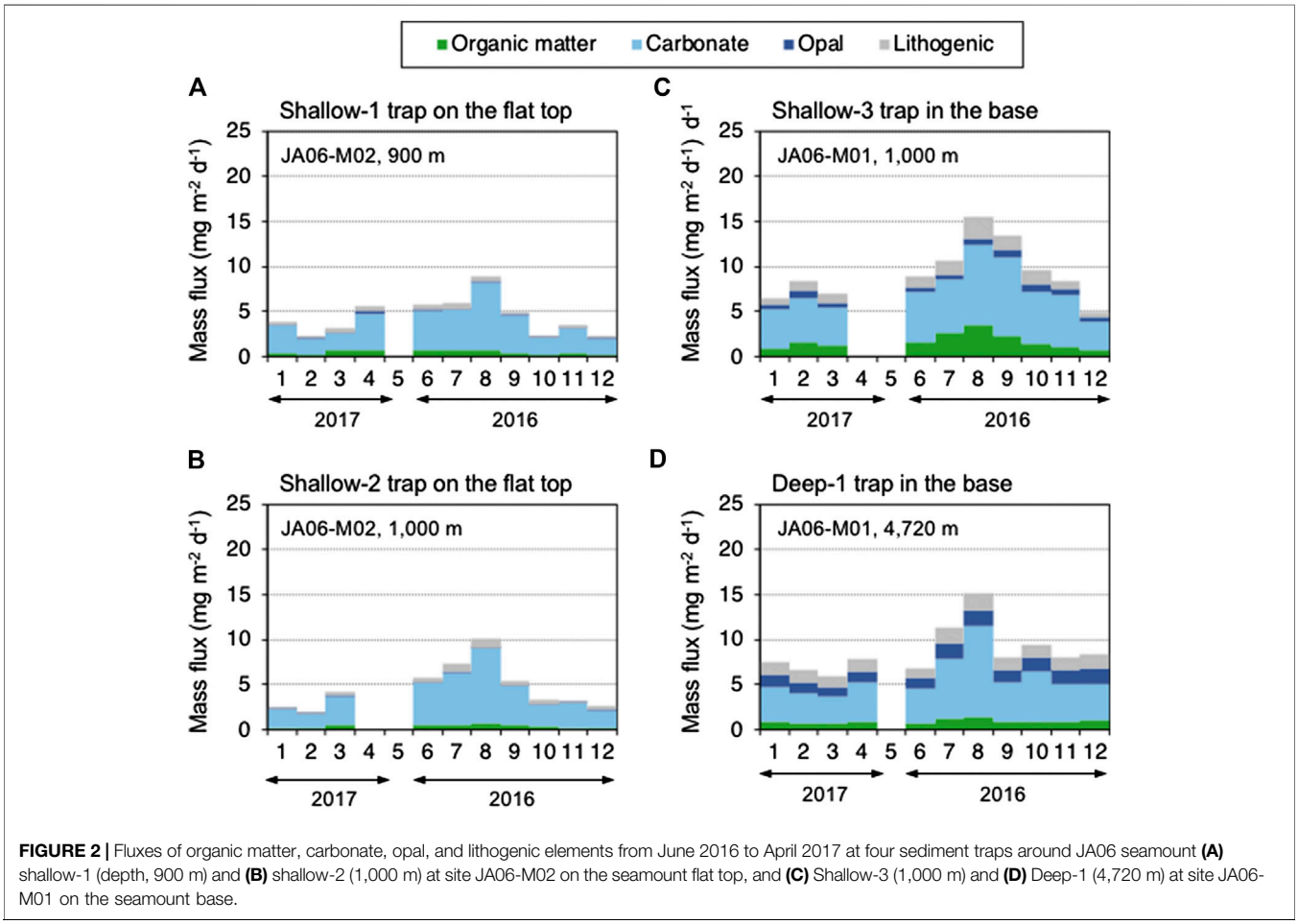

FIGURE 2 | Fluxes of organic matter, carbonate, opal, and lithogenic elements from June 2016 to April 2017 at four sediment traps around JA06 seamount **(A)** shallow-1 (depth, 900 m) and **(B)** shallow-2 (1,000 m) at site JA06-M02 on the seamount flat top, and **(C)** Shallow-3 (1,000 m) and **(D)** Deep-1 (4,720 m) at site JA06-M01 on the seamount base.

can boost primary production (Furuya et al., 1995; Oliveira et al., 2016; Turnewitsch et al., 2016). This effect, however, is inconsistent with the lower primary productivity at the flat top inferred from the sinking fluxes in this study. In fact, seamount effects have only been reported for seamounts with shallow summits (<300 m depth). Due to the much greater depth at the summit of JA06 seamount (~1,500 m), any interaction between the seamount and ocean currents might have little effect on surface ocean structure. This is supported by physicochemical parameters (temperature, salinity, dissolved oxygen, and inorganic nutrient concentrations) measured around the seamount in May, which showed no obvious differences in the vertical profiles measured at the flat top and base (Yamaoka et al., submitted).

Organic matter C/N ratios were similar (around 7–8) in both flat-top traps and in Shallow-3 (the shallow trap at the base site).

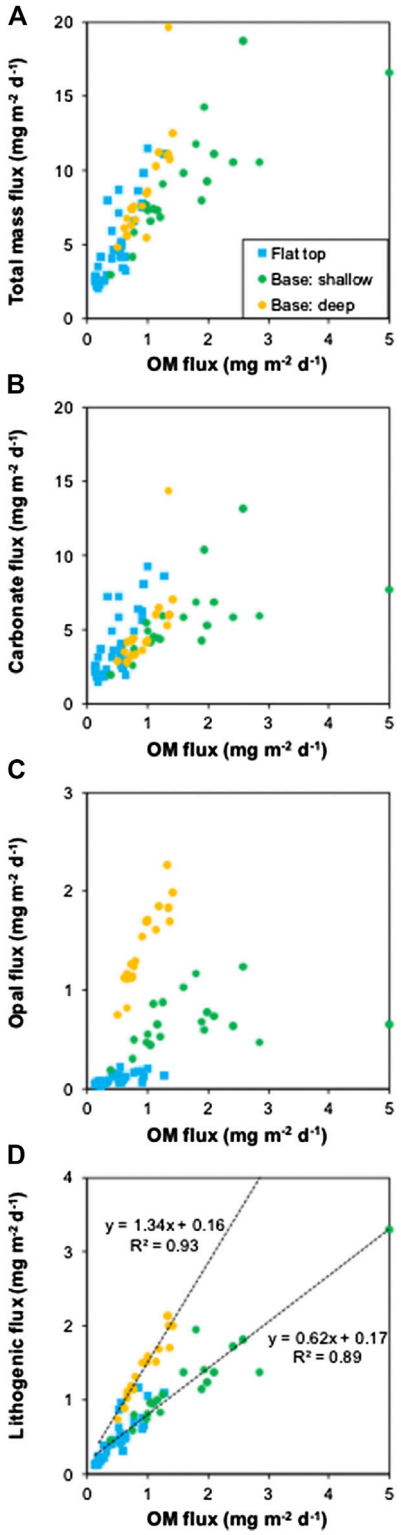

FIGURE 3 | Organic matter (OM) flux vs. **(A)** total mass, **(B)** carbonate, **(C)** opal, and **(D)** lithogenic fluxes. Dashed lines show regression lines for data from shallow and deep sediment traps.

This range is consistent with the C/N ratios of living marine phytoplankton (6.6–7.0; Redfield et al., 1963; Takahashi et al., 1985). However, Shallow-3 had an elevated opal/carbonate ratio (0.12) and C_{org}/C_{inorg} ratio (1.4) compared to the flat-top traps (opal/carbonate ratio, 0.03; C_{org}/C_{inorg} ratio, 0.53–0.67). This suggests that settling organic matter is also associated with other materials besides carbonate.

Figure 3 shows relationships between organic matter flux and fluxes of various components (carbonate, biogenic opal, and lithogenic), as well as total flux, at all the sediment traps. The larger organic matter flux observed in Shallow-3 is associated with increased opal and lithogenic fluxes (**Figures 3C, D**). The lithogenic fraction at sediment traps in the north Pacific is mainly composed of fine clay minerals, which originate in eolian dust transported from the Asian continent by westerly winds (Kawahata, 2002). Atmospheric dust concentrations peak in spring across wide areas of the north Pacific, reflecting frequent dust storms in the source region, with the greatest concentrations occurring at mid-latitudes (Uematsu et al., 1983). However, lithogenic fluxes at JA06 Seamount were relatively low in spring, suggesting small loads and little seasonality of atmospheric dust. Since secular differences in atmospheric input between flat top and base sites are unlikely, lithogenic fluxes probably depend on organic matter flux.

Planktic organisms such as diatoms are known to play an important ballasting role in particulate organic carbon transport due to their propensity to form aggregates and sink rapidly (Smetacek, 1985; Honda and Watanabe, 2010). A two-year observation timeseries at station ALOHA in the oligotrophic north Pacific subtropical gyre demonstrated that diatoms account for only 3–7% of annual primary production but support 9–20% of organic carbon flux at 150 m (Brzezinski et al., 2011). Radiolarians and phaeodarians are another major siliceous microplankton taxon. Although rates of organic carbon export by them have not been quantitatively estimated, it is likely that they also effectively transport organic carbon downward due to their larger size. The mean contents of organic matter, biogenic opal, and lithogenic matter in Shallow-3 were 9%, 5%, and 3% higher, respectively, than in the flat-top traps. By contrast, the mean carbonate content was 17% lower (**Table 1**). Despite the fact that biogenic opal was the smallest constituent of the sinking particles, its efficient vertical transport capacity seems to contribute greatly to total mass fluxes. Based on these observations, we speculated that growth rates of siliceous microplankton may be constrained at the flat top site. However, the environmental basis of this constraint is unclear. Further comparative studies are needed to clarify the mechanisms controlling primary production and particulate fluxes on and off the seamount.

Seasonality of Sinking Particles in Japan's Exploration Area

In **Figure 4**, the total mass fluxes at all three shallow traps at JA06 seamount are compared with those from two other seamounts in Japan's exploration area. The first sediment trap experiment conducted within the area was conducted on the flat top of

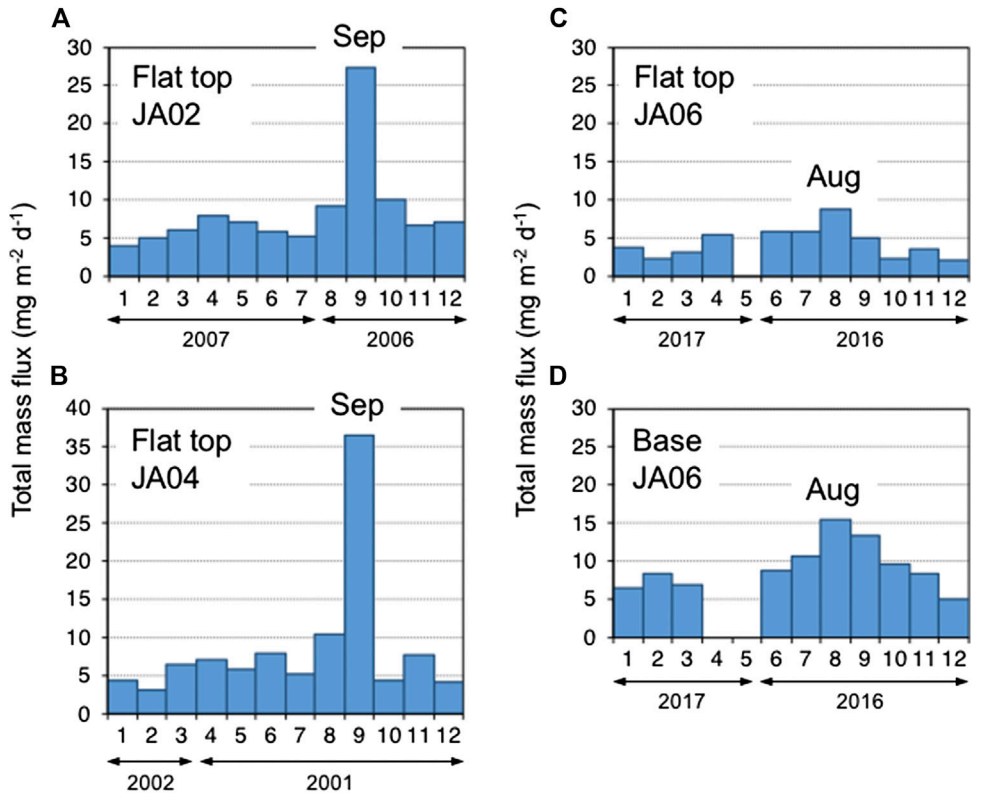

FIGURE 4 | Seasonal variations in total mass fluxes at shallow sediment traps on the **(A)** JA02, **(B)** JA04, and **(C,D)** JA06 seamounts in Japan's exploration area. Three-letter month designations show the month of peak flux for each sediment trap.

JA04 seamount (20°50′N, 157°18′E; water depth 2,257 m), where a single trap was deployed 23 m above the seafloor from April 8, 2001 to May 18, 2002. Another sediment trap was deployed above the flat top of JA02 Seamount (21°19′N, 159°47′E; water depth 1,600 m), where a single trap was deployed 23 m above the seafloor from August 5, 2006 to July 31, 2007. The results from these two seamounts showed a similar low total mass flux with a strong peak in September. These observations suggest that low total mass fluxes with late summer peaks are common in Japan's exploration area in the north Pacific subtropical gyre. The range of total mass fluxes observed in our study is similar to those observed in the oligotrophic region under influence of the equatorial counter current. Kawahata et al. (2000) reported a mean total mass flux of 13.2 mg m^{-2} d^{-1} at their site 4 (8°N, 175°E; water depth 1,637 m), although they did not observe any seasonal patterns.

Interestingly, the observed seasonality in total mass fluxes is inconsistent with satellite-based estimates of NPP in the area. This is an important inconsistency that needs to be addressed. **Figure 5** shows monthly average NPP at three seamounts (JA02, JA04, and JA06) estimated by using a 17-year timeseries (July 2002 to October 2018) of NASA Aqua/MODIS data. The estimated NPP varied seasonally, with an early spring bloom from February to May. This early spring bloom may be related to broader and lower-amplitude peaks in total mass fluxes observed around April in sediment traps at JA02 Seamount (**Figure 4**). Kawahata (2006) reported one broad maximum from January through March in total mass fluxes obtained from a sediment trap (site 6; 30°N, 175°E; water depth 3,873 m). However, the August to October NPP minimums estimated from the satellite data conflict with the late summer peaks in total mass flux observed at JA02, JA04, and JA06 seamounts.

On the basis of a global-scale compilation of sediment trap experiments, Lutz et al. (2007) found that sediment flux maxima are generally synchronous with peaks in primary production and that the oligotrophic subtropical gyres in the Pacific, where production is relatively constant year-round, are characterized by reduced seasonality. Indeed, seasonal maximum-to-minimum monthly flux ratios in the shallow traps on and around JA06 Seamount ranged from 2 to 3. This is clearly lower than the ratios observed at high latitudes and in polar regions, where maximum-to-minimum (summer to winter) flux ratios are ~20 (Lutz et al., 2007). However, it is still unclear why we obtained very high maximum-to-minimum flux ratios (6–10) on JA04 and JA02 seamounts.

The late summer phytoplankton booms and subsequent particle export pulses appear to be a recurring phenomenon in the oligotrophic eastern north Pacific, especially to the northeast of the Hawaiian islands (Karl et al., 2001; Wilson, 2003). The blooms are not associated with deep mixing events or with dust deposition (Wilson, 2003), but rather are fueled by N_2 fixation by

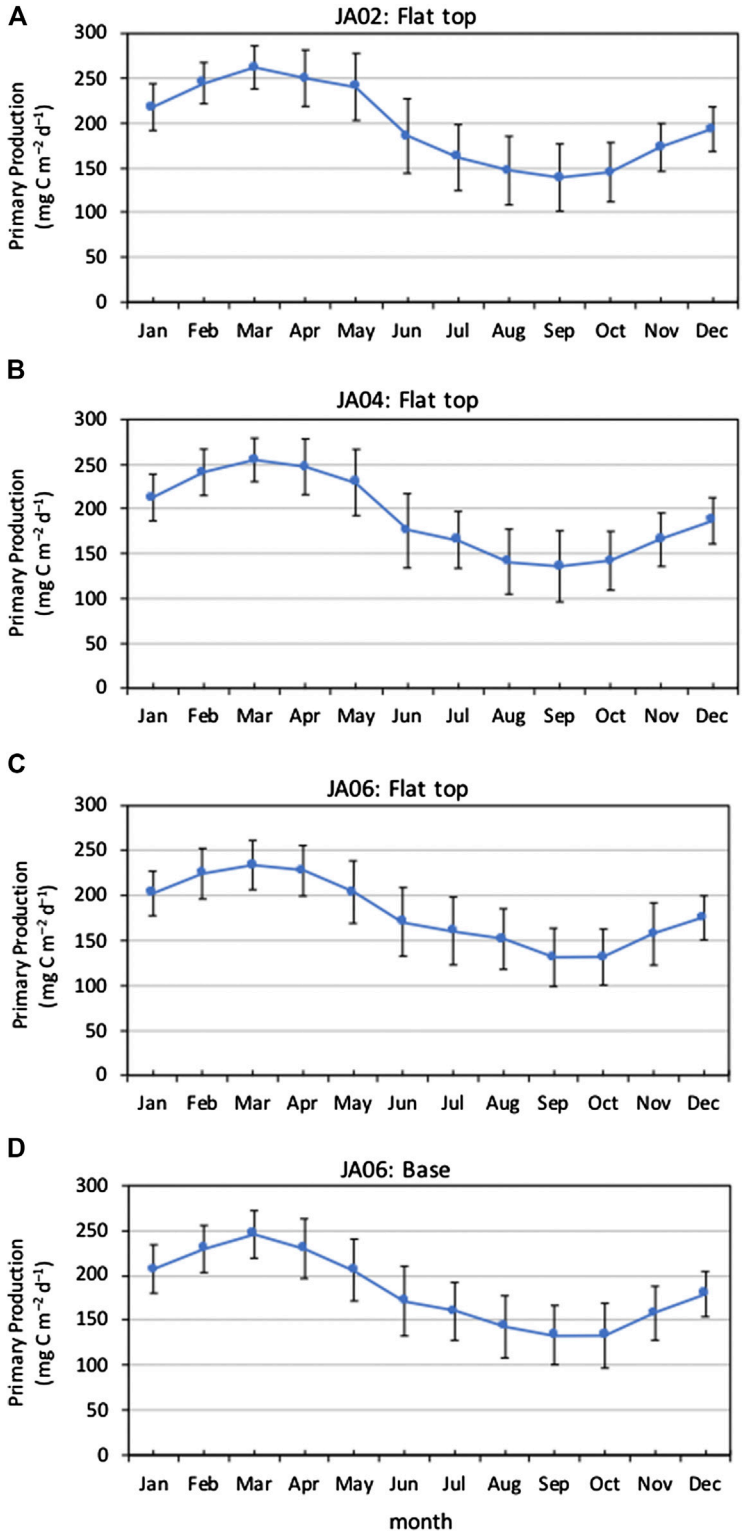

FIGURE 5 | Annual climatology of satellite-based net primary production for the period 2002–2018 around the **(A)** JA02, **(B)** JA04, and **(C,D)** JA06 seamounts.

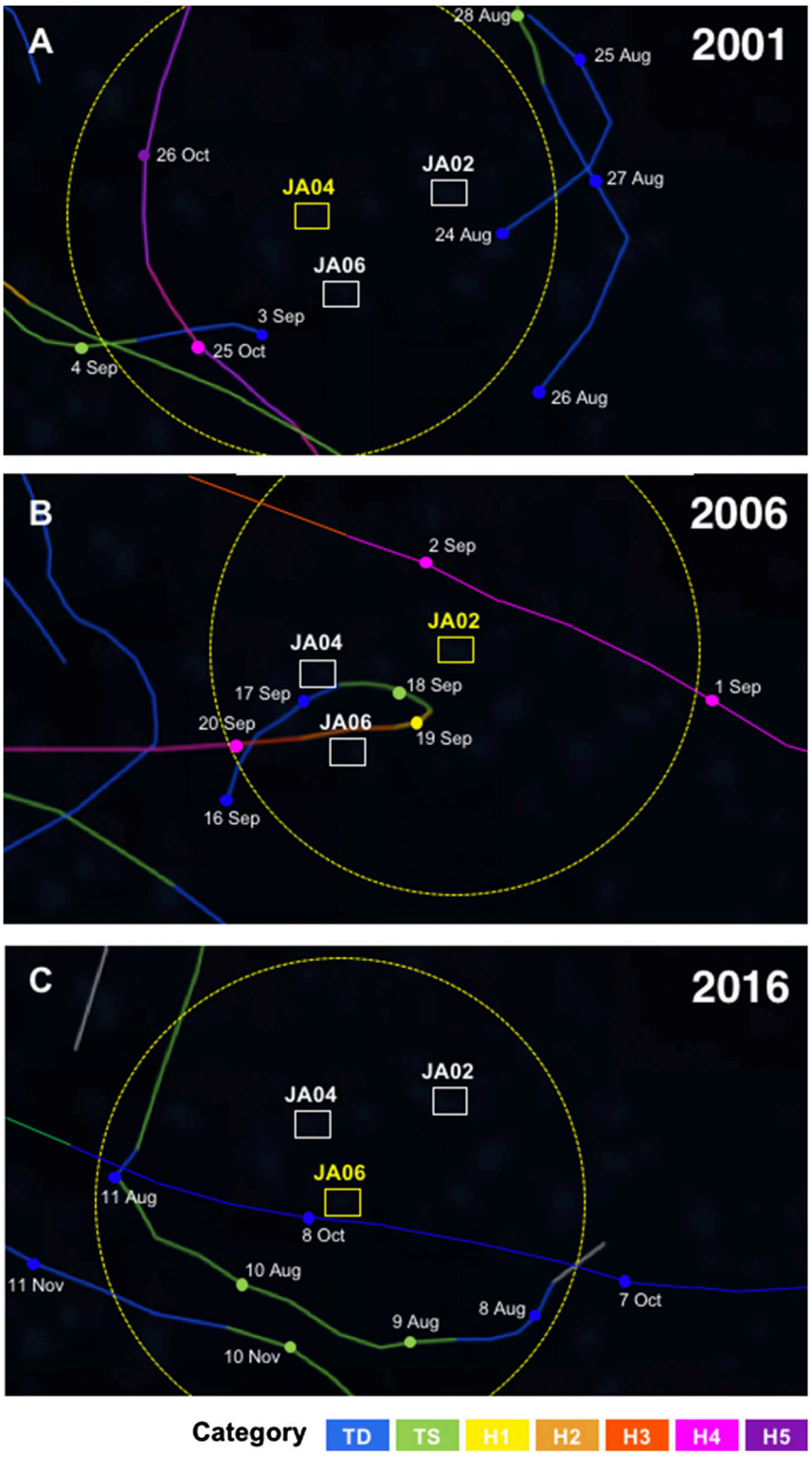

FIGURE 6 | Tracks of hurricanes (typhoons) passing through Japan's exploration area in **(A)** 2001 **(B)** 2006, and **(C)** 2016. Data are from NOAA's historical hurricane tracks (https://coast.noaa.gov/hurricanes/). TD: tropical depression, TS: tropical storm, H1–H5: hurricanes of category 1–5 on the Saffir–Simpson scale. For each year, the seamount where sediment trap observations were conducted is highlighted in yellow. Yellow dashed-line circle indicates radius 500 km from the highlighted seamount.

Trichodesmium and/or diatom–cyanobacteria symbiosis assemblages and nitrogen influx to the euphotic zone from vertical diatom migrations (Wilson et al., 2008; Church et al., 2009; Karl et al., 2012). When analyzing satellite remote sensing data on ocean color, Wilson (2003) used a threshold of chlorophyll *a* concentration >0.15 mg m^{-3} to define a bloom. Based on this definition, blooms have never been observed in the western north Pacific subtropical gyre (Wilson et al., 2008; Wilson and Qiu, 2008). A shallower nutricline and convergent surface conditions in the eastern gyre are considered to be more favorable for the accumulation of buoyant organisms and nitrogen fixers (Dore et al., 2008; Wilson et al., 2008). However, summer blooms are not always detected by satellites and do not always reach the arbitrary 0.15 mg m^{-3} chlorophyll threshold (White et al., 2007; Villareal et al., 2011). Furthermore, Karl et al. (2012) concluded that there is no direct coupling between the appearance of increased surface chlorophyll and the summertime export pulse, based on analysis of a 13-year sediment trap dataset obtained at Station ALOHA (22°45′N, 158°W). Therefore, it is possible that the late summer peak of total mass fluxes observed in this study reflects blooms supported by N_2 fixation that are invisible to satellite observation, although the trigger for these blooms has not yet been thoroughly resolved.

Alternatively, the presence of unusual seasonal peaks in sedimentation fluxes invokes the possibility of an episodic climate event. In late summer, our study area is frequently influenced by hurricanes and tropical depressions. According to historical hurricane tracks obtained from NOAA (**Figure 6**), a tropical depression formed 450 km east-southeast of JA06 seamount on August 8, 2016, then developed into a tropical storm the next day and moved in a clockwise direction from southeast to west around 200–350 km off the seamount over a period of 4 days. Although one more tropical depression quickly passed by the seamount on 7–8 October, its impact would have been limited. The numerical simulations suggested that typhoon-induced blooms in the western north Pacific depend on the moving speeds of typhoons, that is, slow-moving typhoons induce stronger upwelling and vertical mixing (Shibano et al., 2011; Lin, 2012). From 16 to September 19, 2006, a tropical depression rapidly developed into an H3 hurricane 100–350 km southwest of JA02 seamount. In 2001, from the end of August to early September, three tropical depressions appeared 240–600 km south, southeast, and east of JA04 seamount. Hurricane (typhoon)-induced blooming is well established, although its impact on sinking particle flux is still unknown. Strong upper-ocean mixing by intense typhoon winds and the upwelling of nutrient-rich waters have been proposed as a mechanism for storm-induced blooms (Price, 1981; Dickey et al., 1998; Lin et al., 2003; Sanford et al., 2011). Especially, many typhoons-induced phytoplankton blooms have been reported as enhancement of chlorophyll *a* concentration and sea surface temperature cooling of −2 to −7°C in the south China sea (Sun et al., 2010; Lin, 2012; Ye et al., 2013; Zhao et al., 2015; Liu and Tang, 2018; Wang et al., 2020). Based on analyses of satellite data in the subtropical northwest Pacific, Lin (2012) proposed that typhoon-induced phytoplankton blooms require intense wind speed, sufficiently long transit time, and the absence of a warm ocean eddy. A recent study also suggested that heavy rainfall from typhoons could enhance blooming (Lin and Oey, 2016). In addition to the fact that heavy cloud cover inhibits satellite observation, the local and short-lived nature of these blooms may hinder their detection in average monthly NPP data. It is also important to consider the possibility of subsurface phytoplankton bloom. Subsurface chlorophyll *a* maximum (SCM) has been observed frequently in tropical and subtropical oceans. Ye et al. (2013) showed that subsurface chlorophyll *a* bloom was stronger and lasted longer than the surface chlorophyll *a* bloom after the passage of a typhoon in the south China sea. The physical-biogeochemical coupled model supported increase in the chlorophyll *a* lasted for longer in the subsurface layer than in the surface layer (Pan et al., 2017). According to Honda et al. (2018), in the western Pacific subtropical gyre, mesoscale cyclonic eddies enhanced subsurface primary productivity resulting in increase in sinking particle flux. It is likely that such responses of the subsurface chlorophyll *a* were invisible from satellite.

Material Transport From Shallow to Deep

In trap Deep-1 (depth, 4,720 m) at site JA06-M01 (on the northeastern side of the seamount base), mean total mass flux was 8.6 mg m^{-2} d^{-1} (**Figure 2D**). Mean fluxes of organic matter, carbonate, biogenic opal, and lithogenic matter were 0.9, 4.9, 1.5, and 1.4 mg m^{-2} d^{-1}, respectively. Mean contents of organic matter, carbonate, biogenic opal, and lithogenic matter were 11%, 55%, 17%, and 17%, respectively. C/N atomic ratios for most of the samples were about 10. Mean opal/carbonate and C_{org}/C_{inorg} ratios were 0.32 (mass ratio) and 0.96 (molar ratio).

Compared to the shallow trap (Shallow-3), organic matter and carbonate fluxes in the deep trap were low and fluxes of lithogenic matter were almost the same. This is due to the degradation of organic matter and dissolution of carbonate in the water column. Organic matter fluxes correlated more closely with lithogenic fluxes (**Figure 3D**), suggesting an important role of atmospheric dust in downward organic matter transport. The slope of the regression between organic matter and lithogenic fluxes was steeper for the deep trap than for other traps around the seamount (**Figure 3D**). Assuming settling speeds of 160–200 m day^{-1} (e.g., Takahashi, 1986), degradation would decrease organic matter flux from depths of 1,000–4,720 m by half within 19–23 days. The elevated C/N ratio of ~10 at the deep trap is also attributable to organic matter degradation because of the preferential decomposition of organic nitrogen compounds relative to organic carbon. As for carbonate, only 14% of the carbonate at 1,000 m dissolved before leaching at 4,720 m. The local carbonate compensation depth in the area occurs at 4,000–4,500 m (Pälike et al., 2012). Although calcium carbonate solubility (Ω) falls to less than 1 (i.e., is undersaturated) at depth due to the large pressure effect (Kawahata et al., 2019), the dissolution rate of carbonate minerals is likely to be much slower than the sinking speed of settling particles. Surface sediments collected from the base of JA06 seamount (St. B02; water depth 5,009 m) were composed of pelagic clay and contained only 0.1 wt% of total organic carbon (=1.8 wt% organic matter) and 0.5 wt% of carbonate (Yamaoka et al., submitted). Thus, the remaining >50% of organic matter and >80% of carbonate would have degraded or dissolved near or

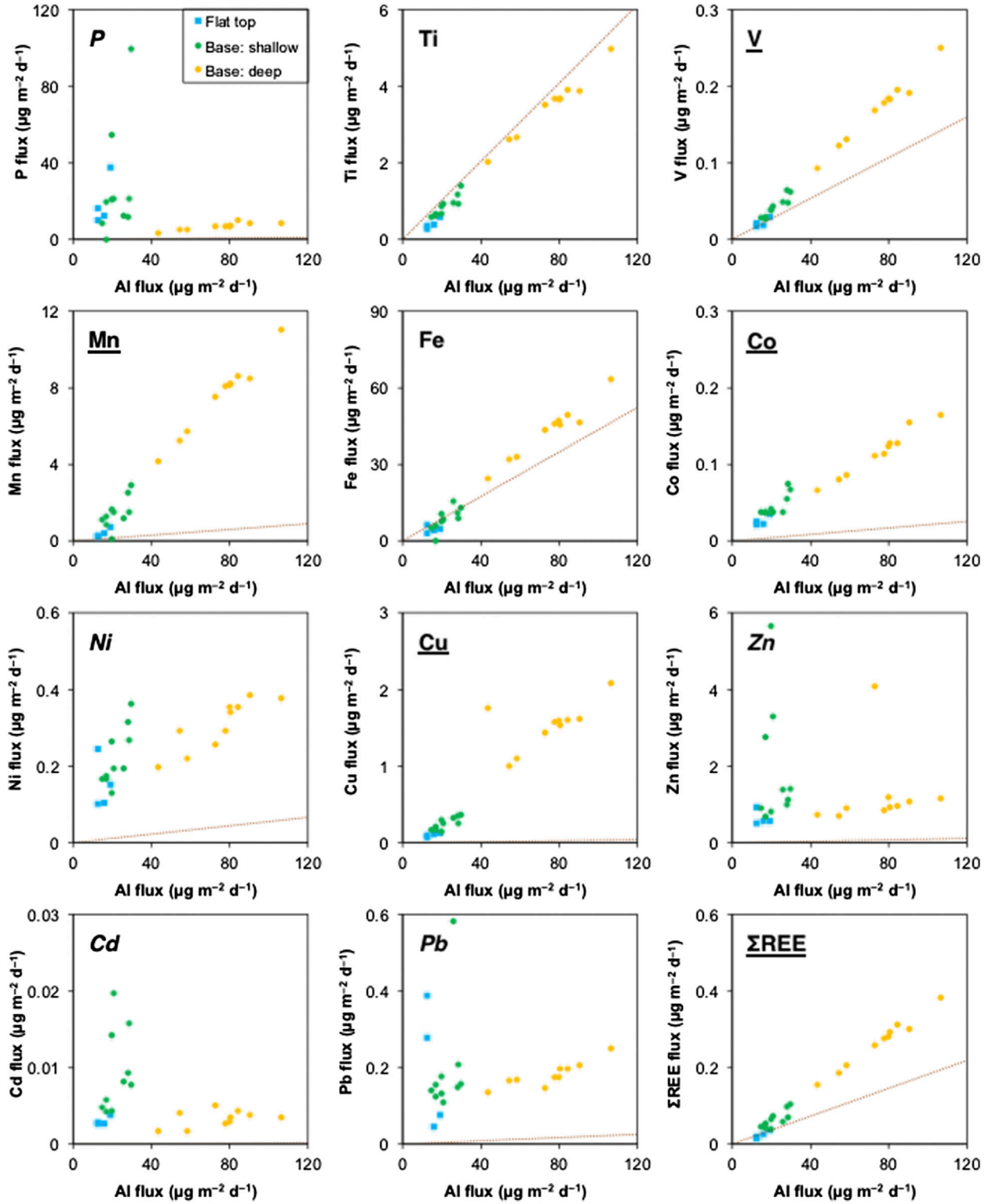

FIGURE 7 | Correlations between trace element and Al fluxes in sediment trap samples from JA06 Seamount. Dashed lines indicate average ratios in upper continental crust (McLennan, 2001). Element names in individual figures with bold, italic, and underline indicate the belonging to lithogenic, biogenic, and scavenging groups, respectively.

on the seafloor. This is consistent with work by Noriki and Tsunogai (1986), which suggested that the regeneration of biogenic particles occurs mainly in the bottom water and at the sediment surface.

The high biogenic opal content in the deep trap is difficult to interpret. Some species of radiolarians inhabit intermediate (200–1,000 m) and deep water (>1,000 m) (e.g., Yamashita et al., 2002). It is likely that the deep trap collected radiolarian shells from these depths.

Elemental Fluxes From Shallow to Deep

Figure 7 shows the relationships between Al and trace element fluxes. The slopes for Ti and Fe are close to the mean values for upper crustal rock (McLennan, 2001), suggesting a lithogenic origin for these elements. On the other hand, Ni, Zn, Cd, and Pb showed elevated fluxes with large variations in the shallow traps. These characteristics resemble P fluxes, implying that these elements are closely related to organic matter. The nutrient-like behaviors of Ni, Zn, and Cd and their correspondence to biogenic flux have been reported in the northeast Atlantic (Kuss and Kremling, 1999; Kuss et al., 2010) and the central Baltic Sea (Pohl et al., 2004). Although the interaction of Pb with sinking particles is still unclear, Pb could be intensively absorbed onto organic matter particles (Schüßler et al., 1997; Pohl et al., 2004). The regression of V, Mn, Co, Cu, and ΣREE fluxes with Al also had elevated slopes. In contrast to the biogenic elements (Ni, Zn, Cd, and Pb), however, fluxes of these elements in the shallow and deep traps were continuously correlated with Al fluxes. These observations suggest that scavenging onto lithogenic materials is the primary process that controls fluxes of these elements.

Although scavenging behaviors of these elements are well known, they have never been detected from the chemical compositions of sinking particles except for Mn due to the large contribution of lithogenic materials. Kuss and Kremling (1999) found a large excess flux of Mn in the deep northeast Atlantic (from 33 to 54°N at ~20°W) but did not observe a corresponding enrichment of elemental fluxes. Similarly, excess Mn fluxes in the northwest Pacific (47°N, 160°E) did not coincide with any elemental fluxes (Lamborg et al., 2008). This is because these Mn enrichments were derived from lateral Mn input from a nearby continental shelf. In contrast, our study area is far from continental shelves. Therefore, scavenging is the dominant process. That is, dissolved Mn in seawater is scavenged onto suspended fine aluminosilicate (i.e., clay mineral) particles and metals are absorbed onto the Mn oxide coating. Then, the Mn-enriched suspended matter is incorporated into sinking particles. The positive correlations between biogenic elemental fluxes (i.e., Ni, Zn, Cd, and Pb) in the deep trap (**Figure 7**) suggest that these elements are also affected by scavenging processes. Previous studies have posited the existence of biological Cu and Co uptake (Saito and Moffett, 2002; Lamborg et al., 2008; Sun et al., 2016). However, the relative impacts of such processes in the removal of elements seems small compared to scavenging in our study area. Although Hwang et al. (2010) suggested that the resuspension of sediments is widespread, especially near continental margins, the direct contribution of resuspended sediments is negligible in our study area. In fact, the chemical composition of sediments in the area is distinct from that of the observed Mn-enriched fraction in sinking particles. As shown in **Table 2**, pelagic clays collected from the base of JA06 Seamount have greater Mn/Al, Co/Al, and Ni/Al ratios by factors of 2–3 than the deep trap samples. Furthermore, the consistent correlations between the shallow and deep traps observed for scavenging elements (V, Mn, Co, Cu, and REE) indicate that the source of the Mn-enriched fraction is independent of distance from the seabed. Loading of resuspended sediments to both the shallow and deep traps is unlikely.

We also compared average element fluxes between the shallow and deep traps at Site JA06-M01 (**Table 2**). Based on the ratio of deep trap/shallow trap fluxes (D/S), the elements can be divided into three groups as follows: group 1: P, Zn, Cd, Pb (D/S < 1); group 2: Mg, Ca, and Sr (D/S = 1); group 3: Al, Ti, V, Mn, Fe, Co, Ni, Cu, and ΣREE (D/S > 1). The group 1 elements correspond to biogenic elements and are characterized by biological uptake and/or adsorption onto organic matter in surface water and low rates of transport to deep waters due to organic matter degradation. These elements (except for P) are also influenced by scavenging, but recycling processes are predominant. The group 2 elements are carbonate elements, which are major and minor of ions of biogenic calcite. The refractory behaviors of these elements are consistent with the low rate of carbonate dissolution in sinking particles, as discussed above. The group 3 elements have larger fluxes in the deep trap, which results from the incorporation of suspended Mn-oxide coated aluminosilicate particles. Despite the biogenic behavior of Ni, its D/S ratio (1.4) is larger than those of other biogenic elements, suggesting the relative importance of scavenging in its vertical transport.

According to Kuss et al. (2010), excess trace element flux (F_{TEexc}) is determined as follows:

$$F_{TEexc} = F_{TE} - F_{Al} \times (TE/Al)_{ucc}$$

where F_{TE} and F_{Al} are the measured fluxes of the trace element and Al, respectively, and $(TE/Al)_{ucc}$ reflects the average TE/Al ratio of the upper continental crust (McLennan, 2001). Based on this calculation, >85% of total fluxes of Mn, Co, Ni, Cu, Zn, Cd, and Pb are attributed to scavenging (+biogenic uptake) processes. These enrichments in excess metal fluxes would be unique to and common across the pelagic and oligotrophic ocean. Recently Hawco et al. (2018) estimated the Co scavenging rate in the water column in the South Pacific to be 0.11 $\mu g\ m^{-2}\ d^{-1}$, which is strongly consistent with the excess Co flux in the deep trap (0.12 $\mu g\ m^{-2}\ d^{-1}$).

Assuming the same Al flux to the sediments as to the deep trap (74.9 $\mu g\ m^{-2}\ d^{-1}$) and a sediment density of 2.6 $g\ cm^{-3}$, the sedimentation rate at the base of JA06 seamount can be roughly estimated as 0.16 $mm\ kyr^{-1}$ based on the Al concentration in the sediments (66,900 $\mu g\ g^{-1}$). We then calculated elemental fluxes to the sediments based on this sedimentation rate (**Table 2**). According to the distribution of metal flux into

TABLE 2 | Average element concentrations, fluxes, and excess fluxes in shallow and deep traps at the base of the JA06 seamount. The corresponding values for pelagic clay sampled at the same seamount are provided for comparison.

	Mg	Al	P	Ca	Ti	V	Mn	Fe	Co	Ni	Cu	Zn	Sr	Cd	Pb	ΣREE
Concentration (μg g^{-1})																
Shallow trap (n = 10)	5,330	2,300	2,680	110,000	92.0	4.48	156	1,010	4.71	23.4	27.1	177	979	0.98	22.0	6.75
Deep trap (n = 10)	5,630	7,800	701	108,000	363	17.7	783	4,510	11.9	32.1	165	142	905	0.36	19.3	27.6
Pelagic clay[a]	16,200	66,900	9,340	26,400	6,060	140	21,600	33,700	427	577	476	208	307	0.84	94.6	777
/Al																
Shallow trap	2.3	–	1.2	48	0.04	0.002	0.1	0.4	0.002	0.01	0.01	0.08	0.4	0.0004	0.01	0.003
Deep trap	0.7	–	0.1	14	0.05	0.002	0.1	0.6	0.002	0.004	0.02	0.02	0.1	0.00005	0.002	0.004
Pelagic clay	0.2	–	0.1	0.4	0.09	0.002	0.3	0.5	0.006	0.009	0.01	0.003	0.005	0.00001	0.001	0.01
Flux (μg m^{-2} d^{-1})																
Shallow trap	55.1	22.1	27.0	1116	0.88	0.04	1.46	8.56	0.05	0.22	0.25	1.90	9.66	0.009	0.19	0.06
Deep trap	54.7	74.9	6.81	1102	3.46	0.17	7.52	43.0	0.12	0.31	1.53	1.26	9.23	0.003	0.18	0.26
D/S	*1.0*	*3.4*	*0.3*	*1.0*	*3.9*	*4.0*	*5.2*	*5.0*	*2.5*	*1.4*	*6.1*	*0.7*	*1.0*	*0.4*	*0.9*	*4.1*
Pelagic clay	18.1	–	10.5	29.6	6.79	0.16	24.2	37.7	0.48	0.65	0.53	0.23	0.34	0.001	0.11	0.87
Excess flux (μg m^{-2} d^{-1})																
Shallow trap	51.5	–	26.8	1108	−0.25	0.01	1.29	−1.04	0.04	0.21	0.24	1.88	9.57	0.009	0.19	0.02
% of total	*93*	–	*99*	*99*	*−28*	*32*	*89*	*−12*	*90*	*95*	*97*	*99*	*99*	*100*	*98*	*38*
Deep trap	42.3	–	6.16	1074	−0.36	0.07	6.96	10.41	0.10	0.27	1.50	1.19	8.90	0.003	0.17	0.13
% of total	*77*	–	*90*	*97*	*−11*	*41*	*93*	*24*	*86*	*87*	*98*	*95*	*96*	*97*	*91*	*49*

[a]*Data are from Yamaoka et al. (submitted).*

modern Pacific ocean basins (Chester, 2003), the Mn and Fe fluxes to the seabed in the study area are <27 and <164 μg m^{-2} d^{-1}, respectively. Thus, our calculated values (24.2 μg m^{-2} d^{-1} for Mn and 37.7 μg m^{-2} d^{-1} for Fe) seem to be reasonable. The Ti, Mn, Co, Ni, and ΣREE fluxes into the sediments are 2–4 times greater than the fluxes in the deep trap, suggesting further accumulations of these metals near and on the sediment surface. In contrast, Cu, Zn, Cd, and Pb show lower fluxes into sediments than those in the deep trap. This could be explained by losses of the labile fraction associated with biogenic materials. The fluxes of carbonate elements, such as Mg, Ca, and Sr, also significantly decreased in the sediments. In other words, the chemical compositions of sinking particles at 500 m above the seafloor are considerably different from those of deep-sea sediments, especially in areas with slow sedimentation rates where sediments are exposed to bottom water for a long period. Sato and Usui (2018) estimated metal fluxes into cobalt-rich crusts on pelagic seamounts in the Northwest Pacific as 1.9–3.0 μg m^{-2} d^{-1} for Mn, 1.4–2.5 μg m^{-2} d^{-1} for Fe, 0.03–0.11 μg m^{-2} d^{-1} for Co, and 0.01–0.11 μg m^{-2} d^{-1} for Ni. Interestingly, the Mn and Co fluxes roughly correspond to the excess fluxes of Mn (1.3–7.0 μg m^{-2} d^{-1}) and Co (0.04–0.1 μg m^{-2} d^{-1}) observed in sinking particles in this study. This similarity supports the newly proposed model that continuous Mn oxidation occurs even within the oxygen minimum zone (OMZ) such that particulate Fe-Mn oxide forms piled ferromanganese crusts and nodules (Usui et al., 2017). Recently, Usui et al. (2020) presented evidence of ongoing precipitation of Fe-Mn oxide particles (a few micrometers in diameter) from normal seawater at 900–4,500 m depth based on *in situ* 15-years exposure tests. Such particulate precipitates could be a common source of Mn for both cobalt-rich crusts and sinking particles.

CONCLUSION

One year of sediment trap observations on and around seamounts in the exploration area for cobalt-rich crusts revealed unique characteristics of sinking particles in the western North Pacific subtropical gyre. The main findings obtained in this study are as follows:

(1) Total mass fluxes on the seamount flat top were half of those on the base throughout the year. This is probably attributable to a lower population of siliceous microplankton, such as diatoms, in the euphotic zone, although the influence of environmental factors including a putative "seamount effect" is still unresolved.
(2) Particle sinking rates in the north Pacific subtropical gyre are characterized by low total mass fluxes with a sharp peak in late summer. However, summer plankton blooms were not detected by satellite observations. The increased fluxes in late summer may be explained by blooms supported by N_2 fixation (similar to those in the eastern gyre but on a smaller scale) or short-lived blooms induced by typhoons (hurricanes) and tropical depressions.
(3) During the vertical transport of particles from depths of 1,000–4,720 m, half of the organic matter was decomposed as compared to only 14% of carbonate elements. Most of the biogenic materials in sinking particles could be regenerated mainly in the bottom water and at the sediment surface.
(4) Elemental analyses of the sinking particles demonstrated that fluxes of metal elements, such as V, Mn, Co, Ni, Cu, Zn, Cd, Pb, and REE, were predominantly driven by scavenging (+biogenic uptake) processes. Such scavenging-dominated metal flux is characteristic of oligotrophic oceans. Among these metals, Ti, Mn, Co, Ni, and REE seem to further accumulate on the seabed.

DATA AVAILABILITY STATEMENT

The raw data supporting the conclusions of this article will be made available by the authors, without undue reservation.

AUTHOR CONTRIBUTIONS

AS, YT, TM, SK, NO, and YI designed the sediment trap experiments. AS and TF collected samples and analyzed chemical compositions. MS and AT analyzed satellite data. KY analyzed elemental composition and wrote the main manuscript text. All authors contributed to the writing and editing of the manuscript.

FUNDING

This project was commissioned by the Agency for Natural Resources and Energy in the Japanese Ministry of Economy, Trade and Industry (METI) and Japan Oil, Gas and Metals National Corporation (JOGMEC). This study was also funded by internal grants from the National Institute of Advanced Industrial Science and Technology (AIST).

ACKNOWLEDGMENTS

The authors express their appreciation to everyone involved in this project. The authors also thank Dr. Hodaka Kawahata for his valuable comments, which helped improve the manuscript. The Associate Editor Dr. Makio Honda and two reviewers provided constructive suggestions.

SUPPLEMENTARY MATERIAL

The Supplementary Material for this article can be found online at: https://www.frontiersin.org/articles/10.3389/feart.2020.558823/full#supplementary-material

REFERENCES

Behrenfeld, M. J., and Falkowski, P. G. (1997). Photosynthetic rates derived from satellite-based chlorophyll concentration. *Limnol. Oceanogr.* 42, 1–20. doi:10.4319/lo.1997.42.1.0001

Brzezinski, M. A., Krause, J. W., Church, M. J., Karl, D. M., Li, B., Jones, J. L., et al. (2011). The annual silica cycle of the North Pacific subtropical gyre. *Deep Sea Res. I* 58, 988–1001. doi:10.1016%2Fj.dsr.2011.08.001

Chester, R. (2003). *Marine geochemistry*. Malden: Blackwell Publ. Co, 442–480

Church, M. J., Mahaffey, C., Letelier, R. M., Lukas, R., Zehe, J. P., and Karl, D. M. (2009). Physical forcing of nitrogen fixation and diazotroph community structure in the North Pacific Subtropical Gyre. *Global Biogeochem. Cyc.* 23, GB2020. doi:10.1029%2F2008GB003418

Dickey, T., Frye, D., McNeil, J., Manov, D., Nelson, N., Sigurdson, D., et al. (1998). Upper-ocean temperature response to hurricane Felix as measured by the Bermuda testbed mooring. *Mon. Weather Rev.* 126, 1195–1201. doi:10.1175/1520-0493(1998)126<1195:UOTRTH>2.0.CO;2

Dore, J. E., Letelier, R. M., Church, M. J., and Karl, D. M. (2008). Summer phytoplankton blooms in the oligotrophic North Pacific subtropical gyre: historical perspective and recent observations. *Prog. Oceanogr.* 76, 2–38. doi:10.1016/j.pocean.2007.10.002

Engleman, E. E., Jackson, L. L., and Norton, D. R. (1985). Determination of carbonate carbon in geological materials by coulometric titration. *Chem. Geol.* 53, 125–128. doi:10.1016/0009-2541(85)90025-7

Field, C. B., Behrenfeld, M. J., Randerson, J. T., and Falkowski, P. (1998). Primary production of the biosphere: integrating terrestrial and oceanic components. *Science* 281, 237–240. doi:10.1126/science.281.5374.237

Furuya, K., Odate, T., and Taguchi, K. (1995). "Effects of a seamount on phytoplankton production in the western Pacific Ocean," in *Biogeochemical processes and ocean flux in the Western Pacific*. Editors H. Sakai and Y. Nozaki, 255–273.

Hawco, N. J., Lam, P. J., Lee, J.-M., Ohnemus, D. C., Noble, A. E., Wyatt, N. J., et al. (2018). Cobalt scavenging in the mesopelagic ocean and its influence on global mass balance: synthesizing water column and sedimentary fluxes. *Mar. Chem.* 201, 151–166. doi:10.1016/j.marchem.2017.09.001

Honda, M. C., Sasai, Y., Siswanto, E., Kuwano-Yoshida, A., Aiki, H., and Cronin, M. F. (2018). Impact of cyclonic eddies and typhoons on biogeochemistry in the oligotrophic ocean based on biogeochemical/physical/meteorological time-series at station KEO. *Prog. Earth Planet. Sci.* 5, 42. 10.1186/s40645-018-0196-3

Honda, M. C., and Watanabe, S. (2010). Importance of biogenic opal as ballast of particulate organic carbon (POC) transport and existence of mineral ballast-associated and residual POC in the Western Pacific Subarctic Gyre. *Geophys. Res. Lett.* 37, L02605. doi:10.1029/2009GL041521

Honjo, S. (1996). "Fluxes of particles to the Interior of the open oceans," in *Particle flux in the ocean. SCOPE*. Editors V. Ittekkot, P. Schafer, S. Honjo, and P. J. Depetris. (Toronto, Canada:Wiley), 91–154

Hwang, J., Druffel, E. R. M., and Eglinton, T. I. (2010). Widespread influence of resuspended sediments on oceanic particulate organic carbon: insights from radiocarbon and aluminum contents in sinking particles. *Global Biogeochem. Cyc.* 24, GB4016. doi:10.1029/2010GB003802

Iguchi, A., Nishijima, M., Yoshioka, Y., Miyagi, A., Miwa, R., Tanaka, Y., et al. (Forthcoming 2020). Deep-sea amphipods around cobalt-rich ferromanganese crusts: taxonomic diversity and selection of candidate species for connectivity analysis. *PLoS ONE*.

Ittekkot, V., Nair, R. R., Honjo, S., Ramaswamy, V., Bartsch, M., Manganini, S. J., et al. (1991). Enhanced particle fluxes in Bay of Bengal induced by injection of fresh water. *Nature* 351, 385–387. doi:10.1038/351385a0

Kameda, T., and Ishizaka, J. (2005). Size-fractionated primary production estimated by a two- phytoplankton community model applicable to ocean color remote sensing. *J. Oceanogr.* 61, 663–672. doi:10.1007%2Fs10872-005-0074-7

Karl, D. M., Björkman, K. M., Dore, J. E., Fujieki, L., Hebel, D. V., Houlihan, T., et al. (2001). Ecological nitrogen-to- phosphorus stoichiometry at station ALOHA. *Deep Sea Res.* 48, 1529–1566. doi:10.1016%2FS0967-0645(00)00152-1

Karl, D. M., Church, M. J., Dore, J. E., Letelier, R. M., and Mahaffey, C. (2012). Predictable and efficient carbon sequestration in the North Pacific Ocean supported by symbiotic nitrogen fixation. *Proc. Natl. Acad. Sci. U. S. A.* 109, 1842–1849. doi:10.1073%2Fpnas.1120312109

Kawahata, H., Fujita, K., Iguchi, A., Inoue, M., Iwasaki, S., Kuroyanagi, A., et al. (2019). Perspective on the response of marine calcifiers to global warming and ocean acidification—behavior of corals and foraminifera in a high CO_2 world "hot house". *Prog. Earth Planet. Sci.* 6, 5. 10.1186/s40645-018-0239-9

Kawahata, H. (2006). "Settling particles in the central North Pacific," in *Global climate change and response of carbon cycle in the equatorial Pacific and Indian oceans and adjacent landmasses, Elsevier oceanography series*. Editors H. Kawahata and Y. Awaya (Amsterdam: Elsevier), Vol. 73, 107–133.

Kawahata, H. (2002). Suspended and settling particles in the Pacific. *Deep-Sea Res. II.* 49, 5647–5664. doi:10.1016/S0967-0645(02)00216-3

Kawahata, H., Suzuki, A., and Ohta, H. (2000). Export fluxes in the western pacific warm pool. *Deep-Sea Res.* 47, 2061–2091. doi:10.1016/S0967-0637(00)00025-X

Kempe, S., and Knaack, H. (1996). "Vertical particle flux in the western pacific below the north equatorial current and the equatorial counter current," in *Particle flux in the ocean. SCOPE*. Editors V. Ittekkot, P. SchŠfer, S. Honjo, and P.J. Depetris Toronto, Canada: Wiley, 313–323.

Kuss, J., and Kremling, K. (1999). Particulate trace element fluxes in the deep northeast Atlantic Ocean. *Deep-Sea Res. I* 46,149–169. doi:10.1016/S0967-0637(98)00059-4

Kuss, J., Waniek, J. J., Kremling, K., and Schulz-Bull, D. E. (2010). Seasonality of particle-associated trace element fluxes in the deep northeast Atlantic Ocean. *Deep-Sea Res. I* 57, 785–796. doi:10.1016/j.dsr.2010.04.002

Lamborg, C. H., Buesseler, K. O., and Lam, P. J. (2008). Sinking fluxes of minor and trace elements in the North Pacific Ocean measured during the VERTIGO program. *Deep-Sea Res. II.* 55, 1564–1577. doi:10.1016%2Fj.dsr2.2008.04.012

Lin, I.-I. (2012). Typhoon-induced phytoplankton blooms and primary productivity increase in the western North Pacific subtropical ocean. *J. Geophys. Res.* 117, C03039. doi:10.1029/2011JC007626

Lin, I., Liu, W. T., Wu, C.-C., Wong, G. T. F., Hu, C., Chen, Z., et al. (2003). New evidence for enhanced ocean primary production triggered by tropical cyclone. *Geophys. Res. Lett.* 30, 1718. doi:10.1029/2003GL017141

Lin, Y.-C., and Oey, L.-Y. (2016). Rainfall-enhanced blooming in typhoon wakes. *Sci. Rep.* 6, 31310. doi:10.1038/srep31310

Liu, F., and Tang, S. (2018). Influence of the interaction between typhoons and oceanic mesoscale eddies on phytoplankton blooms. *J. Geophys. Res.* 123, 2785–2794. 10.1029/ 2017JC013225

Lutz, M. J., Caldeira, K., Dunbar, R. B., and Behrenfeld, M. J. (2007). Seasonal rhythms of net primary production and particulate organic carbon flux to depth describe the efficiency of biological pump in the global ocean. *J. Geophys. Res.* 112, C10011. doi:10.1029/2006JC003706.

McLennan, S. M. (2001). Relationships between the trace element composition of sedimentary rocks and upper continental crust. *Geochem. Geophys. Geosyst.* 2, 2000GC000109. doi:10.1029%2F2000GC000109

Mortlock, R. A., and Froelich, P. N. (1989). A simple method for the rapid determination of biogenic opal in pelagic marine sediments. *Deep-Sea Res. Part A* 36, 1415–1426. doi:10.1016/0198-0149(89)90092-7

Nagao, M., Takasugi, Y., Suzuki, A., Tanaka, Y., Sugishima, H., Matsui, T., et al. (2018). Confirming the validity of ADCP velocity measurements for physical environmental assessment in Exploration Areas for cobalt-rich ferromanganese crusts. *Proc. ISOPE.* 2018, 136–143.

Noriki, S., and Tsunogai, S. (1986). Particulate fluxes and major components of settling particle from sediment trap experiment in the Pacific Ocean. *Deep-Sea Res.* 33, 903–912. doi:10.1016/0198-0149(86)90005-1

Oliveira, A. P., Coutinho, T. P., Cabeçadas, G., Brogueira, M. J., Coca, J., Ramos, M., et al. (2016). Primary production enhancement in a shallow seamount (Gorringe-Northeast Atlantic). *J. Mar. Syst.* 164, 13–29. 10.1016/j.jmarsys.2016.07.012

Pälike, H., Lyle, M. W., Nishi, H., Raffi, I., Ridgwell, A., Gamage, K., et al. (2012). A Cenozoic record of the equatorial Pacific carbonate compensation depth. *Nature* 488, 609–614. doi:10.1038/nature11360.

Pan, S., Shi, J., Gao, H., Guo, X., Yao, X., and Gong, X. (2017). Contributions of physical and biogeochemical processes to phytoplankton biomass enhancement in the surface and subsurface layers during the passage of Typhoon Damrey. *J. Geophys. Res.* 122, 212–229. doi:10.1002/2016JG003331

Pohl, C., Löffler, A., and Hennings, U. (2004). A sediment trap flux study for trace metals under seasonal aspects in the stratified Baltic Sea (Gotland Basin; 57°19.20'N; 20°03.00'E). *Mar. Chem.* 84, 143–160. doi:10.1016/J.MARCHEM.2003.07.002

Price, J. F. (1981). Upper ocean response to a hurricane. *J. Phys. Oceanogr.* 11, 153–175. doi:10.1175/1520-0485(1981)011<0153:UORTAH>2.0.CO;2

Redfield, A. C., Ketchum, B. H., and Richards, F. A. (1963). "The influence of organisms on the composition of seawater," in *The sea.* Editor M. H. Hill (New York, NY: Wiley), 26–77.

Saito, M. A., and Moffett, J. W. (2002). Temporal and spatial variability of cobalt in the Atlantic Ocean. *Geochem. Cosmochim. Acta.* 66, 1943–1953. doi:10.1016/ S0016-7037(02)00829-3

Sanford, T. B., Price, J. F., and Girton, J. B. (2011). Upper ocean response to Hurricane Frances (2004) observed by profiling EM-APEX floats. *J. Phys. Oceanogr.* 41, 1041–1056. doi:10.1175/2010JPO4313.1.

Sato, H., and Usui, A. (2018). Metal flux as an alternative parameter in evaluating the resource potential for co-rich ferromanganese crusts. *Mar. Georesour. Geotechnol.* 36 (7), 768–780. doi:10.1080/1064119X.2017.1378781.

Schüßler, U., Schulz-Bull, D. E., and Bauerfeind, E. (1997). Annual fluxes of particulate chemical trace compounds during the North-East Water Polynya Experiment. *J. Mar. Syst.* 10, 391–400. doi:10.1016/S0924-7963(96)00077-2

Shibano, R., Yamanaka, Y., Okada, N., Chuda, T., Suzuki, S., Niino, H., et al. (2011). Responses of marine ecosystems to typhoon passages in the western subtropical North Pacific. *Geophys. Res. Lett.* 38, L18608. doi:10.1029/ 2011GL048717

Smetacek, V. S. (1985). Role of sinking in diatom life-history cycles: ecological, evolutionary and geological significance. *Mar. Biol.* 84, 239–251. doi:10.1007%2FBF00392493

Sugishima, H., Matsui, T., Okamoto, N., and Fukushima, T. (2018). Distributions of megabenthic organisms in the areas of north-west Pacific seamounts where are covered with cobalt-rich ferromanganese crusts. *Proc. ISOPE.* 2018, 74–80.

Sun, L., Yang, Y.-J., Xian, T., Lu, Z.-M., and Fu, Y.-F. (2010). Strong enhancement of chlorophyll *a* concentration by a weak typhoon. *Mar. Ecol. Prog. Ser.* 404, 39–50. doi:10.3354/meps08477

Sun, W.-P., Han, Z.-B., Hu, C.-Y., and Pan, J.-M. (2016). Source composition and seasonal variation of particulate trace element fluxes in Prydz Bay, East Antarctica. *Chemosphere* 147, 318–327. doi:10.1016/j.chemosphere.2015.12.105

Takahashi, K. (1986). Seasonal fluxes of pelagic diatoms in the subarctic Pacific, 1982–1983. *Deep-Sea Res. I* 33, 1225–1251. doi:10.1016/0198-0149(86)90022-1

Takahashi, T., Broecker, W. S., and Langer, S. (1985). Redfield ratio based on chemical data from isopycnal surfaces. *J. Geophys. Res.* 3, 43–61. doi:10.1029/JC090iC04p06907

Turnewitsch, R., Dumont, M., Kiriakoulakis, K., Legg, S., Mohn, C., Peine, F., et al. (2016). Tidal influence on particulate organic carbon export fluxes around a tall seamount. *Prog. Oceanogr.* 149, 189–213. 10.1016/j.pocean.2016.10.009

Uematsu, M., Duce, R. A., Prospero, J. M., Chen, L., Merrill, J. T., and McDonald, R. L. (1983). Transport of mineral aerosol from Asia over the north Pacific Ocean. *J. Geophys. Res.* 88, 5343–5352. doi:10.1029%2FJC088iC09p05343

Usui, A., Hino, H., Suzushima, D., Tomioka, N., Suzuki, Y., Sunamura, M., et al. (2020). Modern precipitation of hydrogenetic ferromanganese minerals during on-site 15-year exposure tests. *Sci. Rep.* 10, 3558. 10.1038/s41598-020-60200-5

Usui, A., Nishi, K., Sato, H., Nakasato, Y., Thornton, B., Kashiwabara, T., et al. (2017). Continuous growth of hydrogenetic ferromanganese crusts since 17 Myr ago on Takuyo-Daigo Seamount, NW Pacific, at water depths of 800-5500 m. *Ore Geol. Rev.* 87, 71–87. 10.1016/j.oregeorev.2016.09.032

Villareal, T. A., Adornato, L., Wilson, C., and Schoenbaechler, C. A. (2011). Summer blooms of diatom-diazotroph assemblages and surface chlorophyll in the North Pacific gyre: a disconnect. *J. Geophys. Res.* 116, C03001. doi:10.1029%2F2010JC006268

Wang, T., Zhang, S., Chen, F., Ma, Y., Jiang, C., and Yu, J. (2020). Influence of sequential tropical cyclones on phytoplankton blooms in the northwestern South China Sea. *J. Ocean. Limnol.* 10.1007/s00343-020-9266-7

White, A. E., Spitz, Y. H., and Letelier, R. M. (2007). What factors are driving summer phytoplankton blooms in the North Pacific Subtropical Gyre?. *J. Geophys. Res.* 112, C12006. doi:10.1029/2007JC004129

Wilson, C. (2003). Late summer chlorophyll blooms in the oligotrophic North Pacific subtropical gyre. *Geophys. Res. Lett.* 30, 1942. doi:10.1029/2003GL017770

Wilson, C., and Qiu, X. (2008). Global distribution of summer chlorophyll blooms in the oligotrophic gyres. *Prog. Oceanogr.* 78, 107–134. doi:10.1016/j.pocean.2008.05.002

Wilson, C., Villareal, T. A., Maximenko, N., Bograd, S. J., Montoya, J. P., and Schoenbaechler, C. A. (2008). Biological and physical forcings of late summer chlorophyll blooms at 30°N in the oligotrophic Pacific. *J. Mar. Syst.* 69, 164–176. doi:10.1016/j.jmarsys.2005.09.018

Yamashita, H., Takahashi, K., and Fujitani, N. (2002). Zonal and vertical distribution of radiolarians in the western and central Equatorial Pacific in January 1999. *Deep-Sea Res. II* 49, 2823–2862. doi:10.1016%2FS0967-0645(02)00060-7

Ye, H. J., Sui, Y., Tang, D. L., and Afanasyev, Y. D. (2013). A subsurface chlorophyll *a* bloom induced by typhoon in the South China Sea. *J. Mar. Syst.* 128, 138–145. 10.1016/j.jmarsys.2013.04.010

Zhao, H., Shao, J., Han, G., Yang, D., and Lv, J. (2015). Influence of typhoon Matsa on phytoplankton chlorophyll-*a* off east China. *PLoS One* 10 (9), e0137863. doi:10.1371/journal.pone.0137863.

Conflict of Interest: Authors AS and TF were employed by the company KANSO Co., Ltd. Authors TM, SK, NO, and YI were employed by the company Japan Oil, Gas and Metals National Corporation.

The remaining authors declare that the research was conducted in the absence of any commercial or financial relationships that could be construed as a potential conflict of interest.

frontiers in Earth Science

ORIGINAL RESEARCH
published: 08 December 2020
doi: 10.3389/feart.2020.537332

The Impact of Eddies on Nutrient Supply, Diatom Biomass and Carbon Export in the Northern South China Sea

Yung-Yen Shih[1,2], Chin-Chang Hung[2], Sing-how Tuo[3,4], Huan-Jie Shao[2], Chun Hoe Chow[5], François L. L. Muller[2] and Yuan-Hong Cai[1]*

[1]Department of Applied Science, Republic of China (R.O.C.) Naval Academy, Kaohsiung, Taiwan, [2]Department of Oceanography, National Sun Yat-sen University, Kaohsiung, Taiwan, [3]Research Center for Environmental Changes, Academia Sinica, Taipei, Taiwan, [4]Department of Ocean and Earth Sciences, Old Dominion University, Norfolk, VA, United States, [5]Department of Marine Environmental Informatics, National Taiwan Ocean University, Keelung, Taiwan

OPEN ACCESS

Edited by:
Maureen H. Conte, Bermuda Institute of Ocean Sciences, Bermuda

Reviewed by:
Yoshikazu Sasai, Japan Agency for Marine-Earth Science and Technology (JAMSTEC), Japan
Eko Siswanto, Japan Agency for Marine-Earth Science and Technology (JAMSTEC), Japan
Mark Brzezinski, University of California, Santa Barbara, United States

***Correspondence:**
Chin-Chang Hung
cchung@mail.nsysu.edu.tw

Specialty section:
This article was submitted to Biogeoscience, a section of the journal Frontiers in Earth Science

Received: *23 February 2020*
Accepted: *12 November 2020*
Published: *08 December 2020*

Citation:
Shih Y-Y, Hung C-C, Tuo S-h, Shao H-J, Chow CH, Muller FLL and Cai Y-H (2020) The Impact of Eddies on Nutrient Supply, Diatom Biomass and Carbon Export in the Northern South China Sea. Front. Earth Sci. 8:537332. doi: 10.3389/feart.2020.537332

We have investigated the effect of eddies (cold and warm eddies, CEs and WEs) on the nutrient supply to the euphotic zone and the organic carbon export from the euphotic zone to deeper parts of the water column in the northern South China Sea. Besides basic hydrographic and biogeochemical parameters, the flux of particulate organic carbon (POC), a critical index of the strength of the oceanic biological pump, was also measured at several locations within two CEs and one WE using floating sediment traps deployed below the euphotic zone. The POC flux associated with the CEs (85 ± 55 mg-C m^{-2} d^{-1}) was significantly higher than that associated with the WE (20 ± 7 mg-C m^{-2} d^{-1}). This was related to differences in the density structure of the water column between the two types of eddies. Within the core of the WE, downwelling created intense stratification which hindered the upward mixing of nutrients and favored the growth of small phytoplankton species. Near the periphery of the WE, nutrient replenishment from below did take place, but only to a limited extent. By far the strongest upwelling was associated with the CEs, bringing nutrients into the lower portion (~50 m) of the euphotic zone and fueling the growth of larger-cell phytoplankton such as centric diatoms (e.g., *Chaetoceros*, *Coscinodiscus*) and dinoflagellates (e.g., *Ceratium*). A significant finding that emerged from all the results was the positive relationship between the phytoplankton carbon content in the subsurface layer (where the chlorophyll *a* maximum occurs) and the POC flux to the deep sea.

Keywords: eddy, nutrient, diatom, carbon flux, South China Sea, subsurface chlorophyll (phytoplankton) maximum

INTRODUCTION

Eddies are ubiquitous in oligotrophic regions of the open ocean. They are believed to induce an upward mixing of deep, nutrient-enriched waters, alleviating the nutrient limitation of the euphotic zone, and thus resulting in an increase in primary production (PP, as known as biological carbon fixation), which in turn enhances its prospect for export out of the euphotic zone (Hung et al., 2004; Hung et al., 2010a; Zhou et al., 2013; Shih et al., 2015; Boyd et al., 2019). Broadly speaking, the eddies in the Northern Hemisphere can be separated into two types: 1) the cold eddy (CE), also called

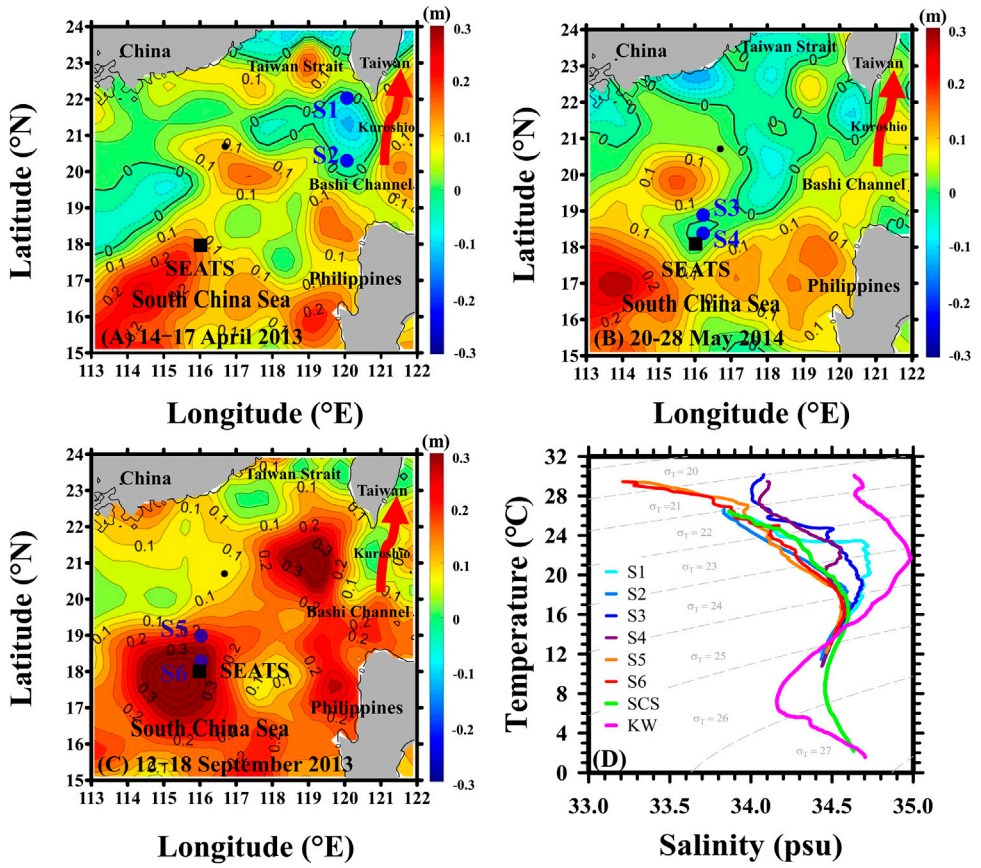

FIGURE 1 | Maps showing the locations of the main sampling stations (solid circles, S1 to S6) in the NSCS in **(A)** April 2013 (cold eddy), **(B)** May 2014 (cold eddy) and **(C)** September 2013 (warm eddy). Contour plots of sea level anomaly (SLA, unit: m) were obtained from the Copernicus Marine Environment Monitoring Service (CMEMS) and are based on comprised daily measurements within 0.25 × 0.25 grid cells (http://marine.copernicus.eu). Solid and dashed lines represent positive (warm eddy) and negative (cold eddy) SLAs, respectively. **(D)** T–S diagrams for the upper 300 m of the water column at stations S1 to S6 including the T–S diagrams of the South China Sea (SCS) and the Kuroshio waters (KW, thick red arrows in **A–C**). The SEATS site is represented with a square symbol.

cyclonic eddy, containing cold nutrient-rich waters and generally associated with higher phytoplankton abundance and PP (Vaillancourt et al., 2003), and 2) the warm eddy (WE), also called anticyclonic eddy, containing warm nutrient-depleted water with lower phytoplankton abundance and low PP. Neighboring eddies of opposite sign, i.e., CE against WE, and vice versa, can also interact with one another to produce an injection of nutrients into the surface layer (McGillicuddy et al., 1998). Warm eddies can further be split into two types depending on whether surface water sinks, depressing the thermocline and taking nutrients away from the photic zone or, on the contrary, the thermocline forms a dome which brings nutrients closer to the sea surface and results high phytoplankton biomass (Sweeney et al., 2003; McGillicuddy et al., 2007). Despite this broad classification, recent research has produced inconsistent results among studies conducted in various marine environments when it comes to the intensity of vertical mixing and/or the stimulation of phytoplankton blooms (Hung et al., 2004; Hung et al., 2010a; Zhou et al., 2013; Chen et al., 2015; Shih et al., 2015). Indeed, it is difficult to resolve biogeochemical responses to eddies, partly because they are superimposed on large regional and seasonal changes in water characteristics, and partly because satellite image observations and field cruise observations only allow large-scale surface signatures and small-scale spatiotemporal variability to be captured, respectively. Satellite observations are limited to surface properties which then need to be extrapolated to the relevant depth horizon. Field observations can provide detailed spatial variations regarding thermocline/pycnocline and nutrients in the water column of the euphotic zone, but only in selected regions and on an episodic basis.

The South China Sea (SCS) is one of the largest marginal seas in the world. It has a complicated flow, with the surface waters of the Kuroshio flowing into the SCS and the surface water of the SCS flowing out to the Taiwan Strait and the Bashi Channel (**Figure 1** of Wong et al., 2007). In terms of its nutrient budget, the main input to the SCS comes mainly from an influx of intermediate and deep waters originating from the western Philippine Sea and flowing west through the Luzon Strait (Chen et al., 2001). Chen (2005) reported that nitrate was more limiting than soluble reactive phosphate in the SCS. Despite nutrients being supplied to ocean gyres by lateral transport and vertical diapycnal diffusion, the rates of supply

involved are generally insufficient to support new production (Liu et al., 2002). Other mixing dynamics associated with eddies must therefore be invoked to account for the nutrient pumping which they are thought to generate (Wong et al., 2007). Nutrient fluxes generated by the eddies are thought to be comparable to benthic nutrient fluxes from shelf sediments (Liu K.-K et al., 2007), Kuroshio intrusions (Liu et al., 2002; Chou et al., 2005; Du et al., 2013; Gan et al., 2016; Li et al., 2016), entrainment by internal waves (Li et al., 2018) or typhoons (Shih et al., 2020) (**Supplementary Figure S1**). Satellite altimetry is one of the most widely used eddy detection methods (Wang et al., 2003). Based on altimetry measurements, Xiu et al. (2010) and Chen et al. (2011) reported that there were approximately thirty eddies appearing in the SCS every year, with no apparent difference between the numbers of CEs and WEs, with radii ranging from 50 to 220 km and with an average lifetime of 8.8 weeks.

Although the diffusional supply of nutrients, phytoplankton abundance and new production associated with eddies were examined by Chen et al. (2007); Chen et al. (2015), little attention has been paid to the direct measurement of carbon fluxes and their modification by eddies over the deep basin of the SCS (Zhou et al., 2013). In particular, particulate organic carbon (POC) measurements are sorely needed to support the contention that POC exports out of the euphotic zone of an eddy are enhanced relative to those outside of the eddy. In this study, we examined this long-neglected issue, first by characterizing the nutrient regime and large algae composition in the water column of three eddies which had formed successively in the SCS. Secondly, POC and particulate nitrogen (PN) export fluxes, together with upward fluxes of dissolved nitrogen associated with these eddies were measured. The results are discussed in relation to the potential mechanisms that control the magnitude and composition of PP and the fate of plankton-fixed carbon in the SCS.

MATERIAL AND METHODS

The daily altimetry sea level anomalies (SLAs) at 1/4° resolution obtained from the Copernicus Marine Environment Monitoring Service (CMEMS) (http://marine.copernicus.eu) were used to detect the CEs and the WE (**Figure 1**) and define their sea surface properties and dynamics at the start of each field survey. Daily satellite measurements of chlorophyll *a* (Chl) and sea surface temperature (SST) provided further indication that the eddies were biogeochemical distinct from the surrounding waters. The Chl data were obtained from the European Space Agency's GlobColour project (http://www.globcolour.info), at 4-km resolution. The SST data were obtained from the Remote Sensing System (http://www.remss.com), at 0.25° resolution.

Three cruises were conducted on April 14–17, 2013 (Stations S1 and S2), September 12–18, 2013 (Stations S5 and S6) and May 20–28, 2014 (Stations S3 and S4) onboard *Ocean Researcher III* (first cruise) and *V* (second and third cruises). Stations S1 and S2 (**Figure 1A**) were located inside a cold eddy at (22.0°N, 120.3°E) and (20.3°N, 120.3°E) and exhibited temperatures at 50 m depth of 25.6°C and 22.9°C, respectively (**Table 1**). Stations S3 and S4 (**Figure 1B**) were located at (18.8°N, 116.2°E) and (18.3°N, 116.2°E) inside the second CE, and both stations exhibited a temperature at 50-m depth of 24.5°C (**Table 1**). Stations S5 and S6 (**Figure 1C**) were located inside a warm eddy at (19.0°N, 116.0°E) and (18.3°N, 116.0°E) where S5 and S6 were close to the periphery and the core of the WE, respectively, and exhibited temperatures at 50 m of 27.9 and 29.0°C, respectively (**Table 1**). It is also worth noting that S4 and S6 were both in the vicinity of the South East Asia Time-series Study (SEATS) site (18°N, 116°E). The CEs and WE displayed by the SLA maps in **Figure 1** were further confirmed by the Okubo-Weiss (OW) parameters (Okubo, 1970; Weiss, 1991; Chen G. et al., 2011; Faghmous et al., 2015), which can provide the difference between deformation rate and rotation rate of ocean currents. If the OW parameters are negative, then the rotation is dominant in the ocean-current field, which is consistent with the presence of an eddy. As can be seen in **Figure 1**, the points of minimum (maximum) SLA in the CEs (WE) corresponded with negative OW parameters (**Supplementary Figure S2**).

An SBE 911 plus mode (SeaBird Scientific Inc.) sensor was deployed to record temperature, density and salinity of seawater. The mixed layer depth (MLD) was defined by the criterion of the depth where the temperature had decreased by 0.8°C from the surface (Kara et al., 2000; Shih et al., 2015). Nitrate + nitrite (N) was analyzed by flow injection analysis according to Gong et al. (2000). Phosphorus (P) was analyzed by the molybdenum blue method (Pai et al., 1990). The concentration of Chl was determined by established fluorometric procedures using a Turner model 10-AU-005 fluorometer. Seawater samples for Chl analysis were directly filtered through 25-mm filters (GF/F) and stored at −20°C pending analysis. The Chl retained on the filter was extracted by 90% acetone and measured by the non-acidification method (Gong et al., 2000; Hung et al., 2000). Particulate matter was collected by filtration of a 2-L volume of seawater through 0.7-μm filtration pre-combusted GF/G filters. Subsamples for POC and PN analyses were then measured with a CHN analyzer following fuming with concentrated HCl in a desiccator to remove particulate inorganic carbon (Liu et al., 2007; Hung and Gong, 2010). Water column inventories of N (I-N), P (I-P), Chl (I-Chl), POC (I-POC) and PN (I-PN) were calculated by the trapezoidal integration for the upper 150 m. The depth of the nitracline (Z_N) was determined as the depth at which N equaled 1 μM (Reynolds et al., 2007).

Phytoplankton size and abundance measurements were undertaken on 50 ml aliquots of seawater sampled at standard depths (e.g., 5, 25, 50, 75 and 100 m) and quickly preserved in acidic Lugol's solution with a volumetric ratio of 1:100. Large phytoplankton cells (>5 μm) were filtered out on 25 mm polycarbonate filters (Whatman Nuclepore Membranes, 5 μm pore size) under the influence of gravity. Large phytoplankton cells and other particles retained on the filter were counted with an optical microscope (OLYMPUS CX31) operating at 400 × magnification. Large phytoplankton abundance was reported at a specific depth while the water column phytoplankton (I-Phytoplankton) and diatom (including centric and pennate diatoms) inventories (I-Diatom) were obtained from

TABLE 1 | Summary of given parameters (mean ± SD), including temperatures at 50 m water depth ($Temp_{50m}$); mean temperature and salinity values of the mixed layer ($Temp_{MLD}$ and $Salinity_{MLD}$); mixed layer, nitracline, euphotic zone and subsurface Chl maximum depths, respectively (MLD, Z_N, Z_{eu} and SCM); surface water concentrations of N, P and Chl, respectively (N, P and Chl); water column inventories (0–150 and 0–100 m) of N and Chl (I-N and I-Chl); inventories in the upper 150 m of POC and PN (I-POC and I-PN); vertical gradients (MLD–150 and MLD–100 m) of N (N-gradient); water column phytoplankton and diatom inventories in the upper 100 m (I-Phyto. and I-Diatom); water column phytoplankton and diatom carbon inventories in the upper 100 m (I-Phyto. C. and I-Diatom C.); export fluxes of POC and PN at 150 m depth (POC flux and PN flux); the periods of deployment; at respective stations of the CEs and the WE relevant to this study.

	CE						WE		
	CE 1 (2013)			CE 2 (2014)			WE (2013)		
Parameters	**S1**	**S2**	**Mean ± 1SD**	**S3**	**S4**	**Maen ± 1SD**	**S5**	**S6**	**Maen ± 1SD**
$Temp_{50m}$ (°C)	25.6	22.9	24.2 ± 2.0	24.5	24.5	24.5 ± 0.0	27.9	29.0	28.5 ± 0.8
$Temp_{MLD}$ (°C)	26.2	26.2	26.2 ± 0.0	29.8	29.3	29.6 ± 0.4	29.4	29.2	29.3 ± 0.1
$Salinity_{MLD}$	33.85	33.84	33.85 ± 0.01	34.06	34.11	34.09 ± 0.04	33.30	33.29	33.30 ± 0.01
MLD (m)	47	36	42 ± 8	13	14	14 ± 1	47	56	52 ± 6
Z_N (m)	56	16	36 ± 28	53	38	46 ± 11	52	61	57 ± 6
Z_{eu} (m)	88	72	80 ± 11	83	88	86 ± 4	82	74	78 ± 6
SCM (m)	53	49	51 ± 3	64	67	66 ± 2	72	79	76 ± 5
N (μM)	0.1	0.9	0.5 ± 0.5	0.1	0.8	0.5 ± 0.6	0.1	<0.1	<0.1
P (μM)	0.02	0.01	0.01 ± 0.01	0.05	0.04	0.04 ± 0.01	<0.01	<0.01	<0.01
Chl (mg m^{-3})	0.16	0.09	0.13 ± 0.05	0.11	0.09	0.10 ± 0.01	0.10	0.10	0.10 ± 0.00
I-N (mmol m^{-2})	—	—	—	—	—	—	—	—	—
(0–150 m)	395	1,155	775 ± 537	780	1,136	958 ± 251	1,268	674	971 ± 420
(0–100 m)	(111)	(475)	(293 ± 257)	(257)	(444)	(351 ± 132)	(524)	(150)	(337 ± 264)
I-Chl (mg m^{-2})	—	—	—	—	—	—	—	—	—
(0–150 m)	38	29	34 ± 6	33	26	29 ± 5	33	28	30 ± 4
(0–100 m)	(38)	(29)	(31 ± 4)	(33)	(26)	(24 ± 4)	(33)	(28)	(22 ± 1)
I-POC (mg-C m^{-2})	4.7	4.5	4.6 ± 0.2	2.7	3.2	3.0 ± 0.3	4.3	4.0	4.1 ± 0.2
I-PN (mg-N m^{-2})	0.4	0.7	0.5 ± 0.2	0.8	0.9	0.8 ± 0.0	0.7	1.2	1.0 ± 0.4
N-gradient (mmol m^{-4})	0.07	0.12	0.10 ± 0.03	0.11	0.12	0.11 ± 0.01	0.20	0.14	0.17 ± 0.04
(MLD–150 m)	—	—	—	—	—	—	—	—	—
(MLD–100 m)	(0.06)	(0.19)	(0.13 ± 0.10)	(0.10)	(0.16)	(0.13 ± 0.04)	(0.31)	(0.14)	(0.22 ± 0.12)
I-Phyto. (10^6 cells m^{-2})	69	32	50 ± 26	67	34	51 ± 23	14	18	16 ± 3
I-Diatom (10^6 cells m^{-2})	63	20	41 ± 31	56	26	41 ± 21	6	8	7 ± 1
I-Phyto. C. (mg-C m^{-2})	20.5	19.6	20.1 ± 0.6	17.4	8.1	12.8 ± 6.6	6.8	6.3	6.6 ± 0.4
I-Diatom C. (mg-C m^{-2})	18.0	16.5	17.3 ± 1.1	14.1	6.4	10.2 ± 5.4	5.6	3.5	4.5 ± 1.5
POC Flux (mg-C m^{-2} d^{-1})	51	72	61 ± 14	166	50	108 ± 82	15	25	20 ± 7
PN Flux (mg-N m^{-2} d^{-1})	6	11	9 ± 3	33	15	24 ± 13	3	7	5 ± 3
Deployment (h)	37	12	—	8	32	—	47	27	—

measurements in the upper 100 m. Phytoplankton species were morphologically distinguished in accordance with the criteria of Hasle and Syvertsen (1997) (diatoms), Steidinger and Tangen (1997) (dinoflagellates) and Throndsen (1997) (other flagellates). Their respective contributions to the phytoplankton carbon inventory were then estimated from cellular carbon contents, as follows: 1) select a geometric shape that best represents each phytoplankton cell and use an ocular micrometer to measure all the dimensions needed to calculate its biovolume (μm^3) (Table 1 and Annex 1 in Olenina et al., 2006); 2) calculate its cellular carbon content (pg-C) by using the carbon to volume ratio commonly found in the relevant plankton group (Menden-Deuer and Lessard 2000); 3) sum up the cellular carbon contents of all the cells contained in a sample; 4) calculate the water column phytoplankton carbon inventory (mg-C m^{-2}) by integrating the depth-dependent carbon contents between 0 and 100 m.

Sinking particles were collected at 150 m using a buoy-tethered drifting sediment trap. This collection depth lay below the euphotic zone (Z_{eu}, **Table 1**), meaning that light intensity had declined to less than 1% of its surface value. The trap array was composed of 12 plastic cylindrical tubes (6.8-cm diameter and 68-cm height) with honeycomb baffles covering the mouth of each tube (Hung and Gong 2010; Hung et al., 2009; Hung et al., 2010b). Each collecting tube was filled with seawater that had been filtered through 0.5-μm and 0.1-μm Sparkling Clear polypropylene filters. The period of deployment was generally 24–48 h (**Table 1**), but less than 24 h if sea state or weather conditions precluded launch and recovery operations. After recovering the trap, samples for POC and PN analysis were filtered on pre-combusted quartz filters (1.0 μm pore size), and swimmers on filters were carefully removed using forceps under a microscope before analysis. POC and PN fluxes were determined by following the detailed procedures mentioned in Hung et al. (2010a). Briefly, POC and PN analyses of the sinking particles were carried out with an elemental analyzer (CHNS/O Elementar, Vario EL) following HCl-fuming to remove particulate inorganic carbon after rinsing and drying of the filters. The analytical errors for POC and PN were 1–3 and 1–5% for duplicate measurements, respectively. Retention times of POC and PN (RT-C and RT-N) within the upper 150 m of the water column were calculated by dividing I-POC and I-PN (mg m^{-2}) by the fluxes of POC and PN (mg m^{-2} d^{-1}) at 150 m (RT-C = I-POC/POC flux; RT-N = I-PN/PN flux).

For the sake of comparison with fluxes obtained from mass balance calculations, the vertical entrainment of N from depth was conservatively estimated by Fick's first law of diffusion:

$$\text{N flux} = K_z dN/dz$$

where N flux (mmol m^{-2} d^{-1}) is the upward vertical diffusive flux of N through the base of the euphotic zone, K_z (m^2 d^{-1}) is the average diffusion coefficient in the upper 150 m water column and dN/dz (mmol m^{-4}) represents the vertical gradient of N between the MLD and 150 m of the depth interval over which turbulent diffusion is occurring. Note that the mixed layer itself, which is characterized by intense vertical advection and mixing, is excluded from that depth interval. The diffusion coefficient K_z is then determined from the formula of Denman and Gargett (1983):

$$K_z = 0.25\,\varepsilon f^{-2}$$

where ε represents the turbulent energy dissipation rate and is computed using the *in situ* density profile to detect overturns of water layer in the whole water column (Thorpe 1977). When density inversions are encountered, the Thorpe scale is defined as the distance by which a water parcel has to be moved to reinstate stability. For each overturn, the overall stratification is computed, and the turbulence dissipation rate can be estimated as the multiplication of Thorpe scale squared by the overall stratification squared (Dillon 1982). The f^{-2} is the Brunt-Välsälä buoyancy frequency, which is derived from the vertical gradient in density between the MLD and 150 m. The values of f^{-2} measured at S1–S6 were 2.1, 2.2, 2.6, 2.7, 3.5 and 3.1 × 10^{-4} s^{-2}, respectively.

To compare sets of measurements made between different eddies, *t* tests (with a one-tailed or two-tailed alternative hypothesis—depending on our biogeochemical knowledge of the sites, please see **Supplementary Table S1** for explanations) with 0.10 of significance level were applied. Linear regressions were used to describe relationships between any two of the parameters. All values are reported as mean ± one standard deviation (SD).

RESULTS

Vertical Hydrographic Characteristics and Biogeochemical Data Distributions

The two CEs of 2013 and 2014, and the WE of 2013 were initially detected through their negative and positive SLAs, respectively, using satellite altimetry records (**Figures 1A–C**). Based on satellite observations, **Supplementary Figure S3** shows that CEs can also be defined by cooler SST (<28°C) and higher Chl (>0.14 mg m^{-3}) while the WE exhibits warmer SST (>28°C) and lower Chl (<0.14 mg m^{-3}), near the eddy cores. The temperature-salinity diagrams of the main sampling stations (S1–S6) are shown in **Figure 1D**. At the four main stations inside the two CEs, the T-S diagrams reflect the mixing between warmer, high-salinity Kuroshio water and cooler, lower-salinity SCS water. By contrast, the two main stations sampled in the WE produced a T-S diagram more representative of a typical SCS water column. The mean temperature and salinity values of the mixed layer were 26.2 ± 0.0°C and 33.85 ± 0.01 in the first CE, 29.6 ± 0.4°C and 34.09 ± 0.04 in the second CE, and 29.3 ± 0.1°C and 33.30 ± 0.01 (**Table 1**) inside the WE. The lower temperature and higher salinity values inside the CEs can likely be attributed to an upward transport of subsurface water at the CE sampling sites (**Table 1**; **Supplementary Figure S4**). Despite these lower temperatures, the mixed layers were no deeper in the second CE (2014) than in the WE. In fact, the MLD was shallower in the second CE (14 ± 1 m) than in either the first CE (42 ± 8 m) ($p < 0.05$) or the WE (52 ± 6 m) ($p < 0.01$) (**Table 1**; **Supplementary Figure S4**).

We have added a figure depicting the seasonal variations of the MLD, as previously recorded in the vicinity of the SEATS station in two published studies (Chen 2005; Chou et al., 2005). It can be observed that the MLD of our second CE is shallower than the value expected in May from the seasonal trend defined by the previous studies; on the other hand, the MLD of the WE is deeper than would be expected in the SEATS area for the month of September (**Supplementary Figure S5**). These anomalies strongly suggest that seasonal effects alone cannot account for our MLD observations. The most likely explanation is that these anomalies are produced by the direct influence of the eddies on the MLD. Indeed, CEs are known to drive the mixed layer shallower and thinner while WEs can drive the mixed layer deeper and suppress mixing of the water column (Chen et al., 2011). As such, we believe that the passage of eddies may induce short-term fluctuations of the MLD in a given location of the SCS. Positive anomalies, i.e., deeper MLD, are expected to be produced by WEs while negative anomalies, i.e., shallower MLD, result from the passage of CEs.

All N and P concentration profiles displayed characteristic surface depletion and increased with depth. Surface concentrations of N and P were analytically detectable in the CEs but not in the WE, as shown in **Table 1**, **Table 2** and **Figure 2** (A1–A3 for N and B1–B3 for P). The Z_N of the WE, CEs sampled in 2013 and 2014 were 57 ± 6, 36 ± 28 and 46 ± 11 m, respectively (**Table 1**, **Figures. 2A1–3**). The difference of Z_N between the CEs and WE was statistically insignificant ($t_{df=4} = -1.13$, $p = 0.162$; **Table 2**). Vertical profiles of POC, PN and Chl concentrations showed strongly similar trends at both CE and WE stations (**Figure 2** C1–C3 for Chl, D1–D3 for POC, E1–E3 for PN). It suggests that POC and PN were mostly derived from phytoplankton biomass. There was no significant difference between the mean surface Chl concentrations measured in the CEs and WE (**Table 2**). However, the subsurface Chl maximum (SCM) was present at shallower depths in the CEs than in the WE, showing the vertical motion induced by the eddies may bring nutrients to the water close to the upper layer (Moloney et al., 1991; Shih et al., 2020). Note that, the satellite-obtained surface Chl concentration (**Supplementary Figure S3**) is not comparable with that obtained from the *in situ* observation (**Table 1**), due to the different time and space scales of these two different observations. Moreover, the Chl concentration obtained from the *in situ* observation may be more sensitive to the changes of physical and biogeochemical processes in the NSCS within a day than the SCM. The concentrations of POC were high in the top

TABLE 2 | Summary of the hydrographic and biogeochemical parameters (±SD) measured in this study of the northern South China Sea, including the temperatures at 50 m water depth ($Temp_{50m}$); mean temperature and salinity values of the mixed layer ($Temp_{MLD}$ and $Salinity_{MLD}$); the mixed layer, nitracline, euphotic zone and subsurface Chl maximum depths, respectively (MLD, Z_N, Z_{eu} and SCM); surface water concentrations of N, P, Chl, POC and PN, respectively (N, P, Chl, POC and PN); the surface abundances of large (>5 μm) phytoplankton and diatoms (Phytoplankton and Diatom); water column inventories (0–150 and 0–100 m) of N, P and Chl (I-N, I-P and I-Chl); inventories in the upper 150 m of POC and PN (I-POC and I-PN); water column phytoplankton and diatom inventories in the upper 100 m (I-Phytoplankton and I-Diatom); water column phytoplankton and diatom carbon inventories in the upper 100 m (I-Phytoplankton C. and I-Diatom C.); the values of diffusion coefficient (K_z); the vertical gradients (MLD–150 and MLD–100 m) of N (N-gradient); the upward vertical diffusive fluxes (0–150 and 0–100 m) of N (N flux); export fluxes of POC and PN at 150 m depth (POC flux and PN flux); retention times of C and N in the upper 150 m (RT-C and RT-N).

parameters	CE (n = 4)	WE (n = 2)	*t* test		
			t	df	*p*
$Temp_{50m}$ (°C)	24.4 ± 1.1	28.5 ± 0.8	−4.53	4	0.005***
$Temp_{MLD}$ (°C)	27.9 ± 1.9	29.3 ± 0.1	−0.98	4	0.384
$Salinity_{MLD}$	33.96 ± 0.14	33.30 ± 0.01	9.54	3	0.002***
MLD (m)	28 ± 17	52 ± 6	−1.86	4	0.068*
Z_N (m)	41 ± 18	57 ± 6	−1.13	4	0.162
Z_{eu} (m)	83 ± 8	78 ± 6	0.77	4	0.484
SCM (m)	58 ± 9	76 ± 5	−2.53	4	0.032**
N (μM)	0.5 ± 0.5	<0.1	1.72	3	0.091*
P (μM)	0.03 ± 0.02	<0.01	2.19	3	0.058*
Chl (mg m^{-3})	0.11 ± 0.04	0.10 ± 0.00	0.76	3	0.250
POC (mg-C m^{-3})	30 ± 8	31 ± 7	−0.12	4	0.913
PN (mg-N m^{-3})	5 ± 1	5 ± 1	0.31	4	0.773
Phytoplankton (10^3 cells L^{-1})	0.62 ± 0.83	0.23 ± 0.04	0.62	4	0.280
Diatom (10^3 cells L^{-1})	0.57 ± 0.80	0.17 ± 0.07	0.67	4	0.270
I-N (mmol m^{-2}) (0–150 m)	867 ± 358	971 ± 420	−0.32	4	0.380
I-N (mmol m–2) (0–100 m)	(322 ± 170)	(337 ± 264)	(−0.09)	(4)	(0.460)
I-P (mmol m^{-2}) (0–150 m)	59 ± 22	48 ± 3	0.67	4	0.260
I-P (mmol m–2) (0–100 m)	(23 ± 11)	(12 ± 0)	(1.88)	(3)	(0.078*)
I-Chl (mg m^{-2}) (0–150 m)	32 ± 5	30 ± 4	0.30	4	0.781
I-Chl (mg m–2) (0–100 m)	(27 ± 5)	(22 ± 1)	(1.28)	(4)	(0.271)
I-POC (g-C m^{-2})	3.8 ± 1.0	4.1 ± 0.2	−0.51	4	0.310
I-PN (g-N m^{-2})	0.7 ± 0.2	1.0 ± 0.4	−1.12	4	0.160
I-phytoplankton (10^6 cells m^{-2})	50 ± 20	16 ± 3	2.27	4	0.043**
I-Diatom (10^6 cells m^{-2})	41 ± 22	7 ± 1	2.13	4	0.050*
I-phytoplankton C. (mg-C m^{-2})	16.4 ± 5.7	6.6 ± 0.4	2.31	4	0.041**
I-Diatom C. (mg-C m^{-2})	13.8 ± 5.2	4.5 ± 1.5	2.35	4	0.039**
K_z (m^2 d^{-1})	4.0 ± 1.5	4.8 ± 4.3	−0.36	4	0.737
N gradient (mmol m^{-4}) (MLD–150 m)	0.10 ± 0.02	0.17 ± 0.04	−2.54	4	0.032**
N gradient (mmol m^{-4}) (MLD–100 m)	(0.13 ± 0.06)	(0.22 ± 0.12)	(−1.39)	(4)	(0.119)
N flux (mmol m^{-2} d^{-1}) (0–150 m)	0.42 ± 0.18	0.90 ± 0.92	−0.74	1.03	0.290
N flux (mmol m^{-2} d^{-1}) (0–100 m)	(0.49 ± 0.26)	(1.34 ± 1.54)	(−0.77)	(1)	(0.290)
POC flux (mg-C m^{-2} d^{-1})	85 ± 55	20 ± 7	1.56	4	0.097*
PN flux (mg-N m^{-2} d^{-1})	16 ± 12	5 ± 3	1.26	4	0.130
RT-C (d)	59 ± 31	226 ± 95	−3.53	4	0.024**
RT-N (d)	938 ± 484	3,328 ± 2,903	−1.16	1	0.454

*The value of CE was the average with 1 SD of first and second CE in 2013 and 2014. *: p < 0.10; **: p < 0.05; ***: p < 0.01.*

50 m of the water column in the CEs, reaching maximum values of 45 and 30 mg-C m^{-3}, and decreasing with depth to less than 30 and 25 mg-C m^{-3} in 2013 and 2014, respectively (**Figures 2D1–D3**). Likewise, high concentrations of POC were observed in the upper 75 m of the WE, reaching a maximum of ~45 mg-C m^{-3}, and declining to less than 20 mg-C m^{-3} at depth. The vertical concentration profiles of PN followed the same pattern as the POC profiles, both in the CEs and the WE (**Figures 2E1–E3**).

Total phytoplankton and diatom abundances showed a much wider range of values in the CEs than in the WE (**Figure 2 F1–F3** for phytoplankton, **G1–G3** for diatom). In the two CEs, cell counts for phytoplankton and diatoms were lowest near the surface (0.12–0.26 and 0.10–0.26 × 10^3 cells L^{-1}, respectively; **Figure 2**) and increased with depth to a subsurface maximum (0.52–2.28 and 0.32–1.94 × 10^3 cells L^{-1}, respectively; **Figure 2**). An unusually high abundance of phytoplankton and diatoms (1.86 and 1.76 × 10^3 cells L^{-1}, respectively; **Figure 2**) was also observed in the surface waters of station S1, inside the first CE. At WE stations S5 and S6, however, cell densities of phytoplankton and diatoms were not only low near the surface (0.20–0.26 and 0.12–0.22 × 10^3 cells L^{-1}, respectively; **Figure 2**), but they also remained uniformly low with increasing depth (0.16–0.34 and 0.06–0.08 × 10^3 cells L^{-1}, respectively; **Figure 2**). In the first CE and the WE, centric diatoms (**Figure 3**, blue) were more abundant than pennate diatoms (**Figure 3**, red) in the surface waters, with the dominant genera being *Bacteriastrum*, *Thalassiosira* and *Chaetoceros*. The most abundant diatoms genera in the surface waters of the second CE were pennate diatoms represented by *Pleurosigma* and *Nitzschia* species

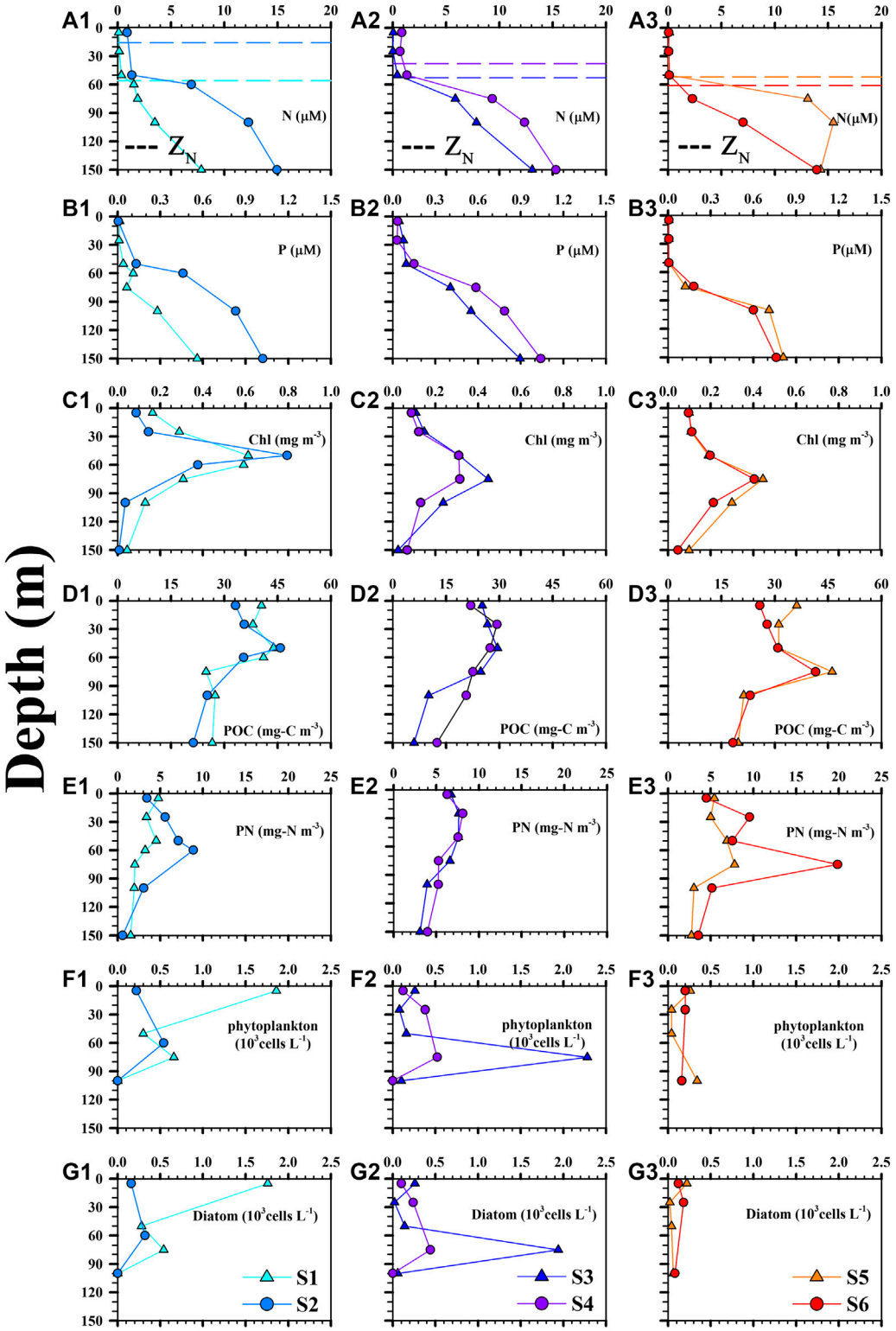

FIGURE 2 | Vertical profiles of **(A1–A3)** nitrate + nitrite (N), **(B1–B3)** phosphate (P), **(C1–C3)** chlorophyll (Chl), **(D1–D3)** POC, **(E1–E3)** PN, **(F1–F3)** phytoplankton abundance and **(G1–G3)** diatom abundance at stations S1 (CE), S2 (CE), S3 (CE), S4 (CE), S5 (WE) and S6 (WE). Horizontal dashed lines in **A1–A3** represent the depth of the nitracline (Z_N).

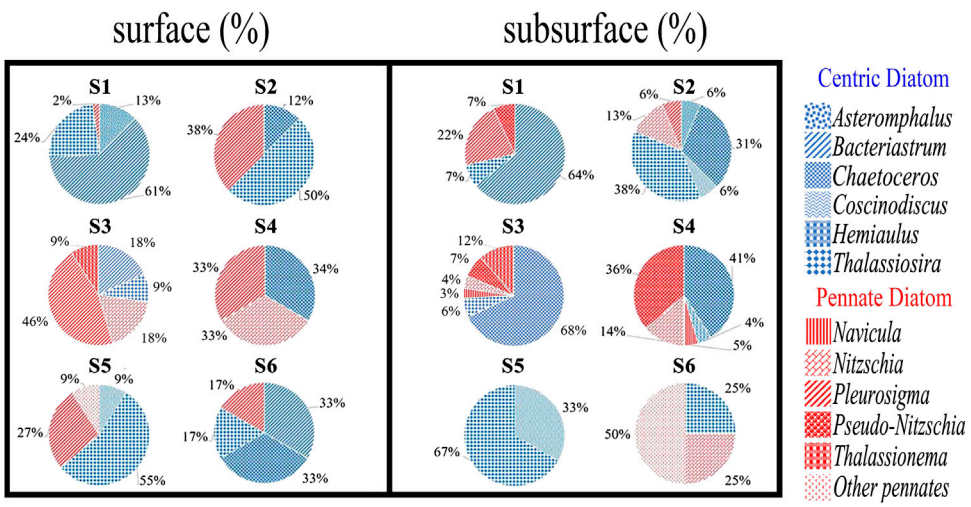

FIGURE 3 | Pie charts showing the relative abundances of centric and pennate diatom cells in surface (5 m) and subsurface (Chl maximum depth) waters.

(**Figure 3**). In subsurface waters (i.e., SCM), centric diatoms were most abundant at stations S1 and S2, with the dominant genera being *Bacteriastrum*, *Thalassiosira* and *Chaetoceros*, while at S3 and S4 the dominant centric and pennate diatoms were genera of *Chaetoceros* and *Pseudo-nitzschia*, respectively. Finally, a clear difference was observed between the periphery (S5) and the core (S6) of the WE, with the centric diatom *Thalassiosira* being dominant at S5 but *Nitzschia* and other unknown pennate diatoms being dominant at S6 (**Figure 3**).

Inventories (I-N, I-P, I-Chl, I-POC, I-PN, I-Phytoplankton and I-Diatom), POC and PN Fluxes, Retention Times (RT-C and RT-N) and Vertical Diffusion Flux of N

It should be noted from the outset that **Figure 4** presents water column inventories calculated from the surface to 150 m (i.e., I-N, I-P, I-Chl). On the other hand, **Tables 1**, **2** also present inventories of the upper 100 m of the water column so as to allow direct comparison with previously published results. **Figures 4A1–A2** showed that the I-N was lower—although not significantly so—in CEs than in the WE ($t_{df=4}$ = −0.32, p = 0.380) whereas I-P tended to be higher in CEs than in the WE ($t_{df=4}$ = 0.67, p = 0.260; **Table 2**). The comparable results of I-N or I-P between the CEs and WE might be attributable to transient spatiotemporal characteristics of the eddies in distinct sampling locations, such as the extremely high value of 1,268 mmol m^{-2} of I-N which occurred at station S5 (**Table 1**; **Figure 4A2**), close to the periphery of the WE as revealed by the satellite SLA map (**Figure 1C**). It is commonly understood that the cores of CEs and WEs are associated with upwelling and downwelling which may correspondingly enhance and suppress nutrients vertical transport, respectively (Sweeney et al., 2003; Zhou et al., 2013; Shih et al., 2015). However, the upwelling can also be induced around the periphery of WEs via the eddy-wind, eddy-eddy and/or eddy-front interactions (McGillicuddy, 2016), supplying more nutrients than near the WE cores (compare the values of I-N at stations S5 and S6 in **Table 1**).

The I-Chl values ranged from 26 to 38 and 28–33 mg m^{-2} for the CEs and WE, respectively (**Table 1**, **Figure 4**). Mean values across the CEs and the WE were 32 ± 5 and 30 ± 4 mg m^{-2} (**Table 2**), respectively. These values were consistent with those previously observed (**Table 3**) in the northern SCS (NSCS) (Chen et al., 2004; Chen 2005; Tseng et al., 2005; Li et al., 2016), with the exception of a higher value (38 ± 4 mg m^{-2}; **Table 1**) recorded in the first CE and which was more comparable with the value (35 mg m^{-2}) reported in winter by Tseng et al. (2005) (**Table 3**). The average I-POC of the CEs and WE were 3.8 ± 1.0 and 4.1 ± 0.2 g-C m^{-2}, respectively (**Table 2**; **Figure 4**). The average I-PN were 0.7 ± 0.2 and 1.0 ± 0.4 g-N m^{-2} for the CEs and WE, respectively (**Table 2**; **Figure 4**). Although there was no significant difference between the mean values of I-POC and I-PN in the different eddies, there were significant differences between the values measured at individual stations: thus I-POC values were 4.7 and 4.5 g-C m^{-2} at S1 and S2, respectively, against 2.7 and 3.2 g-C m^{-2} at S3 and S4; I-PN was 1.2 g-N m^{-2} at S6 against 0.7 g-N m^{-2} at S5 (**Table 1**; **Fig. 4**).

The vertical POC export flux from the WE averaged 20 ± 7 mg-C m^{-2} d^{-1}, which was lower than the fluxes (85 ± 55 mg-C m^{-2} d^{-1}) out of the CEs ($t_{df=4}$ = 1.56, p = 0.097; **Table 2**; **Figures 4C1–C2**). Similarly, the mean export flux of PN tended to be smaller in the WE than that in the CEs ($t_{df=4}$ = 1.26, p = 0.130; **Table 2**; **Figures 4C1–C2**). Although the CEs produced elevated export fluxes of POC and PN, they did not differ noticeably from the WE in terms of their nutrient concentration profiles (**Figures 2A1–A3,B1–B3**) or nutrient inventories (**Figures 4A1–A2**) because nutrients were replenished by upwelling at a greater rate than in the WE. In turn, these elevated fluxes resulted in shorter RT-C and RT-N of the CEs compared with RT-C and RT-N in the upper 150 m of the WE (**Table 2**; **Figures 4D1,D2**). These results thus reinforce the notion of CEs as sites of enhanced

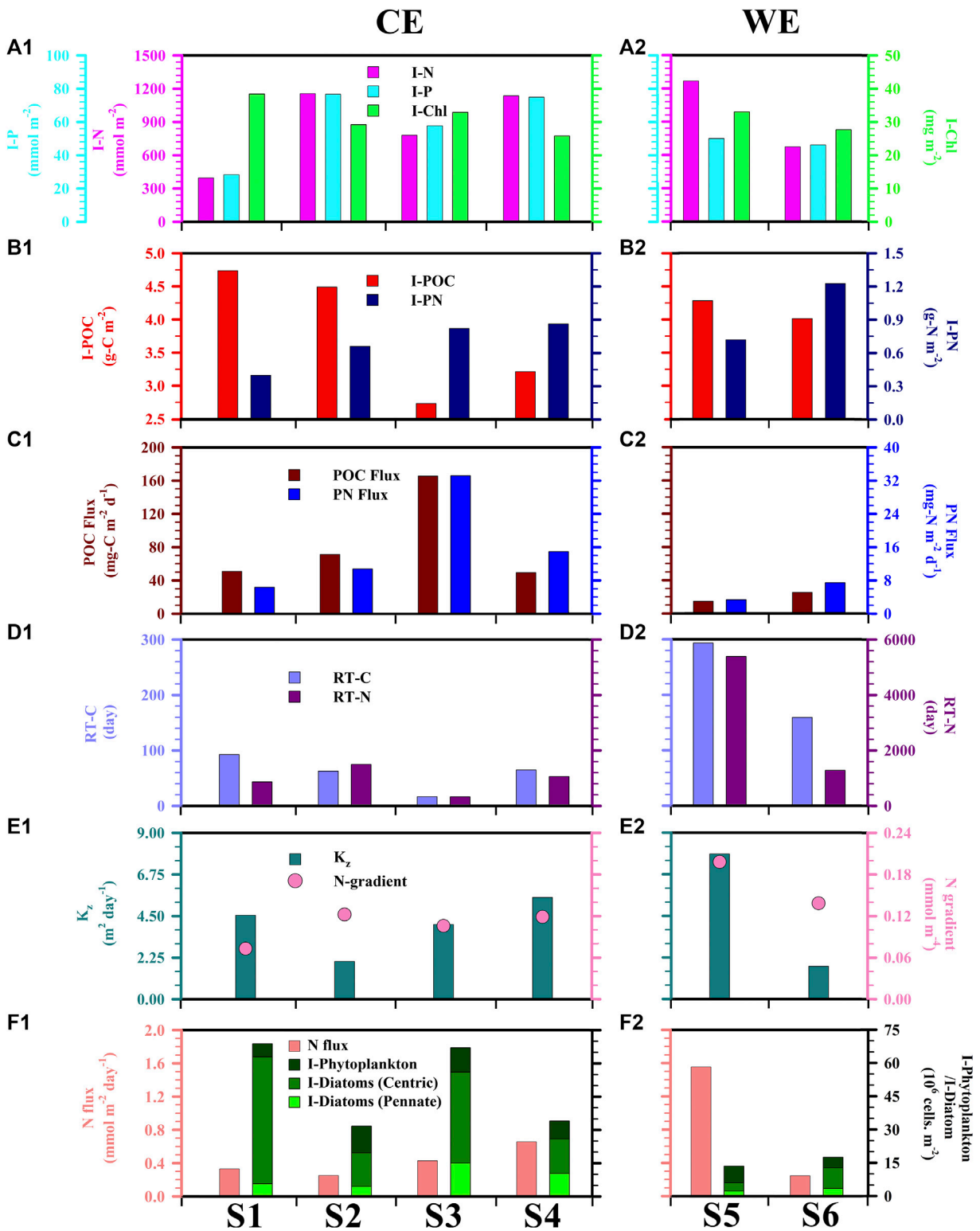

FIGURE 4 | Depth-integrated (0–150 m) values of **(A)** nitrate + nitrite (N), phosphate (P), chlorophyll (Chl) and **(B)** POC and PN; **(C)** POC and PN fluxes measured at a depth of 150 m; **(D)** Retention times of carbon (RT-C) and nitrogen (RT-N) in the upper 150 m representing how long it would take for sedimentation by itself to remove all of POC and PN from the water column (RT-C = I-POC/POC flux; RT-N = I-PN/PN flux); **(E)** Vertical eddy diffusion coefficient (K_z) between MLD and 150-m depth and corresponding nitrate + nitrite (N) concentration gradient; **(F)** Total phytoplankton and diatom inventories (0–100 m) (I-Phytoplankton/I-Diatom), and nitrite + nitrate flux (N flux) due to turbulent mixing.

TABLE 3 | Compilation of published field data on N, P and Chl inventories, N gradients, vertical diffusion coefficients and N fluxes in the upper 100 m of the water column at different locations of the NSCS. Numbers in parentheses represent one standard deviation.

Season (month)	I-N ($mmol\ m^{-2}$)	I-P ($mmol\ m^{-2}$)	I-Chl ($mg\ m^{-2}$)	N gradient ($mmol\ m^{-4}$)	K_z ($m^2\ d^{-1}$)	N flux ($mmol\ m^{-2}\ d^{-1}$)	References
Spring	293	20	31	0.13	3.3	0.33	This study (CE1)[a]
(Apr 2013)	(257)	(18)	(4)	(0.10)	(1.8)	(0.09)	—
Spring	351	25	24	0.13	4.8	0.64	This study (CE2)[a]
(May 2014)	(132)	(5)	(4)	(0.04)	(1.0)	(0.31)	—
Autumn	337	12	22	0.22	4.8	1.34	This study (WE)[a]
(Sep 2013)	(264)	(0)	(1)	(0.12)	(4.3)	(1.54)	—
Spring	—	—	20	—	—	—	Chen et al. 2004[b]
(Mar 2000)	—	—	(4)	—	—	—	—
Spring	—	—	22	—	—	—	Chen et al. 2004[b]
(Mar 2001)	—	—	(4)	—	—	—	—
Spring	—	—	21	—	—	—	Chen 2005[c]
(Mar 01; 02)	—	—	(5)	—	—	—	—
Autumn	—	—	21	—	—	—	Chen 2005[c]
(Oct 2002)	—	—	(1)	—	—	—	—
Winter	—	—	35	—	—	—	Tseng et al., 2005
Other seasons	—	—	15	—	—	—	Tseng et al., 2005
Summer	—	—	—	—	1.8	0.20	Chou et al., 2006
(Jul–Sep)	—	—	—	—	(0.8)	(0.04)	—
Spring	183	—	—	—	—	—	Chen et al., 2007
(Apr–May)	(25)	—	—	—	—	—	—
Spring	252	21	—	—	—	—	Du et al. 2013[d]
(May)	—	—	—	—	—	—	—
Summer	292	24	—	—	—	—	Du et al. 2013[d]
(Jul–Aug)	—	—	—	—	—	—	—
Autumn	245	23	—	—	—	—	Du et al. 2013[d]
(Oct–Nov)	—	—	—	—	—	—	—
Winter	201	13	—	—	—	—	Du et al. 2013[d]
(Jan)	—	—	—	—	—	—	—
Spring	—	—	21	0.07	18.3	1.18	Li et al. 2016[e]
(May)	—	—	(8)	(0.03)	(10.8)	(0.90)	—
Summer	—	—	—	0.01[f]	0.6[g]	0.11[h]	Du et al. 2017[i]
(Aug)	—	—	—	—	—	—	—

[a]*Average inventories of N, P and Chl over the upper 100 m of the water column measured at the two main sampling sites. The one standard deviation had shown in parentheses.*
[b]*Values have been derived from ratios of integrated PP (IPP) and Chl (IPP/IChl) in Table 1 and Table 2 reported by Chen et al. (2004). The values of mean with one standard deviation include the observations at stations 3, A, B, C and D in Chen et al. (2004).*
[c]*The data obtained from Table 3 (Spring; March 2001 and 2002) and Table 4 (Autumn; Oct 2002) reported by Chen (2005). The values of mean with one standard deviation include the observations of slope and basin stations in the NSCS.*
[d]*Nutrient standing stocks of the upper 100 m reported by Du et al. (2013) were divided by the surface area of the studied region ($2.74 \times 10^{11}\ m^2$) to yield water column inventories.*
[e]*Values in Table 1 reported by Li et al. (2016) have been averaged, excluding values at stations C6 and B.*
[f]*The value is derived from Figure 2 of Du et al. (2017).*
[g]*Average of the maximum and minimum values of K_z, upper 100 m.*
[h]*Maximum value at a depth of 68 m.*
[i]*N gradient here refers to nitrate (NO_3^-) only.*

vertical POC fluxes (Bidigare et al., 2003; Hung et al., 2004; Hung et al., 2010a; Zhou et al., 2013; Shih et al., 2015).

Vertical diffusion coefficients (K_z) were calculated as a function of quantities derived from the *in situ* density profiles in the upper 150 m water column. Values of K_z ranged from 2.0 to 5.5 $m^2\ d^{-1}$ with an average of 4.0 ± 1.5 $m^2\ d^{-1}$ in the CEs, ranging from 1.8 to 7.9 $m^2\ day^{-1}$ with an average of 4.8 ± 4.3 $m^2\ day^{-1}$ in the WE (**Table 2**; **Figures 4E1–E2**). These mean values were higher than the value of 2.0 $m^2\ day^{-1}$ derived from the model estimation previously reported in November at low-latitude area of SCS by Cai et al. (2002); the values of 1.2–2.3 $m^2\ day^{-1}$ derived from the constant ε estimation previously reported during the summer period at SEATS site by Chou et al. (2006); the value of 0.6 $m^2\ day^{-1}$ derived from the *in situ* ε estimates recently reported in summer at SEATS site by Du et al. (2017). Reversely, these values were lower than the value of 18.3 ± 10.8 $m^2\ day^{-1}$ averaged from the *in situ* ε calculation recently proposed in spring at NSCS by Li et al. (2016) (**Table 3**). Vertical concentration gradients of N (N gradient) in the CEs ranged from 0.07 to 0.12 $mmol\ m^{-4}$ with an average of 0.10 ± 0.02 $mmol\ m^{-4}$, while in the WE they ranged from 0.14 to 0.20 $mmol\ m^{-4}$ with an average of 0.17 ± 0.04 $mmol\ m^{-4}$ (**Table 2**; **Figures 4E1–E2**). On the other hand, the average value (0.13 ± 0.06 $mmol\ m^{-4}$) of N gradient in the upper 100 m of the CEs was higher ($t_{df=4} = 1.93$, $p = 0.06$) than the value (0.07 ± 0.03 $mmol\ m^{-4}$) investigated in spring by Li et al. (2016); the average value (0.22 ± 0.12 $mmol\ m^{-4}$) of N gradient in the upper 100 m of the WE (in September) was noticeably higher than the value (0.01 $mmol\ m^{-4}$) reported in

the summer (in August) by Du et al. (2017) (**Table 3**). Adopting these values (K_z and N gradient) yields vertical entrainment N fluxes of 0.42 ± 0.18 mmol m^{-2} d^{-1} for the CEs and 0.90 ± 0.92 mmol m^{-2} d^{-1} for the WE from the water depth of 150 m (**Table 2**; **Fig. 4F1–F2**). I-Phytoplankton and I-Diatom in the CEs were higher than in the WE (**Table 2**; **Figures 4F1–F2**). To summarize, phytoplankton and diatom inventories were ~3.1 and ~5.9 times higher in the CEs than in the WE, respectively.

DISCUSSION

Nutrients Dynamics in CE and WE

It has been reported that phytoplankton growth in the SCS is limited by nitrogen availability (Chen 2005; Chen et al., 2004). To put our work in a broader perspective, we therefore began by examining the potential role of eddies in supplying nitrogen to the euphotic zone. To facilitate comparison with reports from previous studies (Chen et al., 2007; Du et al., 2013, 2017; Li et al., 2016), we reported our nitrogen results in terms of depth-integrated inventories in the upper 100 m water column, referred to as I-N. The corresponding values of I-N at stations S1–S6 were exhibited in **Table 1**. On average, I-N was 293 ± 257, 351 ± 132 and 337 ± 264 mmol m^{-2} in the first, second CE and the WE, respectively, i.e., tended to be higher (p = 0.132) than the range of values previously reported in the NSCS (183–292 mmol m^{-2}; **Table 3**) over the entire year (Chen et al., 2007; Du et al., 2013). The mean value of 322 ± 170 mmol m^{-2} in the CEs (**Table 2**) was 76 and 28% higher than the values of 183 ± 25 and 252 mmol m^{-2} in spring by Chen et al. (2007) and Du et al. (2013), respectively (**Table 3**). The average of 337 ± 264 mmol m^{-2} in the WE (**Table 3**) was 15 and 38% higher than the values of 292 and 245 mmol m^{-2} previously reported in summer and autumn (Du et al., 2013), respectively. It is important to note that the individual value we measured close to the WE periphery (524 mmol m^{-2}) was exceptionally high. Indeed, that value was similar to inventories measured in other eddies of the Northern Hemisphere where a clear upwelling of nutrient-rich waters had been demonstrated (Chen et al., 2007; Zhou et al., 2013; Shih et al., 2015).

Here we found that the average water column (0–100 m) concentrations of N increased by 1.04 μM [(322–218) mmol m^{-2}/100 m = 1.04 mmol m^{-3}] and 0.68 μM [(337–269) mmol m^{-2}/100 m = 0.68 mmol m^{-3}] in the CEs and WE, respectively (the detail estimation was listed in **Supplementary Table S2**). The values of 218 and 269 mmol m^{-2} within the estimation above were the mean I-N values calculated from 183 to 252 mmol m^{-2} reported by Chen et al. (2007) and Du et al. (2013) in Spring, from 292 to 245 mmol m^{-2} reported by Du et al. (2013) in Summer and Autumn, respectively (**Table 3**). These net concentration increases took place despite the loss of some quantity of N bound up with sinking particles. Assuming the N concentrations were at steady state over that period, the amount of N associated with this lost particulate matter must therefore be added to the observed net N increases to compute the amount of N injected into the upper layer. Here we conservatively assumed that nutrient injection took place over 7-days (Chelton 2001). During that period, biological uptake caused a drawdown of N at the CEs and the WE were accordingly 0.05 and 0.02 μM (PN flux mg-N m^{-2} d^{-1}/150 m × 7 days/14 mg $mmol^{-1}$), respectively. This would have required a compensating upward transport of N to produce the N concentrations of 1.09 (1.04 + 0.05) and 0.70 (0.68 + 0.02) μM (**Supplementary Table S2**) within the upper layer at the CEs and the WE, respectively. These values tended to be lower (or comparable) (CE: p = 0.10; WE: p = 0.14) than the simulated estimate (3.21 ± 3.04, 0.2–10.7 μM) under the pass of CEs for the time-series study KEO (Kuroshio Extension Observatory) reported by Honda et al. (2018). They were nevertheless sufficient to stimulate the growth of phytoplankton species and to induce biological responses that would otherwise be constrained by the insufficient N-availability in the oligotrophic surface open waters of the NSCS. If we assume steady state and use our particulate N flux value of 16 mg-N m^{-2} d^{-1}/14 g mol^{-1} = 1.14 mmol m^{-2} d^{-1} and upward vertical diffusive flux of N of 0.42 mmol m^{-2} d^{-1} (**Table 2**), we obtain a value of 37% for the approximate contribution of CEs to the nutrient sources to the water column. In terms of the annual budget, however, this figure should only be viewed as a first-order approximation due to the limited temporal dataset of our study.

Figure 5 shows no significant correlation between I-Phytoplankton (or I-Diatom) and I-Chl (or I-N). This might be due in part to the variability in the chemical composition of phytoplankton as a function of taxa and bloom phases. Interestingly, a negative linear relationship was observed between I-Phytoplankton (or I-Diatom) and the vertical N gradient (**Figures 5E–F**). On average, the vertical N-gradient was smaller in the CEs than in the WE (**Table 2**; **Figures 4E1–E2**), which therefore implies that the turbulent diffusion coefficient must have been larger in the CEs than in the WE.

Community Structure of Large Phytoplankton in the CEs and the WE

The phytoplankton species and cell size composition appears to respond to the passage of the eddies in a similar way to that observed after the passage of a winter storm or a typhoon. The upper ocean response to both CE (core zone) and WE (periphery zone) in terms of its water column physical structure is the onset of upwelling and the upward transport of deeper, nutrient-rich water into the photic zone, thus providing suitable conditions for large phytoplankton growth (Chen et al., 2004, Chen et al., 2011, Chen et al., 2015; Chen 2005). The relationship between Chl and large phytoplankton inventories is a matter of continuing debate despite reports of significant positive relationships at a few different areas (Liu et al., 2007). Our observations in both the CEs and the WE do not support the notion of a widely applicable relationship, or indeed a relationship at all. For example, the average I-Chl of the WE and of the CEs were comparable (**Table 2**), however, I-Phytoplankton and I-Diatom were higher in the CEs than in the WE (**Table 2**). The uncoupling between I-Chl and I-Phytoplankton or I-Diatom might be due to different population dynamics and assemblages of phytoplankton at the different locations. The lack of significant relationship between the abundance of large phytoplankton or diatoms and

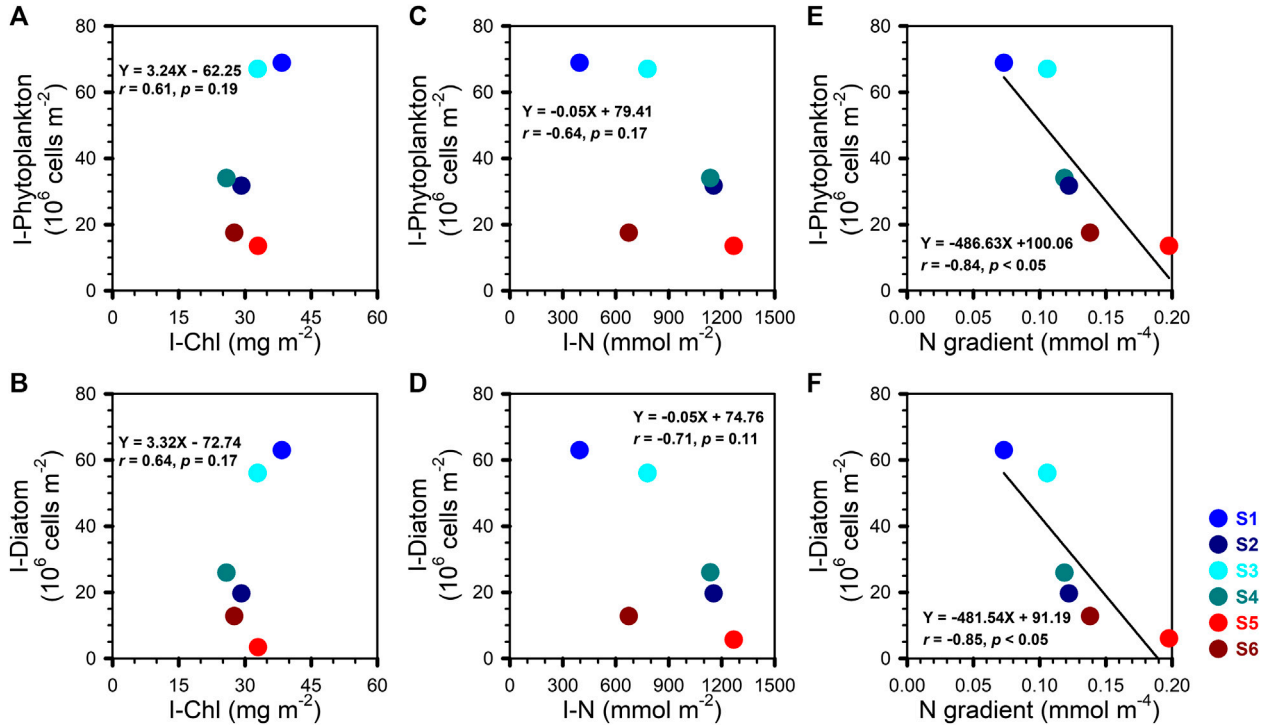

FIGURE 5 | I-Phytoplankton and I-Diatom vs. **(A, B)** I-Chl; **(C, D)** I-N; **(E, F)** N gradient between the lower boundary of the mixed layer and 150 m. The lines in the E and F denoted the result of linear regression.

the Chl stocks can thus be attributed to the differing phytoplankton assemblages and their cellular fluorescence signals in the CEs and the WE. Previous field observations (Chen 2000; Sweeney et al., 2003; Liu et al., 2007) have revealed that small phytoplankton, such as *Synechococcus*, *Prochlorococcus* and picoeukaryotes contribute most of the Chl fluorescence in the upper water column. It follows that the high value of I-Chl at S5, without a correspondingly high POC export, may reflect a greater portion of small-celled phytoplankton compared to the phytoplankton assemblages in the CEs.

Nutrient replenishment, as occurs in the CEs, triggers the growth of the larger phytoplankton species while the N:P ratio further affects their species composition and succession. In this study, the average I-N:I-P ratio in the upper 150 m was 14 ± 1 in the CEs and 20 ± 8 in the WE. In the CEs, diatoms made up 78 ± 13% of all the large-celled phytoplankton, including 59 ± 17% as centric and 19 ± 10% as pennate diatoms (**Figure 4F1**). In the WE, diatoms made up only 59 ± 20% of all the large-celled phytoplankton, including 39 ± 20% as centric and 18 ± 2% as pennate diatoms (**Figure 4F2**). The abundance of large cells, including diatoms (e.g., *Chaetoceros*, *Coscinodiscus*, *Bacteriastrum*) and dinoflagellates (e.g., *Ceratium*), is what resulted in shorter fractional retention times of POC and PN within the CEs than within the WE (**Table 2**). In addition, retention time in the upper layer was shorter for POC than for PN since carbon takes longer to regenerate and hence a greater share of POC than PN is removed by sinking from the euphotic zone (Liu et al., 2002, Liu et al., 2007). Note that the residence time defined here (**Figures 4D1–D2**) represents how long it would take for the process of sinking by itself to vertically remove all the particulate organic matters from the upper 150 m water column. Dividing the distance of transport (150 m) by the residence time of carbon (RT-C (days)) yields an average sinking rate of 3.9 ± 3.5 (1.6–9.1) m d^{-1} in the CEs and 0.7 ± 0.3 (0.5–0.9) m d^{-1} in the WE. We believe that the faster POC sinking velocity and shorter retention time of larger celled phytoplankton in the CEs compared to the WE ($p < 0.10$), has the effect of shortening oceanic food webs and increasing grazing pressure on the other components, thus promoting the repackaging of the organic carbon pool and further strengthening the biological pump (Sweeney et al., 2003; Hung et al., 2010b; Chung et al., 2012).

Origin of the POC Flux in the CEs and the WE

Phytoplankton species composition determines to a large extent the fraction of the total biological production that is exported from the surface ocean. For example, POC generated by diatoms and other large species is more effectively exported than POC generated by smaller and/or soft-bodied plankton (Sweeney et al., 2003 and references therein). It is worth noting that the average POC flux of the first CE (**Table 1**; **Fig. 4C1**) was higher than that reported (50 ± 7 mg-C m^{-2} d^{-1}) in the same area of the NSCS in winter (Hung and Gong, 2010) even though this region as a whole exhibits highest productivity in winter (Liu et al., 2002; Liu et al., 2007; Chen et al., 2007). Likewise, the POC flux driven by the second CE (**Table 1**, **Figure 4C1**) in spring was somewhat higher

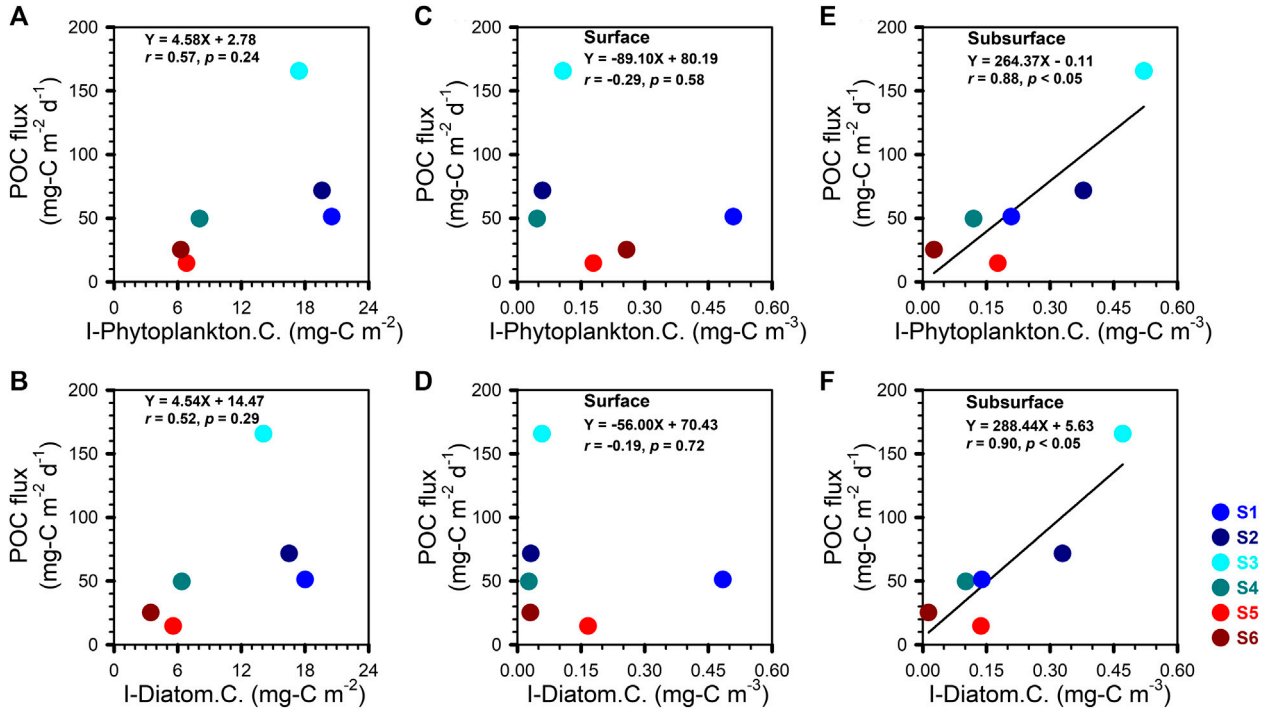

FIGURE 6 | POC fluxes vs. **(A, B)** I-Phytoplankton and I-Diatom carbon inventories (I-Phytoplankton **C**. and I-Diatom **C**.); **(C, D)** phytoplankton and diatom carbon contents (Phytoplankton C. and Diatom C.) in surface waters; **(E, F)** phytoplankton and diatom carbon contents (Phytoplankton C. and Diatom C.) in subsurface waters (i.e., SCM). The lines in the E and F denoted the result of linear regression.

than previously reported (12 mg-C m^{-2} d^{-1}) for the same area and during the same period. Finally, the POC flux driven by the WE (**Table 1**, **Figure 4C2**) in autumn was quite comparable to the value (29 mg-C m^{-2} d^{-1}) reported near the SEATS site by Chen et al. (1998) during the summer monsoon. The major discrepancy with previously reported POC fluxes was at station S3, where the structure of the water column persisted for at least ~15 days (**Supplementary Figure S6**): the POC flux there reached a value of 166 mg-C m^{-2} d^{-1} (**Table 1**; **Figure 4C1**), i.e., well beyond the range of values defined by the time-series observational record (83 ± 34 mg-C m^{-2} d^{-1}) at the SEATS site (Wei et al., 2011). **Supplementary Figure S7** shows how the core of the second CE remained quasi-stationary for more than 2 weeks. This unusual event differs from previous descriptions of eddies in the SCS (Chen et al., 2011). That eddy was a small eddy with a radius of 53–74 km and a lifetime of 1 month (**Supplementary Figure S7**). These observations suggest that the intensity of biogeochemical processes may be stronger in sub-mesoscale than in mesoscale eddies (Chen et al., 2011).

The surface-to-deep ocean transfer efficiency of plankton-fixed POC is affected by the production of biogenic particles in the surface ocean as well as the carbon content of the large, fast-sinking phytoplankton species (Sweeney et al., 2003; Olenina et al., 2006). As such, we had initially expected to find a significant relationship between POC fluxes and the water column carbon inventory from the large phytoplankton and diatoms species we identified. No such relationship held in the upper 100 m (**Figures 6A,B**). We subsequently reexamined this relationship separately in both surface and SCM waters. We found significant linear relationships between the POC export flux and the carbon contents of phytoplankton and diatoms in the waters of the SCM (**Figures 6E–F**) but not in the surface waters (**Figures 6C–D**).

These results provide several vital clues for the further understanding of carbon sequestration caused by eddies and points to the transfer efficiency being related to the type of phytoplankton. Larger cells with heavy, durable shells (e.g., diatoms) sink relatively rapidly and are more efficient carbon carriers than smaller phytoplankton cells (e.g., *Synechococcus*, *Prochlorococcus*) (Karl et al., 2003). Some studies (Karl et al., 2003; Sweeney et al., 2003) have identified diatoms as a principal component for total organic carbon export flux from the upper water column. Yet our compositional data suggest that carbon sources other than diatoms contribute to the flux of sinking particles. Honda and Watanabe (2010) have argued that the association with ballast minerals, opal or $CaCO_3$, can control the export flux of organic matter in the subarctic Pacific Ocean. However, the relative contribution of ballast minerals to the downward POC flux in tropical regions such as the NSCS remains an open question. Answering this question will be the next critical step in explaining and modeling sediment trap results in these regions. A portion of the POC that is unlikely to be associated with ballast minerals consists of zooplankton fecal pellets. These have been identified as one of the main component of sinking particulate matter, but their overall contribution to the

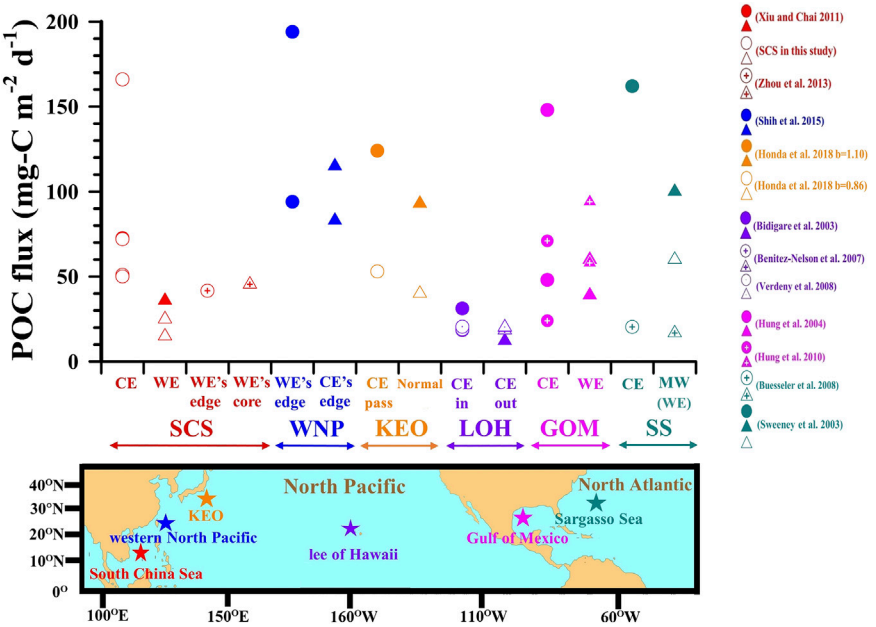

FIGURE 7 | POC fluxes associated with eddies in subtropical regions of the Northern Hemisphere: South China Sea (SCS), Western North Pacific (WNP), Kuroshio Extension Observatory (KEO), Lee of Hawaii (LOH), Gulf of Mexico (GOM), Sargasso Sea (SS). POC fluxes at KEO (Honda et al., 2018), 150-m depth, was estimated according to the Martin's flux attenuation equation, i.e., POC flux = $Flux_{100}$ $(Z/100)^{-b}$ (Martin et al., 1987) with b values from Shih et al. (2019) and Martin et al. (1987) (1.10 and 0.86, respectively); the POC flux denoted by symbols of circle and triangle when CE passed and did not pass over a moored sediment trap, respectively (CE pass and Normal). POC fluxes in the Sargasso Sea, 150-m depth, were calculated according to [POC flux (mg-C m^{-2} d^{-1})] = [^{234}Th flux (dpm m^{-2} d^{-1})] × [POC/^{234}Th (μmol dpm^{-1})], where the flux of ^{234}Th was obtained from Sweeney et al. (2003) and an average value for [POC/^{234}Th] was obtained from the references listed in Hung et al. (2012). Relative to the reference zone or period, i.e., triangle symbols, circle symbols represented the POC flux which the high value was expected to be observed at the target zone or period.

POC flux can be highly variable. Turner (2015) and references therein report contributions of fecal pellets to POC export ranging from less than 1–100%. Clearly, the potential contribution of fecal pellets to POC export cannot be ignored since they may explain the weak and insignificant relationships we obtained between the POC flux and the I-Phytoplankton (I-Diatom included) carbon inventory. Although we did not collect fecal pellets in the present study, it would be important to obtain fecal pellet measurements in future work.

An important positive finding of our study is the significant positive relationship between the POC flux and the phytoplankton carbon content in subsurface waters (i.e., SCM), which holds equally strongly for total phytoplankton or diatom cells alone (**Figures 6E,F**). This finding and our other results underscore the importance of measuring primary production in subsurface waters, especially as it cannot be estimated from satellite measurements of ocean color. All in all, our result suggests that the large phytoplankton and diatoms of the SCM within subsurface waters that appear to govern the POC export to the deep sea. This important finding highlights the limitations of remote sensing as a tool to further our understanding of the impact of eddies on oceanic interior biogeochemical responses, since remote sensing is limited to the very top layer of the sea surface.

Numerous field investigations based on different techniques such as buoy-tethered floating sediment traps (Hung et al., 2004; Hung et al., 2010a; Benitez-Nelson et al., 2007; Buesseler et al., 2008; Shih et al., 2015; this study), moored sediment traps (Honda et al., 2018), neutral buoyancy sediment traps (Buesseler et al., 2007), radioactive isotope disequilibrium (Bidigare et al., 2003; Sweeney et al., 2003; Buesseler et al., 2008; Verdeny et al., 2008; Zhou et al., 2013) as well as modeling approaches (Xiu and Chai 2011) have generally drawn the conclusion that POC export fluxes associated with eddies are high relative to those measured in the surrounding waters. We have compiled POC fluxes collected from "target zones"—where high fluxes are expected—versus POC fluxes from 'reference zones'—where low fluxes are expected (**Figure 7**). In practice, target vs. reference zones (circle and triangle symbols in **Figure 7**) may correspond to CE vs. WE, WE's edge vs. WE's core, WE's edge vs. CE's edge, CE vs. no eddy (external waters), or CE vs. mode water (MW) or WE. Taken collectively, these comparisons serve to evaluate the impact of eddies on the magnitude of the POC export flux (**Figure 7**; **Supplementary Table S3**). Among all references listed in **Figure 7**, the target zone to reference zone POC flux ratios ranged from 1.3 to 5.7 (**Supplementary Table S3**), confirming that enhanced POC export fluxes are associated with eddies. Although our own results fall into this classification, we also found that the two CEs differed in several aspects from each other as well as from the WE. These differences point to the influence of

phytoplankton community structure, which in turns depends on the evolution and stability of the upper water column, as a critical factor controlling the biogeochemistry of the eddy.

SUMMARY

Our study provided *in situ* and direct measurement of POC flux associated with CEs and WE in the NSCS. Both CEs exhibited a shorter retention time, a higher sinking velocity of POC and a higher POC flux than the WE, indicating that carbon export processes were more intense in the CEs than the WE. The enhanced POC export was primarily due to the greater abundance of large cell phytoplankton (e.g., diatoms, large dinoflagellates) at depths ranging between 30 and 90 m (subsurface Chl maximum). These findings highlight the limitations of remote sensing as a tool to study the upper ocean biogeochemical responses to eddies. The lack of correlation between Chl and large phytoplankton inventories in the upper 100 m of the water column was likely due to the variability in the Chl content of the phytoplankton taxa making up the different assemblages in different eddy conditions. Large cell phytoplankton growth was favored under the high-turbulence, weak N-gradient prevailing in the CEs. Conversely, the more stratified, strong N-gradient conditions encountered in the WE encouraged the growth of smaller-celled phytoplankton which may be grazed by small protozoa. Further field investigations are required to clearly elucidate and accurately quantify the evolution and transport of biogeochemical properties induced by cold and warm eddies. This will require new sampling and sensor technologies to extend the spatial and temporal scales of the present study. Especially useful would be the establishment of a long-term observation system to monitor the physical and biogeochemical properties of NSCS waters outside the eddies.

DATA AVAILABILITY STATEMENT

The datasets generated for this study are available on request to the corresponding author.

AUTHOR CONTRIBUTIONS

HC conceived the idea. SY and HC wrote the manuscript with contributions from MF. SY, TS, SH, CC, and CY performed the experiments and created the figures. CC detected the SCS eddies. SY, HC, MF, TS, and CC revised the manuscript. All authors reviewed the manuscript.

FUNDING

This research was supported by the Ministry of Sciences and Technology (MOST) of Republic of China (R.O.C.). Grants numbers are 107-2611-M-019 -020 -MY2, 108-2611-M-012-001, 108-2611M-110-019-MY3, 108-2917-I-564-017, 109-2611-M-019-013 and 109-2611-M-012-001.

ACKNOWLEDGMENTS

We appreciate the assistance given us by the crews and technicians of R/V *OR-3* and R/V *OR-5*.

SUPPLEMENTARY MATERIAL

The Supplementary Material for this article can be found online at: https://www.frontiersin.org/articles/10.3389/feart.2020.537332/full#supplementary-material.

REFERENCES

Benitez-Nelson, C. R., Bidigare, R. R., Dickey, T. D., Landry, M. R., Leonard, C. L., Brown, S. L., et al. (2007). Mesoscale eddies drive increased silica export in the subtropical Pacific Ocean. *Science* 316, 1017–1021. doi:10.1126/science.1136221

Bidigare, R. R., Benitez-Nelson, C., Leonard, C. L., Quay, P. D., Parsons, M. L., Foley, D. G., et al. (2003). Influence of a cyclonic eddy on microheterotroph biomass and carbon export in the lee of Hawaii. *Geophys. Res. Lett.* 30, 1318. doi:10.1029/2002gl016393

Boyd, P. W., Claustre, H., Levy, M., Siegel, D. A., and Weber, T. (2019). Multi-faceted particle pumps drive carbon sequestration in the ocean. *Nature* 568, 327–335. doi:10.1038/s41586-019-1098-2

Buesseler, K. O., Lamborg, C., Cai, P., Escoube, R., Johnson, R., Pike, S., et al. (2008). Particle fluxes associated with mesoscale eddies in the Sargasso Sea. *Deep Sea Res. Part II Top. Stud. Oceanogr.* 55, 1426–1444. doi:10.1016/j.dsr2.2008.02.007

Buesseler, K. O., Lamborg, C. H., Boyd, P. W., Lam, P. J., Trull, T. W., Bidigare, R. R., et al. (2007). Revisiting carbon flux through the Ocean's twilight zone. *Science* 316, 567–570. doi:10.1126/science.1137959

Cai, P., Huang, Y., Chen, M., Guo, L., Liu, G., and Qiu, Y. (2002). New production based on 228Ra-derived nutrient budgets and thorium-estimated POC export at the intercalibration station in the South China Sea. *Deep Sea Res. Oceanogr. Res. Pap.* 49, 53–66. doi:10.1016/s0967-0637(01)00040-1

Chelton, D. (2001). *Report of the high-resolution ocean topography science working group meeting*. Corvallis, Oregon: Oregon State University, College of Oceanic and Atmospheric Science.

Chen, Y. L. L. (2000). Comparisons of primary productivity and phytoplankton size structure in the marginal regions of southern East China Sea. *Continent. Shelf Res.* 20, 437–458. doi:10.1016/S0278-4343(99)00080-1

Chen, Y. L. L. (2005). Spatial and seasonal variations of nitrate-based new production and primary production in the South China Sea. *Deep Sea Res. I Oceanogr. Res. Pap.* 52, 319–340. doi:10.1016/j.dsr.2004.11.001

Chen, C.-T. A., Wang, S.-L., Wang, B.-J., and Pai, S.-C. (2001). Nutrient budgets for the South China sea basin. *Mar. Chem.* 75, 281–300. doi:10.1016/S0304-4203(01)00041-X

Chen, J., Zheng, L., Wiesner, M. G., Chen, R., Zheng, Y., and Wong, H. K. (1998). Estimations of primary production and export production in the South China Sea based on sediment trap experiments. *Chin. Sci. Bull.* 43, 583–586. doi:10.1007/BF02883645

Chen, Y. L. L., Chen, H.-Y., Jan, S., Lin, Y.-H., Kuo, T.-H., and Hung, J.-J. (2015). Biologically active warm-core anticyclonic eddies in the marginal seas of the western Pacific Ocean. *Deep Sea Res. Oceanogr. Res. Pap.* 106, 68–84. doi:10.1016/j.dsr.2015.10.006

Chen, Y. L. L., Chen, H.-Y., Karl, D. M., and Takahashi, M. (2004). Nitrogen modulates phytoplankton growth in spring in the South China Sea. *Continent. Shelf Res.* 24, 527–541. doi:10.1016/j.csr.2003.12.006

Chen, Y. L. L., Chen, H.-Y., Lin, I.-I., Lee, M.-A., and Chang, J. (2007). Effects of cold eddy on phytoplankton production and assemblages in Luzon strait bordering the South China Sea. *J. Oceanogr.* 63, 671–683. doi:10.1007/s10872-007-0059-9

Chen, G., Hou, Y., and Chu, X. (2011). Mesoscale eddies in the South China Sea: mean properties, spatiotemporal variability, and impact on thermohaline structure. *J. Geophys. Res.* 116, C06018. doi:10.1029/2010JC006716

Chen, Y. L. L., Tuo, S., and Chen, H. Y. (2011). Co-occurrence and transfer of fixed nitrogen from *Trichodesmium* spp. to diatoms in the low-latitude Kuroshio Current in the NW Pacific. *Mar. Ecol. Prog. Ser.* 421, 25–38. doi:10.3354/meps08908

Chou, W.-C., Chen, Y.-L. L., Sheu, D. D., Shih, Y.-Y., Han, C.-A., Cho, C. L., et al. (2006). Estimated net community production during the summertime at the SEATS time-series study site, northern South China Sea: implications for nitrogen fixation. *Geophys. Res. Lett.* 33, L22610. doi:10.1029/2005GL025365

Chou, W.-C., Sheu, D. D.-D., Chen, C.-T. A., Wang, S.-L., and Tseng, C.-M. (2005). Seasonal variability of carbon chemistry at the SEATS site, northern South China sea between 2002 and 2003. *Terr. Atmos. Ocean. Sci.* 16, 445–465. doi:10.3319/tao.2005.16.2.445(o)

Chung, C.-C., Gong, G.-C., and Hung, C.-C. (2012). Effect of typhoon morakot on microphytoplankton population dynamics in the subtropical northwest Pacific. *Mar. Ecol. Prog. Ser.* 448, 39–49. doi:10.3354/meps09490

Denman, K. L., and Gargett, A. E. (1983). Time and space scales of vertical mixing and advection of phytoplankton in the upper ocean. *Limnol. Oceanogr.* 28, 801–815. doi:10.4319/lo.1983.28.5.0801

Dillon, T. M. (1982). Vertical overturns: a comparison of Thorpe and Ozmidov length scales. *J. Geophys. Res.* 87, 9601–9613. doi:10.1029/JC087iC12p09601

Du, C., Liu, Z., Dai, M., Kao, S.-J., Cao, Z., Zhang, Y., et al. (2013). Impact of the Kuroshio intrusion on the nutrient inventory in the upper northern South China Sea: insights from an isopycnal mixing model. *Biogeosciences* 10, 6419–6432. doi:10.5194/bg-10-6419-2013

Du, C., Liu, Z., Kao, S. J., and Dai, M. (2017). Diapycnal fluxes of nutrients in an oligotrophic oceanic regime: the South China Sea. *Geophys. Res. Lett.* 44, 11510–11518. doi:10.1002/2017GL074921

Faghmous, J. H., Frenger, I., Yao, Y., Warmka, R., Lindell, A., and Kumar, V. (2015). A daily global mesoscale ocean eddy dataset from satellite altimetry. *Sci. Data* 2, 150028. doi:10.1038/sdata.2015.28

Gan, J., Liu, Z., and Hui, C. R. (2016). A three-layer alternating spinning circulation in the South China Sea. *J. Phys. Oceanogr.* 46, 2309–2315. doi:10.1175/JPO-D-16-0044.1

Gong, G.-C., Shiah, F.-K., Liu, K.-K., Wen, Y.-H., and Ming-Hsin Liang, M. H. (2000). Spatial and temporal variation of chlorophyll *a*, primary productivity and chemical hydrography in the southern East China Sea. *Continent. Shelf Res.* 20, 411–436. doi:10.1016/S0278-4343(99)00079-5

Hasle, G. R., and Syvertsen, E. E. (1997). "Marine diatoms," in: *Identifying marine phytoplankton*. Editor C. R. Tomas (San Diego, CA: Academic Press), 5–385.

Honda, M. C., Sasai, Y., Siswanto, E., Kuwano-Yoshida, A., Aiki, H., and Cronin, M. F. (2018). Impact of cyclonic eddies and typhoons on biogeochemistry in the oligotrophic ocean based on biogeochemical/physical/meteorological time-series at station KEO. *Prog. Earth Planet. Sci.* 5, 42. doi:10.1186/s40645-018-0196-3

Honda, M. C., and Watanabe, S. (2010). Importance of biogenic opal as ballast of particulate organic carbon (POC) transport and existence of mineral ballast-associated and residual POC in the Western Pacific Subarctic Gyre. *Geophys. Res. Lett.* 37, L02605. doi:10.1029/2009gl041521

Hung, C.-C., Gong, G.-C., Chou, W.-C., Chung, C.-C., Lee, M.-A., Chang, Y., et al. (2010b). The effect of typhoon on particulate organic carbon flux in the southern East China Sea. *Biogeosciences* 7, 3007–3018. doi:10.5194/bg-7-3007-2010

Hung, C.-C., Gong, G.-C., Chung, W.-C., Kuo, W.-T., and Lin, F.-C. (2009). Enhancement of particulate organic carbon export flux induced by atmospheric forcing in the subtropical oligotrophic northwest Pacific Ocean. *Mar. Chem.* 113, 19–24. doi:10.1016/j.marchem.2008.11.004

Hung, C.-C., and Gong, G.-C. (2010). POC/^{234}Th ratios in particles collected in sediment traps in the northern South China Sea. *Estuar. Coast Shelf Sci.* 88, 303–310. doi:10.1016/j.ecss.2010.04.008

Hung, C.-C., Gong, G.-C., and Santschi, P. H. (2012). ^{234}Th in different size classes of sediment trap collected particles from the Northwestern Pacific Ocean. *Geochem. Cosmochim. Acta* 91, 60–74. doi:10.1016/j.gca.2012.05.017

Hung, C.-C., Guo, L., Roberts, K. A., and Santschi, P. H. (2004). Upper ocean carbon flux determined by the ^{234}Th approach and sediment traps using size-fractionated POC and ^{234}Th data from the Gulf of Mexico. *Geochem. J.* 38, 601–611. doi:10.2343/geochemj.38.601

Hung, C.-C., Wong, G. T. F., Liu, K.-K., Shiah, F.-K., and Gong, G.-C. (2000). The effects of light and nitrate levels on the relationship between nitrate reductase activity and $^{15}NO_3^-$ uptake: field observations in the East China Sea. *Limnol. Oceanogr.* 45, 836–848. doi:10.4319/lo.2000.45.4.0836

Hung, C.-C., Xu, C., Santschi, P. H., Zhang, S.-J., Schwehr, K. A., Quigg, A., et al. (2010a). Comparative evaluation of sediment trap and ^{234}Th-derived POC fluxes from the upper oligotrophic waters of the Gulf of Mexico and the subtropical northwestern Pacific Ocean. *Mar. Chem.* 121, 132–144. doi:10.1016/j.marchem.2010.03.011

Kara, A. B., Rochford, P. A., and Hurlburt, H. E. (2000). An optimal definition for ocean mixed layer depth. *J. Geophys. Res.* 105, 16803–16821. doi:10.1029/2000jc900072

Karl, D. M., Bates, N. R., Emerson, S., Harrison, P. J., Jeandel, C., Llinâs, O., et al. (2003). "Temporal studies of biogeochemical processes determined from Ocean time-series observations during the JGOFS Era," in *Ocean biogeochemistry: the role of the ocean carbon cycle in global change*. Editor M. J. R. Fasham (New York, Springer), 239–267.

Li, D., Chou, W.-C., Shih, Y.-Y., Chen, G.-Y., Chang, Y., Chow, C. H., et al. (2018). Elevated particulate organic carbon export flux induced by internal waves in the oligotrophic northern South China Sea. *Sci. Rep.* 8, 2042. doi:10.1038/s41598-018-20184-9

Li, Q. P., Dong, Y., and Wang, Y. (2016). Phytoplankton dynamics driven by vertical nutrient fluxes during the spring inter-monsoon period in the northeastern South China Sea. *Biogeosciences* 13, 455–466. doi:10.5194/bg-13-455-2016

Liu, H., Chang, J., Tseng, C.-M., Wen, L.-S., and Liu, K. K. (2007). Seasonal variability of picoplankton in the northern South China sea at the SEATS station. *Deep Sea Res. Part II Top. Stud. Oceanogr.* 54, 1602–1616. doi:10.1016/j.dsr2.2007.05.004

Liu, K.-K., Chao, S.-Y., Shaw, P.-T., Gong, G.-C., Chen, C.-C., and Tang, T. Y. (2002). Monsoon-forced chlorophyll distribution and primary production in the South China Sea: observations and a numerical study. *Deep Sea Res. Oceanogr. Res. Pap.* 49, 1387–1412. doi:10.1016/S0967-0637(02)00035-3

Liu, K.-K., Chen, Y.-J., Tseng, C.-M., Lin, I.-I., Liu, H.-B., and Snidvongs, A. (2007). The significance of phytoplankton photo-adaptation and benthic-pelagic coupling to primary production in the South China Sea: observations and numerical investigations. *Deep Sea Res. Part II Top. Stud. Oceanogr.* 54, 1546–1574. doi:10.1016/j.dsr2.2007.05.009

Martin, J. H., Knauer, G. A., Karl, D. M., and Broenkow, W. W. (1987). VERTEX: carbon cycling in the northeast Pacific. *Deep Sea Res. Part A. Oceanogr. Res. Pap.* 34, 267–285. doi:10.1016/0198-0149(87)90086-0

McGillicuddy, D. J. (2016). Mechanisms of physical-biological-biogeochemical interaction at the Oceanic mesoscale. *Annu. Rev. Mar. Sci.* 8, 125–159. doi:10.1146/annurev-marine-010814-015606

McGillicuddy, D. J., Anderson, L. A., Bates, N. R., Bibby, T., Buesseler, K. O., Carlson, C. A., et al. (2007). Eddy/wind interactions stimulate extraordinary Mid-Ocean plankton blooms. *Science* 316, 1021–1026. doi:10.1126/science.1136256

McGillicuddy, D. J., Robinson, A. R., Siegel, D. A., Jannasch, H. W., Johnson, R., Dickey, T. D., et al. (1998). Influence of mesoscale eddies on new production in the Sargasso Sea. *Nature* 394, 263–266. doi:10.1038/28367

Menden-Deuer, S., and Lessard, E. J. (2000). Carbon to volume relationships for dinoflagellates, diatoms, and other protist plankton. *Limnol. Oceanogr.* 45, 569–579. doi:10.4319/lo.2000.45.3.0569

Moloney, C. L., Field, J. G., and Lucas, M. I. (1991). The size-based dynamics of plankton food webs. II. Simulations of three contrasting southern Benguela food webs. *J. Plankton Res.* 13, 1039–1092. doi:10.1093/plankt/13.5.1039

Okubo, A. (1970). Horizontal dispersion of floatable particles in the vicinity of velocity singularities such as convergences. *Deep Sea Res. Oceanogr. Abstr.* 17, 445–454. doi:10.1016/0011-7471(70)90059-8

Olenina, I., Hajdu, S., Edler, L., Andersson, A., Wasmund, N., Busch, S., et al. (2006). Biovolumes and size-classes of phytoplankton in the Baltic sea. *HELCOM Balt. Sea Environ. Proc.* 106, 144.

Pai, S. C., Yang, C. C., and Riley, J. P. (1990). Effects of acidity and molybdate concentration on the kinetics of the formation of the phosphoantimonylmolybdenum blue complex. *Anal. Chim. Acta* 229, 115–120. doi:10.1016/S0003-2670(00)85116-8

Reynolds, S. E., Mather, R. L., Wolff, G. A., Williams, R. G., Landolfi, A., Sanders, R., et al. (2007). How widespread and important is N_2 fixation in the North Atlantic Ocean? *Global Biogeochem. Cycles* 21, GB4015. doi:10.1029/2006GB002886

Shih, Y.-Y., Hung, C.-C., Gong, G.-C., Chung, W.-C., Wang, Y.-H., Lee, I.-H., et al. (2015). Enhanced particulate organic carbon export at eddy edges in the oligotrophic western north Pacific Ocean. *PloS One* 10, e0131538. doi:10.1371/journal.pone.0131538

Shih, Y.-Y., Hung, C.-C., Huang, S.-Y., Muller, F. L. L., and Chen, Y.-H. (2020). Biogeochemical variability of the upper ocean response to typhoons and storms in the northern South China Sea. *Front. Mar. Sci.* 7, 151. doi:10.3389/fmars.2020.00151

Shih, Y.-Y., Lin, H.-H., Li, D., Hsieh, H.-H., Hung, C.-C., and Chen, C.-T. A. (2019). Elevated carbon flux in deep waters of the South China Sea. *Sci. Rep.* 9, 1496. doi:10.1038/s41598-018-37726-w

Steidinger, K. A., and Tangen, K. (1997). "Dinoflagellates." in: *Identifying marine phytoplankton*. Editor C. R. Tomas (San Diego, CA, Academic Press), 387–584.

Sweeney, E. N., McGillicuddy, D. J., Jr., and Buesseler, K. O. (2003). Biogeochemical impacts due to mesoscale eddy activity in the Sargasso Sea as measured at the Bermuda Atlantic Time-series Study (BATS). *Deep Sea Res. Part II Top. Stud. Oceanogr.* 50, 3017–3039. doi:10.1016/j.dsr2.2003.07.008

Thorpe, S. A. (1977). Turbulence and mixing in a Scottish loch. *Phil. Trans. Roy. Soc. Lond. Math. Phys. Sci.* 286, 125–181. doi:10.1098/rsta.1977.0112

Throndsen, J. (1997). "The planktonic marine flagellates," in: *Identifying marine phytoplankton*. Editor C. R. Tomas (San Diego, CA, Academic Press), 591–729.

Tseng, C.-M., Wong, G. T. F., Lin, I. I., Wu, C. R., and Liu, K. K. (2005). A unique seasonal pattern in phytoplankton biomass in low-latitude waters in the South China Sea. *Geophys. Res. Lett.* 32, L086080. doi:10.1029/2004gl022111

Turner, J. T. (2015). Zooplankton fecal pellets, marine snow, phytodetritus and the ocean's biological pump. *Prog. Oceanogr.* 130, 205–248. doi:10.1016/j.pocean.2014.08.005

Vaillancourt, R. D., Marra, J., Seki, M. P., Parsons, M. L., and Bidigare, R. R. (2003). Impact of a cyclonic eddy on phytoplankton community structure and photosynthetic competency in the subtropical North Pacific Ocean. *Deep Sea Res. Oceanogr. Res. Pap.* 50, 829–847. doi:10.1016/S0967-0637(03)00059-1

Verdeny, E., Masqué, P., Maiti, K., Garcia-Orellana, J., Bruach, J. M., Mahaffey, C., et al. (2008). Particle export within cyclonic Hawaiian lee eddies derived from 210Pb-210Po disequilibrium. *Deep Sea Res. Part II Top. Stud. Oceanogr.* 55, 1461–1472. doi:10.1016/j.dsr2.2008.02.009

Wang, G., Su, J., and Chu, P. C. (2003). Mesoscale eddies in the South China Sea observed with altimeter data. *Geophys. Res. Lett.* 30, 2121. doi:10.1029/2003gl018532

Wei, C.-L., Lin, S.-Y., Sheu, D. D.-D., Chou, W.-C., Yi, M.-C., Santschi, P. H., et al. (2011). Particle-reactive radionuclides (^{234}Th, ^{210}Pb, ^{210}Po) as tracers for the estimation of export production in the South China Sea. *Biogeosciences* 8, 3793–3808. doi:10.5194/bg-8-3793-2011

Weiss, J. (1991). The dynamics of enstrophy transfer in two-dimensional hydrodynamics. *Phys. D.* 48, 273–294. doi:10.1016/0167-2789(91)90088-Q

Wong, G. T. F., Ku, T. L., Mulholland, M., Tseng, C. M., and Wang, D. P. (2007). The SouthEast Asian time-series study (SEATS) and the biogeochemistry of the South China Sea-An overview. *Deep Sea Res. II* 54, 1434–1447. doi:10.1016/J.DSR2.2007.05.012

Xiu, P., and Chai, F. (2011). Modeled biogeochemical responses to mesoscale eddies in the South China Sea. *J. Geophys. Res.* 116, C10006. doi:10.1029/2010jc006800

Xiu, P., Chai, F., Shi, L., Xue, H., and Chao, Yi. (2010). A census of eddy activities in the South China Sea during 1993–2007. *J. Geophys. Res.* 115, C03012. doi:10.1029/2009jc005657

Zhou, K., Dai, M., Kao, S. J., Wang, L., Xiu, P., Chai, F., et al. (2013). Apparent enhancement of ^{234}Th-based particle export associated with anticyclonic eddies. *Earth Planet Sci. Lett.* 381, 198–209. doi:10.1016/j.epsl.2013.07.039

Conflict of Interest: The authors declare that the research was conducted in the absence of any commercial or financial relationships that could be construed as a potential conflict of interest.

frontiers in Earth Science

ORIGINAL RESEARCH
published: 25 February 2021
doi: 10.3389/feart.2021.591948

Atmospheric and Oceanographic Forcing Impact Particle Flux Composition and Carbon Sequestration in the Eastern Mediterranean Sea: A Three-Year Time-Series Study in the Deep Ierapetra Basin

Rut Pedrosa-Pamies[1,2], Constantine Parinos[3], Anna Sanchez-Vidal[2], Antoni Calafat[2], Miquel Canals[2], Dimitris Velaoras[3], Nikolaos Mihalopoulos[4,5], Maria Kanakidou[4], Nikolaos Lampadariou[3] and Alexandra Gogou[3]*

[1]*The Ecosystems Center, Marine Biological Laboratory, Woods Hole, MA, United States,* [2]*Consolidate Research Group in Marine Geosciences, Department of Earth and Ocean Dynamics, Faculty of Earth Sciences, University of Barcelona, Barcelona, Spain,* [3]*Institute of Oceanography, Hellenic Centre for Marine Research (HCMR), Anavyssos, Greece,* [4]*Environmental Chemical Processes Laboratory (ECPL), Department of Chemistry, University of Crete, Heraklion, Greece,* [5]*Institute for Environmental Research and Sustainable Development (IERSD), National Observatory of Athens, Athens, Greece*

OPEN ACCESS

Edited by:
Timothy Ferdelman, Max Planck Institute for Marine Microbiology (MPG), Germany

Reviewed by:
Gerard Versteegh, Alfred Wegener Institute Helmholtz Center for Polar and Marine Research (AWI), Germany
Facundo Matias Barrera, University of Concepción, Chile

***Correspondence:**
Rut Pedrosa-Pamies
rpedrosa@mbl.edu

Specialty section:
This article was submitted to Biogeoscience, a section of the journal Frontiers in Earth Science

Received: *05 August 2020*
Accepted: *06 January 2021*
Published: *25 February 2021*

Citation:
Pedrosa-Pamies R, Parinos C, Sanchez-Vidal A, Calafat A, Canals M, Velaoras D, Mihalopoulos N, Kanakidou M, Lampadariou N and Gogou A (2021) Atmospheric and Oceanographic Forcing Impact Particle Flux Composition and Carbon Sequestration in the Eastern Mediterranean Sea: A Three-Year Time-Series Study in the Deep Ierapetra Basin. Front. Earth Sci. 9:591948. doi: 10.3389/feart.2021.591948

Sinking particles are a critical conduit for the export of organic material from surface waters to the deep ocean. Despite their importance in oceanic carbon cycling, little is known about the biotic composition and seasonal variability of sinking particles reaching abyssal depths. Herein, sinking particle flux data, collected in the deep Ierapetra Basin for a three-year period (June 2010 to June 2013), have been examined at the light of atmospheric and oceanographic parameters and main mass components (lithogenic, opal, carbonates, nitrogen, and organic carbon), stable isotopes of particulate organic carbon (POC) and source-specific lipid biomarkers. Our aim is to improve the current understanding of the dynamics of particle fluxes and the linkages between atmospheric dynamics and ocean biogeochemistry shaping the export of organic matter in the deep Eastern Mediterranean Sea. Overall, particle fluxes showed seasonality and interannual variability over the studied period. POC fluxes peaked in spring April–May 2012 (12.2 mg m^{-2} d^{-1}) related with extreme atmospheric forcing. Summer export was approximately fourfold higher than mean wintertime, fall and springtime (except for the episodic event of spring 2012), fueling efficient organic carbon sequestration. Lipid biomarkers indicate a high relative contribution of natural and anthropogenic, marine- and land-derived POC during both spring (April–May) and summer (June–July) reaching the deep-sea floor. Moreover, our results highlight that both seasonal and episodic pulses are crucial for POC export, while the coupling of extreme weather events and atmospheric deposition can trigger the influx of both marine labile carbon and anthropogenic compounds to the deep Levantine Sea. Finally, the comparison of time series data of sinking particulate flux with the corresponding

biogeochemical parameters data previously reported for surface sediment samples from the deep-sea shed light on the benthic–pelagic coupling in the study area. Thus, this study underscores that accounting the seasonal and episodic pulses of organic carbon into the deep sea is critical in modeling the depth and intensity of natural and anthropogenic POC sequestration, and for a better understanding of the global carbon cycle.

Keywords: sinking particle fluxes, carbon cycle, lipid biomarkers, atmospheric forcing, eastern mediterranean sea, surface sediment, deep ocean, particulate organic carbon

INTRODUCTION

The export of carbon from the surface to the deep ocean through sinking particulate biogenic material, also known as the biological pump (Volk and Hoffert, 1985), is an essential component of the ocean carbon cycle. This plays an important role in atmospheric CO_2 fluctuations (Archer et al., 2000; Kwon et al., 2009; Lima et al., 2014) and in deep ocean ecosystems functioning (Smith et al., 2009 and references therein). The overall fraction of net primary production (NPP) that is exported from the surface ocean to the mesopelagic and bathypelagic layers and the vertical attenuation of this flux with depth are both good measures of the export efficiency (POC export flux/NPP) of the biological pump (De La Rocha and Passow, 2007; DeVries et al., 2012), which is largely being determined by the structure and functioning of the ocean's ecosystem (e.g., Francois et al., 2002; Honjo et al., 2008; Dagg et al., 2014; Le Moigne et al., 2016). However, the processes controlling the biological pump efficiency are not fully understood (Boyd and Trull, 2007). Since oligotrophic waters cover about 75% of the ocean surface (Lewis et al., 1986) and contribute over 30% of the global marine carbon fixation (Longhurst et al., 1995; Marañón et al., 2003), understanding these processes therein is critical in order to assess their biogeochemical functioning and feedbacks between the ocean carbon cycle and human-induced environmental change.

The Eastern Mediterranean Sea (EMS) is one of the most oligotrophic areas of the world ocean, in other words "an oceanic desert" (Azov, 1991). It exhibits ultra-oligotrophic characteristics, related to: 1) a net outflow of nutrients due to its anti-estuarine circulation, 2) nutrient-depleted surface Atlantic Water flowing in through the Strait of Sicily and nutrient-rich Levantine Intermediate Water flowing out at intermediate depths (Ribera d'Alcalà, 2003; Huertas et al., 2012), and 3) extremely low phosphorus levels, which strongly limits both primary and secondary productions (Krom et al., 1991). Carbon vertical flux was found to be differentiated along a north-south oligotrophy gradient and "hot spots" for CO_2 sequestration to the ocean interior on long time scales were detected in the less oligotrophic area (Siokou-Frangou et al., 2002; Gogou et al., 2014; Pedrosa-Pàmies et al., 2016; Pavlidou et al., 2020). The weak seasonality of the phytoplankton biomass and production drives NPP rates below 200 mg C m^{-2} d^{-1} (Psarra et al., 2000; Moutin and Raimbault, 2002; Bosc, 2004), while very low amounts of POC (<0.5% of NPP) reach the deep sea floor (Warnken, 2003; Koppelmann et al., 2004; Stavrakakis et al., 2013; Gogou et al., 2014; Pedrosa-Pàmies et al., 2016; Karageorgis et al., 2018).

The oligotrophic regime of the EMS is modulated by sub-basin gyres and mesoscale features. These may result in distinct changes of the water column biogeochemical properties, through the horizontal and vertical mass transfer that play an important role on nutrient and carbon distribution (Siokou-Frangou et al., 2010, and references therein). Moreover, in the EMS atmospheric deposition plays a major role in the supply of bioavailable nutrients and anthropogenic compounds due to the limited inputs from external sources (Krom et al., 2004; Christodoulaki et al., 2013; Theodosi et al., 2019; Kanakidou et al., 2020). A variety of sources at the regions surrounding the Mediterranean Sea, but also distant sources due to long range transport of air masses, affect the quality of atmospheric deposition which could have important implications on the pelagic productivity and, overall, carbon cycle (Kouvarakis et al., 2001; Jickells et al., 2005; Kanakidou et al., 2012).

Understanding the processes that control the quantity and quality of POC flux to the deep EMS is needed to better characterize the strength and efficiency of the biological pump as well as to accurately project the response of this oligotrophic system to climate fluctuations and anthropogenic perturbations. Bulk geochemical proxies, such as the stable isotopic composition of organic carbon ($\delta^{13}C$), and lipid biomarkers have been widely used as indices of sources and transformation processes of organic matter in marine systems (Meyers, 1994; Wakeham, 1995; Volkman and Tanoue, 2002; Goñi et al., 2003; Hu et al., 2006; Pedrosa-Pàmies et al., 2013; Quirós-Collazos et al., 2017), as well as to assess the biogeochemical dynamics controlling the export of POC to the deep sea (Goutx et al., 2000; Wakeham et al., 2002; Conte et al., 2003; Pedrosa-Pàmies et al., 2018, 2019; De Bar et al., 2019). While there have been several investigations on the $\delta^{13}C$ signature of sinking particles in the Mediterranean Sea (Kerhervé et al., 2001; Turchetto et al., 2012; Pasqual et al., 2015; Theodosi et al., 2019) but also on the molecular composition of POC particulate fluxes in the western Mediterranean Sea, both in the upper mesopelagic layers (100–300 m depth) (e.g., Tolosa et al., 2005; Goutx et al., 2007; Marty et al., 2009; Méjanelle and Dachs, 2009) and the deep sea (Marchand et al., 2005; Wakeham et al., 2009), little is known about the POC molecular composition of the EMS particle fluxes (Tsapakis et al., 2006; Theodosi et al., 2013) and deep-sea floor (Gogou and Stephanou, 2004; Parinos et al., 2013a; Pedrosa-Pàmies et al., 2015).

Herein, we present a 3-year time series of sinking particles flux data in the deep Ierapetra Basin (4,310 m depth). The collected data have been examined at the light of atmospheric and oceanographic parameters and main mass components (lithogenic, calcium carbonate, opal and organic matter), stable isotopic composition of POC and source-specific

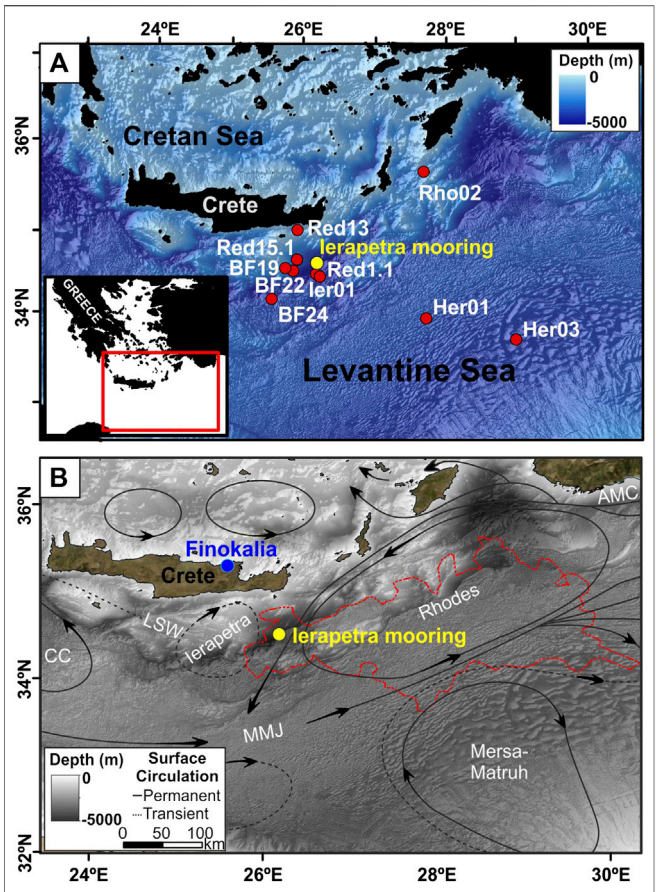

FIGURE 1 | (A) Location of the mooring line deployed in the deep Ierapetra Basin from June 2010 to June 2013 (yellow dot), and 10 surface sediment samples collected in the Levantine Sea (red dots) reported by Pedrosa-Pàmies et al. (2015) (lipid data for sediment samples BF19, BF22 and BF24 are not available). **(B)** Schematic representation of the upper thermocline circulation in the study area (Robinson and Golnaraghi, 1993), and location of Ierapetra mooring (yellow dot), and Finokalia atmospheric station (blue dot). Circulation patterns and water masses: MMJ-Mid-Mediterranean Jet, AMC-Asia Minor Current, LSW-Levantine Surface Water, CC-Cretan Cyclone. The dashed red polygon is the contour of the Rhodes Gyre phytoplankton bloom of March 2012 as indicated by Chlorophyll-*a* concentrations above 0.2 mg m^{-3} (48291.3 km^2). The bathymetric map was produced using metadata from the EMODnet Bathymetry portal—http://www.emodnet-bathymetry.eu.

lipid biomarkers (long chain *n*-alkanes and the unresolved complex mixture of aliphatic hydrocarbons, long-chain *n*-alkanols, long-chain alkenones, long-chain diols&keto-ols and selected sterols). The aim of the present study is to improve the current understanding of the dynamics of particle fluxes and the linkages between atmosphere dynamics and ocean biogeochemistry shaping the export of organic matter in this oligotrophic abyssal region of the EMS. Moreover, in order to evaluate the benthic-pelagic coupling in the study area, the time series of sinking particles flux data were compared to the corresponding data of biogeochemical parameters previously reported for surface sediments from the deep-sea in the study area. To the best of our knowledge, this study presents for the first time the lipid biomarker composition of sinking particles reaching the deep EMS.

OCEANOGRAPHIC AND ATMOSPHERIC SETTINGS

The northwestern part of the Levantine Basin covers an area extending from south of Crete up to the southeast of Rhodes island. It is dominated by the presence of the permanent Rhodes cyclonic gyre centered south of Rhodes but occasionally expanding westwards toward Crete (**Figure 1**). A second feature is the recurrent Ierapetra anticyclonic gyre situated to the southeast of Crete (Larnicol et al., 2002; Mkhinini et al., 2014) showing a climatological mean position close to 26–27°E and 34–35°N. The Ierapetra anticyclone is a mesoscale eddy created by the strong northerly Etesian winds and their interaction with the orography of the island of Crete. Its seasonal variability relates to that of the Etesians, hence it starts developing in summer and intensifies in autumn. Its seasonal variability is correlated with an average three-month lag between maximum negative wind stress curl caused by the Etesians and maximum negative current vorticity linked to the anticyclone (Amitai et al., 2010). The Ierapetra anticyclone entraps water masses exiting from the Cretan straits enhancing the downward fluxes/transport of particulate matter and nutrient-depleted waters with important implications on the biogeochemical functioning of the area (Lampadariou et al., 2009; Pedrosa-Pàmies et al., 2015). The Ierapetra anticyclone also presents interannual variability in intensity and positioning. Nevertheless, during the study period (2010–2013) it had rather typical seasonal behavior (Ioannou et al., 2017).

The Levantine Basin atmosphere is at the crossroad of air masses of various origins that affect atmospheric composition. Air masses coming from the south carry significant amounts of African desert dust, from the northwest/north/northeast carry anthropogenic pollution from Central Europe, Balkans, and Ukraine, and Turkey, respectively from the east air masses are rich in dust mixed with anthropogenic pollution from the Middle-East, while coming from the west air masses are significantly affected by marine emissions (Kanakidou et al., 2011). In addition, when passing over continental regions, air masses are also affected by land sources (i.e., vegetation, forest fires, soil resuspension) (Sciare et al., 2003), and are enriched in air pollutants emitted by land sources (Mihalopoulos et al., 1997; Lelieveld et al., 2002; Kanakidou et al., 2011). Therefore, the quality of atmospheric deposition and its fingerprint in the export of material in the seawater column depend upon the origin of the air masses that are reaching the area during the study period.

METHODS AND DATA

Oceanographic and Atmospheric Data

To investigate the effects of various atmospheric and upper ocean processes on particle fluxes, we consider a variety of environmental parameters for the study area during the investigated period, i.e.

atmospheric deposition, sea surface temperature (SST), surface Chlorophyll *a* (Chl *a*) concentration, and net primary production (NPP). These data were obtained either from *in-situ* observations or satellite data from one grid cell above the location of the sediment trap: 34.3–34.6°N, 26.0–26.3°E (see below for details).

Total atmospheric deposition data (dry and wet deposition) were obtained from the Finokalia atmospheric monitoring station located at a remote site in the northern coast of the island of Crete, Greece (35°20′N, 25°40′E; **Figure 1**). The site is not impacted by local human activities and it is a well characterized location for atmospheric composition and deposition, characteristic for the eastern Mediterranean atmosphere, operating since 1993 (Mihalopoulos et al., 1997). Moreover, in order to investigate the potential sources that contributed to the atmospheric deposition and therefore affected the flux of material into the sea water column during the study period, characteristic air mass 5-days back-trajectories have been calculated and analyzed. The back-trajectories have been computed using the HYSPLIT trajectory model of NOAA (Stein et al., 2015; Rolph et al., 2017) and considering as arriving point the Finokalia atmospheric monitoring station at 1,000 and 3,000 m.

Monthly SST and 8-days Chl *a* concentrations were obtained from the Moderate Resolution Imaging Spectrometer (MODIS), in orbit on the Aqua platform, using 4-km resolution level 3-binned data. Both monthly SST and Chl *a* data are processed and distributed by the NASA Goddard Earth Sciences (GES) Data, Information Services Center (DISC) and Ocean Biology Processing Group (OBPG). Monthly NPP estimates (1/12° resolution) were obtained from the Vertically Generalized Production Model (VGPM) (Behrenfeld and Falkowski, 1997), and provided by the Oregon State University (OSU).

Additionally, deep-sea daily mean current speed and direction at the deep Ierapetra Basin were evaluated. The moored line deployed in the Ierapetra Basin, included an Aanderaa RCM8 current meter deployed at 23 m above the bottom with a measuring interval of 1 h.

Sample Collection

Sinking particles were collected at 4,285 m water depth with a PPS3 Technicap sequential sampling sediment trap (0.125 m^2 collecting area) from June 2010 to June 2013 at the 4,310 m deep Ierapetra Basin (**Figure 1**). The trap was equipped with 12 receiving cups with a sampling interval of 1 month. The collecting cups were filled with a 5% (*v/v*) formaldehyde solution in 0.45 μm filtered seawater buffered with sodium borate. As earlier reported by Altabet (2001), formaldehyde preservative does not add sufficient organic carbon to the sediment trap material to alter organic composition (e.g., $\delta^{13}C$ of POC), and it has been extensively used for the preservation of sediment trap material (Thunell et al., 2000; Tolosa et al., 2003; Struck et al., 2004; Sanchez-Vidal et al., 2008; Tesi et al., 2010; Henley et al., 2012). After recovering, sediment trap samples were stored in the dark at 2–4°C until they were further processed in the laboratory.

Moreover, in order to evaluate the benthic-pelagic linkages in the study area, the time series data of sinking particles flux are being discussed along with the corresponding biogeochemical parameters and lipid compounds/indices data previously reported by Pedrosa-Pàmies et al. (2015) for surface sediment samples (undisturbed top 0–1 cm) collected from January 2007 to June 2012 in the NW Levantine Sea (**Figure 1**, **Supplementary Table S1**). The sedimentation rate in the deep EMS is in the order of 0.003 cm y^{-1} (Van Santvoort et al., 1996).

Analytical Methods

Elemental and Stable Isotope Analysis of Carbon

Sediment trap samples were processed in the laboratory according to a modified version of Heussner et al. (1990). Large swimming organisms were removed by wet sieving through a 1 mm nylon mesh, while organisms <1 mm were handpicked under a microscope with fine tweezers. Samples were repeatedly split into aliquots using a high precision peristaltic pump robot to obtain 10–20 mg subsamples, and then they were stirred three times with ultrapure water, centrifuged and the supernatant removed to eliminate salt and formaldehyde. Samples were finally freeze-dried and weighted for total mass determination.

Total carbon (TC), POC and total nitrogen (TN) contents and stable isotopic composition of POC were analyzed using a Flash 1112 EA elemental analyzer interfaced to a Delta C Finnigan MAT isotope ratio mass spectrometer. Samples analyzed for %OC and $\delta^{13}C$ were initially de-carbonated using repetitive additions of a 25% HCl (*v/v*) solution, separated by 60°C drying steps, until no effervescence was observed (Nieuwenhuize et al., 1994). Uncertainties for elemental composition were lower than 0.1%, while uncertainty for $\delta^{13}C$ was lower than 0.05‰. In consistency with published data in the Mediterranean Sea we assumed OM as twice the OC content (e.g., Heussner et al., 1996; Masqué et al., 2003). The inorganic carbon content was calculated from the difference between TC and OC measurements. Assuming all inorganic carbon is contained within calcium carbonate, $CaCO_3$ content was determined using the molecular mass ratio of 100/12 [(TC%−OC%)×8.33].

Molar TN/POC ratios were also calculated. TN/POC is plotted in order to constrain the elemental ratios of N-depleted samples (i.e. TN/POC ≈0 rather than POC/TN ∞ 0) following Goñi et al. (2006), and to avoid the underestimation of the terrestrial-derived carbon fraction (Perdue and Koprivnjak, 2007).

Biogenic Opal and Lithogenic Fraction Analysis

The biogenic silica content was analyzed using a two-step 2.5 h extraction with a 0.5 M Na_2CO_3 solution, separated by centrifugation of the leachates. Si and Al contents of both leachates were analyzed with a Perkin-Elmer Optima 3200RL Inductive Coupled Plasma Optical Emission Spectrometer (ICP-OES), correcting the Si content of the first leachate by the Si/Al ratio of the second one (Kamatani and Oku, 2000). All values are reported as opal ($SiO_2.0.4H_2O$), a parameter defined by 2.4 times the weight percentage of biogenic Si content determined for each sample (Mortlock and Froelich, 1989). The opal detection limit, associated to the detection limit of the ICP-OES system, is approximately 0.2%. Analytical precision of opal measurements was 4.5%.

The lithogenic fraction was estimated by subtracting the concentration of the major constituents from total dry weight [%lithogenic = 100 – (%OM + %$CaCO_3$ + %opal)]. This fraction represents the residual component of particles such as quartz, feldspars, clay minerals and aluminosilicates (Mortlock and Froelich, 1989).

Lipid Biomarkers

A range of selected lipid biomarkers are considered in this study, namely long chain *n*-alkanes and the unresolved complex mixture of aliphatic hydrocarbons, long-chain *n*-alkanols, long-chain di- and tri-unsaturated C_{37} and C_{38} methyl ketones and C_{38} ethyl ketones, commonly referred to as long-chain alkenones, long-chain diols and keto-ols and a suite of sterols.

The analytical procedure followed for the determination of lipid biomarkers has been previously presented in detail (Gogou et al., 1998, 2000, 2007). Briefly, freeze-dried samples were initially solvent-extracted three times by sonication with dichloromethane. Combined extracts were subsequently separated into different compound classes by column chromatography using silica gel that had been activated for 1 h at 150 °C. The following solvent systems were used to elute the different compound classes of the considered lipid compounds: (1) *n*-hexane (fraction F1; aliphatic hydrocarbons), (2) dichloromethane/*n*-hexane (fraction F2; long-chain alkenones) and (3) ethyl acetate/*n*-hexane (fraction F3; *n*-alkanols, sterols, diols and keto-ols).

F1 and F3 fractions were analyzed by Gas Chromatography-Mass Spectrometry (GC-MS) while F2 fractions were analyzed by Gas Chromatography using Flame Ionization Detection (GC-FID). Hydroxyl-bearing compounds (fraction F3) were derivatized to the corresponding trimethylsilyl ethers prior to GC-MS analysis using N,O-bis-(trimethylsilyl)-trifluoroacetamide (BSTFA) + 1% trimethylchlorosilane (TMCS) for 1 h at 90 °C. Details regarding the GC instrumental parameters are presented elsewhere (Gogou et al., 2007; Parinos et al., 2013a).

The individual lipids were identified by a combination of comparison of GC-retention times to authentic standards and comparison of their mass spectral data to those in the literature. Quantification was based on the GC-MS or GC-FID response and comparison of peak areas with those of known quantities of standards added prior to the extraction of the samples ([$^2H_{50}$] *n*-tetracosane for *n*-alkanes, *n*-hexatriacontane for long-chain alkenones, 5α-androstan-3β-ol for sterols, diols and keto-ols, and *n*-heneicosanol for *n*-alkanols).

Source Indicators of Sinking Particulate Organic Carbon

The study of the natural isotopic variations of organic carbon ($\delta^{13}C$) is a valuable tool to trace sources and transformation processes of the particulate organic matter in the marine environment. The isotopic variations of carbon in the organic particles initially present depletion in ^{13}C, which derives from the formation procedures of the organic matter during primary production (Kerhervé et al., 2001). Then, a stepwise enrichment of ^{13}C occurs in the particles through the food chain and by the processes that are performed at the successive trophic levels (Altabet, 1996). According to this, the isotopic ratios of carbon, should be essentially affected both by the biological sources of the particles and the transformation processes that the latter have to undergo during their transfer through the water column (Kerhervé et al., 2001).

Concerning the suite of lipid biomarkers employed in this study, they have been widely used as proxies to identify the relative importance of natural *vs* anthropogenic, marine- and land-derived, sources for settling particulate matter along with the food web dynamics in the overlying water column (Meyers, 1997; Volkman, 2006; Christodoulou et al., 2009; Close et al., 2014; Pedrosa-Pàmies et al., 2015, 2019).

Herein, the sum of the concentrations of the considered lipid biomarkers having a marine (algal) origin was calculated as follows:

$$\sum \text{Phyto} = \sum (28\Delta^{5,22E} + 4\alpha C_{30}\Delta^{22E} + C_{30}\ \text{diols\&keto-ols} + \text{alkenones}) \quad (1)$$

where $C_{28}\Delta^{5,22E}$ is brassicasterol (24-methyl cholest-5,22-dien-3β-ol), and $4\alpha C_{30}\Delta^{22E}$ is dinosterol (4α,23,24R-trimethyl-5α-cholest-22-en-3β-ol).

Brassicasterol ($C_{28}\Delta^{5,22E}$) is primarily derived from diatoms and *Prymnesiophyta*, while dinosterol ($4\alpha C_{30}\Delta^{22E}$) is a major compound in many dinoflagellates (Volkman, 1986). Long-chain alkenones are produced by some *Prymnesiophyte* class, e.g., *Emiliania huxleyii* (Marlowe et al., 1984) the later constituting the dominant primary producers across the Mediterranean Sea (Ziveri et al., 2000; Triantaphyllou, 2004; Skampa et al., 2019). Long-chain C_{30} *n*-alkan-1,15-diols have been commonly reported in marine and freshwater environments (Versteegh et al., 1997, 2000; Rampen et al., 2012; Pedrosa-Pàmies et al., 2015, 2018, 2019), but little is known about their specific biological sources. They have been identified in the microalgae *Nannochloropsis* sp (class Eustigmatophyceae) (Volkman, 1986; Volkman et al., 1992; Gelin et al., 1997; Versteegh et al., 1997). C_{30} keto-ols might result from oxidation of the corresponding C_{30} diols (Volkman, 1986; Volkman et al., 1999; Rampen et al., 2012), or, on the contrary, as recently suggested by Versteegh and Lipp (2019), might be produced by currently uncharacterized source organisms.

In addition, we have evaluated the abundance of both cholesterol and β-sitosterol. Cholesterol ($C_{27}\Delta^5$, cholest-5-en-3β-ol) is ubiquitous in the marine environment, both in plants and animals (e.g., Harvey et al., 1989; Volkman et al., 1992, 1999). However, high concentrations cholesterol is typically associated with the existence of marine consumers such as zooplankton and benthic animals (Teshima, 1971; Volkman, 1986; Harvey et al., 1989; Grice et al., 1998), and fecal material (Prahl et al., 1984; Neal et al., 1986; Wakeham and Canuel, 1986). β-Sitosterol ($C_{29}\Delta^5$, 24-Ethylcholest-5-en-3β-ol) may derive from both terrigenous and marine sources (Volkman, 1986).

The abundance of the Unresolved Complex Mixture (UCM) of aliphatic hydrocarbons, a commonly observed persistent contaminant mixture in environmental samples consisting of

branched alicyclic hydrocarbons (Gough and Rowland, 1990), is used as an indicator of the contribution of anthropogenic organic matter from degraded petroleum hydrocarbons and/or apolar products deriving from combustion processes, such as grass/wood/coal combustion and/or the incomplete combustion of fossil fuels (e.g., Simoneit, 1984; Wang et al., 1999; Hays, 2004 and references therein).

The carbon preference index of long-chain *n*-alkanes (C*n* with $n \geq 25$; CPI_{NA}) refers to the ratio of the concentrations of the long straight-chain homologues with an odd number of carbon atoms over those with an even number of carbon atoms. Higher (terrestrial) plants produce a higher proportion of odd than even hydrocarbons with a CPI_{NA} of ≥4 (Eglinton and Hamilton, 1967; Collister et al., 1994). Fossil fuels have a CPI_{NA} of ~1 (Wang et al., 1999). For phytoplankton, data are not conclusive, though they generally tend to produce shorter *n*-alkanes (C*n* with $n < 20$) (Volkman et al., 1998). The index is calculated as:

$$CPI_{NA} = \sum([n-C_{25}] - [n-C_{33}])/\sum([n-C_{26}] - [n-C_{34}]) \quad (2)$$

The sum of the concentrations of the most abundant high molecular weight odd *n*-alkanes (TerNA) and even *n*-alkanols (TerN-OH), which are major components of epicuticular higher plant waxes (Eglinton and Hamilton, 1967; Ohkouchi et al., 1997), are defined, respectively, as:

$$\sum \text{TerNA} = \sum n-C_{27,29,31,33} \quad (3)$$

$$\sum \text{TerN-OH} = \sum n-C_{24,26,28,30} \quad (4)$$

With their total sum referred to hereafter as ∑Ter:

$$\sum \text{Ter} = \sum \text{TerNA} + \sum \text{TerN-OH} \quad (5)$$

Since the CPI_{NA} values are indicative of a mixture of both fossil and land-derived long-chain *n*-alkanes in most of the cases (see discussion below), the *n*-alkane contribution by fossil fuels ($CPI_{NA} = 1$) was subtracted in order to obtain the distribution signatures of the plant wax *n*-alkanes. To this, each individual terrestrial higher plant wax *n*-alkane signature considered in ∑TerNA sum was calculated by subtracting the average of the next higher and lower even carbon numbered homolog after Schneider et al. (1983), Simoneit et al. (1990) and Aboul-Kassim and Simoneit (1995) as follows:

$$\text{Wax } n - C_n = [C_n] - 0.5[C_{(n+l)} - C_{(n-1)}] \quad (6)$$

Statistical Analysis

Principal component analysis (PCA) (Meglen, 1992) was performed to identify the dominant factors of the variance within the dataset. Several studies have successfully applied PCA for discriminating organic matter sources (Reemtsma and Ittekkot, 1992; Yunker et al., 1995; Goñi et al., 2000; Pedrosa-Pàmies et al., 2015, 2019) and its transformation patterns in marine systems (Dauwe and Middelburg, 1998; Sheridan et al., 2002; Pedrosa-Pàmies et al., 2018). The observations include 30 sediment trap samples collected during the study period. Samples RedI-3 and RedI-6 are excluded due to lack of atmospheric deposition data for those months, RedII-8 and RedII-9 (Jan–Feb. 2012) and RedIII-4 (Sep. 2012) due to no data for lipids are available, and Red III-11 (Apr. 2013) due to it is an outlier based on the interquartile range of cholesterol (see "**Lipid Biomarkers**" section). The 18 variables considered refer to environmental conditions (SST, NPP, total atmospheric deposition), bulk properties (fluxes of POC, TN, $CaCO_3$, lithogenic, TN/POC ratio, and $\delta^{13}C$) and lipid biomarkers (fluxes of ∑TerNA, ∑TerN-OH, UCM, cholesterol, brassicasterol, β-sitosterol, dinosterol, C_{30}diol&keto-ols, and CPI_{NA}).

Prior to PCA, the data were standardized using the mean values and standard deviations to bring all of the variables into proportion with one another. A subroutine, the Varimax rotation, was applied to the first three factors in order to maximize or minimize loadings within each factor and thus simplify the visual interpretation of PCA projections. Correlation analysis was also performed using the same variables. PCA was carried out by using STATGRAPHICS v. 18.

RESULTS

Environmental Conditions

Total atmospheric deposition ranged from 130 to 5,600 mg m^{-2} $month^{-1}$ (**Figure 2A**). Highest atmospheric wet deposition was recorded in winter, especially in Feb 2011. Highest dry deposition was recorded in summer (Jul 2011), early fall (Sep 2011), and spring (Apr 2013). SST was highest during summer (25.5 ± 1.85°C) and lowest during winter (17.9 ± 1.69°C) (**Figure 2A**). Total Chl *a* concentrations were lowest during summer (0.07 ± 0.01 mg m^{-3}), relatively high during winter-spring (0.14 ± 0.05 mg m^{-3}), and the highest in March 2012 (0.43 mg m^{-3}). NPP followed the same trends as Chl *a* concentrations, with highest values in March 2012 (696 mg C m^{-2} d^{-1}) (**Figure 2B**).

Deep-sea currents at the sediment trap site at in the deep Ierapetra Basin were extremely slow with a predominant S/SW direction of the flow (**Figure 2C**). Intensified current speeds were recorded in January 2011 (up to 8 cm s^{-1}) and March 2012 (up to 9.8 cm s^{-1}) with a SW direction (i.e., topographically constrained). The magnitude of the current speeds and the strong topographic control registered in the deep Ierapetra Basin are of the same magnitude as currents registered at 3,542 m in the Samaria Canyon at the southern Cretan margin (Karageorgis et al., 2018) and at 4,300 m at NESTOR site in the deep Ionian Sea (Stavrakakis et al., 2013).

Sinking Particle Fluxes and Component Ratios

Total mass flux (TMF) and its major constituents (organic matter, opal, $CaCO_3$, and lithogenic matter) were highly variable, including significant seasonal variations (**Figure 3**, **Table 1**). During the three-year deployment, TMF ranged from 1.46 to 306.7 mg m^{-2} d^{-1} (**Figure 3A**). The highest particle flux was in spring 2012 (April-May, from 306.7 to 180.2 mg m^{-2} d^{-1}). Additionally, three other events had relatively high particle fluxes: summer 2010 (June, 174.6 mg m^{-2} d^{-1}), 2011 (June,

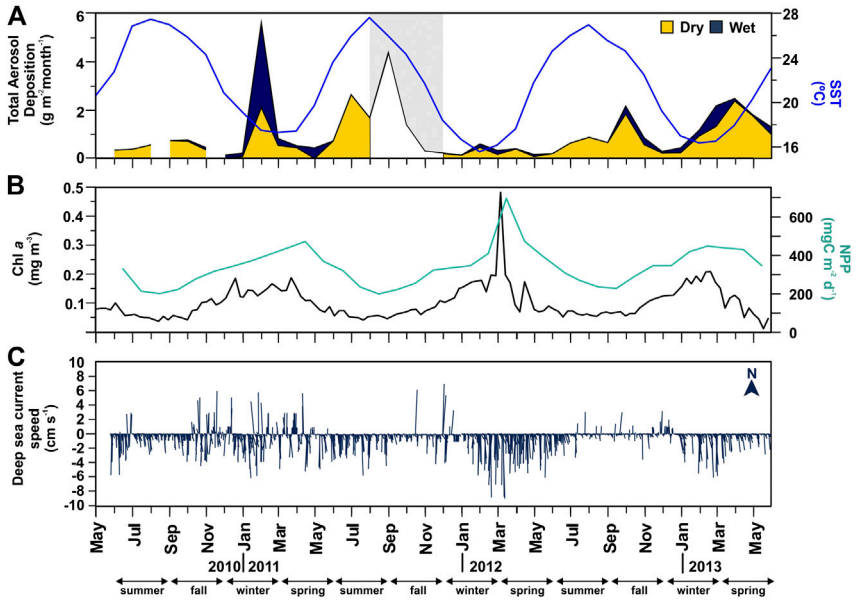

FIGURE 2 | Time-series of atmospheric and oceanographic parameters at the vicinities of the Ierapetra Basin station from June 2010 to June 2013. **(A)** monthly total aerosol [dry (yellow area) + wet (blue area)] deposition (in g m^{-2} $month^{-1}$) at the Finokalia station*, and monthly Sea Surface Temperature (SST, in °C, blue line); **(B)** 8-days surface Chlorophyll *a* concentration (Chl *a*, in mg m^{-3}), and monthly net primary production (NPP, in mg C m^{-2} d^{-1}, green line); and **C)** daily mean deep-sea current speed (in cm s^{-1}) and direction (º) at 4,287 m depth in the Ierapetra Basin (* gray area from September to November 2011 indicates values are available only for total atmospheric deposition, no distinction is made between dry and wet).

105.7 mg m^{-2} d^{-1}) and 2012 (June-July, from 123.2 to 104.5 mg m^{-2} d^{-1}).

During the three-year sampling period POC, opal, $CaCO_3$ and lithogenic fluxes were significantly and positively correlated with TMF (**Figure 4**). Lithogenic matter was the primary flux component, ranging from 0.04 to 156.1 mg m^{-2} day^{-1} and accounting for 86.6 ± 1.2% of TMF on average. Biogenic minerals were the next most abundant, with $CaCO_3$ (0.34–69.5 mg m^{-2} d^{-1}) and opal (0.03–58.7 mg m^{-2} d^{-1}) accounting for 28.6 ± 16.6% and 3.9 ± 4.1%, respectively, of TMF on average. OM contributed from 0.15 to 24.5 mg m^{-2} d^{-1}, accounting for 6.0 ± 3.2% of TMF on average.

POC fluxes ranged from 0.08 to 12.24 mg m^{-2} d^{-1}, and during 64% of the three-years studied the POC flux was <0.60 mg m^{-2} d^{-1} (**Figure 3C**). POC fluxes significantly correlated with the different mineral fractions: lithogenic (r = 0.83, slope = 0.051), $CaCO_3$ (r = 0.93, slope = 0.14) and opal fluxes (r = 0.97, slope = 0.21) (**Figures 4A** and **5**). Correlation of POC *vs* POC percentages was not significant. The highest percentages of POC were observed during the lowest flux periods in fall (5.83 ± 0.80%) and winter 2011 (5.00 ± 0.40%) (**Figure 3B**). POC percentages significantly and negatively correlated with lithogenic percentages, and positively with $CaCO_3$ and opal percentages (**Figure 4A**, **Supplementary Figure S1**).

The opal/$CaCO_3$ mole ratio ranged from 0.01 to 1.60, with an average value of 0.34 ± 0.36, and the POC/$CaCO_3$ mole ratio from 0.38 to 3.58, with an average of 1.06 ± 0.74 (**Table 1**). These two ratios visibly exhibit similar trends, which are positively correlated (r = 0.51, p = 0.004), with the highest opal/$CaCO_3$ and POC/$CaCO_3$ ratios during summer-fall 2011 and spring 2012. The POC/opal ratio ranged from 1.04 to 83.9, with an average of 7.23 ± 15.3, and exhibited exponential negative correlation with opal/$CaCO_3$ (r = 0.73, p < 0.0001).

Bulk Geochemical and Molecular Proxies

TN/POC and $\delta^{13}C$

Total nitrogen (TN) *vs* POC content presents a significant positive correlation (**Figure 4**). The TN/POC molar ratio of the sinking particles ranged from 0.11 to 0.25, with an average of 0.15 ± 0.04 (**Figure 3D**). This ratio was highest during fall 2010 and lowest during fall 2012. The $\delta^{13}C$ values of the sinking POC ranged from −26.53 to −21.33‰, with an average of −24.24 ± 0.96‰ (**Figure 3D**). The heaviest $\delta^{13}C$ was observed during the high-flux period of spring 2012 and the lightest during the relatively low-flux period in winter 2010.

Lipid Biomarkers

The major marine C_{27}-C_{30} sterols considered in this study are cholesterol ($C_{27}\Delta^5$), brassicasterol ($C_{28}\Delta^{5,22E}$), β-sitosterol ($C_{29}\Delta^5$) and dinosterol ($4\alpha C_{30}\Delta^{22E}$). They show total fluxes ranging from 0.15 to 15.8 µg m^{-2} d^{-1}, and concentrations ranging between 4.53 and 1,100 µg g^{-1} (normalized to POC from 0.31 to 31.9 µg mg OC^{-1}) (**Figure 6**, **Table 2**). Cholesterol was the most abundant C_{27}–C_{30} sterol, with fluxes ranging from 0.09 to 14.7 µg m^{-2} d^{-1} at 4,285 m depth, with the highest recorded during spring 2013, spring 2012 and early summer 2011, and the lowest during fall-winter (**Figure 6A**). Cholesterol concentrations ranged between 1.97 and 868 µg g^{-1} (from 0.14 to 29.6 µg mg OC^{-1}). Brassicasterol, dinosterol and β-sitosterol followed similar flux and concentration trends as

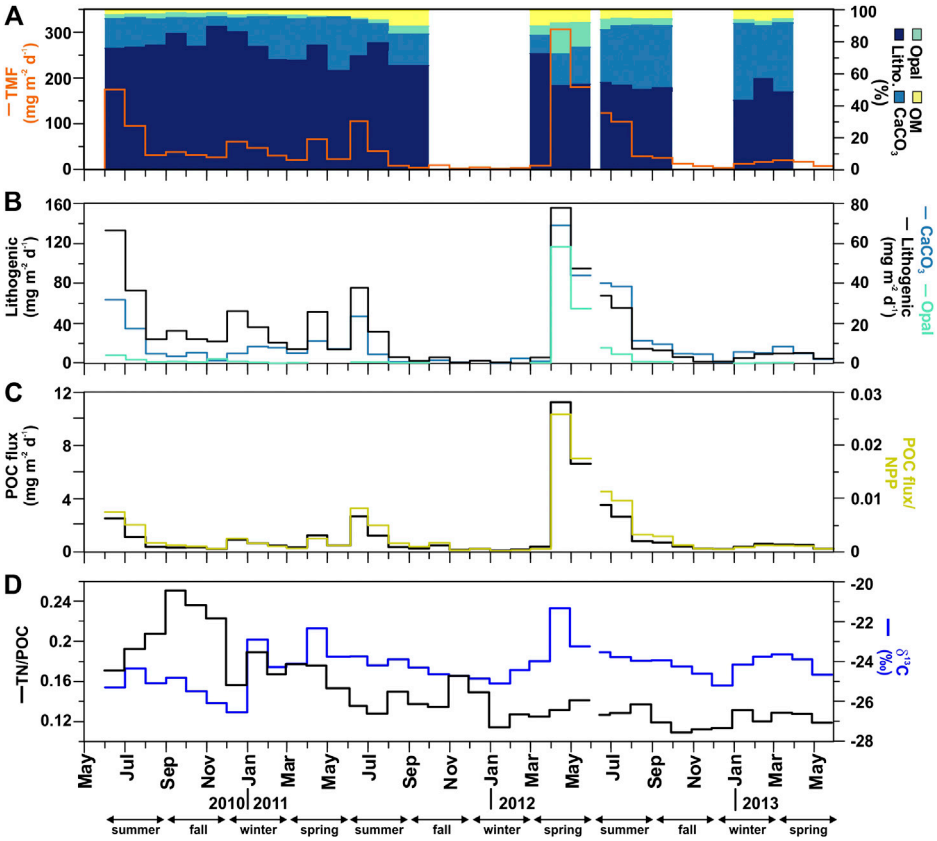

FIGURE 3 | Time-series at the Ierapetra Basin station from May 2010 to June 2013 of **(A)** Total Mass Flux (TMF, in mg m^{-2} d^{-1}), and cumulative percentages* of organic matter (OM), opal, carbonates ($CaCO_3$) and lithogenic; **(B)** Fluxes of lithogenic, opal and $CaCO_3$; **(C)** Particulate organic carbon (POC) flux, and export efficiency ratio (POC flux/NPP); **(D)** TN/POC molar ratio and $\delta^{13}C$ stable isotope (*Gaps of cumulative percentages of flux components correspond to periods where there are no opal data available).

cholesterol, positively correlated (**Figure 4**), but with up to an order of magnitude lower, except during spring of 2012 (**Figure 6B**, **Table 2**). The fluxes of long-chain C_{30} *n*-alkan-1,15-diols and the corresponding C_{30} keto-ols together ranged from 0.01 to 0.70 μg m^{-2} d^{-1}, with the highest values during spring 2012, fall 2011 and winter 2010 (**Figure 6E**). Concentrations ranged from 0.18 to 43.3 μg g^{-1} (from 0.02 to 0.42 μg mg OC^{-1}). Long-chain alkenones, had total fluxes from 0.02 to 1.81 μg m^{-2} d^{-1}, and concentrations from 0.53 to 25.6 μg g^{-1} (from 0.02 to 0.87 μg mg OC^{-1}) (**Figure 6F**). Highest fluxes and concentrations are observed during spring. The fluxes of ∑Phyto, marine phytoplankton-derived lipids, ranged from 0.02 to 5.52 μg m^{-2} d^{-1} and POC-normalized concentrations ranged from 1.07 to 8.99 μg mg OC^{-1} (**Table 2**).

Total aliphatic hydrocarbons (AH) fluxes ranged from 0.44 to 40.6 μg m^{-2} d^{-1}, averaging 3.91 μg m^{-2} d^{-1}. Highest AH fluxes are observed during spring 2012, and in early summers 2010, 2011 and 2012. Total AH concentrations ranged from 23.2 to 492 μg g^{-1} (average 124 μg g^{-1}). POC normalized AH concentrations are 1.07–8.99 μg mg OC^{-1}, with the highest concentrations during fall (**Table 2**). The molecular profile of sinking particle-associated AH is dominated in all cases by a UCM and a series of resolved compounds. UCM, appearing as a unimodal hump centered around *n*-C_{30}, was the major component of sinking particle-associated AH, accounting for up to 91% of their total sum (67% on average). UCM fluxes ranged from 0.29 to 28.7 μg m^{-2} day^{-1}, averaging 3.04 μg m^{-2} day^{-1} (**Figure 7A**). The highest UCM flux was recorded in May 2012, a month after the maximum TMF. UCM concentrations ranged from 15.6 to 372 μg g^{-1}, and from 0.82 to 7.93 μg mg OC^{-1}. *n*-alkanes were the main AH resolved compounds accounting for up to 72% (average 31%) of their total sum and for up to 18% of total AH (average 3.1%). Total *n*-alkanes (∑*n*-$C_{24–33}$) fluxes were 0.04–4.12 μg m^{-2} d^{-1}, and concentrations 0.74–8.45 μg g^{-1} and 0.11–1.31 μg mg OC^{-1}. During the study period, their molecular profile is dominated by long-chain homologues (*n*-C_{20} to *n*-C_{35}) with a CPI_{NA} value from 1.10 to 4.73. Highest CPI_{NA} were observed for summer 2011, and lowest for spring 2012 coupled with the highest UCM flux (**Figures 7A,D**). The flux of the most abundant high molecular weight plant wax *n*-alkanes corrected for the contribution of oil-derived long chain odd-numbered homologues (∑TerNA) ranged from 0.01 to 0.72 μg m^{-2} d^{-1}, and concentrations ranged from 0.74 to 8.45 μg g^{-1} (from 0.06 to 0.27 μg mg OC^{-1}) (**Figure 7B**).

The aliphatic alcohol fraction in the sinking particle samples is dominated in all cases by *n*-C_{24} to *n*-C_{30} alkanols with a maximum at *n*-C_{26}. The plant wax *n*-alkanols (∑TerN-OH) fluxes ranged from 0.03 to 1.65 μg m^{-2} d^{-1}, with the highest

TABLE 1 | Total mass fluxes (TMF) and bulk composition of sinking particles collected at 4,285 m in the Ierapetra Basin (n.d.: no data).

opening day	Sampling days	Season	ID—Bottle	TMF (mg m^{-2} d^{-1})	POC (%)	TN (%)	$\delta^{13}C$ (‰)	Opal (%)	$CaCO_3$ (%)	Lithogenic (%)	$POC/CaCO_3$	POC/opal	$Opal/CaCO_3$
01-Jun-10	30	Summer	RED I-1	174.6	1.42	0.28	−25.29	2.42	18.4	76.3	0.64	2.94	0.22
01-Jul-10	31	Summer	RED I-2	95.1	1.15	0.26	−24.35	2.19	18.5	77.0	0.52	2.63	0.20
01-Aug-10	31	Summer	RED I-3	31.0	1.13	0.27	−25.08	3.21	16.3	78.3	0.58	1.76	0.33
01-Sep-10	30	Fall	RED I-4	38.2	0.75	0.22	−24.81	3.05	9.87	85.6	0.63	1.23	0.51
01-Oct-10	31	Fall	RED I-5	31.3	0.97	0.27	−25.48	2.72	17.7	77.7	0.46	1.78	0.26
01-Nov-10	30	Fall	RED I-6	26.3	0.77	0.20	−26.08	2.45	6.06	83.4	1.06	1.58	0.67
01-Dec-10	31	Winter	RED I-7	60.4	1.46	0.26	−26.53	1.95	8.53	86.6	1.42	3.74	0.38
01-Jan-11	31	Winter	RED I-8	47.0	1.31	0.29	−22.91	1.49	18.4	77.5	0.59	4.40	0.13
01-Feb-11	28	Winter	RED I-9	30.1	1.48	0.29	−24.28	1.08	26.7	69.3	0.46	6.84	0.07
01-Mar-11	31	Spring	RED I-10	20.6	1.50	0.31	−24.10	2.43	25.7	68.9	0.49	3.09	0.16
01-Apr-11	30	Spring	RED I-11	66.1	1.83	0.37	−22.35	0.79	17.3	78.3	0.88	11.59	0.08
01-May-11	31	Spring	RED I-12	22.3	2.01	0.36	−23.76	0.12	33.4	62.4	0.50	83.94	0.01
05-Jun-11	26	Summer	RED II-1	105.7	2.50	0.39	−23.74	0.84	22.5	71.7	0.93	14.90	0.06
01-Jul-11	31	Summer	RED II-2	39.8	2.99	0.44	−24.19	2.31	11.9	79.8	2.09	6.49	0.32
01-Aug-11	31	Summer	RED II-3	8.11	4.09	0.71	−23.89	4.31	12.4	75.1	2.75	4.75	0.58
01-Sep-11	30	Fall	RED II-4	3.80	6.03	0.96	−24.30	n.d.	24.3	63.6	2.07	n.d.	n.d.
01-Oct-11	31	Fall	RED II-5	9.10	4.95	0.77	−24.64	5.02	19.5	65.6	2.11	4.94	0.43
01-Nov-11	30	Fall	RED II-6	1.74	6.51	1.25	−24.71	n.d.	45.7	41.2	1.19	n.d.	n.d.
01-Dec-11	31	Winter	RED II-7	4.49	4.54	0.79	−24.85	n.d.	33.0	57.9	1.15	n.d.	n.d.
01-Jan-12	31	Winter	RED II-8	1.46	5.24	0.69	−25.09	n.d.	23.0	66.5	1.90	n.d.	n.d.
01-Feb-12	29	Winter	RED II-9	3.02	5.23	0.77	−24.42	n.d.	84.6	4.90	0.51	n.d.	n.d.
01-Mar-12	31	Spring	RED II-10	8.34	4.91	0.71	−23.98	5.78	11.4	73.0	3.58	4.25	0.84
01-Apr-12	30	Spring	RED II-11	306.7	3.99	0.61	−21.33	19.1	19.9	53.0	1.67	1.04	1.60
01-May-12	31	Spring	RED II-12	180.2	3.85	0.63	−23.24	15.3	23.1	53.9	1.39	1.26	1.11
15-Jun-12	16	Summer	RED III-1	123.2	2.83	0.42	−23.53	6.47	32.8	55.1	0.72	2.19	0.33
01-Jul-12	31	Summer	RED III-2	104.5	2.50	0.37	−23.78	4.64	37.1	53.3	0.56	2.69	0.21
01-Aug-12	31	Summer	RED III-3	28.9	2.69	0.43	−23.97	3.88	40.2	50.5	0.56	3.47	0.16
01-Sep-12	30	Fall	RED III-4	25.3	2.68	0.37	−23.94	4.15	38.8	51.7	0.57	3.22	0.18
01-Oct-12	31	Fall	RED III-5	12.5	3.04	0.38	−24.25	4.18	40.3	49.4	0.63	3.64	0.17
01-Nov-12	30	Fall	RED III-6	7.13	3.12	0.40	−24.60	n.d.	68.3	25.5	0.38	n.d.	n.d.
01-Dec-12	31	Winter	RED III-7	3.22	5.82	0.76	−25.20	n.d.	27.6	60.8	1.76	n.d.	n.d.
01-Jan-13	31	Winter	RED III-8	12.4	2.92	0.44	−24.16	2.32	48.0	43.8	0.51	6.30	0.08
01-Feb-13	28	Winter	RED III-9	16.4	3.47	0.48	−23.76	2.68	33.0	57.4	0.88	6.47	0.14
01-Mar-13	31	Spring	RED III-10	20.0	2.63	0.39	−23.64	2.53	43.1	49.1	0.51	5.20	0.10
01-Apr-13	30	Spring	RED III-11	16.9	2.94	0.43	−23.89	2.36	30.3	61.5	0.81	6.23	0.13
01-May-13	31	Spring	RED III-12	7.35	2.89	0.40	−24.66	n.d.	30.5	63.7	0.79	n.d.	n.d.

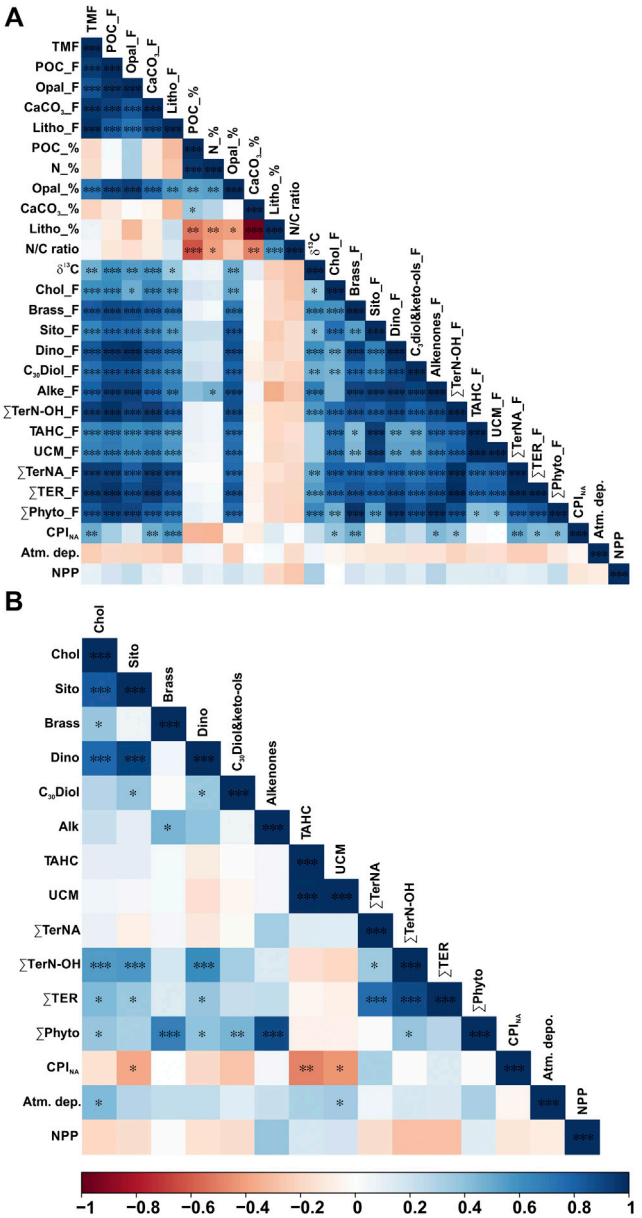

FIGURE 4 | Pearson correlation heatmap matrix with significance level expressed by asterisks (***p-value ≤ 0.001, **p-value ≤ 0.05, *p-value ≤ 0.1) of **A)** fluxes (F) and percentages (%) of bulk parameters, fluxes of lipid biomarkers, CPI_{NA}, total atmospheric deposition, and net primary production, and **(B)** POC-normalized concentrations of lipid biomarkers and CPI_{NA}, total atmospheric deposition, and net primary production. Positive correlations are displayed in blue and negative correlations in red color. Color intensity are proportional to the correlation coefficients.

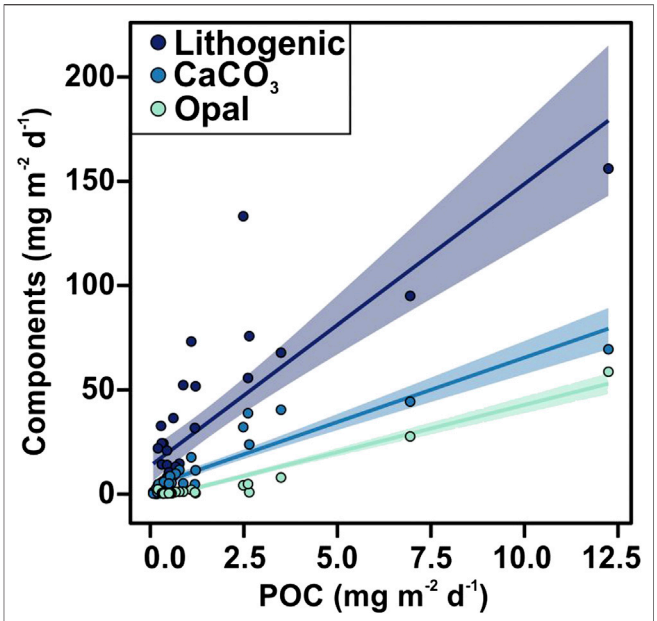

FIGURE 5 | Scatter plot of POC flux *vs.* lithogenic, $CaCO_3$ and opal material fluxes. The shaded areas represent prediction interval at the 95% confidence level.

fluxes during spring 2012, and early summer 2010, 2011 and 2012. Concentrations ranged from 1.22 to 22.5 μg g^{-1} and from 0.11 to 0.38 μg mg OC^{-1}, with the highest values during fall (**Figure 7C**). ∑TerN-OH and ∑Phyto POC-normalized concentrations showed a positive correlation (**Figure 4B**)

Land-derived lipid fluxes (∑Ter) ranged from 0.04 to 2.37 μg m^{-2} d^{-1}, with POC-normalized concentrations from 0.18 to 0.52 μg mg OC^{-1}. ∑Ter fluxes were positively correlated with ∑Phyto fluxes (**Figure 4**), with highest values during spring 2012 and summers 2010 and 2012 (**Figure 8**). Highest ∑Ter POC-normalized concentrations were during fall periods. POC-normalized concentrations of ∑Ter *vs.* ∑Phyto had a very weak positive correlation when considering all sinking particles (**Figure 8**). However, for each season individually, POC-normalized concentrations of ∑Ter *vs.* ∑Phyto of summer sinking particles showed a strong positive correlation (**Figure 8**, **Supplementary Figure S2**).

Multivariate Analysis

PCA was conducted to assess the compositional and temporal evolution of particle fluxes during the studied period. The first two principal components are responsible for 68.8% of the variance (**Figure 9A**). Factor 1 (PC1) explains 57.1% of the total variance and is characterized by positive loadings, above 0.7, for all bulk parameters, brassicasterol, dinosterol and ∑TerNA lipid fluxes, $\delta^{13}C$ and CPI_{NA}, and negative loadings, below −0.15, for SST and atmospheric deposition. PC1 separates samples according to particle fluxes, with the highest factor scores for the extreme episodic event on spring 2012, and summer months (**Figure 9B**). Thus, PC1 reflects the high particle flux periods and the impact of episodic events on the deep particle flux in the EMS. Factor 2 (PC2) explains another 11.7% of the variance and has positive loadings, above 0.7, for UCM, β-sitosterol, ∑TerN-OH fluxes, and negative loadings, below -0.15, for TN/POC ratio and CPI_{NA}. Therefore, PC2 separates samples by relative contribution of land-derived POC sources. Spring and summer samples showed the highest PC2 factor scores, and fall had the lowest. Factor 3 (PC3) explains 7.9% of the total variance

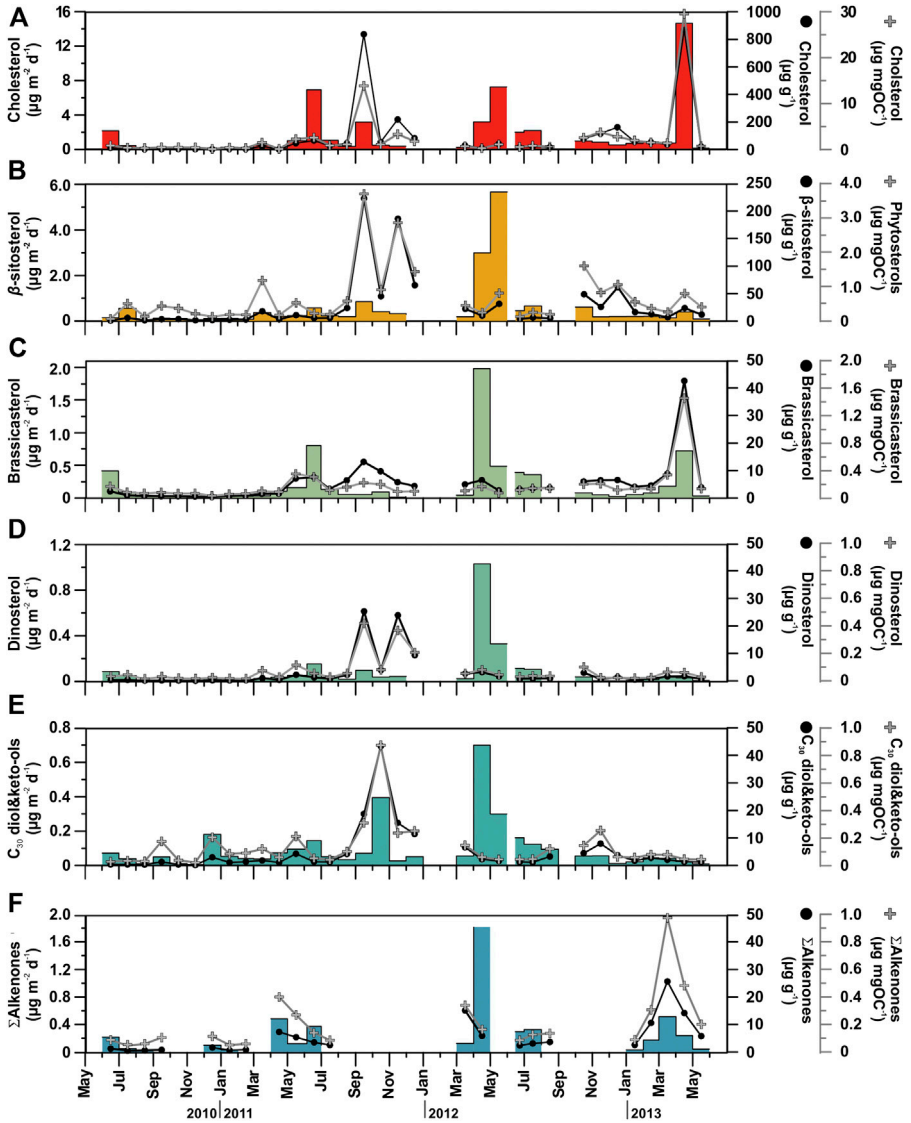

FIGURE 6 | Temporal distribution patterns (fluxes and concentrations) of major phytoplankton- and zooplankton-derived POC compounds (marine origin) in sinking particulate matter collected at 4,285 m in the Ierapetra Basin during the studied period (see section "**Oceanographic and Atmospheric Settings**". for further details).

and is characterized by positive loadings, above 0.5, for NPP, $\delta^{13}C$, and negative loadings, below -0.15, for SST, TN/POC ratio and CPI_{NA}. Highest PC3 factor scores were observed for spring samples. Therefore, PC3 separates samples by the relative contribution of phytoplankton-derived POC.

DISCUSSION

Efficiency of the Biological Pump in the Deep Ierapetra Basin

The mean annual TMF measured in the deep Ierapetra Basin (**Figure 3A**) is fairly comparable with those reported in previous studies that investigated particle fluxes in the bathypelagic EMS (e.g., Kerhervé et al., 1999; Stavrakakis et al., 2000; Patara et al., 2009; Karageorgis et al., 2018; Theodosi et al., 2019). For comparison, in the western Mediterranean Sea, TMF above 500 mg m^{-2} d^{-1} has been reported in the Alboran Sea (e.g., Fabres et al., 2002; Sanchez-Vidal et al., 2005) and submarine canyons of the NW Mediterranean Sea (e.g., Zúñiga et al., 2009; Stabholz et al., 2013).

POC fluxes recorded in this study are also of the same order of magnitude as those reported in previous studies that investigate POC fluxes in the deep EMS. The low POC fluxes during winter and spring are in line with the POC fluxes measured at 2,700 m in the Ierapetra Basin by Koppelmann et al. (2004) during winter/early spring 1999 (0.25–0.57 mg m^{-2} d^{-1}, from January to March) and late spring 1999 (1.16 mg m^{-2} d^{-1} during April). Karageorgis

TABLE 2 | POC-normalized concentrations of selected lipid biomarkers (n.d.: no data).

Opening day	ID - Bottle	Cholesterol $C_{27}\Delta^5$ (µg mg OC^{-1})	Brassicasterol $C_{28}\Delta^{5,22E}$ (µg mg OC^{-1})	Dinosterol $4\alpha C_{30}\Delta^{22E}$ (µg mg OC^{-1})	β-sitosterol $C_{29}\Delta^5$ (µg mg OC^{-1})	C_{30} diols& keto-ols[a] (µg mg OC^{-1})	Alkenone[b] (µg mg OC^{-1})	Total AH (µg mg OC^{-1})	UCM (µg mg OC^{-1})	∑TerNA (µg mg OC^{-1})	∑TerN-OH (µg mg OC^{-1})
01-Jun-10	RED I-1	0.87	0.17	0.03	0.06	0.03	0.09	1.95	1.42	0.15	0.18
01-Jul-10	RED I-2	0.41	0.08	0.05	0.51	0.04	0.05	2.02	1.36	0.09	0.20
01-Aug-10	RED I-3	0.32	0.06	0.02	0.13	0.03	0.06	2.85	2.13	0.09	0.13
01-Sep-10	RED I-4	0.48	0.08	0.03	0.44	0.18	0.10	4.71	3.91	0.10	0.16
01-Oct-10	RED I-5	0.48	0.06	0.02	0.37	0.04	n.d.	4.27	3.31	0.27	0.19
01-Nov-10	RED I-6	0.45	0.06	0.02	0.21	0.02	n.d.	5.45	4.18	0.26	0.26
01-Dec-10	RED I-7	0.14	0.03	0.03	0.12	0.21	0.11	5.65	5.10	0.06	0.12
01-Jan-11	RED I-8	0.42	0.05	0.02	0.19	0.09	0.05	2.72	2.15	0.08	0.11
01-Feb-11	RED I-9	0.32	0.06	0.02	0.18	0.09	0.06	8.71	7.93	0.09	0.11
01-Mar-11	RED I-10	1.51	0.10	0.08	1.18	0.12	n.d.	2.49	1.91	0.08	0.17
01-Apr-11	RED I-11	0.14	0.08	0.03	0.17	0.06	0.40	1.53	1.16	0.07	0.11
01-May-11	RED I-12	2.28	0.35	0.12	0.53	0.21	0.27	2.05	1.54	0.13	0.38
05-Jun-11	RED II-1	2.62	0.30	0.06	0.22	0.05	0.14	1.88	1.52	0.17	0.24
01-Jul-11	RED II-2	0.90	0.11	0.03	0.19	0.04	0.09	1.71	1.32	0.14	0.22
01-Aug-11	RED II-3	1.11	0.16	0.06	0.58	0.10	n.d.	2.48	1.74	0.08	0.25
01-Sep-11	RED II-4	13.9	0.22	0.42	3.72	0.31	n.d.	4.24	3.12	0.14	0.37
01-Oct-11	RED II-5	1.11	0.20	0.08	0.91	0.87	n.d.	2.87	1.96	0.15	0.25
01-Nov-11	RED II-6	3.36	0.09	0.37	2.87	0.24	n.d.	4.88	3.39	0.08	0.28
01-Dec-11	RED II-7	1.82	0.09	0.21	1.44	0.25	n.d.	2.14	1.44	0.07	0.25
01-Jan-12	RED II-8	n.d.	n.d.	n.d.	n.d.	n.d.	n.d.	n.d.	n.d.	n.d.	n.d.
01-Feb-12	RED II-9	n.d.	n.d.	n.d.	n.d.	n.d.	n.d.	n.d.	n.d.	n.d.	n.d.
01-Mar-12	RED II-10	0.61	0.10	0.06	0.46	0.13	0.31	4.88	3.92	0.11	0.22
01-Apr-12	RED II-11	0.26	0.16	0.08	0.24	0.06	0.15	1.07	0.82	0.06	0.14
01-May-12	RED II-12	1.05	0.07	0.05	0.82	0.04	n.d.	5.85	4.13	0.10	0.19
15-Jun-12	RED III-1	0.57	0.11	0.03	0.13	0.05	0.08	2.85	2.43	0.09	0.18
01-Jul-12	RED III-2	0.84	0.14	0.04	0.25	0.05	0.13	2.38	1.96	0.12	0.22
01-Aug-12	RED III-3	0.63	0.13	0.04	0.19	0.12	0.14	5.06	4.48	0.17	0.27
01-Sep-12	RED III-4	n.d.	n.d.	n.d.	n.d.	n.d.	n.d.	n.d.	n.d.	n.d.	n.d.
01-Oct-12	RED III-5	2.58	0.20	0.10	1.61	0.15	n.d.	4.84	4.07	0.17	0.33
01-Nov-12	RED III-6	3.76	0.21	0.03	0.83	0.25	n.d.	8.99	7.55	0.13	0.16
01-Dec-12	RED III-7	2.78	0.11	0.03	1.06	0.06	n.d.	8.45	6.38	0.12	0.16
01-Jan-13	RED III-8	1.97	0.14	0.02	0.56	0.06	0.09	4.47	3.70	0.11	0.16
01-Feb-13	RED III-9	1.53	0.13	0.03	0.37	0.08	0.31	4.66	3.80	0.17	0.20
01-Mar-13	RED III-10	1.42	0.33	0.07	0.26	0.08	0.97	4.31	3.58	0.17	0.19
01-Apr-13	RED III-11	29.6	1.45	0.06	0.81	0.05	0.48	5.26	4.33	0.11	0.20
01-May-13	RED III-12	0.76	0.13	0.03	0.41	0.04	0.20	8.69	7.71	0.12	0.18

[a]*Sum of the concentrations of long-chain C_{30} n-alkan-1,15-diols and C_{30} keto-ols.*

[b]*Sum of the concentrations of $C_{37:3}M$, $C_{37:2}M$, $C_{36:2}FAME$, $C_{38:3}Et$, $C_{38:3}M$, $C_{38:2}Et$, $C_{38:2}M$.*

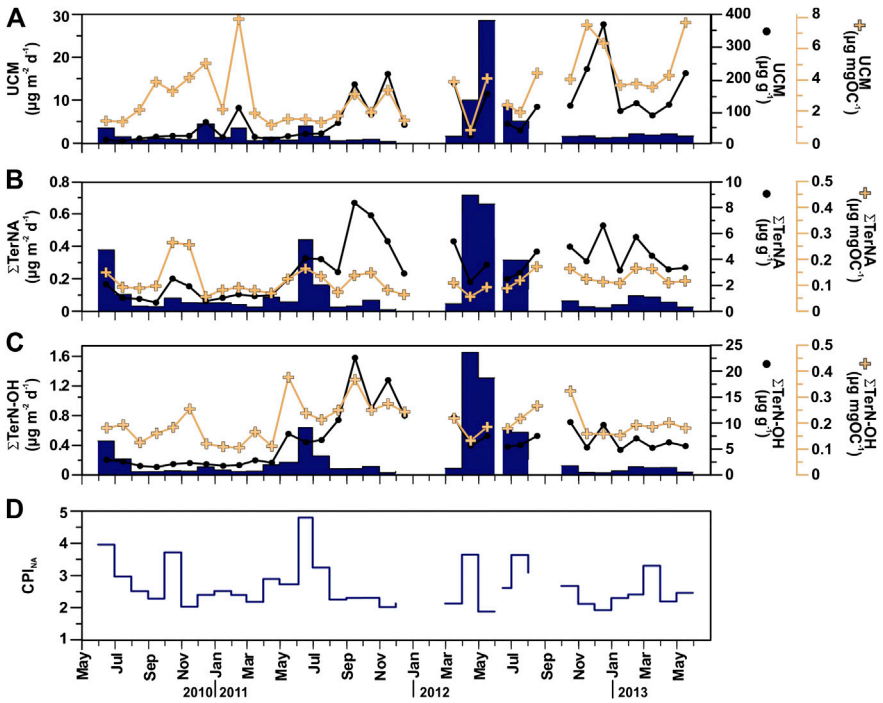

FIGURE 7 | Temporal distribution patterns (fluxes and concentrations) of major terrestrial and anthropogenic-derived POC compounds in sinking particulate matter collected at 4,285 m in the Ierapetra Basin during the studied period: **(A)** Unresolved Complex Mixture of aliphatic hydrocarbons (UCM), **(B)** long-chain *n*-alkanes (∑TerNa), and **(C)** long-chain *n*-alkanols (∑TerN-OH), and **(D)** Carbon Preference Index of long-chain *n*-alkanes (CPI_{NA}) (see section "**Source Indicators of Sinking Particulate Organic Carbon**" for further details).

et al. (2018) reported mean annual POC fluxes between 1.5 and 4.8 mg m^{-2} d^{-1} (May 2005 - June 2006) in the southern Cretan margin at depths from 1,215 to 3,538 m. Gogou et al. (2014) reported mean annual POC fluxes <6 mg m^{-2} d^{-1} (September 2007 to September 2008) in the southern Ionian Sea at 1,400 and 2,800 m water depth. Stavrakakis et al. (2013) reported mean annual POC fluxes between 0.01 and 12.3 mg m^{-2} d^{-1} (February 2006 to March 2010) in the SE Ionian Sea (NESTOR site) at depths from 1,200 to 4,300 m. Finally, Stavrakakis et al. (2000) reported POC fluxes <8.03 and <10.96 mg m^{-2} d^{-1} (November 1994 to November 1995) in the southern Cretan Sea at 200 m and 1,515 m water depth, respectively.

The low POC fluxes reported herein match the very low NPP observed in the Ierapetra Basin during the study period (~118 g C m^{-2} y^{-1}) and reported from other studies in the open waters of the Levantine Basin (97–113 g C m^{-2} y^{-1}) (Antoine et al., 1995; Napolitano et al., 2000; Bosc et al., 2004), which is lower than in the center of large oceanic gyres, such as the Sargasso Sea, where values around 150 g C m^{-2} y^{-1} have been measured (Steinberg et al., 2001; Lomas et al., 2013). For comparison, the primary productivity of coastal and upwelling zones, in some of the most productive areas of the ocean, typically exhibit values close to 250 g C m^{-2} y^{-1} (Longhurst et al., 1995). The fraction of primary production exported to the deep Ierapetra Basin averaged 0.35%, which is comparable to what has been observed in the EMS in the southern Ionian Sea at depths from 2,000 to 2,800 m (Stavrakakis et al., 2013; Gogou et al., 2014), but two-fold higher than what was reported at 4,300 m in the sourtheastern Ionian Sea (Stavrakakis et al., 2013).

Over the study period, the export efficiency was low during 66% (<0.02, twentieth percentile of data) of the time, and moderate during 30.6% of the time (between 0.2 and 0.02) (**Figure 3C**). This underscores the strong oligotrophic conditions of the study area. To further investigate the efficiency of the biological carbon pump we tested the correlation between the export efficiency (POC flux/NPP) and NPP (**Figure 11**). Herein we cannot conclude that in the EMS there is an inverse relationship between PP and export efficiency, as previously identified for the Southern Ocean (Maiti et al., 2013; Cavan et al., 2015; Le Moigne et al., 2016) and globally (Henson et al., 2019). We observed that, overall, there is no clear relationship between the export efficiency and NPP, except when observing seasonal trends (see discussion in section "**Seasonal Export Pulses to the Deep Eastern Mediterranean Sea**" below).

The POC content of sinking particles of the deep Ierapetra Basin (3.00 ± 1.60% POC) was 6-fold higher than the reported for deep-sea surface sediments in the study area (0.49 ± 0.09% POC). Thus, our data indicate that, on average, just about 16% of the POC that reaches the bathypelagic Ierapetra Basin gets settled and preserved to the seafloor sediments.

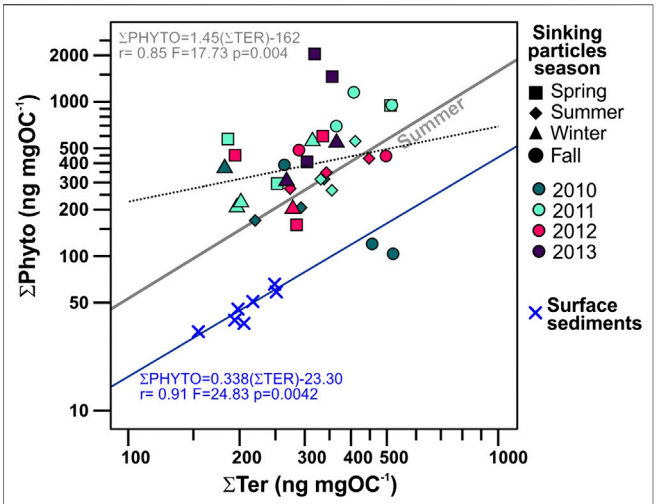

FIGURE 8 | Biplot of POC-normalized concentrations of phytoplankton-derived lipid biomarkers (ΣPhyto) *vs.* terrestrial (ΣTer) of sinking particles collected in the deep Ierapetra Basin from June 2010–June 2013, and surface sediments collected from January 2007 to June 2012 in the NW Levantine Basin (Pedrosa-Pàmies et al., 2015). Symbol shapes correspond to season of the sinking particles and colors correspond to sampling year. Regression lines for all (dashed black line, not significative) and summer period (gray line) sinking particles, as well as for surface sediments (blue line) are represented.

Drivers of Natural and Anthropogenic Particulate Organic Carbon Export

The positive correlation of POC fluxes with the different mineral fractions, especially with the biogenic minerals (**Figure 5**), observed throughout the study period suggests that the ballasting effect of the biogenic minerals is an important factor promoting the export of organic carbon to the deep EMS by increasing the density of settling particles, and/or providing POC protection against remineralization (Armstrong et al., 2002; Francois et al., 2002; Klaas and Archer, 2002). These correlations agree with the study from Klaas and Archer (2002) where they evaluated data from 52 sediment trap experiments worldwide. Low slope of opal *vs* POC flux suggest that in the EMS opal is more effective than carbonates at facilitating the POC flux.

Plankton and microbial community structure in the upper ocean also play a significant role in the export and transfer efficiency of carbon to the ocean interior (Herndl et al., 2008; Guidi et al., 2009; Henson et al., 2012). The main functional groups of phytoplankton contributing to export production through direct sedimentation are nitrogen fixers (e.g., diazotrophic cyanobacteria), silicifiers (e.g., diatoms), calcifiers (e.g., coccolithophores) and other marine plankton (e.g., dinoflagellates) (Agusti et al., 2015; Le Moigne et al., 2015; Turner, 2015; Basu et al., 2018). Generally, in the EMS there is a predominance of dinoflagellates and coccolithophores over diatoms (Malinverno et al., 2003; Ignatiades et al., 2009; Skampa et al., 2020 and references therein), except for the Rhodes gyre area under strong upwelling conditions where diatoms can be dominant (Siokou-Frangou et al., 1999). Therefore, the more stable POC/$CaCO_3$ ratio compared to the POC/opal ratio (**Table 1**) can be associated with the phytoplankton community dynamics and morphological and ecological differences between diatoms and coccolithophorids (De La Rocha and Passow, 2007). Moreover, the relatively high fluxes and POC-normalized concentrations of cholesterol ($C_{27}\Delta^5$) indicate that secondary production has a critical role exporting POC to the deep EMS.

Phytoplankton growth rate, and availability of CO_2, light and nutrients affect isotopic fractionation and thus the $\delta^{13}C$ of POC (Rau et al., 1992; Burkhardt et al., 1999). Winter and spring are the only two seasons when sinking particles reaching the deep Ierapetra Basin show a significant positive correlation (spring: $r = 0.98$, $p < 0.0001$; winter: $r = 0.90$, $p = 0.003$) with sinking POC flux and $\delta^{13}C$ values (**Figure 11**). Because primary production affects the CO_2 concentration near the producers, there is a positive correlation between $\delta^{13}C$ of the phytoplankton and primary production, and consequently, also with sinking POC fluxes (Deuser et al., 1968; Rau et al., 1992). This suggests that during summer and fall, either CO_2 was not depleted enough to cause detectable enrichment of ^{13}C, or $\delta^{13}C$ values were shaped by other processes than primary production. Factors contributing to the decline in $\delta^{13}C$ of POC values can be microbial activity (Lehmann et al., 2002) and inputs from the overlying surface waters of terrestrial or anthropogenic POC. $\delta^{13}C$ values in marine algae from low-to mid-latitude temperate seas vary from -18‰ to -22‰ (Goericke and Fry, 1994; Meyers, 1994; Harmelin-Vivien et al., 2008), whereas most terrestrial POC inputs from C3 plants are -25‰ to -28‰ (Hedges et al., 1997) and POC from crude oil and petroleum products has values between −28.5 and −28.9‰ (Rumolo et al., 2011, and references therein). Therefore, a significant incorporation of terrestrial and anthropogenic POC may be a cause of the more depleted $\delta^{13}C$ values in the summer and fall samples. The $\delta^{13}C$ of the sinking particles was significantly lighter (average isotopic change -1.9‰) than those of surface sediments (**Figure 11**). This isotopic change indicates isotopic discrimination during sinking processes and potential incorporation of allochthonous material from the deep EMS. The isotopic fractionation between sinking particles from the deep ocean and surface sediments has been previously reported (e.g., Fischer and Wefer, 1996; Nakanishi and Minagawa, 2003 and references therein), but this is the first study to document it for the EMS.

The deviation of the TN/POC ratios of the sinking particles from the classical Redfield ratio (Redfield et al., 1963), further indicates POC degradation processes of marine labile compounds during transport from surface waters to the deep Ierapetra Basin (**Figure 11A**). The overall higher TN/POC ratios from the sinking particles *vs* the seafloor sediments (**Figure 11**) further reflect the preferential degradation of labile nitrogen-enriched organic matter and the re-working of marine algal organic matter by zooplankton and benthic invertebrates during transport and deposition (Gogou and Stephanou, 2004; Lampadariou et al., 2009). Additionally, by comparing the lipid biomarker composition of sinking particles *vs* surface sediments, we can provide insight about the pre-depositional processing of the

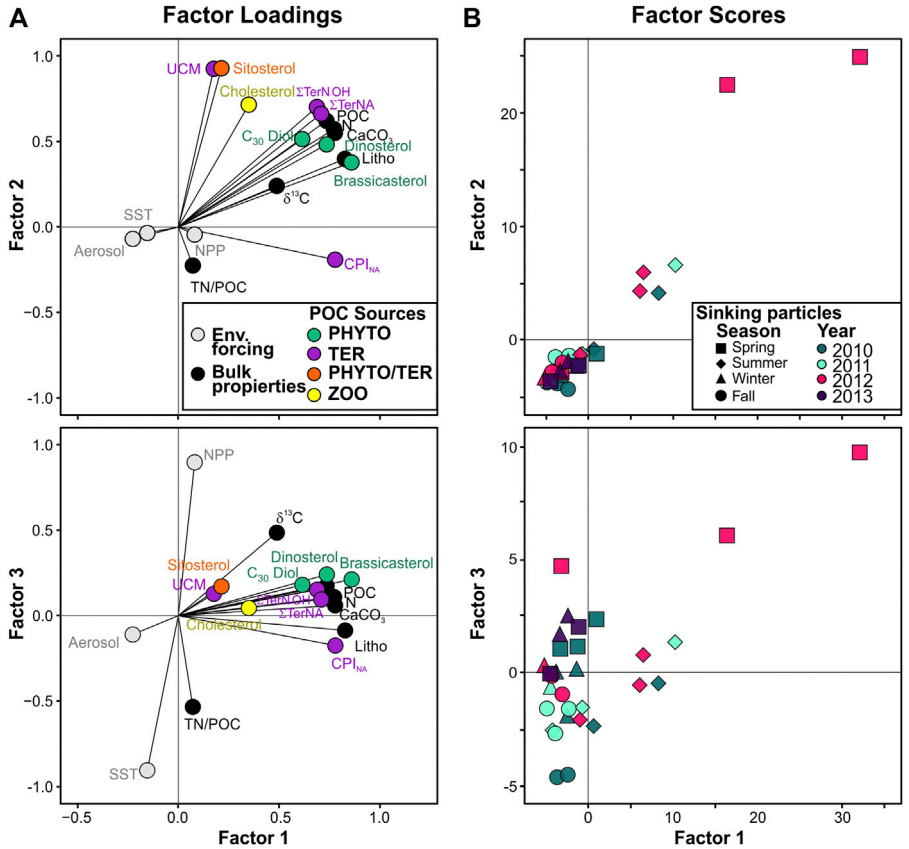

FIGURE 9 | PCA results. **(A)** Factor loadings for environmental forcing, bulk properties, and biomarkers of phytoplankton-derived POC (Phyto, green), zooplankton-derived POC (Zoo, yellow), and land-derived natural and anthropogenic POC (TER, purple) for the collected sinking particles. **(B)** Biplots of main factor scores for sinking particles identified by sampling year (colors) and season: fall (circle: September, October, November), spring (square: March, April, May), summer (diamond, June, July, August) and winter (triangle: December, January, February).

organic matter affecting the POC content and quality in the deep EMS before it gets buried. POC-normalized concentrations of phytoplankton- (∑Phyto) *vs* land-derived (∑Ter) lipid biomarkers of sinking particles compared with surface sediments (**Figure 8**) show that sinking particles are an order of magnitude more enriched in phytoplankton-derived POC, indicating the higher preservation efficiency of terrestrial *vs* marine POC (e.g., Hoefs et al., 2002; Burdige, 2007; Blair and Aller, 2012).

The weak negative correlation between molar TN/POC ratios and $\delta^{13}C$ values of the sinking particles (**Figures 4 and 11b**) indicates that the POC composition of the sinking particles was rather a mixture of marine (high TN/OC and $\delta^{13}C$) and terrestrial (low TN/OC and $\delta^{13}C$) particulate organic matter, but may also suggest significant contribution of other sources (e.g., anthropogenic POC). Indeed, the profile of AHs is indicative of the contribution of anthropogenic POC in the considered samples. Specifically, the CPI_{NA} values of long-chain *n*-alkanes ranging from 1.10 to 4.73 (**Figure 7d**), being, <2 in 61% of the cases, are indicative of a mixture of long straight-chain aliphatic compounds from both fossil (unburned fossil fuels) and land-derived (higher plant waxes) sources (Wang et al., 1999). Moreover, the presence of a UCM in all cases is indicative of anthropogenic POC deriving from degraded petroleum hydrocarbons and/or apolar products deriving from combustion processes (Wang et al., 1999). The entire EMS is a marine setting under intense anthropogenic pressure receiving substantial amounts of petroleum hydrocarbons through direct discharges from merchant shipping and oil transportation, mainly along shipping routes (Gogou et al., 2000; Parinos et al., 2013a; Parinos and Gogou, 2016; Hatzianestis et al., 2020). Furthermore, UCM hydrocarbons can also be derived from combustion processes, such as grass/wood/coal combustion and/or the incomplete combustion of fossil fuels, and are found in atmospheric aerosols collected from marine and urban areas of the EMS constituting a major source of combustion-related AHs through long-range atmospheric transport and subsequent dry/wet deposition (e.g., Tsapakis et al., 2006; Theodosi et al., 2013; Gogou et al., 1998 and references therein).

The strong positive correlation of UCM *vs.* POC fluxes (**Figure 4A**) is in agreement with the widely documented fact that the biogeochemical cycling of anthropogenic hydrocarbons

in marine systems is largely controlled by the biological pump and physico-chemical properties of individual compounds (Farrington and Takada, 2014, and references therein). Fossil hydrocarbons introduced into surface waters via the direct release of petroleum products by ships are more available to the dissolved phase, and are efficiently scavenged by organic rich particles (e.g., phytoplankton and fecal pellets), resulting in their sinking in open seas. Direct and indirect evidence of biodegradation has been shown as an important factor affecting their abundance during their downward transport in the water column. On the other hand, hydrocarbons derived from combustion sources, which are mainly introduced into surface EMS waters through long-range atmospheric transport and subsequent dry/wet deposition, are strongly associated to fine combustion particles that protect them from degradation during their transport through the water column. Sorption of combustion particles onto biogenic aggregates has been highlighted as the important mechanism regulating their cycling in marine systems (Deyme et al., 2011; Parinos et al., 2013b; Theodosi et al., 2013 and references therein)

Seasonal Export Pulses to the Deep Eastern Mediterranean Sea

Export during summer periods in the deep Ierapetra Basin was approximately four-fold greater than the export in wintertime, fall and springtime (except for the episodic event in spring 2012). In summer, the highest relative contribution of lithogenic to the TMF and relatively high POC fluxes coincided with the lowest NPP and high atmospheric dry deposition (**Figures 2** and **3**). It is well-documented that in the Levantine Basin the lowest Chl *a* and primary production levels and the highest transparency are found during the thermally stratified summer period (Gotsis-Skretas et al., 1999; Bosc, 2004; Ignatiades et al., 2009). Our results indicate that the export efficiency is relatively high during summer in the Levantine Basin (below **Figure 3C**). This rather high export efficiency in summertime has been previously reported in a wide range of open oceanic regions (Buesseler, 1998; Henson et al., 2012; Karl et al., 2012; Puigcorbé et al., 2015; Smith et al., 2018), and highlighted by biogeochemical models (Henson et al., 2015). The export efficiency can be highly variable depending on the degree of (de-)coupling between phytoplankton community structure (Buesseler, 1998; Francois et al., 2002), and upper ocean remineralization by zooplankton (Steinberg et al., 2002; Dagg et al., 2014; Cavan et al., 2015) and bacteria (Buchan et al., 2014; Belcher et al., 2016; Le Moigne et al., 2016; Henson et al., 2019). Sinking velocities in the EMS have been estimated to be 100–200 m d^{-1}, and are accelerated by pulses of primary production and grazing and by Saharan dust events that fertilize the upper ocean (Patara et al., 2009)

The fact that the relatively high POC fluxes in summer were enriched with land-derived natural AHs (higher plant waxes) as inferred from both ∑TerNA and ∑TerN-OH concentrations and elevated CPI_{NA} ratio values), anthropogenic AHs (UCM) (relatively high PC1 and PC2 scores), but also from phytoplankton- and zooplankton-derived lipids suggests that POC export to the deep EMS in summer is controlled by the interactions between the biological pump and different types of ballast minerals (dust/-induced POC export by fertilization and aggregation/adsorption processes) (Marañón et al., 2010; Bressac et al., 2014; van der Jagt et al., 2018).

Moreover, the relatively high fluxes of brassicasterol, dinosterol and C_{30} diols&keto-ols, and low POC-normalized concentrations of these phytoplankton-derived lipids coupled with high cholesterol fluxes and relatively high POC-normalized concentration of cholesterol (**Figure 6**), suggest that zooplankton has a significant role in the particle flux and POC degradation in summertime through grazing and repackaging in fecal pellets. This is consistent with previous studies that have reported relatively high export efficiencies during summer, when grazing is able to keep pace with NPP so that the POC flux via fecal pellets increases (Henson et al., 2015). Summertime nutrient limitation in the EMS leads to lower biological production and a plankton community structure dominated by small pico-autotrophic cells (<3 μm) (Psarra et al., 2000; Meador et al., 2010; Siokou-Frangou et al., 2010; Varkitzi et al., 2020). Raveh et al. (2015), revealed that autotrophic cyanobacteria such as *Synechococcus* and *Prochlorococcus* generally dominate the phytoplankton biomass during summer in the eastern Levantine Basin, and are also the main contributors to primary production. Small phytoplankton cells have a higher surface area-to-volume ratio, nutrient assimilation efficiency, photosynthetic activity, faster division rates and lower sinking rates than larger phytoplankton (Raven, 1998; Finkel et al., 2010). Therefore, picoautotroph-dominated communities during summer in the EMS may represent food webs with a high degree of aggregate repackaging with potential for accelerated sinking (Buesseler and Boyd, 2009; Bach et al., 2016).

The strong positive correlation of POC-normalized concentrations of ∑Ter *vs.* ∑Phyto of summer sinking particles (**Figure 8**), but also fluxes of UCM *vs.* ∑TerNA, ∑TerN-OH and ∑Phyto (**Figure 4**, **Supplementary Figure S2**), suggest that coupled with the plankton dynamics, the mineral ballast plays an important role in the export of natural and anthropogenic POC to the deep EMS during summer. For the EMS the periods of increased atmospheric dust are in spring and early summer, followed by autumn, and the dust sources are from the coasts of Africa, Arabian Peninsula and Red Sea (Moulin et al., 1998; Israelevich et al., 2012). Strict dry deposition is a highly effective mechanism of dust deposition in the Mediterranean Sea, and in summer it can contribute up to 93% to the total dust deposition due to the reduction or even absence of wet deposition (Kubilay et al., 2000). The highest summertime atmospheric deposition values were recorded in 2011. During this period, high aerosol dry deposition was recorded, associated with air masses from the south, carrying significant amounts of desert dust, and also air masses marked by local influence (**Supplementary Figure S3**).

In winter-spring (November to May) Chl *a* concentration increased (**Figure 2B**) but compared to summer, POC fluxes to the deep Ierapetra Basin were relatively low (**Figure 3B**), with exceptions, such as spring of 2012 (see discussion below in section "**Extreme Episodic Event in Spring 2012: Coupling of**

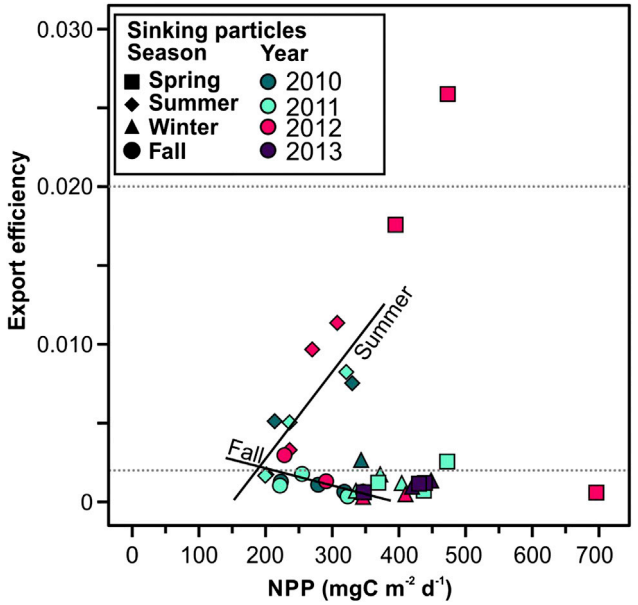

FIGURE 10 | Net primary productivity (NPP) plotted against export efficiency (POC flux/NPP). Horizontal dashed lines indicate threshold for export efficiency regimes: high export efficiency is defined as >0.2 (eightieth percentile of data), low export efficiency is <0.02 (twentieth percentile), and moderate export efficiency lies between. Significative regression lines are shown for summer (Export efficiency = 0.00006NPP–0.0082, r = 0.824, p < 0.05), and fall (Export efficiency = –0.00001NPP+0.0043, r = 0.661, p = 0.053).

Atmospheric Conditions Funneled Labile and Recalcitrant POC to the Deep EMS"). The low export efficiency can be explained by the tight coupling between primary producers and their grazers in the upper ocean layers (Henson et al., 2019 and references therein). The highest fluxes and POC-normalized concentrations of alkenones, and relatively high POC-normalized concentrations of brassicasterol, coupled with relatively enriched $\delta^{13}C$ values, in early spring sinking particles (March/April) (relatively high PC3 factor scores) (**Figure 9**), suggest that this tight coupling is broken intermittently during the onset of the spring bloom, allowing a small export pulse of labile phytoplankton-derived POC to the deep sea. Spring (excluding episodic event 2012) is the only season were we found positive trend of UCM *vs.* ∑Phyto fluxes (r = 0.60, p = 0.15), but also significant positive correlations of UCM fluxes and POC-normalized values *vs* atmospheric dry deposition (r = 0.73 p = 0.06, r = 0.67 p = 0.10, respectively). This suggests that long-range atmospheric transport of combustion emissions is the major source of these compounds, with subsequent sorption of the fine combustion particles onto biogenic aggregates likely regulating their sinking to the deep Ierapetra Basin. A clear coupling of this process is observed in spring of 2013 (March to May), which had relatively high ∑Phyto and UCM concentrations, and was a period with relatively high atmospheric deposition, with air masses arriving at Finokalia enriched in material from land, affected by both south and north continental areas surrounding the Mediterranean Sea (**Supplementary Figure S4**).

Fall and winter had the lowest particle and POC fluxes. These low fluxes could be explained by the microbial communities in the mesopelagic zone reducing sinking velocity of particles during this period and thus low export to the deep Ierapetra Basin (Sempéré et al., 2000; Herndl and Reinthaler, 2013). This hypothesis of POC reworking by microbial communities is supported by the very low POC-normalized concentrations of labile phytoplankton-derived lipids (i.e., brassicasterol and dinosterol), and cholesterol (lowest PC3 factor scores) (**Figure 9**). Fall is the only season where we observed an apparent relationship between NPP and export efficiency (**Figure 10**). This could imply that NPP become decoupled from the processes acting to remineralize POC in the upper ocean during fall periods.

Additionally, during fall period, it is particularly noteworthy to highlight September 2011, which had high total atmospheric deposition (**Figure 2A**). Air masses had significant continental and regional influence, coming from the northeast and east (sweeping the Balkans and Turkey), but also from the west (African continent) (**Supplementary Figure S5**). Therefore, during this period atmospheric deposition provided terrestrial material enriched in soil dust and vegetation, as imprinted in elevated land-derived terrestrial lipids (∑TerNA and ∑TerN-OH) POC-normalized concentrations and CPI_{NA} values (**Figure 7**). Interestingly, the highest POC-normalized concentrations of UCM (but also ∑TerNA, ∑TerN-OH and β-sitosterol) are recorded during late fall and winter periods. This could be attributed to the fact that fall/winter periods have the highest atmospheric wet deposition, especially in February 2011 (**Figure 2A**). During this month, air masses were significantly influenced by land, both coming from the Atlantic close-by the northwest Africa and reaching the EMS after having swept Central and Eastern Europe, and also directly coming from the African continent (**Supplementary Figure S6**). Atmospheric scavenging by rain drops of hydrocarbons emitted from anthropogenic (mainly air masses originating from the NW/N/NE sector) and terrestrial sources (from the SW/S sector), and subsequent efficient sorption of these hydrocarbons on organic-rich particles is likely the main mechanism driving their cycling during this period.

Extreme Episodic Event in Spring 2012: Coupling of Atmospheric Conditions Funneled Labile and Recalcitrant POC to the Deep EMS

In spring 2012, TMF and POC fluxes were one and two orders of magnitude, respectively, higher than in other spring periods over the study period (**Figure 3C**). As highlighted by Pedrosa-Pàmies et al. (2016), winter and spring of 2012 were characterized by exceptional atmospheric conditions. During winter 2011–12, particularly strong cold and dry northerly winds triggered intense convection not only in the EMS but also in the NW Mediterranean Sea (Durrieu de Madron et al., 2013; Palanques and Puig, 2018), and in the Adriatic Sea (Bensi et al., 2013; Janeković et al., 2014). The intense convection in winter 2012 caused an upwelling of relatively nutrient-rich cold water masses into the euphotic zone, triggering an exceptional phytoplankton

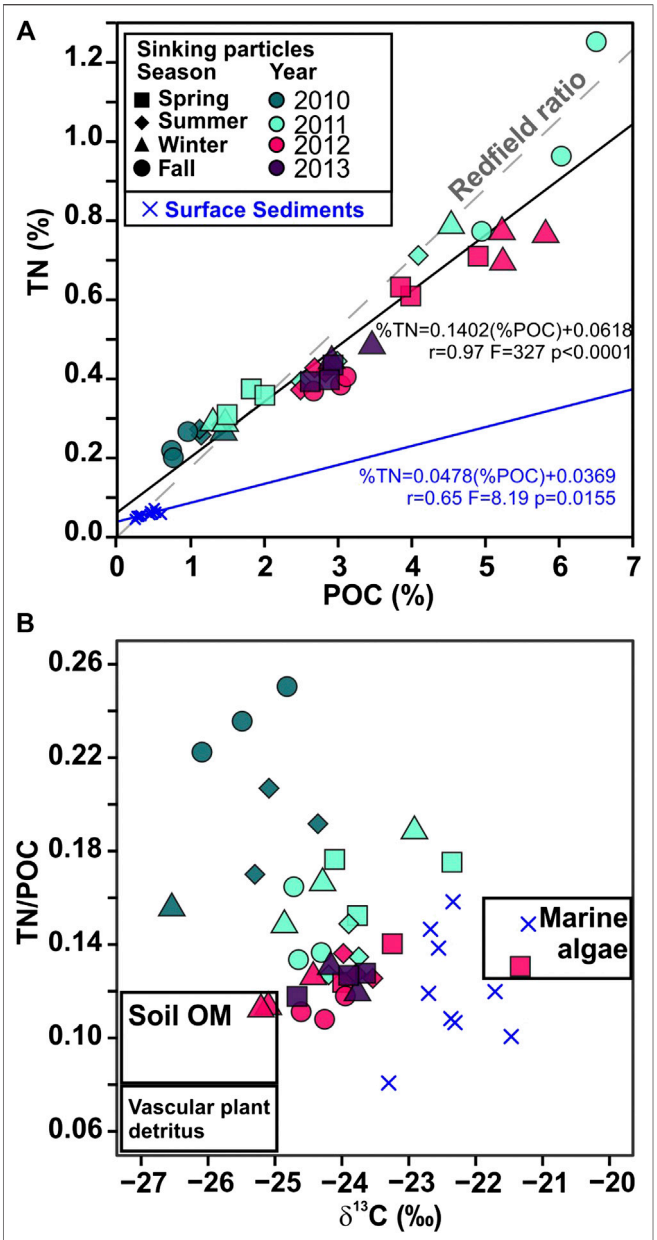

FIGURE 11 | (A) Plot of the weight percent content of nitrogen (TN) *vs.* particulate organic carbon (POC) in settling particles, and surface sediments samples from Pedrosa-Pàmies et al. (2015). The linear fit of the data is shown (solid line) along with the Redfield ratio N_{16}/C_{106} associated with the fresh marine phytoplankton (0.17 *wt/wt*, dashed line), **(B)** Plot of molar TN/OC ratios *vs.* $\delta^{13}C$, in the sediment trap and surface sediment samples. The compositional ranges of end members of organic matter sources (boxes) are derived from previously published studies (Meyers, 1994; Goñi and Hedges, 1995; Hedges et al., 1997; Harmelin-Vivien et al., 2008; Sanchez-Vidal et al., 2013). Symbol shapes correspond to season and colors correspond to sampling year.

bloom on March 2012 (**Figure 2B**). As emphasized by Pedrosa-Pàmies et al. (2016), the exceptional phytoplankton bloom was most probably stimulated by the arrival of Si and Fe from airborne Etna volcano ash during March-April 2012. Volcanic eruptions have the potential to cause regional or even global-scale nutrient (mainly Fe)-fertilization (Olgun et al., 2013; Browning et al., 2015; Weinbauer et al., 2017).

Mount Etna experienced high paroxysmal volcanic activity from January 2011 to April 2012 (Scollo et al., 2014; Giacomoni et al., 2018). In February 2012, the air masses that arrived at Finokalia station from the west had passed over south Italy/Sicily, thus collecting pollutants emitted from Etna (**Supplementary Figure S7**). Similarly, during March air masses remained of west sector and were influenced by volcanic activities in the Etna region together with marine emissions from the Mediterranean Sea, but also from land emissions over Africa (first part of the month) and Central Europe and long-range transport (second part of the month) (**Supplementary Figure S8**). Therefore, atmospheric deposition during this month integrates all potential sources surrounding the East Mediterranean, including Etna's emissions, except the East sector source (sources in the Middle-East).

In spring 2012 there was the highest export efficiency of the study period (**Figure 3C**), indicating that there was a decoupling between primary producers and the grazing population, allowing a strong episodic export pulse to reach the deep Ierapetra Basin (highest PC1, PC2 and PC3 factor scores) (**Figure 9**). The results of this study highlights that POC fluxes during this reported extreme episodic event were enriched in natural and anthropogenic, marine- and land-derived, lipid biomarkers (as inferred from UCM fluxes and CPI_{NA} ratio values ~1) (**Figure 7**). In April 2012, the POC exported during this event shows the highest $\delta^{13}C$ values (−21.33‰) over the study period, suggesting a high contribution of POC derived from marine relatively to land-derived natural sources (Goericke and Fry, 1994; Harmelin-Vivien et al., 2008). It is particularly noteworthy that surface sediment samples collected in the deep Ierapetra Basin (i.e., BF1MC22, Ier01 and Red 11) showed similar $\delta^{13}C$ and TN/POC ratio as sinking particles from the episodic event of spring 2012 (**Figure 11B**), suggesting that pulses of sinking particles during extreme episodic events can have a major role in modulating the seafloor POC composition in the deep Ierapetra Basin.

During the same month, the highest fluxes of brassicasterol of the study period and the highest opal fluxes, indicate the enhanced sedimentation of relatively fresh diatoms reaching bathypelagic depths. Although dinosterol, C_{30}diol and alkenones fluxes also had their maxima in April 2012, the high mole ratios of opal/$CaCO_3$ and POC/$CaCO_3$ in the sinking particles (**Table 2**) suggest that the upwelling event preferentially exported siliceous plankton relative to calcareous plankton (although the calcareous plankton benefitted too). This conclusion agrees with the phytoplankton community dynamics of the Rhodes' Gyre, where high abundances of large diatoms have been found under extreme meteorological conditions resulting in nutrient enrichment (Siokou-Frangou et al., 1999; Siokou-Frangou et al., 2010). In upwelling regions, the phytoplankton communities are often dominated by large diatoms (Malviya et al., 2016).

Supportive to the above, is that the settling particles collected during this period were embedded in a mucilaginous matrix with a high abundance of ash spherules and highly diverse, well-preserved, medium-sized (5–300 μm) long-chain- forming

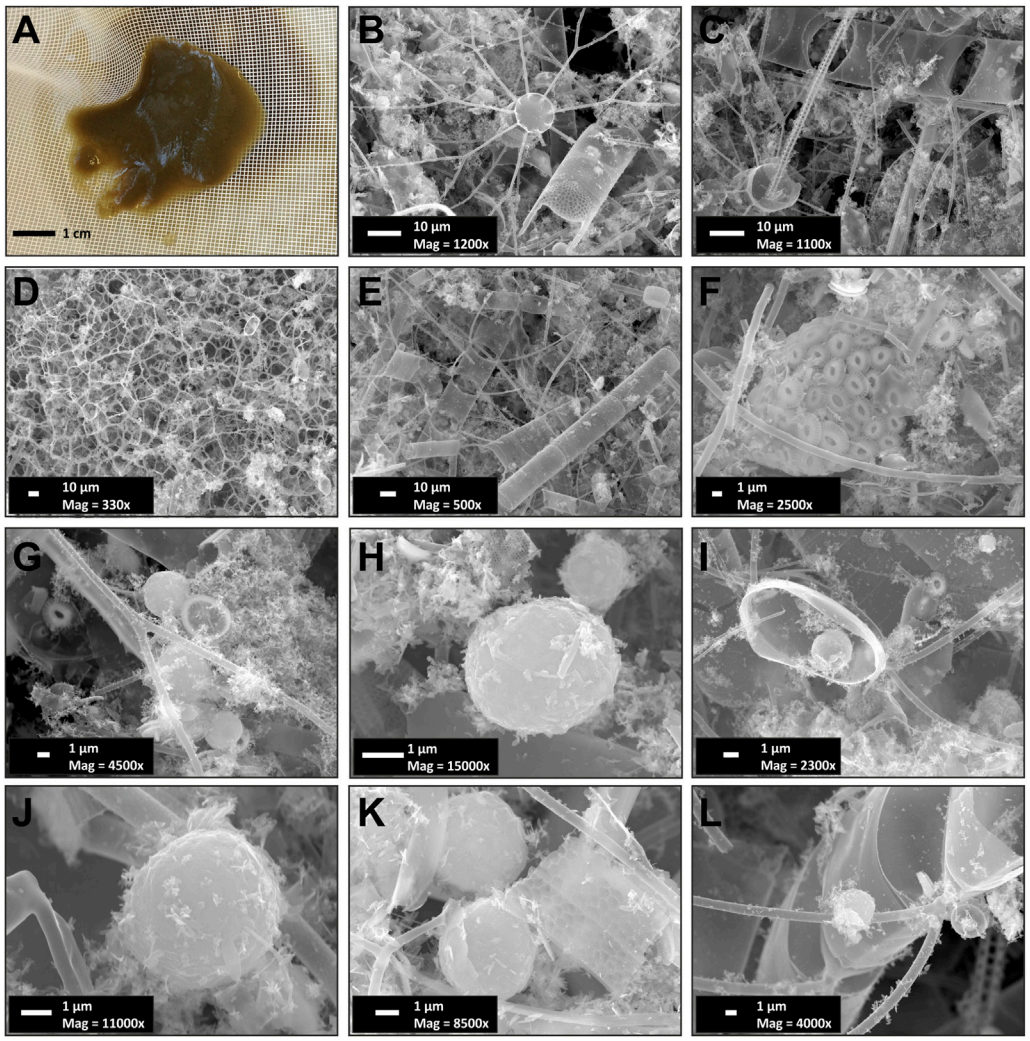

FIGURE 12 | Composite of **(A)** sample lab processing photo and **(B-I)** scanning electron microscopy (SEM) micrographs of sinking particles collected in April 2012 (REDII-11) in the deep Ierapetra Basin. Images reveal the abundant presence of well-preserved diatoms (**B–E**, e.g., *Chaetoceros* spp. and *Thalassioria* spp.), and coccolithophores **(F)** as well as ash microspherules **(G–L)**. Mag: Magnification (see more details in Pedrosa-Pàmies et al., 2016).

centric diatoms such as *Chaetoceros* spp., *Thalassiosira* spp., and *Rhizosolenia* spp (**Figure 12**). This mucilaginous matrix could be attributed to the production of transparent exopolymer particles (TEP) from diatom exudates rich in acidic polysaccharides (Gogou and Repeta, 2010). TEP increase the collision rates between particles, mostly in the form of large, rapidly sinking aggregates, playing an important role in carbon cycling in pelagic/oceanic ecosystems in general (Passow, 2002b and references therein) and the oligotrophic EMS in particular (Bar-Zeev et al., 2011; Parinos et al., 2017; Ortega-Retuerta et al., 2019). Diatoms have been reported to produce large amounts of TEP precursors or TEP directly via sloughing and lysis of senescent colonies under exponentially growing conditions (Passow, 2002a), such as in April of 2012, which are likely to have enhanced post-bloom flocculation and massive sinking of particulate matter in the study area. The ash particles, which typically have a density of twice that of seawater, could have also played an important role for rapid settling of biogenic particles (Passow and De La Rocha, 2006).

Furthermore, the exceptional diatom-dominated bloom fueled higher trophic levels, which further enhanced POC export. The covariation of the heterotrophic activity with the labile phytodetritus flux, producing a pulse of zooplankton-derived POC to the deep waters, is evidenced by the increase of cholesterol fluxes in April and May 2012 (3.20 and 7.23 $\mu g\ m^{-2}\ d^{-1}$, respectively) (**Figure 6A**). In the oligotrophic Sargasso Sea (N Atlantic), a similar ecosystem response has been observed as a result of the impact of mesoscale ocean features (fronts and eddies) (Conte et al., 1998, 2003) and extreme weather events (Pedrosa-Pàmies et al., 2019), locally enhancing vertical advection and stimulating production and sinking export of labile marine carbon to the deep ocean (e.g., increased cholesterol fluxes of 4.95 $\mu g\ m^{-2}\ d^{-1}$ at 3,200 m depth after a hurricane passage).

Sinking particles during this event were relatively depleted in land-derived natural POC and anthropogenic compounds due to dilution from biogenic material. Nevertheless, in April 2012, the highest fluxes of ∑TerNA and ∑TerN-OH, a decrease of CPI_{NA} and an increase in UCM fluxes (**Figure 7**) indicate that there was an efficient transfer of anthropogenic and higher plant wax-derived hydrocarbons to the deep Ierapetra Basin.

CONCLUSION

In the Ierapetra basin, particle flux data have been examined in combination with atmospheric and oceanographic parameters and main mass flux components (lithogenic, calcium carbonate, opal and organic matter), stable isotopes of POC ($\delta^{13}C$) and source-specific lipid biomarkers, aiming to improve the current understanding of the dynamics of particle fluxes and the impact of external forcing on the deep Eastern Mediterranean Sea. This study highlights that both seasonal and episodic pulses are crucial for POC export to the deep Ierapetra Basin, and likely most of the deep EMS. Overall, summer particle export to the deep EMS fuels more efficient carbon sequestration than during the other seasons. Our results also show that the combination of extreme weather events and aerosol deposition can trigger an influx of marine organic matter to the deep EMS. This influx is a critical factor determining food supply for deep ocean ecosystems, but also induces an increased influx of anthropogenic organic carbon to the deep EMS. Therefore, this study underscores the importance of accounting both seasonal and episodic pulses of POC to the deep sea when modeling the sequestration of natural and anthropogenic POC, and for a better understanding of the global carbon cycle. Finally, the comparison of biogeochemical parameters of the sinking particles flux data with previously reported surface sediments from the deep-sea in the study area revealed an isotopic discrimination, as also as a preferential degradation of labile organic matter during deposition and burial, along with higher preservation of land-derived POC in the underlying sediments. This line of research provides key knowledge to better understand the export, fate and preservation *vs.* degradation of marine and land-derived organic carbon and for modeling the organic carbon burial rates in the Mediterranean Sea.

DATA AVAILABILITY STATEMENT

The original contributions presented in the study are included in the article/**Supplementary Material**, further inquiries can be directed to the corresponding author.

AUTHOR CONTRIBUTIONS

RP-P performed the sample analyses and data processing and lead the interpretation of the results and wrote the manuscript. CP aided in interpreting the results and worked on the manuscript. RP-P and AS-V participated in the sample collection. AS-V and AC were involved in the design of the study, and supervised RP-P work during the early stage of the study. AG and CP supervised RP-P during the lipid biomarkers analyses at the Organic Chemistry Laboratory at HCMR. NL and MC were the REDECO's project co-ordinator and the lead of the University of Barcelona research team, respectively. DV contributed to the interpretation of the oceanographic settings of the study area. NM and MK contributed with Finokalia atmospheric observatory data and atmospheric data interpretation. All authors provided feedback on the manuscript.

FUNDING

This research was supported by the REDECO (CTM2008-04973-E/MAR) and PERSEUS (GA 287600) projects. We further acknowledge support by the projects PANACEA—'PANhellenic infrastructure for Atmospheric Composition and climatE chAnge' (MIS 5021516) and ENIRISST—'Intelligent Research Infrastructure for Shipping, Supply Chain, Transport and Logistics' (MIS 5027930), which are implemented under the Action "Reinforcement of the Research and Innovation Infrastructure," funded by the Operational Program "Competitiveness, Entrepreneurship and Innovation" (NSRF 2014-2020) and co-financed by Greece and EU; and by the Action "National Network on Climate Change and its Impacts - Climpact" which is implemented under the sub-project 3 of the project "Infrastructure of national research networks in the fields of Precision Medicine, Quantum Technology and Climate Change," funded by the Public Investment Program of Greece, General Secretary of Research and Technology/Ministry of Development and Investments." Researchers from GRC Geociències Marines benefited from a Grups de Recerca Consolidats grant (2017 SGR 315) by Generalitat de Catalunya autonomous government.

ACKNOWLEDGMENTS

We sincerely thank the officers, crews of *R/V* Aegaeo (HCMR), C. Pasqual, O. Veres, and P. Lopez- Fernandez for their precious help during cruises, and A. Rumín-Caparrós for his valuable inputs and comments on the currentmeter data. Additionally, we sincerely thank Giorgos Kouvarakis for his contribution with the Finokalia station data and the back-trajectory calculations. The authors gratefully acknowledge the NOAA Air Resources Laboratory (ARL) for the provision of the HYSPLIT transport and dispersion model and/or READY website (https://www.ready.noaa.gov) used in this publication. Elemental analyses were performed at the Scientific and Technological Centers of the University of Barcelona. We would like to thank the Editor Timothy Ferdelman and the reviewers Gerard Versteegh and Facundo Matias Barrera for their very constructive comments that helped significantly to improve the quality of this paper.

SUPPLEMENTARY MATERIAL

The Supplementary Material for this article can be found online at: https://www.frontiersin.org/articles/10.3389/feart.2021.591948/full#supplementary-material.

REFERENCES

Aboul-Kassim, T. A. T., and Simoneit, B. R. T. (1995). Petroleum hydrocarbon fingerprinting and sediment transport assessed by molecular biomarker and multivariate statistical analyses in the Eastern Harbour of Alexandria, Egypt. *Mar. Pollut. Bull.* 30, 63–73. doi:10.1016/0025-326X(94)00102-F

Agusti, S., González-Gordillo, J. I., Vaqué, D., Estrada, M., Cerezo, M. I., Salazar, G., et al. (2015). Ubiquitous healthy diatoms in the deep sea confirm deep carbon injection by the biological pump. *Nat. Commun.* 6, 7608. doi:10.1038/ncomms8608

Altabet, M. A. (1996). "Nitrogen and carbon isotopic traces of the source and transformation of particles in the deep sea," in *Particle flux in the ocean*. Editors V. Ttekkot, P. Schufer H. S., and P. J. Depetris (Hoboken: John Wiley & Sons Ltd), 155–184.

Altabet, M. A. (2001). Nitrogen isotopic evidence for micronutrient control of fractional NO_3^- utilization in the equatorial Pacific. *Limnol. Oceanogr.* 46, 368–380. doi:10.4319/lo.2001.46.2.0368

Amitai, Y., Lehahn, Y., Lazar, A., and Heifetz, E. (2010). Surface circulation of the eastern Mediterranean Levantine basin: insights from analyzing 14 years of satellite altimetry data. *J. Geophys. Res.* 115, C10058. doi:10.1029/2010JC006147

Antoine, D., Morel, A., and André, J.-M. (1995). Algal pigment distribution and primary production in the eastern Mediterranean as derived from coastal zone color scanner observations. *J. Geophys. Res.* 100, 16193–16209. doi:10.1029/95JC00466

Archer, D., Winguth, A., Lea, D., and Mahowald, N. (2000). What caused the glacial/interglacial atmospheric pCO_2 cycles?. *Rev. Geophys.* 38, 159–189. doi:10.1029/1999RG000066

Armstrong, R. A., Lee, C., Hedges, J. I., Honjo, S., and Wakeham, S. G. (2002). A new, mechanistic model for organic carbon fluxes in the ocean based on the quantitative association of POC with ballast minerals. *Deep Sea Res. Part II Top. Stud. Oceanogr.* 49, 219–236. doi:10.1016/S0967-0645(01)00101-1

Azov, Y (1991). Eastern Mediterranean—a marine desert?. *Mar. Pollut. Bull.* 23, 225–232.

Bach, L. T., Boxhammer, T., Larsen, A., Hildebrandt, N., Schulz, K. G., and Riebesell, U. (2016). Influence of plankton community structure on the sinking velocity of marine aggregates. *Global Biogeochem. Cycles* 30, 1145–1165. doi:10.1002/2016GB005372

Bar-Zeev, E., Berman, T., Rahav, E., Dishon, G., Herut, B., and Berman-Frank, I. (2011). Transparent exopolymer particle (TEP) dynamics in the Eastern Mediterranean Sea. *Mar. Ecol. Prog. Ser.* 431, 107–118. doi:10.3354/meps09110

Basu, S., Mackey, K. R. M., Basu, S., and Mackey, K. R. M. (2018). Phytoplankton as Key mediators of the biological carbon pump: their responses to a changing climate. *Sustainability* 10, 869. doi:10.3390/su10030869

Behrenfeld, M. J., and Falkowski, P. G. (1997). Photosynthetic rates derived from satellite-based chlorophyll concentration. *Limnol. Oceanogr.* 42, 1–20. doi:10.4319/lo.1997.42.1.0001

Belcher, A., Iversen, M., Giering, S., Riou, V., Henson, S. A., Berline, L., et al. (2016). Depth-resolved particle-associated microbial respiration in the northeast Atlantic. *Biogeosciences* 13, 4927–4943. doi:10.5194/bg-13-4927-2016

Bensi, M., Cardin, V., Rubino, A., Notarstefano, G., and Poulain, P. M. (2013). Effects of winter convection on the deep layer of the Southern Adriatic Sea in 2012. *J. Geophys. Res. Ocean.* 118, 6064–6075. doi:10.1002/2013JC009432

Blair, N. E., and Aller, R. C. (2012). The fate of terrestrial organic carbon in the marine environment. *Ann. Rev. Mar. Sci.* 4, 401–423. doi:10.1146/annurev-marine-120709-142717

Bosc, E., Bricaud, A., and Antoine, D. (2004). Seasonal and interannual variability in algal biomass and primary production in the Mediterranean Sea, as derived from 4 years of SeaWiFS observations. *Global Biogeochem. Cycles* 18, GB1005. doi:10.1029/2003GB002034

Bosc, E. (2004). Seasonal and interannual variability in algal biomass and primary production in the Mediterranean Sea, as derived from 4 years of SeaWiFS observations. *Global Biogeochem. Cycles* 18, GB1005. doi:10.1029/2003GB002034

Boyd, P. W., and Trull, T. W. (2007). Understanding the export of biogenic particles in oceanic waters: is there consensus?. *Prog. Oceanogr.* 72, 276–312. doi:10.1016/j.pocean.2006.10.007

Bressac, M., Guieu, C., Doxaran, D., Bourrin, F., Desboeufs, K., Leblond, N., et al. (2014). Quantification of the lithogenic carbon pump following a simulated dust-deposition event in large mesocosms. *Biogeosciences* 11, 1007–1020. doi:10.5194/bg-11-1007-2014

Browning, T. J., Stone, K., Bouman, H. A., Mather, T. A., Pyle, D. M., Moore, C. M., et al. (2015). Volcanic ash supply to the surface ocean-remote sensing of biological responses and their wider biogeochemical significance. *Front. Mar. Sci.* 2, 14. doi:10.3389/fmars.2015.00014

Buchan, A., LeCleir, G. R., Gulvik, C. A., and González, J. M. (2014). Master recyclers: features and functions of bacteria associated with phytoplankton blooms. *Nat. Rev. Microbiol.* 12, 686–698. doi:10.1038/nrmicro3326

Buesseler, K. O., and Boyd, P. W. (2009). Shedding light on processes that control particle export and flux attenuation in the twilight zone of the open ocean. *Limnol. Oceanogr.* 54, 1210–1232. doi:10.4319/lo.2009.54.4.1210

Buesseler, K. O. (1998). The decoupling of production and particulate export in the surface ocean. *Global Biogeochem. Cycles* 12, 297–310. doi:10.1029/97GB03366

Burdige, D. J. (2007). Preservation of organic matter in marine sediments: controls, mechanisms, and an imbalance in sediment organic carbon budgets?. *Chem. Rev.* 107, 467–485. doi:10.1021/cr050347q

Burkhardt, S., Riebesell, U., and Zondervan, I. (1999). Stable carbon isotope fractionation by marine phytoplankton in response to daylength, growth rate, and CO_2 availability. *Mar. Ecol. Prog. Ser.* 184, 31–41. doi:10.3354/meps184031

Cavan, E. L., Le Moigne, F. A. C., Poulton, A. J., Tarling, G. A., Ward, P., Daniels, C. J., et al. (2015). Attenuation of particulate organic carbon flux in the Scotia Sea, Southern Ocean, is controlled by zooplankton fecal pellets. *Geophys. Res. Lett.* 42, 821–830. doi:10.1002/2014GL062744

Christodoulaki, S., Petihakis, G., Kanakidou, M., Mihalopoulos, N., Tsiaras, K., and Triantafyllou, G. (2013). Atmospheric deposition in the Eastern Mediterranean. A driving force for ecosystem dynamics. *J. Mar. Syst.* 109–110, 78–93. doi:10.1016/j.jmarsys.2012.07.007

Christodoulou, S., Marty, J.-C., Miquel, J.-C., Volkman, J. K., and Rontani, J.-F. (2009). Use of lipids and their degradation products as biomarkers for carbon cycling in the northwestern Mediterranean Sea. *Mar. Chem.* 113, 25–40. doi:10.1016/j.marchem.2008.11.003

Close, H. G., Wakeham, S. G., and Pearson, A. (2014). Lipid and ^{13}C signatures of submicron and suspended particulate organic matter in the Eastern Tropical North Pacific: implications for the contribution of Bacteria. *Deep. Res. Part I* 85, 15–34. doi:10.1016/j.dsr.2013.11.005

Collister, J. W., Rieley, G., Stern, B., Eglinton, G., and Fry, B. (1994). Compound-specific δ13C analyses of leaf lipids from plants with differing carbon dioxide metabolisms. *Org. Geochem.* 21, 619–627. doi:10.1016/0146-6380(94)90008-6

Conte, M. H., Dickey, T. D., Weber, J. C., Johnson, R. J., and Knap, A. H. (2003). Transient physical forcing of pulsed export of bioreactive material to the deep Sargasso Sea. *Deep-Sea Res. Part I Oceanogr. Res. Pap.* 50, 1157–1187. doi:10.1016/S0967-0637(03)00141-9

Conte, M. H., Weber, J. C., and Ralph, N. (1998). Episodic particle flux in the deep Sargasso Sea. *Deep-Sea Res. Part I Oceanogr. Res. Pap.* 45, 1819–1841. doi:10.1016/S0967-0637(98)00046-6

Dagg, M. J., Jackson, G. A., and Checkley, D. M. (2014). The distribution and vertical flux of fecal pellets from large zooplankton in Monterey bay and coastal California. *Deep. Res. Part I Oceanogr. Res. Pap.* 94, 72–86. doi:10.1016/j.dsr.2014.09.001

Dauwe, B., and Middelburg, J. J. (1998). Amino acids and hexosamines as indicators of organic matter degradation state in North Sea sediments. *Limnol. Oceanogr.* 43, 782–798. doi:10.4319/lo.1998.43.5.0782

De Bar, M. W., Ullgren, J. E., Thunnell, R. C., Wakeham, S. G., Brummer, G. J. A., Stuut, J. B. W., et al. (2019). Long-chain diols in settling particles in tropical oceans: insights into sources, seasonality and proxies. *Biogeosciences* 16, 1705–1727. doi:10.5194/bg-16-1705-2019

De La Rocha, C. L., and Passow, U. (2007). Factors influencing the sinking of POC and the efficiency of the biological carbon pump. *Deep. Res. Part II Top. Stud. Oceanogr.* 54, 639–658. doi:10.1016/j.dsr2.2007.01.004

Deuser, W. G., Degens, E. T., and Guillard, R. R. L. (1968). Carbon isotope relationships between plankton and sea water. *Geochem. Cosmochim. Acta* 32, 657–660. doi:10.1016/0016-7037(68)90055-0

DeVries, T., Primeau, F., and Deutsch, C. (2012). The sequestration efficiency of the biological pump. *Geophys. Res. Lett.* 39, 114. doi:10.1029/2012GL051963

Deyme, R., Bouloubassi, I., Taphanel-Valt, M. H., Miquel, J. C., Lorre, A., Marty, J. C., et al. (2011). Vertical fluxes of aromatic and aliphatic hydrocarbons in the Northwestern Mediterranean Sea. *Environ. Pollut.* 159, 3681–3691. doi:10.1016/j.envpol.2011.07.017

Durrieu de Madron, X., Houpert, L., Puig, P., Sanchez-Vidal, A., Testor, P., Bosse, A., et al. (2013). Interaction of dense shelf water cascading and open-sea convection in the northwestern Mediterranean during winter 2012. *Geophys. Res. Lett.* 40, 1379–1385. doi:10.1002/grl.50331

Eglinton, G., and Hamilton, R. J. (1967). Leaf epicuticular waxes. *Science* 156, 1322–1335. doi:10.1126/science.156.3780.1322

Fabres, J., Calafat, A., Sanchez-Vidal, A., Canals, M., and Heussner, S. (2002). Composition and spatio-temporal variability of particle fluxes in the western Alboran Gyre, Mediterranean Sea. *J. Mar. Syst.* 33, 431–456. doi:10.1016/S0924-7963(02)00070-2

Farrington, J., and Takada, H. (2014). Persistent organic pollutants (POPs), polycyclic aromatic hydrocarbons (PAHs), and plastics: examples of the status, trend, and cycling of organic chemicals of environmental concern in the ocean. *Oceanography* 27, 196–213. doi:10.5670/oceanog.2014.23

Finkel, Z. V, Beardall, J., Flynn, K. J., Quigg, A., Rees, T. A. V, and Raven, J. A. (2010). Phytoplankton in a changing world: cell size and elemental stoichiometry. *J. Plankton Res.* 32, 119–137. doi:10.1093/plankt/fbp098

Fischer, G., and Wefer, G. (1996). "Long-term observation of particle fluxes in the eastern Atlantic: seasonality, changes of flux with depth and comparison with the sediment record," in *The South Atlantic: present and past circulation*. Editors G. Wefer, W. H. Berger, G. Siedler, and G. Webb (Berlin.: Springer-Verlag), 325–344.

Francois, R., Honjo, S., Krishfield, R., and Manganini, S. (2002). Factors controlling the flux of organic carbon to the bathypelagic zone of the ocean. *Global Biogeochem. Cycles* 16, 34–41. doi:10.1029/2001GB001722

Gelin, F., Boogers, I., Noordeloos, A. A. M., Damste, J. S. S., Riegman, R., and De Leeuw, J. W. (1997). Resistant biomacromolecules in marine microalgae of the classes Eustigmatophyceae and Chlorophyceae: geochemical implications. *Org. Geochem.* 26, 659–675. doi:10.1016/S0146-6380(97)00035-1

Giacomoni, P. P., Coltorti, M., Mollo, S., Ferlito, C., Braiato, M., and Scarlato, P. (2018). The 2011–2012 paroxysmal eruptions at Mt. Etna volcano: insights on the vertically zoned plumbing system. *J. Volcanol. Geoth. Res.* 349, 370–391. doi:10.1016/j.jvolgeores.2017.11.023

Goericke, R., and Fry, B. (1994). Variations of marine plankton δ13C with latitude, temperature, and dissolved CO_2 in the world ocean. *Global Biogeochem. Cycles* 8, 85–90. doi:10.1029/93GB03272

Gogou, A., Apostolaki, M., and Stephanou, E. G. (1998). Determination of organic molecular markers in marine aerosols and sediments: one-step flash chromatography compound class fractionation and capillary gas chromatographic analysis. *J. Chromatogr. A* 799, 215–231. doi:10.1016/S0021-9673(97)01106-0

Gogou, A., Bouloubassi, I., Lykousis, V., Arnaboldi, M., Gaitani, P., and Meyers, P. A. (2007). Organic geochemical evidence of late glacial–holocene climate instability in the north Aegean sea. *Palaeogeogr. Palaeoclimatol. Palaeoecol.* 256, 1–20. doi:10.1016/j.palaeo.2007.08.002

Gogou, A., Bouloubassi, I., and Stephanou, E. G. (2000). Marine organic geochemistry of the Eastern Mediterranean: 1. Aliphatic and polyaromatic hydrocarbons in Cretan Sea surficial sediments. *Mar. Chem.* 68, 265–282. doi:10.1016/S0304-4203(99)00082-1

Gogou, A., and Repeta, D. J. (2010). Particulate-dissolved transformations as a sink for semi-labile dissolved organic matter: chemical characterization of high molecular weight dissolved and surface-active organic matter in seawater and in diatom cultures. *Mar. Chem.* 121, 215–223. doi:10.1016/j.marchem.2010.05.001

Gogou, A., Sanchez-Vidal, A., Durrieu de Madron, X., Stavrakakis, S., Calafat, A., Stabholz, M., et al. (2014). Carbon flux to the deep in three open sites of the Southern European Seas (SES). *J. Mar. Syst.* 129, 224–233. doi:10.1016/j.jmarsys.2013.05.013

Gogou, A., and Stephanou, E. G. (2004). Marine organic geochemistry of the Eastern Mediterranean: 2. Polar biomarkers in Cretan Sea surficial sediments. *Mar. Chem.* 85, 1–25. doi:10.1016/j.marchem.2003.08.005

Goñi, M. A., and Hedges, J. I. (1995). Sources and reactivities of marine-derived organic matter in coastal sediments as determined by alkaline CuO oxidation. *Geochem. Cosmochim. Acta* 59, 2965–2981. doi:10.1016/0016-7037(95)00188-3

Goñi, M. A., Monacci, N., Gisewhite, R., Ogston, A., Crockett, J., and Nittrouer, C. (2006). Distribution and sources of particulate organic matter in the water column and sediments of the Fly River Delta, Gulf of Papua (Papua New Guinea). *Estuar. Coast Shelf Sci.* 69, 225–245. doi:10.1016/j.ecss.2006.04.012

Goñi, M. A., Teixeira, M. J., and Perkey, D. W. (2003). Sources and distribution of organic matter in a river-dominated estuary (Winyah Bay, SC, USA). *Estuar. Coast Shelf Sci.* 57, 1023–1048. doi:10.1016/S0272-7714(03)00008-8

Goñi, M. A., Yunker, M. B., Macdonald, R. W., and Eglinton, T. I. (2000). Distribution and sources of organic biomarkers in arctic sediments from the Mackenzie River and Beaufort Shelf. *Mar. Chem.* 71, 23–51. doi:10.1016/S0304-4203(00)00037-2

Gotsis-Skretas, O., Pagou, K., Moraitou-Apostolopoulou, M., and Ignatiades, L. (1999). Seasonal horizontal and vertical variability in primary production and standing stocks of phytoplankton and zooplankton in the Cretan Sea and the Straits of the Cretan Arc (March 1994-January 1995). *Prog. Oceanogr.* 44, 625–649. doi:10.1016/S0079-6611(99)00048-8

Gough, M. A., and Rowland, S. J. (1990). Characterization of unresolved complex mixtures of hydrocarbons in petroleum. *Nature* 344, 648–650. doi:10.1038/344648a0

Goutx, M., Momziko, A., Striby, L., Andersen, V., Marty, J. C., and Vescovali, I. (2000). High-frequency fluxes of labile compounds in the central Ligurian Sea. *Northwestern Mediterranean* 47, 3–4.

Goutx, M., Wakeham, S. G., Lee, C., Duflos, M., Guigue, C., Liu, Z., et al. (2007). Composition and degradation of marine particles with different settling velocities in the northwestern Mediterranean Sea. *Limnol. Oceanogr.* 52, 1645–1664. doi:10.4319/lo.2007.52.4.1645

Grice, K., Klein Breteler, W., Schouten, S., Grossi, V., de Leeuw, J. W., and Sinninghe-Damsté, J. S. (1998). Effects of zooplankton herbivory on biomarker proxy records. *Paleoceanography* 13, 686–693. doi:10.1029/98PA01871

Guidi, L., Stemmann, L., Jackson, G. A., Ibanez, F., Claustre, H., Legendre, L., et al. (2009). Effects of phytoplankton community on production, size, and export of large aggregates: a world-ocean analysis. *Limnol. Oceanogr.* 54, 1951–1963. doi:10.4319/lo.2009.54.6.1951

Harmelin-Vivien, M., Loizeau, V., Mellon, C., and Beker, B. (2008). Comparison of C and N stable isotope ratios between surface particulate organic matter and microphytoplankton in the Gulf of Lions (NW Mediterranean). *Continent. Shelf Res.* 28, 1911–1919. doi:10.1016/j.csr.2008.03.002

Harvey, H. R., O'Hara, S. C. M., Eglinton, G., and Corner, E. D. S. (1989). The comparative fate of dinosterol and cholesterol in copepod feeding: implications for a conservative molecular biomarker in the marine water column. *Org. Geochem.* 14, 635–641. doi:10.1016/0146-6380(89)90042-9

Hatzianestis, I., Parinos, C., Bouloubassi, I., and Gogou, A. (2020). Polycyclic aromatic hydrocarbons in surface sediments of the Aegean Sea (Eastern Mediterranean Sea). *Mar. Pollut. Bull.* 153, 111030. doi:10.1016/j.marpolbul.2020.111030

Hays, M. D. (2004). Nature of unresolved complex mixture in size-distributed emissions from residential wood combustion as measured by thermal desorption-gas chromatography-mass spectrometry. *J. Geophys. Res.* 109, D16S04. doi:10.1029/2003JD004051

Hedges, J. I., Keil, R. G., and Benner, R. (1997). What happens to terrestrial organic matter in the ocean?. *Org. Geochem.* 27, 195–212. doi:10.1016/S0146-6380(97)00066-1

Henley, S. F., Annett, A. L., Ganeshram, R. S., Carson, D. S., Weston, K., Crosta, X., et al. (2012). Factors influencing the stable carbon isotopic composition of suspended and sinking organic matter in the coastal Antarctic sea ice environment. *Biogeosciences* 9, 1137–1157. doi:10.5194/bg-9-1137-2012

Henson, S. A., Sanders, R., and Madsen, E. (2012). Global patterns in efficiency of particulate organic carbon export and transfer to the deep ocean. *Global Biogeochem. Cycles* 26, 33. doi:10.1029/2011GB004099

Henson, S. A., Yool, A., and Sanders, R. (2015). Variability in efficiency of particulate organic carbon export: a model study. *Global Biogeochem. Cycles* 29, 33–45. doi:10.1002/2014GB004965

Henson, S., Le Moigne, F., and Giering, S. (2019). Drivers of carbon export efficiency in the global ocean. *Global Biogeochem. Cycles* 33, 891–903. doi:10.1029/2018GB006158

Herndl, G. J., Agogué, H., Baltar, F., Reinthaler, T., Sintes, E., and Varela, M. (2008). Regulation of aquatic microbial processes: the 'microbial loop' of the sunlit

surface waters and the dark ocean dissected. *Aquat. Microb. Ecol.* 53, 59–68. doi:10.3354/ame01225

Herndl, G. J., and Reinthaler, T. (2013). Microbial control of the dark end of the biological pump. *Nat. Geosci.* 6, 718–724. doi:10.1038/ngeo1921

Heussner, S., Calafat, A., and Palanques, A. (1996). Quantitative and qualitative features of particle fluxes in *the north-balearic basin. EUROMARGE-NB final report*, Editors M. Canals, J. L. Casamor, I. Cacho, A. M. Calafat, and A. Monaco, (MAST II Program), 41–66.

Heussner, S., Ratti, C., and Carbonne, J. (1990). The PPS 3 time-series sediment trap and the trap sample processing techniques used during the ECOMARGE experiment. *Continent. Shelf Res.* 10, 943–958. doi:10.1016/0278-4343(90)90069-X

Hoefs, M. J. L., Rijpstra, W. I. C., and Damsté, J. S. S. (2002). The influence of oxic degradation on the sedimentary biomarker record I: evidence from Madeira Abyssal Plain turbidites. *Geochem. Cosmochim. Acta* 66, 2719–2735. doi:10.1016/S0016-7037(02)00864-5

Honjo, S., Manganini, S. J., Krishfield, R. a., and Francois, R. (2008). Particulate organic carbon fluxes to the ocean interior and factors controlling the biological pump: a synthesis of global sediment trap programs since 1983. *Prog. Oceanogr.* 76, 217–285. doi:10.1016/j.pocean.2007.11.003

Hu, J., Peng, P., Jia, G., Mai, B., and Zhang, G. (2006). Distribution and sources of organic carbon, nitrogen and their isotopes in sediments of the subtropical Pearl River estuary and adjacent shelf, Southern China. *Mar. Chem.* 98, 274–285. doi:10.1016/j.marchem.2005.03.008

Huertas, I. E., Ríos, A. F., García-Lafuente, J., Navarro, G., Makaoui, A., Sánchez-Román, A., et al. (2012). Atlantic forcing of the Mediterranean oligotrophy. *Global Biogeochem.* 26, 127. doi:10.1029/2011GB004167

Ignatiades, L., Gotsis-Skretas, O., Pagou, K., and Krasakopoulou, E. (2009). Diversification of phytoplankton community structure and related parameters along a large-scale longitudinal east–west transect of the Mediterranean Sea. *J. Plankton Res.* 31, 411–428. doi:10.1093/plankt/fbn124

Ioannou, A., Stegner, A., Le Vu, B., Taupier-Letage, I., and Speich, S. (2017). Dynamical evolution of ontense Ierapetra eddies on a 22 year long period. *J. Geophys. Res. Ocean.* 122, 9276–9298. doi:10.1002/2017JC013158

Israelevich, P., Ganor, E., Alpert, P., Kishcha, P., and Stupp, A. (2012). Predominant transport paths of saharan dust over the Mediterranean Sea to Europe. *J. Geophys. Res. Atmos.* 117, 33. doi:10.1029/2011JD016482

Janeković, I., Mihanović, H., Vilibić, I., and Tudor, M. (2014). Extreme cooling and dense water formation estimates in open and coastal regions of the Adriatic Sea during the winter of 2012. *J. Geophys. Res. Ocean.* 119, 3200–3218. doi:10.1002/2014JC009865

Jickells, T. D., An, Z. S., Andersen, K. K., Baker, A. R., Bergametti, G., Brooks, N., et al. (2005). Global iron connections between desert dust, ocean biogeochemistry, and climate. *Science* 308, 67–71. doi:10.1126/science.1105959

Kamatani, A., and Oku, O. (2000). Measuring biogenic silica in marine sediments. *Mar. Chem.* 68, 219–229. doi:10.1016/S0304-4203(99)00079-1

Kanakidou, M., Duce, R. A., Prospero, J. M., Baker, A. R., Benitez-Nelson, C., Dentener, F. J., et al. (2012). Atmospheric fluxes of organic N and P to the global ocean. *Global Biogeochem. Cycles* 26, 67. doi:10.1029/2011GB004277

Kanakidou, M., Mihalopoulos, N., Kindap, T., Im, U., Vrekoussis, M., Gerasopoulos, E., et al. (2011). Megacities as hot spots of air pollution in the East Mediterranean. *Atmos Environ* 45, 1223–1235. doi:10.1016/j.atmosenv.2010.11.048

Kanakidou, M., Myriokefalitakis, S., and Tsagkaraki, M. (2020). Atmospheric inputs of nutrients to the Mediterranean Sea. *Deep. Res. Part II Top. Stud. Oceanogr.* 171, 104606. doi:10.1016/j.dsr2.2019.06.014

Karageorgis, A. P., Kontoyiannis, H., Stavrakakis, S., Krasakopoulou, E., Gogou, A., Papadopoulos, A., et al. (2018). Particle dynamics and fluxes in canyons and open slopes of the southern Cretan margin (Eastern Mediterranean). *Prog. Oceanogr.* 169, 33–47. doi:10.1016/j.pocean.2017.12.009

Karl, D. M., Church, M. J., Dore, J. E., Letelier, R. M., and Mahaffey, C. (2012). Predictable and efficient carbon sequestration in the North Pacific Ocean supported by symbiotic nitrogen fixation. *Proc. Natl. Acad. Sci. U. S. A* 109, 1842–1849. doi:10.1073/pnas.1120312109

Kerhervé, P., Heussner, S., Charrière, B., Stavrakakis, S., Ferrand, J.-L., Monaco, A., et al. (1999). Biogeochemistry and dynamics of settling particle fluxes at the Antikythira strait (eastern mediterranean). *Prog. Oceanogr.* 44, 651–675. doi:10.1016/S0079-6611(99)00040-3

Kerhervé, P., Minagawa, M., Heussner, S., and Monaco, A. (2001). Stable isotopes ($^{13}C/^{12}C$ and $^{15}N/^{14}N$) in settling organic matter of the northwestern Mediterranean Sea: biogeochemical implications. *Oceanol. Acta* 24, 77–85. doi:10.1016/s0399-1784(00)01111-7

Klaas, C., and Archer, D. E. (2002). Association of sinking organic matter with various types of mineral ballast in the deep sea: implications for the rain ratio. *Global Biogeochem. Cycles* 16, 63–71. doi:10.1029/2001GB001765

Koppelmann, R., Weikert, H., Halsband-Lenk, C., and Jennerjahn, T. (2004). Mesozooplankton community respiration and its relation to particle flux in the oligotrophic eastern Mediterranean. *Global Biogeochem.* 18, 64. doi:10.1029/2003GB002121

Kouvarakis, G., Mihalopoulos, N., Tselepides, A., and Stavrakakis, S. (2001). On the importance of atmospheric inputs of inorganic nitrogen species on the productivity of the Eastern Mediterranean Sea. *Global Biogeochem. Cycles* 15, 805–817. doi:10.1029/2001GB001399

Krom, M. D., Herut, B., and Mantoura, R. F. C. (2004). Nutrient budget for the eastern mediterranean: implications for phosphorus limitation. *Limnol. Oceanogr.* 49, 1582–1592. doi:10.4319/lo.2004.49.5.1582

Krom, M. D., Kress, N., Brenner, S., and Gordon, L. I. (1991). Phosphorus limitation of primary productivity in the Eastern Mediterranean Sea. *Limnol. Oceanogr.* 36, 424–432. doi:10.4319/lo.1991.36.3.0424

Kubilay, N., Nickovic, S., Moulin, C., and Dulac, F. (2000). An illustration of the transport and deposition of mineral dust onto the eastern Mediterranean. *AtmosEnviron* 34, 1293–1303. doi:10.1016/S1352-2310(99)00179-X

Kwon, E. Y., Primeau, F., and Sarmiento, J. L. (2009). The impact of remineralization depth on the air–sea carbon balance. *Nat. Geosci.* 2, 630–635. doi:10.1038/ngeo612

Lampadariou, N., Tselepides, A., and Hatziyanni, E. (2009). Deep-sea meiofaunal and foraminiferal communities along a gradient of primary productivity in the Eastern Mediterranean Sea. *Sci. Mar.* 73, 337–345. doi:10.3989/scimar.2009.73n2337

Larnicol, G., Ayoub, N., and Le Traon, P. Y. (2002). Major changes in Mediterranean sea level variability from 7 years of TOPEX/Poseidon and ERS-1/2 data. *J. Mar. Syst.* 33–34, 63–89. doi:10.1016/S0924-7963(02)00053-2

Le Moigne, F. A. C., Henson, S. A., Cavan, E., Georges, C., Pabortsava, K., Achterberg, E. P., et al. (2016). What causes the inverse relationship between primary production and export efficiency in the Southern Ocean?. *Geophys. Res. Lett.* 43, 4457–4466. doi:10.1002/2016GL068480

Le Moigne, F. A. C., Poulton, A. J., Henson, S. A., Daniels, C. J., Fragoso, G. M., Mitchell, E., et al. (2015). Carbon export efficiency and phytoplankton community composition in the Atlantic sector of the Arctic Ocean. *J. Geophys. Res. Ocean.* 120, 3896–3912. doi:10.1002/2015JC010700

Lehmann, M. F., Bernasconi, S. M., Barbieri, A., and McKenzie, J. A. (2002). Preservation of organic matter and alteration of its carbon and nitrogen isotope composition during simulated and *in situ* early sedimentary diagenesis. *Geochem. Cosmochim. Acta* 66, 3573–3584. doi:10.1016/S0016-7037(02)00968-7

Lelieveld, J., Berresheim, H., Borrmann, S., Crutzen, P. J., Dentener, F. J., Fischer, H., et al. (2002). Global air pollution crossroads over the Mediterranean. *Science 84* 298, 794–799. doi:10.1126/science.1075457

Lewis, M. R., Hebert, D., Harrison, W. G., Platt, T., and Oakey, N. S. (1986). Vertical nitrate fluxes in the oligotrophic ocean. *Science* 234, 870–873. doi:10.1126/science.234.4778.870

Lima, I. D., Lam, P. J., and Doney, S. C. (2014). Dynamics of particulate organic carbon flux in a global ocean model. *Biogeosciences* 11, 1177–1198. doi:10.5194/bg-11-1177-2014

Lomas, M. W., Bates, N. R., Johnson, R. J., Knap, A. H., Steinberg, D. K., and Carlson, C. A. (2013). Two decades and counting: 24-years of sustained open ocean biogeochemical measurements in the Sargasso Sea. *Deep Sea Res. Part II Top. Stud. Oceanogr.* 93, 16–32. doi:10.1016/J.DSR2.2013.01.008

Longhurst, A., Sathyendranath, S., Platt, T., and Caverhill, C. (1995). An estimate of global primary production in the ocean from satellite radiometer data. *J. Plankton Res.* 17, 1245–1271. doi:10.1093/plankt/17.6.1245

Maiti, K., Charette, M. A., Buesseler, K. O., and Kahru, M. (2013). An inverse relationship between production and export efficiency in the Southern Ocean. *Geophys. Res. Lett.* 40, 1557–1561. doi:10.1002/grl.50219

Malinverno, E., Ziveri, P., and Corselli, C. (2003). Coccolithophorid distribution in the Ionian Sea and its relationship to eastern Mediterranean circulation during

late fall to early winter 1997. *J. Geophys. Res. C Oceans* 108, 33. doi:10.1029/2002jc001346

Malviya, S., Scalco, E., Audic, S., Vincent, F., Veluchamy, A., Poulain, J., et al. (2016). Insights into global diatom distribution and diversity in the world's ocean. *Proc. Natl. Acad. Sci. U. S. A* 113, E1516–E1525. doi:10.1073/pnas.1509523113

Marañón, E., Behrenfeld, M. J., González, N., Mouriño, B., and Zubkov, M. V. (2003). High variability of primary production in oligotrophic waters of the Atlantic Ocean: uncoupling from phytoplankton biomass and size structure. *Mar. Ecol. Prog. Ser.* 257, 1–11. doi:10.3354/meps257001

Marañón, E., Fernández, A., Mouriño-Carballido, B., MartÍnez-GarcÍa, S., Teira, E., Cermeño, P., et al. (2010). Degree of oligotrophy controls the response of microbial plankton to Saharan dust. *Limnol. Oceanogr.* 55, 2339–2352. doi:10.4319/lo.2010.55.6.2339

Marchand, D., Marty, J. C., Miquel, J. C., and Rontani, J. F. (2005). Lipids and their oxidation products as biomarkers for carbon cycling in the northwestern Mediterranean Sea: results from a sediment trap study. *Mar. Chem.* 95, 129–147. doi:10.1016/j.marchem.2004.09.001

Marlowe, I. T., Green, J. C., Neal, A. C., Brassell, S. C., Eglinton, G., and Course, P. A. (1984). Long chain (*n*-C37–C39) alkenones in the Prymnesiophyceae. Distribution of alkenones and other lipids and their taxonomic significance. *Br. Phycol. J.* 19, 203–216. doi:10.1080/00071618400650221

Marty, J. C., Goutx, M., Guigue, C., Leblond, N., Raimbault, P., Villefranche, D., et al. (2009). Short-term changes in particulate fluxes measured by drifting sediment traps during end summer oligotrophic regime in the NW Mediterranean Sea. *Biogeosciences* 6, 887–899. doi:10.5194/bg-6-887-2009

Masqué, P., Fabres, J., Canals, M., Sanchez-Cabeza, J. A., Sanchez-Vidal, A., Cacho, I., et al. (2003). Accumulation rates of major constituents of hemipelagic sediments in the deep Alboran Sea: a centennial perspective of sedimentary dynamics. *Mar. Geol.* 193, 207–233. doi:10.1016/S0025-3227(02)00593-5

Meador, T. B., Gogou, A., Spyres, G., Herndl, G. J., Krasakopoulou, E., Psarra, S., et al. (2010). Biogeochemical relationships between ultrafiltered dissolved organic matter and picoplankton activity in the Eastern Mediterranean Sea. *Deep Sea Res. Part II Top. Stud. Oceanogr.* 57, 1460–1477. doi:10.1016/j.dsr2.2010.02.015

Meglen, R. R. (1992). Examining large databases: a chemometric approach using principal component analysis. *Mar. Chem.* 39, 217–237.

Méjanelle, L., and Dachs, J. (2009). Short scale (6 h) temporal variation of sinking fluxes of planktonic and terrigeneous lipids at 200 m in the NW Mediterranean Sea. *Biogeosciences* 6, 3017–3034. doi:10.5194/bg-6-3017-2009

Meyers, P. A. (1997). Organic geochemical proxies of paleoceanographic, paleolimnologic, and paleoclimatic processes. *Org. Geochem.* 27, 213–250. doi:10.1016/S0146-6380(97)00049-1

Meyers, P. A. (1994). Preservation of elemental and isotopic source identification of sedimentary organic matter. *Chem. Geol.* 114, 289–302. doi:10.1016/0009-2541(94)90059-0

Mihalopoulos, N., Stephanou, E., Kanakidou, M., Pilitsidis, S., and Bousquet, P. (1997). Tropospheric aerosol ionic composition in the Eastern Mediterranean region. *Tellus Ser. B Chem. Phys. Meteorol.* 49, 314–326. doi:10.3402/tellusb.v49i3.15970

Mkhinini, N., Coimbra, A. L. S., Stegner, A., Arsouze, T., Taupier-Letage, I., and Béranger, K. (2014). Long-lived mesoscale eddies in the Eastern Mediterranean Sea: analysis of 20 years of AVISO geostrophic velocities. *J. Geophys. Res. Ocean.* 119, 8603–8626. doi:10.1002/2014JC010176

Mortlock, R. A., and Froelich, P. N. (1989). A simple method for the rapid determination of biogenic opal in pelagic marine sediments. *Deep Sea Res. Part A. Oceanogr. Res. Pap.* 36, 1415–1426. doi:10.1016/0198-0149(89)90092-7

Moulin, C., Lambert, C. E., Dayan, U., Masson, V., Ramonet, M., Bousquet, P., et al. (1998). Satellite climatology of African dust transport in the Mediterranean atmosphere. *J. Geophys. Res. Atmos.* 103, 13137–13144. doi:10.1029/98JD00171

Moutin, T., and Raimbault, P. (2002). Primary production, carbon export and nutrients availability in western and Eastern Mediterranean Sea in early summer 1996 (MINOS cruise). *J. Mar. Syst.* 33–34, 273–288. doi:10.1016/S0924-7963(02)00062-3

Nakanishi, T., and Minagawa, M. (2003). Stable carbon and nitrogen isotopic compositions of sinking particles in the northeast Japan Sea. *Geochem. J.* 37, 261–275. doi:10.2343/geochemj.37.261

Napolitano, E., Oguz, T., Malanotte-Rizzoli, P., Yilmaz, A., and Sansone, E. (2000). Simulations of biological production in the Rhodes and Ionian basins of the eastern Mediterranean. *J. Mar. Syst.* 24, 277–298. doi:10.1016/S0924-7963(99)00090-1

Neal, A. C., Prahl, F. G., Eglinton, G., O'Hara, S. C. M., and Corner, E. D. S. (1986). Lipid changes during a planktonic feeding sequence involving unicellular algae, *Elminius nauplii* and adult *Calanus*. *J. Mar. Biol. Assoc. U. K.* 66, 1. doi:10.1017/S0025315400039606

Nieuwenhuize, J., Maas, Y. E. M., and Middelburg, J. J. (1994). Rapid analysis of organic carbon and nitrogen in particulate materials. *Mar. Chem.* 45, 217–224. doi:10.1016/0304-4203(94)90005-1

Ohkouchi, N., Kawamura, K., Kawahata, H., and Taira, A. (1997). Latitudinal distributions of terrestrial biomarkers in the sediments from the Central Pacific. *Geochem. Cosmochim. Acta* 61, 1911–1918. doi:10.1016/S0016-7037(97)00040-9

Olgun, N., Duggen, S., Andronico, D., Kutterolf, S., Croot, P. L., Giammanco, S., et al. (2013). Possible impacts of volcanic ash emissions of Mount Etna on the primary productivity in the oligotrophic Mediterranean Sea: results from nutrient-release experiments in seawater. *Mar. Chem.* 152, 32–42. doi:10.1016/j.marchem.2013.04.004

Ortega-Retuerta, E., Mazuecos, I. P., Reche, I., Gasol, J. M., Álvarez-Salgado, X. A., Álvarez, M., et al. (2019). Transparent exopolymer particle (TEP) distribution and *in situ* prokaryotic generation across the deep Mediterranean Sea and nearby North East Atlantic Ocean. *Prog. Oceanogr.* 173, 180–191. doi:10.1016/j.pocean.2019.03.002

Palanques, A., and Puig, P. (2018). Particle fluxes induced by benthic storms during the 2012 dense shelf water cascading and open sea convection period in the northwestern Mediterranean basin. *Mar. Geol.* 406, 119–131. doi:10.1016/j.margeo.2018.09.010

Parinos, C., Gogou, A., Bouloubassi, I., Pedrosa-Pàmies, R., Hatzianestis, I., Sanchez-Vidal, A., et al. (2013a). Occurrence, sources and transport pathways of natural and anthropogenic hydrocarbons in deep-sea sediments of the Eastern Mediterranean Sea. *Biogeosciences* 10, 6069–6089. doi:10.5194/bg-10-6069-2013

Parinos, C., Gogou, A., Bouloubassi, I., Stavrakakis, S., Plakidi, E., and Hatzianestis, I. (2013b). Sources and downward fluxes of polycyclic aromatic hydrocarbons in the open southwestern Black Sea. *Org. Geochem.* 57, 65–75. doi:10.1016/j.orggeochem.2013.01.007

Parinos, C., Gogou, A., Krasakopoulou, E., Lagaria, A., Giannakourou, A., Karageorgis, A. P., et al. (2017). Transparent exopolymer particles (TEP) in the NE Aegean sea frontal area: seasonal dynamics under the influence of black sea water. *Continent. Shelf Res.* 149, 112–123. doi:10.1016/j.csr.2017.03.012

Parinos, C., and Gogou, A. (2016). Suspended particle-associated PAHs in the open Eastern Mediterranean Sea: occurrence, sources and processes affecting their distribution patterns. *Mar. Chem.* 180, 42–50. doi:10.1016/j.marchem.2016.02.001

Pasqual, C., Calafat, A., Lopez-Fernandez, P., and Pusceddu, A. (2015). Organic carbon inputs to the sea bottom of the Mallorca continental slope. *J. Mar. Syst.* 148, 142–151. doi:10.1016/j.jmarsys.2015.02.006

Passow, U., and De La Rocha, C. L. (2006). Accumulation of mineral ballast on organic aggregates. *Global Biogeochem. Cycles* 20, 17. doi:10.1029/2005GB002579

Passow, U. (2002a). Production of transparent exopolymer particles (TEP) by phyto- and bacterioplankton. *Mar. Ecol. Prog. Ser.* 236, 1–12. doi:10.3354/meps236001

Passow, U. (2002b). Transparent exopolymer particles (TEP) in aquatic environments. *Prog. Oceanogr.* 55, 287–333. doi:10.1016/S0079-6611(02)00138-6

Patara, L., Pinardi, N., Corselli, C., Malinverno, E., Tonani, M., Santoleri, R., et al. (2009). Particle fluxes in the deep Eastern Mediterranean basins: the role of ocean vertical velocities. *Biogeosciences* 6, 29. doi:10.5194/bg-6-333-2009

Pavlidou, A., Velaoras, D., Karageorgis, A. P., Rousselaki, E., Parinos, C., Dähnke, K., et al. (2020). Seasonal variations of biochemical and optical properties, physical dynamics and N stable isotopic composition in three northeastern Mediterranean basins (Aegean, Cretan and Ionian Seas). *Deep. Res. Part II Top. Stud. Oceanogr.* 171, 104704. doi:10.1016/j.dsr2.2019.104704

Pedrosa-Pàmies, R., Conte, M. H., Weber, J. C., and Johnson, R. (2018). Carbon cycling in the Sargasso Sea water column: insights from lipid biomarkers in

suspended particles. *Prog. Oceanogr.* 168, 248–278. doi:10.1016/J.POCEAN.2018.08.005

Pedrosa-Pàmies, R., Conte, M. H., Weber, J. C., and Johnson, R. (2019). Hurricanes enhance labile carbon export to the deep ocean. *Geophys. Res. Lett.* 46, 10484–10494. doi:10.1029/2019GL083719

Pedrosa-Pàmies, R., Parinos, C., Sanchez-Vidal, A., Gogou, A., Calafat, A., Canals, M., et al. (2015). Composition and sources of sedimentary organic matter in the deep Eastern Mediterranean Sea. *Biogeosciences* 12, 7379–7402. doi:10.5194/bgd-12-9935-2015

Pedrosa-Pàmies, R., Sanchez-Vidal, A., Calafat, A., Canals, M., and Durán, R. (2013). Impact of storm-induced remobilization on grain size distribution and organic carbon content in sediments from the Blanes Canyon area, NW Mediterranean Sea. *Prog. Oceanogr.* 118, 122–136. doi:10.1016/j.pocean.2013.07.023

Pedrosa-Pàmies, R., Sanchez-Vidal, A., Canals, M., Lampadariou, N., Velaoras, D., Gogou, A., et al. (2016). Enhanced carbon export to the abyssal depths driven by atmosphere dynamics. *Geophys. Res. Lett.* 43, 8626–8636. doi:10.1002/2016GL069781

Perdue, E. M., and Koprivnjak, J.-F. (2007). Using the C/N ratio to estimate terrigenous inputs of organic matter to aquatic environments. *Estuar. Coast Shelf Sci.* 73, 65–72. doi:10.1016/j.ecss.2006.12.021

Prahl, F. G., Eglinton, G., Corner, E. D. S., O'Hara, S. C. M., and Forsberg, T. E. V. (1984). Changes in plant lipids during passage through the gut of Calanus. *J. Mar. Biol. Assoc. U. K.* 64, 317. doi:10.1017/S0025315400030022

Psarra, S., Tselepides, A., and Ignatiades, L. (2000). Primary productivity in the oligotrophic Cretan Sea (NE Mediterranean): seasonal and interannual variability. *Prog. Oceanogr.* 46, 187–204. doi:10.1016/S0079-6611(00)00018-5

Puigcorbé, V., Benitez-Nelson, C. R., Masqué, P., Verdeny, E., White, A. E., Popp, B. N., et al. (2015). Small phytoplankton drive high summertime carbon and nutrient export in the Gulf of California and Eastern Tropical North Pacific. *Global Biogeochem. Cycles* 29, 1309–1332. doi:10.1002/2015GB005134

Quirós-Collazos, L., Pedrosa-Pàmies, R., Sanchez-Vidal, A., Guillén, J., Duran, R., and Cabelloa, P. (2017). Distribution and sources of organic matter in size-fractionated nearshore sediments off the Barcelona city (NW Mediterranean). *Estuar. Coast Shelf Sci.* 189, 47. doi:10.1016/j.ecss.2017.03.004

Rampen, S. W., Willmott, V., Kim, J.-H., Uliana, E., Mollenhauer, G., Schefuß, E., et al. (2012). Long chain 1,13- and 1,15-diols as a potential proxy for palaeotemperature reconstruction. *Geochem. Cosmochim. Acta* 84, 201–216. doi:10.1016/j.gca.2012.01.024

Rau, G. H., Takahashi, T., Des Marais, D. J., Repeta, D. J., and Martin, J. H. (1992). The relationship between $\delta^{13}C$ of organic matter and $[CO_2(aq)]$ in ocean surface water: data from a JGOFS site in the northeast Atlantic Ocean and a model. *Geochem. Cosmochim. Acta* 56, 1413–1419. doi:10.1016/0016-7037(92)90073-R

Raveh, O., David, N., Rilov, G., and Rahav, E. (2015). The temporal dynamics of coastal phytoplankton and bacterioplankton in the Eastern Mediterranean Sea. *PloS One* 10, e0140690. doi:10.1371/journal.pone.0140690

Raven, J. A. (1998). The twelfth Tansley Lecture. Small is beautiful: the picophytoplankton. *Funct. Ecol.* 12, 503–513. doi:10.1046/j.1365-2435.1998.00233.x

Redfield, A. C., Ketchum, B. H., and Richards, F. A. (1963). "The influence of organisms on the composition of sea-water," in *The Sea*. Editor M. N. Hill (New York: Interscience), 26–77.

Reemtsma, T., and Ittekkot, V. (1992). Determination of factors controlling the fatty acid composition of settling particles in the water column by principal-component analysis and their quantitative assessment by multiple regression. *Org. Geochem.* 18, 121–129. doi:10.1016/0146-6380(92)90149-R

Ribera d'Alcalà, M. (2003). Nutrient ratios and fluxes hint at overlooked processes in the Mediterranean Sea. *J. Geophys. Res.* 108, 8106. doi:10.1029/2002JC001650

Robinson, A. R., and Golnaraghi, M. (1993). Circulation and dynamics of the Eastern Mediterranean Sea; quasi-synoptic data-driven simulations. *Deep Sea Res. Part II Top. Stud. Oceanogr.* 40, 1207–1246. doi:10.1016/0967-0645(93)90068-X

Rolph, G., Stein, A., and Stunder, B. (2017). Real-time environmental Applications and display sYstem: READY. *Environ. Model. Software* 95, 210–228. doi:10.1016/j.envsoft.2017.06.025

Rumolo, P., Barra, M., Gherardi, S., Marsella, E., and Sprovieri, M. (2011). Stable isotopes and C/N ratios in marine sediments as a tool for discriminating anthropogenic impact. *J. Environ. Monit.* 13, 3399–3408. doi:10.1039/c1em10568j

Sanchez-Vidal, A., Calafat, A., Canals, M., Frigola, J., and Fabres, J. (2005). Particle fluxes and organic carbon balance across the eastern Alboran Sea (SW Mediterranean Sea). *Continent. Shelf Res.* 25, 609–628. doi:10.1016/j.csr.2004.11.004

Sanchez-Vidal, A., Higueras, M., Martí, E., Liquete, C., Calafat, A., and Kerhervé, P. (2013). Riverine transport of terrestrial organic matter to the North Catalan margin, NW Mediterranean Sea. *Prog. Oceanogr.* 118, 71–80. doi:10.1016/j.pocean.2013.07.020

Sanchez-Vidal, A., Pasqual, C., Kerhervé, P., Calafat, A., Heussner, S., Palanques, A., et al. (2008). Impact of dense shelf water cascading on the transfer of organic matter to the deep western Mediterranean basin. *Geophys. Res. Lett.* 35, L05605. doi:10.1029/2007GL032825

Schneider, J. K., Gagosian, R. B., Cochran, J. K., and Trull, T. W. (1983). Particle size distributions of n-alkanes and 210Pb in aerosols off the coast of Peru. *Nature* 304, 429–432. doi:10.1038/304429a0

Sciare, J., Bardouki, H., Moulin, C., and Mihalopoulos, N. (2003). Aerosol sources and their contribution to the chemical composition of aerosols in the Eastern Mediterranean Sea during summertime. *Atmos. Chem. Phys.* 3, 291–302. doi:10.5194/acp-3-291-2003

Scollo, S., Prestifilippo, M., Pecora, E., Corradini, S., Merucci, L., Spata, G., et al. (2014). Eruption column height estimation of the 2011-2013 Etna lava fountains. *Ann. Geophys.* 57, S0214. doi:10.4401/ag-6396

Sempéré, R., Yoro, S., Van Wambeke, F., and Charrière, B. (2000). Microbial decomposition of large organic particles in the northwestern Mediterranean Sea: an experimental approach. *Mar. Ecol. Prog. Ser.* 198, 61–72. doi:10.3354/meps198061

Sheridan, C. C., Lee, C., Wakeham, S. G., and Bishop, J. K. B. (2002). Suspended particle organic composition and cycling in surface and midwaters of the equatorial Pacific Ocean. *Deep-Sea Res. Part I Oceanogr. Res. Pap.* 49, 1983–2008. doi:10.1016/S0967-0637(02)00118-8

Simoneit, B. R. T., Cardoso, J. N., and Robinson, N. (1990). An assessment of the origin and composition of higher molecular weight organic matter in aerosols over Amazonia. *Chemosphere* 21, 1285–1301. doi:10.1016/0045-6535(90)90145-J

Simoneit, B. R. T. (1984). Organic matter of the troposphere-III. Characterization and sources of petroleum and pyrogenic residues in aerosols over the western United States. *Atmos. Environ.* 18, 51–67. doi:10.1016/0004-6981(84)90228-2

Siokou-Frangou, I., Bianchi, M., Christaki, U., Christou, E. D., Giannakourou, A., Gotsis, O., et al. (2002). Carbon flow in the planktonic food web along a gradient of oligotrophy in the Aegean Sea (Mediterranean Sea). *J. Mar. Syst.* 33–34, 335–353. doi:10.1016/S0924-7963(02)00065-9

Siokou-Frangou, I., Christaki, U., Mazzocchi, M. G., Montresor, M., Ribera d'Alcalá, M., Vaqué, D., et al. (2010). Plankton in the open Mediterranean Sea: a review. *Biogeosciences* 7, 1543–1586. doi:10.5194/bg-7-1543-2010

Siokou-Frangou, I., Gotsis-Skretas, O., Christou, E. D., and Pagou, K. (1999). *The eastern Mediterranean as a laboratory Basin for the Assessment of contrasting ecosystems*. Berlin: Springer Netherlands, 205–223. doi:10.1007/978-94-011-4796-5_15Plankton characteristics in the Aegean, ionian and NW Levantine seas

Skampa, E., Triantaphyllou, M. V., Dimiza, M. D., Gogou, A., Malinverno, E., Stavrakakis, S., et al. (2020). Coccolithophore export in three deep-sea sites of the Aegean and Ionian Seas (Eastern Mediterranean): biogeographical patterns and biogenic carbonate fluxes. *Deep. Res. Part II Top. Stud. Oceanogr.* 171, 104690. doi:10.1016/j.dsr2.2019.104690

Skampa, E., Triantaphyllou, M. V., Dimiza, M. D., Gogou, A., Malinverno, E., Stavrakakis, S., et al. (2019). Coupling plankton—sediment trap—surface sediment coccolithophore regime in the North Aegean Sea (NE Mediterranean). *Mar. Micropaleontol.* 152, 101729. doi:10.1016/j.marmicro.2019.03.001

Smith, K. L., Ruhl, H. A., Bett, B. J., Billett, D. S. M., Lampitt, R. S., and Kaufmann, R. S. (2009). Climate, carbon cycling, and deep-ocean ecosystems. *Proc. Natl. Acad. Sci. U. S. A* 106, 19211. doi:10.1073/pnas.0908322106–8

Smith, K. L., Ruhl, H. A., Huffard, C. L., Messié, M., and Kahru, M. (2018). Episodic organic carbon fluxes from surface ocean to abyssal depths during long-term monitoring in NE Pacific. *Proc. Natl. Acad. Sci. U. S. A.* 115, 12235–12240. doi:10.1073/PNAS.1814559115

Stabholz, M., Durrieu de Madron, X., Canals, M., Khripounoff, A., Taupier-Letage, I., Testor, P., et al. (2013). Impact of open-ocean convection on particle fluxes and sediment dynamics in the deep margin of the Gulf of Lions. *Biogeosciences* 10, 1097–1116. doi:10.5194/bg-10-1097-2013

Stavrakakis, S., Chronis, G., Tselepides, A., Heussner, S., Monaco, A., and Abassi, A. (2000). Downward fluxes of settling particles in the deep Cretan Sea (NE Mediterranean). *Prog. Oceanogr.* 46, 217–240. doi:10.1016/S0079-6611(00)00020-3

Stavrakakis, S., Gogou, A., Krasakopoulou, E., Karageorgis, A. P., Kontoyiannis, H., Rousakis, G., et al. (2013). Downward fluxes of sinking particulate matter in the deep Ionian Sea (NESTOR site), eastern Mediterranean: seasonal and interannual variability. *Biogeosciences* 10, 7235–7254. doi:10.5194/bg-10-7235-2013

Stein, A. F., Draxler, R. R., Rolph, G. D., Stunder, B. J. B., Cohen, M. D., and Ngan, F. (2015). Noaa's hysplit atmospheric transport and dispersion modeling system. *Bull. Am. Meteorol. Soc.* 96, 2059–2077. doi:10.1175/BAMS-D-14-00110.1

Steinberg, D. K., Carlson, C. A., Bates, N. R., Johnson, R. J., Michaels, A. F., and Knap, A. H. (2001). Overview of the US JGOFS Bermuda Atlantic Time-series Study (BATS): a decade-scale look at ocean biology and biogeochemistry. *Deep Sea Res. Part II Top. Stud. Oceanogr.* 48, 1405–1447. doi:10.1016/S0967-0645(00)00148-X

Steinberg, D. K., Goldthwait, S. A., and Hansell, D. A. (2002). Zooplankton vertical migration and the active transport of dissolved organic and inorganic nitrogen in the Sargasso Sea. *Deep. Res. Part I Oceanogr. Res. Pap.* 49, 1445–1461. doi:10.1016/S0967-0637(02)00037-7

Struck, U., Pollehne, F., Bauerfeind, E., and Bodungen, B. V. (2004). Sources of nitrogen for the vertical particle flux in the Gotland Sea (Baltic Proper) - results from sediment trap studies. *J. Mar. Syst.* 45, 91–101. doi:10.1016/j.jmarsys.2003.11.012

Teshima, S.-I. (1971). Bioconversion of β-sitosterol and 24-methylcholesterol to cholesterol in marine crustacea. *Comp. Biochem. Physiol. Part B Comp. Biochem.* 39, 815–822. doi:10.1016/0305-0491(71)90105-2

Tesi, T., Puig, P., Palanques, A., and Goñi, M. A. (2010). Lateral advection of organic matter in cascading-dominated submarine canyons. *Prog. Oceanogr.* 84, 185–203. doi:10.1016/j.pocean.2009.10.004

Theodosi, C., Markaki, Z., Pantazoglou, F., Tselepides, A., and Mihalopoulos, N. (2019). Chemical composition of downward fluxes in the Cretan Sea (Eastern Mediterranean) and possible link to atmospheric deposition: a 7 year survey. *Deep. Res. Part II Top. Stud. Oceanogr.* 164, 89–99. doi:10.1016/j.dsr2.2019.06.003

Theodosi, C., Parinos, C., Gogou, A., Kokotos, A., Stavrakakis, S., Lykousis, V., et al. (2013). Downward fluxes of elemental carbon, metals and polycyclic aromatic hydrocarbons in settling particles from the deep Ionian Sea (NESTOR site), Eastern Mediterranean. *Biogeosciences* 10, 4449–4464. doi:10.5194/bg-10-4449-2013

Thunell, R. C., Varela, R., Llano, M., Collister, J., -Karger, F. M., and Bohrer, R. (2000). Organic carbon fluxes, degradation, and accumulation in an anoxic basin: sediment trap results from the Cariaco Basin. *Limnol. Oceanogr.* 45, 300–308. doi:10.4319/lo.2000.45.2.0300

Tolosa, I., LeBlond, N., Copin-Montégut, C., Marty, J.-C., de Mora, S., and Prieur, L. (2003). Distribution of sterol and fatty alcohol biomarkers in particulate matter from the frontal structure of the Alboran Sea (S.W. Mediterranean Sea). *Mar. Chem.* 82, 161–183. doi:10.1016/S0304-4203(03)00051-3

Tolosa, I., LeBlond, N., Marty, J.-C., de Mora, S., and Prieur, L. (2005). Export fluxes of organic carbon and lipid biomarkers from the frontal structure of the Alboran Sea (SW Mediterranean Sea) in winter. *J. Sea Res.* 54, 125–142. doi:10.1016/J.SEARES.2005.04.002

Triantaphyllou, M. V. (2004). Coccolithophore export production and response to seasonal surface water variability in the oligotrophic Cretan Sea (NE Mediterranean). *Micropaleontology* 50, 127–144. doi:10.2113/50.Suppl_1.127

Tsapakis, M., Apostolaki, M., Eisenreich, S., and Stephanou, E. G. (2006). Atmospheric deposition and marine sedimentation fluxes of polycyclic aromatic hydrocarbons in the eastern Mediterranean basin. *Environ. Sci. Technol.* 40, 4922–4927. doi:10.1021/es060487x

Turchetto, M., Boldrin, A., Langone, L., and Miserocchi, S. (2012). Physical and biogeochemical processes controlling particle fluxes variability and carbon export in the Southern Adriatic. *Continent. Shelf Res.* 44, 72–82. doi:10.1016/j.csr.2011.05.005

Turner, J. T. (2015). Zooplankton fecal pellets, marine snow, phytodetritus and the ocean's biological pump. *Prog. Oceanogr.* 130, 205–248. doi:10.1016/J.POCEAN.2014.08.005

van der Jagt, H., Friese, C., Stuut, J.-B. W., Fischer, G., and Iversen, M. H. (2018). The ballasting effect of Saharan dust deposition on aggregate dynamics and carbon export: aggregation, settling, and scavenging potential of marine snow. *Limnol. Oceanogr.* 63, 1386–1394. doi:10.1002/lno.10779

Van Santvoort, P. J. M., de Lange, G. J., Thomson, J., Cussen, H., Wilson, T. R. S., Krom, M. D., et al. (1996). Active post-depositional oxidation of the most recent sapropel (S1) in sediments of the Eastern Mediterranean Sea. *Geochem. Cosmochim. Acta* 60, 4007–4024. doi:10.1016/S0016-7037(96)00253-0

Varkitzi, I., Psarra, S., Assimakopoulou, G., Pavlidou, A., Krasakopoulou, E., Velaoras, D., et al. (2020). Phytoplankton dynamics and bloom formation in the oligotrophic eastern mediterranean: field studies in the Aegean, Levantine and ionian seas. *Deep. Res. Part II Top. Stud. Oceanogr.* 171, 104662. doi:10.1016/j.dsr2.2019.104662

Versteegh, G. J., Bosch, H.-J., and De Leeuw, J. W. (1997). Potential palaeoenvironmental information of C_{24} to C_{36} mid-chain diols, keto-ols and mid-chain hydroxy fatty acids; a critical review. *Org. Geochem.* 27, 1–13. doi:1016/S0146-6380(97)00063-6

Versteegh, G. J. M., Jansen, J. H. F., Schneider, R. R., and De Leeuw, J. W. (2000). Mid-chain diols and keto-ols in SE atlantic sediments: a new tool for tracing past sea surface water masses?. *Geochem. Cosmochim. Acta* 64, 1879–1892. doi:10.1016/S0016-7037(99)00398-1

Versteegh, G. J. M., and Lipp, J. (2019). Detection of new long-chain mid-chain keto-ol isomers from marine sediments by means of HPLC–APCI-MS and comparison with long-chain mid-chain diols from the same samples. *Org. Geochem.* 133, 92–102. doi:10.1016/j.orggeochem.2019.04.004

Volk, T., and Hoffert, M. I. (1985). "Ocean carbon pumps: analysis of relative strengths and efficiencies in ocean-driven atmospheric CO_2 changes," in *The carbon cycle and atmospheric CO_2: natural variations Archean to present*. New York, NY: American Geophysical Union, 99–110. doi:10.1029/GM032p0099

Volkman, J. K. (1986). A review of sterol markers for marine and terrigenous organic matter. *Org. Geochem.* 9, 83–99. doi:10.1016/0146-6380(86)90089-6

Volkman, J. K., Barrett, S. M., and Blackburn, S. I. (1999). Eustigmatophyte microalgae are potential sources of C29 sterols, C22–C28 n-alcohols and C28–C32 n-alkyl diols in freshwater environments. *Org. Geochem.* 30, 307–318. doi:10.1016/S0146-6380(99)00009-1

Volkman, J. K., Barrett, S. M., Blackburn, S. I., Mansour, M. P., Sikes, E. L., and Gelin, F. (1998). Microalgal biomarkers: a review of recent research developments. *Org. Geochem.* 14, 1163–1179. doi:10.1016/S0146-6380(98)00062-X

Volkman, J. K., Barrett, S. M., Dunstan, G. A., and Jeffrey, S. W. (1992). C_{30} C_{32} alkyl diols and unsaturated alcohols in microalgae of the class Eustigmatophyceae. *Org. Geochem.* 18, 131–138. doi:10.1016/0146-6380(92)90150-V

Volkman, J. K. (2006). "Lipid markers for marine organic matter," in *Marine organic matter: biomarkers, isotopes and DNA*. Editor J. K. Volkman (Berlin: Springer-Verlag), 27–70.

Volkman, J. K., and Tanoue, E. (2002). Chemical and biological studies of particulate organic matter in the ocean. *J. Oceanogr.* 58, 265–279. doi:10.1023/A:1015809708632

Wakeham, S. G., Canuel, E. A., Lerberg, E. J., Mason, P., Sampere, T. P., and Bianchi, T. S. (2009). Partitioning of organic matter in continental margin sediments among density fractions. *Mar. Chem.* 115, 211–225. doi:10.1016/j.marchem.2009.08.005

Wakeham, S. G., and Canuel, E. A. (1986). Lipid composition of the pelagic crab *Pleuroncodes planipes*, its feces, and sinking particulate organic matter in the Equatorial North Pacific Ocean. *Org. Geochem.* 9, 331–343. doi:10.1016/0146-6380(86)90114-2

Wakeham, S. G. (1995). Lipid biomarkers for heterotrophic alteration of suspended particulate organic matter in oxygenated and anoxic water columns of the ocean. *Deep-Sea Res. Part I Oceanogr. Res. Pap.* 42, 1749–1771. doi:10.1016/0967-0637(95)00074-G

Wakeham, S. G., Peterson, M. L., Hedges, J. I., and Lee, C. (2002). Lipid biomarker fluxes in the Arabian sea, with a comparison to the equatorial pacific ocean. *Deep Sea Res. Part II Top. Stud. Oceanogr.* 49, 2265–2301. doi:10.1016/S0967-0645(02)00037-1

Wang, Z., Fingas, M., and Page, D. S. (1999). Oil spill identification. *J. Chromatogr. A* 843, 369–411. doi:10.1016/S0021-9673(99)00120-X

Warnken, C. (2003). Biogeochemie von Schwebstoffen, Sinkstoffen und Sedimenten im Ierapetra-Tief (östliches Mittelmeer). Diploma thesis. Inst. für Biogeochem. und Meereschem. Hamburg: University of Hamburg.

Weinbauer, M. G., Guinot, B., Migon, C., Malfatti, F., and Mari, X. (2017). Skyfall—neglected roles of volcano ash and black carbon rich aerosols for microbial plankton in the ocean. *J. Plankton Res.* 39, 187–198. doi:10.1093/plankt/fbw100

Yunker, M. B., Macdonald, R. W., Veltkamp, D. J., and Cretney, W. J. (1995). Terrestrial and marine biomarkers in a seasonally ice-covered Arctic estuary — integration of multivariate and biomarker approaches. *Mar. Chem.* 49, 1–50. doi:10.1016/0304-4203(94)00057-K

Ziveri, P., Rutten, A., de Lange, G. J., Thomson, J., and Corselli, C. (2000). Present-day coccolith fluxes recorded in central eastern Mediterranean sediment traps and surface sediments. *Palaeogeogr. Palaeoclimatol. Palaeoecol.* 158, 175–195. doi:10.1016/S0031-0182(00)00049-3

Zúñiga, D., Flexas, M. M., Sanchez-Vidal, A., Coenjaerts, J., Calafat, A., Jordà, G., et al. (2009). Particle fluxes dynamics in Blanes submarine canyon (Northwestern Mediterranean). *Prog. Oceanogr.* 82, 239–251. doi:10.1016/j.pocean.2009.07.002

Conflict of Interest: The authors declare that the research was conducted in the absence of any commercial or financial relationships that could be construed as a potential conflict of interest.

frontiers in Earth Science

BRIEF RESEARCH REPORT
published: 17 June 2021
doi: 10.3389/feart.2021.579198

Sinking Diatom Assemblages as a Key Driver for Deep Carbon and Silicon Export in the Scotia Sea (Southern Ocean)

D. Zúñiga[1,2,3], A. Sanchez-Vidal[4], M. M. Flexas[5], D. Carroll[6], M. M. Rufino[2,7], G. Spreen[8], A. Calafat[4] and F. Abrantes[2,3]*

[1]Instituto de Investigacións Mariñas, Spanish National Research Council (CSIC), Vigo, Spain, [2]Div. Geologia e Georecursos Marinhos, Portuguese Institute for the Sea and Atmosphere (IPMA), Lisbon, Portugal, [3]CCMAR - Centre of Marine Sciences, University of Algarve, Faro, Portugal, [4]GRC Geociències Marines, Universitat de Barcelona, Barcelona, Spain, [5]California Institute of Technology, Pasadena, CA, United States, [6]Moss Landing Marine Laboratories, San José State University, Moss Landing, CA, United States, [7]CEAUL, Centre of Statistics and its Applications, Faculty of Sciences, University of Lisbon, Lisbon, Portugal, [8]Institute of Environmental Physics, University of Bremen, Bremen, Germany

OPEN ACCESS

Edited by:
Maureen H Conte, Bermuda Institute of Ocean Sciences, Bermuda

Reviewed by:
Ian Salter, Alfred Wegener Institute Helmholtz Centre for Polar and Marine Research (AWI), Germany
Tom Trull, Commonwealth Scientific and Industrial Research Organisation (CSIRO), Australia

***Correspondence:**
D. Zúñiga
imissons@gmail.com

Specialty section:
This article was submitted to Biogeoscience, a section of the journal Frontiers in Earth Science

Received: *01 July 2020*
Accepted: *26 May 2021*
Published: *17 June 2021*

Citation:
Zúñiga D, Sanchez-Vidal A, Flexas MM, Carroll D, Rufino MM, Spreen G, Calafat A and Abrantes F (2021) Sinking Diatom Assemblages as a Key Driver for Deep Carbon and Silicon Export in the Scotia Sea (Southern Ocean). Front. Earth Sci. 9:579198. doi: 10.3389/feart.2021.579198

Physical and biogeochemical processes in the Southern Ocean are fundamental for modulating global climate. In this context, a process-based understanding of how Antarctic diatoms control primary production and carbon export, and hence global-ocean carbon sequestration, has been identified as a scientific priority. Here we use novel sediment trap observations in combination with a data-assimilative ocean biogeochemistry model (ECCO-Darwin) to understand how environmental conditions trigger diatom ecology in the iron-fertilized southern Scotia Sea. We unravel the role of diatoms assemblage in controlling the biogeochemistry of sinking material escaping from the euphotic zone, and discuss the link between changes in upper-ocean environmental conditions and the composition of settling material exported from the surface to 1,000 m depth from March 2012 to January 2013. The combined analysis of *in situ* observations and model simulation suggests that an anomalous sea-ice episode in early summer 2012–2013 favored (*via* restratification due to sea-ice melt) an early massive bloom of *Corethron pennatum* that rapidly sank to depth. This event drove high biogenic silicon to organic carbon export ratios, while modulating the carbon and nitrogen isotopic signals of sinking organic matter reaching the deep ocean. Our findings highlight the role of diatom ecology in modulating silicon vs. carbon sequestration efficiency, a critical factor for determining the stoichiometric relationship of limiting nutrients in the Southern Ocean.

Keywords: diatoms, sea ice, marginal ice zone, carbon export, biogenic silicon, scotia sea, southern ocean, corethron pennatum

INTRODUCTION

The Southern Ocean (SO) is one of the most productive regions in the global ocean, and through its connection with all other basins, has sparked intense debate of how this remote region modulates global climate (Falkowski et al., 1998; Sarmiento et al., 2004). In this context, phytoplankton are of utmost importance due to their critical role in ocean carbon sequestration. These tiny organisms are fundamental for modulating climate change through their capacity to consume and export

atmospheric carbon dioxide (CO_2) to bottom sediments (Smetacek et al., 2012; Boyd et al., 2016; Tréguer et al., 2017). Furthermore, phytoplankton in the SO may influence productivity at global scales by modifying the stoichiometric relationships of SO nutrients that are transported to distant regions around the global ocean (Pondaven et al., 2000; Ragueneau et al., 2000; Brzezinski et al., 2002; Matsumoto and SarmientoBrzezinski, 2002).

While the phytoplankton community varies between different SO biogeochemical provinces, there is clear consensus that diatoms, which are unicellular organisms with silica skeletons, are the dominant phytoplankton group during elevated primary productivity events (Bathmann et al., 1997; Arrigo et al., 1999; Landry et al., 2002). In the remote SO, where macronutrients remain high, dissolved iron (dFe) content in combination with light availability acts as the limiting factor for diatom growth (Martin et al., 1990; Buma et al., 1991; Boyd et al., 2007). Furthermore, dFe variability can also shift diatoms community structure, through the promotion of different physiological and survival strategies (Hutchins and Bruland, 1998; Takeda, 1998; Marchetti and Cassar, 2009; Quéguiner, 2013). The largest ecological manipulation experiment to date in the SO revealed that Fe addition promoted thin-shelled small diatoms, while Fe-limited conditions led to the dominance of heavily-silicified diatoms (Assmy et al., 2013). While the results from this groundbreaking experiment provide invaluable information linking diatom ecology to SO biogeochemistry, other critical aspects, such as how other environmental factors (e.g., irradiance, temperature, and water column stability) control the diatom species succession remain poorly understood (Boyd, 2013).

Due to their high sinking rates, diatoms have the capacity to transfer organic carbon (OC) and biogenic silicon (bioSi) from the productive surface layer to the deep ocean. As a result, diatoms are widely identified as the most relevant phytoplankton group for unraveling SO organic carbon cycling (Bathmann et al., 1991; Smetacek et al., 2012; Krause and Lomas, 2020). To fully understand diatom-driven export, and hence how carbon and silicon are sequestered, it is also critical to consider diatom ecological traits. These traits respond to favorable growth conditions, determine the survival of one species vs. another, and consequently impacts settling velocity. While sinking, the intact survival of diatom frustules depends on the resistance of their siliceous skeletons to dissolution and the impact of remineralization processes on their cell's organic content. These two aspects, along with the capability of diatoms to avoid grazing by pelagic zooplankton, must be considered for a complete understanding of which diatom species reach the seafloor and impact sediment composition. In this context, studies based on sediment trap data are especially important, since they represent the missing link between processes occurring at the ocean surface and the seafloor. Despite sparse sediment trap observations in the SO, previous *in-situ* studies have been fundamental for understanding the role of seasonal diatom assemblages in determining the transfer efficiency of biogenic matter escaping the epipelagic domain (Fischer et al., 2002; Pilskaln et al., 2004; Salter et al., 2007; Ichinomiya et al., 2008; Salter et al., 2012; Grigorov et al., 2014; Rembauville et al., 2015; Rigual-Hernández et al., 2015, 2016; Rigual-Hernandez et al., 2019). However, only few studies discuss variability in export rates by considering environmental factors to regulate seasonal diatom production in the upper water column (Salter et al., 2012; Rigual-Hernández et al., 2015, 2019; Rembauville et al., 2018).

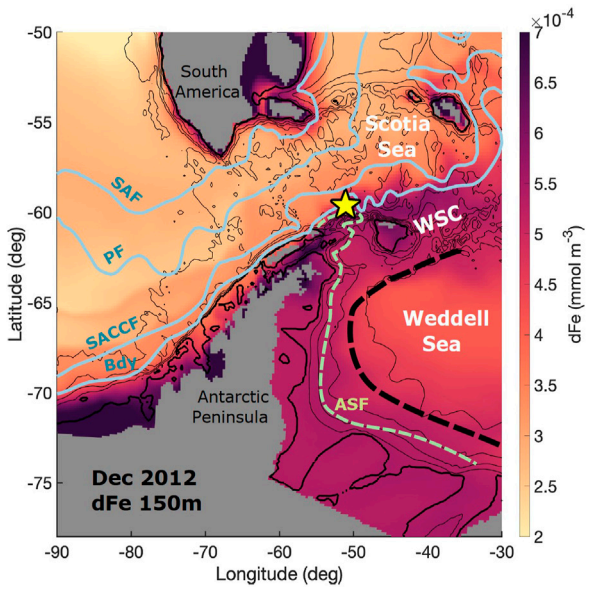

FIGURE 1 | Map of the study region depicting bathymetry, main oceanographic fronts and the sediment trap location (yellow star). ECCO-Darwin dissolved iron concentration (dFe, in color) for the month of December 2012 at 150 m depth shows the supply of dFe from the tip of the Antarctic Peninsula. Antarctic Circumpolar fronts (Orsi et al., 1995) are shown in gray (SAF: Sub-Antarctic front; PF: Polar Front; SACCF: Southern Antarctic Circumpolar Current Front; Bdy: Southern boundary of the Antarctic Circumpolar Current); the Antarctic Slope Front (ASF) is shown in light green; and the outer limit of the Weddell Gyre is indicated with a dashed black line. The zonal band between the southern boundary (Bdy) of the ACC and the northern limit of the Weddell Gyre is known as the Weddell Scotia Confluence (WSC; Patterson and Sievers, 1980). Isobaths are shown as black contours (500 m, thick line; every 1,000 m, thin lines).

In the South Atlantic sector of the SO, naturally Fe-enriched shelf waters from the Antarctic Peninsula meet the southern boundary of the Antarctic Circumpolar Current (**Figure 1**) (Orsi et al., 1995; Dulaiova et al., 2009; DeJong et al., 2012; Jiang et al., 2019; Sanchez et al., 2019). This leads to relatively high rates of primary production compared to other SO biogeochemical regions (de Baar et al., 1995; Holm-Hansen et al., 2004; Ardelan et al., 2010). Despite their importance in terms of quantifying productivity, previous particle flux studies in this region are scarce and are based on free-drifting traps deployed for short time periods (Bodungen et al., 1986; Gersonde and Wefer, 1987; Abelmann and Gersonde, 1991; Leventer, 1991), which limits our understanding of carbon and silicon sequestration on seasonal and longer timescales.

The primary goal of this study is to determine the role of diatoms in driving the export of OC and bioSi to depth in the Fe-fertilized southern Scotia Sea by analyzing sinking diatom

assemblage, along with isotopic and major element composition of settling particles. These data provide unprecedented detail on: 1) how diatom survival strategies regulate the biogeochemical signature of exported particles and 2) how diatom floristics respond to changing environmental conditions. Our work fills a critical gap in understanding the role of diatom ecology in the SO carbon cycle, while providing novel information on the use of fossil diatom assemblages as a proxy for past primary production. Ultimately, our results provide new insight on the role of diatoms in the biogeochemistry cycle of SO waters.

DATA AND METHODS

Study Region

The study site is located in the Weddell-Scotia Confluence (WSC, **Figure 1**), a weakly-stratified region with sub-surface temperature and salinity that is lower than waters located to the north and the south (Patterson and Sievers, 1980; Orsi et al., 1993; Whitworth et al., 1994). Relatively warm sub-surface waters in the north (Circumpolar Deep Water, in the Scotia Sea) and the south (Warm Deep Water, in the Weddell Sea) mark the meridional extension of the Confluence Zone. The currents associated with these water masses (the Antarctic Circumpolar Current and the Weddell Gyre) confer a general eastward zonal flow on both limits. The weak stratification of the WSC is caused by strong lateral mixing along isopycnals (Whitworth et al., 1994), and enhanced diapycnal mixing near the bottom (Naveira-Garabato et al., 2002). Rectified tidal flows are responsible for sustaining the Antarctic Slope Front (Jacobs, 1991) over the complex double-ridge topography (Heywood et al., 2004; Flexas et al., 2015). Wind forcing controls the surface circulation over the South Scotia Ridge. In particular, wind stress curl over the Weddell Gyre determines the pathway of surface waters exported into the Scotia Sea (Youngs et al., 2015) and thus has a large impact on surface-ocean chlorophyll patterns in this region (Thompson and Youngs, 2013). Sea ice from the continental shelf and slope of the Weddell Sea is advected by local winds, which also control sea-ice concentration trends (Holland and Kwok, 2012) (**Supplementary Figure S1**).

Sediment Trap Observations

In the framework of a multi-year international program focused on studying the Antarctic Slope Front over the South Scotia Ridge (Palmer et al., 2012; Flexas et al., 2015), an instrumented mooring with a near-bottom sediment trap (1,000 m depth) was deployed from March 2012 toJanuary 2013 at the northern slope of the South Scotia Ridge (60°S, 53°W; 1,130 m isobath) with sampling periods of one month. Representing dates are referred to the middle point of each sampling period that begins the first day of the corresponding month. The sediment trap was a Technicap PPS3 (0.125 m^2 collecting area) with a cylindroconical collection funnel and 12 polypropylene collecting cups, which were set to rotate every month. Before the deployment, the cups were cleaned with 0.5 N HCl, rinsed with ultrapure water, and filled with buffered 5% (v/v) formaldehyde solution in 0.45 μm filtered seawater. After recovery, the closed cups were stored in the dark at 2–4°C until they were processed in the laboratory, within a maximum delay of a few weeks. After decantation of the supernatant, particles were wet-sieved through a 1 mm nylon mesh to retain the largest swimmers, while the smaller ones were removed under a dissecting microscope using fine tweezers. The sample was then divided into 6–12 equal wet aliquots for biogeochemical analyses and diatom identification using a rotary splitting method following the methodology described in Heussner et al. (1990).

The total mass was determined gravimetrically on two or three sub-samples. The replicates were filtered onto cellulose acetate membranes (0.45 μm pore size, 47 mm diameter), rinsed with distilled water to remove salts and excess formalin, and dried to constant weight at 40 C during 24 h. One of the aliquots of each sediment trap sample was freeze-dried, ground and homogenized. Assuming that all the inorganic carbon was constituted by calcium carbonate, the organic matter (organic carbon × 2) and the calcium carbonate [(total carbon–organic carbon) × 8.33] were calculated. The lithogenic (terrigenous) fraction was obtained by the difference between the total mass and the sum of the biogenic compounds [organic matter, calcium carbonate and biogenic silicon (bioSi)].

Total and organic carbon (OC) and total nitrogen (TN) contents, and the stable isotope composition of OC and TN, were measured on an elemental analyzer interfaced to an isotope ratio mass spectrometer at the Scientific and Technological Centers of the University of Barcelona. Samples for OC analysis were first treated with HCl 25% to remove inorganic carbon. The results of isotopic analyses are presented in the conventional δ notation, which is defined as $\delta X = [(Rsample/Rstandard)- 1] \times 1{,}000$, where X is ^{13}C or ^{15}N and R is the isotopic ratio of $^{13}C/^{12}C$ or $^{15}N/^{14}N$. Isotopic ratios of the samples (Rsample) are expressed relative to those of a standard (Rstandard), the Pee Dee Belemnite for C and atmospheric N_2 for N.

BioSi was analyzed using a two-step extraction with 0.5 M Na_2CO_3 (2.5 h each) separated after filtration of the leachate. Inductive Coupled Plasma Atomic Emission Spectroscopy (ICP-AES) was used to analyze Si and Al contents in the leachates, and a correction of the Si of the first leachate by the Si/Al relation of the second leachate was applied in order to correct for the excess Si dissolved from aluminosilicates and obtain the bioSi concentration (Kamatani and Oku, 2000). Thus, in this paper we provide bioSi (silicon) strictly speaking, not silica (SiO_2) neither amorphous hydrated silica (opal, SiO_2 $0.4H_2O$) as reported by Mortlock and Froelich (1989). Dissolved elements in the supernatant overlying the trap particulate samples were not measured and thus particulate fluxes have not been corrected for total fluxes.

Diatom counting and identification was performed using a full sediment trap sample aliquot (Abrantes et al., 2005). Each sample was first cleaned of organic matter and carbonate by additions of H_2O_2 30% and HCl 10%, respectively. Permanent slides of the entire aliquots (2 fractions <63 μm and >63 μm) were prepared using the evaporation n-tray method (Battarbee, 1973) and the Norland optical adhesive (NOA61) as mounting medium. Diatom counting and species identification was performed at 1000 X (×10 eyepieces and ×100 objectives), using a Nikon Eclipse E100 microscope equipped with Differential Interference Contrast. Exactly 100 randomly-selected fields of view were counted in three replicate slides. For each sample,

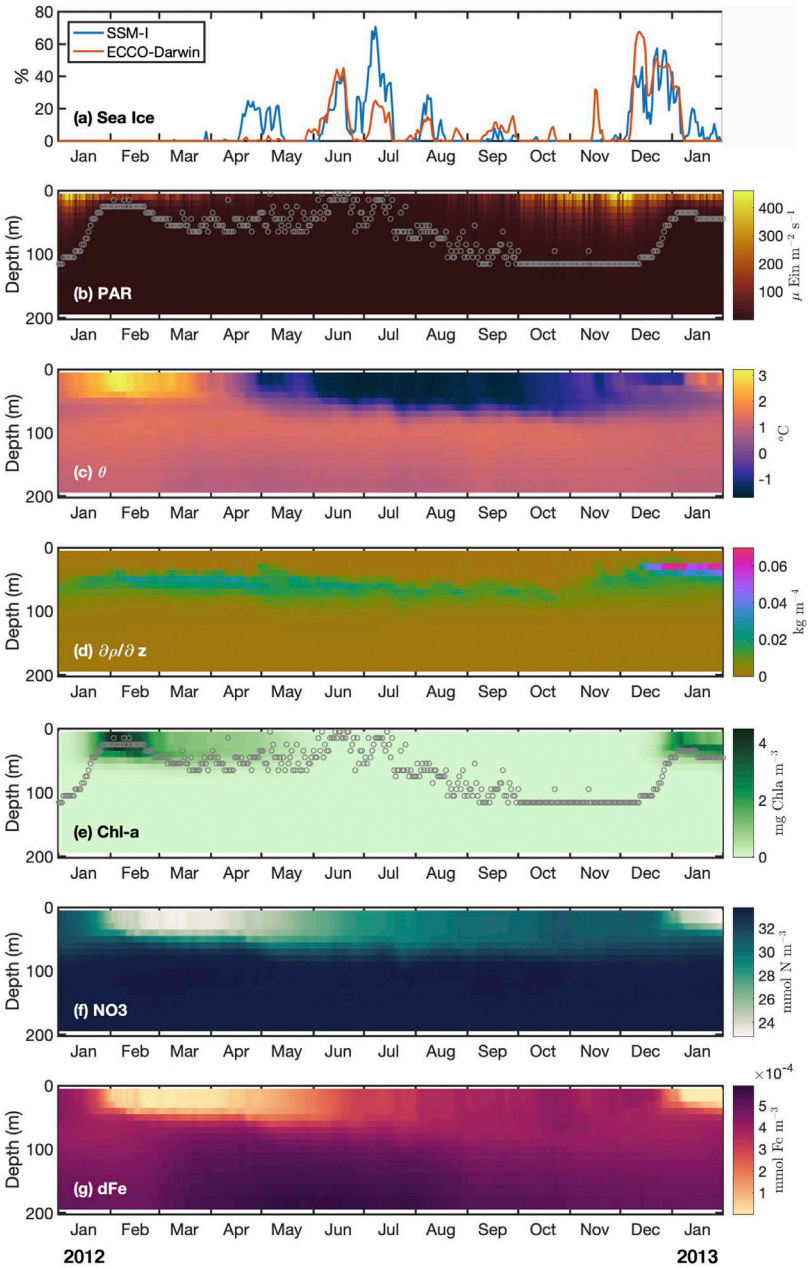

FIGURE 2 | Sea-ice concentration from satellite observations (SSM-I) and environmental variables from ECCO-Darwin at the sediment trap location. **(A)** Sea-ice concentration, **(B)** Photosynthethic Active Radiation (PAR, μ Eins m^{-2} s^{-1}), **(C)** potential temperature, **(D)** stratification (-dρ/dz, kg m^{-4}), **(E)** Chlorophyll *a* (Chl *a*, mg m^{-3}), **(F)** and **(G)** concentration of dissolved nitrate (NO_3, mmol m^{-3}) and dissolved iron (dFe, mmol m^{-3}), respectively. Photic layer depth is shown as gray circles in panels **(B)** and **(E)**.

300 specimens were identified to the species level and raw counts were then converted to percent abundance. Data presented in this work only includes the dominant diatom species, which represent >70% of the total diatom assemblage.

Sea-Ice Concentrations

Sea-ice velocity fields (**Supplementary Figure S1**) were obtained from Tschudi et al. (2016). Sea-ice concentration data for years 2012 and 2013 were obtained from the 89 GHz channels of the AMSR2 satellite microwave radiometer with a grid resolution of 6.25 km (Spreen et al., 2008, data available from www.seaice.uni-bremen.de). Sea-ice concentration anomalies (**Supplementary Figure S2**) were calculated as differences relative to the December 1979–2016 mean sea-ice concentration based on SMMR and SSM/I-SSMIS data at 25 km grid resolution (Cavalieri et al., 2016). The same sea-ice data were also used to calculate sea-ice persistence (**Supplementary Figure S3**) and the sea ice concentration time series in **Figure 2A** for a 75 × 81 km region surrounding the mooring.

ECCO-Darwin

The state-of-the-art ECCO-Darwin ocean biogeochemistry model and its performance has been extensively discussed in the literature (Brix et al., 2015; Manizza et al., 2019; Carroll et al., 2020). ECCO-Darwin is based on a global ocean and sea-ice configuration of the Massachusetts Institute of Technology general circulation model (MITgcm) (Marshall et al., 1997). The physical ocean circulation is from the Estimating the Circulation and Climate of the Ocean (ECCO) consortium (Wunsch et al., 2009), which synthesizes the MITgcm with nearly all available ocean observations since the era of satellite altimetry (~1992), and provides an adjoint-method-based reconstruction of the three-dimensional, time-varying global ocean and sea-ice state. The ECCO circulation estimates are used to drive an online ecosystem model provided by the MIT Darwin Project (Follows et al., 2007; Follows and Dutkiewicz, 2011; Dutkiewicz et al., 2015), which in turn drives and interacts with marine chemistry variables. ECCO-Darwin uses physical fields from the recently released ECCO LLC270 global ocean and sea-ice data synthesis (Zhang et al., 2018); ECCO LLC270 has ~18 km horizontal grid spacing at high latitudes.

The MIT Darwin Project ecosystem model is used to couple the ECCO physical solution with ocean ecology and carbon chemistry (Brix et al., 2015; Manizza et al., 2019; Carroll et al., 2020). Standard ecological equations and parameters (Dutkiewicz et al., 2019) are employed; the Darwin ecology includes five large-to-small phytoplankton function types (diatoms, other large eukaryotes, *Synechococcus*, and low- and high-light adapted *Prochlorococcus*) and two zooplankton types that graze preferentially on either the large eukaryotes or small picoplankton. Biogeochemical tracers (inorganic nutrients, phytoplankton, zooplankton, dissolved organic matter, and detrital particles) are advected and mixed online by the ECCO LLC270 physical fields. The carbon and nitrogen cycle in Darwin is explicitly represented, along with phosphorus, iron, silicon, oxygen, and alkalinity. To provide an estimate of realistic physical and biogeochemical conditions in the water column we use daily model outputs from January 2012 to March 2013, taken at the grid cell closest to the mooring location.

Statistical Analysis

The relationship between the relative abundance of diatom species assemblages and upper-ocean environmental variables obtained from ECCO-Darwin model during the period March 2012 – January 2013 were analyzed using the ordination technique canonical correspondence analysis (CCA) (vegan package, R-project; ter Braak, 1986; Oksanen et al., 2015).

The water-column environmental data used for this exploration is the result of averaging or integrating each value to the photic layer depth after determining the depth where photosynthetic available radiation (PAR) is 1% of its surface value and above a minimum threshold of 1 μ Ein m^{-2} s^{-1} (**Table 1**).

Preliminary variable reduction was carried out through hierarchical cluster analysis using euclidean distance, principal component analysis, and correlation matrix plots, which were used to determine the main groups of variables (not shown for brevity). Within each main group, a representative variable was selected, based on the relationship with other variables and on previous scientific knowledge, to avoid issues with collinearity and for variable reduction. Thus, for the final analysis, sampling time (month), temperature (temp), sea-ice concentration (seaice), dissolved iron (dFe), stratification (strat), particulate organic carbon (POC), Photosynthethic Active Radiation (PAR) and chlorophyll *a* (chl) were considered. The effect of multicollinearity of environmental variables was checked after modeling using variance inflation factors (VIFs) applied to the CCA. For the species matrix, Hellinger distance was used, as recommended for community compositional data (Legendre and Gallagher, 2001). Significant environmental variables were identified *via* a stepwise procedure, using permutation tests (999 permutations). After the selection of the significant variables, the model was tested a second time through a Monte Carlo global permutation test (999 permutations) to assess the significance of ordination axes, partial terms and global model.

The results of the CCA are presented as an ordination triplot diagram containing the explanatory variables plotted as arrows along with numbers for samples (dates) and diatom species (main groups of diatoms). All statistical analysis was carried out using r-project (ter Braak, 1986; Oksanen et al., 2015).

RESULTS

Environmental Data and Water-Column Characteristics From ECCO-Darwin

We first use ECCO-Darwin, which provides a best-possible estimate of the global-ocean state by assimilating both physical and biogeochemical observation to infer the environmental conditions and the associated seasonal variability at the mooring location during 2012–2013. Larger concentrations of sea ice were observed in June–July 2012 and in December 2012 (**Figure 2A**), when sea ice was advected into the study region from the Weddell Sea (**Supplementary Figure S1**). Sea ice is typically present in the area during austral winter but not in summer. In December 2012 the sea-ice edge was located 200–300 km northward from its typical location, causing the study area to be anomalously covered by 30% sea-ice concentration (**Supplementary Figure S2**). The sea-ice anomaly was such that in over 38 years of satellite data, sea ice was never observed in the area during December (**Supplementary Figure S3**).

Sea-ice concentration from ECCO-Darwin showed general agreement with satellite observations (**Figure 2A**). Upper-ocean properties (surface to 150-m depth) extracted from ECCO-Darwin at the mooring location are shown in **Figure 2** and **Table 1**. Relatively high PAR was observed in austral spring and summer months (January – March 2012, and from October 2012 to January 2013; **Figure 2B**) due to net heat gain from the atmosphere into the ocean. Mean ocean temperatures within the photic layer ranged between −0.1 and 1.8°C and presented maximum values in concordance with high PAR and absence of sea ice (**Figures 2A–C** and **Table 1**). The relatively low stratification increased three-fold in January 2013, due to sea-

TABLE 1 | Water-column environmental variables obtained from ECCO-Darwin at the mooring location. Daily data were averaged (indicated with *) or integrated within the photic layer depth after determining the depth at which photosynthetic available radiation (PAR) equals 1% of its surface value, and above a minimum threshold of 1 μ Ein m^{-2} s^{-1}. Data was subsequently averaged over the time interval corresponding to each trap sample (code E1 to E11). PAR: Photosynthethic Active Radiation; MLD, mixed layer depth; Temp, potential temperature; Sal, salinity; Strat, stratification; NO3, nitrate concentration; PO4, phosphate concentration; SiO_2, silicate concentration; dFe, total dissolved iron concentration; bioSi/OC, biogenic silicon/organic carbon molar ratio; Chl *a*, chlorophyll *a* concentration.

	Date	PAR	MLD	Temp*	Sal*	Strat*	NO3	PO4	SiO4	dFe	bioSi/OC*	Chla
		(μ Ein m-2 s-1)	(m)	(°C)		(kg m-4)	(mmol m-3)	(mmol m-3)	(mmol m-3)	(mmol m–3)	(mol:mol)	(mg Chla m–3)
E1	March 16, 2012	159.1	30	1.81	33.71	-0.0085	150.2	10.8	393.2	0.70	0.450	6.35
E2	April 16, 2012	71.5	28	0.59	33.60	-0.0074	143.7	10.3	364.4	0.74	0.450	4.18
E3	May 16, 2012	33.4	23	–0.61	33.41	–0.0063	140.3	10.0	349.5	0.93	0.449	1.61
E4	June 16, 2012	7.4	33	–1.50	33.42	–0.0009	81.3	5.8	207.9	0.75	0.449	0.12
E5	July 16, 2012	21.9	38	–1.41	33.62	–0.0021	138.2	9.7	314.1	1.53	0.451	0.01
E6	August 16, 2012	76.8	39	–0.88	33.86	–0.0041	250.4	17.5	567.8	3.08	0.452	0.00
E7	September 16, 2012	186.9	36	–0.37	34.00	–0.0043	327.5	22.8	729.0	4.11	0.452	0.00
E8	October 16, 2012	601.0	44	–0.06	34.10	–0.0035	380.3	26.5	857.1	4.95	0.451	0.00
E9	November 16, 2012	801.4	26	0.15	34.05	–0.0048	383.1	26.7	842.8	4.86	0.450	0.01
E10	December 16, 2012	705.5	12	0.20	33.81	–0.0111	325.7	22.7	715.6	3.95	0.448	1.85
E11	January 12, 2013	290.5	13	0.45	33.17	–0.0234	121.3	8.6	289.7	0.70	0.448	8.52

ice melt (**Figure 2D**). Spring-summer peaks of Chl *a* between second half of January–March 2012 and January 2013 were associated with dissolved iron and nitrate consumption by model phytoplankton (**Figures 2E–G**).

Sinking Particulate Material Time Series

Biosiliceous organism fluxes at 1000-m depth ranged between a maximum of 5.6 10^6 valves $m^{-2}d^{-1}$ in June 2012 to a minimum of 2.5 10^6 valves $m^{-2}d^{-1}$ in September 2012 (**Figure 3A**). Diatoms dominated the total siliceous microorganisms during all months, whilst silicoflagellates constitute less than 1% (**Figure 3A**). Diatom fluxes averaged 3.5 10^6 valves $m^{-2}d^{-1}$ and showed marked inter-month variability in terms of assemblage. The large-sized diatom *Corethron pennatum* (Grunow) Ostenfeld (diameter ~47 μm; pervalvar axis ~149 μm) (Annett et al., 2010) and *Chaetoceros* sp. resting spores were dominant during summer (March 2012 and December 2012–January 2013), reaching up to 67% (January 2013) and 25% (March 2012) of the total flux, respectively (**Figures 3B**, **4A,D**). Thalassiosira gracilis (Karsten) Hustedt became more abundant during winter, representing up to 43% of the total diatom flux in June 2012 (**Figures 3B**, **4C**). The diatom assemblage in sinking particles was also explained by the highly silicified *Fragilariopsis kerguelensis* (O'Meara) Hustedt (whose relative contribution remained relatively constant throughout the year, ~26%), the sea-ice related species Fragilariopsis curta (Van Heurck) Hustedt and Fragilariopsis cylindrus (Grunow ex Cleve) Helmcke and Krieger (<7% on average), and the large O*odontellaceae* diatom *Odontella weissflogii* (Grunow) Grunow (reached up to 7%) (**Figures 3B**, **4B,E,F**).

OC and bioSi fluxes varied around averages of 1.53 mmol OC $m^{-2}d^{-1}$ and 2.86 mmol bioSi $m^{-2}d^{-1}$, respectively, and showed clear differences between months (**Figure 3C** and **Table 2**). OC represented 1–2.3% of the total mass flux, and varied from minimum OC values of 0.76 mmol OC $m^{-2}d^{-1}$ in August 2012 to maximum values of 2.38 mmol OC $m^{-2}d^{-1}$ in March 2012. bioSi fluxes were also higher in summer months, especially in December 2012, when bioSi fluxes achieved a maximum of 6.82 bioSi $m^{-2}d^{-1}$ (**Figure 3C** and **Table 2**). Furthermore, the bioSi/OC ratio that varied around a mean of 1.8 showed marked differences during the year, with a maximum of 2.95 in December 2012 (**Figure 3D** and **Table 2**). The carbon ($\delta^{13}C$) and nitrogen ($\delta^{15}N$) isotopic signal of sinking particles varied around mean values of −27.52 and 2.24, respectively; these also showed significant differences over the study period, with summer samples characterized by lower values compared to winter samples (**Figure 3E** and **Table 2**).

Relationships Between Sediment Trap Data and Modeled Environmental Variables

canonical correspondence analysis (CCA; **Figure 5**) evidenced the importance of both 1) upper-ocean hydrographic conditions and 2) sea-ice concentration, in determining diatom species assemblages collected by the sediment trap. The initial model CCA included: Photosynthethic Active Radiation (PAR), sea-ice concentration (sea ice), temperature, dissolved iron (dFe), stratification, chlorophyll a (chl), and particulate organic carbon (POC). POC was excluded due to VIF results, whereas PAR and Chl *a* were excluded on the stepwise procedure from the CCA analysis, due to non significance and low contribution to the model. The CCA final model with only four variables (stratification, temperature, sea ice, and dissolved iron content) explained 89% of the total variance in the species assemblage (adjusted R^2) (**Figure 5**). The model was significant (F = 21.064 m

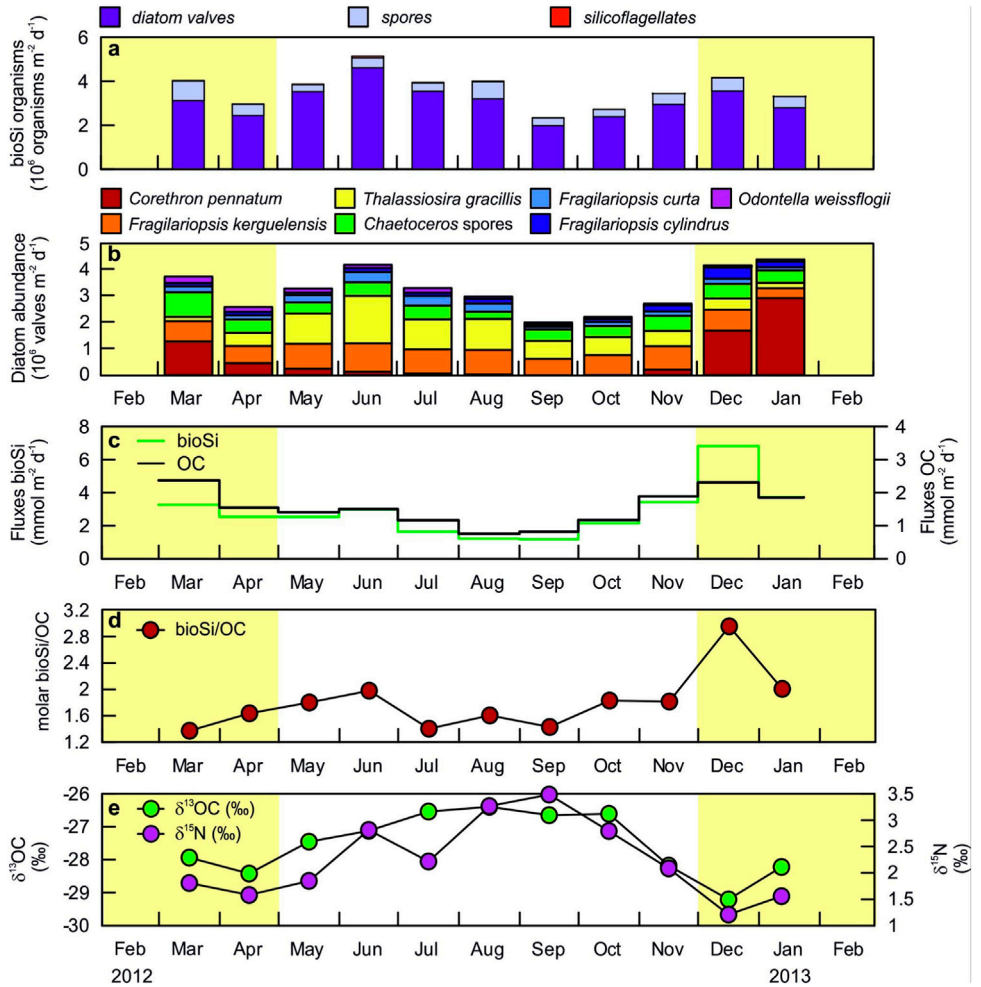

FIGURE 3 | Time series for biosiliceous organisms, diatom assemblage and biogeochemical signals of the settling material recovered by a sediment trap at 1,000 m depth in 2012/13. **(A)** Total biosiliceous (bioSi) organisms. **(B)** main diatom species abundance. **(C)** Fluxes of biogenic silicon (bioSi) and organic carbon (OC). **(D)** OC normalized bioSi molar ratio. **(E)** Stable isotope ratios of C (δ^{13}OC) and N (δ^{15}N). Shaded areas correspond to periods with relatively high Chl *a* concentration in the upper photic layer according to ECCO-Darwin model data (see **Figure 2E**).

p = 0.001), as well as the four environmental terms, with iron being marginally significant (F = 4.38, p = 0.06). The first two axes explained 85 and 5% respectively. Variance inflation factors (VIF) of the four terms were all below two.

The first canonical axis is primarily associated with temperature and stratification. The analysis discriminates between high/low productivity conditions, along with the species associated with each season. Month 1 (January 2013) is representative of a highly-productive period associated with *Corethron pennatum*. Months 6 (June 2012), 8 (August 2012), 9 (September 2012), and 10 (October 2012) correspond to periods of low productivity, associated with *T. gracillis, F. cylindrus,* and *F. curta*. The second canonical axis reflects sea-ice concentration and shows a separation of species associated with sea-ice in summer (*C. pennatum*) and winter (*T. gracillis*, *F. cylindrus,* and *F. curta*) from species less impacted by sea ice (*Chaetoceros* spores and *Odontella weissflogii*). Note also that the oceanographic variables were associated with the first canonical axis, explaining 85% of the variability in species assemblages, whereas sea ice, associated with the second axis, represents only 5% of the species assemblage variability.

DISCUSSION

Biosiliceous organisms sinking at 1,000 m depth in the South Scotia Ridge -a naturally Fe-enriched region (Fugre 1)-, were primarily represented by diatom valves (**Figure 3A**). Silicoflagellates contributed only a small fraction (mean of 0.6%), and based on previous studies, radiolarians, another key contributor to biogenic silicon fluxes, appear in minor proportions in our study site (less than 1%) (Gersonde and Wefer, 1987; Abelmann and Gersonde, 1991). Our data thus corroborates that diatoms are the largest contributors of bioSi fluxes in the study area.

The fact that diatom assemblages observed at depth were primarily composed of heavily silicified species

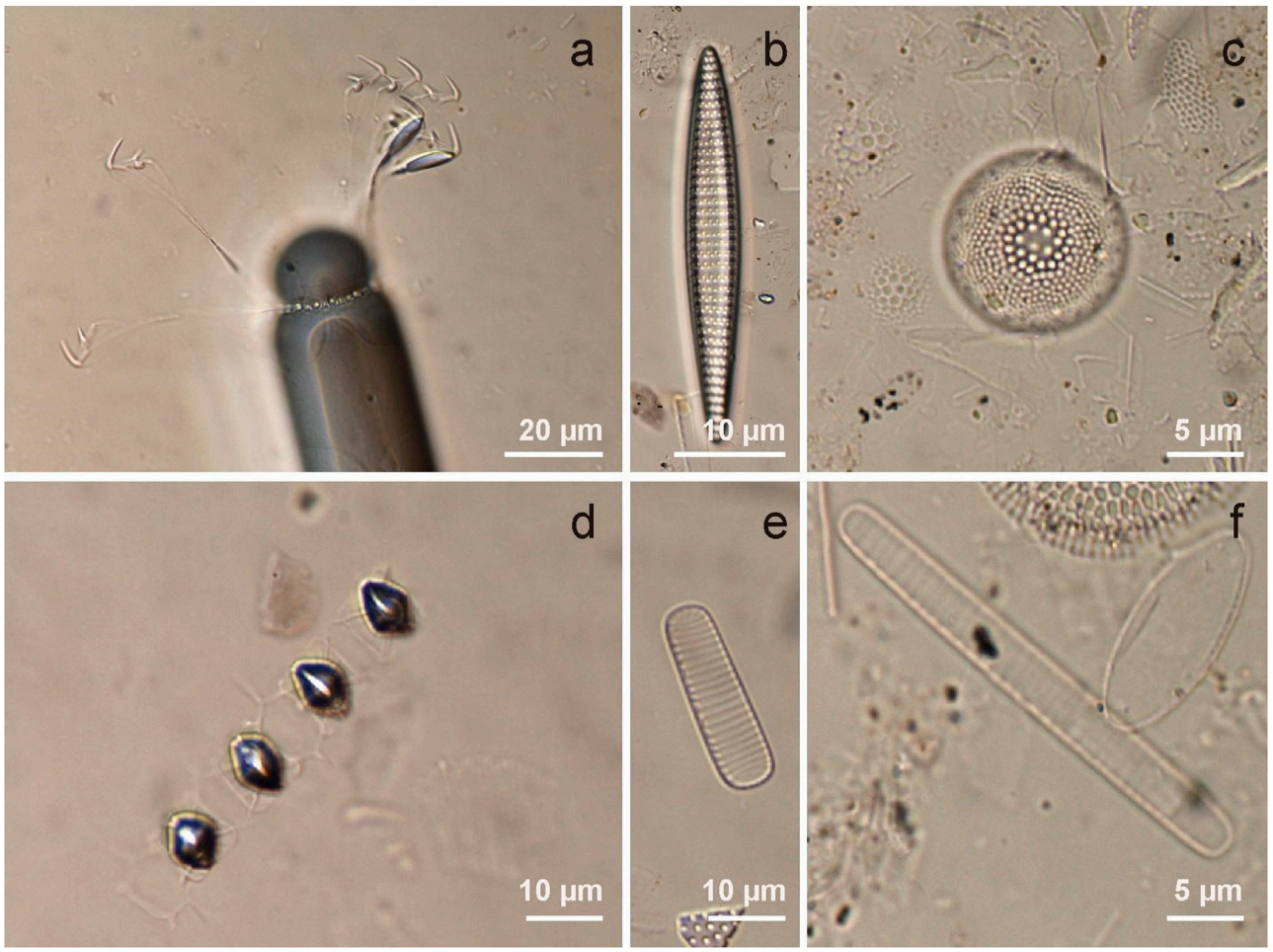

FIGURE 4 | Main diatom species found by microscope examination of the sediment trap samples (<63 µm and >63 µm fractions). **(A)** *Corethron pennatum*. **(B)** *Fragilariopsis kerguelensis.* **(C)** *Thalassiosira gracilis*. **(D)** *Chaetoceros* sp. resting spores. **(E)** *Fragilariopsis curta*. **(F)** *Fragilariopsis cylindrus*).

TABLE 2 | Total mass fluxes (TMF), fluxes and concentrations of main components (OC, organic carbon; IC, inorganic carbon; bioSi, biogenic silicon) and lithogenics (litho). The C and N isotope ratios ($\delta^{13}C$ and $\delta^{15}N$), and molar bioSi/OC ratio are also presented.

	Date	TMF	OC	OC	IC	IC	bioSi	bioSi	Litho	Litho flux	$\delta^{13}C$	$\delta^{15}N$	bioSi/OC
		(mg $m^{-2}d^{-1}$)	%	(mmol $m^{-2}d^{-1}$)	%	(mmol $m^{-2}d^{-1}$)	%	(mmol $m^{-2}d^{-1}$)	%	(mg $m^{-2}d^{-1}$)	(‰)	(‰)	molar
E1	March 16, 2012	1230.45	2.32%	2.38	0.21%	0.21	7.43%	3.26	75.79%	932.54	−27.94	1.81	1.37
E2	April 16, 2012	826.60	2.25%	1.55	0.58%	0.40	8.61%	2.53	69.98%	578.45	−28.42	1.58	1.63
E3	May 16, 2012	1028.76	1.64%	1.41	0.14%	0.12	6.90%	2.53	78.97%	812.40	−27.45	1.85	1.80
E4	June 16, 2012	1560.22	1.16%	1.51	0.14%	0.18	5.35%	2.97	83.65%	1305.14	−27.12	2.82	1.98
E5	July 16, 2012	1097.53	1.28%	1.17	0.18%	0.17	4.19%	1.64	85.87%	942.41	−26.54	2.22	1.40
E6	August 16, 2012	886.28	1.03%	0.76	0.21%	0.16	3.86%	1.22	86.90%	770.18	−26.39	3.27	1.60
E7	September 16, 2012	741.11	1.34%	0.82	0.21%	0.13	4.46%	1.18	84.87%	628.99	−26.65	3.48	1.43
E8	October 16, 2012	892.53	1.58%	1.18	0.19%	0.14	6.76%	2.15	79.01%	705.17	−26.61	2.79	1.83
E9	November 16, 2012	1041.74	2.18%	1.89	0.15%	0.13	9.23%	3.42	72.22%	752.38	−28.18	2.08	1.81
E10	December 16, 2012	1410.86	1.97%	2.31	0.25%	0.30	13.57%	6.82	61.38%	865.94	−29.21	1.21	2.95
E11	January 12, 2013	1227.85	1.81%	1.86	0.44%	0.45	8.50%	3.72	72.34%	888.21	−28.22	1.56	2.00

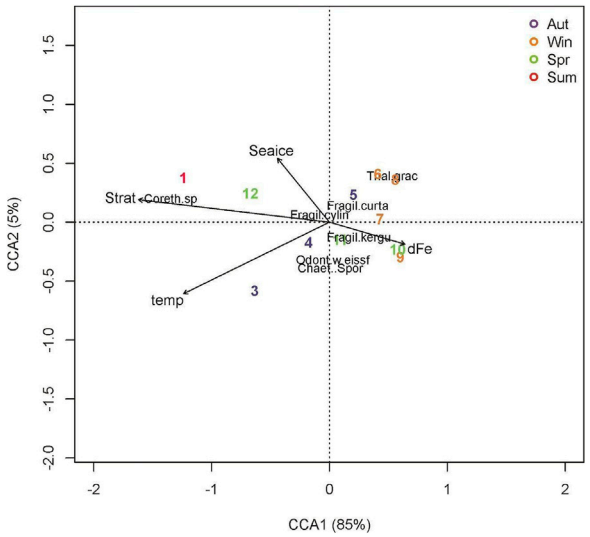

FIGURE 5 | RDA triplot results of the final canonical correspondence analysis (CCA) for the most relevant fossil diatom species registered in our sediment trap during the period March 2012-January 2013 (*Corethron pennatum*: Coreth. sp; *Chaetoceros* spores: Chaet. Spor.; *Fragilariopsis kerguelensis*: Fragil. kergu.; *Thalassiosira gracilis*: Tha. grac; *Fragilariopsis curta*: Fragil. curta; *Fragilariopsis cylindrus*: Fragil. cylin; *Odontella weisflogii:* Odont. weissf), and environmental variables (Seaice: sea ice; Strat: stratification; temp; temperature; dFe: dissolved iron). Numbers from 1 to 12 represent months from January–December. Aut: autumn (purple); Win: winter (orange); Spr: spring (green); Sum: summer (red).

with well-preserved valves (**Figure 4**) highlights the role of silicification in export production, as less-silicified species may be more prone to dissolution in the upper-water column (Annett et al., 2010). We note that other diatom survival strategies such as their huge size (e.g., *C. pennatum*; **Figure 4A**) or the formation of chains (e.g., *F. kerguelensis;* **Figure 4B**) may also protect diatoms against grazing pressure (Hamm et al., 2003; Smetacek et al., 2004), and thus aiding in their ability to reach deep waters. However, the observation of small fragments during microscopic analysis also suggests the presence of less-silicified species, likely affected by dissolution during vertical export (Abelmann and Gersonde, 1991). In this regard, Nelson and Gordon (1982) estimated that, in the SO, up to 18–58% of biogenic opal might be dissolved in the upper 100 m. This implies that our bioSi content, which does not exceed 14% of the total flux (**Table 2**), could represent a relatively small fraction of the bioSi in the productive upper water column.

Diatom assemblage in sinking particles appear to have a major role in setting OC and bioSi export rates during our experiment year, with mean fluxes of 1.53 mmol OC $m^{-2}d^{-1}$ and 2.86 mmol bioSi m^{-2} d^{-1} (**Figure 3C** and **Table 2**)—these are in the higher range of those reported for the SO at 1000-m depth (Honjo, 2004). Strong evidence that enhanced settling of biogenic compounds occurred in close correlation with primary production in the upper water column is provided by the fact that lithogenic fluxes, as a tracer of the input of continental particles, even representing a significant fraction of the sinking material (**Table 2**), were not correlated with either OC nor bioSi fluxes (r^2 = 0.07 and r^2 = 0.05, respectively; **Supplementary Figure S4**). Instead, sinking OC was closely related to bioSi downward flux (r^2 = 0.7; **Supplementary Figure S4**), suggesting that both biogenic compounds are closely linked to diatom's production. This finding and the high proportion of well-preserved valves in the samples also suggests that the majority of diatoms recorded at depth sank from the surface, either as solitary cells or as part of fast-sinking fecal pellets and aggregates (i.e., Smetacek, 1985; Manno et al., 2015). In spite of that, OC and bioSi behave differently during their way down to the bottom. The higher bioSi/OC molar ratios in settling material (mean value of 1.8) when compared with those from ECCO-Darwin in the photic layer (average of ~0.4) (**Table 1** and **Table 2**), point to a preferential export of bioSi relative to OC (DeMaster, 2002; Rembauville et al., 2016). Against this background, Pilskaln et al. (2004) show that the OC exported to 1000-m depth in the SO may represent only 1% of the annual OC production in surface waters, while the preservation efficiency for bioSi is 19%. This means that deep particle fluxes obtained with sediment traps need to be carefully interpreted when attributing OC and bioSi export rates directly to exported particles and diatoms sinking.

Seasonal Succession of Diatoms Assemblage Determining bioSi/OC Variations

OC sinking fluxes down to 1000-m depth were significantly higher during austral summer periods, reflecting the end of the 2012 bloom and the early summer 2012–2013 in agreement with ECCO-Darwin Chl a concentrations (**Figures 2E**, **3C**). The diatom assemblages during these productive periods were principally explained by two bloom-forming diatoms: *Chaetoceros* spp. (represented by their resting spores) and the giant *C. pennatum* (**Figure 3B**). The chain-forming, highly-silicified *Fragilariopsis kerguelensis* also achieved significant proportions (maximum of 25%) during those intervals. This structure of the diatom's community corroborates that OC sequestration was characterized by species that build up high biomass under favorable growth conditions (e.g., *Chaetoceros* and *C. pennatum*) rather than species whose survival strategy is based on the maintenance of relatively constant stocks throughout the year (*F. kerguelensis*) (Smetacek et al., 2002; Timmermans et al., 2004; Peloquin and Smith, 2006).

Corethron pennatum fluxes seems to reflect both the end of the 2012 and the early summer 2012–13 blooms (**Figures 2E**, **3B**). Indeed, the high correlation of *C. pennatum* abundances and δ^{13}OC and δ^{15}N isotopic signals (r^2 = 0.76 and r^2 = 0.77, respectively; **Supplementary Figure S4**) points to this species exert an important role in determining biogeochemical signature of the sinking organic matter (**Figures 3B,E**). This is consistent with previous findings that show a lowering δ^{13}C (−30–−32) of settling OC when *C. pennatum* dominates (Bathmann et al., 1991). Moreover, our data agrees with *in-situ* observations at Marguerite Bay (West Antarctic Peninsula) that attribute the shift in δ^{13}OC isotopic signals of sinking material to contrasting

carbon utilization mechanisms by different diatom species (Henley et al., 2012; Shen et al., 2017).

However, we found some differences in how diatoms community structure regulate bioSi/OC molar ratio during these highly productive periods. In March 2012, despite *Corethron pennatum* is a relevant species, the comparatively high contribution of dense *Chaetoceros* spp. resting spores during this month may explain the relatively low bioSi/OC molar ratio (~1.4) (**Figures 3B,D**). The reduction in this ratio due to enhanced carbon export by diatom resting spores has been observed in other Fe-rich regions of the SO (Salter et al., 2012; Rembauville et al., 2016). In contrast, during early summer 2012–2013, we found a relatively higher export of bioSi relative to OC (**Figure 3D**). The relatively low Chl a during December 2012, coinciding with the arrival of sea ice to our study site, suggests that in addition to the onset of the *Corethron pennatum* bloom (**Figures 2A**,E, **3B**), the high bioSi export occurring during this month might be also explained by advective processes (Abelmann and Gersonde, 1991). The particular increase of the diatom species *F. cylindrus*, which is associated with coastal regions of Antarctica and consolidated sea ice, would also support this hypothesis (Armand et al., 2005; Lundholm and Hasle, 2008). However, the January 2013 maximum in Chl a in the photic layer, which coincide with the massive bloom of *C. pennatum* (**Figures 2E**, **3B**,D) indicates that this large diatom has a significant role in favoring the export of bioSi relatively to OC to the deep ocean (bioSi/OC ratio close to two).

Environmental Factors in the Upper Photic Layer Triggering Seasonal Diatom Assemblage

Environmental conditions from ECCO-Darwin show a seasonal productivity pattern in the photic layer with a maximum of Chl a occurring during summer, in agreement with low macronutrients levels reflecting phytoplankton consumption (**Figures 2E,F**). Modeled Chl *a* and nutrient concentrations generally agree with field data previously obtained near our study site (Korb et al., 2005; Ardelan et al., 2010). The model also reproduces the consumption of dissolved Fe associated with increased summer productivity in the upper layer (**Figure 2G**), although the dFe background levels of ~0.4 nM are typical of non Fe-limited regions (Dulaiova et al., 2009; DeJong et al., 2012; Measures et al., 2013). The Fe-enrichment in this study area is primarily attributed to the arrival of shelf waters from the Antarctic Peninsula (Hatta et al., 2013; Klunder et al., 2014). Additionally, local sea-ice melt -as occurred in January 2013-, is another known source of dissolved Fe in this region (Wang et al., 2014; Lannuzel and Chever, 2016; Monien et al., 2017).

Sinking diatom assemblages, which follow the seasonal trend of environmental variables in the upper photic layer was reflected in the ordination technique canonical correspondence analysis, where we assume that sinking rates are high enough for the particles to sink to 1,000 m depth in less than 30 days (**Figure 5**). This assumption has been considered in previous SO studies (e.g., Pilskaln et al., 2004; Fisher and Karakaç, 2009; Rigual-Hernandez et al., 2019). Considering this, our analysis shows that, apart from irradiance and dFe, other environmental factors such as water column stratification of the water column need to be considered as triggers of phytoplankton blooms. This means that increased stratification, whether it occurs at the end of summer due to heating of the surface layer (March-April 2012), or it is associated with sea ice melt, as occurred in early summer 2012–2013, plays a key role in promoting *C. pennatum* blooms (**Figures 2D**, **3B**, **5**). Such massive blooms have been previously observed close to our study site (Gersonde and (Wefer, 1987; Fryxell, 1989) as well as in the vicinity of South Georgia Island (Froneman et al., 1995, 1997), and at frontal zones in the Atlantic sector of the SO (Laubscher et al., 1993; Bathmann et al., 1997). Our data suggests that sea ice may trigger an early summer bloom, as recently observed in the Arctic Ocean (Boetius et al., 2013; Clement-Kinney et al., 2020). This may occur *via* two main processes. First, local melting of sea ice can result in an additional flux of dissolved nutrients (such as Fe) to near-surface waters (Lannuzel and Chever, 2016). This might provide the extra nutrient supply needed to promote blooms and the high ambient Fe concentrations required by the large, slow growing *C. pennatum* to reach optimal growth rates (Timmermans et al., 2004; Smetacek et al., 2004; Hoffmann et al., 2006). Second, the capacity of *C. pennatum* to adjust its buoyancy would provide an advantage for exploiting nutrients in stratified waters, allowing for blooms under low-light conditions (as reproduced by ECCO-Darwin; **Figure 2B**). Though *C. pennatum* buoyancy adjustment has only been reported by Crawford (1995), this mechanism was observed for other large diatoms (e.g. *Rhizosolenia* and *Proboscia*) (Villareal et al., 1993, 1999a, 1999b; Moore and Villareal, 1996; Singler and Villareal, 2005; Kemp et al., 2006). This supports the idea that *Corethron* might also be adapted to exploit a stratified water column (via sea ice melt) and deep nutrient sources. In this context, Chl *a* maxima associated with sea-ice melt was attributed to *C. pennatum* in the Atlantic sector of the SO (Fryxell, 1989), and in the South Georgia region (Whitehouse et al., 2008; Nunes et al., 2019). The blooming of this large diatom, combined with its morphological characteristics (such as the presence of a set of shorted barbed spines that favor entanglement and aggregation, or its large size that allow scape grazing, probably favor larger export into the deep ocean (Smetacek, 1985; Alldredge and Gotschalk, 1989; Smetacek et al., 2004). Increased sinking of *C. pennatum* half-cell walls may occur due to the fall-down of a sexual reproductive phase event (Crawford, 1995), but the absence of half-cells in the samples prevent us from confirming this hypothesis. Accordingly, this data supports the assumption used by paleoceanographers where *C. pennatum* creates and rapidly exports substantial biomass under stratified conditions during times of enhanced sea-ice melt (Jordan et al., 1991; Leventer et al., 1993; Sedwick et al., 2001; Leventer et al., 2002; Taylor and Sjunneskog, 2002; Maddison et al., 2012; Alley et al., 2018).

The role of stratification in promoting *C. pennatum* blooms is also supported by the observed changes in the sinking organic matter total nitrogen (TN) and OC isotopic composition, which are well-established proxies for assimilation of surface-ocean nitrate and dissolved inorganic carbon (DIC) by phytoplankton (Sigman et al., 1999). Exported organic matter shows relatively low $\delta^{15}N$ values (1.2–1.6‰) in periods when *C. pennatum* dominates the diatoms assemblage (**Figures 3B,E**). These values are significantly lower than the typical summer $\delta^{15}N$ values of surface-ocean nitrate (>5‰) (Sigman et al., 2000), suggesting a shift from high $\delta^{15}N$ -NO3 to low $\delta^{15}N$ -NH_4^+ as the primary nitrogen source exploitable by these large

blooming diatoms. However, this does not agree with the assumption that NH_4^+-assimilating phytoplankton are typically smaller in size (Berg et al., 2011). Another possibility is that phytoplankton utilize under-ice NH_4^+ and DIC with low $\delta^{13}C$ (because of low ventilation). However, low $\delta^{15}N$ and $\delta^{13}OC$ were also recorded during sea-ice free conditions in February 2012. Yet, the robust positive correlation of $\delta^{13}OC$ and $\delta^{15}N$ (r^2 = 0.74; **Supplementary Figure S4**) suggests that the mechanism responsible for low $\delta^{15}N$ is also decreasing the $\delta^{13}OC$ of sinking particles. If assimilation of low ^{13}OC DIC relatively to ambient DIC occurs deeper in the water column, then vertical migration due to buoyancy regulation of *C. pennatum* would also explain the use of lighter ^{14}N from the nutricline and near-surface waters, triggering lower $\delta^{15}N$ in settling particles.

CONCLUSION

Settling material collected by a sediment trap at 1000 m depth in the South Scotia Ridge provides, for the first time, an almost complete annual cycle of diatom abundance and composition in the southern sector of the Scotia Sea. A statistical analysis of in-situ data and realistic ocean biogeochemistry simulation shows that the material collected by the sediment trap reflects changes in upper-ocean environmental conditions. Additionally, sediment trap data provide geochemical evidence that massive *C. pennatum* blooms occuring in highly-stratified waters thrive during early summer sea-ice melt conditions. Consequently, the sedimentation of these large diatoms enhance silicon removal from SO waters. Our results, together with similar studies that report high bioSi/OC ratios in other Fe-rich SO regions, challenge the conventional view of diatoms growing under Fe-replete conditions as drivers of sinking high OC to bioSi fluxes. We conclude that, along with irradiance and dFe, sea ice concentration (which modulates changes in upper-ocean stratification), needs to be considered when determining which environmental factors trigger specific diatoms blooms, that, in turn, determine carbon sequestration. To our knowledge, this is a novel aspect of diatoms ecology in setting bioSi vs. OC sequestration efficiency—a key controlling factor that regulates the stoichiometric relationship of limiting nutrients for primary production. Ultimately, additional studies that combine water column environmental conditions and surface-to-bottom sediment trap data are required to improve our understanding of diatom dynamics and the coupled physical-biogeochemical processes that regulate export in the Southern Ocean.

DATA AVAILABILITY STATEMENT

The datasets presented in this study can be found in online repositories. The names of the repository/repositories and accession number(s) can be found below: The datasets analyzed for this study have been deposited at the Spanish National Polar Data Center (CNDP), http://hielo.igme.es/index.php/en/. ECCO-Darwin model fields are available at: https://data.nas.nasa.gov/ecco.

AUTHOR CONTRIBUTIONS

DZ, AS-V and MMF contributed equally to the writing of the manuscript. MMF conceived, designed the monitoring experiment and acquired the data. AS-V. performed biogeochemical analyses and acquired the data. DZ counted and identified diatom assemblage. DC provided ECCO-Darwin time series and helped with manuscript editing and figure creation. MR performed the statistical analysis. FA provided relevant information for diatoms identification and contributed to the writing of the manuscript. GS contributed with sea-ice analysis and prepared **Supplementary Figures S1–S3**. TC contributed to the writting of the manuscript and provide valuable support during the whole process. All authors read, edited, and approved the final version of the manuscript.

FUNDING

This work was funded by the Spanish Polar Program through the Spanish Research and Innovation (I+D+i) National Plan (grant numbers CTM2009-08287-E/ANT and CTM2011-14056-E/ANT), and supported by the Catalan Government Grups de Recerca Consolidats Grant (2017 SGR 315) and the Internal Research and Technology Development program of the Jet Propulsion Laboratory, California Institute of Technology. DZ was funded by a postdoctoral fellowship (Plan I2C) from Xunta de Galicia (Spain) and performed diatom analysis during her stay at Instituto Português do Mar e da Atmosfera (IPMA), Lisbon, Portugal. Diatom analysis was sponsored by Portuguese national funding through FCT-Fundação para a Ciência e a Tecnologia (UIDB/04326/2020 and DiatBIo PTDC/AAG-GLO/3737/2012 projects). GS was supported by the Deutsche Forschungsgemeinschaft (DFG) in the framework of the priority programme "Antarctic Research with comparative investigations in Arctic ice areas" SPP 1158 by Grant SITAnt (365778379).

ACKNOWLEDGMENTS

The authors are deeply grateful to Joan Puigdefàbregas and Jordi Cateura for their technical assistance in mooring deployment and recovery; Rut Pedrosa-Pàmies and Montse Guart for their help with analytical tasks; the Captain and crew of the R/V Hespérides for their support during the 2012 and 2013 Antarctic cruises.

SUPPLEMENTARY MATERIAL

The Supplementary Material for this article can be found online at: https://www.frontiersin.org/articles/10.3389/feart.2021.579198/full#supplementary-material

Supplementary Figure 1 | Sea ice velocity fields for the months of November 2012, December 2012 and January 2013 obtained from the NASA National Snow and Ice Data Center Distributed Active Archive Center (Tschudi et al.,

2016). Sea ice was strongly advected into the study area during November and December, and the advection stopped in January.

Supplementary Figure 2 | December 2012 sea ice concentration anomaly relative to the reference period 1979–2016. Antarctic Circumpolar Current fronts, after Orsi et al. (1995), are indicated as dashed contours (names labeled). The sediment trap location (60° 24'S; 52° 58'W) is marked by a black star. Gray lines mark parallels and meridians.

Supplementary Figure 3 | Sea ice persistence for the month of December during the 1979–2016 period. Sea-ice persistence gives the frequency of sea ice occurrence (how often sea ice is present) at a given location. Sea ice persistence of 100% means that the area was always covered by sea ice throughout December within the 38-year period 1979–2016; 0% means the opposite: no sea ice was ever present. The mooring location is marked with a star. Sea ice persistence at the mooring location is 2% or 24 days, i.e., 2012 was the only year in which sea ice was observed at that location during the month of December.

Supplementary Figure 4 | Pearson correlation matrix for the sediment trap data. Lithog flux: lithogenic flux (mmol m^{-2} d^{-1}), OC: organic carbon flux (mmol m^{-2} d^{-1}) and relative contribution (%), bioSi: biogenic silicon flux (mmol m^{-2} d^{-1}) and relative contribution (%), biogeochemical variables (d13C= organic carbon isotope ratio; d15N= total nitrogen isotope ratio; bioSi/OC: biogenic silicon/organic carbon molar ratio), and most representative fossil diatoms species (*Corethron pennatum*: Coreth. sp; *Chaetoceros spores*: Chaet.Spor.; *Fragilariopsis kerguelensis*: Fragil.kergu.; *Thalassiosira gracilis*: Thal.grac; *Fragilariopsis curta*: Fragil. curta; *Fragilariopsis cylindrus*: Fragil. cylin; *Odontella weisflogii*: Odont.weissf) abundances expressed in valves m^{-2} d^{-1}).

REFERENCES

Abelmann, A., and Gersonde, R. (1991). Biosiliceous Particle Flux in the Southern Ocean. *Mar. Chem.* 35, 503–536. doi:10.1016/s0304-4203(09)90040-8

Abrantes, F., Gil, I., Lopes, C., and Castro, M. (2005). Quantitative Diatom Analyses-A Faster Cleaning Procedure. *Deep Sea Res. Oceanographic Res. Pap.* 52, 189–198. doi:10.1016/j.dsr.2004.05.012

Alldredge, A., and Gotschalk, C. (1989). Direct Observations of the Mass Flocculation of Diatomblooms - Characteristics, Settling Velocities and Formation of Diatom Aggregates. *Deep- Sea Res.* 36 (2), 159–171 .

Alley, K., Patacca, K., Pike, J., Dunbar, R., and Leventer, A. (2018). Iceberg Alley, East Antarctic Margin: Continuously Laminated Diatomaceous Sediments from the Late Holocene. *Mar. Micropaleontology* 140, 56–68. doi:10.1016/j.marmicro.2017.12.002

Annett, A. L., Carson, D. S., Crosta, X., Clarke, A., and Ganeshram, R. S. (2010). Seasonal Progression of Diatom Assemblages in Surface Waters of Ryder Bay, Antarctica. *Polar Biol.* 33 (1), 13–29. doi:10.1007/s00300-009-0681-7

Ardelan, M. V., Holm-Hansen, O., Hewes, C. D., Reiss, C. S., Silva, N. S., Dulaiova, H., et al. (2010). Natural Iron Enrichment Around the Antarctic Peninsula in the Southern Ocean. *Biogeosciences* 7, 11–25. doi:10.5194/bg-7-11-2010

Armand, L. K., Crosta, X., Romero, O., and Pichon, J.-J. (2005). The Biogeography of Major Diatom Taxa in Southern Ocean Sediments. *Palaeogeogr. Palaeoclimatol. Palaeoecol.* 223, 93–126. doi:10.1016/j.palaeo.2005.02.015

Arrigo, K. R., Robinson, D. H., Worthen, D. L., Dunbar, R. B., DiTullio, G. R., VanWoert, M., et al. (1999). Phytoplankton Community Structure and the Drawdown of Nutrients and CO2 in the Southern Ocean. *Science* 283, 365–367. doi:10.1126/science.283.5400.365

Assmy, P., Smetacek, V., Montresor, M., Klaas, C., Henjes, J., Strass, V. H., et al. (2013). Thick-shelled, Grazer-Protected Diatoms Decouple Ocean Carbon and Silicon Cycles in the Iron-Limited Antarctic Circumpolar Current. *Proc. Natl. Acad. Sci. U.S.A.* 110, 633–638. doi:10.1073/pnas.1309345110

Bathmann, U., Fisher, G., Müller, P. J., and Gerdes, D. (1991). Short-term Variations in Particulate Matter Sedimentation off Kapp Norvegia, Weddell Sea, Antarctica: Relation to Water Mass Advection, Ice Cover, Plankton Biomass and Feeding Activity. *Polar Biol.* 11, 185–195. doi:10.1007/bf00240207

Bathmann, U. V., Scharek, R., Klaas, C., Dubischar, C. D., and Smetacek, V. (1997). Spring Development of Phytoplankton Biomass and Composition in Major Water Masses of the Atlantic Sector of the Southern Ocean. *Deep Sea Res. Part Topical Stud. Oceanography* 44, 51–67. doi:10.1016/s0967-0645(96)00063-x

Battarbee, R. W. (1973). A New Method for the Estimation of Absolute Microfossil Numbers, with Reference Especially to Diatoms. *Limnol. Oceanogr.* 18, 647–653. doi:10.4319/lo.1973.18.4.0647

Berg, G. M., Mills, M. M., Long, M. C., Bellerby, R., Strass, V., Savoye, N., et al. (2011). Variation in Particulate C and N Isotope Composition Following Iron Fertilization in Two Successive Phytoplankton Communities in the Southern Ocean. *Glob. Biogeochem. Cycles* 25, a–n. doi:10.1029/2010gb003824

Bodungen, B. v., Smetacek, V. S., Tilzer, M. M., and Zeitzschel, B. (1986). Primary Production and Sedimentation during spring in the Antarctic Peninsula Region. *Deep Sea Res. A. Oceanographic Res. Pap.* 33, 177–194. doi:10.1016/0198-0149(86)90117-2

Boetius, A., Albrecht, S., Bakker, K., Bienhold, C., Felden, J., Fernandez-Mendez, M., et al. (2013). Export of Algal Biomass from the Melting Arctic Sea Ice. *Science*, 339, 1430–1432. doi:10.1126/science.1231346

Boyd, P. W. (2013). Diatom Traits Regulate Southern Ocean Silica Leakage. *Proc. Nat. Acad. Sci. U.S.A.* 110 (20), 358–359.,

Boyd, P. W., Dillingham, P. W., McGraw, C. M., Armstrong, E. A., Cornwall, C. E., Feng, Y.-y., et al. (2016). Physiological Responses of a Southern Ocean Diatom to Complex Future Ocean Conditions. *Nat. Clim Change* 6, 207–213. doi:10.1038/nclimate2811

Boyd, P. W., Jickells, T., Law, C. S., Blain, S., Boyle, E. A., Buesseler, K. O., et al. (2007). Mesoscale Iron Enrichment Experiments 1993-2005: Synthesis and Future Directions. *Science* 315, 612–617. doi:10.1126/science.1131669

Brix, H., Menemenlis, D., Hill, C., Dutkiewicz, S., Jahn, O., Wang, D., et al. (2015). Using Green's Functions to Initialize and Adjust a Global, Eddying Ocean Biogeochemistry General Circulation Model. *Ocean Model.* 95, 1–14. doi:10.1016/j.ocemod.2015.07.008

Brzezinski, M. A., Pride, C. J., Franck, V. M., Sigman, D. M., Sarmiento, J. L., Matsumoto, K., et al. (2002). A Switch from Si(OH)4to NO3−depletion in the Glacial Southern Ocean. *Geophys. Res. Lett.* 29 (12), 5-1–5-4. doi:10.1029/2001GL014349

Buma, A. G. J., de Baar, H. J. W., Nolting, R. F., and van Bennekom, A. J. (1991). Metal Enrichment Experiments in the Weddell-Scotia Seas: Effects of Iron and Manganese on Various Plankton Communities. *Limnol. Oceanogr.* 36 (8), 1865–1878. doi:10.4319/lo.1991.36.8.1865

Carroll, D., Menemenlis, J. F., Bowman, K. W., Brix, H., Dutkiewicz, S., et al. (2020). Seasonal to Multi-Decadal Air-Sea CO_2 Fluxes from the Data-Constrained ECCO-Darwin Global Ocean Biogeochemistry Model. *J. Adv. Model. Earth Sy.* 12, e2019MS001888. doi:10.1029/2019ms001888

Cavalieri, D., Parkinson, C., Gloersen, P., and Zwally, H. (2016). *Sea Ice Concentrations from Nimbus-7 SMMR and DMSP SSM/I-SSMIS Passive Microwave Data, Version 1. Boulder*, Colorado USA. NASA National Snow and Ice Data Center Distributed Active Archive Center. 1996, updated yearly). doi:10.5067/8GQ8LZQVL0VL

Crawford, R. M. (1995). The Role of Sex in the Sedimentation of a marine Diatom Bloom. *Limnol. Oceanogr.* 40 (1), 200–204. doi:10.4319/lo.1995.40.1.0200

de Baar, H. J. W., de Jong, J. T. M., Bakker, D. C. E., Loscher, B. M., Veth, C., Bathmann, U., et al. (1995). Importance of Iron for Plankton Blooms and Carbon Dioxide Drawdown in the Southern Ocean. *Nature* 373, 6513. doi:10.1038/373412a0

de Jong, J., Schoemann, V., Lannuzel, D., Croot, P., de Baar, H., and Tison, J.-L. (2012). Natural Iron Fertilization of the Atlantic Sector of the Southern Ocean by continental Shelf Sources of the Antarctic Peninsula. *J. Geophys. Res.* 117, G01029. doi:10.1029/2011JG001679

DeMaster, D. J. (2002). The Accumulation and Cycling of Biogenic Silica in the Southern Ocean: Revisiting the marine Silica Budget. *Deep Sea Res. Part Topical Stud. Oceanography* 49, 3155–3167. doi:10.1016/s0967-0645(02)00076-0

Dulaiova, H., Ardelan, M. V., Henderson, P. B., and Charette, M. A. (2009). Shelf-derived Iron Inputs Drive Biological Productivity in the Southern Drake Passage. *Glob. Biogeochem. Cycles* 23, a–n. doi:10.1029/2008GB003406

Dutkiewicz, S., Hickman, A. E., Jahn, O., Gregg, W. W., Mouw, C. B., and Follows, M. J. (2015). Capturing Optically Important Constituents and Properties in a

marine Biogeochemical and Ecosystem Model. *Biogeosciences* 12 (14), 4447–4481. doi:10.5194/bg-12-4447-2015

Dutkiewicz, S., Hickman, A. E., Jahn, O., Henson, S., Beaulieu, C., and Monier, E. (2019). Ocean Colour Signature of Climate Change. *Nat. Commun* 10 (1), 578. doi:10.1038/s41467-019-08457-x

Falkowski, P. G., Barber, R., and Smetacek, V. (1998). Biogeochemical Controls and Feedbacks on Ocean Primary Production. *Science* 281, 200–206. doi:10.1126/science.281.5374.200

Fischer, G., Gersonde, R., and Wefer, G. (2002). Organic Carbon, Biogenic Silica and Diatom Fluxes in the Marginal winter Sea-Ice Zone and in the Polar Front Region: Interannual Variations and Differences in Composition. *Deep Sea Res. Part Topical Stud. Oceanography* 49, 1721–1745. doi:10.1016/s0967-0645(02)00009-7

Fisher, G., and Karakaç, G. (2009). Sinking Rates and Ballast Composition of Particles in the Atlantic Ocean: Implications for the Organic Carbon Fluxes to the Deep Ocean. *Biogeosciences* 6, 85–102. doi:10.5194/bg-6-85-2009

Flexas, M. M., Schodlok, M. P., Padman, L., Menemenlis, D., and Orsi, A. H. (2015). Role of Tides on the Formation of the Antarctic Slope Front at the Weddell-Scotia Confluence. *J. Geophys. Res. Oceans* 120, 3658–3680. doi:10.1002/2014jc010372

Follows, M. J., Dutkiewicz, S., Grant, S., and Chisholm, S. W. (2007). Emergent Biogeography of Microbial Communities in a Model Ocean. *Science* 315, 1843–1846. doi:10.1126/science.1138544

Follows, M. J., and Dutkiewicz, S. (2011). Modeling Diverse Communities of marine Microbes. *Annu. Rev. Mar. Sci.* 3 (1), 427–451. doi:10.1146/annurev-marine-120709-142848

Froneman, P. W., Pakhomov, E. A., and Laubscher, R. K. (1997). Microphytoplankton Assemblages in the Waters Surrounding South Georgia, Antarctica during Austral Summer 1994. *Polar Biol.* 17, 515–522. doi:10.1007/s003000050150

Froneman, P. W., Perissinotto, R., McQuaid, C. D., and Laubscher, R. K. (1995). Summer Distribution of Netphytoplankton in the Atlantic Sector of the Southern Ocean. *Polar Biol.* 15, 77–84. doi:10.1007/bf00241045

Fryxell, G. (1989). Marine Phytoplankton at the Weddell Sea Ice Edge: Seasonal Changes at the Specific Level. *Polar Biol.* 10, 1–18. doi:10.1007/bf00238285

Gersonde, R., and Wefer, G. (1987). Sedimentation of Biogenic Siliceous Particles in Antarctic Waters from the Atlantic Sector. *Mar. Micropaleontology* 11, 311–332. doi:10.1016/0377-8398(87)90004-1

Grigorov, I., Rigual-Hernandez, A. S., Honjo, S., Kemp, A. E. S., and Armand, L. K. (2014). Settling Fluxes of Diatoms to the interior of the Antarctic Circumpolar Current along 170°W. *Deep Sea Res. Part Oceanographic Res. Pap.* 93, 1–13. doi:10.1016/j.dsr.2014.07.008

Hamm, C. E., Merkel, R., Springer, O., Jurkojc, P., Maier, C., Prechtel, K., et al. (2003). Architecture and Material Properties of Diatom Shells Provide Effective Mechanical protection. *Nature* 421, 841–843. doi:10.1038/nature01416

Hatta, M., Measures, C. I., Selph, K. E., Zhou, M., and Hiscock, W. T. (2013). Iron Fluxes from the Shelf Regions Near the South Shetland Islands in the Drake Passage during the Austral-winter 2006. *Deep Sea Res. Part Topical Stud. Oceanography* 90, 89–101. doi:10.1016/j.dsr2.2012.11.003

Henley, S. F., Annett, A. L., Ganeshram, R. S., Carson, D. S., Weston, K., Crosta, X., et al. (2012). Factors Influencing the Stable Carbon Isotopic Composition of Suspended and Sinking Organic Matter in the Coastal Antarctic Sea Ice Environment. *Biogeosciences* 9, 1137–1157. doi:10.5194/bg-9-1137-2012

Heussner, S., Ratti, C., and Carbonne, J. (1990). The PPS 3 Time-Series Sediment Trap and the Trap Sample Processing Techniques Used during the ECOMARGE experiment. *Continental Shelf Res.* 10, 943–958. doi:10.1016/0278-4343(90)90069-x

Heywood, K. J., Naveira Garabato, A. C., Stevens, D. P., and Muench, R. D. (2004). On the Fate of the Antarctic Slope Front and the Origin of the Weddell Front. *J. Geophys. Res.* 109, C06021. doi:10.1029/2003JC002053

Hoffmann, L., Peeken, I., Lochte, K., Assmy, P., and Veldhuis, M. (2006). Different Reactions of Southern Ocean Phytoplankton Size Classes to Iron Fertilization. *Limnol. Oceanogr.* 51 (3), 4231217–4231229. doi:10.4319/lo.2006.51.3.1217

Holland, P. R., and Kwok, R. (2012). Wind-driven Trends in Antarctic Sea-Ice Drift. *Nat. Geosci* 5, 872–875. doi:10.1038/ngeo1627

Holmhansen, O., Naganobu, M., Kawaguchi, S., Kameda, T., Krasovski, I., Tchernyshkov, P., et al. (2004). Factors Influencing the Distribution, Biomass, and Productivity of Phytoplankton in the Scotia Sea and Adjoining Waters. *Deep Sea Res. Part Topical Stud. Oceanography* 51, 1333–1350. doi:10.1016/s0967-0645(04)00083-9

Honjo, S. (2004). Particle export and the Biological Pump in the Southern Ocean. *Antarct. Sci.* 16, 430–501. doi:10.1017/s0954102004002287

Hutchins, D. A., and Bruland, K. W. (1998). Iron-limited Diatom Growth and Si:N Uptake Ratios in a Coastal Upwelling Regime. *Nature* 393, 561–564. doi:10.1038/31203

Ichinomiya, M., Gomi, Y., Nakamachi, M., Honda, M., Fukuchi, M., and Taniguchi, A. (2008). Temporal Variations in the Abundance and Sinking Flux of Diatoms under Fast Ice in Summer Near Syowa Station, East Antarctica. *Polar Sci.* 2, 33–40. doi:10.1016/j.polar.2008.01.001

Jacobs, S. S. (1991). On the Nature and Significance of the Antarctic Slope Front. *Mar. Chem.* 35, 9–24. doi:10.1016/s0304-4203(09)90005-6

Jiang, M., Measures, C. I., Barbeau, K. A., Charette, M. A., Gille, S. T., Hatta, M., et al. (2019). Fe Sources and Transport from the Antarctic Peninsula Shelf to the Southern Scotia Sea. *Deep Sea Res. Part Oceanographic Res. Pap.* 150, 103060. doi:10.1016/j.dsr.2019.06.006

Jordan, R. W., Priddle, J., Pudsey, C. J., Barker, P. F., and Whitehouse, M. J. (1991). Unusual Diatom Layers in Upper Pleistocene Sediments from the Northern Weddell Sea. *Deep Sea Res. Part A. Oceanographic Res. Pap.* 38 (7), 829–843. doi:10.1016/0198-0149(91)90021-7

Kamatani, A., and Oku, O. (2000). Measuring Biogenic Silica in marine Sediments. *Mar. Chem.* 68 (3), 219–229. doi:10.1016/s0304-4203(99)00079-1

Kemp, A. E. S., Pearce, R. B., Grigorov, I., Rance, J., Lange, C. B., Quilty, P., et al. (2006). Production of Giant marine Diatoms and Their export at Oceanic Frontal Zones: Implications for Si and C Flux from Stratified Oceans. *Glob. Biogeochem. Cycles* 20, a–n. doi:10.1029/2006GB002698

Kinney, J. C., Maslowski, W., Osinski, R., Jin, M., Frants, M., Jeffery, N., et al. (2020). Hidden Production: On the Importance of Pelagic Phytoplankton Blooms beneath Arctic Sea Ice. *J. Geophys. Res. Oceans* 125, e2020JC016211. doi:10.1029/2020JC016211

Klunder, M. B., Laan, P., De Baar, H. J. W., Middag, R., Neven, I., and Van Ooijen, J. (2014). Dissolved Fe across the Weddell Sea and Drake Passage: Impact of DFe on Nutrient Uptake. *Biogeosciences* 11, 651–669. doi:10.5194/bg-11-651-2014

Korb, R. E., Whitehouse, M. J., Thorpe, S. E., and Gordon, M. (2005). Primary Production across the Scotia Sea in Relation to the Physico-Chemical Environment. *J. Mar. Syst.* 57, 231–249. doi:10.1016/j.jmarsys.2005.04.009

Krause, J. W., and Lomas, M. W. (2020). Understanding Diatoms' Past and Future Biogeochemical Role in High-Latitude Seas. *Geophys. Res. Lett.* 47, e2019GL085602. doi:10.1029/2019GL085602

Landry, M. R., Selph, K. E., Brown, S. L., Abbott, M. R., Measures, C. I., Vink, S., et al. (2002). Seasonal Dynamics of Phytoplankton in the Antarctic Polar Front Region at 170°W. *Deep Sea Res. Part Topical Stud. Oceanography* 49, 1843–1865. doi:10.1016/s0967-0645(02)00015-2

Lannuzel, D., Chever, F., van der Merwe, P. C., Janssens, J., Roukaerts, A., Cavagna, A.-J., et al. (2016). Iron Biogeochemistry in Antarctic Pack Ice during SIPEX-2. *Deep Sea Res. Part Topical Stud. Oceanography* 131, 111–122. doi:10.1016/j.dsr2.2014.12.003

Laubscher, R. K., Perissinotto, R., and McQuaid, C. D. (1993). Phytoplankton Production and Biomass at Frontal Zones in the Atlantic Sector of the Southern Ocean. *Polar Biol.* 13, 471–481. doi:10.1007/bf00233138

Legendre, P., and Gallagher, E. D. (2001). Ecologically Meaningful Transformations for Ordination of Species Data. *Oecologia* 129, 271–280. doi:10.1007/s004420100716

Leventer, A., Domack, E., Barkoukis, A., McAndrews, B., and Murray, J. (2002). Laminations from the Palmer Deep: A Diatom-Based Interpretation. *Paleoceanography* 17, 3–1. doi:10.1029/2001PA000624

Leventer, A., Dunbar, R. B., and DeMaster, D. J. (1993). Diatom Evidence for Late Holocene Climatic Events in Granite Harbor, Antarctica. *Paleoceanography* 8 (3), 373–386. doi:10.1029/93pa00561

Leventer, A. (1991). Sediment Trap Diatom Assemblages from the Northern Antarctic Peninsula Region. *Deep Sea Res. Part A. Oceanographic Res. Pap.* 38, 1127–1143. doi:10.1016/0198-0149(91)90099-2

Lundholm, N., and Hasle, G. R. (2008). Are Fragilariopsis Cylindrus and Fragilariopsis Nana Bipolar Diatoms? - Morphological and Molecular Analyses of Two Sympatic Species. *Nova Hedwigia* 133, 231–250 .

Maddison, E. J., Pike, J., and Dunbar, R. (2012). Seasonally Laminated Diatom-Rich Sediments from Dumont d'Urville Trough, East Antarctic Margin: Late-

Holocene Neoglacial Sea-Ice Conditions. *The Holocene* 22 (8), 857–875. doi:10.1177/0959683611434223

Manizza, M., Menemenlis, D., Zhang, H., and Miller, C. E. (2019). Modeling the Recent Changes in the Arctic Ocean CO 2 Sink (2006-2013). *Glob. Biogeochem. Cycles* 33, 420–438. doi:10.1029/2018gb006070

Manno, C., Stowasser, G., Enderlein, P., Fielding, S., and Tarling, G. A. (2015). The Contribution of Zooplankton Faecal Pellets to Deep-Carbon Transport in the Scotia Sea (Southern Ocean). *Biogeosciences* 12, 1955–1965. doi:10.5194/bg-12-1955-2015

Marchetti, A., and Cassar, N. (2009). Diatom Elemental and Morphological Changes in Response to Iron Limitation: a Brief Review with Potential Paleoceanographic Applications. *Geobiology* 7 (4), 419–431. doi:10.1111/j.1472-4669.2009.00207.x

Marshall, J., Adcroft, A., Hill, C., Perelman, L., and Heisey, C. (1997). A Finite-Volume, Incompressible Navier Stokes Model for Studies of the Ocean on Parallel Computers. *J. Geophys. Res.* 102, 5753–5766. doi:10.1029/96jc02775

Martin, J. H., Gordon, R. M., and Fitzwater, S. E. (1990). Iron in Antarctic Waters. *Nature* 345, 156–158. doi:10.1038/345156a0

Matsumoto, K., SarmientoBrzezinski, J. L. M. A., and Brzezinski, M. A. (2002). Silicic Acid Leakage from the Southern Ocean: A Possible Explanation for Glacial atmosphericpCO2. *Glob. Biogeochem. Cycles* 16, 5–1. doi:10.1029/2001GB001442

Measures, C. I., Brown, M. T., Selph, K. E., Apprill, A., Zhou, M., Hatta, M., et al. (2013). The Influence of Shelf Processes in Delivering Dissolved Iron to the HNLC Waters of the Drake Passage, Antarctica. *Deep Sea Res. Part Topical Stud. Oceanography* 90, 77–88. doi:10.1016/j.dsr2.2012.11.004

Monien, D., Monien, P., Brünjes, R., Widmer, T., Kappenberg, A., Silva Busso, A. A., et al. (2017). Meltwater as a Source of Potentially Bioavailable Iron to Antarctica Waters. *Antarctic Sci.* 29, 277–291. doi:10.1017/S095410201600064X

Moore, J., and Villareal, T. (1996). Buoyancy and Growth Characteristics of Three Positively Buoyant marine Diatoms. *Mar. Ecol. Prog. Ser.* 132 (1–3), 203–213. doi:10.3354/meps132203

Mortlock, R. A., and Froelich, P. N. (1989). A Simple Method for the Rapid Determination of Biogenic Opal in Pelagic marine Sediments. *Deep Sea Res. Part A. Oceanographic Res. Pap.* 36, 1415–1426. doi:10.1016/0198-0149(89)90092-7

Naveira Garabato, A. C., Heywood, K. J., and Stevens, D. P. (2002). Modification and Pathways of Southern Ocean Deep Waters in the Scotia Sea. *Deep Sea Res. Part Oceanographic Res. Pap.* 49, 681–705. doi:10.1016/s0967-0637(01)00071-1

Nelson, D. M., and Gordon, L. I. (1982). Production and Pelagic Dissolution of Biogenic Silica in the Southern Ocean. *Geochimica et Cosmochimica Acta* 46, 491–501. doi:10.1016/0016-7037(82)90153-3

Nunes, S., Latasa, M., Delgado, M., Emelianov, M., Simó, R., and Estrada, M. (2019). Phytoplankton Community Structure in Contrasting Ecosystems of the Southern Ocean: South Georgia, South Orkneys and Western Antarctic Peninsula. *Deep Sea Res. Part Oceanographic Res. Pap.* 151, 103059. doi:10.1016/j.dsr.2019.06.005

Oksanen, J., Blanchet, F. G., Friendly, M., Kindt, R., Legendre, P., McGlinn, D., et al. (2015). Vegan: Community Ecology. Avaliable at: http://CRAN.R-project.org/package=vegan (Accessed March 20, 2016).

Orsi, A. H., Nowlin, W. D., Jr., and Whitworth, T., III (1993). On the Circulation and Stratification of the Weddell Gyre. *Deep Sea Res. Part Oceanographic Res. Pap.* 40, 169–203. doi:10.1016/0967-0637(93)90060-g

Orsi, A. H., Whitworth, T., III, and Nowlin, W. D., Jr (1995). On the Meridional Extent and Fronts of the Antarctic Circumpolar Current. *Deep Sea Res. Part Oceanographic Res. Pap.* 42, 641–673. doi:10.1016/0967-0637(95)00021-w

Palmer, M., Gomis, D., Flexas, M. d. M., Jordà, G., Jullion, L., Tsubouchi, T., et al. (2012). Water Mass Pathways and Transports over the South Scotia Ridge West of 50°W. *Deep Sea Res. Part Oceanographic Res. Pap.* 59, 8–24. doi:10.1016/j.dsr.2011.10.005

Patterson, S. L., and Sievers, H. A. (1980). The Weddell-Scotia Confluence. *J. Phys. Oceanogr.* 10, 1584–1610. doi:10.1175/1520-0485(1980)010<1584:twsc>2.0.co;2

Peloquin, J. A., and Smith, W. O., Jr (2006). The Role of Phytoplankton Size on Photochemical Recovery during the Southern Ocean Iron experiment. *J. Phycol.* 42, 1016–1027. doi:10.1111/j.1529-8817.2006.00266.x

Pilskaln, C. H., Manganini, S. J., Trull, T. W., Armand, L., Howard, W., Asper, V. L., et al. (2004). Geochemical Particle Fluxes in the Southern Indian Ocean Seasonal Ice Zone: Prydz Bay Region, East Antarctica. *Deep Sea Res. Part Oceanographic Res. Pap.* 51, 307–332. doi:10.1016/j.dsr.2003.10.010

Pondaven, P., Ragueneau, O., Tréguer, P., Hauvespre, A., Dezileau, L., and Reyss, J. L. (2000). Resolving the 'opal Paradox' in the Southern Ocean. *Nature* 405, 168–172. doi:10.1038/35012046

Quéguiner, B. (2013). Iron Fertilization and the Structure of Planktonic Communities in High Nutrient Regions of the Southern Ocean. *Deep Sea Res. Part Topical Stud. Oceanography* 90, 43–54. doi:10.1016/j.dsr2.2012.07.024

Ragueneau, O., Tréguer, p., Leynaert, A., Anderson, R. F., Brzezinski, M. A., DeMaster, D. J., et al. (2000). A Review of the Si Cycle in the Modern Ocean: Recent Progress and Missing Gaps in the Application of Biogenic Opal as a Paleoproductivity Proxy. *Glob. Planet. Change* 26, 317–365. doi:10.1016/s0921-8181(00)00052-7

Rembauville, M., Blain, S., Blain, S., Armand, L., Quéguiner, B., and Salter, I. (2015). Export Fluxes in a Naturally Iron-Fertilized Area of the Southern Ocean - Part 2: Importance of Diatom Resting Spores and Faecal Pellets for export. *Biogeosciences* 12, 3171–3195. doi:10.5194/bg-12-3171-2015

Rembauville, M., Manno, C., Tarling, G. A., Blain, S., and Salter, I. (2016). Strong Contribution of Diatom Resting Spores to Deep-Sea Carbon Transfer in Naturally Iron-Fertilized Waters Downstream of South Georgia. *Deep Sea Res. Part Oceanographic Res. Pap.* 115, 22–35. doi:10.1016/j.dsr.2016.05.002

Rembauville, M., Salter, I., Dehairs, F., Miquel, J.-C., and Blain, S. (2018). Annual Particulate Matter and Diatom export in a High Nutrient, Low Chlorophyll Area of the Southern Ocean. *Polar Biol.* 41, 25–40. doi:10.1007/s00300-017-2167-3

Rigual-Hernández, A. S., Pilskaln, C. H., Cortina, A., Abrantes, F., and Armand, L. K. (2019). Diatom Species Fluxes in the Seasonally Ice-Covered Antarctic Zone: New Data from Offshore Prydz Bay and Comparison with Other Regions from the Eastern Antarctic and Western Pacific Sectors of the Southern Ocean. *Deep Sea Res. Part Topical Stud. Oceanography* 161, 92–104. doi:10.1016/j.dsr2.2018.06.005

Rigual-Hernández, A. S., Trull, T. W., Bray, S. G., and Armand, L. K. (2016). The Fate of Diatom Valves in the Subantarctic and Polar Frontal Zones of the Southern Ocean: Sediment Trap versus Surface Sediment Assemblages. *Palaeogeogr. Palaeoclimatol. Palaeoecol.* 457, 129–143. doi:10.1016/j.palaeo.2016.06.004

Rigual-Hernández, A. S., Trull, T. W., Bray, S. G., Closset, I., and Armand, L. K. (2015). Seasonal Dynamics in Diatom and Particulate export Fluxes to the Deep Sea in the Australian Sector of the Southern Antarctic Zone. *J. Mar. Syst.* 142, 62–74. doi:10.1016/j.jmarsys.2014.10.002

Salter, I., Kemp, A. E. S., Moore, C. M., Lampitt, R. S., Wolff, G. A., and Holtvoeth, J. (2012). Diatom Resting Spore Ecology Drives Enhanced Carbon export from a Naturally Iron-Fertilized Bloom in the Southern Ocean. *Glob. Biogeochem. Cycles* 26, a–n. doi:10.1029/2010GB003977

Salter, I., Lampitt, R. S., Sanders, R., Poulton, A., Kemp, A. E. S., Boorman, B., et al. (2007). Estimating Carbon, Silica and Diatom export from a Naturally Fertilised Phytoplankton Bloom in the Southern Ocean Using PELAGRA: A Novel Drifting Sediment Trap. *Deep Sea Res. Part Topical Stud. Oceanography* 54, 2233–2259. doi:10.1016/j.dsr2.2007.06.008

Sanchez, N., Reiss, C. S., Holm-Hansen, O., Hewes, C. D., Bizsel, K. C., and Ardelan, M. V. (2019). Weddell-Scotia confluence Effect on the Iron Distribution in Waters Surrounding the South Shetland (Antarctic Peninsula) and South Orkney (Scotia Sea) Islands during the Austral Summer in 2007 and 2008. *Front. Mar. Sci.* 6, 771. doi:10.3389/fmars.2019.00771

Sarmiento, J. L., Gruber, N., Brzezinski, M. A., and Dunne, J. P. (2004). High-latitude Controls of Thermocline Nutrients and Low Latitude Biological Productivity. *Nature* 427, 56–60. doi:10.1038/nature02127

Sedwick, P. N., Harris, P. T., Robertson, L. G., McMurtry, G. M., Cremer, M. D., and Robinson, P. (2001). Holocene Sediment Records from the continental Shelf of Mac. Robertson Land, East Antarctica. *Paleoceanography* 16 (2), 212–225. doi:10.1029/2000pa000504

Shen, C., Dupont, C. L., and Hopkinson, B. M. (2017). The Diversity of CO2-concentrating Mechanisms in marine Diatoms as Inferred from Their Genetic Content. *J. Exp. Bot.* 68, 3937–3948. doi:10.1093/jxb/erx163

Sigman, D. M., Altabet, M. A., McCorkle, D. C., Francois, R., and Fischer, G. (1999). The δ15N of Nitrate in the Southern Ocean: Consumption of Nitrate in

Surface Waters. *Glob. Biogeochem. Cycles* 13, 1149–1166. doi:10.1029/1999gb900038

Sigman, D. M., Altabet, M. A., McCorkle, D. C., Francois, R., and Fischer, G. (2000). The δ15N of Nitrate in the Southern Ocean: Nitrogen Cycling and Circulation in the Ocean interior. *J. Geophys. Res.* 105, 19599–19614. doi:10.1029/2000jc000265

Singler, H. R., and Villareal, T. A. (2005). Nitrogen Inputs into the Euphotic Zone by Vertically Migrating Rhizosolenia Mats. *J. Plankton Res.* 27, 545–556. doi:10.1093/plankt/fbi030

Smetacek, V., Assmy, P., and Henjes, J. (2004). The Role of Grazing in Structuring Southern Ocean Pelagic Ecosystems and Biogeochemical Cycles. *Antartic Sci.* 16 (4), 541–558. doi:10.1017/s0954102004002317

Smetacek, V., Klaas, C., Menden-Deuer, S., and Rynearson, T. A. (2002). Mesoscale Distribution of Dominant Diatom Species Relative to the Hydrographical Field along the Antarctic Polar Front. *Deep Sea Res. Part Topical Stud. Oceanography* 49, 3835–3848. doi:10.1016/s0967-0645(02)00113-3

Smetacek, V., Klaas, C., Strass, V. H., Assmy, P., Montresor, M., Cisewski, B., et al. (2012). Deep Carbon export from a Southern Ocean Iron-Fertilized Diatom Bloom. *Nature* 487, 313–319. doi:10.1038/nature11229

Smetacek, V. S. (1985). Role of Sinking in Diatom Life-History Cycles: Ecological, Evolutionary and Geological Significance. *Mar. Biol.* 84, 239–251. doi:10.1007/bf00392493

Spreen, G., Kaleschke, L., and Heygster, G. (2008). Sea Ice Remote Sensing Using AMSR-E 89-GHz Channels. *J. Geophys. Res.* 113, C02S03. doi:10.1029/2005JC0033810.1029/2005jc003384

Takeda, S. (1998). Influence of Iron Availability on Nutrient Consumption Ratio of Diatoms in Oceanic Waters. *Nature* 393, 774–777. doi:10.1038/31674

Taylor, F., and Sjunneskog, C. (2002). Postglacial marine Diatom Record of the Palmer Deep, Antarctic Peninsula (ODP Leg 178, Site 1098) 2. Diatom Assemblages. *Paleoceanography* 17 (3), 2–1. doi:10.1029/2000pa000564

ter Braak, C. J. F. (1986). Canonical Correspondence Analysis: a New Eigenvector Technique for Multivariate Direct Gradient Analysis. *Ecology* 67, 1167–1179. doi:10.2307/1938672

Thompson, A. F., and Youngs, M. K. (2013). Surface Exchange between the Weddell and Scotia Seas. *Geophys. Res. Lett.* 40, 5920–5925. doi:10.1002/2013gl058114

Timmermans, K. R., van der Wagt, B., and de Baar, H. J. W. (2004). Growth Rates, Half-Saturation Constants, and Silicate, Nitrate, and Phosphate Depletion in Relation to Iron Availability of Four Large, Open-Ocean Diatoms from the Southern Ocean. *Limnol. Oceanogr.* 49, 2141–2151. doi:10.4319/lo.2004.49.6.2141

Tréguer, P., Bowler, C., Moriceau, B., Dutkiewicz, S., Gehlen, M., Aumont, O., et al. (2017). Influence of Diatom Diversity on the Ocean Biological Carbon Pump. *Nat. Geosci* 11, 27–37. doi:10.1038/s41561-017-0028-x

Tschudi, M., Fowler, C., Maslanik, J., Stewart, J. S., and Meier, W. (2016). *Polar Pathfinder Daily 25 Km EASE-Grid Sea Ice Motion Vectors, Version 3. Boulder*, Colorado USA. NASA National Snow and Ice Data Center Distributed Active Archive Center. doi:10.5067/O57VAIT2AYYY

Villareal, T. A., Altabet, M. A., and Culver-Rymsza, K. (1993). Nitrogen Transport by Vertically Migrating Diatom Mats in the north Pacific Ocean. *Nature* 363, 709–712. doi:10.1038/363709a0

Villareal, T. A., Joseph, L., Brzezinski, M. A., Shipe, R. F., Lipschultz, F., and Altabet, M. A. (1999b). Biological and Chemical Characteristics of the Giant Diatom Ethmodiscus (Bacillariophyceae) in the central North Pacific Gyre. *J. Phycol.* 35, 896–902. doi:10.1046/j.1529-8817.1999.3550896.x

Villareal, T. A., Pilskaln, C., Brzezinski, M., Lipschultz, F., Dennett, M., and Gardner, G. B. (1999a). Upward Transport of Oceanic Nitrate by Migrating Diatom Mats. *Nature* 397, 423–425. doi:10.1038/17103

Wang, S., Bailey, D., Lindsay, K., Moore, J. K., and Holland, M. (2014). Impact of Sea Ice on the marine Iron Cycle and Phytoplankton Productivity. *Biogeosciences* 11, 4713–4731. doi:10.5194/bg-11-4713-2014

Whitehouse, M. J., Korb, R. E., A., A., Atkinson, S. E., and Gordon, M. (2008). Formation, Transport and Decay of an Intense Phytoplankton Bloom within the High-Nutrient Low-Chlorophyll belt of the Southern Ocean. *J. Mar. Syst.* 70, 150–167. doi:10.1016/j.jmarsys.2007.05.003

Whitworth, T., III, Nowlin, W. D., Jr., Orsi, A. H., Locarnini, R. A., and Smith, S. G. (1994). Weddell Sea Shelf Water in the Bransfield Strait and Weddell-Scotia Confluence. *Deep Sea Res. Part Oceanographic Res. Pap.* 41, 629–641. doi:10.1016/0967-0637(94)90046-9

Wunsch, C., Heimbach, P., Ponte, R., and Fukumori, I. (2009). The Global General Circulation of the Ocean Estimated by the ECCO-Consortium. *Oceanog.* 22, 88–103. doi:10.5670/oceanog.2009.41

Youngs, M. K., Thompson, A. F., Flexas, M. M., and Heywood, K. J. (2015). Weddell Sea export Pathways from Surface Drifters. *J. Phys. Oc.* 45, 1068–1085. doi:10.1175/jpo-d-14-0103.1

Zhang, H., Menemenlis, D., and Fenty, I. G. (2018). ECCO LLC270 Ocean-Ice State Estimate. Available at: http://hdl.handle.net/1721.1/119821 (Accessed October 14, 2020).

Conflict of Interest: The authors declare that the research was conducted in the absence of any commercial or financial relationships that could be construed as a potential conflict of interest.

frontiers in Earth Science

ORIGINAL RESEARCH
published: 16 August 2021
doi: 10.3389/feart.2021.614703

Optical Properties and Biochemical Indices of Marine Particles in the Open Mediterranean Sea: The *R/V* Maria S. Merian Cruise, March 2018

*Spyros Chaikalis[1,2], Constantine Parinos[1], Jürgen Möbius[3], Alexandra Gogou[1], Dimitris Velaoras[1], Dagmar Hainbucher[4], Sarantis Sofianos[2], Toste Tanhua[5], Vanessa Cardin[6], Emmanouil Proestakis[7], Vassilis Amiridis[7], Afrodite Androni[1] and Aristomenis Karageorgis[1]**

[1]Institute of Oceanography, Hellenic Centre for Marine Research (HCMR), Anavyssos, Greece, [2]Ocean Physics and Modelling Group, National and Kapodistrian University of Athens, Athens, Greece, [3]Institute for Coastal Research, Helmholtz-Zentrum Geesthacht, Geesthacht, Germany, [4]Institut für Meereskunde, CEN, Universität Hamburg, Hamburg, Germany, [5]GEOMAR Helmholtz Centre for Ocean Research Kiel, Kiel, Germany, [6]Istituto Nazionale di Oceanografia e di Geofisica Sperimentale - OGS, Sgonico, Italy, [7]Institute for Astronomy, Astrophysics, Space Applications and Remote Sensing, National Observatory of Athens, Athens, Greece

OPEN ACCESS

Edited by:
Gerhard Josef Herndl,
University of Vienna, Austria

Reviewed by:
Alexander B. Bochdansky,
Old Dominion University,
United States
Travis Blake Meador,
Academy of Sciences of the Czech Republic (ASCR), Czechia

***Correspondence:**
Aristomenis Karageorgis
ak@hcmr.gr

Specialty section:
This article was submitted to Biogeoscience, a section of the journal Frontiers in Earth Science

Received: 06 October 2020
Accepted: 30 July 2021
Published: 16 August 2021

Citation:
Chaikalis S, Parinos C, Möbius J, Gogou A, Velaoras D, Hainbucher D, Sofianos S, Tanhua T, Cardin V, Proestakis E, Amiridis V, Androni A and Karageorgis A (2021) Optical Properties and Biochemical Indices of Marine Particles in the Open Mediterranean Sea: The R/V Maria S. Merian Cruise, March 2018. Front. Earth Sci. 9:614703. doi: 10.3389/feart.2021.614703

A rich data set on particulate matter optical properties and parameters (beam attenuation coefficient, volume concentration, particle size and PSD slope), accompanied by measurements of biochemical indices (particulate organic carbon, particulate nitrogen and their stable isotopic composition) was obtained from the surface to deep waters across the Mediterranean Sea, in March-April 2018. A decrease of beam attenuation coefficients, total particle volume concentrations, particulate organic carbon and nitrogen concentrations was noted towards the eastern Mediterranean Sea (EMed) in comparison to the western Mediterranean Sea (WMed). LISST-derived optical properties were significantly correlated with water mass characteristics. Overall, the most turbid water mass identified in the Mediterranean Sea was the Surface Atlantic water (AW), and the most transparent was the Transitional Mediterranean Water (TMW) in the Cretan Sea, whereas a general decrease in particulate matter concentration is observed from the WMed towards the EMed. Relatively depleted δ^{13}C-POC values in the particle pool of the open Mediterranean Sea can be attributed to contribution from terrestrial inputs, mainly via atmospheric deposition. Throughout the entire water column, a significant positive correlation between particle beam attenuation coefficient and particulate organic carbon concentration is observed in the open Mediterranean Sea. Such relationship suggests the predominance of organic particles with biogenic origin. POC concentration and particle median diameter D_{50} are significantly and negatively correlated both in the WMed and the EMed Sea, confirming that small particles are POC-rich. At depth, a prominent decrease of most measured parameters was observed, with the exception of particle median diameter that increased substantially in the EMed towards the deep sea, suggesting potentially enhanced aggregation processes. The low particle size distribution slope ξ observed in the EMed, corresponding to larger particle populations, supports the above notion. Basin-wide Rayleigh-type isotopic fractionation in vertical profiles of

δ^{15}N-PN across the Mediterranean Sea, underlines the differences in the trophic characters of the two sub-basins and highlights the role of circulation changes on biogeochemical parameters and the redistribution of particulate matter as a source of nutrients in the water column.

Keywords: particle dynamics, optical oceanography, LISST-Deep, PSD slope, POC, PN, δ^{13}C-POC, δ^{15}N-PN

INTRODUCTION

The vertical distribution, horizontal distribution, and export at depth of particulate matter (PM) in the world ocean have been the subject of numerous studies over the past decades (Volk and Hoffert, 1985; Honjo et al., 2008; Jeandel et al., 2015). PM is mostly generated in the ocean's surface layers through primary production and the small fraction that survives remineralization in the upper ocean is exported through physical mixing, aggregation and disaggregation, repackaging and gravitational sinking downwards to the deep sea. During its transit towards the seafloor, most of the particulate organic carbon (POC) particulate nitrogen (PN) and particulate organic phosphorus (POP) is returned to their inorganic forms and redistributed into the water column. This redistribution determines the surface concentration of dissolved CO_2 and inorganic nutrients and hence the rate at which the ocean can absorb CO_2 from the atmosphere. The ability to quantitatively predict the depth profile of POC remineralization is therefore critical for evaluating the response of the ocean carbon cycle to global change. Processes involved in particle formation, remineralization and transport from the epipelagic to the mesopelagic and bathypelagic ocean are tightly connected to the biochemistry of marine organisms and the biodiversity and health of marine ecosystems.

Optical methods have been used for decades to describe PM behavior in the marine environment, as particle quality, distribution, abundance and size, directly affect light scattering in the ocean, and subsequently regulate the oceans' optical properties and the water-leaving radiance measured remotely from satellites (Twardowski et al., 2001; Buonassissi and Dierssen, 2010; Karageorgis et al., 2012; Kostadinov et al., 2012; Xi et al., 2014). In particular, particle size distribution quantifies the concentration of particles as a function of particle size, playing a critical role in the determinations of the light scattering and absorption properties of seawater, and thus the penetration of light within the ocean (Runyan et al., 2020). Despite its utility, little is known about the natural variability of the particle size distribution (PSD) due to challenges inherent with its measurement (Buonassissi and Dierssen, 2010). This holds particularly true in the case of deep regional seas, such as the oligotrophic ocean, where very limited particle size data are available to the oceanographic community, mainly due to instrumental limitations, since instruments measuring *in-situ* particle size at deep waters are so few.

Optical studies in the oligotrophic, open Mediterranean Sea have been limited over past decades, yet can be traced back to the 1990s with the pioneering work of Bricaud et al. (1995, 1998) and Loisel and Morel (1998), and more recently by Loisel et al. (2011), Moutin et al. (2012). Utilizing beam transmissometers, optical instruments routinely used to measure the concentration of suspended particulate matter, and describe the temporal and spatial variability of PM in marine waters, Karageorgis et al. (2008) synthesized numerous transmissometer profiles in the eastern Mediterranean Sea, whereas Karageorgis et al. (2012) reported the PM optical and size properties in the Ionian Sea.

Concerning the quality and origin of the marine PM, valuable information can be obtained by the stable isotopic composition of significant elements such as carbon and nitrogen, which constitutes a tracer of surface biological and biochemical processes, thus providing deeper insight into the physical and biogeochemical processes during its transport towards the deep ocean (Wu et al., 1999). The use of stable isotopes as a mean for source identification is based on the concept that carbon and nitrogen are interrelated in many forms, and measurable differences in the isotopic composition of the source-materials will persist through their biogeochemical cycling (Stumm and Morgan, 1981; Peterson and Fry, 1987). Moreover, transformation processes cause isotopic fractionation between substrates and products (Kerhervé et al., 2001).

As the ^{15}N atom is heavier than the ^{14}N atom, molecules containing ^{15}N are usually less reactive than those containing ^{14}N, leading to a slight discrimination against ^{15}N in almost every no-equilibrium transformation in the N-cycle (Wada and Hattori, 1991; Altabet, 1996; Waser et al., 1998; Möbius, 2013). According to the ^{14}N preference, residual substrate of any reaction (i.e. NO_3) becomes enriched in ^{15}N, whereas the product (i.e. assimilated N) is depleted in ^{15}N compared to the substrate. For this "Rayleigh" type fractionation, the intensity, the so-called fractionation factor $^{15}\varepsilon$ (‰), is defined either as the difference in δ^{15}N between product and substrate or as the slope of the logarithmic function δ^{15}N *vs* the concentration of product or substrate (Mariotti et al., 1981) if additional sources or sinks are negligible. Because of the aforementioned processes, each N-pool has a specific isotopic signature, resulting from the balance of source and sink terms and their isotopic fractionation. Accordingly, the δ^{15}N of marine particulate matter reflects the interplay of isotopically distinct N sources as well as the isotopic fractionation processes during both its formation (as a product of assimilation) and its decomposition (as the substrate of ammonification).

The study of the natural isotopic variations of organic carbon ($\delta^{13}C_{org}$) presents another important method used to trace sources and transformation processes of the particulate organic matter in the marine environment. The isotopic variations of carbon in the organic particles initially present depletion in ^{13}C, which derives from the formation procedures of the organic matter during primary production (Kerhervé et al., 2001). Then, as in the case of nitrogen, a stepwise enrichment of ^{13}C occurs in the particles through the food chain and by the

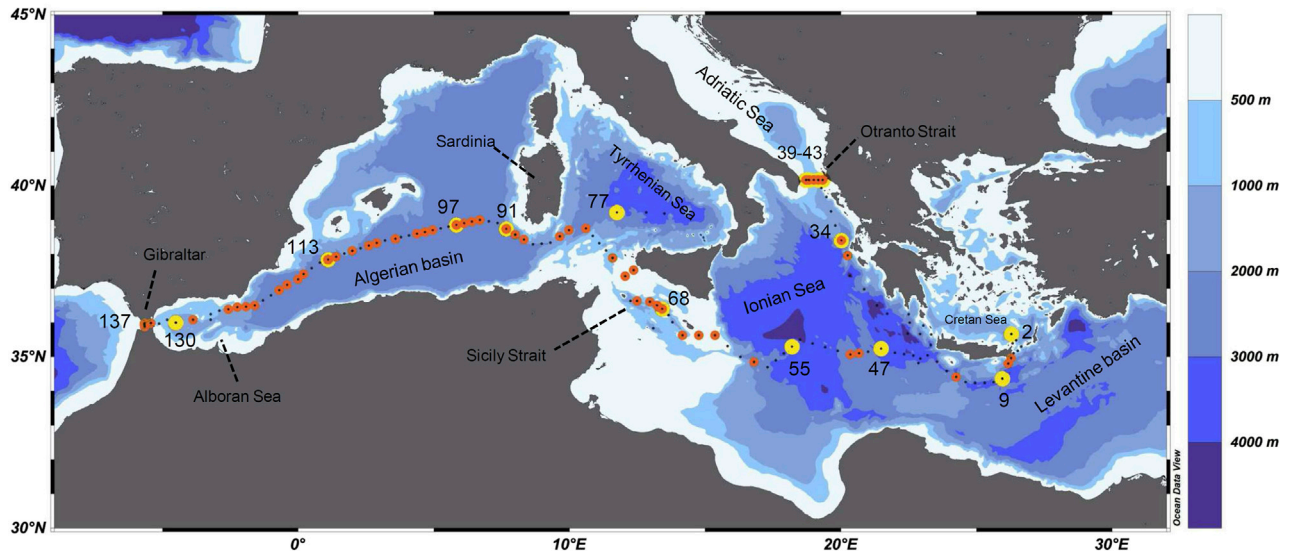

FIGURE 1 | The study area map annotated with major features discussed in the text. Black dots correspond to CTD casts; orange circles correspond to stations where optical parameters of particulate matter were obtained by using the LISST-Deep; while yellow circles correspond to stations where seawater samples were collected for the elemental and stable isotopic analysis of carbon and nitrogen of particulate matter.

processes that are performed at the successive trophic levels (Altabet, 1996). Accordingly to this, the isotopic ratios of carbon, are affected both by the biological sources of the particles and the transformation processes that they undergo during their transfer (Kerhervé et al., 2001).

The oligotrophic seas are ideal settings for studying isotopic composition patterns because sources of nitrogen and carbon vary spatially and temporally, and each with a distinct isotopic composition (Meador et al., 2007). So far, the studies that have been performed on δ^{13}C-POC and δ^{15}N-PN in the Mediterranean Sea were focused mainly on sinking organic matter (Kerhervé et al., 2001; Çoban-Yildiz et al., 2006; Emeis et al., 2010; Möbius et al., 2010; Pedrosa-Pàmies et al., 2016). To the best of our knowledge, there are only a few studies reporting on the isotopic composition of PN in suspended particles in the Mediterranean Sea (Struck et al., 2001; Pantoja et al., 2002; Çoban-Yildiz et al., 2006; Koppelmann et al., 2009; Emeis et al., 2010; Pavlidou et al., 2020) and none that provide the isotopic composition of POC in suspended particles along the entire water column, from the surface to deep waters, across the open Mediterranean Sea.

In this study, optical (transmissometry and particle-size spectra) and biochemical (POC, PN concentrations, and their stable isotopic composition δ^{13}C-POC and δ^{15}N-PN respectively) data of marine PM were collected during the MSM72 trans-Mediterranean Sea oceanographic cruise onboard the German *R/V* Maria S. Merian in spring 2018. The cruise was designed to contribute towards the understanding of interannual changes and trends in the physical and biogeochemical status of the oligotrophic Mediterranean Sea and to further record the hydrological status following the climatological shifts that were observed in the eastern and western part of the basin during the last decades (Durrieu De Madron et al., 2011; Cardin et al., 2015). An east-to-west transect across the EMed and the WMed was conducted, and multidisciplinary measurements took place on an almost zonal section throughout the Mediterranean Sea, following the principle and requirements of the global GO-SHIP repeated oceanographic survey program, tailored for the Mediterranean Sea (CIESM, 2012) (GO-SHIP line MED-01).

The present work combines optical and biochemical data for the Mediterranean Sea to: 1) present the spatial distribution of particle-related optical properties and considered biochemical indices in the study area; 2) examine the potential relationship between hydrology and optical properties of main water masses; and 3) explore the associations of optical parameters with PM, and in particular its organic forms, to gain new insights into the main physical and biogeochemical features driving particle dynamics in the oligotrophic Mediterranean Sea.

METHODOLOGY

Cruise Description and Sampling

The survey was carried out on board the German *R/V* Maria S. Merian from March 2nd to April 3rd 2018 (**Figure 1**). The cruise started at Heraklion, Crete, Greece and ended in Cadiz, Spain (Hainbucher et al., 2020). In total, 136 CTD casts were conducted during the cruise materializing a complete east-to-west Mediterranean transect plus another one in the Ionian Sea. The CTD system used was a Seabird SBE911plus and a Seabird SBE32 carousel equipped with 24/10lt Niskin bottles. Dual sensors for temperature and conductivity were employed. Salinity values were checked against water salinity samples with the help of a Guildline Autosal salinometer in the laboratory. Overall accuracies were within the expected instrument range of salinity. More details for the instruments setup and the sampling

strategy can be found in Hainbucher et al. (2020). At 62 stations (with depth <3,000 m) the LISST-Deep was deployed along with the rosette system to obtain optical parameters i.e., beam attenuation coefficient, particle volume concentration, particle median diameter, and the slope of PSD. At 15 stations, seawater samples were also collected for the elemental and stable isotopic analysis of carbon and nitrogen of PM.

Beam Attenuation Coefficient, Particle Volume Concentration and Particle Median Diameter

Laser diffraction is a method that permits nondestructive *in situ* measurements of the particle size distribution over a relatively large size range, implemented in Laser *in Situ* Scattering and Transmissometry (LISST–Deep), an autonomous instrument manufactured by Sequoia Scientific Inc., to measure particle size distribution and the beam attenuation coefficient in the deep sea (Agrawal and Pottsmith, 2000). LISST-Deep derived variables are the beam attenuation coefficient due to particles (c_p at 670 nm in m^{-1}), the total particle volume concentration (VC in $\mu L\ L^{-1}$ or ppm), and the particle median diameter (D_{50} in μm). A detailed description of the methodology applied is given in the **Supplementary Material**.

Estimation of Particle Size Distribution Slope, ξ

The PSD slope, ξ, provides information on the relative concentration of small to large particles, i.e. steep slopes correspond to higher abundance of small particles and flatter slopes to the opposite; its mathematical description using the power-law model is used most often in marine studies (Buonassissi and Dierssen, 2010; Xi et al., 2014). For the estimation of ξ, we followed Xi et al. (2014). Methodological details are given in the **Supplementary Material**.

Elemental and Stable Isotope Analysis of Carbon and Nitrogen

For the determination of POC, PN contents and stable isotopic composition (δ^{13}C-POC and δ^{15}N-PN), seawater samples (5–10 L) were collected close to the sea surface, within the maximum of chlorophyll fluorescence and main water masses from 15 stations across the study area (98 samples in total; **Figure 1**). The POC and PN contents and their stable isotopic composition were determined at the Stable Isotope Facility at the University of California Davis (Davis, CA, United States), using a PDZ Europa ANCA-GSL elemental analyzer coupled to a PDZ Europa 20-20 isotope ratio mass spectrometer (Sercon Ltd., Chesire, United Kingdom). Methodological details are given in the **Supplementary Material**.

Surface Chl-α Satellite Imagery

To evaluate the sea surface productivity in the study area for the duration of the cruise, monthly mean and 8 day average sea surface chlorophyll-*a* concentrations (Chl-*a*) were obtained using the Ocean Color (OC) climate record developed by the European Space Agency (ESA) in the framework of its Climate Change Initiative (CCI) activity. Detailed description is given in the **Supplementary Material**.

Visualization and Statistical Analysis of Data

The spatial distribution of the various optical and geochemical parameters considered herein was visualized by using Ocean Data View - ODV (Schlitzer, 2018). The dataset variables are normally distributed (passed Kolmogorov–Smirnov tests) thus, the determined optical and biochemical parameters, including water depth, were tested on their potential statistical relationships by using 2-tailed Pearson correlation analysis (SPSS statistics software v. 17.0); the data set was divided into western and eastern Mediterranean data points and Otranto Strait data points, since those regions exhibited considerable differences in the spatial distribution of the studied parameters (see *Discussion* below).

RESULTS AND DISCUSSION

Hydrological Setting

The Theta-S diagram of the stations sampled during the MSM72 cruise is presented in **Figure 2**. The profiles have been assigned into four different groups each with different hydrological characteristics. Two profile groups represent stations in the WMed, one sampled from the Gibraltar Strait up to the Sardinia channel and a second one in the Sardinia channel until the Tyrrhenian Sea. Two profile groups represent stations sampled in the EMed, one sampled in the western part of the EMed (mostly in the Ionian Sea), and a second one sampled in the eastern Ionian Sea, Otranto strait, Cretan Passage and Cretan Sea. The reader is referred to the caption of **Figure 2** for information about the group color-coding. For further information related to this section, the reader is referred to Astraldi et al. (1999), Wüst (1961), Millot (1999), Malanotte-Rizzoli (2001), Millot and Taupier-Letage (2005), Tanhua et al. (2013), and references therein.

The Mediterranean Sea is a concentration basin where the amount of water lost to the atmosphere through evaporation is larger than the water added into the basin through precipitation and riverine input. In order to balance this water budget deficit, low salinity Atlantic Water (AW) enters the basin through the Gibraltar Strait in the WMed and follows an eastward path towards the Sicily strait, before advancing into the EMed. The low salinity signal of the entering AW surface mass is much stronger close to the entrance point, and whilst it is still evident along its eastward route in the Tyrrhenian and Ionian Seas, salinity is increased. Finally, in the eastern part of the EMed, surface AW masses are transformed into a high salinity, warm surface water mass known as Levantine Surface Water (LSW), which is the most saline surface mass of the Mediterranean Sea. Levantine Intermediate Water (LIW) formed mainly in the Levantine Sea during winter is a saline water mass with a density not high enough to penetrate the Mediterranean deep layers. Thus, it is usually traced as a local salinity maximum at

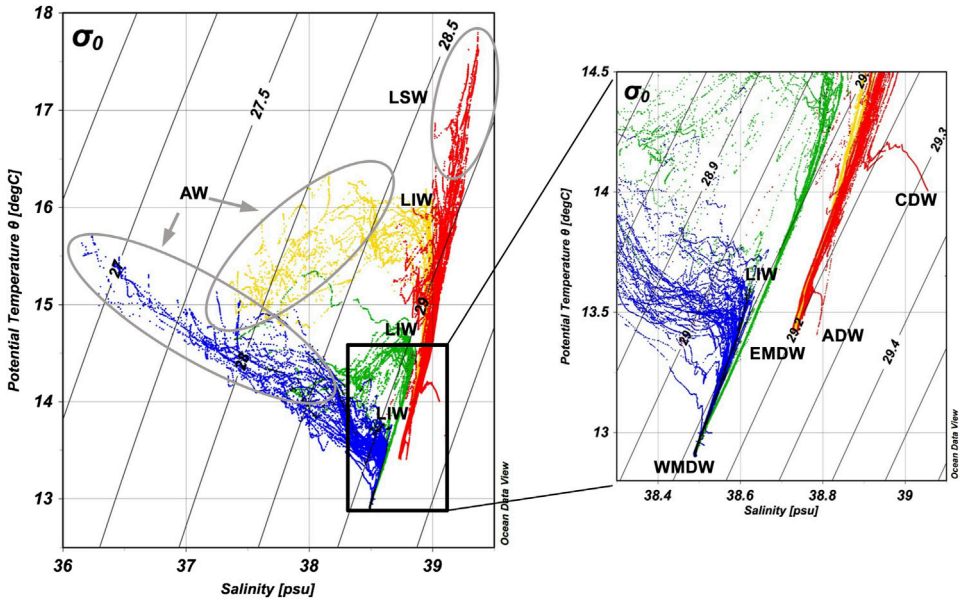

FIGURE 2 | Theta-S diagram of the stations sampled during the MSM72 cruise. The profiles have been grouped into four categories assigning different colors to different hydrological characteristics. Blue and green profiles represent stations in the WMed: Gibraltar Strait up to the Sardinia channel; Sardinia channel and the Tyrrhenian Sea, respectively. Yellow and red profiles represent stations sampled in the EMed: western part of the EMed (mostly in the Ionian Sea); east Ionian Sea, Otranto strait, Cretan Passage and Cretan Sea, respectively. The abbreviations of the identified main water masses are defined in the text.

intermediate depths. In general, intermediate waters in the Mediterranean are defined as those occupying the layer between ~150 and 600 m. After formation, LIW follows a path opposite to that of AW, and finally exits the Mediterranean through the Gibraltar Strait below the AW layer. This dual flow regime constitutes the upper thermohaline conveyor belt that runs throughout the whole Mediterranean Sea.

Close to the formation sites, LIW masses cannot be clearly observed, as the shallower layers in the absence of AW are more saline than LIW (**Figure 2**). However, along its westward route, local salinity LIW core maxima can easily be discerned. From the Ionian Sea, through the Tyrrhenian basin and further on towards Gibraltar, LIW becomes colder and less saline, thus increasing its density (σ_θ) from ~29 kg m^{-3} in the Ionian Sea to ~29.05 kg m^{-3} in the Tyrrhenian and ≤29.10 kg m^{-3} in the western part of the WMed. During this route, LIW core depth increases from 200 to 250 dbar in the Ionian Sea, to 250–300 dbar in the Tyrrhenian, and to 400–500 dbar in the WMed.

The Mediterranean deep water formation areas are different for the west and east sub-basins. The Gulf of Lions in the west and the Adriatic Sea in the east, are the most active formation sources. The deep waters formed are practically isolated by the shallow (~400 m) strait of Sicily. Hence, East Mediterranean Deep Water (EMDW) is easily distinguishable from West Mediterranean Deep Water (WMDW), as the former is warmer, more saline and denser than the latter. The density (σ_θ) of these two different water masses is ≥29.20 and <29.15 kg m^{-3} respectively. In the lower part of the Theta-S diagram (**Figure 2**) blue and green WMed profiles merge as WMDW shares almost the same properties throughout the basin. The same applies to the lower part of the yellow and red EMed profiles, with two exceptions. Firstly, the isolated high temperature, salinity and density, hook-shaped profile observed in the red group, is a profile in the Cretan Sea, where deep water density is over σ_θ 29.30 kg m^{-3}. This Cretan Deep Water (CDW) mass has stagnated inside the Cretan Sea for the last two decades (Velaoras et al., 2019). Secondly, the profile sampled in the Otranto strait appears to be slightly denser (σ_θ ≥29.24 kg m^{-3}) at a depth of ~760–900 dbar. This marks the winter-formed Adriatic Deep Water (ADW) which plunges through the shallow Otranto strait towards the Ionian abyssal plain. Between the intermediate and bottom layers (approximately from 700 to 1,600 m) of the EMed, a low salinity and oxygen water mass is found called the Transitional Mediterranean Water (TMW). This is the oldest water in the eastern Mediterranean (Stöven and Tanhua, 2014) and is the product of the uplift of deep masses by intrusions of bottom water masses of Adriatic and/or Aegean origin (Velaoras et al., 2019). In the literature (Stöven and Tanhua, 2014; Li and Tanhua, 2020) TMW can be also found as Tracer Minimum Zone (TMZ) due to its low concentration in transient tracers (i.e., CFC-12, SF_6).

Finally, it should be noted that during the last decades both Mediterranean sub-basins have been subjected to severe overturning circulation changes. In the EMed during the early 1990s a shift in the dominant dense water formation source from the Adriatic to the Aegean Sea was observed. This event is known as the Eastern Mediterranean Transient (EMT) and resulted in the massive export of dense, warm and saline deep waters from the Aegean Sea to the EMed abyssal reservoirs. The Adriatic Sea gradually regained its role as the

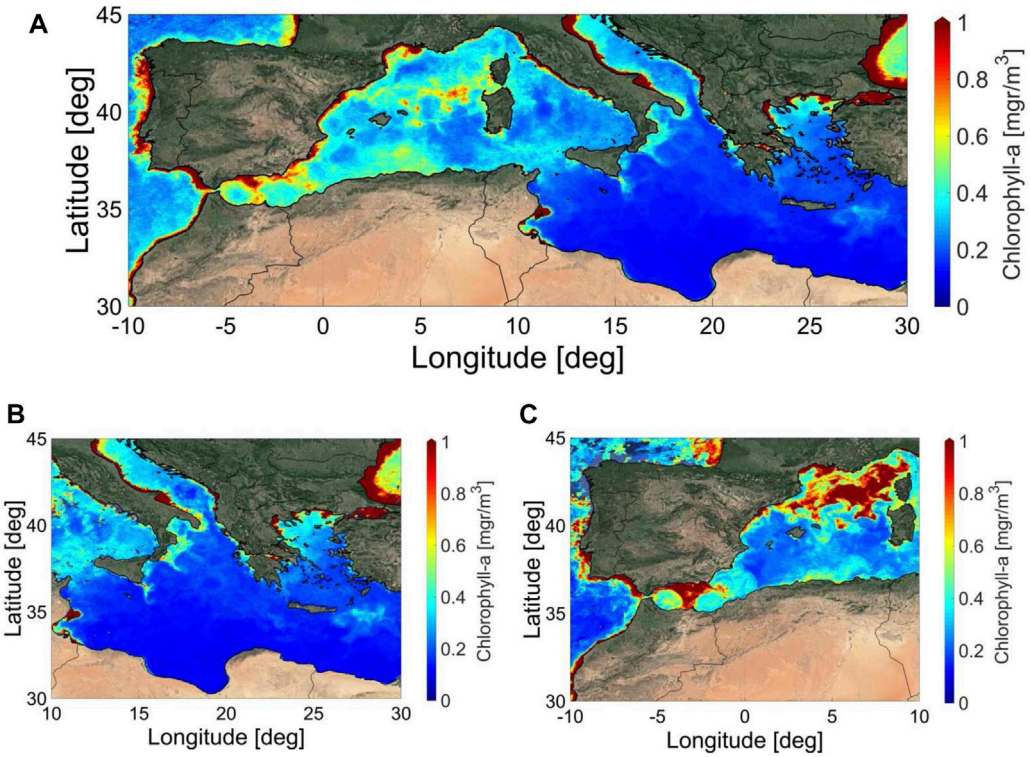

FIGURE 3 | Monthly mean (March 2018) **(A)** and 8 day average sea surface Chlorophyll-*a* concentration in the Mediterranean Sea for the first (06-13/03/2018) **(B)** and second (30/03/2018-06/04/2018-right) **(C)** part of the MSM72 cruise.

main dense water source of the EMed only after the early 2000s (Roether et al., 2007; Cardin et al., 2015). Between 2004 and 2006 significant dense water formation events were observed in the WMed, producing larger quantities of warmer, saltier and denser deep waters masses than ever before. This event is known as the Western Mediterranean Transition (WMT) and is partly attributed to salinity preconditioning caused by the import from the EMed through the Sicily Strait of intermediate water masses with higher-than-usual salinity due to the preceding EMT event (Schroeder et al., 2016; Schroeder et al., 2017).

Biogeochemical Setting

The Mediterranean Sea is a semi-enclosed deep basin (maximum depth 5,125 m offshore Peloponnese, Greece, EMed) characterized by oligotrophy, an overall result of low nutrient inputs into the basin (Krom et al., 2014). Nutrient concentrations in the Mediterranean Sea are characterized by a decreasing trend from the oligotrophic WMed to the ultra-oligotrophic EMed (Azov, 1991; Ignatiades et al., 2002). Redfield-deviated (i.e. higher than 16:1) N/P ratios become more pronounced eastwards and are essentially explained by the excess N over P in all nutrient sources arriving in the basin via atmospheric deposition (Mara et al., 2009; Markaki et al., 2010) and river discharge (Ludwig et al., 2009; Krom et al., 2010). The large loss of inorganic nutrients, through the inflow of relatively nutrient-depleted Atlantic water at surface layers and the outflow of the underlying nutrient-rich Mediterranean waters through the Strait of Gibraltar (Béthoux et al., 1998), prevents nutrient accumulation in deep waters, strongly limiting both primary and secondary production and thus particulate matter formation.

Within the Mediterranean, the EMed waters are very transparent and exhibit unique optical characteristics such as very low beam attenuation coefficient (c_p) values at depths >200 m (<0.04 m^{-1} in the open Ionian Sea), associated with very low particulate matter and particulate organic carbon concentrations (PMC <100 $\mu g\ L^{-1}$, POC <40 $\mu g\ L^{-1}$, respectively) (Karageorgis et al., 2008; Zaccone et al., 2012; Ortega-Retuerta et al., 2019). Overall, the oligotrophy in combination with the dominance of the microbial food web in the pelagic ecosystem results in low food availability for top predators (Turley et al., 2000; Siokou-Frangou et al., 2002) and low levels of carbon sequestration to depth (Gogou et al., 2014).

Satellite chlorophyll-*a* concentrations during the MSM72 cruise are presented in **Figures 3A–C**. **Figure 3A** shows the monthly mean average sea surface chlorophyll-*a* concentration in the Mediterranean Sea for March 2018, while **Figures 3B,C** shows the 8 day average sea surface chlorophyll-*a* concentrations in the Mediterranean Sea for the first (06-13/03/2018) and second (30/03/2018-06/04/2018) legs of the MSM72 cruise, which corresponds to the sampling periods in the EMed and WMed Mediterranean sub-basins, respectively.

According to this, during the MSM72 cruise, a west-to-east, as well as a north-to-south gradient in oligotrophy, was observed in the two sub-basins (**Figures 3A–C**), which is in accordance with

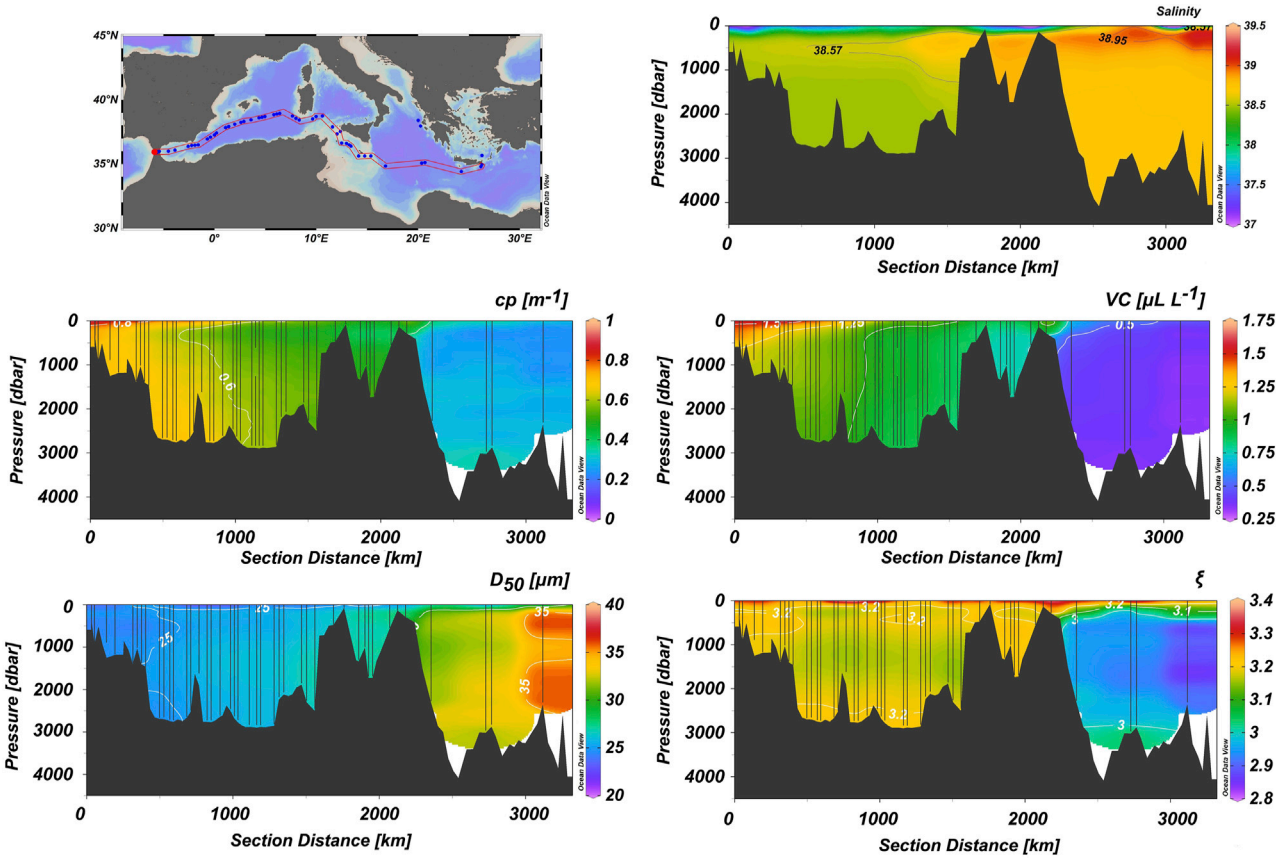

FIGURE 4 | West-east section of salinity, c_p, VC, D_{50} and ξ in the Mediterranean Sea. Section location is shown in the **upper left** panel. Vertical lines correspond to LISST-Deep casts.

what has previously been described for the different Mediterranean bioregions (D'Ortenzio and Ribera d'Alcalà, 2009; Mayot et al., 2016). In these studies, the biogeography of the Mediterranean Sea and the seasonal cycle of the surface biomass were characterized in different areas of the basin by analyzing 10-year satellite surface Chl-*a* concentrations, and the results showed that the Mediterranean sub-regions have varying physical, chemical and biological forcing factors. However, it is important to note that surface Chl-*a* as seen by satellites, is not representative of the total phytoplankton biomass in the Mediterranean waters, i.e. subsurface phytoplankton dynamics, in particular those associated with the Deep Chlorophyll Maximum (DCM) at the base of the upper mixed layer (Barbieux et al., 2019; D'Ortenzio et al., 2021) could be highly underestimated.

Spatial and Vertical Variations of Particulate Matter Optical Properties

A west-east section of c_p, VC, D_{50}, and ξ distribution in the study area is presented in **Figure 4**, and **Table 1** summarizes the range and mean values in the entire Mediterranean as well as the considered sub-regions, i.e., Gibraltar and Algerian Basin, Sardinia and Tyrrhenian Sea, Sicily Strait and western Ionian Sea, Otranto Strait, Ionian Sea (excluding the Otranto Strait) and the Cretan Sea. The beam attenuation coefficient, c_p, clearly exhibits higher values throughout the water column in the WMed, especially in the upper ~100 m, and progressively the c_p signal decreases towards the east, at first towards the Sicily strait, and then it becomes very weak in the EMed, with values <0.1 m^{-1}. The cruise average c_p was 0.53 ± 0.17 m^{-1} and the highest values were recorded in the upper ~200 m of the westernmost part of the section (>1.0 m^{-1}). The maximum value of 1.77 m^{-1} was recorded near-bottom in the Otranto strait, and the minimum (0.025 m^{-1}) in the intermediate waters east of Crete.

The particle volume concentration, VC, along the section shows similar characteristics to c_p, with higher values in the WMed and progressively lower values towards the central Mediterranean and the EMed. It exhibits an average of 0.89 ± 0.31 µl L^{-1} in the entire Mediterranean Sea. Similarly to c_p, the maximum value occurs near-bottom in the Otranto strait (3.7 µl L^{-1}), whereas the minimum value appears south of Crete (0.33 µl L^{-1}); overall, we observe a higher abundance of particles in the WMed and a scarcity of particles in the EMed.

Furthermore, the particle median diameter D_{50}, in the Mediterranean shows an average of 27 ± 3 µm (particle size was estimated in the range 1.25–92.6 µm; see **Supplementary**

TABLE 1 | Ranges and mean values of the determined optical and biochemical parameters considered in this study in the entire Mediterranean Sea as well as in the various considered sub-regions, i.e., Gibraltar/Algerian Basin (stations 94–137), Sardinia/Tyrrhenian Sea (stations 75–93), Sicily Strait/western Ionian Sea (stations 50–72), Otranto Strait (stations 39–42), Ionian Sea (stations 7–50 excluding the Otranto Strait) and the Cretan Sea (station 2). Within each of the considered sub-regions mean values of all parameters are also reported for the identified main water masses. The abbreviations of the identified main water masses are defined in the text. "Inter" signifies intermediate water masses regardless of their origin (LIW, CIW, etc.).

Area	Water mass	Biochemicals						Optics				
		POC (μmol L^{-1})	PN (μmol L^{-1})	δ^{13}C-POC (‰)	δ^{15}N-PN (‰)	POC/PN	*n*	c_p (m^{-1})	VC (μl L^{-1})	D_{50} (μm)	ξ	*n*
Gibraltar—Algerian Basin	Surface	6.02	0.79	−25.80	2.14	7.68	3	0.69	1.31	24	3.26	2,621
	DCM	4.07	0.72	−25.11	2.71	6.19	2	0.66	0.53	25	3.23	402
	Inter	1.81	0.42	−27.86	3.72	7.06	3	0.60	1.12	25	3.19	5,564
	WMDW	1.62	0.36	−28.16	4.35	6.55	9	0.63	1.02	25	3.18	17,228
	Max (all)	7.11	1.05	−24.45	5.85	10.4	17	1.56	2.78	29	3.76	25,815
	Min (all)	1.17	0.12	−29.87	1.88	1.9	17	0.30	0.88	19	3.10	25,815
	Average (all)	2.72	0.50	−27.33	3.62	6.8	17	0.63	1.07	25	3.19	25,815
Sardinia—Tyrrhenian Sea	Surface	4.45	0.77	−26.0	2.85	6.07	2	0.54	0.99	25	3.25	800
	DCM	3.86	0.52	−25.0	1.90	7.39	1	0.53	1.00	25	3.23	145
	Inter	2.07	0.22	−28.1	5.92	9.57	3	0.49	0.91	26	3.20	1,705
	WMDW	1.87	0.20	−27.7	6.43	9.57	8	0.55	0.88	26	3.17	5,250
	Max (all)	5.55	1.06	−25.02	8.10	11.0	14	0.82	1.31	31	3.42	7,900
	Min (all)	1.30	0.16	−28.87	1.90	5.2	14	0.31	0.72	23	3.03	7,900
	Average (all)	2.42	0.32	−27.33	5.41	8.9	14	0.54	0.90	26	3.18	7,900
Sicily Strait—Western Ionian Sea	Surface	4.71	0.57	−26.28	3.05	8.43	2	0.45	0.81	26	3.27	837
	DCM	3.86	1.15	−27.31	3.35	5.96	2	0.45	0.84	26	3.24	133
	Inter	2.28	0.23	−28.47	5.82	9.85	2	0.38	0.69	28	3.14	1,527
	TMW	1.67	0.24	−28.73	5.51	7.75	3	0.41	0.63	29	3.22	2,189
	WMDW	1.78	0.19	−28.21	6.63	9.55	5	0.34	0.46	32	3.21	3,445
	Max (all)	4.96	1.99	−25.31	7.79	11.2	14	0.94	1.83	33	3.51	8,131
	Min (all)	1.56	0.15	−29.58	2.02	2.4	14	0.07	0.34	22	2.87	8,131
	Average (all)	2.54	0.40	−27.96	5.29	8.5	14	0.32	0.64	29	3.12	8,131
Otranto Strait	Surface	5.00	0.75	−26.07	−0.40	6.74	4	0.33	0.55	28	3.16	498
	DCM	3.61	0.51	−27.18	1.96	7.24	4	0.32	0.52	29	3.01	159
	Inter	2.47	0.29	−27.53	4.17	9.23	8	0.32	0.53	30	3.10	1,063
	ADW	2.37	0.27	−27.36	3.88	9.34	8	0.47	0.76	30	3.16	572
	Max (all)	7.12	1.06	−25.44	6.41	13.7	24	1.78	3.70	37	3.76	2,292
	Min (all)	1.66	0.16	−28.82	−1.31	4.0	24	0.05	0.38	19	2.92	2,292
	Average (all)	3.08	0.40	−27.16	2.80	8.6	24	0.44	0.72	29	3.13	2,292
Ionian Sea	Surface	4.37	0.55	−25.46	0.56	7.99	3	0.30	0.49	30	3.19	687
	DCM	4.01	0.87	−25.40	0.98	5.99	3	0.28	0.47	30	3.17	81
	Inter	1.77	0.17	−27.87	5.50	10.3	3	0.23	0.40	34	2.97	1,478
	TMW	1.74	0.16	−27.70	5.81	11.1	6	0.27	0.38	34	2.92	2,720
	EMDW	1.88	0.17	−27.83	6.13	10.9	7	0.30	0.37	34	2.95	1,961
	Max (all)	5.62	1.51	−24.64	7.58	12.5	22	0.76	0.69	37	3.46	6,927
	Min (all)	1.06	0.09	−28.83	−0.88	2.3	22	0.03	0.33	24	2.83	6,927
	Average (all)	2.46	0.31	−27.14	4.43	9.8	22	0.27	0.39	34	2.97	6,927
Cretan Sea	Surface	5.26	0.67	−26.40	0.20	7.83	1	0.25	0.45	31	3.04	97
	DCM	3.59	0.65	−26.77	3.30	5.50	1	0.27	0.43	32	2.99	1
	Inter	3.03	0.51	−27.10	2.67	7.11	2	0.21	0.39	35	2.90	207
	TMW	2.78	0.38	−27.93	4.06	8.50	2	0.20	0.35	34	2.95	180
	CDW	1.97	0.17	−28.46	2.99	11.5	1	—	—	—	—	—
	Max (all)	5.26	1.22	−26.40	4.20	11.5	7	0.76	0.69	36	3.18	485
	Min (all)	1.97	0.17	−28.46	0.20	3.1	7	0.03	0.34	28	2.86	485
	Average (all)	3.21	0.53	−27.39	2.65	7.9	7	0.23	0.39	34	2.95	485
All dataset	Max	7.12	1.99	−24.45	8.10	13.7	98	1.78	3.70	37	3.76	49,361
	Min	1.06	0.09	−29.87	−1.31	1.9	98	0.03	0.33	19	2.83	49,361
	Average	2.71	0.40	−27.34	4.07	8.5	98	0.53	0.41	27	3.15	49,361

Material for details). Its evolution from the west to the east is reversed with respect to the previously discussed parameters. D_{50} exhibits lower values in the WMed up to the Sicily strait, which increases substantially towards the east (>25 μm). The minimum value of D_{50} is recorded in the Otranto Strait (19 μm), whereas the largest is found in the EMed, south of Crete (37 μm).

Finally, the PSD slope ξ, along the section shows similar characteristics to c_p and VC with high values in WMed and lower values in EMed, thus confirming the predominance of relatively smaller particle populations in the western basin over the larger particles dominating the eastern basin. The minimum value is 2.83 at the mid and deep waters of the Ionian Sea; on the other hand, the maximum value is 3.76 in the deepwater of the Otranto Strait. In the WMed, the average ξ is 3.2 ± 0.1; the average value in the EMed is 3 ± 0.1, whereas the Mediterranean Sea average ξ is estimated at 3.1 ± 0.1.

Beam c_p values from the present study appear to be high when compared to other data sets from the Mediterranean Sea (cruise average 0.53 m^{-1}). Karageorgis et al. (2008) compiled 11 years of transmissometry data from the EMed and reported that the average cp value in the open sea is ~0.1 m^{-1}, i.e. five-fold lower than the present case. It should be noted however, that absolute cp values depend highly on the acceptance angle of the transmissometer employed. Boss et al. (2009) concluded that eight different transmissometers' mean attenuation values differ markedly and in a consistent way with instrument acceptance angle: smaller acceptance angles provide higher beam attenuation values. Later, Boss et al. (2018) tested cp obtained from LISST-100X (5 cm pathlength, acceptance angle 0.069°) against cp from a hyperspectral spectrophotometer and transmissometer (ac-s, Sea-Bird Scientific, Bellevue, WA, United States, formerly WET Labs, 25 cm pathlength, acceptance angle 0.93°) and found particulate beam attenuation coefficients to be well correlated, with LISST values being slightly larger. LISST's cp values, because of the very small-angle transmissometer employed, would be higher than the ones measured with conventional instruments. In that respect, direct cp comparisons should be avoided, with the exception of cp variation studies conducted in a relative manner.

Data for LISST-Deep derived parameters VC, D50, and occasionally ξ, presented in the current study represent a ~30% increase relative to that available in the literature (Karageorgis et al., 2012; Karageorgis et al., 2014; Karageorgis et al., 2017b; Parinos et al., 2017; Turner et al., 2017; Leroux et al., 2018). A substantial amount of data have been previously reported with LISST-100X, i.e. the 'shallow' version of the instrument, operating up to 300 m depth (Mikkelsen et al., 2006; Barone et al., 2015; White et al., 2015; Yamada et al., 2015; Many et al., 2016; Qiu et al., 2016).

Literature mean VC values from the coastal and shallow (10–12 m depth) Adriatic Sea were two orders of magnitude higher than our measurements (Mikkelsen et al., 2006). In the northwestern Mediterranean, Gulf of Lions, VC average values in the vicinity of the Rhône River plume decreased progressively (Many et al., 2016) in the offshore direction. The latter notion is further strengthened by the observations of Leroux et al. (2018), who reported VC values well below 1 μl L^{-1} in the open northwestern Mediterranean. In the open Ionian and Levantine Seas, Karageorgis et al. (2012) reported mean VC values in the range 0.29–0.30 μl L^{-1}.

The mean D50 literature values for the coastal Adriatic Sea varied from 112 to 291 μm, much higher than the values reported here. With respect to the Gulf of Lions, in the northwestern Mediterranean Sea, Many et al. (2016) reported PSD in the range of 30–200 μm offshore the Rhône River; it should be noted, however, that those values were derived from a combination of LISST-100X and LISST-HOLO instruments thus covering a wider particle size range, including micro-aggregates or macro-aggregates. In the open northwestern Mediterranean Sea, Leroux et al. (2018) identified particle populations in the range of 2–109 μm that were attributed to river-derived fine silts and microflocs. In the Ionian, Aegean, and Levantine Seas, D50 varied between 86 and 88 μm (note that the latter D50 values have been estimated using different methodological assumptions; Karageorgis et al., 2012). The aforementioned literature excerpts, as well as the MSM72 new data, exemplify the pronounced variety of particle sizes encountered in the marine environment of the Mediterranean Sea, resulting from the interplay of numerous biogeochemical processes, and thus enhancing the complexity of the particle pool and its composition dynamics.

With respect to the PSD slope ξ, very little information exists for the Mediterranean Sea. Many et al. (2016) estimated the spectral PSD slope γ from backscattering measurements and reported values in the range of 0.3–0.7, approximately corresponding to ξ values 3.3–3.7, thus similar to the MSM72 cruise values. Another example of ξ estimates from the north Aegean Sea (Karageorgis et al., 2017a) reports higher values varying from 3.46 to 4.86 which corresponds to smaller particle populations than the present study. In most oceanic observations ξ values range from 2.5 to 5 (Boss et al., 2001; Kostadinov et al., 2012), which, according to our measurements, is the case for the WMed and the EMed as well. Nevertheless, the PSD slope is highly dependent on: 1) the method of calculation; 2) the size range used, and 3) the existence or not of large deviations from the power law distribution. Regardless of methodological differences, the present data set on PSD slope ξ in the Mediterranean Sea indicates that there exists a substantial difference between the small particle abundance in the WMed in comparison to the larger particle populations in the EMed. The potential causes of this consistent pattern will be investigated hereafter using the biochemical data set obtained during the cruise.

Spatial and Vertical Variations of Particulate Organic Carbon & Particulate Nitrogen Contents and Their Stable Isotopic Composition

A west-east section of POC and PN contents and their isotopic composition in the study area is presented in **Figure 5**, while as in the case of optical properties above, **Table 1** summarizes their ranges and mean values in the entire Mediterranean as well as in the various sub-regions considered here. POC and PN concentrations in the study area, considering the entire water

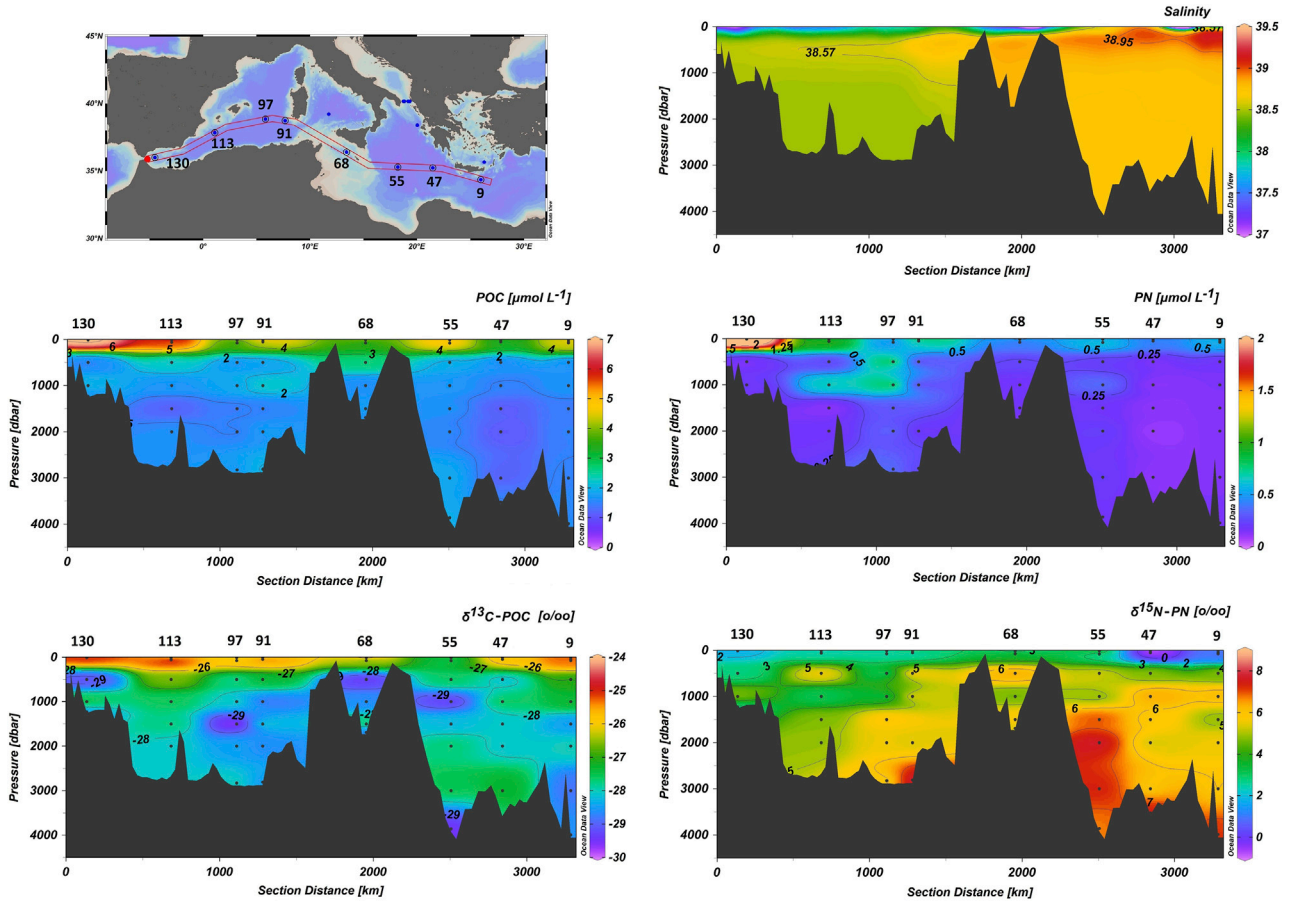

FIGURE 5 | West-east section of salinity, POC and PN contents, δ^{13}C-POC and δ^{15}N-PN values in the Mediterranean Sea. Section location is shown in the **upper left** panel. Dots correspond to the sampled depths.

column, ranged from 1.06 to 7.12 µmol L^{-1}, 2.71 ± 1.40 µmol L^{-1} on average, and from 0.09 to 1.99 µmol L^{-1}, 0.40 ± 0.32 µmol L^{-1} on average, respectively. Consequently, the POC/PN molar ratio ranged from 1.9 to 13.7, with an average of 8.5 ± 2.6. Higher POC and PN concentrations were consistently recorded within surface waters or the maximum of chlorophyll fluorescence of all stations with the highest values being detected in the Alboran Sea and Algerian Basin while lower concentrations were observed in the eastern Ionian Sea and South Cretan margin (**Figure 5**; **Table 1**). Within intermediate and deep water layers of the studied sub-basins, POC and PN concentrations gradually decrease exhibiting a rather uniform distribution. The POC/PN ratio values exhibited a uniform distribution within surface waters or the maximum chlorophyll fluorescence depth of all stations with an average of 6.9 ± 0.9. Within intermediate and deep water layers, POC/PN ratio values increase with higher values, up to 11.5, being detected in the EMed stations and the Otranto Strait (**Table 1**).

δ^{13}C-POC ranged between −28.73 and −25.02‰. Close and Henderson (2020) reported δ^{13}C-POC values in open oceanic waters that span over a broad range, varying from −35‰ at high latitudes to −16‰ at low-mid latitudes. Less depleted values of δ^{13}C-POC were recorded within surface waters or the maximum chlorophyll fluorescence depth in all stations. Intermediate and deep water δ^{13}C-POC values varied between −28.73 and −27.10‰, averaging −27.89‰. Within the considered sub-regions, δ^{13}C-POC values in near-surface waters of the WMed are comparable to those recorded within the Ionian Sea in the EMed, while more depleted values are evident within surface waters of the Sicily Strait, Otranto and the Cretan Sea. At deeper water depths, δ^{13}C-POC values in the WMed, the Ionian Sea and the Cretan Sea average −27.96‰ while in the Sicily Strait δ^{13}C-POC values average −28.47‰. In the Otranto Strait, more enriched δ^{13}C-POC values are observed, with the ADW value being −27.36‰ (**Table 1**; **Figure 5**).

δ^{15}N-PN values in our data set spans a range from −1.31 to 8.10‰. Depleted values are recorded within surface waters or the maximum of chlorophyll fluorescence in all stations, ranging from −1.31 to 3.35‰ (average 1.88‰), while enriched δ^{15}N-PN values are recorded in deeper water layers ranging between 2.67 and 8.10‰ (average 4.91‰). Within the considered sub-regions, δ^{15}N-PN values in near-surface waters of the WMed averaged 2.40‰, in the Sicily Strait averaged 3.20‰, while in the Ionian Sea, the Otranto Strait and the Cretan Sea δ^{15}N-PN values averaged 1.10‰, with the minimum value being recorded in

the surface waters of the Otranto Strait and maximum δ^{15}N-PN value at the maximum of Chl-α fluorescence depth in the Cretan Sea. In deeper water layers, δ^{15}N-PN values in the Gibraltar and the Algerian Basin range from 2.63 to 5.85‰, averaging 4.18‰, while more enriched values are recorded westwards in Sardinia and Sicily Strait, averaging 6.07‰, and the Ionian Sea, 5.64‰ on average with a maximum of 7.79‰ within the EMDW layer in station 55. Less enriched values are evident in the Otranto Strait, where values reaching 1.92‰ for ADW are recorded (**Table 1**; **Figure 5**).

The POC and PN contents of PM reported in our study fall within the ranges of previously published data for open Mediterranean Sea waters. POC values up to 16.5 μmol L^{-1} have been reported for the top 400 m of the water column in open Mediterranean waters (Struck et al., 2001), up to 13.8 μmol L^{-1} for near surface waters of the open Levantine Basin (Tanaka et al., 2007; Bar-Zeev et al., 2011), up to 7.2 μmol L^{-1} in epipelagic waters of the open northwestern Mediterranean Sea (Ortega-Retuerta et al., 2017) and up to 9.8 μmol L^{-1} in near surface waters of the north Aegean Sea (Parinos et al., 2017). Zaccone et al. (2012) has reported mean POC values of 2.29, 0.60, and 0.59 μmol L^{-1} in epipelagic, mesopelagic and bathypelagic layers of the WMed, with the corresponding values for the EMed being 1.82, 0.77 and 0.59 μmol L^{-1}, respectively. Karageorgis et al. (2018) reported POC values in the range 2.3–11.8 μmol L^{-1} in canyons and open slopes of the southern Cretan margin (EMed), while Ortega-Retuerta et al. (2019), reported POC values ranging from 0.10 to 8.60 μmol L^{-1} along an east-west transect across the Mediterranean Sea. Concerning PN contents, Emeis et al. (2010) have reported similar values in vertical profiles of pelagic stations in the Ionian Sea and NW Levantine Sea as has Struck et al. (2001) for the top 400 m of the water column in open Mediterranean waters. Pavlidou et al. (2020) reported mean PN contents values of 3.17, 2.40, and 0.94 μmol L^{-1} in epipelagic, mesopelagic and bathypelagic layers, in the NE Ionian Sea. It is noteworthy that POC concentrations encountered in the present study are amongst the lowest values observed in the global ocean, as values <10 μmol L^{-1} were found only in the open Pacific Ocean and Bermuda in the Atlantic Ocean (Gardner et al., 2006).

Concerning δ^{13}C-POC, and to the best of our knowledge, there are no previous published data along the entire water column, from the surface to deep waters, across the open Mediterranean Sea. Çoban-Yildiz et al. (2006) reported an δ^{13}C-POC average value of -22.9‰ in the euphotic zone of the Rhodes Gyre in the Levantine Basin, while Struck et al. (2001) reported an δ^{13}C-POC range between −28.41 and −24.50‰ for the top 400 m of the water column in open Mediterranean waters. In the case of δ^{15}N-PN, the values reported herein fall within the range of previously published data for open Mediterranean Sea waters. Emeis et al. (2010) reported δ^{15}N-PN values averaging 1.3 ± 0.7‰ in the mixed layer and up to 8.1‰ in deeper waters of the EMed. In a transect across the Mediterranean Sea, Pantoja et al. (2002) observed a significant west-to-east decrease in the isotopic composition of PN from the upper 200 m of the water column. In the western basin, δ^{15}N-PN averaged 2.7 ± 1.2‰, in contrast to −0.2 ± 0.7‰ in the eastern basin. Çoban-Yildiz et al. (2006) reported an δ^{15}N-PN average value of 2.2‰ in the euphotic zone of the Rhodes Gyre in the Levantine Basin. Koppelmann et al. (2009) reported δ^{15}N-PN values within a range of 0.43–1.19‰ in surface waters of the Levantine Basin, while slightly higher values were found in the DCM and mesopelagic and bathypelagic depths, ranging between 6.19 and 8.49‰. Struck et al. (2001) reported δ^{15}N-PN values ranging from 2.64 to 13.7‰ for the top 400 m of the water column in open Mediterranean waters, while finally, Pavlidou et al. (2020) reported mean δ^{15}N-PN values of −0.57, 2.98 and 4.18‰ in epipelagic, mesopelagic and bathypelagic layers, in the NE Ionian Sea (Nestor site).

Particle Dynamics in the Mediterranean Sea as Inferred From Optical Properties and Biochemical Indices

In order to gain insights on the relationships between measured optical properties and identified water masses in the Mediterranean Sea, T-S diagrams superimposed with c_p, VC, D_{50}, and ξ information were used (**Figure 6**). Surface Atlantic waters (AW) are clearly characterized as the most turbid waters in the Mediterranean Sea, with average beam c_p of 0.68 ± 0.01 m^{-1}. On the other hand, TMW constitutes another extreme; one of the lowest observed c_p values averaging 0.20 m^{-1}. AW spreading towards the EMed and particularly in the Ionian Sea exhibits moderate beam c_p values. Intermediate waters masses as LIW show overall c_p values in-between AW and LSW (average 0.57 ± 0.03 m^{-1}), whereas deep water masses have different c_p values according to their location. This pattern is closely followed in the case of VC and is inversed for D_{50}. Average D_{50} in AW is 25 ± 3 μm, in LSW 35 ± 2 μm, in LIW 28 ± 4 μm, whereas the lowest average D_{50} value of 19 μm is observed in ADW. AW in the western basin is characterized by low salinities, relatively high turbidity and VC, low particle size, and higher ξ. The highest ξ values (>3.15) are observed within AW in the WMed, which decrease as AW spreads out towards the east. LIW on the other hand, exhibits the smallest ξ values, especially in the EMed.

The differentiation between the WMed and the EMed is also illustrated in the variability of mean differential particle volume V'(D) (see **Supplementary Material** for definition), D_{50}, and PSD slope ξ (**Figure 7**). Mean V'(D) and ξ are higher in the WMed than in the EMed, whereas the opposite is recorded for mean D_{50} values. These observations demonstrate that in the EMed particle concentration is overall lower than the WMed, whilst mean particle size increases with depth, suggesting that aggregation processes are active in the EMed.

The results of the correlation analysis of the determined optical and biochemical parameters considered in this study are shown in **Supplementary Table 1**. POC is significantly and positively correlated with VC, negatively with D_{50}, and positively with ξ in both the WMed and the EMed. The elevated VC, POC, and PN concentrations recorded within surface waters of the WMed stations, highlight the enhanced surface production therein, compared to the EMed, resulting in a higher abundance of particles within the upper water column. POC concentration and ξ are strongly, significantly, and

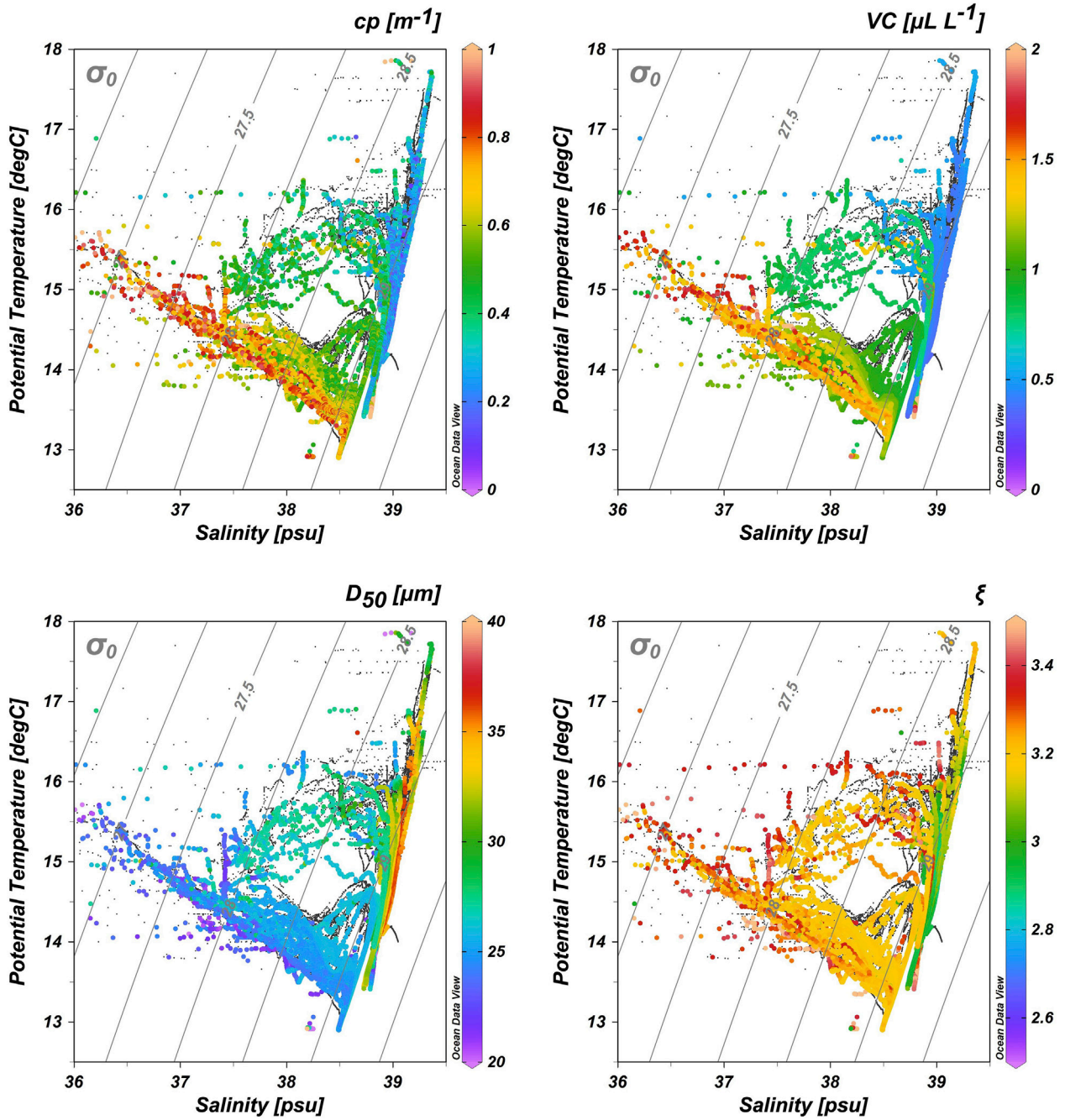

FIGURE 6 | Theta-S diagram of the stations sampled during the MSM72 cruise superimposed with c_p, VC, D_{50} and ξ data. Abbreviations of optical parameters and main water masses are defined in the text.

positively correlated in the Mediterranean Sea, confirming that small particles are POC-rich. Finally, the combined positive correlation of VC with POC concentrations and δ^{13}C-POC can be attributed to surface productivity.

The positive and significant relationship between c_p, as a proxy of suspended particle concentration (or turbidity), and POC, has been acknowledged for decades in global ocean studies (Bishop, 1999; Gardner et al., 2006) as well as the Mediterranean Sea (Loisel et al., 2011); this also holds for the EMed, as demonstrated by Karageorgis et al. (2008) who reported a significant positive correlation between beam c_p and POC concentrations. However, it should be mentioned that the level of relationship also depends on the acceptance angle of the transmissometer used, and in the present case, LISST employs a very narrow angle transmissometer, hence correlations may differ substantially. In any case, the observed positive and significant correlation

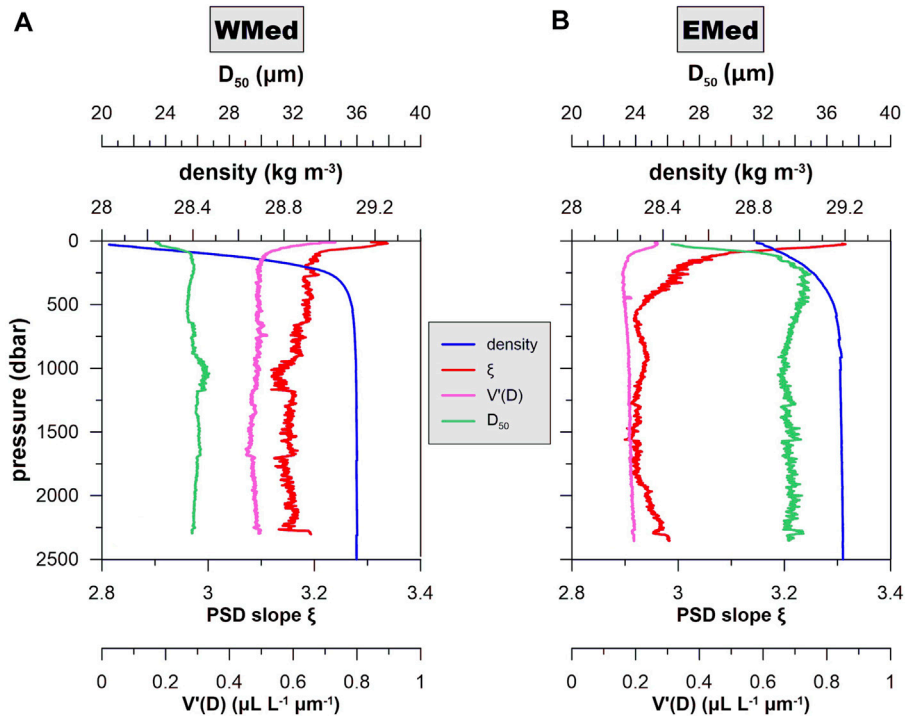

FIGURE 7 | Profiles of mean (smoothed by a 10-point moving average) density, V'(D), D_{50}, and PSD slope ξ for the WMed **(A)** and EMed **(B)**. Differential particle volume V'(D) in the WMed is almost double in the WMed than in the EMed. Mean ξ in the WMed is overall higher than the EMed demonstrating the presence of larger particle pools below ~500 m in the latter, corresponding at a mean D_{50} of ~35 µm.

($r = 0.613$, $p = 0.002$) in the WMed highlights the predominance of organic particles in the water column, whereas this relationship weakens in the EMed ($r = 0.613$, $p = 0.002$) probably due to: 1) the narrow acceptance angle of LISST's transmissometer resulting in small sampled water volume (Boss et al., 2009), in combination with the extreme scarcity of particles observed in the EMed, and 2) the presence of generally larger particles in the EMed, greater than the 0.5–20 µm range, where most of the light attenuation and scattering occurs, and is detected by transmissometers (Gardner et al., 2006).

D_{50} is significantly positively correlated with water column depth in both the WMed and the EMed (excluding the Otranto Strait) (**Supplementary Table 1**) likely suggesting that the process of aggregation of PM with increasing depth is probably present in the study area. Interestingly, D_{50} is significantly positively correlated with POC/PN ratio values only within the EMed stations (excluding the Otranto Strait), while a significant correlation of the POC/PN ratio *vs.* depth is also evident ($r = 0.422$, $p = 0.02$, $n = 30$). Various reasons could account for this result. In oligotrophic systems, such as the EMed, a faster and more efficient decomposition of N versus C has been highlighted by previous studies (Altabet, 1996; Meador et al., 2010), which could potentially account for the observed elevated POC/PN values with depth. Moreover, in the EMS, a significant proportion of C fixed by phytoplankton is released to the dissolved phase (Teira et al., 2001; Lagaria et al., 2011; López-Sandoval et al., 2011), leading to the enhanced extracellular release of organic carbon mainly in the form of carbon-rich acidic polysaccharides (Passow, 2002; Gogou and Repeta, 2010; Parinos et al., 2017). The coagulation of this colloidal dissolved organic matter could lead to the formation of extracellular polymeric substances, mainly transparent exopolymer particles (TEP), bearing a C/N ratio signature well above Redfield, i.e. mean value >20 (Engel and Passow, 2001; Mari et al., 2001). The observed significant positive correlation of D_{50} *vs* POC/PN ratio *vs* depth (**Supplementary Table 1**) could be indicative of the efficiency of aggregation mechanisms within the EMed, with carbon-rich surface active organic particles (i.e. TEPs) acting as "biological glue" for the formation of larger sized aggregates (Bar-Zeev et al., 2011; Parinos et al., 2017; Ortega-Retuerta et al., 2019). In support of this, Martínez-Pérez et al. (2017), recorded a substantial increase of high molecular weight dissolved organic matter (TEP precursors) in a transect spanning from the Atlantic and Gibraltar to the Levantine Sea (from 40–55% to 68–76%, respectively) thus providing independent evidence of more important aggregation potential in the eastern sub-basin.

The horizontal patterns of δ^{15}N-PN observed in the mixed layer of the EMed reflect the interplay of isotopically distinct N sources and the degree of N utilization during primary production. Extremely low δ^{15}N-PN values in NO_3^- replete waters (Hainbucher et al., 2020) at stations 47 and 9 give evidence for diazotrophic N_2 fixation or atmospheric NO_x deposition in the ultra-oligotrophic EMed (Pantoja et al., 2002; Emeis et al., 2010; Moon et al., 2016). Moreover, low values at still

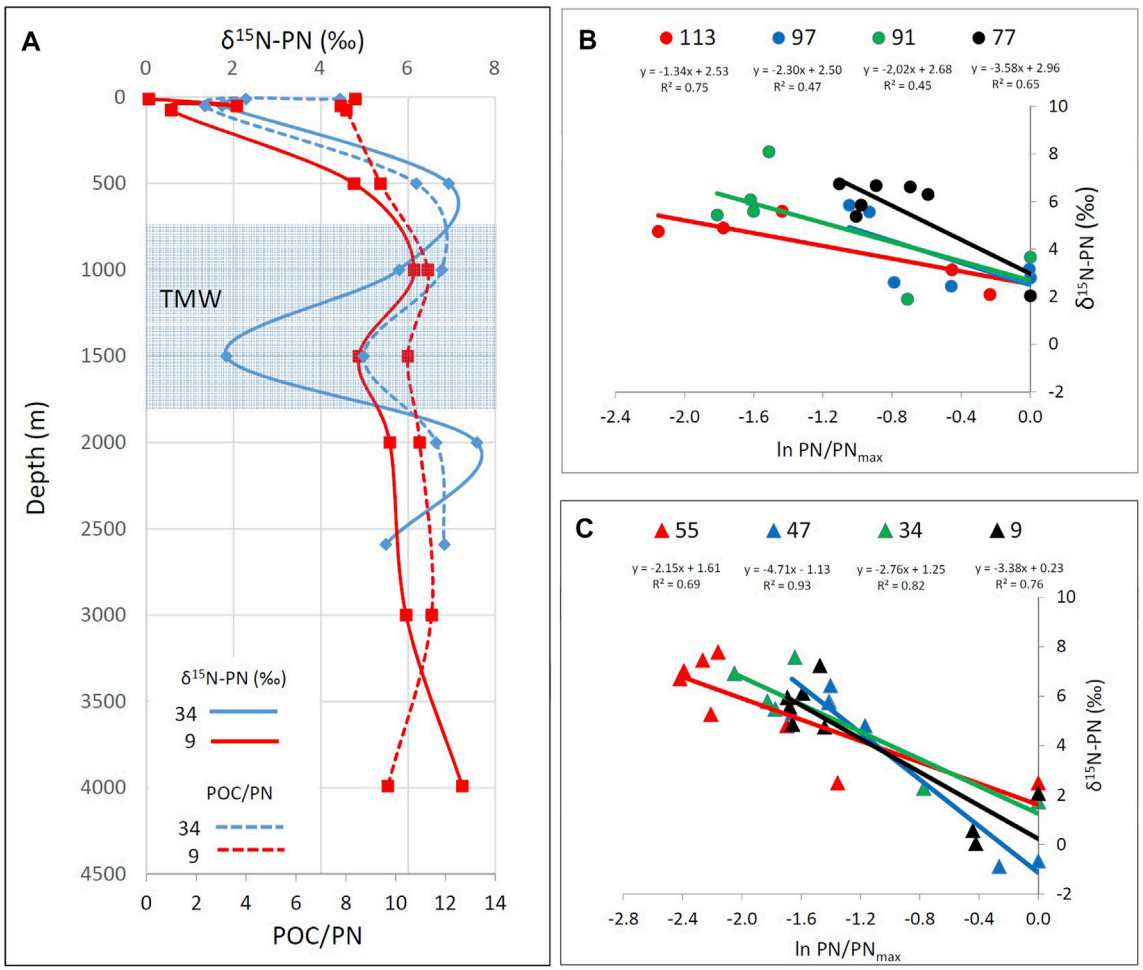

FIGURE 8 | Vertical profiles of δ^{15}N-PN (in ‰; solid lines) and POC/PN ratio (dotted lines) for stations 34 (blue lines) and 9 (red lines) showing outliers within the TMW mass **(A)**. PN concentrations per liter, normalized to maximum PN concentrations of surface waters (10 m or DCM depth for each station, except of station 97 for which the max PN values were observed in subsurface waters) *vs* δ^{15}N-PN (in ‰) for pelagic stations in the WMed **(B)** and EMed **(C)** respectively, indicating Rayleigh-type isotope fractionation. The fractionation factors $^{15}\varepsilon$ calculated from the slope of the logarithmic functions and r^2 significance in all cases show a clear tendency towards stronger fractionation in the EMed (2.15–4.71‰) compared to the WMed (1.34–3.58‰). Y-intercepts indicate initial δ^{15}N values of the substrate (from −1.13 to 2.97‰).

relatively high nitrate levels in the Alboran Sea point towards preferential assimilation of ^{14}N, however, the ambient nitrate most probably had a higher δ^{15}N signature due to its Atlantic origin (Pantoja et al., 2002). Slightly elevated values, in concert with almost depleted NO_3^- concentrations in the surface waters of remaining stations, imply the assimilation of ^{15}N enriched NO_3^- at the end of a blooming period, but may, to some extent, also reflect the increasing importance of ^{15}N enriched sources such as Atlantic water and riverine inputs in the WMed as proposed by Struck et al. (2001) and Pantoja et al. (2002).

The striking segregation of relatively depleted δ^{15}N-PN in the surface or mixed layer waters and enriched values in deep Mediterranean waters has been also observed by Emeis et al. (2010) and Pavlidou et al. (2020). Both attributed the higher δ^{15}N-PN values in deep waters to the enrichment of residual ^{15}N during progressive decay of organic matter, whereas the latter for the first time described a systematic relationship to PN concentrations. In contrast to Pavlidou et al. (2020), our EMed data show several (less enriched) outliers in the δ^{15}N-PN of deep waters. Together with lower POC/PN ratios, these values imply less degraded organic matter (**Figure 8A**). On the other hand, particle concentrations and particle mean sizes remain stable, in defiance of signals from the surface waters such as a sinking algal bloom. At the same time, nitrate concentrations reach their maxima and O_2 concentrations their minima (Hainbucher et al., 2020). Interestingly, all these outliers (even in the Sicily Strait) have been sampled between 500 and 1,500 m within the TMW. The TMW contains former bottom waters that have been uplifted during the EMT (Stöven and Tanhua, 2014; Velaoras et al., 2019). We consider it possible that fresh organic matter has been released from larger disaggregating particles settling in the bottom water, which remained in the water mass during uplift.

The high apparent oxygen utilization (AOU) rates recorded before in the mesopelagic and bathypelagic waters of the EMed (Meador et al., 2010; Santinelli et al., 2010) are indicative of exhaustive organic matter recycling, but the remaining (semi-refractory to refractory) organic matter may not be readily available to deep-sea microbes (Rahav et al., 2019) or is highly diluted (Arrieta et al., 2015).

In support of this hypothesis, Sisma-Ventura et al. (2016) reported depleted values of δ^{13}C-DIC in the LIW and the EMDW of Aegean origin, claiming that isotopically light anthropogenic carbon penetrates the Levantine interior during pronounced convection events such as the EMT. Alternatively, we cannot exclude that lower δ^{15}N-PN values result from surface waters that have downwelled in the Cretan Sea and the EMed during more recent, extreme winter mixing events (i.e. in 2012 and 2014–2015) (Gačić et al., 2014; Pedrosa-Pàmies et al., 2016; Velaoras et al., 2017; Pedrosa-Pamies et al., 2021).

Similar processes could account for the less enriched values of δ^{15}N-PN being observed in some cases at the subsurface layers of the WMed, as a western Mediterranean Transient after the EMT, and extensive downwelling events, have been reported in this sub-basin (Durrieu De Madron et al., 2013; Stöven and Tanhua, 2014; Testor et al., 2018). Finally, we should also mention the possibility that the outliers could give evidence for *in-situ* aphotic diazotrophic N_2 fixation as earlier described for the Mediterranean Sea (Rahav et al., 2013; Benavides et al., 2016; Moisander et al., 2017), although the isotopic fractionation of the processes and sources involved are not yet delineated.

δ^{13}C-POC values show a surface enrichment-depth depletion profile in all stations. A plausible explanation for the relatively depleted δ^{13}C-POC values in the marine organic pool of the open Mediterranean Sea can be the contribution of terrestrial organic matter, mainly via atmospheric dry and wet deposition (Gogou et al., 1996; Guerzoni et al., 1999; Pedrosa-Pamies et al., 2021; Stavrakakis et al., 2013). Vertical differences in organic matter quality and quantity are also reflected in lower N concentrations and the increase of the POC/PN ratio in deep waters of all studied sites. Following the approach of Pavlidou et al. (2020), we assume a Rayleigh type isotope fractionation discriminating ^{15}N during the decomposition of sinking and suspended PN (Möbius, 2013). Evidenced by their data, basic assumptions of Pavlidou et al. (2020) are: 1) PN distribution in the water column is almost solely driven by vertical transport (sinking) from sea surface to bottom waters and 2) additional sources and sinks of PN are negligible. In this case, the strength of fractionation (fractionation factor ε^{15}) is expressed by the slope of the logarithmic function of δ^{15}N-PN *vs* PN in depth profiles. In our study, fractionation factors calculated vary from 1.34 to 4.66‰ (**Figures 8B,C**) and thus are similar to those published in Pavlidou et al. (2020). In contrast to Pavlidou et al. (2020) excellent correlations that cover the full range between both endmembers, our data show stronger scatter and concentrate on the endmembers with only few exceptions. We explain the scattering by both, the above-mentioned outliers in the TMW and by the fact that our sampling sites in the open and deep Mediterranean Sea may be biased by horizontal transport. As correlations in our data set are weaker, we consider the absolute values of fractionation factors with care—nevertheless, a tendency towards stronger fractionation in the EMed can be noted (**Figures 8B,C**). This could either simply reflect the stronger vertical gradients in δ^{15}N-PN in the EMed (extremely low in surface waters) or it is plausible as organic matter decomposition is expected to be more complete in the nutrient starving ultra-oligotrophic EMed in comparison to the oligotrophic WMed.

Apart from biogeochemical properties, local mesoscale features' variability and dynamics seem to play an important role in regulating the optical and biochemical characteristics of particulate matter in the study area. **Supplementary Figure 1**, shows the variability of salinity and beam attenuation coefficient in the Alboran Sea and the Algerian basin. Therein, a sinusoidal variation of salinity is observed, possibly caused by the presence of anticyclonic eddies (Millot, 1999). A similar variation is also observed in the distribution of the beam attenuation coefficient, suggesting that the inherent optical properties of the water masses, and in particular the spatial variability of the beam attenuation coefficient, are largely controlled by mesoscale dynamics.

Interesting optical and biochemical features were also observed in the Otranto Strait which separates the Adriatic and the Ionian Seas (**Supplementary Figures 1, 2**). Dense waters formed locally in the Adriatic during winter, exit through the bottom of the Otranto Strait, while LIW enters the basin at intermediate layers. The result is a cyclonic flow pattern, with water entry at the eastern part of the Strait and exit through the western part (Kovačević et al., 1999; Yari et al., 2012). Indeed, in the studied section, we observed that waters of Adriatic origin occupy the western Otranto Strait and are characterized by higher c_p and VC, and inverse D_{50} values when compared to the LIW waters prevailing in the eastern Otranto Strait. This is accompanied by elevated POC concentrations along with enriched δ^{13}C-POC, and depleted values for δ^{15}N-PN at intermediate and near bottom-waters in the western part of the section, likely attributed to the newly formed dense water-bearing the biochemical signature of surface waters that they originated from. Finally, maximum values of c_p and VC are observed near the bottom layers of the central part of the section. This could likely be attributed to surface sediment resuspension due to currents, a commonly observed feature in the world ocean and the Mediterranean Sea as well (Karageorgis and Anagnostou, 2003; Karageorgis et al., 2008; Karageorgis et al., 2012). In support to this, minimum values for D_{50} are observed in the same area, probably due to the fact that resuspension favors the detachment of smaller particles from the seabed.

CONCLUSION

A data set of beam attenuation coefficient, total particle volume concentration, particle median diameter, and PSD slope ξ up to

3,000 m depth was obtained across the Mediterranean Sea during cruise MSM72 in March-April 2018, a relatively high productivity period for the region, accompanied by standard CTD, biochemical (POC and PN contents) and isotopic data (δ^{13}C-POC and δ^{15}N-PN) of PM. Surface Atlantic waters were identified as the most turbid waters in the Mediterranean Sea, whilst Transitional Mediterranean Water represents the most transparent water mass. A direct relationship between hydrological parameters, water masses and LISST-derived particle optical properties was observed throughout the Mediterranean Sea. The significant correlation between beam attenuation coefficient c_p and POC concentration, consistently observed in the world ocean (Gardner et al., 2006), demonstrates that most particles and particulate organic matter -of marine and/or terrestrial biological origin - predominate in the entire water column of the open Mediterranean Sea. POC concentrations increase inversely with D_{50} and proportionally with ξ, indicating higher organic carbon contents within smaller particle populations. Our data showed substantial differences between the western-central and the eastern sector of the basin, highlighting the transition from mesotrophic to oligotrophic conditions, as well as the overall decrease in suspended particles concentrations. This pattern is observed both in the euphotic zone as well as within the mesopelagic and bathypelagic waters. A predominance of larger particles in the eastern Mediterranean Sea compared to the western Mediterranean Sea was observed, a pattern that is probably associated with more favorable conditions for aggregation in the eastern sub-basin. Basin-wide Rayleigh-type isotope fractionation of δ^{15}N-PN along the water column and gradients in intensity underline the differences in the trophic characters of the two sub-basins. The presence of relatively depleted δ^{15}N-PN values in the Transitional Mediterranean Water mass highlights the role changes in circulation patterns have on biogeochemical parameters and the redistribution of particulate matter as a source of nutrients.

DATA AVAILABILITY STATEMENT

The datasets presented in this study can be found in online repositories. The names of the repository/repositories and accession number(s) can be found below: CTD data: https://doi.org/10.1594/PANGAEA.905902 (Hainbucher et al., 2020); Laser *in situ* Scattering and Transmissometry (LISST–Deep) data: https://doi.pangaea.de/10.1594/PANGAEA.934055; Biochemical data of marine PM (POC, PN, δ^{13}C-POC, δ^{15}N-PN): https://www.ncei.noaa.gov/data/oceans/ncei/ocads/metadata/0218894.html and https://doi.org/10.1594/PANGAEA.905887.

AUTHOR CONTRIBUTIONS

SC, CP, AG, DV, SS, and AK conceived the idea, designed the experiment and wrote the manuscript. JM completed the data analysis of nitrogen isotopes and contributed in writing the manuscript. DH, TT, and VC were chief scientist and PIs of the biogeochemistry and physical oceanography groups of the MSM72 cruise, respectively. SC, DV, VC, TT, and DH collected data aboard the cruise. EP and VA contributed the satellite Chl-α data and wrote the relevant text in the manuscript. All authors aided in editing the manuscript.

FUNDING

This research was supported by the Action "National Network on Climate Change and its Impacts – Climpact" which is implemented under the sub-project 3 of the project "Infrastructure of national research networks in the fields of Precision Medicine, Quantum Technology and Climate Change," funded by the Public Investmen Program of Greece, General Secretary of Research and Technology/Ministry of Development and Investments; and by the "MARine monitoring system of the Hellenic Seas using REmote sensing satellite data and insitu measurements - MARRE" project (T1EDK-02966) financed by the Operational Programme Competitiveness, Entrepreneurship and Innovation (EPAnEK, ESPA 2014–2020) of the Greek Ministry of Economy and Development, and co-funded by the EU (European Regional Development Fund) and by national funds. VA acknowledges support by the ERC Consolidator Grant 2016 D-TECT: "Does dust TriboElectrification affect our ClimaTe?" (grant no. 725698). EP acknowledges support by Greece and the European Union (European Social Fund-ESF) through the Operational Programme "Human Resources Development, Education and Lifelong Learning" in the context of the project "Reinforcement of Postdoctoral Researchers-2nd Cycle" (MIS-5033021), implemented by the State Scholarships Foundation (ΙΚΥ).

ACKNOWLEDGMENTS

Dr. Laura Bray (Hellenic Centre for Marine Research - Oxbridge English) performed proofreading and linguistic corrections of the manuscript. We sincerely thank the officers and crew of *R/V* Maria S. Merian for their precious help during the MSM72 cruise. We would also like to thank the Guest Editor Prof. Gerhard Josef Herndl and the two Reviewers, Prof. A.B. Bochdansky and Dr. T.B. Meador, for their precious comments that helped us to significantly improve the manuscript during the revision process.

SUPPLEMENTARY MATERIAL

The Supplementary Material for this article can be found online at: https://www.frontiersin.org/articles/10.3389/feart.2021.614703/full#supplementary-material

REFERENCES

Agrawal, Y. C., and Pottsmith, H. C. (2000). Instruments for Particle Size and Settling Velocity Observations in Sediment Transport. *Mar. Geol.* 168, 89–114. doi:10.1016/s0025-3227(00)00044-x

Altabet, M. A. (1996). "Nitrogen and Carbon Isotopic Tracers of the Source and Transformation of Particles in the Deep Sea," in *Particle Flux in the Ocean*. Editors V. Ittekkot, P. Schufer, S. Honjo, and P. J. Depetris (Hoboken, NJ: John Wiley & Sons), 155–184.

Arrieta, J. M., Mayol, E., Hansman, R. L., Herndl, G. J., Dittmar, T., and Duarte, C. M. (2015). Dilution Limits Dissolved Organic Carbon Utilization in the Deep Ocean. *Science* 348, 331–333. doi:10.1126/science.1258955

Astraldi, M., Balopoulos, S., Candela, J., Font, J., Gacic, M., Gasparini, G. P., et al. (1999). The Role of Straits and Channels in Understanding the Characteristics of Mediterranean Circulation. *Prog. Oceanogr.* 44, 65–108. doi:10.1016/s0079-6611(99)00021-x

Azov, Y. (1991). Eastern Mediterranean-A marine Desert?. *Mar. Pollut. Bull.* 23, 225–232. doi:10.1016/0025-326x(91)90679-m

Bar-Zeev, E., Berman, T., Rahav, E., Dishon, G., Herut, B., and Berman-Frank, I. (2011). Transparent Exopolymer Particle (TEP) Dynamics in the Eastern Mediterranean Sea. *Mar. Ecol. Prog. Ser.* 431, 107–118. doi:10.3354/meps09110

Barbieux, M., Uitz, J., Gentili, B., Pasqueron De Fommervault, O., Mignot, A., Poteau, A., et al. (2019). Bio-Optical Characterization of Subsurface Chlorophyll Maxima in the Mediterranean Sea from a Biogeochemical-Argo Float Database. *Biogeosciences* 16, 1321–1342. doi:10.5194/bg-16-1321-2019

Barone, B., Bidigare, R. R., Church, M. J., Karl, D. M., Letelier, R. M., and White, A. E. (2015). Particle Distributions and Dynamics in the Euphotic Zone of the North Pacific Subtropical Gyre. *J. Geophys. Res. Oceans* 120, 3229–3247. doi:10.1002/2015jc010774

Benavides, M., Bonnet, S., Hernández, N., Martínez-Pérez, A. M., Nieto-Cid, M., Álvarez-Salgado, X. A., et al. (2016). Basin-wide N2 Fixation in the Deep Waters of the Mediterranean Sea. *Glob. Biogeochem. Cycles* 30, 952–961. doi:10.1002/2015gb005326

Béthoux, J. P., Morin, P., Chaumery, C., Connan, O., Gentili, B., and Ruiz-Pino, D. (1998). Nutrients in the Mediterranean Sea, Mass Balance and Statistical Analysis of Concentrations with Respect to Environmental Change. *Mar. Chem.* 63, 155–169. doi:10.1016/s0304-4203(98)00059-0

Bishop, J. K. B. (1999). Transmissometer Measurement of POC. *Deep Sea Res. Oceanogr. Res. Pap.* 46, 353–369. doi:10.1016/s0967-0637(98)00069-7

Boss, E., Haëntjens, N., Westberry, T. K., Karp-Boss, L., and Slade, W. H. (2018). Validation of the Particle Size Distribution Obtained with the Laser Iin-Ssitu Scattering and Transmission (LISST) Meter in Flow-Through Mode. *Opt. Express* 26, 11125–11136. doi:10.1364/oe.26.011125

Boss, E., Slade, W. H., Behrenfeld, M., and Dall'olmo, G. (2009). Acceptance Angle Effects on the Beam Attenuation in the Ocean. *Opt. Express* 17, 1535–1550. doi:10.1364/oe.17.001535

Boss, E., Twardowski, M. S., and Herring, S. (2001). Shape of the Particulate Beam Attenuation Spectrum and its Inversion to Obtain the Shape of the Particulate Size Distribution. *Appl. Opt.* 40, 4885–4893. doi:10.1364/ao.40.004885

Bricaud, A., Babin, M., Morel, A., and Claustre, H. (1995). Variability in the Chlorophyll-Specific Absorption Coefficients of Natural Phytoplankton: Analysis and Parametrization. *Journal of Geophysical Research Atmospheres* 100 (C7), 13,321–13,332. doi:10.1029/95JC00463

Bricaud, A., Morel, A., Babin, M., Allali, K., and Claustre, H. (1998) Variations of light absorption by suspended particles with chlorophyll a concentration in oceanic (case 1) waters: Analysis and implications for bio-optical models. *Journal of Geophysical Research Atmospheres* 103 (C4), 31,033–31,044. doi:10.1029/98JC02712

Buonassissi, C. J., and Dierssen, H. M. (2010). A Regional Comparison of Particle Size Distributions and the Power Law Approximation in Oceanic and Estuarine Surface Waters. *J. Geophys. Res. Oceans* 115, C10028. doi:10.1029/2010jc006256

Cardin, V., Civitarese, G., Hainbucher, D., Bensi, M., and Rubino, A. (2015). Thermohaline Properties in the Eastern Mediterranean in the Last Three Decades: Is the basin Returning to the Pre-EMT Situation?. *Ocean Sci.* 11, 53–66. doi:10.5194/os-11-53-2015

Close, H. G., and Henderson, L. C. (2020). Open-Ocean Minima in δ13C Values of Particulate Organic Carbon in the Lower Euphotic Zone. *Front. Mar. Sci.* 7, 540165. doi:10.3389/fmars.2020.540165

Çoban-Yildiz, Y., Altabet, M. A., Yilmaz, A., and Tuğrul, S. (2006). Carbon and Nitrogen Isotopic Ratios of Suspended Particulate Organic Matter (SPOM) in the Black Sea Water Column. *Deep-Sea Res. Part Topical Stud. Oceanogr.* 53, 1875–1892. doi:10.1016/j.dsr2.2006.03.021

D'Ortenzio, F., and Ribera d'Alcalà, M. (2009). On the Trophic Regimes of the Mediterranean Sea: A Satellite Analysis. *Biogeosciences* 6, 139–148. doi:10.5194/bg-6-139-2009

D'Ortenzio, F., Taillandier, V., Claustre, H., Coppola, L., Conan, P., Dumas, F., et al. (2021). BGC-Argo Floats Observe Nitrate Injection and Spring Phytoplankton Increase in the Surface Layer of Levantine Sea (Eastern Mediterranean). *Geophys. Res. Lett.* 48, e2020GL091649. doi:10.1029/2020gl091649

Durrieu De Madron, X., Guieu, C., Sempéré, R., Conan, P., Cossa, D., D'Ortenzio, F., et al. (2011). Marine Ecosystems' Responses to Climatic and Anthropogenic Forcings in the Mediterranean. *Prog. Oceanogr.* 91, 97–166. doi:10.1016/j.pocean.2011.02.003

Durrieu De Madron, X., Houpert, L., Puig, P., Sanchez-Vidal, A., Testor, P., Bosse, A., et al. (2013). Interaction of Dense Shelf Water Cascading and Open-Sea Convection in the Northwestern Mediterranean During Winter 2012. *Geophys. Res. Lett.* 40, 1379–1385. doi:10.1002/grl.50331

Emeis, K.-C., Mara, P., Schlarbaum, T., Möbius, J., Dähnke, K., Struck, U., et al. (2010). External N Inputs and Internal N Cycling Traced by Isotope Ratios of Nitrate, Dissolved Reduced Nitrogen, and Particulate Nitrogen in the Eastern Mediterranean Sea. *J. Geophys. Res.* 115, G04041. doi:10.1029/2009jg001214

Engel, A., and Passow, U. (2001). Carbon and Nitrogen Content of Transparent Exopolymer Particles (TEP) in Relation to Their Alcian Blue Adsorption. *Mar. Ecol. Prog. Ser.* 219, 1–10. doi:10.3354/meps219001

CIESM (2012). "Designing Med-SHIP: a Program for Repeated Oceanographic Surveys." in *CIESM Workshop Monograph n. 43*, Editor F. Briand (Monaco: CIESM Publisher), 164.

Gačić, M., Civitarese, G., Kovačević, V., Ursella, L., Bensi, M., Menna, M., et al. (2014). Extreme winter 2012 in the Adriatic: An Example of Climatic Effect on the biOS Rhythm. *Ocean Sci.* 10, 513–522. doi:10.5194/os-10-513-2014

Gardner, W. D., Mishonov, A. V., and Richardson, M. J. (2006). Global POC Concentrations from Iin-Ssitu and Satellite Data. *Deep Sea Res. Part Topical Stud. Oceanogr.* 53, 718–740. doi:10.1016/j.dsr2.2006.01.029

Gogou, A., and Repeta, D. J. (2010). Particulate-dissolved Transformations as a Sink for Semi-labile Dissolved Organic Matter: Chemical Characterization of High Molecular Weight Dissolved and Surface-Active Organic Matter in Seawater and in Diatom Cultures. *Mar. Chem.* 121, 215–223. doi:10.1016/j.marchem.2010.05.001

Gogou, A., Sanchez-Vidal, A., Durrieu De Madron, X., Stavrakakis, S., Calafat, A. M., Stabholz, M., et al. (2014). Carbon Flux to the Deep in Three Open Sites of the Southern European Seas (SES). *J. Mar. Syst.* 129, 224–233. doi:10.1016/j.jmarsys.2013.05.013

Gogou, A., Stratigakis, N., Kanakidou, M., and Stephanou, E. G. (1996). Organic Aerosols in Eastern Mediterranean: Components Source Reconciliation by Using Molecular Markers and Atmospheric Back Trajectories. *Org. Geochem.* 25, 79–96. doi:10.1016/s0146-6380(96)00105-2

Guerzoni, S., Chester, R., Dulac, F., Herut, B., Loÿe-Pilot, M.-D., Measures, C., et al. (1999). The Role of Atmospheric Deposition in the Biogeochemistry of the Mediterranean Sea. *Prog. Oceanogr.* 44, 147–190. doi:10.1016/s0079-6611(99)00024-5

Hainbucher, D., Álvarez, M., Astray Uceda, B., Bachi, G., Cardin, V., Celentano, P., et al. (2020). Physical and Biogeochemical Parameters of the Mediterranean Sea During a Cruise with RV Maria S. Merian in March 2018. *Earth Syst. Sci. Data* 12, 2747–2763. doi:10.5194/essd-12-2747-2020

Honjo, S., Manganini, S. J., Krishfield, R. A., and Francois, R. (2008). Particulate Organic Carbon Fluxes to the Ocean interior and Factors Controlling the Biological Pump: A Synthesis of Global Sediment Trap Programs since 1983. *Prog. Oceanogr.* 76, 217–285. doi:10.1016/j.pocean.2007.11.003

Ignatiades, L., Psarra, S., Zervakis, V., Pagou, K., Souvermezoglou, E., Assimakopoulou, G., et al. (2002). Phytoplankton Size-Based Dynamics in the Aegean Sea (Eastern Mediterranean). *J. Mar. Syst.* 36, 11–28. doi:10.1016/s0924-7963(02)00132-x

Jeandel, C., Rutgers Van Der Loeff, M., Lam, P. J., Roy-Barman, M., Sherrell, R. M., Kretschmer, S., et al. (2015). What Did We Learn about Ocean Particle Dynamics in the GEOSECS-JGOFS Era?. *Prog. Oceanogr.* 133, 6–16. doi:10.1016/j.pocean.2014.12.018

Karageorgis, A. P., and Anagnostou, C. L. (2003). Seasonal Variation in the Distribution of Suspended Particulate Matter in the Northwest Aegean Sea. *J. Geophys. Res. Oceans* 108, 30–31. doi:10.1029/2002jc001672

Karageorgis, A. P., Drakopoulos, P. G., Chaikalis, S., Spyridakis, N., and Psarra, S. (2017a). "Estimation of the Particle Size Distribution Slope with 3 Methods: Implications for the Optical Backscattering Ratio and the Bulk Refractive index," in Proceedings of SPIE - The International Society for Optical Engineering, 10444.

Karageorgis, A. P., Drakopoulos, P. G., Psarra, S., Pagou, K., Krasakopoulou, E., Banks, A. C., et al. (2017b). Particle Characterization and Composition in the NE Aegean Sea: Combining Optical Methods and Biogeochemical Parameters. *Cont. Shelf Res.* 149, 96–111. doi:10.1016/j.csr.2017.03.008

Karageorgis, A. P., Gardner, W. D., Georgopoulos, D., Mishonov, A. V., Krasakopoulou, E., and Anagnostou, C. (2008). Particle Dynamics in the Eastern Mediterranean Sea: A Synthesis Based on Light Transmission, PMC, and POC Archives (1991-2001). *Deep Sea Res. Part Oceanogr. Res. Pap.* 55, 177–202. doi:10.1016/j.dsr.2007.11.002

Karageorgis, A. P., Gardner, W. D., Mikkelsen, O. A., Georgopoulos, D., Ogston, A. S., Assimakopoulou, G., et al. (2014). Particle Sources over the Danube River delta, Black Sea Based on Distribution, Composition and Size Using Optics, Imaging and Bulk Analyses. *J. Mar. Syst.* 131, 74–90. doi:10.1016/j.jmarsys.2013.11.013

Karageorgis, A. P., Georgopoulos, D., Kanellopoulos, T. D., Mikkelsen, O. A., Pagou, K., Kontoyiannis, H., et al. (2012). Spatial and Seasonal Variability of Particulate Matter Optical and Size Properties in the Eastern Mediterranean Sea. *J. Mar. Syst.* 105–108, 123–134. doi:10.1016/j.jmarsys.2012.07.003

Karageorgis, A. P., Kontoyiannis, H., Stavrakakis, S., Krasakopoulou, E., Gogou, A., Kanellopoulos, Th. D., Rousakis, G., Malinverno, E., Triantaphyllou, M. V., and Lykousis, V. (2018). Particle dynamics and fluxes in canyons and open slopes of the southern Cretan margin (Eastern Mediterranean). *Progress in Oceanography.* 169, 33–47. doi:10.1016/j.pocean.2017.12.009

Kerhervé, P., Minagawa, M., Heussner, S., and Monaco, A. (2001). Stable Isotopes (13C/12C and 15N/14N) in Settling Organic Matter of the Northwestern Mediterranean Sea: Biogeochemical Implications. *Oceanol. Acta* 24, S77–S85. doi:10.1016/s0399-1784(00)01111-7

Koppelmann, R., Böttger-Schnack, R., Möbius, J., and Weikert, H. (2009). Trophic Relationships of Zooplankton in the Eastern Mediterranean Based on Stable Isotope Measurements. *J. Plankton Res.* 31, 669–686. doi:10.1093/plankt/fbp013

Kostadinov, T. S., Siegel, D. A., Maritorena, S., and Guillocheau, N. (2012). Optical Assessment of Particle Size and Composition in the Santa Barbara Channel, California. *Appl. Opt.* 51, 3171–3189. doi:10.1364/ao.51.003171

Kovačević, V., Gačić, M., and Poulain, P.-M. (1999). Eulerian Current Measurements in the Strait of Otranto and in the Southern Adriatic. *J. Mar. Syst.* 20, 255–278.

Krom, M. D., Emeis, K.-C., and Van Cappellen, P. (2010). Why Is the Eastern Mediterranean Phosphorus Limited?. *Prog. Oceanogr.* 85, 236–244. doi:10.1016/j.pocean.2010.03.003

Krom, M., Kress, N., Berman-Frank, I., and Rahav, E. (2014). "Past, Present and Future Patterns in the Nutrient Chemistry of the Eastern Mediterranean," in *The Mediterranean Sea: Its History and Present Challenges*. Editors Goffredo, S., and Dubinsky, Z., 49–68. doi:10.1007/978-94-007-6704-1_4

Lagaria, A., Psarra, S., Lefèvre, D., Van Wambeke, F., Courties, C., Pujo-Pay, M., et al. (2011). The Effects of Nutrient Additions on Particulate and Dissolved Primary Production and Metabolic State in Surface Waters of Three Mediterranean Eddies. *Biogeosciences* 8, 2595–2607. doi:10.5194/bg-8-2595-2011

Leroux, R., Gregori, G., Leblanc, K., Carlotti, F., Thyssen, M., Dugenne, M., et al. (2018). Combining Laser Diffraction, Flow Cytometry and Optical Microscopy to Characterize a Nanophytoplankton Bloom in the Northwestern Mediterranean. *Prog. Oceanogr.* 163, 248–259. doi:10.1016/j.pocean.2017.10.010

Li, P., and Tanhua, T. (2020). Recent Changes in Deep Ventilation of the Mediterranean Sea; Evidence From Long-Term Transient Tracer Observations. *Front. Mar. Sci.* 7, 594. doi:10.3389/fmars.2020.00594

Loisel, H, and Morel, A. (1998). Light scattering and chlorophyll concentration in Case 1 waters: A reexamination. *Limnology and Oceanography.* doi:10.4319/lo.1998.43.5.0847

Loisel, H., Vantrepotte, V., Norkvist, K., Mériaux, X., Kheireddine, M., Ras, J., et al. (2011). Characterization of the Bio-Optical Anomaly and Diurnal Variability of Particulate Matter, as Seen from Scattering and Backscattering Coefficients, in Ultra-Oligotrophic Eddies of the Mediterranean Sea. *Biogeosciences* 8, 3295–3317. doi:10.5194/bg-8-3295-2011

López-Sandoval, D. C., Fernández, A., and Marañón, E. (2011). Dissolved and Particulate Primary Production along a Longitudinal Gradient in the Mediterranean Sea. *Biogeosciences* 8, 815–825. doi:10.5194/bg-8-815-2011

Ludwig, W., Dumont, E., Meybeck, M., and Heussner, S. (2009). River Discharges of Water and Nutrients to the Mediterranean and Black Sea: Major Drivers for Ecosystem Changes during Past and Future Decades?. *Prog. Oceanogr.* 80, 199–217. doi:10.1016/j.pocean.2009.02.001

Malanotte-Rizzoli, P. (2001). "Current Systems in the Mediterranean Sea," in *Encyclopedia of Ocean Sciences*. 2nd Edn. 744–751. doi:10.1016/b978-012374473-9.00375-1

Many, G., Bourrin, F., Durrieu De Madron, X., Pairaud, I., Gangloff, A., Doxaran, D., et al. (2016). Particle Assemblage Characterization in the Rhone River ROFI. *J. Mar. Syst.* 157, 39–51. doi:10.1016/j.jmarsys.2015.12.010

Mara, P., Mihalopoulos, N., Gogou, A., Daehnke, K., Schlarbaum, T., Emeis, K. C., et al. (2009). Isotopic Composition of Nitrate in Wet and Dry Atmospheric Deposition on Crete in the Eastern Mediterranean Sea. *Glob. Biogeochem. Cycles* 23, GB4002. doi:10.1029/2008gb003395

Mari, X., Beauvais, S., Lemée, R., and Pedrotti, M. L. (2001). Non-Redfield C:N Ratio of Transparent Exopolymeric Particles in the Northwestern Mediterranean Sea. *Limnol. Oceanogr.* 46, 1831–1836. doi:10.4319/lo.2001.46.7.1831

Mariotti, A., Germon, J. C., Hubert, P., Kaiser, P., Letolle, R., Tardieux, A., et al. (1981). Experimental Determination of Nitrogen Kinetic Isotope Fractionation: Some Principles; Illustration for the Denitrification and Nitrification Processes. *Plant Soil* 62, 413–430. doi:10.1007/bf02374138

Markaki, Z., Loÿe-Pilot, M. D., Violaki, K., Benyahya, L., and Mihalopoulos, N. (2010). Variability of Atmospheric Deposition of Dissolved Nitrogen and Phosphorus in the Mediterranean and Possible Link to the Anomalous Seawater N/P Ratio. *Mar. Chem.* 120, 187–194. doi:10.1016/j.marchem.2008.10.005

Martínez-Pérez, A. M., Álvarez-Salgado, X. A., Arístegui, J., and Nieto-Cid, M. (2017). Deep-Ocean Dissolved Organic Matter Reactivity Along the Mediterranean Sea: Does Size Matter?. *Sci. Rep.* 7, 5687. doi:10.1038/s41598-017-05941-6

Mayot, N., D'ortenzio, F., Ribera d'Alcalà, M., Lavigne, H., and Claustre, H. (2016). Interannual Variability of the Mediterranean Trophic Regimes from Ocean Color Satellites. *Biogeosciences* 13, 1901–1917. doi:10.5194/bg-13-1901-2016

Meador, T. B., Aluwihare, L. I., and Mahaffey, C. (2007). Isotopic Heterogeneity and Cycling of Organic Nitrogen in the Oligotrophic Ocean. *Limnol. Oceanogr.* 52, 934–947. doi:10.4319/lo.2007.52.3.0934

Meador, T. B., Gogou, A., Spyres, G., Herndl, G. J., Krasakopoulou, E., Psarra, S., et al. (2010). Biogeochemical Relationships between Ultrafiltered Dissolved Organic Matter and Picoplankton Activity in the Eastern Mediterranean Sea. *Deep Sea Res. Part Topical Stud. Oceanogr.* 57, 1460–1477. doi:10.1016/j.dsr2.2010.02.015

Mikkelsen, O. A., Hill, P. S., and Milligan, T. G. (2006). Single-Grain, Microfloc and Macrofloc Volume Variations Observed with a LISST-100 and a Digital Floc Camera. *J. Sea Res.* 55, 87–102. doi:10.1016/j.seares.2005.09.003

Millot, C. (1999). Circulation in the Western Mediterranean Sea. *J. Mar. Syst.* 20, 423–442. doi:10.1016/s0924-7963(98)00078-5

Millot, C., and Taupier-Letage, I. (2005). Additional Evidence of LIW Entrainment across the Algerian Subbasin by Mesoscale Eddies and Not by a Permanent Westward Flow. *Prog. Oceanogr.* 66, 231–250. doi:10.1016/j.pocean.2004.03.002

Möbius, J. (2013). Isotope Fractionation during Nitrogen Remineralization (Ammonification): Implications for Nitrogen Isotope Biogeochemistry. *Geochim. Cosmochim. Acta* 105, 422–432. doi:10.1016/j.gca.2012.11.048

Möbius, J., Lahajnar, N., and Emeis, K.-C. (2010). Diagenetic Control of Nitrogen Isotope Ratios in Holocene Sapropels and Recent Sediments from the Eastern Mediterranean Sea. *Biogeosciences* 7, 3901–3914. doi:10.5194/bg-7-3901-2010

Moisander, P. H., Benavides, M., Bonnet, S., Berman-Frank, I., White, A. E., and Riemann, L. (2017). Chasing after Non-cyanobacterial Nitrogen Fixation in

marine Pelagic Environments. *Front. Microbiol.* 8, 1736. doi:10.3389/fmicb.2017.01736

Moon, J. Y., Lee, K., Tanhua, T., Kress, N., and Kim, I. N. (2016). Temporal Nutrient Dynamics in the Mediterranean Sea in Response to Anthropogenic Inputs. *Geophys. Res. Lett.* 43, 5243–5251. doi:10.1002/2016gl068788

Moutin, T., Van Wambeke, F., and Prieur, L. (2012). Introduction to the Biogeochemistry from the Oligotrophic to the Ultraoligotrophic Mediterranean (BOUM) experiment. *Biogeosciences* 9, 3817–3825. doi:10.5194/bg-9-3817-2012

Ortega-Retuerta, E., Mazuecos, I. P., Reche, I., Gasol, J. M., Álvarez-Salgado, X. A., Álvarez, M., et al. (2019). Transparent Exopolymer Particle (TEP) Distribution and *In Situ* Prokaryotic Generation across the Deep Mediterranean Sea and Nearby North East Atlantic Ocean. *Prog. Oceanogr.* 173, 180–191. doi:10.1016/j.pocean.2019.03.002

Ortega-Retuerta, E., Sala, M. M., Borrull, E., Mestre, M., Aparicio, F. L., Gallisai, R., et al. (2017). Horizontal and Vertical Distributions of Transparent Exopolymer Particles (TEP) in the NW Mediterranean Sea Are Linked to Chlorophyll a and O2 Variability. *Front. Microbiol.* 7, 2159. doi:10.3389/fmicb.2016.02159

Pantoja, S., Repeta, D. J., Sachs, J. P., and Sigman, D. M. (2002). Stable Isotope Constraints on the Nitrogen Cycle of the Mediterranean Sea Water Column. *Deep Sea Res. Part Oceanogr. Res. Pap.* 49, 1609–1621. doi:10.1016/s0967-0637(02)00066-3

Parinos, C., Gogou, A., Krasakopoulou, E., Lagaria, A., Giannakourou, A., Karageorgis, A. P., et al. (2017). Transparent Exopolymer Particles (TEP) in the NE Aegean Sea Frontal Area: Seasonal Dynamics under the Influence of Black Sea Water. *Cont. Shelf Res.* 149, 112–123. doi:10.1016/j.csr.2017.03.012

Passow, U. (2002). Production of Transparent Exopolymer Particles (TEP) by Phyto- and Bacterioplankton. *Mar. Ecol. Prog. Ser.* 236, 1–12. doi:10.3354/meps236001

Pavlidou, A., Velaoras, D., Karageorgis, A. P., Rousselaki, E., Parinos, C., Dähnke, K., et al. (2020). Seasonal Variations of Biochemical and Optical Properties, Physical Dynamics and N Stable Isotopic Composition in Three Northeastern Mediterranean Basins (Aegean, Cretan and Ionian Seas). *Deep Sea Res. Part Topical Stud. Oceanogr.* 171, 104704. doi:10.1016/j.dsr2.2019.104704

Pedrosa-Pamies, R., Parinos, C., Sanchez-Vidal, A., Calafat, A., Canals, M., Velaoras, D., et al. (2021). Atmospheric and Oceanographic Forcing Impact Particle Flux Composition and Carbon Sequestration in the Eastern Mediterranean Sea: A Three-Year Time-Series Study in the Deep Ierapetra Basin. *Front. Earth Sci.* 9, 591948. doi:10.3389/feart.2021.591948

Pedrosa-Pàmies, R., Sanchez-Vidal, A., Canals, M., Lampadariou, N., Velaoras, D., Gogou, A., et al. (2016). Enhanced Carbon export to the Abyssal Depths Driven by Atmosphere Dynamics. *Geophys. Res. Lett.* 43, 8626–8636. doi:10.1002/2016gl069781

Peterson, B. J., and Fry, B. (1987). Stable Isotopes in Ecosystem Studies. *Annu. Rev. Ecol. Syst.* 18, 293–320. doi:10.1146/annurev.es.18.110187.001453

Qiu, Z., Sun, D., Hu, C., Wang, S., Zheng, L., Huan, Y., et al. (2016). Variability of Particle Size Distributions in the Bohai Sea and the Yellow Sea. *Remote Sens.* 8, 949. doi:10.3390/rs8110949

Rahav, E., Bar-Zeev, E., Ohayon, S., Elifantz, H., Belkin, N., Herut, B., et al. (2013). Dinitrogen Fixation in Aphotic Oxygenated marine Environments. *Front. Microbiol.* 4, 227. doi:10.3389/fmicb.2013.00227

Rahav, E., Silverman, J., Raveh, O., Hazan, O., Rubin-Blum, M., Zeri, C., et al. (2019). The Deep Water of Eastern Mediterranean Sea is a Hotspot for Bacterial Activity. *Deep Sea Res. Part Topical Stud. Oceanogr.* 164, 135–143. doi:10.1016/j.dsr2.2019.03.004

Roether, W., Klein, B., Manca, B. B., Theocharis, A., and Kioroglou, S. (2007). Transient Eastern Mediterranean Deep Waters in Response to the Massive Dense-Water Output of the Aegean Sea in the 1990s. *Prog. Oceanogr.* 74, 540–571. doi:10.1016/j.pocean.2007.03.001

Runyan, H., Reynolds, R. A., and Stramski, D. (2020). Evaluation of Particle Size Distribution Metrics to Estimate the Relative Contributions of Different Size Fractions Based on Measurements in Arctic Waters. *J. Geophys. Res. Oceans* 125, e2020JC016218. doi:10.1029/2020jc016218

Santinelli, C., Nannicini, L., and Seritti, A. (2010). DOC Dynamics in the Meso and Bathypelagic Layers of the Mediterranean Sea. *Deep Sea Res. Part Topical Stud. Oceanogr.* 57, 1446–1459. doi:10.1016/j.dsr2.2010.02.014

Schlitzer, R. (2018). Ocean Data View. Available at: http://odv.awi.de.

Schroeder, K., Chiggiato, J., Bryden, H. L., Borghini, M., and Ben Ismail, S. (2016). Abrupt Climate Shift in the Western Mediterranean Sea. *Sci. Rep.* 6, 23009. doi:10.1038/srep23009

Schroeder, K., Chiggiato, J., Josey, S. A., Borghini, M., Aracri, S., and Sparnocchia, S. (2017). Rapid Response to Climate Change in a Marginal Sea. *Sci. Rep.* 7, 4065. doi:10.1038/s41598-017-04455-5

Siokou-Frangou, I., Bianchi, M., Christaki, U., Christou, E. D., Giannakourou, A., Gotsis, O., et al. (2002). Carbon Flow in the Planktonic Food Web along a Gradient of Oligotrophy in the Aegean Sea (Mediterranean Sea). *J. Mar. Syst.* 33-34, 335–353. doi:10.1016/s0924-7963(02)00065-9

Sisma-Ventura, G., Yam, R., Kress, N., and Shemesh, A. (2016). Water Column Distribution of Stable Isotopes and Carbonate Properties in the South-Eastern Levantine basin (Eastern Mediterranean): Vertical and Temporal Change. *J. Mar. Syst.* 158, 13–25. doi:10.1016/j.jmarsys.2016.01.012

Stavrakakis, S., Gogou, A., Krasakopoulou, E., Karageorgis, A. P., Kontoyiannis, H., Rousakis, G., Velaoras, D., Perivoliotis, L., Kambouri, G., Stavrakaki, I., and Lykousis, V. (2013). Downward fluxes of sinking particulate matter in the deep Ionian Sea (NESTOR site), Eastern Mediterranean: Seasonal and interannual variability. *Biogeosciences* 10, 7235–7254. doi:10.5194/bg-10-7235-2013

Stöven, T., and Tanhua, T. (2014). Ventilation of the Mediterranean Sea Constrained by Multiple Transient Tracer Measurements. *Ocean Sci.* 10, 439–457. doi:10.5194/os-10-439-2014

Struck, U., Emeis, K.-C., Voß, M., Krom, M. D., and Rau, G. H. (2001). Biological Productivity during Sapropel S5 Formation in the Eastern Mediterranean Sea: Evidence from Stable Isotopes of Nitrogen and Carbon. *Geochim. Cosmochim. Acta* 65, 3249–3266. doi:10.1016/s0016-7037(01)00668-8

Stumm, W., and Morgan, J. J. (1981). *Aquatic Chemistry: An Introduction Emphasizing Chemical Equilibria in Natural Waters*. 2nd Edn. New York: John Wiley & Sons.

Tanaka, T., Zohary, T., Krom, M. D., Law, C. S., Pitta, P., Psarra, S., et al. (2007). Microbial Community Structure and Function in the Levantine Basin of the Eastern Mediterranean. *Deep Sea Res. Part Oceanogr. Res. Pap.* 54, 1721–1743. doi:10.1016/j.dsr.2007.06.008

Tanhua, T., Hainbucher, D., Schroeder, K., Cardin, V., Álvarez, M., and Civitarese, G. (2013). The Mediterranean Sea System: A Review and an Introduction to the Special Issue. *Ocean Sci.* 9, 789–803. doi:10.5194/os-9-789-2013

Teira, E., José Pazó, M., Serret, P., and Fernández, E. (2001). Dissolved Organic Carbon Production by Microbial Populations in the Atlantic Ocean. *Limnol. Oceanogr.* 46, 1370–1377. doi:10.4319/lo.2001.46.6.1370

Testor, P., Bosse, A., Houpert, L., Margirier, F., Mortier, L., Legoff, H., et al. (2018). Multiscale Observations of Deep Convection in the Northwestern Mediterranean Sea During Winter 2012-2013 Using Multiple Platforms. *J. Geophys. Res. Oceans* 123, 1745–1776. doi:10.1002/2016jc012671

Turley, C., Bianchi, M., Christaki, U., Conan, P., Harris, J., Psarra, S., et al. (2000). Relationship Between Primary Producers and Bacteria in an Oligotrophic Sea-The Mediterranean and Biogeochemical Implications. *Mar. Ecol. Prog. Ser.* 193, 11–18. doi:10.3354/meps193011

Turner, J. S., Pretty, J. L., and Mcdonnell, A. M. P. (2017). Marine Particles in the Gulf of Alaska Shelf System: Spatial Patterns and Size Distributions from *In Situ* Optics. *Cont. Shelf Res.* 145, 13–20. doi:10.1016/j.csr.2017.07.002

Twardowski, M. S., Boss, E., Macdonald, J. B., Pegau, W. S., Barnard, A. H., and Zaneveld, J. R. V. (2001). A Model for Estimating Bulk Refractive index from the Optical Backscattering Ratio and the Implications for Understanding Particle Composition in Case I and Case II Waters. *J. Geophys. Res.* 106, 14129–14142. doi:10.1029/2000jc000404

Velaoras, D., Papadopoulos, V. P., Kontoyiannis, H., Cardin, V., and Civitarese, G. (2019). Water Masses and Hydrography during April and June 2016 in the Cretan Sea and Cretan Passage (Eastern Mediterranean Sea). *Deep Sea Res. Part Topical Stud. Oceanogr.* 164, 25–40. doi:10.1016/j.dsr2.2018.09.005

Velaoras, D., Papadopoulos, V. P., Kontoyiannis, H., Papageorgiou, D. K., and Pavlidou, A. (2017). The Response of the Aegean Sea (Eastern Mediterranean) to the Extreme 2016-2017 Winter. *Geophys. Res. Lett.* 44, 9416–9423. doi:10.1002/2017gl074761

Volk, T., and Hoffert, M. I. (1985). "Ocean Carbon Pumps: Analysis of Relative Strengths and Efficiencies in Ocean-Driven Atmospheric CO_2 Changes," in *The Carbon Cycle and Atmospheric CO_2: Natural Variations Archean to present. Chapman Conference Papers, 1984*. Editors Sundquist, E. T., and Broecker, W. S. (New York University, NY: American Geophysical Union), 99–110.

Wada, E., and Hattori, A. (1991). *Variation of Nitrogen in the Sea: Forms, Abundances and Rate Processes*. Boca Raton, FL: CRC Press, 208.

Waser, N., Yin, K., Yu, Z., Tada, K., Harrison, P., Turpin, D., et al. (1998). Nitrogen Isotope Fractionation During Nitrate, Ammonium and Urea Uptake by marine Diatoms and Coccolithophores under Various Conditions of N Availability. *Mar. Ecol. Prog. Ser.* 169, 29–41. doi:10.3354/meps169029

White, A. E., Letelier, R. M., Whitmire, A. L., Barone, B., Bidigare, R. R., Church, M. J., et al. (2015). Phenology of Particle Size Distributions and Primary Productivity in the N Orth P Acific Subtropical Gyre (S Tation ALOHA). *J. Geophys. Res. Oceans* 120, 7381–7399. doi:10.1002/2015jc010897

Wu, J., Calvert, S. E., Wong, C. S., and Whitney, F. A. (1999). Carbon and Nitrogen Isotopic Composition of Sedimenting Particulate Material at Station Papa in the Subarctic Northeast Pacific. *Deep Sea Res. Part Topical Stud. Oceanogr.* 46, 2793–2832. doi:10.1016/s0967-0645(99)00084-3

Wüst, G. (1961). On the Vertical Circulation of the Mediterranean Sea. *J. Geophys. Res.* 66, 3261–3271. doi:10.1029/jz066i010p03261

Xi, H., Larouche, P., Tang, S., and Michel, C. (2014). Characterization and Variability of Particle Size Distributions in Hudson Bay, Canada. *J. Geophys. Res. Oceans* 119, 3392–3406. doi:10.1002/2013jc009542

Yamada, Y., Fukuda, H., Uchimiya, M., Motegi, C., Nishino, S., Kikuchi, T., et al. (2015). Localized Accumulation and a Shelf-Basin Gradient of Particles in the Chukchi Sea and Canada Basin, Western Arctic. *J. Geophys. Res. Oceans* 120, 4638–4653. doi:10.1002/2015jc010794

Yari, S., Kovačević, V., Cardin, V., Gačić, M., and Bryden, H. L. (2012). Direct Estimate of Water, Heat, and Salt Transport through the Strait of Otranto. *J. Geophys. Res. Oceans* 117, C09009. doi:10.1029/2012jc007936

Zaccone, R., Boldrin, A., Caruso, G., La Ferla, R., Maimone, G., Santinelli, C., et al. (2012). Enzymatic Activities and Prokaryotic Abundance in Relation to Organic Matter along a West-East Mediterranean Transect (TRANSMED Cruise). *Microb. Ecol.* 64, 54–66. doi:10.1007/s00248-012-0011-4

Conflict of Interest: The authors declare that the research was conducted in the absence of any commercial or financial relationships that could be construed as a potential conflict of interest.

The reviewer TBM declared a past co-authorship with one of the authors AG to the handling editor.

Publisher's Note: All claims expressed in this article are solely those of the authors and do not necessarily represent those of their affiliated organizations, or those of the publisher, the editors and the reviewers. Any product that may be evaluated in this article, or claim that may be made by its manufacturer, is not guaranteed or endorsed by the publisher.

Advantages of publishing in Frontiers

OPEN ACCESS
Articles are free to read for greatest visibility and readership

FAST PUBLICATION
Around 90 days from submission to decision

HIGH QUALITY PEER-REVIEW
Rigorous, collaborative, and constructive peer-review

TRANSPARENT PEER-REVIEW
Editors and reviewers acknowledged by name on published articles

Frontiers
Avenue du Tribunal-Fédéral 34
1005 Lausanne | Switzerland

Visit us: www.frontiersin.org
Contact us: frontiersin.org/about/contact

REPRODUCIBILITY OF RESEARCH
Support open data and methods to enhance research reproducibility

DIGITAL PUBLISHING
Articles designed for optimal readership across devices

FOLLOW US
@frontiersin

IMPACT METRICS
Advanced article metrics track visibility across digital media

EXTENSIVE PROMOTION
Marketing and promotion of impactful research

LOOP RESEARCH NETWORK
Our network increases your article's readership